



Zerbst, Désirée (2024) *An investigation into the role of autophagy in mediating leukaemic cell location in the bone marrow niche*. PhD thesis.

<http://theses.gla.ac.uk/84311/>

Copyright and moral rights for this work are retained by the author

A copy can be downloaded for personal non-commercial research or study, without prior permission or charge

This work cannot be reproduced or quoted extensively from without first obtaining permission in writing from the author

The content must not be changed in any way or sold commercially in any format or medium without the formal permission of the author

When referring to this work, full bibliographic details including the author, title, awarding institution and date of the thesis must be given

Enlighten: Theses

<https://theses.gla.ac.uk/>  
[research-enlighten@glasgow.ac.uk](mailto:research-enlighten@glasgow.ac.uk)



# University of Glasgow

## **An investigation into the role of autophagy in mediating leukaemic cell location in the bone marrow niche**

**Désirée Zerbst, BSc., MSc.**

Thesis submitted to the University of Glasgow in fulfilment of the requirements  
for the degree of Doctor of Philosophy

School of Cancer Sciences

College of Medical, Veterinary and Life Sciences

University of Glasgow

January 2024

## Abstract

Leukaemic stem cell (LSC) persistence is the prevailing issue in curing chronic myeloid leukaemia (CML) with the current gold-standard treatment – tyrosine kinase inhibitors (TKIs). To fully comprehend how LSCs evade targeted treatment, it is essential to study LSCs in their natural environment: the bone marrow (BM) niche. In the last few decades, advances have been made to better understand how the niche influences the maintenance and regulation of healthy haematopoietic stem cells (HSCs), as well as the role of the niche in malignancies. LSCs have been shown to be metabolically adapted to survive within the BM niche and outcompete healthy haematopoiesis.

Previous research in CML aimed to unravel the role of autophagy in LSC survival. This revealed that autophagy inhibition induced LSCs differentiation and sensitization to TKI treatment. As autophagy is influenced by the environment, such as hypoxia, nutrient availability, and inflammation, our study aimed to investigate the complex interplay of CML cells within the BM niche, with a specific focus on the role of autophagy. Moreover, we aimed to unravel the role of mitophagy, the selective degradation of mitochondria, in TKI resistance *in vitro*.

Through a minimally invasive surgery, high-resolution intravital microscopy (IVM) can be utilised to image cells within the BM in the mouse calvarium. We aimed to assess changes in the niche with leukaemia development and dynamics upon treatment response by developing xenograft and genetically engineered mouse models (GEMM) suitable for confocal IVM.

To model CML, we utilised the SCL-tTA/BCR::ABL1 mouse model – an inducible mouse model resembling human CML-like disease development upon BCR::ABL1 expression. To study autophagy in primitive leukaemic cells, we used a fluorescent BCR::ABL1 mouse expressing the autophagy marker GFP-LC3. While we could observe autophagic flux *in vitro*, we faced challenges in detecting the GFP signal within the BM niche. Various strategies, including injectable fluorescent antibodies and *ex vivo* dyes for long-term tracking, were explored to overcome these challenges. Lastly, we generated a fluorescent version of the SCL-tTA/BCR::ABL1 model by crossing it with the mTmG mouse, which expresses

membrane-targeted tdTomato (tdTom). Encouragingly, transplantation of BCR::ABL1<sup>tdTom+</sup> haematopoietic cells allowed us to visualise leukaemic cells within the BM niche in WT recipient mice, providing a solid foundation for future studies.

The investigation extends to xenograft mouse models, aiming to understand the *in vivo* localisation and interactions of human leukaemic cells in the BM microenvironment. We observed highly variable BM engraftment of different cell lines, particularly concerning localisation within the calvarial BM compared to localisation within the long bones. This posed challenges for attempts to unravel the role of autophagy in BM engraftment and *in vivo* localisation. Furthermore, we noted different migration patterns of transplanted cells, with extramedullary tumour formation dependent on the mouse's sex occurring in female mice but not males.

Finally, we investigated the role of mitophagy in response to TKI treatment. High-resolution confocal live-cell microscopy was used with KCL22 and K562 cell lines expressing the reporter gene mCherry-GFP-Fis1, referred to as MitoQC. This fluorescent tandem-dye allows distinction of healthy mitochondria and those undergoing mitophagy due to the pH-sensitivity of GFP. We observed an increase in mitophagy upon TKI treatment, mediated by the autophagy machinery, which, to our knowledge, has not been demonstrated previously. To validate our results, we inhibited autophagy by blocking ULK1 activity and by using ATG7 knockout (KO) cells. We explored different canonical mitophagy pathways, focusing on Nix and BNIP3, key proteins in hypoxia-mediated mitophagy. Our results provide initial insights that Nix and, in a broader sense, BNIP3 may be involved in this process, although further investigation is required to unravel their specific roles in TKI-induced mitophagy.

# Table of Contents

Abstract .....	i
List of Tables.....	v
List of Figures .....	vi
Acknowledgement .....	xiii
Author's Declaration .....	xv
Abbreviations .....	xvi
Chapter 1 Introduction .....	1
1.1 Haematopoiesis and haematopoietic stem cells .....	1
1.2 The bone marrow niche.....	10
1.3 Chronic myeloid leukaemia .....	23
1.4 Intravital microscopy.....	37
1.5 Autophagy .....	41
1.6 Aims .....	54
Chapter 2 Materials and Methods.....	55
2.1 Materials .....	55
2.2 Composition of buffers and media .....	62
2.3 Animal work .....	66
2.4 Culturing of cells .....	69
2.5 Processing animal tissue.....	70
2.6 Flow cytometry .....	72
2.7 Immunoblotting .....	74
2.8 Microscopy .....	76
2.9 Generation of stable cell lines and CRISPR/Cas9-mediated gene editing	81
2.10 Statistical analysis.....	88
Chapter 3 Modelling GEMMs to track leukaemic cells in the BM niche and study the role of autophagy upon BM microenvironment interaction.....	89
3.1 Introduction .....	89
3.2 Validating the SCL-tTA/BCR::ABL1 GFP-LC3 model for <i>in vivo</i> LSCs localisation .....	90
3.3 Investigating lipophilic dyes for <i>in vivo</i> tracking of LSCs in the BM microenvironment .....	116
3.4 Establishing a fluorescent mouse model expressing tdTomato for <i>in vivo</i> tracing of LSCs in CML.....	128
3.5 Discussion .....	141
Chapter 4 Investigating leukaemic cell location in the BM niche by developing a cell line xenograft mouse model.....	148
4.1 Introduction .....	148

4.2	Generating GFP <sup>+</sup> human CML cell lines for the xenograft mouse model	149
4.3	Investigating short- and long-term homing to the BM by K562-GFP cells	150
4.4	Visualising K562-GFP <sup>+</sup> cells in murine calvarium.....	155
4.5	Hypoxia-priming of K562-GFP cells prior to xenograft did not impact BM engraftment .....	160
4.6	Migration of K562-GFP to the brain in male mice instead of BM engraftment or formation of extramedullary tumours .....	167
4.7	Autophagy-deficient K562 cells had reduced tumour formation capacity	174
4.8	Human Jurl cells engrafted close to vasculature in mouse calvarium BM	182
4.9	Intravital localisation of Jurl-GFP five weeks after transplantation in the BM	192
4.10	Autophagy-deficient Jurl cells exhibited higher engraftment potential to control cells and increased localisation to the spleen .....	199
4.11	Discussion .....	207
Chapter 5	Investigating the role of mitophagy in TKI resistance in CML.....	211
5.1	Introduction .....	211
5.2	Leukaemic cells displayed reduced mitochondrial mass upon TKI treatment .....	212
5.3	Generation of MitoQC stable CML cell lines .....	216
5.4	TKI treatment led to mitophagy induction in CML cells .....	218
5.5	Development of a high-throughput assay to measure mitophagy in CML cells	238
5.6	Discussion .....	253
Chapter 6	Discussion.....	257
6.1	Introduction .....	257
6.2	Future outlook investigating LSCs in the BM niche .....	257
6.3	Future outlook on investigating the leukaemic niche by using xenograft mouse models .....	259
6.4	Investigation into the role of mitophagy in TKI resistance in CML .....	261
6.5	Summary .....	264
List of References	.....	265

## List of Tables

Table 1 Filter settings for the MitoQC flow assay on the Attune NxT .....	73
Table 2 Antibodies used <i>in vivo</i> .....	79
Table 3 CRISPR/Cas9 guides targeting sequence .....	82
Table 4 Lentiviral transfection mix .....	87
Table 5 Retroviral transfection mix .....	88

## List of Figures

Figure 1-1 Classical model of the haematopoietic tree.....	3
Figure 1-2 Stem cell fate and metabolic reprogramming.....	9
Figure 1-3 Schematic illustration depicting the regulation of HSCs within the BM niche .....	12
Figure 1-4 Schematic illustration of HIF1 $\alpha$ regulation .....	20
Figure 1-5 The origin of the Philadelphia chromosome .....	24
Figure 1-6 Schematic illustration of BCR::ABL1 signalling pathways.....	28
Figure 1-7 Kaplan-Meier survival curve of CML patients .....	30
Figure 1-8 Schematic representation of autophagy .....	42
Figure 1-9 Schematic illustration of mitochondrial dynamics of fission and fusion .....	46
Figure 1-10 Schematic representation of Pink1/Parkin-mediated mitophagy ....	47
Figure 1-11 Schematic illustration of mitophagy mediated by mitophagy receptors .....	49
Figure 2-1 Schematic illustration of the inducible the SCL-tTA/BCR::ABL1 mouse model.....	67
Figure 2-2 Assembly of the Western blot 'sandwich' for wet transfer. ....	76
Figure 2-3 Setup of the IVM on the calvarium on the microscope stage .....	77
Figure 2-4 Schematic representation of CRISPR/Cas9 .....	82
Figure 2-5 Vector map of LentiCRISPR V2 plasmid .....	83
Figure 2-6 Vector map of pLKO.1 GFP shRNA .....	84
Figure 2-7 Vector map of pLVX mCherry-GFP-mtFIS1(101-152) .....	85
Figure 2-8 Vector map of mtKeima .....	86
Figure 3-1 GFP-LC3 expression is notably high in primitive BM cells within the SCL-tTA/BCR::ABL1 GFP-LC3 mouse model .....	91
Figure 3-2 GFP-LC3 enables the monitoring of autophagic flux in primary mouse BM cells .....	94
Figure 3-3 Increased autophagosome formation in GFP <sup>+</sup> LSK cells upon metabolic stress .....	96
Figure 3-4 Experimental setup for BM engraftment in conditioned and non-conditioned mice .....	98
Figure 3-5 LSK-SLAM populations in whole BM compared to cKit enriched sample .....	99
Figure 3-6 Detection of leukaemia development indicated by trend towards splenomegaly in the irradiated transplant group .....	100
Figure 3-7 BM transplant requires irradiation of recipient mice for long-term BM reconstitution .....	101

Figure 3-8 Experimental setup for competitive transplant of GFP <sup>high</sup> and GFP <sup>low</sup> DTG cells.....	102
Figure 3-9 GFP <sup>high</sup> cell population exhibits a substantial enrichment for primitive cells .....	103
Figure 3-10 Progression of long-term engraftment in GFP <sup>high</sup> transplant group measured by blood sampling.....	105
Figure 3-11 Failure of GFP <sup>low</sup> population in long-term engraftment in irradiated recipient mice .....	106
Figure 3-12 Myeloproliferation in the GFP <sup>high</sup> transplant group was observed eleven days after induction.....	106
Figure 1-13 Granulocyte infiltration of spleen observed in GFP <sup>high</sup> transplant group .....	107
Figure 3-14 Detection of GFP <sup>+</sup> cells in the calvarium isolated from a GFP-LC3 mouse using <i>ex vivo</i> microscopy.....	109
Figure 3-15 Insufficient detection of GFP <sup>+</sup> cells in induced recipient mice transplanted with DTG GFP-LC3 BM cells .....	110
Figure 3-16 Minimal detection of GFP <sup>+</sup> cells in the calvarium two weeks post-transplantation in DTG GFP-LC3 allografted mouse using <i>ex vivo</i> microscopy ..	111
Figure 3-17 Lack of detection of GFP <sup>+</sup> cells observed in the calvarium three weeks post-transplantation in DTG GFP-LC3 allografted mouse using <i>ex vivo</i> microscopy .....	112
Figure 3-18 Validation of GFP expression in CD45.2 <sup>+</sup> cells in allografted mice .	113
Figure 3-19 <i>In vivo</i> labelling with fluorescent antibody targeting CD48 and CD150 .....	114
Figure 3-20 <i>In vivo</i> labelling using a fluorescent antibody against CD150.....	115
Figure 3-21 Experimental design for <i>in vivo</i> tracing of DiD-stained LT-HSCs transplanted to WT recipient mice .....	116
Figure 3-22 DiD labelling of sorted LT-HSCs for transplantation .....	117
Figure 3-23 Detection of DiD <sup>+</sup> LT-HSCs was inconclusive four to five weeks after transplantation .....	118
Figure 3-24 Primary murine cells require an adjusted protocol compared to human cell lines for DiD cell labelling.....	119
Figure 3-25 Optimising DiD-labelling in cKit-enriched primary mouse BM cells .	120
Figure 3-26 Transplantation of cKit-enriched DiD <sup>+</sup> into conditioned and non-conditioned WT mice .....	121
Figure 3-27 Absence of DiD <sup>+</sup> cells in BM cells in induced mice one to three weeks post-transplantation .....	122
Figure 3-28 Lack of clear localisation of DiD <sup>+</sup> cells observed one week post-transplantation using <i>ex vivo</i> microscopy.....	123
Figure 3-29 Absence of DiD <sup>+</sup> cells in calvarium imaged two weeks post-transplantation using <i>ex vivo</i> microscopy.....	123
Figure 3-30 Higher DiD-signal in calvarium obtained from the non-engrafted mouse compared to successfully engrafted mouse .....	124

Figure 3-31 Experimental design aimed to compare the suitability of DiD-labelled LT-HSC transplantation for <i>in vivo</i> tracing in leukaemic and non-leukaemic mice .....	125
Figure 3-32 BM chimerism reveals lack of engraftment of DiD-stained LT-HSCs	127
Figure 3-33 Experimental design of allografting tdTom <sup>+</sup> BM cells to WT CD45.1 for <i>in vivo</i> tracing.....	129
Figure 3-34 Visualising mTmG BM cells transplanted to CD45.1 WT recipient mice via microscopy .....	130
Figure 3-35 Tile scan of the calvarium of mTmG chimeric mouse .....	131
Figure 3-36 Experimental design aimed to evaluate busulfan-conditioning of mice prior to transplant with whole BM and cKit-enriched tdTom <sup>+</sup> cells .....	132
Figure 3-37 Chimerism in cKit <sup>+</sup> recipient mice established eight weeks after transplantation .....	133
Figure 3-38 Experimental setup of investigating leukaemic vs non-leukaemic BM cells in busulfan conditioned mice.....	134
Figure 3-39 Unsuccessful engraftment of STG and DTG mTmG BM cells in busulfan conditioned mice .....	135
Figure 3-40 Experimental setup of allografting DTG and STG cKit <sup>+</sup> cells to busulfan conditioned mice .....	136
Figure 3-41 Highly variable engraftment of STG and DTG mTmG BM cells in busulfan conditioned mice .....	136
Figure 3-42 Experimental design for localising therapy resistant LSCs within the BM niche .....	137
Figure 3-43 Leukaemia development was detected in DTG mice after two weeks of BCR::ABL1 expression .....	139
Figure 3-44 Splenomegaly and myeloid cell infiltration were observed in the spleens of DTG recipient mice.....	140
Figure 4-1 Generation of GFP-expressing human CML cell lines.....	149
Figure 4-2 Expression levels of hCD45 on human CML cell lines .....	150
Figure 4-3 Experimental design aimed to investigate BM engraftment of human cell lines .....	151
Figure 4-4 Neither KCL22 nor K562 cells showed engraftment in the BM within three days post-injection.....	152
Figure 4-5 Absence of GFP <sup>+</sup> cells in the BM of mice sacrificed three days after transplantation .....	152
Figure 4-6 BM engraftment of K562-GFP 21 days after transplantation .....	153
Figure 4-7 Total cell count of the BM, spleen, and tumour at three and 21 days post-transplantation .....	153
Figure 4-8 GFP <sup>+</sup> cells detected in the BM and tumour of the K562 recipient mouse 21 days post-transplant.....	154
Figure 4-9 Haematological mouse cells remained GFP <sup>neg</sup> .....	154
Figure 4-10 Experimental design aimed to localise K562-GFP cells in mouse BM .....	156

Figure 4-11 K562-GFP showed no engraftment in male recipient mice within 23 days post-transplantation .....	157
Figure 4-12 Non-transplanted control mice assayed for hCD45 <sup>+</sup> to identify background staining.....	158
Figure 4-13 Confocal microscopy detection of GFP <sup>+</sup> cells in the calvarium of xenograft mice.....	159
Figure 4-14 Reduced cell proliferation of K562 in hypoxia.....	160
Figure 4-15 Experimental design aimed to investigate BM engraftment of hypoxia-primed K562-GFP cells .....	161
Figure 4-16 Indication of reduced tumour formation of hypoxia-primed K562-GFP cells .....	162
Figure 4-17 BM engraftment of hCD45 <sup>+</sup> of hypoxia- vs. normoxia-primed cells .	164
Figure 4-18 Human cells were not detected in the blood of immunocompromised mice .....	165
Figure 4-19 K562-GFP cells did not localise to the spleen when primed in hypoxia .....	165
Figure 4-20 Hypoxia-priming had no effect on BM engraftment in the calvarium of NRGW mice.....	166
Figure 4-21 Experimental design aimed to investigate BM engraftment of human cells in male mice .....	167
Figure 4-22 Male xenograft recipients showed proliferation of K562 in the brain .....	168
Figure 4-23 Microscopy image of K562-GFP recipient male GWNW13.3a .....	170
Figure 4-24 Microscopy image of K562-GFP recipient male mouse GWNW13.3b	171
Figure 4-25 Microscopy image of K562-GFP recipient male mouse GWNW13.3c	172
Figure 4-26 Microscopy image of K562-GFP recipient male mouse GWNW13.3d	173
Figure 4-27 Validation of ATG7 knockout in K562 GFP cells .....	175
Figure 4-28 Experimental design aimed to investigate BM engraftment of autophagy-deficient cells .....	175
Figure 4-29 K562-GFP WT or ATG7 KO cells are not able to be localised in the BM of the calvarium by microscopy .....	176
Figure 4-30 Tumour formation capacity reduced by ATG7 KO in K562-GFP cells .....	177
Figure 4-31 K562-GFP control cells showed limited potential of BM engraftment in female mice .....	178
Figure 4-32 BM engraftment of K562-GFP ATG7 KO cells in female NRGW mice	180
Figure 4-33 Analysis of BM engraftment of K562-GFP ATG7 KO compared to control cells .....	181
Figure 4-34 K562-GFP cells tended to not migrate to the brain in female NRGW mice .....	181
Figure 4-35 Generation of Jurl cells to stably express GFP .....	182
Figure 4-36 Validation of human CD45 <sup>+</sup> expression on Jurl-GFP cells .....	183

Figure 4-37 Experimental design aimed to investigate BM engraftment dynamics of Jurl-GFP cells .....	183
Figure 4-38 Time course of Jurl-GFP engraftment in the BM .....	185
Figure 4-39 Analysis of BM and spleen of Jurl-GFP recipient mice .....	186
Figure 4-40 Microscopy image of Jurl-GFP recipient 20 days post-transplantation .....	187
Figure 4-41 Microscopy of calvarium from Jurl-GFP recipient mouse four weeks post-transplantation .....	188
Figure 4-42 Microscopy of calvarium from Jurl-GFP recipient mouse 32 days post-transplantation .....	189
Figure 4-43 Microscopy of calvarium from Jurl-GFP recipient mouse 39 days-post-transplantation detects GFP <sup>+</sup> close to vasculature .....	190
Figure 4-44 Microscopy of calvarium from Jurl-GFP recipient mouse 39 days-post-transplantation detects accumulation of GFP <sup>+</sup> cells .....	191
Figure 4-45 Experimental design for localising Jurl-GFP in the BM microenvironment using IVM.....	192
Figure 4-46 Flow cytometry analysis of Jurl-GFP in NRGW mice five weeks after transplantation .....	194
Figure 4-47 Splenomegaly in NRGW mice five weeks after transplant with Jurl-GFP cells .....	195
Figure 4-48 IVM of xenograft mice transplanted with Jurl-GFP revealed large clusters of leukaemic cells .....	196
Figure 4-49 IVM of xenograft mice transplanted with Jurl-GFP mice .....	197
Figure 4-50 IVM of xenograft mouse transplanted with Jurl-GFP cells reveals minimal localisation within the calvarium.....	198
Figure 4-51 Validation of ATG7 KO in Jurl-GFP cells .....	199
Figure 4-52 Experimental design aimed to investigate the impact of autophagy deficiency on BM engraftment of Jurl-GFP .....	200
Figure 4-53 Tissue analysis of Jurl-GFP control cells transplanted to NRGW mice .....	202
Figure 4-54 Tissue analysis of Jurl-GFP ATG7 KO in NRGW mice .....	203
Figure 4-55 Autophagy-deficient Jurl-GFP recipient mice exhibited splenomegaly .....	204
Figure 4-56 Jurl-GFP ATG7 KO cells exhibited higher engraftment potential at 4 ½ weeks post-transplantation .....	204
Figure 4-57 Jurl cells detected in the female reproductive organs .....	205
Figure 4-58 Sparse localisation of Jurl-GFP cells in proximity to vasculature...	206
Figure 5-1 Mitochondrial content reduced in KCL22 Tom20-GFP cells upon TKI treatment.....	212
Figure 5-2 Decrease of mitochondrial mass in TKI-resistant cells measured using MitoTracker .....	214
Figure 5-3 Reduction in Tom20 protein levels following imatinib treatment....	215

Figure 5-4 The concept of MitoQC for measuring mitophagy .....	216
Figure 5-5 Generation of MitoQC CML cell lines via retroviral transduction .....	217
Figure 5-6 Lysosomal staining co-localised with mCherry-'puncta' from MitoQC probe .....	219
Figure 5-7 Slightly increased mitophagy induction upon TKI treatment in CML cells .....	220
Figure 5-8 mCherry-'puncta' formation in KCL22 upon TKI treatment .....	221
Figure 5-9 Significant increase in mitophagy upon BCR::ABL1 inhibition in K562 MitoQC cells .....	222
Figure 5-10 Detection of mitophagy in K562 MitoQC cells upon TKI treatment ..	223
Figure 5-11 Imatinib inhibited BCR::ABL1 signalling validated by reduced phosphorylation of CrkL .....	225
Figure 5-12 Inhibition of ULK1 halts the autophagic flux triggered by TKI treatment.....	225
Figure 5-13 MRT403 inhibits mitophagy induced by TKI treatment in KCL22 MitoQC cells .....	227
Figure 5-14 ULK1 inhibition prevented TKI-mediated mitophagy induction in K562 MitoQC cells .....	228
Figure 5-15 ATG7 KO impeded TKI-mediated mitophagy induction in KCL22 cells .....	230
Figure 5-16 TKI-mediated mitophagy induction required ATG7 for autophagic flux in K562 cells.....	231
Figure 5-17 Nix protein levels increased upon imatinib treatment .....	233
Figure 5-18 Validation of BNIP3 and Nix knockout in K562 MitoQC cells .....	233
Figure 5-19 Measuring mitophagy in Nix KO cells upon TKI treatment .....	235
Figure 5-20 Measuring mitophagy in BNIP3 KO cells in response to TKI treatment .....	236
Figure 5-21 Nix or BNIP3 are not essential for imatinib-mediated mitophagy...	237
Figure 5-22 Induction of mitophagy by CCCP and AA-OL peaked between three to six hours in KCL22 MitoQC cells .....	239
Figure 5-23 Mitophagy induction by AA-OL or CCCP reaches maximum between three to six hours in K562 MitoQC.....	240
Figure 5-24 Minimal cell death upon treatment with AA-OL or CCCP in KCL22 and K562 over 24 hours .....	241
Figure 5-25 Prolonged autophagic flux results in the degradation of GFP and mCherry.....	242
Figure 5-26 Imatinib treatment induced mitophagy in a time-dependent manner in KCL22 and K562 cells .....	244
Figure 5-27 Autophagy suppression with a ULK1 inhibitor did not prevent mitophagy induction .....	246
Figure 5-28 ULK1 inhibition minimally reduced TKI-induced mitophagy in K562 MitoQC cells .....	247

Figure 5-29 Pre-treating K562 cells with an autophagy inhibitor did not counteract imatinib-induced mitophagy .....	248
Figure 5-30 Autophagy inhibitors BafA and HCQ failed to impede imatinib-induced mitophagy .....	249
Figure 5-31 Autophagy-deficient CML cells exhibited induction of mitophagy upon imatinib treatment.....	250
Figure 5-32 Sensitivity of the mtKeima probe in flow cytometry analysis for detecting mitophagy induction in K562 cells.....	252

## Acknowledgement

First and foremost, I want to express my gratitude to my supervisors Vignir Helgason and Leo Carlin for giving me the opportunity to undertake this project under their guidance. During this time, I have not only learned a great deal as a scientist but have also grown on a personal level. I am particularly thankful to Vignir for his unwavering support and encouragement throughout the years – thank you for always being available for insightful discussions and chats, especially during challenging times, and for giving me the necessary push when I needed it. I want to thank Leo for his enthusiasm and for sharing his expertise and advice in microscopy. I am grateful for the countless hours spent together at the microscope that taught me so much.

My gratitude goes out to all current and past members of M08 for their support throughout the years. Working in this team has been a wonderful experience, and I am forever grateful for all the memories made in the lab and beyond. I also like to extend my thanks to everyone from Level 3 for creating a lovely and lively work environment that I looked forward to everyday. A special thanks to Daniele, my Italian soulmate, for your friendship and your positivity through the dark and challenging times. To everyone in R26, thank you for welcoming me with open arms and for the shared advice, laughter, and antibodies. I especially want to thank Fred for generously sharing his knowledge in microscopy.

I would like to thank and acknowledge all the people who have made this work possible and supported my research in various ways. To Cristina Lo Celso for providing her expertise in the IVM setup, and to Chiara Pirillo for teaching me the IVM surgery with her encouraging personality. To Ewan McGee for designing the IVM tools. To the BAIR team for the assistance with the microscopes, and to Tom Gilbey and Yi-Hsia Liu for their support with flow cytometry. I appreciate the efforts of the BRU staff and Central Services for ensuring a reliable work environment and keeping everything running. I want to extend a special acknowledgement to Karen Dunn, who has supported every animal experiment in this work and has been flexible with times if needed. Additionally, I would like to express my gratitude to the funding bodies Medical Research Scotland and LifeArc for their generous support, which made this research possible.

I want to thank my partner Iain, for being my safe haven throughout the last years and for making Glasgow feel like home. Thank you for your support, love and for the countless trips to the lab, making mouse checks easier and turning every late night into a reassuring journey home.

Finally, I want to thank my friends and family, especially my parents. Without you, none of this would be possible. Thank you for always believing in me. Your unconditional love and support are a constant reminder to keep going, no matter what.

## **Author's Declaration**

I declare that, except where explicit reference is made to the contribution of others, this thesis is the result of my own work and has not been submitted for any other degree at the University of Glasgow or any other institution.

Désirée Zerbst

## Abbreviations

403	MRT403, inhibitor for ULK1
5-FU	5-fluorouracil
7AAD	7-Aminoactinomycin D, nuclear dye
AA	Antimycin A
ABC	ATP-binding cassette
ABL1	Abelson1
ADP	Adenosine-5'-diphosphate
aEC	Arteriolar EC
AKT	Protein kinase B
ALOX15	Arachidonate 5-lipoxygenase 15
ALOX5	Arachidonate 5-lipoxygenase 5
AMBRA1	Activating molecule in Beclin1-regulated autophagy protein 1
AML	Acute myeloid leukaemia
AMP	Adenosine-5'-monophosphate
AMPK	AMP-activated protein kinase
ANGPT1	Angiopoietin 1
ANT	ADP/ATP translocase
AP	Accelerated phase
ATAD3A	ATPase Family AAA Domain-containing protein 3A
ATG	Autophagy-related gene/protein
ATG10	Autophagy related 10
ATG12	Autophagy related 12
ATG16L	Autophagy related 16L
ATG4	Autophagy related 4
ATG5	Autophagy related 5
ATG7	Autophagy related 7
ATP	Adenosine-5'-triphosphate
BafA	Bafilomycin A1
BC	Blast crisis
BCA	Bicinchoninic acid assay
BCR	Breakpoint cluster region
BH3-only	Members of the Bcl-2 family containing only a single BH domain (BH3)
BM	Bone marrow
BNIP3	BCL2 interacting protein 3
BSA	Bovin serum albumin
CAFC	Cobblestone area-forming cells
CAR cells	CXCL12-abundant reticular stromal cells
Cas9	CRISPR-associated protein 9
CCCP	Carbonyl cyanide 3-chlorophenylhydrazone
CD	Cluster of differentiation
CD105 <sup>+</sup> CD51 <sup>+</sup>	Marker for MSCs in mouse

CD117 (cKit)	Stem cell factor receptor
CD11b (Mac-1)	Integrin $\alpha$ M or Macrophage-1 antigen
CD145 <sup>+</sup>	Marker for MSCs in human
CD150/SLAM	Signalling lymphocytic activation molecule Family Member1
CD31	Platelet endothelial cell adhesion molecules
CD34	Cluster of differentiation 34
CD38	Cyclic ADP ribose hydroxylase
CD4	Surface marker for helper T cells
CD41	Integrin $\alpha$ Ib
CD45	Surface marker for haematopoietic cells
CD45.1	Isotype <i>Ptprc</i> <sup>a</sup>
CD45.2	Wild type isotype <i>Ptprc</i> <sup>b</sup>
CD45R (B220)	Surface marker for B cells
CD48	Cluster of differentiation 48
CD5	Lymphocyte antigen 1
CD82	Cluster of differentiation 82
CD8a	Surface marker for cytotoxic T cells
CFU-S	Colony forming unit-spleen
CK2	Casein-kinase 2
CLP	Common lymphoid progenitor
CMA	Chaperon-mediated autophagy
CML	Chronic myeloid leukaemia
CMP	Common myeloid progenitor
CP	Chronic phase
CRISPR	Clustered Regularly Interspaced Short Palindromic Repeats
CrkL	CRK like proto-oncogene adaptor protein
CTL	Cytotoxic T cells
CTLA-4	Cytotoxic T-lymphocyte associated protein 4
CXCL12	C-X-C motif chemokine 12
CXCL4	C-X-C motif chemokine 4
CXCR2	C-X-C motif chemokine receptor 2
CXCR4	C-X-C motif chemokine receptor 4
DAPI	4',6-diamidino-2-phenylindole
DC	Dendritic cell
DFP	Deferiprone
DiD	Carbocyanine DiD
DMEM	Dulbecco's Modified Eagle Medium
DMR	Deep molecular response
DMSO	Dimethyl sulfoxide
DNA	Deoxyribonucleic acid
Dnm2	Dynamin-2
DPP4	dipeptidyl peptidase 4
DRAC	Duffy antigen receptor for chemokines

Drp1	Dynamin-related protein 1
DTG	Double transgenic mice
EC	Endothelial cell
ECL	Enhanced chemiluminescence
ECM	Extracellular matrix
Edu	5-ethynyl 2'-deoxyuridine
ER	Endoplasmic reticulum
ERK	Extracellular signal-regulated kinases
ETC	Electron transport chain
FACS	Fluorescence activated cell sorting
FAO	Fatty acid oxidation
FBS	Foetal bovine serum
FGF1	Fibroblast growth factor 1
FIP200	Focal adhesion kinase family-interaction protein of 200 kDa
Fis1	Mitochondrial fission 1 protein
FISH	Fluorescence <i>in situ</i> hybridisation
Flk2	CD135, Fms-related receptor tyrosine kinase 3
FLT3-ITD	Driver mutation in AML
FoxO	Forkhead O transcription factor
FOXO3a	Forkhead box protein O 3a
FUNDC1	FUN14 domain-containing protein-1
G6PDH	Glucose-6-phosphate dehydrogenase
GAB2	GRB2-associated-binding protein 2
GABARAP	GABA type A receptor-associated protein
G-CSF	Granulocyte colony-stimulating factor
GEF	Guanin nucleotide exchange factors
GEMM	Genetically engineered mouse models
GFP	Green fluorescent protein
GMP	Granulocyte-macrophage progenitor
Gr-1 (Ly-6G/Ly-6C)	Lymphocyte antigen 6 complex locus G6D
GRB2	Growth factor receptor-bound protein 2
gRNA	Guide RNA
GTP	Guanosine-5'-triphosphate
GTPase	Guanosine-5'-triphosphate hydrolases
HBSS	Hank's Balanced Salt Solution
HCQ	Hydroxychloroquine
HIF1 $\alpha$	Hypoxia inducible factor 1 subunit alpha
HIF1 $\beta$	Hypoxia inducible factor 1 subunit beta
Hoechst	Hoechst33342
HRE	Hypoxia response elements
HRP	Horseradish peroxidase
HSC	Haematopoietic stem cell
HSP90	Heat shock protein 90

HSPC	haematopoietic stem and progenitor cell
ICAM-1	Intercellular adhesion molecule 1
IFN- $\alpha$	Interferon- $\alpha$
IFN- $\gamma$	Interferon- $\gamma$
IGF-1	Insulin-like growth factor 1
IL-1	Interleukin-1
IL-3	Interleukin-3
IL-4	Interleukin-4
IL-7	Interleukin-7
Ima	Imatinib
IMDM	Iscove's Modified Dulbecco's Medium
IR	Infrared
IV	Intravenous
IVM	Intravital microscopy
JAK	Janus kinases
KD	Knockdown
Ki67	Kiel 67, cellular marker for proliferation
KO	Knockout
LC3	Microtubule-associated protein 1A/1B-light chain 3
LC3B	Microtubule associated protein 1 light chain 3 beta
LepR	Leptin Receptor
LFA-1	Lymphocyte function-associated molecule ( $\alpha$ LB2 integrin)
LIC	Leukaemia-initiating cell
Lin <sup>-</sup>	Lineage <sup>+</sup> depleted population
LIR	LC3-interacting region
LSC	Leukaemic stem cell
LSK	Lin <sup>-</sup> Sca1 <sup>+</sup> cKit <sup>+</sup> cells
LSKT	Lin <sup>-</sup> Sca-1 <sup>+</sup> cKit <sup>+</sup> Thy1 <sup>+</sup> cells
LTC-IC	Long-term culture-initiating cell
LT-HSC	Long-term haematopoietic stem cell
mAb	Monoclonal antibody
MAPK	Mitogen-activated protein kinases
MDR	Multiple drug resistance
MEP	Megakaryocyte-erythroid progenitor
MFI	Median fluorescent intensity
Mfn1/2	Mitofunsin 1 or 3
MHC	Major histocompatibility complex
mIL-3	Mouse interleukin-3
mIL-6	Mouse interleukin-6
MIP-1 $\alpha$	Macrophage inflammatory protein 1 alpha
miR-126	MicroRNA-126
MitoQC	Mitochondria quality control, reporter gene
MMP	Matrix metalloproteinases
MMR	Major molecular response

MP	Multiphoton
MPN	Myeloproliferative neoplasm
MPP	Multipotent progenitor
MPP1	Multipotent progenitor subset 1
MPP2	Multipotent progenitor subset 2
MPP3	Multipotent progenitor subset 3
MPP4	Multipotent progenitor subset 4
MSC	Mesenchymal stem cells
mSCF	Mouse stem cell factor
mTOR	mechanistic target of rapamycin
mTORC1/2	Mechanistic target of rapamycin complex 1/2
mtPP	Mitochondrial processing peptidase
MYC	Proto-oncogene
NAC	N-acetyl-L-cysteine
NAD	Nicotinamide adenine dinucleotide
NBR1	NBR1 autophagy cargo receptor
NDC	No drug control
Nes	Nestin
NFκB	Nuclear factor kappa b
NG2	Nerve/glia antigen-2
NHEJ	Non-homologous end joining
NIR	Near-infrared
Nix	BNIP3-like
NK	natural killer cell
NO	Nitric oxide
NRGW	NOD.Cg-Rag1 <sup>tm1Mom</sup> Kit <sup>W-41J</sup> Il2rg <sup>tm1Wjl</sup> /EavJ mice
OCR	Oxygen consumption rate
OL	Oligomycin
Opa1	Optic atrophy 1
OPN	Osteopontin
Optn	Optineurin
OSM	Oncostatin M
OXPPOS	Oxidative phosphorylation
PAM	Proto-spacer adjacent
PARL	Presenilin-associated rhomboid-like
pATG14	Phosphorylated ATG14
PB	Peripheral blood
PBS	Phosphate Buffered Saline
PCR	Polymerase chain reaction
pCrkL	Phosphorylated CrkL
PD1	Programmed death 1
PDH	pyruvate dehydrogenase
PDK	pyruvate dehydrogenase kinases
PDPN	Podoplanin

PDX	Patient-derived xenografts
PE	Phosphatidylethanolamine
PGAM5	phosphoglycerate mutase family member 5
PGE <sub>2</sub>	Prostaglandin E <sub>2</sub>
Ph	Philadelphia chromosome
PHD	Prolyl hydroxylases domain
PI	Phosphatidylinositol
PI3K	Phosphoinositide 3-kinase
PI3P	Phosphatidylinositol-3-phosphate
Pimo	Pimodiazole
Pink1	PTEN induced kinase 1
pO <sub>2</sub>	Partial pressure of oxygen
PPAR $\delta$	Peroxisome-proliferator activated receptor delta
PS	Phosphatidylserine
PSGL-1	P-selectin glycoprotein ligand-1
PTEN	Phosphatase and tensin homolog
PTH	Parathyroid hormone
PTPMT1	Protein tyrosine phosphatase mitochondrial 1
PVDF	Polyvinylidene fluoride
Rh-123	Rhodamine-123
RISP	Rieske iron-sulphur protein
RNA	Ribonucleic acid
ROS	Reactive oxygen species
RPMI	Roswell Park Memorial Institute media
Sca-1	Stem cells antigen-1
SCF	Stem cell factor
SCID	Severe combined immunodeficient
sEC	Sinusoidal EC
SHG	Second harmonic generation
SIRT1	Sirtuin 1
SMO	Smoothened
SNAP-29	Synaptosomal-associated protein 29
SNARE	Soluble N-ethylmaleimide-sensitive factor attachment protein receptor
SOS	Son of sevenless
SP	Side population
SRC	Steroid receptor coactivator
STAT	Signal transducer and activator of transcription
Stbl3	Stbl3 chemically competent E. coli
STG	Single transgenic mice
ST-HSC	Short-term haematopoietic stem cell
Stx17	Syntaxin17
T-ALL	T-cell acute lymphoblastic leukaemia
TBK1	Tank-binding kinase 1

TBST	Tris-buffered saline with Tween
tCrkL	Total CrkL
Ter119	Marker for erythroid cells
tet	Tetracycline
TF	Transcription factor
TFR	Treatment-free remission
TGF- $\beta$	Transforming growth factor beta
THG	Third harmonic generation
TIM3	T cell immunoglobulin and mucin domain-containing protein 3
TIM	Translocase of the inner membrane
TK	Tyrosine kinase
TKI	Tyrosine kinase inhibitor
TNF- $\alpha$	Tumour necrosis factor alpha
TOM	Translocase of the outer membrane
Tom20	Translocase of outer mitochondrial membrane 20
TPO	Thrombopoietin
Treg cells	Regulatory T cells
tTA	Tetracycline-controlled transcription factor
ULK1	Unc-51-like kinase 1
UV	Ultraviolet
VCAM-1	Vascular cell adhesion molecule 1
VDAC1	Voltage-dependent anion channel 1
VHL	Von Hippel Lindau ubiquitin ligase
VIS	Visible light
VLA-4	Very late antigen-4 ( $\alpha$ 4 $\beta$ 1 integrin)
VLA-5	$\alpha$ 5 $\beta$ 1 integrin
VPS34	Vacuolar protein sorting 34
vWF	von Willebrand factor
WIPI	WD-repeat domain phosphoinositide-interacting
WT	Wild type
$\alpha$ -SMA-	Alpha-smooth muscle actin

# Chapter 1 Introduction

## 1.1 Haematopoiesis and haematopoietic stem cells

### 1.1.1 A brief history of haematopoiesis

Haematopoiesis translates from the Greek ‘blood’ (*haima*) and ‘to produce’ (*poiēsis*) and describes the process of generating new blood cells. Mature blood cells have a limited lifespan and require continuous replacement. An adult human produces billions of new blood cells per day, approximately 200 billion red blood cells, 100 billion white blood cells, and 100 billion platelets<sup>1</sup>.

Microscopy played a pivotal role in the early history of blood research and the discovery of blood cells. The development of high-quality lenses in the 17<sup>th</sup> century enabled the first observations of red blood cells by Jan Swammerdam (1667) and Marcello Malpighi (1673)<sup>2</sup>. However, it was Antonie van Leeuwenhoek who made the first comprehensive report of red blood cells, publishing an illustration of ‘red corpuscles’ in 1695<sup>3,4</sup>. In 1868, German pathologist Franz Christian Neumann observed nucleated red blood cells in the bone marrow (BM), leading to the conclusion that the marrow is the site of blood formation<sup>5</sup>. Neuman also postulated the controversial theory that all blood cells develop from a single precursor cell<sup>5</sup>. Subsequently, around the turn of the century, other scientist utilised observational methods to support Neumann’s theory and began to refer to the progenitor cell as a ‘stem cell’<sup>6</sup>.

However, it was not until the early 1960s that Till and McCulloch’s groundbreaking animal experiments confirmed this theory. Initially, they discovered that injecting BM cells into irradiated mice resulted in the formation of large haematopoietic colonies in the spleen, referred to as colony forming unit-spleen (CFU-S)<sup>7</sup>. These colonies contained immature progenitor cells as well as cells of different lineages<sup>7</sup>. By introducing random chromosome breakage through irradiating donor cells, they demonstrated that each colony originated from a single initiating cell<sup>8</sup>. Furthermore, experiments showing the transplantation of CFU-S into secondary recipient mice demonstrated their self-renewal capacity<sup>9</sup>.

### 1.1.2 The haematopoietic tree

Haematopoietic stem cells (HSCs) are at the top of the hierarchy on the haematopoietic tree (**Figure 1-1**) and are characterised by their multipotency – their ability to give rise to all blood cell types – and their inherent capacity for self-renewal. Self-renewal refers to the ability to generate two long-term (LT)-HSCs when dividing to sustain the pool of stem cells. Asymmetric division produces a stem cell and a committed daughter cell destined for differentiation into a progenitor cell. These progenitors, categorised into short-term (ST)-HSCs and multipotent progenitors (MPPs), still maintain multipotency but have lost their self-renewal potential.

MPPs subsequently progress to generate more lineage committed progenitors: common lymphoid progenitors (CLPs) and common myeloid progenitors (CMPs). CLPs give rise to cells of the adaptive immune system, including B cells, T cells, natural killer (NKs) cells and dendritic cells (DCs). On the other hand, CMPs generate the megakaryocyte-erythroid progenitor (MEP) lineage, which further branches into erythropoiesis for red cell production or thrombopoiesis for platelet formation. Furthermore, CMPs produce granulocyte-macrophage progenitors (GMPs), that differentiate into various white blood cells belonging to the myeloid lineage, such as neutrophils, basophils and eosinophils, as well as monocytes. Monocytes further mature into macrophages or myeloid-derived DCs.

The haematopoietic tree serves as a valuable model for studying haematopoiesis, yet it does not display the complexity and heterogeneity within the population of haematopoietic stem and progenitor cells (HSPCs) and their lineage biases. While MPPs are classically considered to be able to give rise to any lineage progenitor, Pietras *et al.* applied immunophenotyping to analyse subpopulations of MPPs, referred to as MPP1-4, regarding their lineage bias<sup>10</sup>. They showed that MPP1 cells exhibited strong similarities to ST-HSCs, displaying a higher metabolic activity compared to LT-HSCs<sup>10</sup>. MPP2 and MPP3 demonstrated a marked myeloid lineage bias while still generating small quantities of B and T cells<sup>10</sup>. MPP2 predominantly produced megakaryocytes, while MPP3 exhibited a higher bias towards myeloid cells, such as granulocytes and macrophages<sup>10</sup>. On the other hand, MPP4 showed a propensity towards the lymphoid lineage, producing mainly B and T cells, although they initially

displayed myeloid cell production<sup>10</sup>. Interestingly, in transplant reconstitution assays myeloid-primed MPPs emerged earlier, with megakaryocyte-primed MPPs appearing most rapidly, while MPP4 was the last population to emerge<sup>10</sup>.

Overall, this study suggests that HSCs dictate blood production by generating specific lineage biased MPPs according to demand<sup>10,11</sup>.

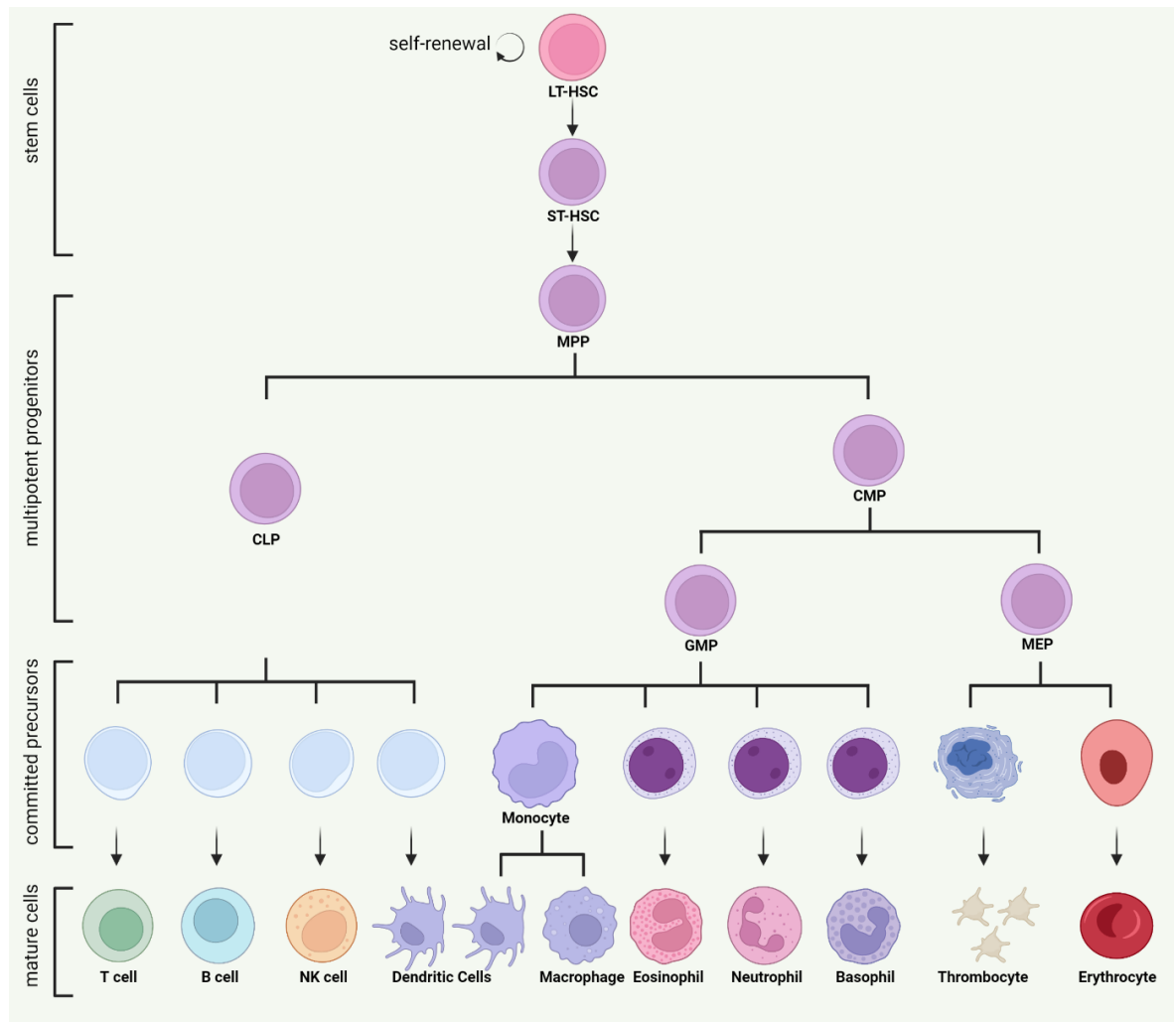


**Figure 1-1 Classical model of the haematopoietic tree.** Long-term haematopoietic stem cells (LT-HSCs) are the most primitive stem cells with the ability to self-renew. They generate short-term (ST)-HSCs, which have lost the self-renewal capacity and give rise to less primitive but highly proliferative multipotent progenitors (MPPs). The tree branches into lineage-specific progenitors, notably the common lymphoid progenitor (CLP) and the common myeloid progenitor (CMP). CLP initiate the lymphoid lineage, giving rise to precursor cells that undergo differentiation into T, B, natural killer (NK) and dendritic cells (DCs). Conversely, the myeloid lineage diverges into granulocyte-macrophage progenitor (GMP) cells, responsible for generating precursor cells that differentiate into granulocytes and monocytes. Additionally, the megakaryocyte-erythroid progenitors (MEPs) branch out, producing precursor cells committed to thrombopoiesis and erythropoiesis. Created with BioRender.com.

Another study unveiled the presence of a platelet-biased stem cell expressing von Willebrand factor (vWF), exclusively found on platelets and endothelial cells (ECs)<sup>12</sup>. These cells displayed a strong bias towards myeloid lineage, particularly in megakaryocyte differentiation and platelet generation<sup>12</sup>. Subsequent

transplantation of single vWF<sup>+</sup> LT-HSCs confirmed the existence of a platelet-restricted subset, contributing solely to the megakaryocyte-platelet lineage without contributing to any other lineage cell<sup>13</sup>. Moreover, single cell transplantation demonstrated the existence of myeloid-restricted progenitor cells that maintained self-renewal potential without multilineage-repopulation capacity<sup>14</sup>. These studies show that the classical model of haematopoiesis, describing a discrete stepwise differentiation process with functional homogenous progenitor cells, does not encompass the complexity of stem cell differentiation. In the last decade, studies combining surface marker analysis with advanced methods such as transcriptomics and transcription factor analysis, suggest haematopoiesis follows a continuum or partial continuum differentiation model<sup>15</sup>. This model describes the differentiation process of progenitor cells as a continuous process with variable lineage biased progenitor cells<sup>15</sup>. Velten *et al.* utilised single cell RNA sequencing to demonstrate that unilineage-restricted HSCs derive from low-primed undifferentiated HSPCs, which gradually acquire lineage priming<sup>16</sup>. While the HSPC continuum contains phenotypic MPPs and multi-lymphoid progenitors, these populations are not discrete progenitor populations and are functionally and transcriptionally distinct<sup>16,17</sup>.

### 1.1.3 Isolation of haematopoietic stem cells

Over the past decades, several strategies have been developed to isolate HSCs, which have become increasingly more accessible due to technological advances in flow cytometry and the vast array of commercially available monoclonal antibodies (mAbs) targeting cell surface markers, cytokine receptors, adhesion markers or integrins, typically referred to within the nomenclature as clusters of differentiation (CD).

The Weissman laboratory made significant contributions to identifying stem cell markers in mice and introduced the concept of 'lineage negative' (Lin<sup>-</sup>) selection. Their research revealed that stem cells lack surface markers found on mature blood cells<sup>18</sup>. They developed a Lin<sup>-</sup> antibody cocktail to deplete B and T cells, erythrocytes, granulocytes, and macrophages through fluorescence activated cell sorting (FACS), successfully isolating a stem-cell enriched population<sup>18</sup>. This population could be further enriched for stem cells by positive selection for Sca-1, cKit and Thy1 (known as the LSKT scheme), as demonstrated

by long-term culture and successful long-term repopulation in lethally irradiated mice<sup>18-20</sup>.

The primary human surface marker for HSC enrichment is CD34, as shown by Baum *et al.* who achieved engraftment of human CD34<sup>+</sup> cells in severe combined immunodeficient mice (SCID) mice, sustaining long-term repopulating multilineage capacity<sup>21</sup>. Further refinement involved the separation of cells into CD34<sup>+</sup>CD38<sup>-</sup>, as the CD34<sup>+</sup>CD38<sup>+</sup> subset is more heterogeneous, containing more committed progenitors<sup>22</sup>.

There are species differences between human and murine surface markers as the CD34<sup>+</sup> fraction in adult mouse BM has been shown to contain HSCs<sup>23</sup>. Kiel *et al.* developed a purification strategy utilising the SLAM family for HSC purification (CD150<sup>+</sup>CD48<sup>-</sup>CD41<sup>-</sup>), which resulted in a higher purity than the LSKT strategy with fewer surface markers, making it more feasible for immunohistology<sup>24</sup>. Additionally, this strategy has been shown to be more consistent between different mouse strains as well as when isolating HSCs from older mice<sup>25</sup>.

Another method for stem cell isolation exploits the low retention capacity of the DNA-binding dye Hoechst33342 (Hoechst). While progenitor and mature cells exhibit high staining for this dye, HSCs rapidly efflux Hoechst due to their high expression of ATP-binding cassette (ABC) transporters, which are implicated in multiple drug resistance (MDR)<sup>25</sup>. This resulted in a tail of low-fluorescent cells detected by flow cytometry called the side population (SP)<sup>26</sup>. Similarly, rhodamine-123 (Rh-123), another dye, has also been shown to exhibit low retention in HSCs<sup>27</sup>. It is noteworthy that Rh-123 is a mitochondrial dye, specifically staining active mitochondria with high membrane potential, resulting in lower intensity in quiescent cells with less active mitochondria<sup>28</sup>. The efflux of Rh-123 in a manner akin to Hoechst further enhances this effect resulting in low staining of more primitive cells<sup>28</sup>.

It should be noted that immunophenotyping using surface markers enriches for stem cells; however, functional characterisation by transplantation is the gold standard method to confirm self-renewal and multipotency<sup>25</sup>.

## 1.1.4 Stem cell fate decisions: Don't exhaust yourself.

### 1.1.4.1 Quiescence as a pathway to longevity

HSCs exhibit remarkable adaptability throughout their lifespan, balancing the demand of sustaining steady state blood production with the necessity to safeguard their integrity and self-renewal potential. During embryonic development, foetal HSCs display a high proliferative capacity, establishing diverse haematopoietic lineages and building a reserve of stem cells within the developing organism<sup>29</sup>. Studies conducted in mice have revealed a significant shift in proliferation around three to four weeks of age, coinciding with the achievement of steady state haematopoiesis<sup>29</sup>. Around 75% of adult HSCs enter and persevere in a quiescent state, while a small fraction engages in active cycling to maintain blood homeostasis<sup>30,31</sup>. Notably, investigations combining label or clonal tracing with computational modelling in genetically engineered mouse models (GEMM) have indicated that progenitor cells, rather than actively cycling LT-HSCs, predominantly contribute to steady state blood production<sup>31-34</sup>.

However, HSCs can respond dynamically to injury or infection, transitioning between dormant and active states. This adaptability is evident in experiments where mice treated with mobilising factors such as granulocyte colony-stimulating factor (G-CSF) or the cytotoxin 5-fluorouracil (5-FU) display altered cell cycle dynamics<sup>31</sup>. Dormancy serves as a protective mechanism for HSCs, shielding them from acquiring DNA mutations and preventing stem cell exhaustion, which could otherwise lead to dysfunction in haematopoiesis<sup>35</sup>. Despite their self-renewal capacity, serial transplant models in mice suggests that the ability of HSCs for continuous self-renewal might be limited<sup>36,37</sup>.

Dormancy, therefore, plays an essential role in averting stem cell exhaustion and maintaining proper functionality. Upon activation, HSCs respond to extrinsic signals whether to undergo asymmetric or symmetric division, depending on the required support for blood production or the need to increase the stem cell population. Consequently, stem cell fate decisions are pivotal in determining the continuation of life or the onset of exhaustion. This intricate mechanism controlling this process is of significant interest in scientific research aimed at

elucidating their role in various pathologies, especially those accompanied with ageing and cancer.

#### 1.1.4.2 Metabolism in quiescent haematopoietic stem cells

Metabolic rewiring has been shown to be implicated in stem cell fate decisions when analysing quiescent and active HSCs (**Figure 1-2**). Quiescent HSCs are found to be in an anaerobic state favouring glycolysis over oxidative phosphorylation (OXPHOS) for energy production<sup>38,39</sup>. Around 80% of LT-HSCs (LSK CD34<sup>-</sup>Flk2<sup>-</sup>) have been found to have a lower mitochondrial potential than more committed progenitors<sup>38</sup>. Further, their oxygen consumption rate (OCR) was found to be the lowest within the haematopoietic lineage but increased upon differentiation to ST-HSCs<sup>39</sup>. Metabolic analysis revealed that glycolytic enzymes were more abundant in LT-HSCs than their progeny or mature haematopoietic cells<sup>39</sup>. Moreover, Takubo *et al.* discovered that LT-HSCs exhibit high expression levels of pyruvate dehydrogenase kinases (PDKs), enzymes that stop pyruvate from entering TCA cycle by phosphorylating pyruvate dehydrogenase (PDH)<sup>39</sup>.

Although glycolysis is less efficient in ATP production, it is accompanied with low reactive oxygen species (ROS). High levels of ROS promote not only HSCs differentiation but also mobilisation from the BM<sup>40-42</sup>. As mitochondria are the main source of ROS, avoiding cellular respiration reduces intracellular stress. Interestingly, studies on stem-like cells showed that these cells selectively pass on aged mitochondria to their daughter cells with less stem cell properties<sup>43</sup>.

Further, the BM niche creates a protective environment maintaining HSCs in hypoxia, further reducing exposure to intracellular as well as extracellular stress<sup>44</sup>. Tothova *et al.* conducted studies elucidating the role of the transcription factor (TF) family forkhead O (FoxO) in regulating ROS levels in quiescent HSCs. Conditional deletion of FoxO 1, 3 and 4 in mice resulted in increased ROS levels specifically in the HSCs compartment, without affecting myeloid progenitors<sup>45</sup>. FoxO-deficient HSCs lost their repopulation ability, exhibited increased cell death and cell cycle entry, which could be rescued by treating the mice with the antioxidant N-acetyl-L-cysteine (NAC)<sup>45</sup>.

### 1.1.4.3 Haematopoietic stem cell proliferation and commitment

It has been shown that quiescent HSCs increase their mitochondrial mass and switch to a high OXPHOS state upon activation and entry into the cell cycle<sup>46</sup>. Deletion of the PTEN-like mitochondrial phosphatase PTPMT1 obstructed mitochondrial respiration, preventing HSCs from initiating differentiation due to an inability to meet the energy demands required for proliferation<sup>47,48</sup>. Ansó *et al.* demonstrated similar outcomes, where the loss of the mitochondrial complex III subunit, Rieske iron-sulphur protein (RISP), resulted in the failure of differentiation in foetal HSCs, although they retained the ability to proliferate<sup>49</sup>.

Interestingly, fatty acid oxidation (FAO) has been identified as a crucial factor for maintaining the HSCs pool, as it supports asymmetric division. Inhibition of FAO, either pharmacologically or through the deletion of PPAR $\delta$ , a nuclear receptor regulating FAO, resulted in increased symmetric division, leading both progenies to undergo differentiation<sup>50,51</sup>. Growing evidence suggests that ROS play a signalling role in stem cell fate decisions by inducing differentiation through the activation of various signalling pathways and modulation of epigenetic regulators<sup>50</sup>. *In vivo* experiments with HSCs in *Drosophila* demonstrated that scavenging ROS blocked HSC differentiation entirely<sup>52</sup>.

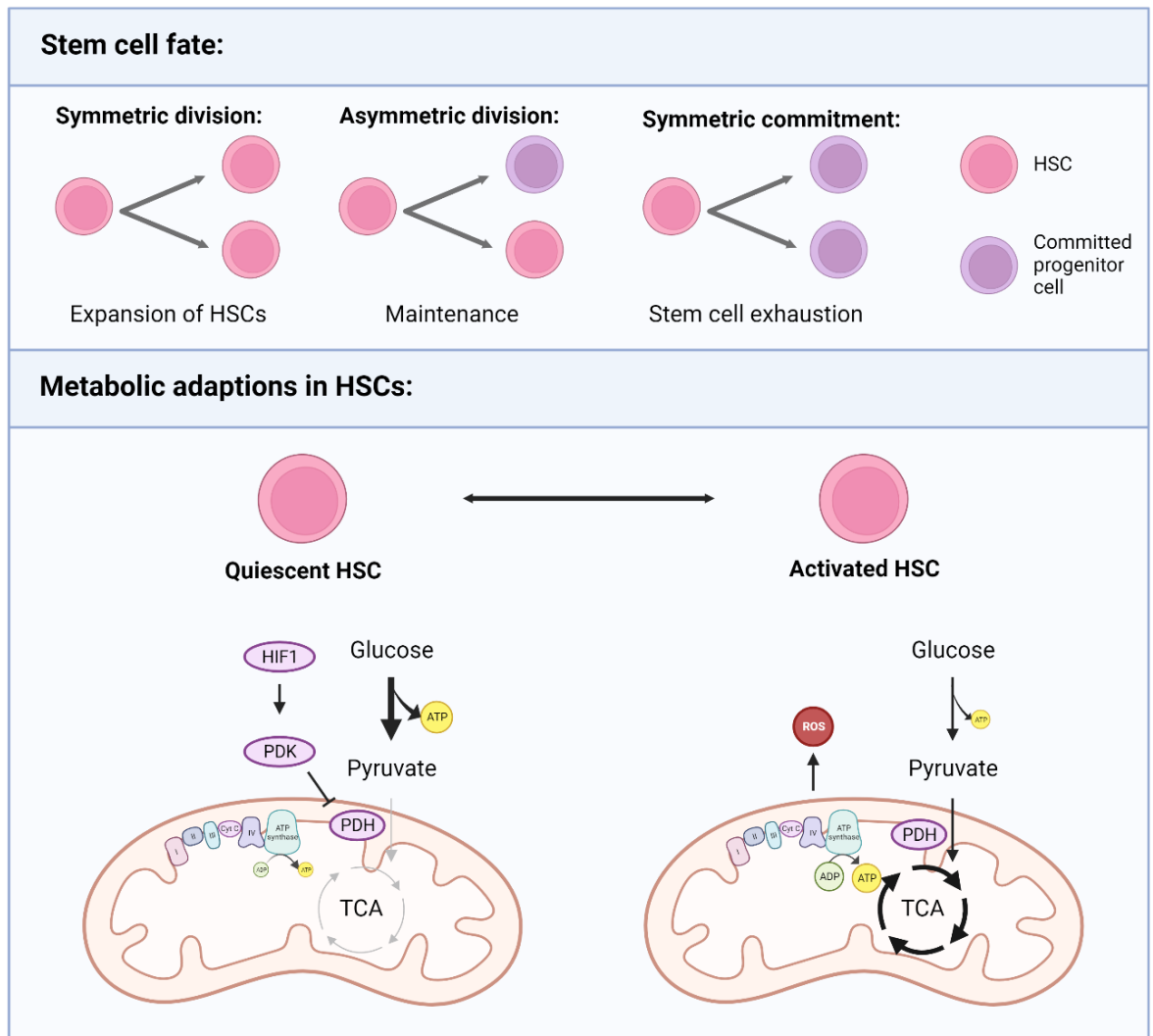


**Figure 1-2 Stem cell fate and metabolic reprogramming.** Cycling stem cells can undergo symmetric division, resulting into two stem cells or asymmetric division, leading to one stem cell and one committed progenitor cell. Stem cell exhaustion results in both progenies committing to differentiation. To prevent stem cell exhaustion, the majority of cells remain in a quiescent state with low OXPHOS to mitigate DNA damage caused by ROS. Cycling HSCs transition to a high OXPHOS state due to increased energy demand (adapted from Ito *et al.*<sup>48</sup> and Rattigan *et al.*<sup>53</sup>). Created with BioRender.com.

## 1.2 The bone marrow niche

### 1.2.1 Where the haematopoietic stem cells live

The site of haematopoiesis changes during embryogenesis, originating in the yolk sac where primitive haematopoiesis occurs, with definitive haematopoiesis occurring later in development in the aorta-gonad-mesonephros region where the first HSCs emerge<sup>54-56</sup>. In parallel, HSCs are generated *de novo* in the placenta, originating from the chorionic and allantoic mesodermal tissue, and functions as a prehepatic niche<sup>57-59</sup>. HSCs are then seeded to the foetal liver, which is the primary foetal haematopoietic organ supporting HSC expansion and differentiation during development<sup>60,61</sup>. HSCs migrate to the spleen and the BM, which are the main postnatal haematopoietic sites, with the BM remaining the primary site of haematopoiesis throughout life<sup>61</sup>.

The BM is a complex environment where HSCs are shielded, protected, and tightly regulated. The concept of the BM niche and its influence on HSCs maintenance and proliferation was introduced by Schofield in 1978<sup>62</sup>. Initial evidence of a stem cell-supporting mechanism was demonstrated by *in vitro* expansion culture of BM stem cells on a layer of stromal cells while preserving their stem cell characteristics<sup>63</sup>. Since then, extensive research has aimed to investigate the regulation of HSCs by the microenvironment.

However, studying the BM poses challenges due to its limited accessibility, being surrounded by calcified bone. Additionally, there is no single surface marker exclusively expressed by HSCs. Nevertheless, with advancements in imaging techniques over the last two decades, significant contributions have been made to elucidate the location of the stem cell niche and the players involved in regulating HSCs.

#### 1.2.1.1 Bone and marrow architecture

In adult humans, not all bones remain active sites of haematopoiesis. During adolescence, red marrow undergoes progressive replacement by yellow marrow, which comprises mostly fat and stromal cells but can support haematopoiesis in emergency situations such as blood loss<sup>64</sup>. Red marrow is primarily located in the axial skeleton, including the sternum, cranium, ribs, vertebrae and proximal

epiphyseal ends of long bones<sup>64</sup>. In contrast, in mice all bones support haematopoiesis, allowing for extensive study and a high publication output on HSCs in the murine BM<sup>65</sup>.

Long bones are divided into three regions: the epiphysis, which refers to both ends of the bone and consists of trabecular bone – a spongy, porous bone. The diaphysis constitutes the bone's shaft, primarily composed of thick, compact cortical bone enclosing the central marrow<sup>66</sup>. Meanwhile, the metaphysis, a small region between the epiphysis and diaphysis, plays a crucial role in bone development<sup>66</sup>. Flat Bones, such as the skull, are comprised of compact bone with pockets of medullary space<sup>66</sup>.

Despite being perceived as static mineralised structures, bones possess a high level of vascularity facilitated by thin layers of connective tissue<sup>66</sup>. The endosteum lines the bone's interior, while the periosteum forms its outer layer, allowing entry of nerve fibres and blood vessels to deliver oxygen-rich blood and nutrients to the marrow<sup>65</sup>. Arteries enter the bone through the nutrient canal, branching into smaller arterioles near the endosteum and are surrounded by pericytes<sup>67</sup>. Transitional vessels, referred to as type H vessels, serve as connectors between arterioles and a dense, irregular network of sinusoids characterised by a wider lumen and a reticulated pattern of interconnections<sup>68</sup>. These sinusoids extensively vascularise the BM, eventually draining into collecting veins that exit the bone through the nutrient canal<sup>68</sup>.

#### **1.2.1.2 The perivascular and endosteal niche**

The BM niche is commonly classified into two regions: the endosteal niche close to the bone and endosteum and the vascular niche. Initially, the prevailing belief was that the HSCs predominantly inhabit the more hypoxic endosteal niche, owing to substantial evidence of their interaction and dependence on osteoblasts. However, emerging studies have challenged this perspective by detecting HSCs residing in the perivascular region. These findings have led to the concept of niche heterogeneity, suggesting that more quiescent HSCs may reside in the endosteal niche, while actively cycling HSCs might favour the perivascular region. This concept will be discussed in more detail, along with exploring the influence of niche cells on HSCs (**Figure 1-3**).

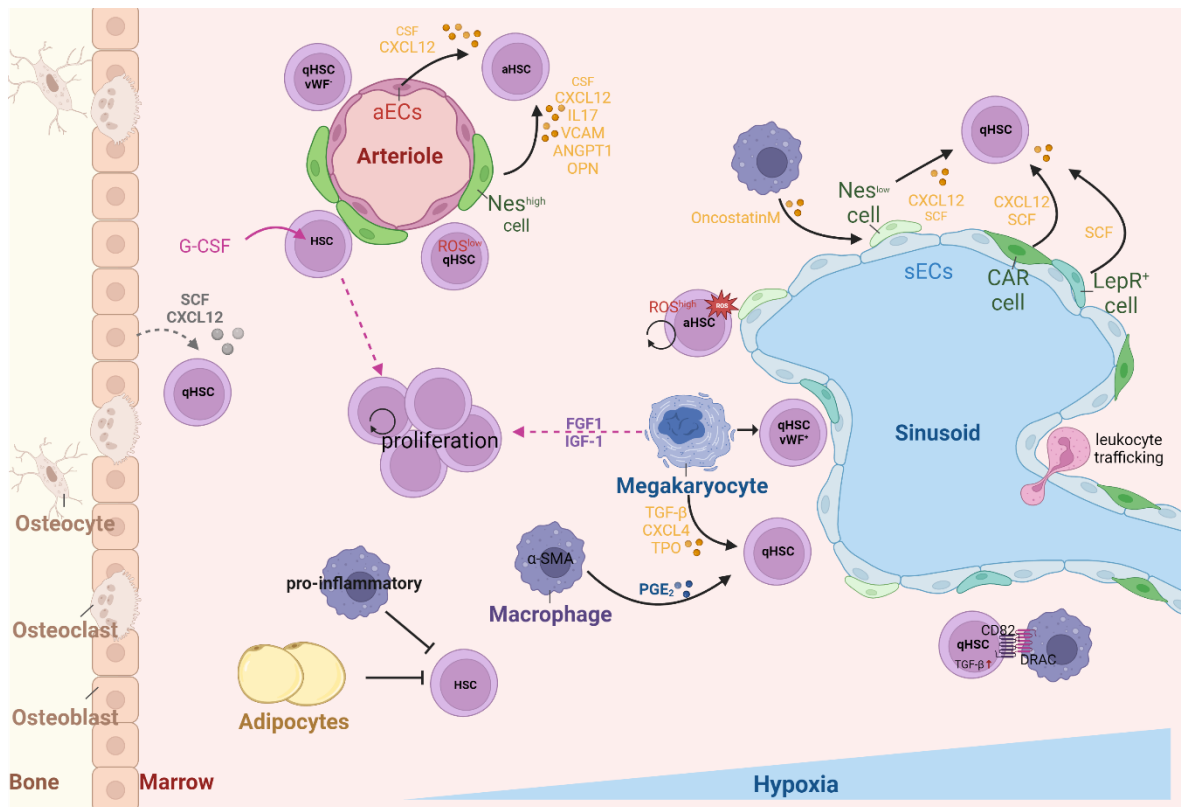


**Figure 1-3 Schematic illustration depicting the regulation of HSCs within the BM niche.** Various niche cells play crucial roles in influence HSC function. Perivascular stromal cells, including periaarteriolar Nestin (Nes<sup>high</sup>) cells, CXCL12-abundant reticular (CAR) cells, Leptin-receptor (LepR<sup>+</sup>)-positive cells, and perisinusoidal Nes<sup>low</sup> cells, have been identified as key regulators for stem cell quiescence by secreting CXCL12 and SCF. While osteoblasts produce relevant cytokines, their contribution to maintain HSCs, specifically in terms of CXCL12 and SCF production, appears less significant. Contradicting finding exists regarding activated (aHSCs) and quiescent (qHSCs), yet evidence suggest that HSCs predominantly reside in perivascular rather than endosteal regions. ROS levels within HSCs are influenced by exposure to blood plasma, particular evident in cells residing in the perisinusoidal niche. Hypoxia plays a role in HSC regulation, with a gradient observed from the bone to the sinusoidal niche. Megakaryocyte have been found to mediate quiescence through TGF- $\beta$ , CXCL4 and thrombopoietin (TPO) secretion and may specifically regulate vWF<sup>+</sup> HSC, inducing activation via FGF1 signalling. Macrophages contribute to maintaining HSC quiescence through signalling pathways involving prostaglandin E<sub>2</sub> (PGE<sub>2</sub>) and oncostatin M (OSM). A subset of macrophages directly maintains HSCs quiescence by DRAC-CD82 interaction, leading to TGF- $\beta$  signalling. In contrast, pro-inflammatory primed macrophages and adipocytes negatively impact HSC regulation and maintenance. Created with BioRender.com.

## 1.2.2 The influence of niche cells on haematopoietic stem cells

### 1.2.2.1 Osteoblasts and the endosteal niche

Osteoblasts were the first candidates to be proposed as a stem cell regulator as they supported HSC expansion *in vitro*<sup>69</sup>. Conditional elimination of osteoblasts in GEMMs led to reduced HSC numbers and impaired haematopoiesis, affirming their essential role in HSC maintenance<sup>70</sup>. Moreover, increasing osteoblast numbers via parathyroid hormone (PTH) receptor signalling resulted in an increased number of HSC and enhanced survival after HSC transplantation<sup>71</sup>.

Several imaging-based studies in mice showed HSCs to be enriched in the endosteal region, in proximity to osteoblasts<sup>24,72,73</sup>. Notably, while Zhang *et al.* suggested direct contact between LT-HSCs and endosteal osteoblasts mediated by the adherens junction molecule N-cadherin<sup>73</sup>, this finding was later challenged by Kiel *et al.*, who did not detect N-cadherin expression in HSCs<sup>74</sup>. Similarly, N-cadherin-positive BM cells showed no reconstitution capacity in transplant assays, indicating that HSCs likely do not express N-cadherin<sup>74</sup>.

Multiple studies indicated murine HSCs preferentially home to the endosteal niche<sup>75-77</sup>. Along similar lines, human HSCs favoured homing to the endosteal region of trabecular bone and exhibited a higher stem cell potential compared to cells localising to the diaphyseal area in mouse xenograft studies<sup>78</sup>. However, detecting more committed progenitors further away from the bone surface fostered the idea that there might be different niches for LT-HSCs and less primitive progenitors, suggesting distinct microenvironments<sup>75,79</sup>.

Though, evidence is increasing showing primitive HSCs in the endosteal niche but closely associated with vasculature<sup>67,80</sup>. Indeed, conditional deletion of crucial cytokines for HSCs maintenance, for example C-X-C motif chemokine 12 (CXCL12) and stem cell factor (SCF), in osteoblasts did not affect endogenous HSC number<sup>81-83</sup>. Therefore, it is unlikely that osteoblasts are the sole determinant in HSCs maintenance.

### 1.2.2.2 Stromal cells and the perivascular niche

Mesenchymal stem cells (MSCs), like HSCs, possess self-renewal capabilities and can give rise to multiple cell types such as osteocytes, chondrocytes, adipocytes and stromal cells<sup>84</sup>. Studies with human (CD146<sup>+</sup>) or foetal mouse (CD105<sup>+</sup>CD51<sup>+</sup>) BM cells enriched for MSCs demonstrated their ability to form an ectopic haematopoietic niche capable of harbouring host-derived HSCs after *in vivo* transplantation<sup>85,86</sup>.

Several genetic markers have been used to explore the relationship between MSCs and the HSC niche. CXCL12 was identified as an essential factor for HSCs maintenance, with conditional deletion of its receptor CXCR4 in HSCs leading to a significant reduction in HSC frequency<sup>87</sup>. CXCL12-abundant reticular (CAR)

stromal cells, defined by their high expression of CXCL12 and primarily observed surrounding sinusoidal vessels, were found to be crucial for maintaining HSCs in the niche<sup>24,87,88</sup>. These cells also provide the cytokine SCF, which contributes to HSC maintenance<sup>88</sup>.

A similar strategy was applied to identify a cell population expressing high levels of SCF by genetic knock-in of GFP into the *Scf* locus<sup>82</sup>. These GFP-expressing cells, predominantly wrapped around sinusoids and were found adjacent to HSCs, were of mesenchymal origin and exhibited high expression of leptin receptor (LepR)<sup>82</sup>. Homozygous progeny for conditionally deleted *Scf* in these cells were not viable, providing strong evidence that SCF-GFP/LepR cells are essential to the BM niche<sup>82</sup>.

Another possible candidate contributing to the niche are Nestin-GFP MSCs (Nes-GFP) as they were found closely associated with HSCs and produce high levels of CXCL12 and SCF<sup>89</sup>. Kunisaki *et al.* further defined Nes-GFP cells into Nes-GFP<sup>low</sup> cells with a reticular phenotype positioned closer to sinusoids, and Nes-GFP<sup>high</sup> cells located exclusively periarteriolar<sup>67</sup>. Notably, HSCs near Nes-GFP<sup>high</sup> arterioles were predominantly quiescent, as indicated by staining characteristics (Ki67<sup>-/low</sup> and high Edu<sup>+</sup> retention)<sup>67</sup>. Interestingly, stimulation with G-CSF, which mobilises HSCs and induces proliferation, resulted in relocation of HSCs with greater distance to Nes-GFP<sup>high</sup> vessels suggesting different niches for quiescent and activated HSCs<sup>67</sup>. Likewise, CXCL12-deletion using NG2-Cre, which population strongly overlaps with Nes-GFP, LepR<sup>+</sup> and CAR cells<sup>84</sup>, induces not only a decrease in HSC frequency and quiescence, but also a redistribution further away from arterioles<sup>90</sup>. Furthermore, Nes-GFP<sup>+</sup> cells were found to produce other factors, such as interleukin-7 (IL-7), vascular cell adhesion molecule 1 (VCAM-1), angiopoietin 1 (ANGPT1), osteopontin (OPN), found to be of importance for HSCs maintenance<sup>65,89</sup>. In contrast, SCF from Nes-GFP cells revealed not to be essential for HSC maintenance<sup>82</sup>.

To integrate microscopy with *in situ* analysis, Acar *et al.* generated a new reporter gene mouse  $\alpha$ -catulin<sup>GFP</sup>, that in combination with cKit<sup>+</sup> staining, enables the identification of a cell population enriched in HSCs. Using optically cleared BM, their research demonstrated a higher frequency of HSCs within the central marrow of the diaphysis compared to the metaphysis<sup>91</sup>. Computational

comparisons against randomly placed spots, reinforced that HSCs, regardless their cycling state, were not located near arterioles (less than 10% within 10 $\mu$ m) nor the bone surface (less than 1% within 10 $\mu$ m), but more than 80% were within 10 $\mu$ m of sinusoids<sup>91</sup>. Consistent with these observations, another study supported the prevalence of HSCs localised predominantly perisinusoidally<sup>74</sup>. Furthermore, an extensive analysis of over 150 bone sections from various bones corroborated these findings<sup>92</sup>. The vast majority of HSCs were closely situated near vasculature (within 10 $\mu$ m), with 66% proximate to sinusoids and CXCL12<sup>+</sup> stroma cells<sup>92</sup>. However, 80% of HSCs were not associated with arterioles or NG2<sup>+</sup> periarteriolar cells (at distances greater than 20 $\mu$ m)<sup>92</sup>. Further, the study revealed no distinct disparity in location between dormant and actively cycling HSCs<sup>92</sup>.

### 1.2.2.3 Endothelial Cells

Endothelial cells (ECs) form the lining of all blood vessels and are abundantly present in the BM, playing a crucial role in creating the BM niche. Apart from their distinctive morphology, surface markers can be utilised to distinguish arteriolar ECs (aECs), identified by CD45<sup>-</sup>Ter119<sup>-</sup>Sca1<sup>high</sup>PDPN<sup>-</sup> staining and sinusoidal ECs (sECs), recognised by CD45<sup>-</sup>Ter119<sup>-</sup>Sca1<sup>+</sup>PDPN<sup>+</sup><sup>65</sup>. Ding *et al.* provided evidence supporting the essential role of EC-derived SCF<sup>82</sup>. Intriguingly, the substantial portion of SCF produced by ECs appears to originate from aECs, and targeted deletion of SCF in aECs resulted in decreased numbers of functional HSCs<sup>93</sup>. Apart from SCF, ECs secrete various factors regulating HSCs, including CXCL12, Notch ligands and pleiotrophin<sup>65</sup>. However, studies have shown that the intracellular protein expression of CXCL12 and SCF were significantly higher in MSCs than in ECs, suggesting a minor role of ECs in stem cell maintenance<sup>90</sup>.

Besides secreting factors, ECs can influence the location of HSCs by creating specific vascular architecture that determines vasculature permeability. Arteries possess a continuous basement membrane and exhibit lower permeability, whereas the sinusoidal lining is fenestrated, allowing perfusion of the surrounding tissue. According to Itkin *et al.* periarteriolar HSCs reside in a ROS<sup>low/neg</sup> state, while sinusoidal HSCs exhibit higher levels of ROS, promoting HSC activation<sup>40</sup>. Inducing endothelial disruption utilising Endo <sup>$\Delta$ Fgfr1/2</sup> mice increased ROS levels in HSCs, resulting in a reduction in HSCs numbers along with an increase in cell cycle entry<sup>40</sup>. Prolonged treatment with NAC to reduce ROS

levels, completely abolished the effects induced by exposure to blood plasma<sup>40</sup>. This strongly suggests that vascular integrity mediated by ECs influences both HSCs maintenance and activation.

Furthermore, permeability of the vasculature appears to determine leukocyte trafficking, despite aECs expressing higher levels of surface molecules for leukocyte rolling, such as VCAM-1, ICAM-1, P-selectin, than sECs<sup>40</sup>. Extravasation of leukocytes and HSC precursors was only detected in sinusoids<sup>40</sup>. Similarly, in irradiated mice, HSCs were observed to home closer to the endosteum compared to non-irradiated mice, because irradiation disrupted vascular integrity<sup>75</sup>.

#### 1.2.2.4 Adipocytes

Throughout human life red marrow is progressively replaced by yellow ‘fatty’ marrow that does not contribute to blood production. Only in emergency situations like chronic anaemia and other diseases with higher need for haematopoiesis can yellow marrow support blood production by reverting back to active red marrow<sup>64</sup>. Mice tail vertebrae are rich in adipocytes and show reduced HSCs frequency compared to the thorax vertebrae, which contain significantly fewer fat cells<sup>94</sup>. BM transplant was improved when recipient mice were either genetically depleted of adipocytes or treated to inhibit adipogenesis concluding that adipocytes negatively influence HSC<sup>94</sup>. Further, adiponectin secreted specifically by adipocytes impairs *in vitro* culture and proliferation of HSC<sup>95</sup>. Overall, adipocytes appear to exert a negative regulatory effect on HSCs, which may be associated with the higher prevalence of blood-related malignancies in older patients with more yellow marrow. However, further exploration is needed to comprehensively investigate this relationship.

#### 1.2.2.5 Descendants of HSCs

Megakaryocytes have been found to play an important role in regulating HSCs and influence their quiescence through the secretion of various cytokines, such as promoting quiescence via TPO secretion<sup>96</sup> or inducing proliferation by IGF-1<sup>97</sup>. Studies indicate that megakaryocytes express the highest level of CXCL4 among BM residing cells<sup>98</sup>, which facilitates HSC quiescence via the CXCR2 receptor<sup>99</sup>. Conditional depletion of CXCR4 in mice resulted in increased proliferation of

HSCs, while injecting CXCL4 led to decreased HSC count due to increased quiescence<sup>98</sup>.

Additionally, Zhao *et al.* demonstrated that megakaryocytes regulate quiescence by expressing high levels of TGF- $\beta$ . Notably, upon injury, megakaryocytes activate HSCs via fibroblast growth factor 1 (FGF1) signalling, temporarily overriding quiescence signals<sup>100</sup>. Depletion of megakaryocytes or depletion of FGF1 in megakaryocytes resulted in impairment of restoring HSC after 5-FU treatment in mice<sup>100</sup>.

Both studies utilised imaging techniques to assess the co-localisation of megakaryocytes and HSCs, identifying approximately 20% in direct or close contact<sup>98,100</sup>. While Bruns and colleagues used computational random dots analysis to confirm the specificity of co-localisation to megakaryocytes, Kokkaliaris *et al.* obtained similar results, although theirs did not differ significantly from randomly assigned dots<sup>92</sup>. Although these studies provide evidence of megakaryocytes as an important factor in stem cell regulation, the existence of a megakaryocyte-defined niche remains controversial and emphasizes the need for cautious interpretation of imaging-based results.

Contradictory findings could also arise due to difference in the specific cell populations under investigation. Pinho *et al.* revealed that megakaryocytes might specifically regulate vWF<sup>+</sup> HSCs, which primarily co-localised with sinusoids<sup>101</sup>. On the other hand, lymphoid-primed vWF<sup>-</sup> HSCs were shown to reside periarteriolar<sup>101</sup>.

Macrophages have been demonstrated to influence HSC quiescence directly and indirectly by affecting other niche cells. Depletion of macrophages overall disrupted the endosteal niche, leading to egress of HSPCs into the bloodstream, similar to the effects observed with G-CSF treatment<sup>102</sup>. Furthermore, another study showed that depletion of CD169<sup>+</sup> macrophages not only reduced CXCL12 levels in the BM, resulting in HSC mobilisation, but also downregulated the genes responsible for HSC retention in Nes<sup>+</sup>-MSCs<sup>103</sup>. Additionally, Albiero *et al.* proposed that macrophages support HSCs retention in the BM by inducing CXCL12 expression in Nes-GFP<sup>+</sup> MSCs through the secretion of oncostatin M (OSM)<sup>104</sup>. Another study suggested that a rare subpopulation of  $\alpha$ -SMA<sup>+</sup> monocytes and

macrophages, that show a high expression of COX-2, prevent HSC exhaustion by reducing ROS levels via prostaglandin E<sub>2</sub> (PGE<sub>2</sub>) secretion in response to genotoxic insults (e.g., 5-FU), in addition to increasing CXCL12 expression in BM stromal cells<sup>105</sup>. Another subset of macrophages characterised by their expression levels of DRAC, which binds to CD82 on LT-HSCs, was found to mediate quiescence and cell cycle arrest via TGF- $\beta$  signalling<sup>106</sup>. Knocking out DRAC in macrophages reduced surface levels of CD82 on LT-HSCs<sup>106</sup>. Depletion of DRAC-expressing macrophages increased cell cycling and differentiation of LT-HSCs<sup>106</sup>.

A recent study unveiled that macrophages can influence HSC self-renewal based on their polarisation<sup>107</sup>. *In vitro* co-culture with anti-inflammatory primed macrophages via IL-4 stimulation increased engraftment of HSPCs into irradiated recipient mice as well as promoted expansion of cobblestone area-forming cells (CAFC), compared to monocytes or pro-inflammatory primed macrophages via Interferon- $\gamma$  (IFN- $\gamma$ )<sup>107</sup>. This effect was partly attributed to nitric oxide (NO) production of inflammatory macrophages<sup>107</sup>.

### 1.2.3 Homing

HSCs homing to the BM niche is a rapid process, occurring within minutes of intravenous (IV) transplantation of cells<sup>108,109</sup>. It involves multiple steps, including chemokine signalling to induce cell rolling, adhesion, and migration. Trans-endothelial migration and extravasation of HSCs primarily occurs in the sinusoidal vessels with the CXCL12/CXCR4 axis playing a central role in facilitating cell adhesion to the BM endothelium<sup>110-112</sup>.

Adhesion molecules, such as selectins and integrins, mediate rolling and adhesion of cells as they extravasate from blood vessels. Multiple molecules have been identified as mediating stem cell adhesion. While L-selectins predominantly facilitate lymphocyte rolling, studies have revealed that P- and E-selectins are required for the homing of human CD34<sup>+</sup> cells to SCID mice<sup>109</sup>. Hidalgo *et al.* identified the P-selectin ligand PSGL-1 on CD34<sup>+</sup> cells to play a key role in initiation the interaction with the BM endothelium<sup>109</sup>.

Investigations into VCAM-1 and its receptor VLA-4 have highlighted their significance in homing, demonstrated by studies blocking either molecule using mAbs<sup>113,114</sup>. Consistent with these findings, Mazo *et al.* showed that VCAM-1 mediates progenitor cell rolling on endothelial cells via the  $\alpha 4\beta 1$  integrin VLA-4<sup>115</sup>. Blocking of VCAM-1 in selectin-deficient mice nearly abolished HSCs homing, underscoring the vital role of selectins and adhesion molecules in this process<sup>116</sup>. Despite reducing the number of rolling cells with VCAM-1 inhibition, VCAM-1 could not compensate CD34<sup>+</sup> cell homing in the absence of endothelial selectins, suggesting that selectins are key players in initiating cell rolling and adhesion molecules such as VCAM-1 and ICAM-1 mediate shear-resistant adhesion to the vessel wall<sup>109</sup>. Scott *et al.* further contributed to our understanding the homing process by demonstrating that conditional deletion of  $\alpha 4$  integrins, including VLA-4, impaired homing, with integrin-deficient HSPCs remaining in the peripheral blood<sup>117</sup>. A study by Peled *et al.* further identified VLA-5 and to a lesser extent LFA-1 to mediate cell adhesion and trans-endothelial migration of circulating HSPCs<sup>118</sup>. VLA-4 and VLA-5 have been shown to not only mediate extravasation of HSPCs, but also facilitate migration along a CXCL12-gradient on extracellular matrix proteins such as fibronectin<sup>119</sup>.

## 1.2.4 Hypoxia

### 1.2.4.1 Haematopoietic stem cells reside in a hypoxic environment

The BM has long been described as a hypoxic organ, displaying a gradient of highest oxygen tension at the endosteal niche. It was believed that HSCs not only adapted to reside in hypoxia but also depend on it to remain quiescent. This theory has been supported by studies detecting a hypoxic profile in HSCs. Parmer *et al.* perfused the BM with the nucleic dye Hoechst and demonstrated the most primitive HSCs residing in a low perfusion area, indicating a hypoxic region<sup>120</sup>. Importantly, they confirmed that this phenomenon is not attributed to higher dye efflux in more primitive HSCs<sup>120</sup>. Pimodiazole (Pimo) is a compound that forms protein adducts in low oxygen conditions, making it a marker for hypoxia. HSCs residing in low-perfusion area exhibited the highest staining for Pimo among all BM cells and displayed the least resistance to tirapazamine, a cytotoxin that induces DNA damage in hypoxic conditions<sup>120</sup>.

### 1.2.4.2 HIF1 $\alpha$ regulation in haematopoietic stem cells

Another common way of investigating cellular hypoxic status is through the measurement of hypoxia inducible factor 1 subunit alpha (HIF1 $\alpha$ ) protein levels. Under normal oxygen levels (normoxia), HIF1 $\alpha$  undergoes hydroxylation by prolyl hydroxylases domain (PHD) enzyme, followed by ubiquitination by the E3 ubiquitin ligase von Hippel Lindau (VHL), and finally subsequent degradation by the proteasome (**Figure 1-4**)<sup>121</sup>. In hypoxic conditions, the oxygen-sensitive PHD is inactivated, leading to stabilisation of HIF1 $\alpha$ <sup>121</sup>. HIF1 $\alpha$  forms a heterodimer with HIF1 $\beta$ , translocating to the nucleus and activating the hypoxia response elements (HREs)<sup>121</sup>.

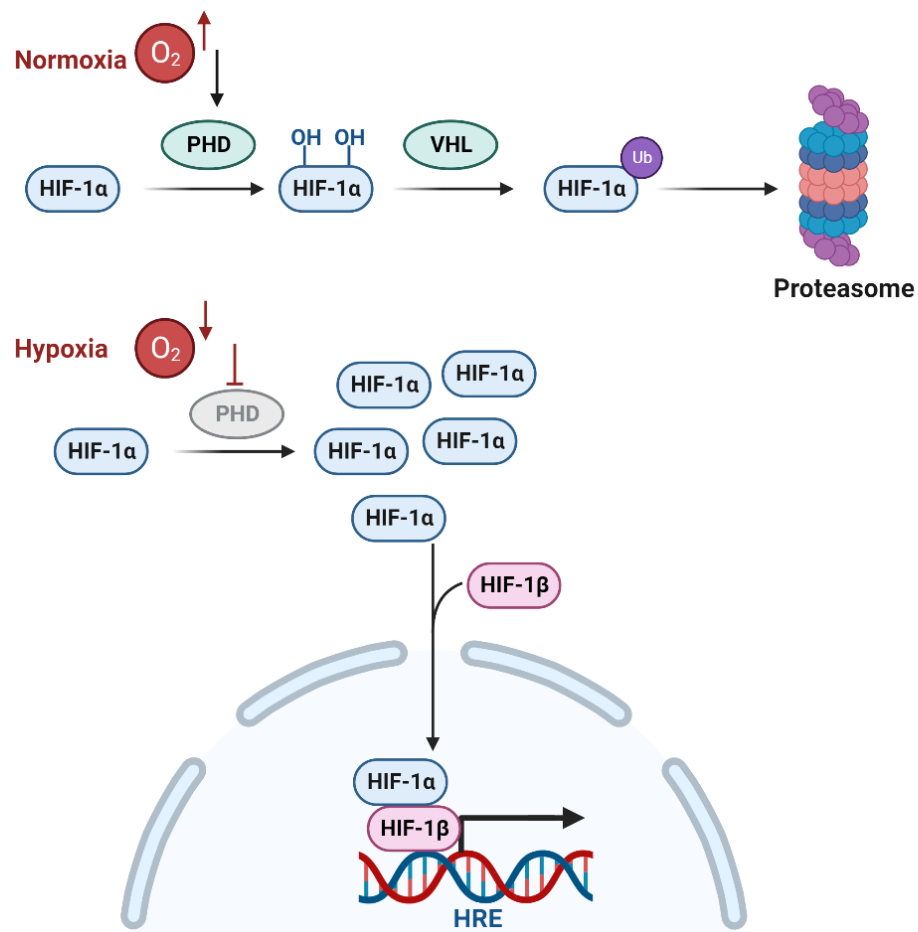


**Figure 1-4 Schematic illustration of HIF1 $\alpha$  regulation.** HIF1 $\alpha$  is consistently expressed and degraded in normoxia, undergoing hydroxylation by prolyl hydroxylases (PHD). This is followed by ubiquitination via the von Hippel Lindau E3 ligase (VHL) and subsequent degradation by the proteasome. PHDs act as oxygen sensors and remain inactive in hypoxic conditions. Consequently, HIF1 $\alpha$  accumulates and forms a heterodimer with HIF1 $\beta$  to activate the hypoxia response elements (HRE). Created with BioRender.com.

Comparative analysis of HIF1 $\alpha$  levels revealed stable levels in the majority of LT-HSCs (89%), but less than 30% in the entirety of BM-residing cells<sup>38,122</sup>. Alterations in HIF1 $\alpha$  levels within HSCs, either through HIF1 $\alpha$  knockout (KO) or over-

stabilisation by VHL KO, significantly impaired HSC homeostasis and notably reduced reconstitution capacity after transplantation<sup>122</sup>. Furthermore, HIF1 $\alpha$  deletion increased intracellular ROS levels, triggered cell cycle entry, and promoted HSC mobilisation from the BM<sup>38,122</sup>. Although KO of VHL induced quiescence, it still negatively impacted engraftment<sup>122</sup>. Moreover, HIF1 $\alpha$  has been linked to metabolic rewiring by promoting the expression of PDKs, which suppress OXPHOS<sup>39</sup>. Overall, precise regulation of HIF1 $\alpha$  appears crucial for normal HSCs function.

In contrast to these findings, Nombela-Arrieta *et al.* demonstrated that HSCs exhibit a hypoxic profile (Pimo<sup>high</sup>, HIF1 $\alpha$ <sup>high</sup>) independent of their location within the BM. Notably, they observed Pimo<sup>high</sup> HSCs (cKit<sup>+</sup> progenitors) adjacent to Pimo<sup>low/neg</sup> mature B220<sup>+</sup> cells, suggesting that Pimo does not reflect local oxygen tension<sup>80</sup>. Furthermore, circulating HSCs, induced by AMD3100 treatment, and splenic HSCs not only displayed high staining for Pimo but also exhibited similar HIF1 $\alpha$  levels compared to BM-residing HSCs<sup>80</sup>. Therefore, the hypoxic profile of HSCs appears to be independent of local oxygen levels, instead reflecting their metabolic phenotype. It is recognised that other factors such as TPO and SCF contribute to HIF1 $\alpha$  stabilisation<sup>123,124</sup>.

#### 1.2.4.3 Oxygen levels in the bone marrow

Previous studies suggesting the hypoxic niche were based on indirect measurements<sup>120,122</sup>. Spencer *et al.* conducted the first study that directly measured hypoxia. They utilised intravital microscopy (IVM) with a metalloporphyrin-based two-photon-enhanced-phosphorescent nanoprobe in the mouse calvarium to detect local oxygen levels<sup>125</sup>. This method involved measuring the probe's triplet lifetime, which is reduced in the presence of oxygen, causing the quenching of its phosphorescence<sup>125</sup>. Their findings revealed a mean partial pressure of oxygen (pO<sub>2</sub>) of 2.7% in the BM, which was lower compared to other tissues such as the brain, periosteum, or the cortical bone, despite high vascular density<sup>125</sup>. Within the BM, the highest oxygen concentration was observed in the endosteal zone (0-20 $\mu$ m from the bone), measuring at 2.9% within the vasculature and 1.8% outside of vasculature<sup>125</sup>. Furthermore, they confirmed a pO<sub>2</sub> gradient in the BM, revealing an unexpected increase in oxygen tension with increasing distance from the endosteum<sup>125</sup>.

Beyond 40 $\mu$ m from the endosteum, oxygen levels were measured at 2.4% within the vasculature, and 1.3% in the BM stroma<sup>125</sup>.

Contrary to general assumptions that sinusoidal areas may be less hypoxic due to their higher permeability compared to arterioles, Spencer and colleagues provided evidence that BM arterioles vessels (located endosteal and diameter <15 $\mu$ m) exhibited a higher pO<sub>2</sub> (3.0%) compared to sinusoids (diameters >15 $\mu$ m, 2.6%), demonstrating the highest oxygen tension is in the perisinusoidal niche<sup>125</sup>.

## 1.3 Chronic myeloid leukaemia

### 1.3.1 Oncology of chronic myeloid leukaemia

Chronic myeloid leukaemia (CML) is a blood cancer with approximately 800 new cases reported annually in the UK according to Cancer Research UK<sup>126</sup>. This malignancy is a relatively rare malignancy, and accounts for less than 1% of all new cancer cases. Median diagnostic age is between 57-60 years, with slightly higher prevalence in males<sup>127</sup>. CML rarely develops in children and has no known risk factors, except high exposure to radiation<sup>127</sup>.

CML arises from reciprocal translocation of chromosome 9 and 22, resulting in the formation of the Philadelphia chromosome (Ph), named after the city where it was discovered<sup>128-130</sup>. This translocation fuses the genes *Abelson (ABL1)* and *breakpoint cluster region (BCR)*, leading to expression of the constitutive active tyrosine kinase (TK) BCR::ABL1. Typically diagnosed in the chronic phase (CP), CML is characterised by an abnormal but still functional number of myeloid cells in the peripheral blood (PB)<sup>131</sup>. Left untreated, the disease progresses to the accelerated phase (AP) and, with the acquisition of additional genetic mutations, leads to blast crisis (BC), during which cells lose their ability to differentiate<sup>132</sup>. Recently, the WHO has redefined the classification of CML into only two phases, CP and BC, excluding AP due to its rarity since the use of TKIs<sup>133</sup>. This redefinition aims to emphasise BC risk features and TKI resistance, which are better indicators of whether BC transition will occur<sup>133</sup>. The primary goal in treating CML is to prevent BC, as this form is very aggressive with a very short median survival of 3-11 months, depending on treatment<sup>132</sup>.

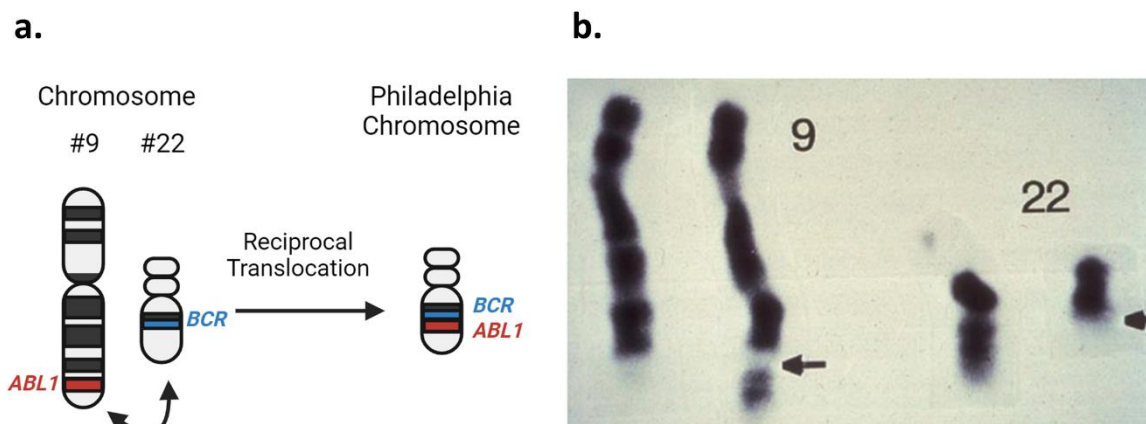


**Figure 1-5 The origin of the Philadelphia chromosome.** Reciprocal translocation of chromosome 9 and 22 leads to the formation of the Philadelphia chromosome (Ph) that carries the fusion gene *BCR::ABL1* (a). Karyotype preparation from a patient diagnosed with CML shows the minute chromosome 22 (arrow)<sup>134</sup>. Created with BioRender.com.

### 1.3.2 *BCR::ABL1* signalling pathways

The fusion of *ABL1* to *BCR* creates a potent oncogene that not only influences cell cycle regulation but also profoundly impacts cell death pathways (**Figure 1-6**). *ABL1* encodes the crucial kinase domain, essential for autophosphorylation at Tyr177<sup>135</sup>. Phosphorylated *BCR::ABL1* enhances the binding affinity of its SH2 domain, facilitating the interaction with the adaptor protein growth factor receptor-bound protein 2 (*GRB2*)<sup>136</sup>. Consequently, guanine nucleotide exchange factors (*GEF*), such as *GAB2* and *SOS* are recruited and phosphorylated, thus linking *BCR::ABL1* signalling to the *RAS-MAPK* pathway<sup>137,138</sup>. This has been shown as transduction of *HSCs* with *BCR::ABL1* impede cell cycle arrest, pushing cells into transition from the *G*<sub>1</sub> phase into the *S*-phase through *Ras* and *ERK* signalling pathways<sup>139</sup>.

Furthermore, *BCR::ABL1* activates the *PI3K/AKT* signalling pathway<sup>140</sup> affecting a multitude of pathways in support of proliferation and survival such as suppression of *FoxO*, a TF that regulates apoptosis, cell-cycle progression and oxidative-stress resistance<sup>141</sup>. Additionally, mechanistic target of rapamycin (*mTOR*) is upregulated, inhibiting autophagic flux but increasing protein translation required for transition from *G*<sub>1</sub> to *S*-phase<sup>142,143</sup>. Moreover, active *PI3K/AKT* signalling cascade suppresses apoptosis by inhibiting proapoptotic factors such as *Bad* and *caspase-9*<sup>144</sup>. The *PI3K/AKT* pathway might also be activated by elevated levels of *ROS*<sup>145</sup> or *CrkL*, which is phosphorylated by *BCR::ABL1* on Tyr207 by a second phosphorylation site on *BCR::ABL1*<sup>146,147</sup>.

Other effectors of BCR::ABL1 are members of the signal transducer and activator of transcription (STAT) protein family, which regulate proliferation, apoptosis and differentiation<sup>143</sup>. Generally, these are only activated by cytokines via Janus kinases (JAK). However, BCR::ABL1 signalling bypasses JAK and constitutively activate STAT proteins, primarily STAT1, STAT3 and STAT4<sup>148</sup>. Interestingly, while activation of STAT3 and STAT5 were initially required for oncogenic transformation, BCR::ABL1-transformed cells became dependent of STAT5<sup>149</sup>. Gallipoli *et al.* demonstrated in pre-clinical studies that intervening the Jak2/STAT5 signalling pathway, in combination with TKI, induces apoptosis in CD34<sup>+</sup> cells, indicating that it could be a valuable pathway to target LSCs<sup>150</sup>.

MYC is a known oncogene and dysregulated in over 50% of all cancers<sup>151</sup>. Multiple studies have indicated that MYC is elevated in CML<sup>152,153</sup>. Interfering with MYC signalling despite active BCR::ABL1 eliminated leukaemia potential *in vivo*<sup>154,155</sup>. Some studies found higher levels of MYC in patients in BC and indicate MYC being involved in disease progression<sup>153,154</sup>.

Another pathway of interest in CML treatment is the Hedgehog pathway, which is critical during embryonic haematopoiesis but not required for steady-state adult haematopoiesis<sup>156</sup>. Multiple studies have shown that inhibition of the Hedgehog pathway negatively affects CML LSCs<sup>157,158</sup>. Irvine *et al.* utilised an inhibitor targeting Smoothed (SMO), the main mediator of the Hedgehog pathway, and showed that patient-derived CML cells had a reduced CFC replating capacity and a lower long-term culture-initiating cell (LTC-IC) frequency<sup>159</sup>. Moreover, SMO inhibition in combination with nilotinib reduced engraftment of CML cells in PDX studies<sup>159</sup>. Therefore, combination therapy of TKI treatment with inhibition of the Hedgehog pathway could improve clinical outcomes. However, one clinical study evaluated a SMO inhibitor (BMS-833923) in combination with dasatinib, which showed no evidence of efficacy in CP-CML patients compared to dasatinib alone<sup>160</sup>. More clinical trials testing various inhibitors targeting the Hedgehog pathway in haematological malignancies are ongoing, with Glasdegib being already approved for AML treatment<sup>161</sup>.

In the efforts of understanding the relevance of the Wnt pathway in CML, studies have elucidated multiple mechanism that led to stabilisation of  $\beta$ -catenin, the

main mediator of the Wnt signalling pathway, improving survival of CML cells and mediating TKI resistance<sup>162-164</sup>. Conditional deletion of  $\beta$ -catenin led to lower number of CML LSCs and reduced CML progression *in vivo*<sup>165</sup>. Furthermore, the authors could show that loss of  $\beta$ -catenin led to reduced p-STAT5 $\alpha$  levels, a signal transducer activated by BCR::ABL1 driving cell proliferation<sup>165</sup>. A study by Hu *et al.* demonstrated that BCR::ABL1 signalling directly leads to  $\beta$ -catenin accumulation via inhibition of GSK-3 $\beta$  through the PI3K/AKT pathway<sup>166</sup>. Another study found a synergy of imatinib treatment, and the use of a COX-2 inhibitor called indomethacin to block prostaglandin E<sub>2</sub> signalling<sup>167</sup>. This combination suppressed  $\beta$ -catenin accumulation and effectively targeted LSCs *in vivo*<sup>167</sup>. An interesting study by Schürch *et al.* revealed that stimulation of the receptor CD27, belonging to the TNF receptor family, enhances Wnt stimulation in LSCs<sup>168</sup>. Deletion of CD27 on Ph<sup>+</sup> LSCs significantly improved survival of recipient mice compared to mice receiving wild type (WT) LSCs<sup>168</sup>. Interfering with the CD70-CD27 interaction via mAbs reduced  $\beta$ -Catenin translocation to the nuclei and improved primary and secondary recipient survival<sup>168</sup>. As under physiological conditions CD70 is primarily expressed by activated lymphocytes and a subset of DCs, this study shows how the adaptive immune system could potentially contribute to leukaemia progression opening up the possibility of immunotherapy in combination with TKI to eliminate LSCs<sup>168-170</sup>. However, a study by Riether *et al.* demonstrated that CD70 is upregulated in CML LSCs upon TKI treatment, thereby contributing to increased CD27 signalling in a cell-autonomous manner<sup>171</sup>. A phase 1/2 clinical trial with AML patients using a combination treatment with a monoclonal antibody for CD70 ARGX-110 is ongoing as of 2018<sup>172</sup>.

Notch signalling is known to be involved in preservation and maintenance of healthy HSCs<sup>173</sup>. BM niche cells, especially trabecular osteoblasts, have been found to express higher levels of the Notch ligand Jagged-1 and to be involved in preservation of self-renewable LT-HSCs<sup>71,78</sup>. Studies in myeloproliferative neoplasms (MPN) revealed aberrant Notch signalling sustaining self-renewal potential in hyperproliferative LT-HSCs with myeloid lineage bias<sup>174-176</sup>. While the previous authors reported a decrease in Notch signalling along with BCR::ABL1 expression<sup>175</sup>, a study by Bowers *et al.* found increased Notch signalling to accelerate leukaemia development<sup>177</sup>. The authors demonstrated

that osteoblasts in Ph<sup>+</sup> mice expressed higher levels of Jagged-1, compared to healthy mice<sup>177</sup>. Ablation of osteoblasts accelerated leukaemia development with an increased number of LSCs along with reduced survival of mice compared to control animals<sup>177</sup>. However, LSCs from osteoblast-ablated mice showed reduced long-term repopulation in secondary transplantation compared to LSCs acquired from control mice<sup>177</sup>. Whether this effect is attributed to reduced LSCs self-renewal potential without Notch stimulation, or if osteoblast ablation changed homing and engraftment properties, requires further investigation<sup>177</sup>. Similarly, analysis of patient-derived CD34<sup>+</sup> cells revealed upregulation of Notch signalling in CML cells compared to healthy cells<sup>178</sup>. Furthermore, CD34<sup>+</sup> CML cells treated with imatinib showed increased Notch signalling, which was not found in imatinib-resistant cells indicating a potential resistance mechanism to imatinib treatment<sup>178</sup>. Furthermore, Nakahara *et al.* detected an increase in Notch signalling with CML progression, as evidenced by higher expression levels of the downstream effector Hes1 in samples obtained from BC patients compared to patients in CP<sup>179,180</sup>. The authors previously reported that Hes1 overexpression, along with BCR::ABL1, resulted in a more aggressive form of CML resembling BC in mice<sup>180</sup>.

Interestingly, a study in AML showed that  $\beta$ -catenin stimulates Notch signalling in HSCs, which can be prevented by deletion of Jagged-1 signalling in osteoblasts<sup>181</sup>. A crosstalk between Wnt and Notch signalling is not surprising, as previous studies reported their involvement in regulating the differentiation of healthy HSCs<sup>182</sup>. A study by Naef *et al.* elucidated an interesting mechanism involving IL-33 signalling and activation of its IL1RL1 receptor (encoded by the ST2 gene), which was higher expressed on the cell surface of Ph<sup>+</sup> CD34<sup>+</sup> cells compared to healthy HSCs<sup>183</sup>. *In vitro* activation of IL-33/ST2 signalling led expansion of LSCs, caused by Wnt activation while autonomously inhibiting Notch signalling<sup>183</sup>. Furthermore, activation of ST2 signalling circumvented BCR::ABL1 inhibition via TKI, leading to TKI resistance<sup>183</sup>. This was further supported by showing that TKI treatment was more effective in mice lacking ST2<sup>183</sup>. Kang *et al.* reported a similar signalling profile of lower Notch signalling and increased Wnt activation to be associated with myeloid-driven malignancies pushing MPPs into myeloid lineage differentiation<sup>184</sup>. Overall, Notch signalling represents a complex and multifaceted pathway in LSCs, and further research is required to

elucidate its precise mechanism and crosstalk to other signalling pathways to determine the therapeutic potential in leukaemia treatment.

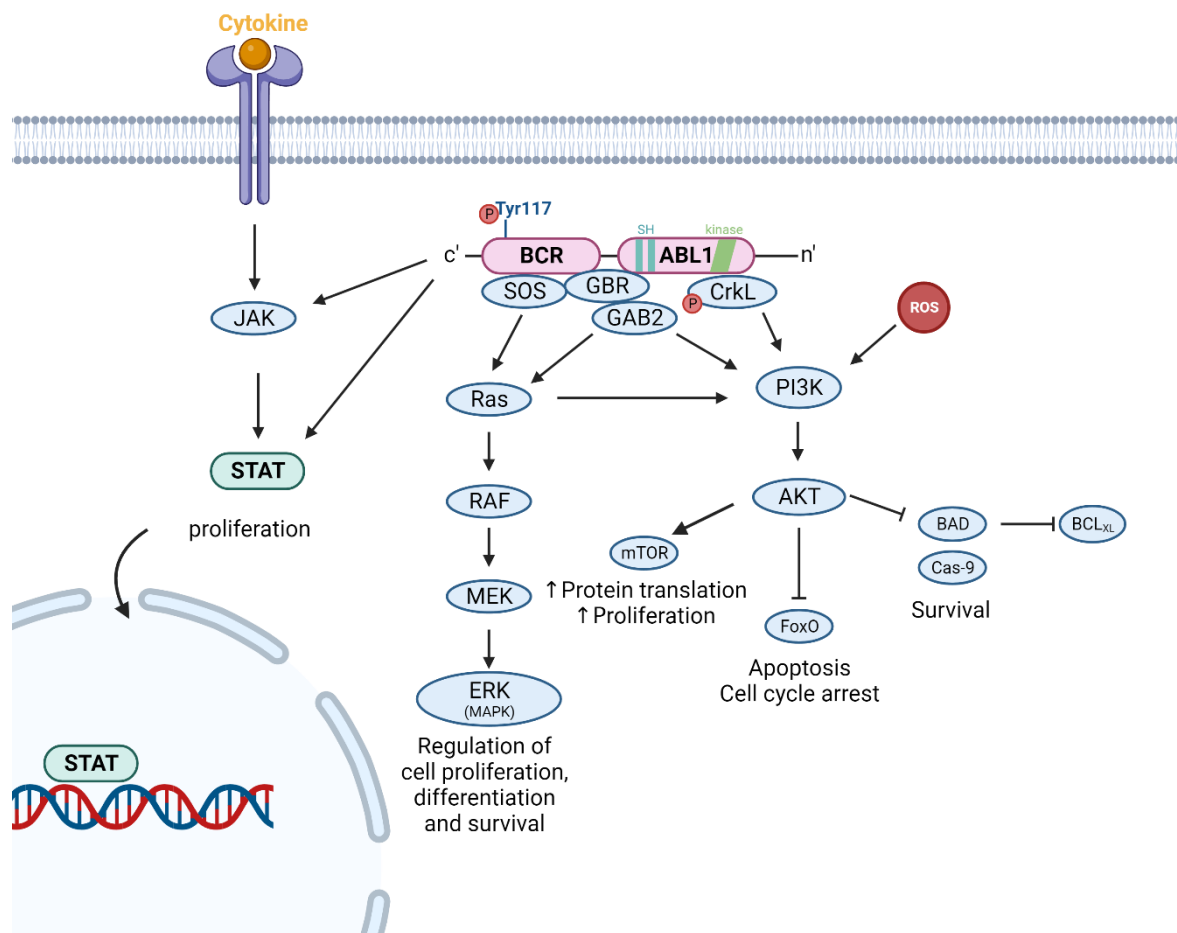


**Figure 1-6 Schematic illustration of BCR::ABL1 signalling pathways.** BCR::ABL1, as a constitutive active kinase, initiates aberrant cell cycle progression by activating several pathways. It triggers the MAPK/ERK pathway via Ras, as well as the PI3K/AKT pathway, leading to mTOR activation, which promotes cell cycle entry while inhibiting FoxO and pro-apoptotic proteins such as BAD, enabling evasion of apoptosis and cell cycle arrest. BCR::ABL1 has the ability to directly activate STAT bypassing JAK signalling, which normally requires cytokine activation. Created with BioRender.com.

### 1.3.3 Targeted therapy with tyrosine kinase inhibitors

The introduction of tyrosine kinase inhibitors (TKIs) has revolutionised the treatment of CML (Figure 1-7). The first TKI, imatinib, marketed as Gleevec by Novartis, exhibited successful haematological response in 53 out of 54 patients<sup>185,186</sup>. Imatinib, a small molecule inhibitor, targets the ATP binding site of ABL1<sup>186</sup>. Subsequently, second-generation TKIs, nilotinib and dasatinib, were approved as frontline treatments in 2010<sup>131,187,188</sup>. Dasatinib as well as bosutinib, another second-generation inhibitor, are designed not to only inhibit ABL1 but also members of the Src kinase family to enhance their efficacy<sup>189</sup>. Research has shown, that BCR::ABL1 activates Src kinases through direct binding as well as

phosphorylation<sup>189-191</sup>. Furthermore, Src kinases such as Hck have been shown to activate BCR::ABL1 via phosphorylation, potentiating BCR::ABL1 activity<sup>192,193</sup>. In clinical trials dasatinib has been shown to have higher efficacy than imatinib in newly diagnosed patients in CP<sup>187,194</sup>. Furthermore, dasatinib can overcome certain point mutations in the ABL1 ATP-binding site that render patients resistant to imatinib<sup>195</sup>.

Approximately three-quarters of patients respond to TKI therapy, achieving major molecular response (MMR), significantly improving progression-free survival compared to the previous first-line treatments with interferon- $\alpha$  (IFN- $\alpha$ )<sup>131,196-198</sup>. Patients treated with TKIs, where BCR::ABL1 expression was nearly undetectable by polymerase chain reaction (PCR) for two years (10-20%), discontinued treatment, but within 24 months, approximately 50% experienced relapse<sup>198-200</sup>. However, around 40% of patients remained in remission<sup>199</sup>. Current data indicate that around one-quarter of CP patients fail first-line therapy, with half of these cases attributed to point mutations in the kinase domain of BCR::ABL1<sup>131,201</sup>. One notable point mutation is T315I, which prevents imatinib and other TKIs from binding the kinase domain<sup>138</sup>. To address this, the third generation TKI ponatinib was developed specifically targeting T315I-mutated BCR::ABL1<sup>202</sup> and has been approved for patients with this point mutation. Notably, ponatinib has also shown effectiveness in patients without this specific mutation but who have failed first- and second-generation TKI treatment<sup>203</sup>. However, besides the risk for point mutations and failure of TKIs, lifelong treatment with TKIs may lead to multiple side effects and complications, like vascular events or pleural effusion<sup>204,205</sup> and poses a high economic burden on healthcare systems<sup>206</sup>.

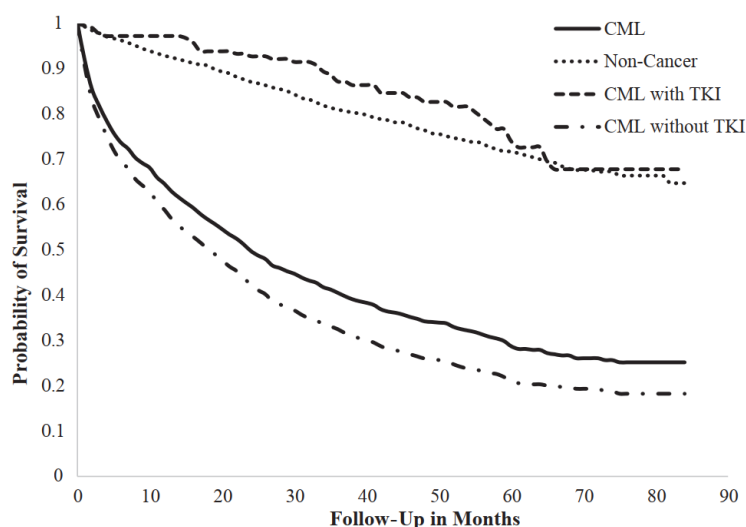


**Figure 1-7 Kaplan-Meier survival curve of CML patients showing life-expectancy with TKI treatment (97% receiving Imatinib) in line with aged-matched general population (Patients from the USA, age >66 years)<sup>205</sup>.**

### 1.3.4 Leukaemic stem cells and LSC persistence

CML has been shown to be a stem cell-driven disease, characterised by transformation occurring in the most primitive HSCs, referred to as leukaemic stem cell (LSC) or leukaemia-initiating cell (LIC). Evidence supporting this proposition was provided by x-linked clonality testing utilising the marker glucose-6-phosphate dehydrogenase (G6PDH)<sup>207</sup>. In females heterozygous for the x-linked enzyme G6PDH, active expression of either isotype A or B occurs, but never within the same cell<sup>207</sup>. Among healthy individuals, blood granulocytes were found to express either isotype<sup>207</sup>. However, in CML patients, exclusive expression of one isotype was observed in all leukaemia cells<sup>207</sup>. Later, fluorescence *in situ* hybridisation (FISH) was used to detect the Ph not only in myeloid cells but also in lymphoid cells, demonstrating that the cell of origin must be multipotent excluding more committed myeloid progenitors<sup>208</sup>. In addition, BCR::ABL1 transformation of committed progenitor cells, such as CMP and GMP, does not enable self-renewal, unlike the case observed with an acute myeloid leukaemia (AML) oncogene<sup>209</sup>.

Although LSCs express BCR::ABL1, promoting cell cycling, Holyoake *et al.* identified a rare population of deeply quiescent LSCs isolated from CML patients<sup>210</sup>. These LSCs reversibly enter cycling both *in vivo* and *in vitro*<sup>210</sup>. Coexisting alongside cycling LSCs, these quiescent LSCs exhibit similar characteristics to quiescent HSCs and could be the root cause of CML relapse<sup>210</sup>.

This discovery fostered the concept of LSC persistence, where a small dormant Ph<sup>+</sup> cell population remains unresponsive to TKI treatment. Subsequent studies have detected BCR::ABL1<sup>+</sup> primitive cells in patients achieving MMR with TKI therapy, explaining the 50% relapse rate after TKI discontinuation<sup>198,211,212</sup>.

Further research by Corbin *et al.* demonstrated that LSCs are not reliant on BCR::ABL1 signalling for survival<sup>213</sup>. Patient-derived CML LSCs (CD34<sup>+</sup>CD38<sup>-</sup> and CD34<sup>+</sup>CD38<sup>+</sup>) cultured under the same conditions as healthy counterparts displayed similar growth and survival patterns, even with suppressed BCR::ABL1 signalling by imatinib treatment<sup>213</sup>. Supporting the idea that LSCs are non-‘oncogene-addicted’, healthy HSCs typically require addition of growth factors for *in vitro* culture, normally provided by cells in the BM niche. Conversely, LSCs have been shown to produce their own cytokines, such as IL-3 and GM-CSF, thereby sustaining proliferation by autocrine signalling<sup>214,215</sup>. In addition, Hamilton *et al.* demonstrated that abolishing BCR::ABL1 signalling through TKI treatment (dasatinib, 12 days) induced reversible quiescence in CD34<sup>+</sup> CML cells instead of cell death<sup>216</sup>. These studies collectively highlight that solely inhibiting BCR::ABL1 may not suffice to eradicate LSCs, emphasising the need to target alternative pathways for a more curative approach in CML treatment.

### 1.3.5 Metabolic adaptations in leukaemic stem cells

#### 1.3.5.1 Cancer cells and the Warburg effect

Otto Warburg discovered that cancer cells, which are highly proliferative and consequently require substantial energy, exhibit a preference for glycolysis even in the presence of oxygen<sup>217</sup>. This metabolic phenomenon, termed the Warburg effect, has been marked as a hallmark of cancer<sup>218</sup>. Contrary to Warburg’s initial suggestion of dysfunctional mitochondria as the primary cause, research indicates that cancer cells prioritise aerobic glycolysis due to their high demand for metabolic intermediates<sup>219</sup>. Apart from the need for ATP as energy, rapidly dividing cells require increased supply of fatty acids, nucleotides, and amino acids for continuous mitosis<sup>219</sup>.

### 1.3.5.2 Metabolic adaptations in leukaemic stem cells

Despite sharing the capacity of self-renewal with their healthy counterpart, studies have revealed that LSCs sustained their elevated energy requirements through increased levels of OXPHOS and exhibited higher mitochondrial activity<sup>220</sup>. Investigations using primary CML cells (CD34<sup>+</sup>CD38<sup>-</sup>) demonstrated that a higher dependency on active OXPHOS as treatment with the antibiotic tigecycline, known for inhibiting mitochondrial ribosomes and protein synthesis, effectively eradicated human LSCs in pre-clinical studies<sup>220</sup>. Recent research has showcased a role of SIRT1, a NAD<sup>+</sup> dependent deacetylase, in enhancing OXPHOS in CML independently of BCR::ABL1<sup>221</sup>. In contrast, SIRT1 deletion did not affect OXPHOS in HSCs<sup>221</sup>. Given this dependency on OXPHOS, there has been a growing interest in pharmacologically targeting this metabolic vulnerability in LSCs while avoiding impacts on HSCs<sup>222</sup>. Metabolic profiling of human LSCs revealed that TKI treatment can partly reverse some of the metabolic changes induced by BCR::ABL1 signalling<sup>223</sup>. Identifying and targeting metabolic pathways deregulated independently of BCR::ABL1 signalling, such as pyruvate anaplerosis, could sensitise LSCs to imatinib treatment in pre-clinical studies<sup>223</sup>.

Further, fatty acid metabolism has been linked to sustain LSC survival, evidenced by the impairment in LSC function upon loss of ALOX5 and ALOX15, enzymes involved in fatty acid metabolism<sup>224</sup>. However, the precise mechanism, such as their contribution to fuel the citric acid cycle, is largely unexplored. Notably, a subset of LSCs expressing the fatty acid transporter CD36 were found to evade chemotherapy in adipose tissue, while exhibiting elevated levels of FAO and a state of quiescence<sup>225</sup>. Given that amino acids can supplement the TCA cycle as well, current research is concentrating on evaluating the dependence of specific amino acids for LSC function<sup>53</sup>.

### 1.3.6 The bone marrow microenvironment in chronic myeloid leukaemia

Similar to HSCs, LSCs reside within the BM niche, a protective environment shielding them from targeted therapy. Numerous efforts have been undertaken to understand how LSC persistence is facilitated by the niche and how LSCs exploit and manipulate the niche to their advantage.

### 1.3.6.1 Inflammatory environment

Welner and colleagues demonstrated that CML cells negatively impacted self-renewal of healthy HSCs by inducing proliferation, mediated by IL-6 secretion<sup>226</sup>. Single-cell transcriptomics revealed increased expression of inflammatory-related genes, such as IL-6, TGF- $\beta$  and TNF $\alpha$ , in BCR::ABL1<sup>+</sup> stem cells compared to HSCs from healthy donors<sup>227</sup>. Several studies have reported a pro-inflammatory milieu, favouring CML cells at the expense of healthy haematopoiesis<sup>228</sup>. TNF- $\alpha$  and IL-1, both increased in LSCs, promoted survival via NF $\kappa$ B signalling<sup>229,230</sup>. Inhibition of autocrine signalling of either TNF- $\alpha$ <sup>229</sup> or IL-1<sup>231</sup> has shown to sensitise CML CD34<sup>+</sup> cells to TKI treatment. Furthermore, BCR::ABL1<sup>+</sup> cells were found to influence MSCs via direct cell-cell contact, resulting in the accumulation of inflammatory myelofibrotic cells, ultimately leading to fibrosis<sup>232</sup>. In this study, TPO and MIP-1 $\alpha$  were identified as major drivers, contributing to a niche detrimental to normal HSCs but favourable for LSCs<sup>232</sup>.

### 1.3.6.2 Interaction with niche cells

LSCs show reduced dependence on the BM niche compared to HSCs. CXCL12, known to mediate HSCs homing, is found to be decreased in BM of CML mice but instead increased in the spleen, leading to higher mobilisation to the spleen<sup>228</sup>. Consistent with this, CXCL12 levels were reduced in BM samples from CML patients compared to healthy individuals<sup>228</sup>. *In vitro* co-culture of primary CD34<sup>+</sup>CD38<sup>-</sup> cells and immortalised stromal cells confirmed that high expression levels of G-CSF are responsible for reduced CXCL12 levels<sup>228</sup>. Conditioned medium from CML LSCs suppressed cell growth selectively in healthy CD34<sup>+</sup>CD38<sup>-</sup> cells without affecting CML LSCs expansion<sup>228</sup>. Although the majority of LSCs appear to grow independently of stem cell factors, recent research has revealed that CXCL12-expressing MSCs play a role in maintaining a population of quiescent and TKI-resistant LSCs<sup>233</sup>. These findings highlight the potential significance of MSCs and CXCL12 in the persistence of LSCs, maintaining a small reservoir of TKI-resistant LSCs.

CD44, a cell-surface glycoprotein, has been found to be elevated on LSCs, drawing attention for its role in mediating LSC homing to the BM<sup>234</sup>. Krause *et al.*

demonstrated that CML stem cells exhibited a higher dependency on CD44 expression for successful engraftment compared to healthy HSCs<sup>234</sup>.

Furthermore, Godavarthy *et al.* identified that CD44 homing was mediated by binding to the endothelium via E-selectin<sup>235</sup>. Interestingly, the authors could establish a link between BCR::ABL1 signalling that modulated CD44 expression and suggested that increased CD44 expression contributes to LSCs quiescence and TKI resistance<sup>235</sup>.

Furthermore, Zhang *et al.* discovered an intriguing mechanism by which ECs support LSC quiescence in CML through microRNA transfer<sup>236</sup>. Specifically, miRNA-126 (miR-126) has been reported to play a regulatory role in maintaining quiescence in healthy stem cells and AML LSCs<sup>237,238</sup>. Despite BCR::ABL1 signalling suppressing the biogenesis of miR-126, CML LSCs were found to have higher levels of miR-126 compared to more committed progenitors<sup>236</sup>. As ECs express the highest levels of miR-126 within the BM niche, the researchers proposed the potential transfer of miR-126 to LSCs, possibly through extracellular vesicles<sup>236</sup>. In an *in vitro* co-culture setup, CML LSCs cultured with WT ECs exhibited lower rates of cell cycling and apoptosis, accompanied by increased engraftment and reduced survival upon transplantation, compared to LSCs cultured with ECs lacking miR-126<sup>236</sup>. Furthermore, TKI treatment increased miR-126 expression within LSCs but sensitivity to TKI treatment could be restored by knockdown (KD) or inhibition of miR-126<sup>236</sup>.

Multiple studies have demonstrated that osteoblasts contribute to HSCs maintenance through Jagged-1/Notch-mediated regulation of the cell cycle<sup>71,177</sup>. In particular, Jagged-1 exhibited higher expression levels in osteoblasts from BCR::ABL1<sup>+</sup> mice compared to WT mice<sup>177</sup>. Deletion of osteoblasts accelerated leukaemia, suggesting that osteoblasts might contribute to LSCs quiescence<sup>177</sup>. Furthermore, overstimulation of osteoblasts through continuous PTH signalling improved survival of BCR::ABL1-expressing mice and was associated with increased release of TGF- $\beta$  during bone remodelling<sup>239</sup>. KD of TGF- $\beta$  via lentiviral shRNA resulted in accelerated CML development<sup>239</sup>. However, other studies found TGF- $\beta$  signalling to increase FoxO3a translocation to the nucleus supporting LSCs maintenance<sup>141</sup>. Inhibition of TGF- $\beta$  and FoxO3a in combination

with TKI treatment improved the eradication of CML cells<sup>141</sup>, indicating the need for further investigation into this complex interplay.

### 1.3.6.3 Dysfunctional immunosurveillance in CML

Despite the high inflammatory signals observed in the CML niche, immune cells in the BM niche are surprisingly suppressed – a phenomenon partly reversible by TKI treatment<sup>240</sup>. The composition of immune cells within the BM has been correlated with patients achieving deep molecular response (DMR)<sup>240</sup>. Notably, the presence of mature NK cells has been associated with DMR and treatment-free remission (TFR)<sup>241,242</sup>. Furthermore, regulatory T (Treg) cells, a population suppressing both T and NK cell activity against leukaemic cells, were shown to be increased in CML patients at diagnosis<sup>240,243</sup>. A study by Najima *et al.* found a correlation between reduced Treg presence and restored NK cell differentiation in patients who achieved DMR with dasatinib treatment over 36 months<sup>244</sup>.

Studies profiling T cells in CML patients revealed that their T cells express higher levels of inhibitory checkpoint molecules, such as PD1, TIM3 and CTLA4, which were reduced to normal levels during TKI therapy<sup>240,245</sup>. Interestingly, a study focused on LSCs found them to exhibit high levels of MHC class I and II, stimulating the proliferation of naïve cytotoxic T lymphocytes (CTLs), which were able to eliminate these LSCs *in vitro*<sup>246</sup>. However, in *in vivo* studies with therapeutic infusion of effector CTLs, the cells had the opposite of the desired effect and activated LSCs thereby inducing their proliferation via INF- $\gamma$  secretion<sup>246</sup>.

Another immunosuppressive population associated with reduced T cell activity is the increased presence of myeloid-derived suppressor cells (MDSCs), a heterogeneous, immature cell population of myeloid origin with an immunosuppressive function<sup>247,248</sup>. MDSCs have been found to be increased in patients newly diagnosed with CML compared to healthy controls<sup>245,249</sup>. Both studies showed that TKI treatment reduced MDSC presence to normal levels in patients who reached MMR or DMR<sup>245,249</sup>. MDSCs were shown to directly inhibit T cell activation by producing ROS and nitrogen species, as well as arginase1, an enzyme that depletes arginine in the microenvironment<sup>249-251</sup>. Arginine is essential for proper T cell function, and its depletion further contributes to a

favourable microenvironment for leukaemic cells escaping immunosurveillance<sup>250</sup>. Studies monitoring the immune profile in TKI discontinuation trials could be useful to evaluate patients' potential for TFR<sup>252</sup>.

## 1.4 Intravital microscopy

### 1.4.1 A brief historical background on microscopy and intravital microscopy

The earliest notion of IVM, a technique for observing biological dynamic processes *in situ*, goes back to Marcello Malpighi, who studied the function of the lung and discovered the structure of the alveoli in frogs<sup>253</sup>. His observations included witnessing the movement of blood within the arteries, making a crucial step in the history of IVM over 350 years ago<sup>254</sup>. However, observations had to be published as descriptions and drawings of live processes, such as leukocyte rolling in the vasculature by Rulolph Wagner in 1839<sup>255</sup>. In the early 20<sup>th</sup> century, the development of microcinematography allowed time-lapse recordings to demonstrate cellular movements such as pinocytosis<sup>256</sup>. Advancements in imaging biological material progressed steadily, incorporating techniques like phase contrast and the development of dyes<sup>257</sup>. The introduction of the first fluorescence microscope in 1911 marked a significant breakthrough. Subsequent innovations in fluorescent probes not only enhanced contrast but also enabled highly specific labelling with antibodies<sup>257</sup>. Further improvements were made in the second half of the 20<sup>th</sup> century with the development of laser scanning confocal microscopy. In this technique, a single focal plane is illuminated by using a pinhole in front of the detector to reflect out-of-focus light, allowing acquisition of thin focal sections<sup>258</sup>. In contrast, conventional fluorescence microscopy, which illuminates the entire specimen while collecting all emitted light, results in a fuzzier image due to out-of-focus signal<sup>257</sup>.

### 1.4.2 Multiphoton microscopy

Although laser scanning confocal microscopy has greatly enhanced the quality of IVM, it faces challenges when imaging whole tissues, including increasing light scattering and limitations in light penetration. Further advances, such as the development of multiphoton (MP) microscopy with pulsed near infrared or infrared lasers, have improved resolution of whole tissue imaging<sup>259</sup>. Two-photon excitation, also called nonlinear excitation, refers to the excitation of a fluorophore with two photons by near simultaneous absorption within a few atto- or femto-seconds with wavelengths in near infrared or infrared<sup>260</sup>. Each photon

has half the energy required to excite the fluorophore, but hit the fluorophore at almost exactly the same time to excite it<sup>259</sup>. Longer wavelengths penetrate deeper than light from the visible or ultraviolet spectrum due to reduced scattering<sup>261</sup>. Moreover, light with longer wavelengths is thought to cause less photodamage, reducing the potential for bleaching the sample, as well as preventing out-of-focus bleaching, as only fluorophores in the focal plane get excited<sup>261,262</sup>. Additionally, this negates the need for a pinhole to reject out-of-focus light at the detector.

### 1.4.3 Second harmonic generation

Bone can be visualised without any fluorescent markers due to the intrinsic property of densely packed collagen fibres for second harmonic generation (SHG). SHG describes a phenomenon in nonlinear optical imaging when the detected signal originates from two photons with the same frequency, that interact with a nonlinear material, are combined and generate a new photon with twice the energy of the initial photon, also called frequency doubling<sup>263</sup>. Rather than the material being excited by absorption, photons are scattered and combined into a single photon without losing energy<sup>259</sup>. Highly ordered structures such as collagen, microtubules and muscle tissue have the intrinsic potential for SHG without photobleaching occurring<sup>264</sup>. Therefore, this imaging technique can be used to make out endosteal surfaces, while the BM cavity remains dark.

With advancing techniques in MP laser development and optics, third harmonic generation (THG) has become available, which does not require a specific asymmetry, predominantly occurring at aqueous and lipid-rich interfaces, thereby extending nonfluorescent imaging to cellular membranes and lipid droplets<sup>260,265,266</sup>.

### 1.4.4 Spectral imaging

Spectral imaging is a technique that can decipher fluorescence spectral overlap and artefacts that would be unable to separate using conventional fluorescent microscopy. Generally, the number of fluorophores used in a specimen is limited by overlapping emission spectra, leading to bleed-through into other channels.

Narrow bandwidth emission filters and sequential excitation reduce the chance of spill-over signals but result in signal loss and increased acquisition time<sup>267</sup>. This is not ideal in live-cell microscopy or imaging of whole tissues as signal loss might need to be compensated with higher level of excitation.

Spectral imaging utilises detectors that divide the spectrum of emitted light across an array of subdetectors with assigned wavelength 'bins' to measure the emission fingerprint of each voxel creating an image known as a lambda-stack<sup>268</sup>. Linear unmixing using reference spectra acquired for each individual fluorophore can separate the signal and determine the contribution of each fluorophore to each voxel<sup>267</sup>. This technique allows for the use of more fluorescent probes within one specimen, even though there is signal overlap. In contrast to using bandpass filters, almost all fluorescent emission signal is collected in spectral microscopy, reducing signal loss and bleaching due to lower laser power<sup>269</sup>. Moreover, autofluorescence can be unmixed by acquiring a spectrum for the unstained tissue<sup>267</sup>.

### 1.4.5 Intravital microscopy in the bone marrow niche

The accessibility of *in vivo* studies has significantly improved not only with advances in microscopy techniques but also due to the increased availability of fluorescent dyes, antibodies, and fluorescent reporter mice. In contrast to analysis of *ex vivo* tissue, capturing only a momentary snapshot in time, IVM allows real-time studies of cells within their physiological environment, addressing cell interaction dynamics at steady state and in disease<sup>75</sup>. IVM to investigate cells in the BM niche can be performed on the skull bone, achieving an imaging depth of ~100-200 $\mu\text{m}$ <sup>270</sup>, or the long bones, a more invasive technique requiring thinning of the thick compact bone<sup>263</sup>. In both cases, mice are stabilised on the microscope stage to minimize motion artefacts generated by heartbeat, respiration, and peristaltic movements<sup>261</sup>.

IVM has provided insights into general HSC cell motility<sup>40,75,271</sup> as well as into disease development and progression, which cannot be detected in tissue sections. For instance, Hawkins *et al.* utilised IVM to observe T-ALL cells *in situ* during treatment<sup>272</sup>. Initially, T-ALL cells were observed to be more motile than healthy HSCs but showed no selectivity for infiltrating a specific BM stroma<sup>272</sup>.

Analysing chemotherapy-resistant T-ALL cells provided further information that these cells do not depend on a specific niche, but overall T-ALL infiltration led to remodelling of the endosteal space, resulting in the depletion of osteoblastic cells affecting healthy haematopoiesis<sup>272</sup>. Duarte *et al.* utilised IVM to study vascular remodelling in AML-burdened mice affecting healthy haematopoiesis<sup>273</sup>. Their findings revealed that AML cells directly alter the BM stroma, correlating with high AML infiltration and collapse of endosteal vessels<sup>273</sup>. Transplanting healthy HSCs into lethally irradiated control and leukaemic mice showed that the altered BM mediated by AML cells could no longer home healthy HSCs<sup>273</sup>. Interestingly, the use of deferoxamine, a compound that stabilises HIF1 $\alpha$  and induces endosteal vessel expansion, prevented vascular remodelling by AML cells, protected healthy HSCs and improved chemotherapy treatment<sup>273</sup>. Another study by the Lo Celso group revealed that matrix metalloproteinases (MMPs) are dysregulated in AML cells, leading to ECM remodelling, and increased vascular permeability<sup>274</sup>. This leads to dislodgment of healthy haematopoietic cells<sup>274</sup>. Inhibition of MMPs using prinomastat protected healthy haematopoiesis and prevented vascular leakiness in AML-burdened mice, overall improving their survival when combined with chemotherapy compared to chemotherapy alone<sup>274</sup>.

IVM, when combined with other techniques, can offer deeper mechanistic insights along with observational data. A technique developed by Haase *et al.*, called Image-seq, allows tracking of single cells within the BM, followed by extraction and single-cell RNA sequencing<sup>275</sup>. This technique revealed that in a highly proliferative subpopulation of AML cells, dipeptidyl peptidase 4 (DPP4) among other cell cycle-related genes, was highly upregulated, which was not found when analysing AML cells in culture<sup>275</sup>.

IVM stands out as a unique technique to enhance our understanding of disease development and progression. It offers real-time, *in situ* observations, providing information of structural changes and mechanistic insights into how malignant cells manipulate the BM and how the microenvironment contributes to therapy-resistance.

## 1.5 Autophagy

### 1.5.1 General overview

Autophagy, derived from the Greek term 'self-eating', is an evolutionarily conserved catabolic process describing the degradation and recycling of cellular material in eukaryotic cells, a concept first described by Christian De Duve<sup>276</sup>. Initially, autophagy was perceived as a non-selective process that maintains cellular homeostasis during nutrient deprivation. However, it has since been recognised that autophagy can selectively degrade damaged organelles such as mitochondria and protein aggregates, serving a cytoprotective role by mitigating cellular stress. Moreover, research has revealed autophagy being involved in microbial defence and to play a role in non-apoptotic programmed cell death<sup>277,278</sup>. About three decades after the discovery of the autophagosome, Yoshinori Ohsumi had characterised 15 essential autophagy-related proteins (ATGs) in yeast, laying the foundation for understanding the mechanism and regulation of autophagy<sup>279</sup>. Ohsumi's groundbreaking work in autophagy research earned him the Nobel Prize in 2016.

Throughout the past decades, three forms of autophagy have been identified: chaperon-mediated autophagy (CMA), microautophagy and macroautophagy. CMA describes the selective degradation of cytosolic proteins that are directly delivered to the lysosome. This process is a highly energy-efficient method of eliminating dysfunctional proteins, while also capable of playing a regulatory role by targeting enzymes or TFs<sup>280</sup>. Microautophagy, previously believed to lack selectivity entirely, is characterised by sequestering cytosolic cargo via lysosomal or endosomal invagination<sup>281</sup>. Macroautophagy, hereinafter referred to as autophagy, remains the most well-understood pathway. It involves five distinctive steps: initiation, nucleation, membrane elongation, fusion with lysosome and degradation of cargo (**Figure 1-8**).

Briefly, the initiation complex orchestrates autophagy induction, prompting the formation of a double membrane known as the phagophore. While the precise origin of the phagophore remains uncertain, it may stem from the endoplasmic reticulum (ER), Golgi apparatus, plasma membrane, or assemble *de novo*<sup>282</sup>. During membrane elongation, cargo is enclosed and isolated within the newly

formed autophagosome. Fusion with a lysosome, termed the autolysosome at this stage, facilitates the degradation of the cargo. Subsequently, the resulting degradation products are released into the cytoplasm for reuse as building blocks by the cell. However, in the recent years, studies have shown that tumour cells can be supported by autophagy in neighbouring cells through increased metabolite secretion, sustaining the high metabolic needs in tumour cells<sup>283,284</sup>. Moreover, autophagy has become a field of interest in studying tumour microenvironment. Rather than solely focusing on cargo degradation, studies suggest that autophagy is involved in secreting non-degraded cargo, such as cytokines<sup>285</sup>.

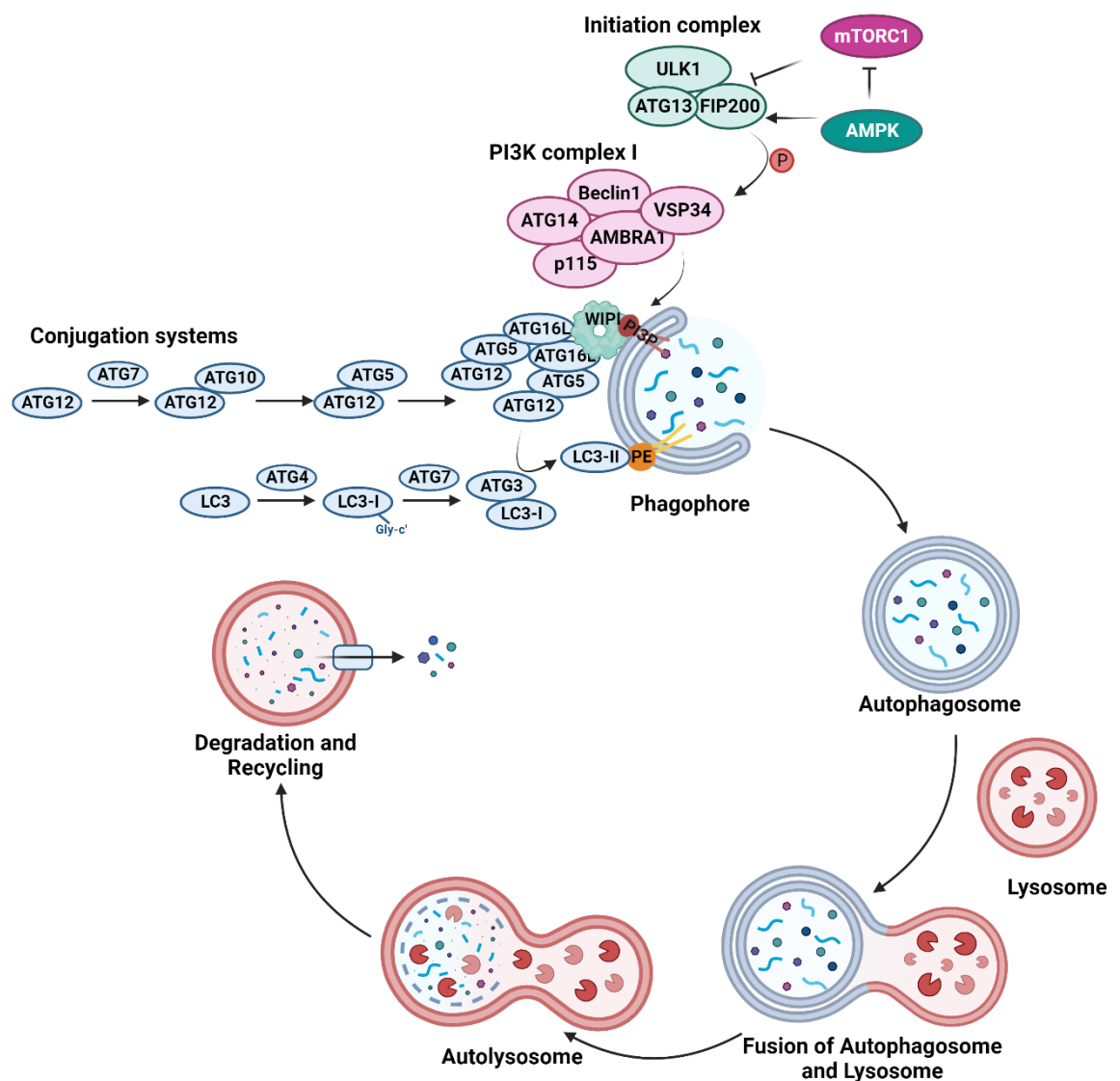


**Figure 1-8 Schematic representation of autophagy.** The initiation complex ULK1 is regulated by mTOR and AMPK. Upon activation, the PI3K complex I is recruited to the phagophore. Two conjugation systems are required for membrane elongation and binding cargo. Upon completion, the autophagosome fuses with the lysosome, leading to the degradation of its inner membrane and its contents. Degradation products are subsequently released into the cytosol for reuse. Created with BioRender.com.

## 1.5.2 Regulation of autophagy

### 1.5.2.1 Initiation of autophagy and nucleation of the phagophore

The Unc-51-like kinase 1 (ULK1) initiation complex comprises the Ser/Thr protein kinase ULK1 bound to ATG13 and focal adhesion kinase family-interaction protein of 200kDa (FIP200). mTOR regulates cell growth and consists of two distinct protein complexes, mTOR complex 1 and 2 (mTORC1/2), while only mTORC1 regulates autophagy<sup>286</sup>. In inactive state ULK1 and ATG13 are associated with and phosphorylated by mTORC1<sup>287</sup>. Nutrient deficiency induces dephosphorylation of ULK1 at its mTORC1 sites, leading to dissociation from mTORC1 and subsequent autophosphorylation<sup>288</sup>. Following this, ULK1 phosphorylates ATG13, which enables the interaction between FIP200 and ULK1, facilitating the phosphorylation of FIP200<sup>289</sup>. Another key regulator for autophagy initiation during starvation is AMP-activated protein kinase (AMPK). AMPK not only directly activates ULK1 via phosphorylation but also represses mTORC1, thereby counteracting its inhibitory effect<sup>290,291</sup>.

The activated ULK1 complex plays a pivotal role in initiating phagophore nucleation by phosphorylating Beclin1, an integral component of the class III PI3K complex 1, which includes VPS34, ATG14 and p115<sup>292</sup>. Studies by Fimia *et al.* have highlighted the essential role of activating molecule in Beclin1-regulated autophagy protein 1 (AMBRA1) in Beclin1's function within autophagy regulation<sup>293</sup>. The conversion of phosphatidylinositol (PI) to phosphatidylinositol-3-phosphate (PI3P) is a critical step primarily mediated by VPS34. This conversion is vital for recruitment of PI3P effector proteins, such as WD-repeat domain phosphoinositide-interacting (WIPI) proteins. These WIPI proteins serve as docking stations for ATG proteins, enabling proper assembly and functioning of the autophagic machinery<sup>294,295</sup>.

### 1.5.2.2 Phagophore expansion and formation of the autophagosome

Phagophore expansion involves two conjugation systems. First discovered by Mizushima *et al.*, ATG12 is activated by the E1-like enzyme ATG7, transferred to ATG10, an E2-like molecule and finally conjugated to ATG5<sup>296</sup>. ATG16L1 interacts with ATG12-ATG5 conjugate, and upon homodimerization of two ATG12-ATG5-ATG16L1 conjugates binds to PIP3 effector proteins, promoting the lipidation of

microtubule-associated protein 1A/1B-light chain 3 (MAP1LC3/LC3), which represents the second conjugation system<sup>297,298</sup>.

Hereby, LC3 is covalently conjugated to the membrane lipid phosphatidylethanolamine (PE) via a process akin to ubiquitination. First, cytosolic LC3 is cleaved by the protease ATG4, revealing a glycine at the c-terminus. This activated LC3 is then transferred to the E2 enzyme ATG3 by ATG7<sup>299</sup>. Finally, the ATG12-ATG5 complex functions as an E3-like enzyme, facilitating LC3 lipidation to PE<sup>299,300</sup>. Notably, ATG4 can also cleave LC3 from PE, causing LC3 to detach from the membrane<sup>299,301</sup>. LC3 is important for phagophore elongating, but it has been shown that LC3 molecules are partly removed upon near completion of the autophagosome<sup>302</sup>. The LC3 family consists of two subfamilies, LC3 and GABARAP. All proteins carry the LC3-interacting region (LIR) motif, enabling the selective targeting of cargo via autophagy adaptors such as p62<sup>303</sup>.

### 1.5.2.3 Lysosomal fusion and cargo degradation

The final step involves the fusion of the autophagosome with the lysosome, a process that remains poorly characterised. Similarly to fusion of late endosomes with lysosomes, which are mediated by soluble N-ethylmaleimide-sensitive factor attachment protein receptor (SNARE) complex tethering, the SNARE protein Syntaxin 17 (Stx17) has been identified to be required and localises to the outer membrane of autophagosomes in the late stage<sup>304</sup>. Although the precise mechanism underlying the incorporation of autophagosomal SNARE proteins remains unknown, it has been shown that Stx17 interacts with the lysosomal SNARE protein VAMP8, facilitating membrane proximity through the typical zippering of SNARE motifs supported by SNAP-29<sup>304</sup>. Upon completion of fusion, pH-sensitive lysosomal hydrolases, primarily cathepsins, degrade the inner autophagosomal membrane and its cargo.

## 1.5.3 Mitophagy

### 1.5.3.1 Mitochondrial dynamics

Mitochondria serve as the main energy suppliers in cells but can also pose a threat as they are generating most of the endogenous ROS<sup>305</sup>. Furthermore, mitochondria themselves are susceptible to damage by ROS, amplifying their potential to be dysfunctional further elevating oxidative stress, while their energy output via OXPHOS becomes inefficient. Moreover, damaged mitochondria can trigger apoptosis by releasing cytochrome c. Therefore, the elimination of damaged mitochondria is crucial for cellular survival.

Mitochondria are known as dynamic organelles with an intricate network of mitochondria tubules that continuously undergo fission and fusion (**Figure 1-9**). This balance between fission and fusion influences mitochondrial clearance. Mitochondrial fusion is mediated by the GTPases Mitofusin 1 and 2 (Mfn1/Mfn2), which are both essential orthologues<sup>306</sup>, and the dynamin-like GTPase Optic atrophy 1 (Opa1)<sup>307</sup>. While the intricate molecular mechanism underlying mitochondrial fusion remains not entirely understood, the current model suggests opposing mitochondria fuse through tethering via their Mfn proteins on the outer mitochondrial membrane, thereby pulling the mitochondria together<sup>308-310</sup>. Opa1, located in the inner mitochondrial membrane, interacts with Mfn1/2, leading to the fusion of the inner mitochondrial membranes<sup>311</sup>.

The primary protein orchestrating fission is dynamin-related protein 1 (DRP1), a cytosolic protein that attaches to the outer mitochondrial membrane, where it forms a multimeric ring-like structure<sup>312</sup>. Similar to its namesake dynamin, following GTP hydrolysis the DRP1-ring tightens around the mitochondria, constricting the tubular organelle until the targeted part separates<sup>313</sup>. The final membrane scission step is executed by dynamin-2 (Dnm2)<sup>314,315</sup>. Loss of DRP1 functionality, for example by overexpressing double negative mutant versions, led to highly interconnected mitochondria<sup>313</sup>. Another protein involved in mitochondrial fission is Mitochondrial fission 1 protein (Fis1). Similar to DRP1, Fis1 depletion resulted in elongated mitochondria tubules, whereas overexpression of Fis1 led to highly fragmented mitochondria<sup>316-318</sup>. Contrary to yeast, where Fis1 acts as an adaptor for Dnm1, the homologue of DRP1, Fis1 in

mammalian cells promotes fission independently of DRP1<sup>318</sup>. Instead, Fis1 interferes with the fusion machinery by binding Opa1, Mfn1 and 2<sup>318</sup>.

Mitophagy refers to the selective degradation of mitochondria. In specific instances, certain cells require the complete removal of mitochondria, such as in maturing erythrocytes<sup>319</sup> or sperm-derived mitochondria after fertilisation<sup>320</sup>. However, the removal of damaged mitochondria necessitates their selective isolation from the healthy network by interfering with fusion and inducing mitochondrial fission.

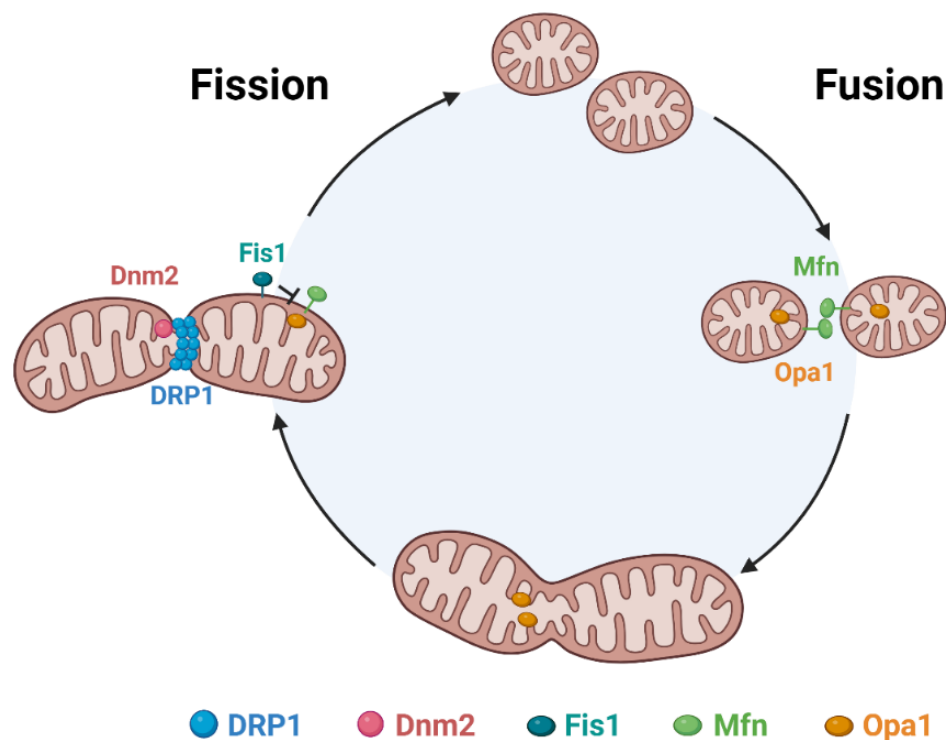


**Figure 1-9 Schematic illustration of mitochondrial dynamics of fission and fusion.** Fusion of mitochondria is primarily mediated by Mfn1 and Mfn2, which facilitate the fusion of the outer membrane, while Opa1 mediates fusion of the inner membrane. DRP1 and Fis1 are involved in mitochondrial fission, with DRP1 actively constricting and separating mitochondria, while Fis1 primarily prevents the fusion of mitochondria by blocking Mfn and Opa1. Created with BioRender.com.

### 1.5.3.2 Pink1/Parkin-mediated mitophagy

The Pink1/Parkin mitophagy pathway (**Figure 1-10**) utilises the Ser/Thr PTEN-induced kinase 1 (Pink1) as a sensor for mitochondrial damage. Under normal conditions, Pink1 is imported to the inner mitochondrial membrane via the translocase of the outer membrane (TOM) and the translocase of the inner membrane (TIM). Subsequently, Pink1 is cleaved by the mitochondrial processing

peptidase (mtPP) and the presenilin-associated rhomboid-like protein (PARL) leading to its degradation by the proteasome, thereby maintaining low Pink1 levels<sup>321,322</sup>.

In the case of damaged mitochondria, Pink1 fails to translocate to the inner mitochondrial membrane. Instead, it accumulates on the outer mitochondrial membrane. *In vitro* experiments suggest that proteolytic cleavage of Pink1 is dependent on the membrane potential<sup>323,324</sup>. Furthermore, the ADP/ATP translocase (ANT) can impede TIM-mediated protein translocation when mitochondria are depolarisation or when there is insufficient OXPHOS<sup>325</sup>. Mitochondrial uncouplers, like carbonyl cyanide m-chlorophenylhydrazone (CCCP), have been shown to trigger Pink1/Parkin-mediated mitophagy<sup>326</sup>. Consequently, Pink1 accumulates on the outer mitochondrial membrane, ultimately leading to recruitment of Parkin<sup>324,326</sup>. Pink1 autophosphorylation stabilises Pink1 dimers on the outer membrane<sup>327</sup>.

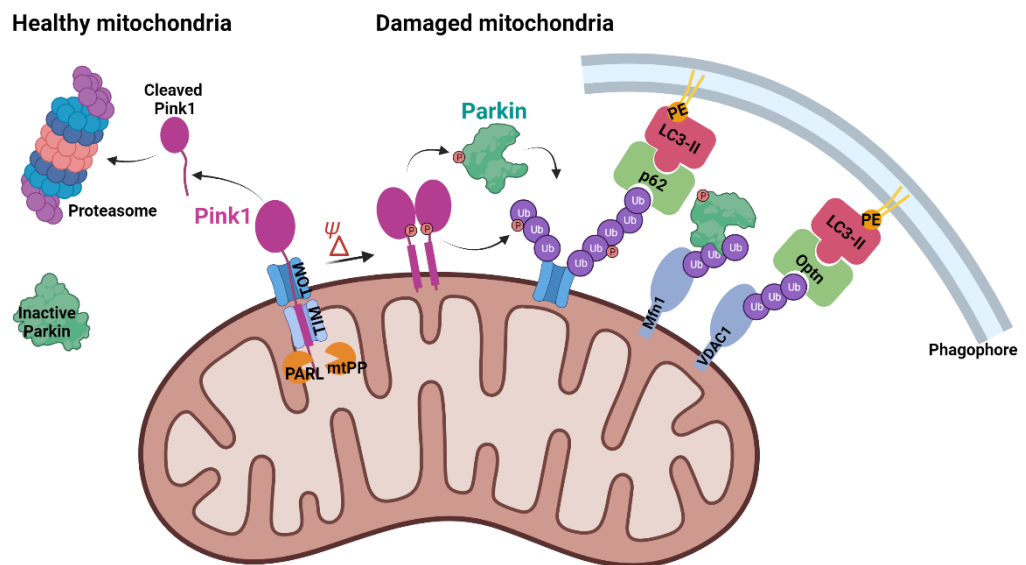


**Figure 1-10 Schematic representation of Pink1/Parkin-mediated mitophagy.** In healthy mitochondria Pink1 is imported to the inner mitochondrial membrane, where it undergoes cleavage by proteolytic enzymes (PARL and mtPP) and subsequent degradation by the proteasome. Mitochondrial damage, such as loss of mitochondrial potential, results in accumulation of Pink1 dimers on the outer membrane. Consequently, Pink1 activates Parkin by phosphorylation. Parkin, an E3 ubiquitin ligase, attaches ubiquitin chains to various proteins on the mitochondrial surface. This process functions as an 'eat-me' signal to autophagy receptors like p62 and Optn. Autophagy receptors can bind to LC3 in the autophagosomal membrane via the LIR motif. Created with BioRender.com.

Parkin, a E3 ubiquitin ligase, typically resides in an inactive state within the cytosol. Upon phosphorylation by Pink1 at Ser65, Parkin undergoes a conformational change that activates its ligase activity, enabling the

ubiquitination of key proteins on the outer mitochondrial membrane such as Tom20, Tom70 and voltage-dependent anion channel 1 (VDAC1)<sup>328</sup>. Parkin has been demonstrated to ubiquitinate Mfn1, further impeding mitochondrial fusion and resulting in isolation of the targeted organelle<sup>329,330</sup>. Pink1 additionally enhances Parkin recruitment by phosphorylating the ubiquitin chains fuelling a feedforward loop<sup>321,328</sup>. Accumulation of polyubiquitinated proteins on the mitochondrial surface attracts binding of autophagy adaptor proteins such as p62<sup>331</sup>. The role of p62 (also referred to as SQSTM1) in Pink1/Parkin-mediated mitophagy remains a topic of debate. While p62 is not required for Parkin translocation to the mitochondrial membrane, studies indicate its crucial role in clearing mitochondria<sup>332</sup>. Other studies suggest that p62 supports mitophagy by mediating aggregation of damaged mitochondria but does not aid in their delivery to the autophagosome<sup>333,334</sup>. This perspective finds support in the work of Wong *et al.*, who identified Optineurin (Optn) as an essential autophagy adaptor that facilitates the transport to the autophagosome formation during Pink1/Parkin-initiated mitophagy<sup>335</sup>.

### 1.5.3.3 Receptor-mediated mitophagy

A mitophagy pathway, mostly associated with hypoxia, involves two proteins containing a LC3-binding sequence and are regulated by HIF1 $\alpha$ : BCL2 interacting protein 3 (BNIP3) and BNIP3-like protein (BNIP3L), mostly referred to as Nix<sup>336</sup>. These proteins are located on the outer mitochondrial membrane (**Figure 1-11**). Phosphorylation of the LIR domain in BNIP3 (Ser17 and Ser24) or Nix (Ser34 and Ser35) through tank-binding kinase 1 (TBK1) increases their LC3-binding affinity<sup>337-340</sup>. Robust autophagosome recruitment requires formation of homodimers, which also increase affinity to LC3 proteins<sup>341,342</sup>.

In contrast to Pink1/Parkin-mediated mitophagy, mitophagy receptors like BNIP3 and Nix, do not require polyubiquitination and can directly interact with LC3 proteins. A similar mechanism has been observed in yeast involving the mitophagy receptor ATG23<sup>343,344</sup>, indicating that LIR phosphorylation might be a conserved mechanism for selective autophagy<sup>345</sup>. As both proteins belong to the pro-apoptotic family of BH3-only proteins, it has been suggested that phosphorylation of the LIR domain acts as the main switch towards survival function via mitophagy induction<sup>337,338</sup>.

Interestingly, evidence suggests a crossover between mitophagy pathways, wherein BNIP3 and Nix can enhance or aid in Pink1/Parkin-mediated mitophagy<sup>321</sup>. Notably, BNIP3 not only supports mitochondrial fragmentation by interaction with Opa1<sup>346</sup> as well as inducing DRP1 translocation to the mitochondria<sup>347</sup>, but also aids in Pink1 accumulation by inhibiting proteolytic cleavage of Pink1 as well as inducing Pink1 expression<sup>348</sup>. Moreover, Nix has been identified as a substrate of Parkin, and upon ubiquitination recruits the autophagy cargo receptor NBR1 to the mitochondria<sup>349</sup>.

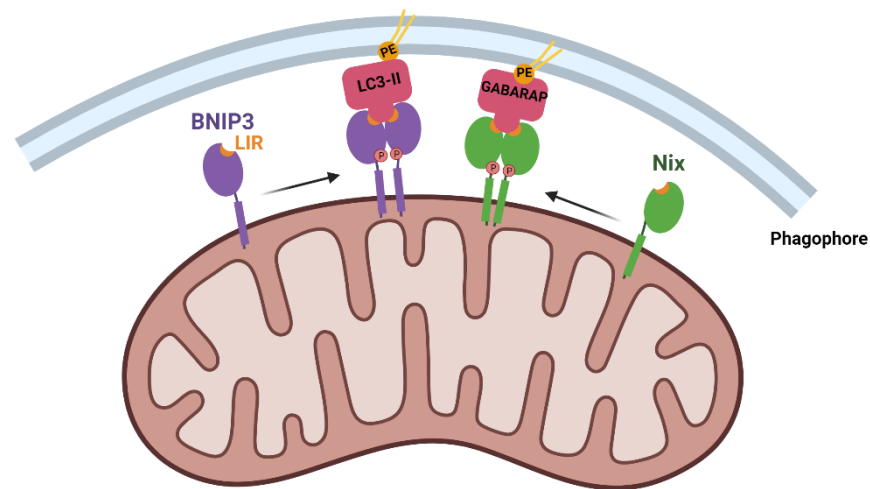


**Figure 1-11 Schematic illustration of mitophagy mediated by mitophagy receptors.** Nix and BNIP3 are proteins located on the outer mitochondrial membrane, forming homodimers upon activation. Both proteins contain LIR binding domains, enabling direct binding to autophagy adaptor proteins of the LC3/GABARAP family. Created with BioRender.com.

Another regulator of mitophagy is FUN14 domain-containing protein-1 (FUNDC1), which, like Nix and BNIP3, localises to the outer mitochondrial membrane and has the potential for direct interaction with LC3. Notably, in contrast to BNIP3 and Nix, phosphorylation of its LIR domain decreases its affinity for LC3<sup>350,351</sup>. Under basal conditions, FUNDC1 is phosphorylated at two amino acid residues: casein-kinase 2 (CK2) phosphorylates Ser13 and the steroid receptor coactivator (SRC) kinase at Tyr18<sup>350,351</sup>. Stress factors such as hypoxia induce dephosphorylation by the phosphoglycerate mutase family member 5 (PGAM5) phosphatase, leading to efficient binding of FUNDC1 to LC3 and initiation of mitophagy<sup>350,351</sup>. Similar to BNIP3, FUNDC1 can modulate the fission and fusion of mitochondria by interaction with Opa1 and DRP1<sup>351</sup>.

#### 1.5.3.4 Mitophagy in erythropoiesis

In addition to its role in clearing damaged mitochondria, Nix is best known for its involvement in the mitochondrial clearance during erythropoiesis. Nix-deficient mice display severe defects in reticulocyte maturation, characterised by retention of mitochondria in peripheral red blood cells<sup>319</sup>. This leads to anaemia and abnormal expansion of erythroid precursor cell, resulting in a reduced lifespan<sup>319</sup>. However, canonical autophagy is involved in mitochondrial clearance in reticulocytes, although this does not seem to be essential<sup>352</sup>. Deletion of ATG7 delayed mitochondria clearance but did not completely prohibit it<sup>352</sup>.

#### 1.5.4 Autophagy and mitochondrial metabolism in haematopoietic stem cells

Autophagy is known to reduce with age, which correlates with an increased risk of age-related blood pathologies like leukaemia<sup>353</sup>. Several studies support the notion that autophagy contributes significantly to maintaining healthy stem cells. Initial evidence revealed higher mTORC1 levels in aged HSCs, compared to younger counterparts<sup>354</sup>. Manipulating autophagy by deleting FIP200 in HSCs resulted in decreased HSC numbers, elevated mitochondrial mass, and ROS levels, prompting active cycling of HSCs<sup>355</sup>. Demonstrating the essential role of autophagy in normal HSCs function, Mortensen *et al.* showed that conditional ATG7 deletion in HSCs led to severe myeloproliferation and a reduced lifespan in mice<sup>356</sup>. In line with previous findings, autophagy-deficient LSK cells exhibited mitochondrial accumulation, increased ROS and consequently DNA damage<sup>356</sup>. Analysis of human and murine HSPCs (CD34<sup>+</sup> or LSK cells, respectively) revealed overall higher basal autophagy and lower ROS compared to more mature haematopoietic cells<sup>357</sup>.

According to the research conducted by Warr *et al.*, HSCs increased autophagic flux upon starvation to ensure survival, whereas their short-lived progeny lacked this ability<sup>358</sup>. Notably, autophagy-deficient HSCs from conditional ATG12 KO mice shifted from a quiescent to an activated state when starved, displaying high OXPHOS and loss of stemness<sup>46</sup>. Additionally, these cells displayed epigenetic changes akin to cytokine-activated HSCs<sup>46</sup>. Interestingly, HSCs from aged mice displayed higher basal autophagic levels, yet they still showed robust

autophagy induction upon metabolic stress and maintained HSCs function<sup>358</sup>. In a follow up study, old HSCs that exhibit high levels of basal autophagy were successful in long-term engraftment to lethally irradiated mice, whereas old HSCs with low basal levels and high mTOR activity failed to engraft<sup>46</sup>. Overall, autophagy plays a pivotal role that ensures slow aging of the stem cell by maintaining a quiescence state and preventing stem cell exhaustion.

Multiple studies have demonstrated that manipulating autophagy in HSCs affects mitochondrial homeostasis, potentially due to a blockage in mitophagy. An intriguing finding was observed in a study by Jin *et al.*, where hyperactivation of mitophagy, achieved through the deletion of ATAD3A required for Pink1 import to the inner mitochondrial membrane, resulted in impaired erythropoiesis<sup>359</sup>. Unlike inhibition, which had no effect on erythroid precursors but impacted the final maturation stage<sup>319</sup>, hyperactivation led to diminished differentiation of erythroid progenitors<sup>359</sup>. Another study emphasised the significance of a high mitochondrial turnover mediated by PPAR-FAO pathway, which regulates Pink1 on a transcriptional level via FoxO3a<sup>360</sup>. FoxO3a has been recognised as a crucial factor in HSC self-renewal<sup>41</sup>. Previous studies have associated FoxO3a with the regulation of autophagy in HSCs to minimise oxidative stress<sup>358</sup>. However, recent insights suggest that its role may extend beyond mitigating oxidative stress, focusing more on preserving healthy mitochondrial function and OXPHOS. Notably, experiments employing NAC treatment failed to restore the FoxO3a KO phenotype in mice, indicating broader impact on mitochondrial integrity rather than solely oxidative stress reduction<sup>361</sup>. This perspective gains further support from investigations conducted by Ansó *et al.*, wherein deliberate disruption of OXPHOS through manipulation of the electron transport chain (ETC) complex III resulted in apoptosis, substantial impairment of HSC differentiation, and adverse effects on HSCs function, such as loss of quiescence and competitive repopulation capacity<sup>49</sup>.

### 1.5.5 Autophagy in leukaemia

Autophagy in context with cancer is a double-edged sword. While autophagy has implications that can prevent malignant cell transformation, it has also been shown to serve various tumour-supporting functions, such as maintenance of cancer stem cells and mediating therapy resistance<sup>362</sup>. It has been demonstrated

that after treatment of CML Ph<sup>+</sup> cells with imatinib, there is an increase in autophagic flux<sup>363</sup>. This increase is specifically linked to the inhibition of BCR::ABL1, as this phenotype was not detected in Ph<sup>-</sup> cells, such as HeLa cells, or in imatinib-resistant cells expressing the mutant version T315I BCR::ABL1<sup>363</sup>. Moreover, in a study by Karvela *et al.*, the KD of ATG7 in primary CML CD34<sup>+</sup> progenitor cells resulted in increased OXPHOS accompanied with an increase in ROS levels. Further, this KD sensitised the cells to targeted treatment with imatinib and induced apoptosis<sup>364</sup>. Experiments conducted using a CML mouse model demonstrated that while imatinib treatment successfully reduced leukaemia burden, it also resulted in an increase in the primitive stem cell compartment (LSK CD48<sup>-</sup>CD150<sup>+</sup>)<sup>365</sup>. However, the combination treatment of imatinib with an autophagy inhibitor, significantly reduced LSCs suggesting that autophagy inhibition sensitises TKI-resistant LSCs to targeted therapy<sup>365</sup>. The Phase II clinical trial, CHOICES<sup>366</sup> (CHLOROquine and Imatinib Combination to Eliminate Stem cells), investigated a combined treatment approach using the front-line CML treatment imatinib, along with the autophagy inhibitor hydroxy chloroquine (HCQ). HCQ, a clinically available yet non-specific autophagy inhibitor, was administered at a tolerable dose (400-800mg daily) but did not lead to a significant improvement in treatment response compared to patients treated solely with imatinib. The authors concluded that HCQ lacks potency to sufficiently inhibit autophagy in patients at the maximum tolerated dose, thereby not providing a beneficial effect in LSC eradication<sup>366</sup>. A recent study used a novel small molecule (MRT403) that inhibits ULK1 and led to oxidative stress-related differentiation in CML LSCs without affecting healthy CD34<sup>+</sup> primary cells<sup>367</sup>. Combination treatment with imatinib in the inducible CML mouse model, showed higher efficacy with MRT403 compared to the non-specific autophagy inhibitor HCQ at targeting LSCs<sup>367</sup>. The study presents a promising perspective suggesting that exploiting the metabolic vulnerability in LSCs through highly efficacious autophagy inhibitors could offer a curative approach in CML treatment.

Inhibition of autophagy might not only be interesting for CML treatment as a similar dependency on high autophagic flux has been shown in AML<sup>357</sup>. Studies showed that a poor prognosis of AML correlates with high autophagic flux in the patients CD34<sup>+</sup> cells<sup>368</sup>. Conversely, CD34<sup>+</sup> cells from AML patients in the

intermediate- or favourable risk group exhibited high levels of ROS and low autophagic flux<sup>368</sup>. *In vitro* treatment of primary AML cells showed that ROS<sup>low</sup> cells with high autophagic flux showed greater susceptibility to autophagy inhibition than ROS<sup>high</sup> cells<sup>368</sup>. However, the authors also found that autophagy inhibition had no effect in AML cells with mutated p53, a common mutation found in AML patients with poor prognosis<sup>368</sup>. Furthermore, Qui *et al.* demonstrated a synergistic effect when targeting AML cells using the autophagy inhibitor Lys05 in combination with TKI treatment (AC220)<sup>369</sup>. A competitive transplant study involving FLT3-ITD AML mice revealed an antagonistic interaction between suppression of TKI signalling and autophagy inhibition<sup>369</sup>. While the single treatments overall reduced the repopulation potential of LSCs, the combination treatment primarily affected AML progenitors but failed to reduce and impair LSC reconstitution capacity<sup>369</sup>. Moreover, Pei *et al.* investigated mitophagy modulation via Fis1 and found it a critical pathway in AML LSCs<sup>370</sup>. Fis1 depletion led to an increase in ROS and induced myeloid differentiation in primary AML cells<sup>370</sup>. Therefore, autophagy inhibition could pose a potential treatment option for certain AML patients. However, AML is highly heterogeneous disease, and more research is needed to carefully evaluate the influence of autophagy in LSCs, especially regarding TKI treatment.

## 1.6 Aims

The aim of this study was to investigate the leukaemia niche with focus on the influence of autophagy upon TKI resistance.

Therefore, we aimed to establish genetic engineered and xenograft mouse models to enable visualisation of leukaemic cells and LSCs within the BM microenvironment. Using IVM microscopy on the calvarium for longitudinal tracking of leukaemic cells in response to TKI treatment and autophagy inhibition will deepen our insight in how the niche protects CML cells.

Furthermore, we aimed to improve our understanding of metabolic adaptation of CML cells through autophagy, particularly focusing on mitophagy.

## Chapter 2 Materials and Methods

### 2.1 Materials

#### 2.1.1 General Reagents

Product	Manufacturer	Catalogue Number
2-Mercaptoethanol 55mM	Gibco	21985-023
7-AAD	BD Pharmingen	51-6898IE
Ammonium acetate NH <sub>4</sub> Ac	Sigma Aldrich	A1542-500G
Ampicillin	Sigma Aldrich	A5354-10ML
Anhydrous DMSO	Sigma Aldrich	276855-100ML
AnnexinV APC	BioLegend	640941
Antimycin A	Fisher Scientific	15495729
Bafilomycin A1	Strattech Scientific	A8627-APE
BIT 9500 Serum Substitute, containing BSA, insulin and transferrin in Iscove's MDM	Stem Cell Technologies	9500
Bovin Serum Albumin (BSA)	VWR	422361V
Busulfan	Merck	B2635-25G
Calcium chloride (CaCl <sub>2</sub> )	Sigma Aldrich	1023780500
Carbonyl cyanide 3-chlorophenylhydrazone (CCCP)	Sigma Aldrich	C2759
CD117 MicroBeads	Miltenyi Biotech	130-091224
Chlorhexidine 0.5% in 70% Ethanol Pink Spray	Co-Clens	500mL
Compensation beads	Thermo Fisher	01-2222-42
Cytiva Amersham ECL Prime Western Blotting Detection Reagent	Amersham	RPN2235
DAPI	Merck Life Sciences	MBD0015-10ML
Deferiprone (DFP)	ApexBio	B1723
Dextran Fluorescein (FITC), 500,000MW, Anionic, lysine fixable	Invitrogen	D7136
Dextran Tetramethylrhodamine isothiocyanate TRITC	Sigma-Aldrich	52197
Dextran TexasRed, 70,000 MW, lysine fixable	Invitrogen	D1864
Diamond Carve A3	Kemdent	
Dimethyl Sulfoxide (DMSO), for freezing cell lines	Alfa Aesar	J66650
Dimethyl Sulfoxide DMSO, anhydrous	Thermo Fischer Scientific	43998
DNase I	Sigma Aldrich	11284923001
DNase Set - RNase free	Qiagen	79254
Dulbecco's Phosphate Buffered Saline (DPBS)	Gibco	14190-094
Dulbecco's Modified Eagle Medium (DMEM)	Gibco	21969-035

EasyStrainer 40µm, for 50mL tubes	Greiner	542040
ECL Western Blotting substrate	Fisher Scientific	10005943
Fc block	BioLegend	553142
Foetal Bovine Serum (FBS)	Gibco	10500064
Hair removal cream	Veet	N/A
Hank's Balanced Salt Solution (HBSS) (10X), calcium, magnesium, no phenol red	Gibco	14065049
HEPES	Sigma Aldrich	H3375-100G
High-Capacity cDNA Reverse Transcription Kit	Thermo Fisher Scientific	4387406
Hoechst 33342, Trihydrochloride, Trihydrate 10mg/mL solution in water	Invitrogen	H3570
Hydroxychloroquine (HCQ)	Fischer Scientific	10646271
Hygromycin B	Thermo Fisher Scientific	10687010
Imatinib Mesylate	LC Laboratories	I-5508
Iscove's Modified Dulbecco's Medium (IMDM)	Gibco	21980
L-Glutamine	Life Technologies	25030-024
Low density lipoprotein	Sigma Aldrich	L4646
LS Separation columns	Miltenyi Biotec	130-042-401
LysoTracker Blue DND-22	Invitrogen	L7525
Magnesium chloride	Sigma Aldrich	208337
MES SDS running buffer powder	Merck Millipore	MPMES
Methanol	Fisher Scientific	M/4056/17
MidiMACS Starting Kit	Miltenyi Biotec	130-042-301
mIL-3	BioLegend	575502
mIL-6	BioLegend	575702
MitoTracker Green	Life Technologies	M46750
mPAGE 4-12% Bis-Tris Precast Gel, 10-well/12-well/15-well	Merck Millipore	MP41G10/MP41G12/MP41G15
mPAGE Transfer Buffer	Merck	MPTRB
MRT403	LifeArc	
mSCF	BioLegend	579702
Normal goat serum (NSG)	Sigma-Aldrich	G9023-10ML
Nunc Lab-Tek Chambered Coverglass, 4-wells and 8-wells	Thermo Scientific	155411PK
NuPAGE™ LDS Sample Buffer (4X)	Invitrogen	2152677
Oligomycin	Strattech Scientific	C3007-APE
One Shot™ Stbl3™ Chemically Competent E. coli	Thermo Fisher Scientific	C737303
PageRuler™ Plus Prestained Protein Ladder	Thermo Fisher Scientific	26619
Paraformaldehyde 16%, methanol free	Alfa Aesar	043368.9L
Penicillin Streptomycin	Life Technologies	15140-122
PhosSTOP (phosphatase inhibitors)	Roche	4906845001
Pierce ECL Western Blotting Substrate	Thermo Scientific	32106
Pierce™ BCA Protein Assay Reagent A	Thermo Fischer Scientific	123221

Pierce™ BCA Protein Assay Reagent B	Thermo Fischer Scientific	23224
Pierce™ BSA Standard Ampules, 2 mg/mL	Thermo Fischer Scientific	23209
Polybrene Transfection Reagent	Merck	TR-1003-G
Poly-D-Lysine 0.1 mg/ml	Gibco	A38904-01
Potassium bicarbonate KHCO <sub>3</sub>	Sigma Aldrich	60339
Potassium Chloride (KCl)	Thermo Fisher Scientific	10684732
Pre-Separation Filters (30 µm)	Miltenyi Biotec	130-041-407
Prestained protein marker, 10-180kDa	Proteintech	PL00001
PVDF Transfer Membrane	Thermo Fisher Scientific	88520
Rapamycin	LC Laboratories	R-5000
RNase Inhibitor	Thermo Fisher Scientific	N8080119
Roswell Park Memorial Institute media (RPMI) 1640	Gibco	31870-025
Rotenone	Sigma Aldrich	R8875
Sigma 7-9 (Trizma® base, Tris base)	Sigma Aldrich	T1378
Sodium chloride (NaCl)	Sigma Aldrich	S5886
Sodium dodecyl sulfate (SDS)	Sigma Aldrich	L5750
Sodium hydroxide (NaOH)	Sigma Aldrich	S0899
Sodium phosphate dibasic dihydrate (Na <sub>2</sub> HPO <sub>4</sub> · 2H <sub>2</sub> O)	Sigma Aldrich	10028-24-7
Transfer buffer powder for use with mPAGE Bis-Tris gels, 1L	Millipore	MPTRB
Trypsin-EDTA (0.05%), phenol red	Thermo Fisher Scientific	25300054
Tween 20	Sigma Aldrich	P9416-100ML
UltraPure Ethylenediaminetetraacetic acid, EDTA	Invitrogen	15576028
Vybrant Mulicolor Cell-Labeling Kit (DiO, DiI, DiD Solutions, 1mL each)	Invitrogen	V22889

## 2.1.2 Antibodies

### 2.1.2.1 Antibodies for flow cytometry

#### Conjugated anti-human antibodies

Target	Manufacturer	Catalogue Number	Stock	Final concentration
CD45 AlexaFluor647	BioLegend	304056	0.5mg/mL	5ug/ml

## Primary anti-mouse lineage-cocktail

Target	Manufacturer	Catalogue Number	Final concentration	Recipe for 125µL
B220/CD45 R	BD Pharmingen	553086	310µg/mL	6.2µL
CD11b (Mac-1)	BD Pharmingen	553309	310µg/mL	6.2µL
CD4	BD Pharmingen	553649	40µg/mL	0.8µL
CD5	BD Pharmingen	553019	80µg/mL	1.6µL
CD8a	BD Pharmingen	553029	80µg/mL	1.6µL
Gr-1 (Ly-6G and Ly-6C)	BD Pharmingen	553125	610µg/mL	12.5µL
Ter119	BD Pharmingen	553672	1,250µg/mL	25.0µL

## Conjugated anti-mouse antibodies

Target	Manufacturer	Catalogue Number	Stock	Final concentration
CD150 (SLAM) APC	BioLegend	115910	0.2mg/mL	2µg/mL
CD45 PE	BioLegend	103106	0.2mg/mL	2µg/mL
CD45.1 FITC	BioLegend	110706	0.5mg/mL	5µg/mL
CD45.1 BV510	BioLegend	110741	0.5mg/mL	5µg/mL
CD45.2 Pacific Blue	BioLegend	109820	0.5mg/mL	5µg/mL
CD45.2 PerCP-Cy5.5	BioLegend	109828	0.2mg/mL	2µg/mL
CD48 PE	BioLegend	103406	0.2mg/mL	6µg/mL
CD48 AlexaFluor488	BioLegend	103414	0.2mg/mL	6µg/mL
cKit (CD117) APC/Cyanine7	BioLegend	105826	0.2mg/mL	2µg/mL
Gr-1 (Ly-G/Ly6C) PE	BioLegend	108408	0.2mg/mL	2µg/mL
Gr-1 (Ly-G/Ly6C) PE/Cyanine7	BioLegend	108416	0.2mg/mL	2µg/mL
Lineage cocktail Pacific Blue	BioLegend	133310	N/A	10µL in 100µL
Mac-1 (CD11b) APC	BioLegend	101212	0.2mg/mL	2µg/mL
Sca-1 PE/Cyanine7	BioLegend	108114	0.2mg/mL	2µg/mL
Ter119 APC-Cy7	BioLegend	116223	0.2mg/mL	2µg/mL

**Secondary antibodies for lineage cocktail**

Target	Manufacturer	Catalogue Number	Final concentration
Streptavidin, Pacific Blue conjugate	Molecular probes	S11222	1µg/mL

**2.1.2.2 Antibodies for microscopy****Anti-mouse antibodies used in vivo:**

Target	Manufacturer	Catalogue Number	Clone	Stock concentration
CD150 AlexaFluor647	BioLegend	115918	TC15-12F12.2	0.5mg/mL
CD31 AlexaFluor594	BioLegend	102432	390	0.5mg/mL
CD41 BV421	BD Biosciences	747729	MWReg30	0.2mg/mL
CD48 AlexaFluor488	BioLegend	103414	HM48-1	0.5mg/mL
CD48 PE	BioLegend	103406	HM48-1	0.2mg/mL
CD48 BV421	BD Biosciences	747718	HM48-1	0.2mg/mL
CD48 AlexaFluor700	BioLegend	103426	HM48-1	0.5mg/mL

**2.1.2.3 Antibodies for Western blotting****Primary antibodies**

Target	Manufacturer	Catalogue Number	Host/Source	Dilution
ATG7	Cell Signalling	8558S	Rabbit	1:500
BNIP3	Cell Signalling	44060	Rabbit	1:500
CrkL	Cell Signalling	3182S	Mouse	1:500
GAPDH	Cell Signalling	5174S	Rabbit	1:1000
HSP90	Proteintech	60318-1-Ig	Mouse	1:1000
LC3B	Cell Signalling	2775S	Rabbit	1:500
Nix/BNIP3L	Cell Signalling	12396S	Rabbit	1:500
p62	BD Biosciences	610833	Mouse	1:1000
pAGT14 (S29)	Cell Signalling	92340S	Rabbit	1:500
Phospho-CrkL (Tyr207)	Cell Signalling	3181S	Rabbit	1:500
Pink1	Cell Signalling	6949	Rabbit	1:500
B-tubulin	Cell Signalling	2146S	Mouse	1:1000

### Secondary antibodies

Target	Manufacturer	Catalogue Number	Host/Source	Dilution
Anti-mouse IgG, HRP-linked	Cell Signalling	7076S	Horse	1:10,000
Anti-rabbit IgG, HRP-linked	Cell Signalling	7074S	Goat	1:10,000

### 2.1.3 Cell Lines

The cell lines K562, KCL22 and HEK293 were available in house. Jurl-MK1 cells were kindly provided by the Vetrie lab. All cell lines were routinely tested for mycoplasma contamination.

### 2.1.4 Drugs preparation

Drug	Supplier	Catalogue Number	Vehicle	Required concentration	Storage
Antimycin A	Fisher Scientific	15495729	DMSO	4 $\mu$ M	-20 $^{\circ}$ C
Bafilomycin A1	Stratech Scientific	A8627-APE	DMSO	100nM	-20 $^{\circ}$ C
CCCP	Sigma Aldrich	C2759	DMSO	10-20 $\mu$ M	-20 $^{\circ}$ C
DFP	ApexBio	B1723	Water	1mM	-20 $^{\circ}$ C
HCQ	Fisher Scientific	10646271	DMSO	10-20 $\mu$ M	-20 $^{\circ}$ C
Imatinib	LC Laboratories	I55-08	Water	600nM-2 $\mu$ M	4 $^{\circ}$ C
MRT403	Supplied by LifeArc	N/A	DMSO	1-10 $\mu$ M	-20 $^{\circ}$ C
Oligomycin	Stratech Scientific	C3007-APE	DMSO	10 $\mu$ M	-20 $^{\circ}$ C

### 2.1.5 Equipment

Name	Supplier
Attune NxT Flow Cytometer	Thermo Fischer Scientific
CASY Cell Counter and Analyser	Roche
Electrophoresis Tank	GenScript
FACS Fusion	BD Biosciences
FACS Verse	BD Bioscience
Infinite M200 Pro Plate Reader	Tecan
IVIS Spectrum In Vivo Imaging System	Perkin Elmer
Nanodrop 2000	Thermo Fischer Scientific
Odyssey XF	Li-Cor
Peltier Thermal Cycler PTC 225	MJ Research
Western Blotting Tank	BioRad
Zeiss LSM 880 inverted confocal microscope with Airyscan	Zeiss
Zeiss LSM 880 upright confocal multiphoton microscope	Zeiss

## 2.2 Composition of buffers and media

### Complete RPMI

Component	Final Concentration
RPMI 1640	N/A
FBS, heat inactivated	10%
L-Glutamine	2mM
Penicillin-Streptomycin (Pen/Strep)	100 IU/mL

### Complete DMEM

Component	Final Concentration
DMEM	N/A
FBS, heat inactivated	10%
L-Glutamine	2mM
Penicillin-Streptomycin (Pen/Strep)	100 IU/mL

### Serum free medium (SFM)

Component	Final Concentration
IMDM	N/A
BIT 9500 Serum Substitute	20%
2-Mercaptoethanol	0.2%
L-Glutamine	2mM
Low Density Lipoprotein	40µg/mL
Pen/Strep	100 IU/mL

**SFM supplemented with murine growth factors (GF)**

Component	Final Concentration
SFM	N/A
mIL-3	10ng/mL
mIL-6	25ng/mL
mSCF	50ng/mL

**Cell freezing medium**

Component	Final Concentration
FBS	90%
DMSO	10%

**Red blood cell lysis buffer**

Component	Recipe for 1L
Milli-Q water	N/A
NH <sub>4</sub> Ac Ammonium acetate	8.02g
KHCO <sub>3</sub> Potassium Bicarbonate	1.00g
EDTA	0.02g

**Protein Lysis Buffer**

Component	Final Concentration
RIPA Buffer	N/A
PhosphoSTOP	10% of 1 tablet dissolved in 1mL RIPA buffer
Protease Inhibitor	10% of 1 tablet dissolved in 1mL RIPA buffer
SDS	10%

**Western transfer buffer**

Component	Recipe for 2L
Milli-Q water	N/A
Transfer buffer powder for use with mPAGE Bis-Tris gels, 1L	2 sachets
Methanol	200mL

**10x TBS (pH 7.5)**

Component	Recipe for 1L
Milli-Q water	N/A
Tris	60.5g
NaCl	87.6g

**1x TBST**

Component	Recipe for 1L
Milli-Q water	899mL
10x TBS	100mL
Tween20	1mL

**Western blocking buffer**

Component	Final Concentration
1x TBST	N/A
BSA	2%

**2X HEPES-Buffered Saline (HBS) (pH 7.0)**

Component	Recipe for 500mL
Milli-Q water	480mL
NaCl	8.00g
KCl	0.37g
Glucose	1.00g
HEPES	5.00g
Na <sub>2</sub> HPO <sub>4</sub> * 7H <sub>2</sub> O	500μL

**2X CaCl<sub>2</sub>**

Component	Recipe for 500mL
Milli-Q water	500mL
CaCl <sub>2</sub> * 2H <sub>2</sub> O	147g

**Flow cytometry staining buffer (2% FBS)**

Component	Final concentration
Milli-Q water	N/A
FBS	2%

## 2.3 Animal work

### 2.3.1 Ethical approval

All animal studies were conducted in accordance with the Animals Scientific Procedures Act 1986 and UK Home Office regulations. All animals were housed at the Beatson Institute for Cancer Research. Experiments were carried out under Prof. Alison Michie's project license (PD6C67A47) or Prof. Vignir Helgason's project license (PP2518370) and my personal license (PP2518370). Number and sex for each experiment is provided in each figure legend.

Pilot experiments were performed with small cohorts of mice, generally making use of surplus littermates resulting from excess breeding. In this way, we ensured optimum use of bred mice, in accordance with the ARRIVE guidelines and the 3Rs.

### 2.3.2 Genetically engineered mouse models

#### 2.3.2.1 SCLtTA/BCR::ABL1 mouse

The inducible transgenic mouse model resembling CML was generated by Koschmieder *et al.* in which p210 BCR::ABL1 is expressed in stem and progenitor cells using a tet-off system (**Figure 2-1**). This allows gene regulation by putting mice on and off tetracycline, as that prevents the tTA transcription factor from binding DNA at the promoter. The tTA was generated to be under the control of the murine stem cell leukaemia (SCL) gene 3' enhancer. Tetracycline in the drinking water (0.5g/L) prevents expression of BCR::ABL1, while removal of tetracycline induces BCR::ABL1 expression and leads to neutrophilia, anaemia, splenomegaly and extramedullary haematopoiesis in the spleen resembling CML in patients<sup>371</sup>.

Single transgenic mice (STG) describe mice that only have one of the relevant genes (either SCL-tTA or BCR::ABL1) and cannot be induced to develop leukaemia by tetracycline removal. Double transgenic mice (DTG) describe mice that have both transgenes and consistently develop a CML-like disease upon tetracycline removal within two to four weeks.

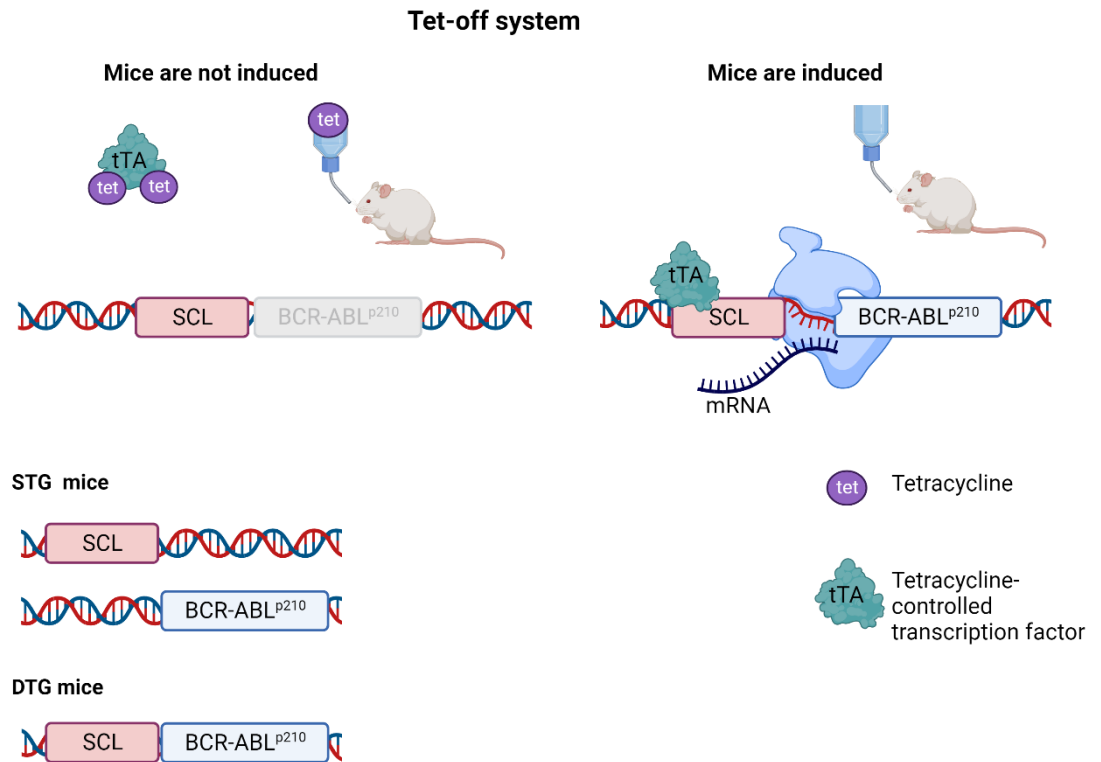


**Figure 2-1 Schematic illustration of the inducible the SCL-tTA/BCR::ABL1 mouse model.** Tetracycline (tet), administered orally via drinking water, prevents the transcription factor (tTA) from binding to the SCL promoter. Upon withdrawal of tetracycline, tTA can bind to the SCL promoter, thereby inducing the transcription of BCR::ABL1. Single-transgenic (STG) mice possess only one of the necessary genes and cannot be induced, functioning instead as control mice. Double-transgenic (DTG) mice carry both the SCL enhancer gene and BCR::ABL1, allowing for induction of leukaemia. Created with BioRender.com.

### 2.3.2.2 CD45.1 mouse

The B6.SJL-*Ptprc<sup>a</sup> Pepc<sup>b</sup>*/BoyJ (JAX Stock #002014) strain is used for allograft studies and serve as recipient mice. These mice carry the differential marker CD45.1 (*Ptprc<sup>a</sup>*) to allow differentiation from transplanted cells.

### 2.3.2.3 GFP-LC3 mouse

The GWLC mouse strain describes SCL-tTA/BCR::ABL1 mice that were crossed with the GFP-LC3 mouse model<sup>372</sup>, where GFP-LC3 is exogenously overexpressed (pCAG-GFP-LC3). The Ohsumi lab generated the GFP-LC3 mouse by transferring microinjected eggs containing the isolated DNA fragment (3.4-kbp) to pseudopregnant foster females<sup>372</sup>.

#### 2.3.2.4 mTmG mouse

The GWTM mouse was established by crossing the SCL-tTA/BCR::ABL1 mouse with the mTmG mouse (Gt(ROSA)26Sor<sup>tm4</sup>(ACTB-tdTomato,-EGFP)<sup>Luo</sup>; JAX Stock #007576)<sup>373</sup>. This mouse contains an mTmG cassette in the ubiquitously expressed endogenous ROSA26 locus on chromosome six leading to global expression of membrane-targeted tdTomato. Expression of Cre would lead to excision of tdTomato and activation of membrane targeted GFP. The SCL-tTA/BCR::ABL1 model does not have any Cre expression, therefore the cells can only ever express tdTomato.

#### 2.3.2.5 Generating chimeras by sublethal irradiation

Recipient mice (8-12 weeks old) were irradiated at two doses of 4.25Gy, three hours apart. The cells were transplanted via tail vein injection of 200µL cell suspension. Mice were kept on antibiotics for up to five days prior and two weeks following irradiation.

#### 2.3.2.6 Generating chimeras using busulfan conditioning

Mice were treated with 15mg/kg busulfan 24 hours apart with last dose 24 hours before transplant. The drug was prepared freshly just before dosing. To prepare the drug, 12.5mg busulfan was resuspended in 250µL of DMSO. Then 6mL pre-warmed (37°C) PBS was added, vortexed vigorously and kept at 37°C to prevent drug from precipitating. Dosing was done via intraperitoneal injection. The cells were transplanted via tail vein injection of 200µL cell suspension. Mice were kept on antibiotics for up to five days prior and two weeks following transplantation.

### 2.3.3 Xenograft mouse model

#### 2.3.3.1 Severe combined immunodeficient mice

Severe combined immunodeficient (SCID) mice are most widely used for xenograft studies. All studies were done with the NRGW<sup>41</sup> strain, which stands for NOD.Cg-Rag1<sup>tm1Mom</sup> Kit<sup>W-41J</sup> Il2rg<sup>tm1Wjl</sup>/EavJ (JAX Stock #026014)<sup>374</sup>. These mice are homozygous for the *Rag1*<sup>null</sup> and the *IL2*<sup>null</sup> genotypes which disrupts

maturation of T, B and NK cells. Additionally, introduction mutation in *c-kit* alleles have been shown to improve xenograft of human haematopoietic cells<sup>374</sup>.

### **2.3.3.2 Xenograft transplant with CML cell lines**

CML cells were harvested and resuspended to contain four million cells in 200 $\mu$ L of PBS. Cells were administered via IV tail vein injection.

## **2.4 Culturing of cells**

### **2.4.1 Maintenance of cell lines**

CML cell lines (K562, KCL22, Jurl) were cultured in complete RPMI (2.2) at 5% CO<sub>2</sub> at 37°C. The cells were passaged every two days and maintained at a density of 200,000 cells/mL. HEK293 cells were cultured in complete DMEM (2.2). The cells were passaged every two days using trypsin-EDTA to detach the cells from the culture flask and maintained at a density of 500,000 cells/mL.

### **2.4.2 Cryopreservation of cell lines**

Cells lines were cryopreserved by suspending the cell pellet in 1.5mL freezing medium (2.2). The cell suspension was transferred to a 2mL cryopreservation vial and placed in a -80°C freezer within a protective container (Mr. Frosty freezing container, Thermo Fischer Scientific). After 24 hours, the cryovials were transferred to liquid nitrogen containers.

### **2.4.3 Thawing of cell lines**

Cells were retrieved from the liquid nitrogen containers using dry ice. The cell suspension was rapidly thawed in a 37°C water bath. After complete thawing, the solution was transferred into a tube containing 10mL pre-warmed (37°C) complete medium (2.2). The tubes were centrifuged at 300xg for 5 minutes to pellet the cells. The supernatant containing DMSO was removed, and the cells were suspended in fresh complete medium.

## 2.5 Processing animal tissue

### 2.5.1 Red blood cell lysis

To analyse granulocytes in the blood, red blood cells were removed using the red blood cell lysis buffer (2.2). Therefore, 30-50 $\mu$ L of blood was incubated in 1mL of the lysis buffer for 10 minutes at room temperature. Afterwards, 2mL of PBS was added, and the tubes were centrifuged for 5 minutes at 350xg. The supernatant was discarded, and the cells were resuspended in flow cytometry staining solution for further analysis.

### 2.5.2 Processing bones

For cell transplantation, cells were harvested using the 'spin'-method. Small Eppendorf tubes (500 $\mu$ L) were perforated at the bottom with a 18G needle and then placed into a 1.5mL Eppendorf cup. The bones were each cut into two pieces and positioned with the opening facing downwards in the small Eppendorf cup. These tubes were subsequently centrifuged in a benchtop centrifuge for approximately 20 seconds until reaching 10,000xg. The resulting cell pellet was resuspended in 1mL of flow cytometry staining buffer and passed through a filter (0.45 $\mu$ m) into a 50mL Falcon tube. Then, 24mL of staining buffer was added and cells were counted using the Casy cell counter.

For tissue analysis, cells were harvested by crushing the bones in a mortar. The bones were placed into a clean and sterile mortar with 5mL of PBS. Gentle rocking of the pestle back and forth was employed to crush the bones without grinding, as this could damage the cells. The resulting solution was passed through a filter (0.45 $\mu$ m) into a 50mL Falcon tube. This process was repeated twice with 10mL of fresh staining buffer each time. Finally, the cells were counted using the Casey cell counter.

The cells from the calvarium were consistently obtained by crushing the bones in a total volume of 10mL staining buffer.

### 2.5.3 Processing soft tissue

Soft tissue, such as the spleen, tumours, and the brain, were processed into a single-cell solution by placing the organ onto a 0.45µm filter, which was attached to a 50mL Falcon tube. The organ was then pressed through the filter using a plunger from a 5mL or 10mL syringe. Subsequently, 5mL of PBS was added to the filter, and any remaining tissue was further pressed through. The plunger was then removed, and PBS was added to ensure equal volumes across all sample.

### 2.5.4 cKit enrichment

The cells from the leg bones were harvested using the 'spin' method and centrifuged for 10 minutes at 300xg. The supernatant was removed, and the cell pellet resuspended in the remaining solution. Subsequently, 20µL of magnetic cKit-labelled beads (CD117 MicroBeads, Miltenyi Biotech) was added to each cell pellet and carefully resuspended. The mixture was refrigerated for 15 minutes. Following this, 20mL of fresh PBS was added, and the cells were centrifuged for 10 minutes at 300xg.

During this time, the columns were equilibrated with PBS. The columns were positioned in a magnetic holder, and 30µm filter was placed on top of each column. A 15mL collection tube was set underneath the column. Then, 3mL of PBS was added to the filter atop the columns and allowed to pass through. This step was repeated twice until no liquid dropped out of the column, and the 15mL collection tube was emptied.

After centrifugation, the cell supernatant was discarded, and the pellet was resuspended in 500µL of PBS and placed onto the filter. After the solution passed through, 1mL of PBS was added to the Falcon tube to collect any remaining cells, which were then pipetted onto the filter. This step was repeated once more. Once the column stopped dripping, the filter was discarded, and the column washed with 3mL PBS three times.

The column was removed from the magnetic holder and placed in a fresh 15mL Falcon tube. Then, 5mL of PBS was added to the column, and pushed through

the column using the plunger. This process was repeated once more to achieve a final volume of 10mL. The cells were subsequently harvested by spinning for 10 minutes at 300xg.

## **2.6 Flow cytometry**

### **2.6.1 Antibody staining panels**

Cells were harvested in flow cytometry staining buffer (2% FBS) and spun down at 300xg for 5 minutes. The supernatant was discarded, and cells resuspended in 50µL of 2% FBS. Subsequently, 1µL of Fc block was added to each sample. Antibodies master mix solutions, prepared of 2% FBS, were then added to the tube. Before acquisition on a flow cytometer, the cells were filtered through a 40µm cell strainer. Detailed information about each antibody can be found in section 2.1.2.1.

### **2.6.2 Apoptosis assay**

The apoptosis assay is based on the combination of a non-permeant nucleic acid dye and detection of phosphatidylserine (PS) on the outer cell membrane. In healthy cells, PS is located on the cytoplasmic side in the plasma membrane, but a redistribution of phospholipids in early cell death leads to exposure of PS on the outer membrane. Fluorescent conjugates of AnnexinV, which has a high affinity to PS, allows identification of early apoptotic cells. Nuclear dyes, such as 7-AAD stain late apoptotic cells as their cell membranes are permeable.

Cells seeded at a density of 170,000cells/mL, were harvested by centrifugation at 300xg for 5 minutes and washed with PBS. The staining solution was prepared by adding 3µL each of 7-AAD and AnnexinV to 50µL of HBSS containing calcium and magnesium ( $\text{Ca}^{2+}$   $\text{Mg}^{2+}$ ). The staining solution was added to the cells, which were then incubated for 20 minutes at room temperature in the dark. Afterwards, 200µL of HBSS was added to each sample, followed by flow cytometry.

### 2.6.3 Mitochondrial content

Cell-permeant MitoTracker dyes were utilised to measure mitochondrial content via flow cytometry. Cells seeded at a density of 170,000cells/mL in a total volume of 5mL medium. Cells were stained with 100nM MitoTracker Green and then incubated at for 30min at 37°C in the dark. Following incubation, the cells were washed with PBS and resuspended in PBS for subsequent analysis by flow cytometry.

### 2.6.4 MitoQC high-throughput assay

Cells were seeded at a density of 170,000cells/mL with a total volume of 200µL per 96-well. Cell cultures set up in 96-well plates (flat-bottom) were transferred to 96-well plates with a V-bottom and centrifuged at 350xg for 10 minutes at 4°C. The supernatant was discarded, and cells were washed with 100µL of PBS followed by centrifugation. The cells were then resuspended in 150µL flow cytometry staining buffer containing 1µg/ml DAPI. Subsequently, the cells were acquired using the Attune NxT autosampler using the following lasers and bandpass filters:

**Table 1 Filter settings for the MitoQC flow assay on the Attune NxT**

Fluorophore	Laser	Bandpass Filter
DAPI	405nm	440/50
GFP	488nm	530/30
mCherry	561nm	620/15

### 2.6.5 Fluorescence-activated cell sorting (FACS)

Cells were harvested and resuspended at a density of 10<sup>7</sup> cells/mL in 2% FBS, followed by filtration through a cell strainer (40µm). Typically, cells were collected in 15mL tubes containing 1mL 2% FBS. Cells were isolated using the FACS Fusion.

### 2.6.6 Acquisition and analysis

All experiments were conducted using the FACSVerse or the Attune NxF. Compensation beads, stained with respective antibodies, were employed for

compensation purposes. Fluorescence Minus One (FMO) samples were acquired when necessary. All flow cytometry analysis was performed with the latest version of FlowJo.

## 2.7 Immunoblotting

### 2.7.1 Cell lysis and protein extraction

The cells were harvested by centrifugation at 300xg for 5 minutes. The resulting pellet was resuspended in 1mL ice-cold PBS and centrifuged again for at 300xg for 5 minutes. At this stage, cell pellets were either stored at -20°C or subjected to immediate protein extraction. For protein extraction, 100-300µL (depending on cell count) of lysis buffer (2.2) was added, and the cells were resuspended. Thorough cell lysis was achieved by passing the suspension through a 25 gauge needle 10-20 times until the lysate was no longer viscous, followed by centrifugation at 21,300xg for 15 minutes at 4°C. The resulting supernatant was collected in a 1.5mL Eppendorf tube and stored at -20°C until further use.

### 2.7.2 Protein quantification

The Bicinchoninic acid (BCA) assay was used to quantify the protein content in protein extractions, ensuring equal loading on protein separation gels. This assay relies on the colour change induced by the presence of proteins, resulting in the reduction of  $\text{Cu}^{+2}$  ions to  $\text{Cu}^{+}$  ions. BCA acts as a chelating agent for  $\text{Cu}^{+}$  ions, forming a purple complex that exhibits high absorbance at 562nm.

The Pierce BCA reagent kit involves a two-solution mixture. Buffer A comprises a carbonate buffer with BCA at an alkaline pH of 11, while buffer B contains a cupric-sulphate ( $\text{CuSO}_4$ ) solution. Reagent A and B were mixed in a ratio 50:1 leading to a green starting solution.

Samples preparation involves pipetting 2µL of each sample into triplicate wells of a 96-well plate. Subsequently, 198µL of freshly prepared BCA solution was added to each well. Each sample was vigorously mixed by vortexing to ensure an equal distribution of proteins. For the generation of a standard curve, triplicate wells received serially diluted BSA standards (2, 1.5, 1, 0.5, 0.25, 0.125, 0mg/mL) prepared in water. These standards, typically stored at -20°C, were

thawed at room temperature before use. For the standard curve, 10 $\mu$ L of each standard was pipetted into triplicate wells, followed by the addition of 190 $\mu$ L of BCA solution.

The plate was incubated at 37°C for 30 minutes in the dark. Protein content was subsequently measured by quantifying absorbance using a spectrophotometer plate reader. The protein quantity in the samples was determined by interpolating their absorbance values with the standard curve.

### **2.7.3 SDS-PAGE separation of proteins**

Samples were prepared by diluting 15 $\mu$ g protein in water to a final volume of 20-25 $\mu$ L, including protein loading buffer (4X). The prepared samples were thoroughly mixed and incubated at 95°C for 10 minutes to denature proteins. After brief centrifugation, the samples were carefully vortexed to ensure an even distribution of proteins within the solution. The samples were loaded into precast gels (4-12% Bis-Tris) positioned in an electrophoresis tank (GenScript), which was filled with MES running buffer. To estimate molecular weight, a protein ladder (PageRuler prestain protein ladder, ranging from 10 to 180kDa) was loaded into the first well (5 $\mu$ L). Empty lanes were loaded with 2 $\mu$ L of 4X protein loading buffer to ensure an even run. Gels were run at 120V for 75 minutes or longer, depending on protein of interest.

### **2.7.4 Western blotting**

The gels were transferred to a PVDF membrane using a wet Western blot transfer system. Consequently, the PVDF membrane was activated in methanol for 5 minutes on a shaker. The Western blot 'sandwich' was assembled as shown in **Figure 2-2**.

These 'sandwiches' were placed into a transfer chamber containing transfer buffer (2.2), with the PVDF membrane being positioned on the anode side, while the gel side faced the cathode. As the proteins are negatively charged, they are transferred to the membrane when electric current is applied for 120 minutes with 120V.

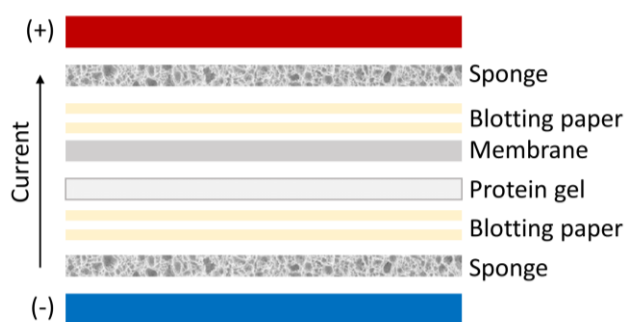


Figure 2-2 Assembly of the Western blot 'sandwich' for wet transfer.

## 2.7.5 Blocking and immunolabelling

The membranes were incubated in 10mL of Western blocking buffer (2.2) for 60 minutes at room temperature on a shaker. After blocking, the membranes were incubated with primary antibodies (2.1.2.3), which were diluted in blocking buffer, overnight at 4°C on a tube roller. The following day, the membranes underwent three washes for 10 minutes with TBST at room temperature, followed by incubation with secondary antibody (2.1.2.3) for 60 minutes. The secondary antibody is conjugated to the enzyme horseradish peroxidase (HRP), enabling visualisation via chemiluminescence. The membrane was developed using enhanced chemiluminescence (ECL) with either the Pierce ECL substrate or the Cytiva solution (Amersham), employing the Odyssey FC imaging system.

## 2.8 Microscopy

### 2.8.1 Calvarium intravital microscopy (IVM)

Non-recovery intravital microscopy (IVM) was performed according to the SOP we established at the BRU Facility of the Beatson Institute (SOP120). The technique was adapted from the Lo Celso lab at the Imperial College London. The imaging was performed with a Zeiss LSM 880 NLO MP system fitted with a 32-channel 'spectral' detector.

#### 2.8.1.1 Surgery and microscopy stage setup

Two heat pads were affixed onto the stage. The temperature was monitored to remain stable at 37°C. A sterile surgical drape was placed on top of the heat pad.

### 2.8.1.2 Preparing mouse for surgery

The mouse was weighed before surgery and an appropriate level of analgesia administered. Imaging probes were introduced via tail vein injection. Anaesthesia was induced using isoflurane at a flow rate of level 4 in 95% oxygen-enriched air at 1L/min. Hair removal cream was applied to eliminate fur on the skull. Lacri-lube eye ointment was applied to the eye using a clean cotton swab. Throughout the anaesthesia, fluids were administered by injecting 200 $\mu$ L of PBS subcutaneously every 45 minutes. Subsequently, the mouse was then moved onto the stage and positioned on the nose cone supplying isoflurane, while the flow rate was reduced to achieve stable surgical anaesthesia, confirmed by the absence of pedal reflex and stable breathing. The front paws were affixed onto the surgical stage with tape. The surgical area on the skull was disinfected using chlorhexidine solution.



Figure 2-3 Setup of the IVM on the calvarium on the microscope stage.

### 2.8.1.3 Surgery and imaging

The skin on the skull was removed to reveal the calvarium. Dental cement was freshly prepared and applied to the titanium window piece, which was immediately attached to the bone of the calvarium. After the cement was set (5-8 minutes) the metal piece was attached to stage holder. A cotton swab soaked with PBS was used to remove the periosteum carefully. Imaging was performed while monitoring stable anaesthesia.

Generally, dyes were imaged using either continuous wave excitation at specific wavelengths appropriate for the fluorophores used or using a Coherent Discovery

('two-photon') pulsed laser tuned to the appropriate wavelength. Signals were detected using a 32-array GaAsP 'spectral' detector either in wavelength mode and subsequently unmixed using reference spectra or by dividing the detector into specific wavelength 'bands' if the experiment allowed. 20x 1.0 NA water immersion (UV) VIS IR or VIS IR objectives were used.

The mouse was humanely killed with an overdose of anaesthesia. While the isoflurane flow rate was raised to level 4, 200 $\mu$ L of pentobarbital was administered via intraperitoneal injection.

### **2.8.2 *Ex vivo* calvarium imaging**

Imaging of the *ex vivo* calvarium was conducted in two ways. The mouse was humanely killed 10 to 20 minutes after IV injection. Immediately after death was ensured, the mouse was prepared similarly to IVM surgery to install a calvarium window. Another method of imaging the calvarium *ex vivo* involved excising the calvarium and subsequently affixing it to a culture dish filled with PBS. Confocal microscopy was performed immediately.

### **2.8.3 Imaging probes**

Freshly prepared in sterile PBS were stored at 4°C in the dark until administered via IV tail vein injection in the mouse.

Fluorescent dextran, suspended in sterile water at concentrations of 10 or 20 $\mu$ g/ $\mu$ L, was stored in aliquots at -20°C in the dark. Before imaging, 640 $\mu$ g Dextran was diluted in a total volume of 100 $\mu$ L of sterile PBS. Amounts were adjusted for 20% excess solution to account for dead space volume.

Fluorescent antibodies were suspended in 100 $\mu$ L of sterile PBS with administering 5 $\mu$ g per mouse. For *ex vivo* imaging in the calvarium, mice were humanely killed after 15-20 minutes to allow antibody binding.

Table 2 Antibodies used *in vivo*

Target	Manufacturer	Catalogue Number	Clone	Stock concentration	Amount
CD150 AlexaFluor647	BioLegend	115918	TC15-12F12.2	0.5mg/mL	5µg
CD31 AlexaFluor594	BioLegend	102432	390	0.5mg/mL	5-10µg
CD41 BV421	BD Biosciences	747729	MWReg30	0.2mg/mL	5µg
CD48 AlexaFluor488	BioLegend	103414	HM48-1	0.5mg/mL	5µg
CD48 PE	BioLegend	103406	HM48-1	0.2mg/mL	5µg
CD48 BV421	BD Biosciences	747718	HM48-1	0.2mg/mL	5µg
CD48 AlexaFluor700	BioLegend	103426	HM48-1	0.5mg/mL	5µg

## 2.8.4 Cell labelling with lipophilic dyes

### 2.8.4.1 Protocol for cell lines

Cells were resuspended at a density of  $1 \times 10^6$  cells/mL. 5µL per 1mL of the cell-labelling solution DiD was added and the tube was gently vortexed and incubated at 37°C for 30 minutes. The cells were then washed 2x with 2mL PBS.

### 2.8.4.2 Protocol for staining cKit enriched primary cells

Cells are pelleted and up to  $1 \times 10^6$  cells were resuspended in 400µL PBS. 10µL DiD was added followed immediately by vortexing to prevent lipophilic dye going out of solution. Cells were incubated at 37°C for 10 minutes. Cells were washed with PBS.

### 2.8.4.3 Protocol for staining LT-HSCs enriched primary cells:

Cells are pelleted and up to 100,000 cells were resuspended in 100µL PBS. 0.5µL DiD was added followed immediately by vortexing to prevent lipophilic dye going out of solution. Cells were incubated at 37°C for 10 minutes. Cells were washed with PBS.

## **2.8.5 Live cell microscopy**

### **2.8.5.1 Poly-D-Lysine coating of imaging chamber slides**

Glass bottom chamber slides were coated with a 1mg/mL poly-D-lysine solution and stored up to two months at 4°C. To each well enough solution was added to cover the surface (100µL in 8-well chamber, 250µL in 4-well chamber slides) and incubated at room temperature for 30 minutes. The solution was carefully discarded, and the wells washed twice with 0.5mL/1mL sterile PBS. The slides were then left to dry out in a sterile environment for up to three hours.

### **2.8.5.2 Cell culture setup and staining**

Cells were plated at 40.000 cells/mL in a 5mL cell culture in a 6-well plate. Treatment was added to the medium as indicated in each figure legend. After 16 hours the cell culture was resuspended and 0.5mL (for 8-well dish) or 1mL (for 4-well dish) was transferred to an Eppendorf tube. Hoechst33342 was added to a final concentration 10µg/mL. Cells were mixed well and carefully plated on a glass-bottom chamber slide and incubated in a 5% CO<sub>2</sub> incubator at 37°C in the dark for 60 minutes.

LysoTracker Blue DND-22 was added 60 minutes before microscopy to the cell medium at a final concentration of 50nM.

### **2.8.5.3 Live cell microscopy**

Cells were imaged using a LSM Zeiss880 inverted confocal fluorescent microscope fitted with an Airyscan fast detector and an 63x oil immersion objective. The microscope chamber and stage were heated to 37°C and supplied with 5% CO<sub>2</sub>. Images were acquired with the 405nm, 488nm and 561nm lasers and processed in Zen black.

### **2.8.5.4 Opera Phenix high content imaging of autophagosomes**

BM cells from a WT GFP-LC3 mouse were isolated and sorted for LSK GFP<sup>+</sup> cells into a 96-well plate (Greiner µClear) at a density of 500 cells per well. Cells were cultured in SFM (2.2) for 24 hours in an incubator set to 37°C with 5% CO<sub>2</sub>. Live-cell imaging was conducted with the Opera Phenix high content imaging

system and analysis was conducted using the Harmony software, quantifying GFP spots per cell.

### **2.8.6 Image processing**

Images acquired in spectral mode were processed in Zen (black) using linear unmixing with reference spectra from single colours. Images acquired with the Airyscan detector were also processed in Zen (black).

## **2.9 Generation of stable cell lines and CRISPR/Cas9-mediated gene editing**

### **2.9.1 Transformation into Stbl3 bacteria**

Stbl3 bacteria were thawed on ice, followed by the addition of 5 $\mu$ L of DNA. The solution was gently mixed, and vials were incubated on ice for 30 minutes. The bacteria underwent a heat-shock for 45 seconds in a water bath set to 42 $^{\circ}$ C, followed by 2 minutes on ice. Subsequently, 250 $\mu$ L pre-warmed S.O.C medium was added to each vial. The vials were placed in a shaker set to 37 $^{\circ}$ C for one hour at 225rpm. Then, 100 $\mu$ L from each vial was spread onto pre-warmed ampicillin selective plates and incubated overnight at 37 $^{\circ}$ C. The following day, three colonies from each plate were collected in 5mL LB medium and placed in the shaker for the remaining day. The pre-inoculum was then added to 250mL of LB medium supplemented with ampicillin (50 $\mu$ g/mL) and incubated overnight while shaking at 37 $^{\circ}$ C. The next day, the culture was centrifuged at 3,500 $\times$ g for 30 minutes at 4 $^{\circ}$ C, and the pellet was stored at -20 $^{\circ}$ C until DNA was isolated via maxi-prep. Glycerol stocks were prepared by mixing 500 $\mu$ L of bacterial culture with 500 $\mu$ L of 50% glycerol and stored at -80 $^{\circ}$ C.

## 2.9.2 CRISPR/Cas9

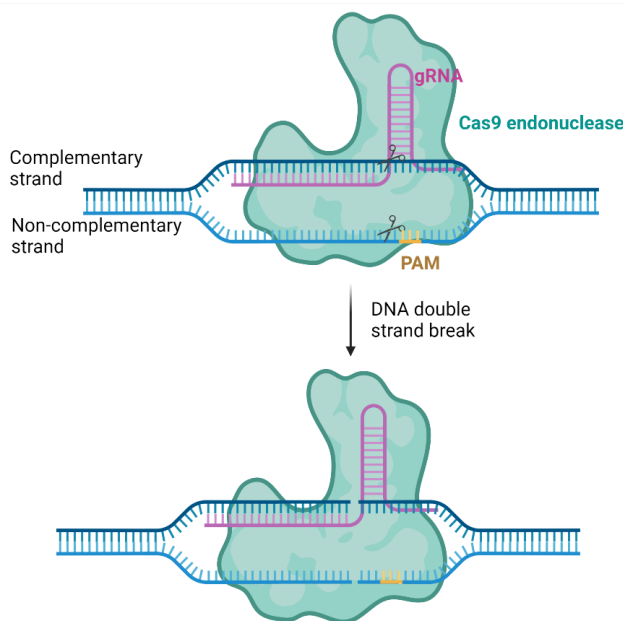


**Figure 2-4 Schematic representation of CRISPR/Cas9.** Guide RNA recruits the Cas9 endonuclease to the target gene and binds the complementary strand. A proto-spacer adjacent motif (PAM) has to be present when designing the target sequence. Created with BioRender.com.

Clustered Regularly Interspaced Short Palindromic Repeats (CRISPR)/Cas9 genome editing can be utilised to generate gene-specific knockout cell lines<sup>375</sup>. The Cas9 enzyme binds a short guide RNA (gRNA) and forms a binary complex (**Figure 2-4**). When designing the target sequence, it is crucial to look for a proto-spacer adjacent motif (PAM) upstream of the target sequence<sup>376</sup>. Cas9 is directed to the target site by the gRNA, and its two nuclease domains cause a double strand break. Non-homologous end joining (NHEJ) leads to insertion or deletion of base pairs during the repair process of the double strand break, resulting in the loss of function in the desired gene<sup>376</sup>.

**Table 3 CRISPR/Cas9 guides targeting sequence**

Gene	Targeting Sequence
ATG7	5'-GAAGCTGAACGAGTATCGGC-3'
Nix	5'-GTTCTGTGTCTTTAAGCATG-3'
BNIP3	5'-ATGGGATTGGTCAAGTCGGC- 3'

The targeting sequence for ATG7 were designed and generated by Dr. Angela Ianniciello, who also performed the cloning into the LentiCRISPR plasmid. The targeting sequence for Nix and BNIP3 were generated by Daniele Sarnello, who also performed the cloning into the LentiCRISPR plasmid.

2.9.3 Plasmid vectors

Created with SnapGene®

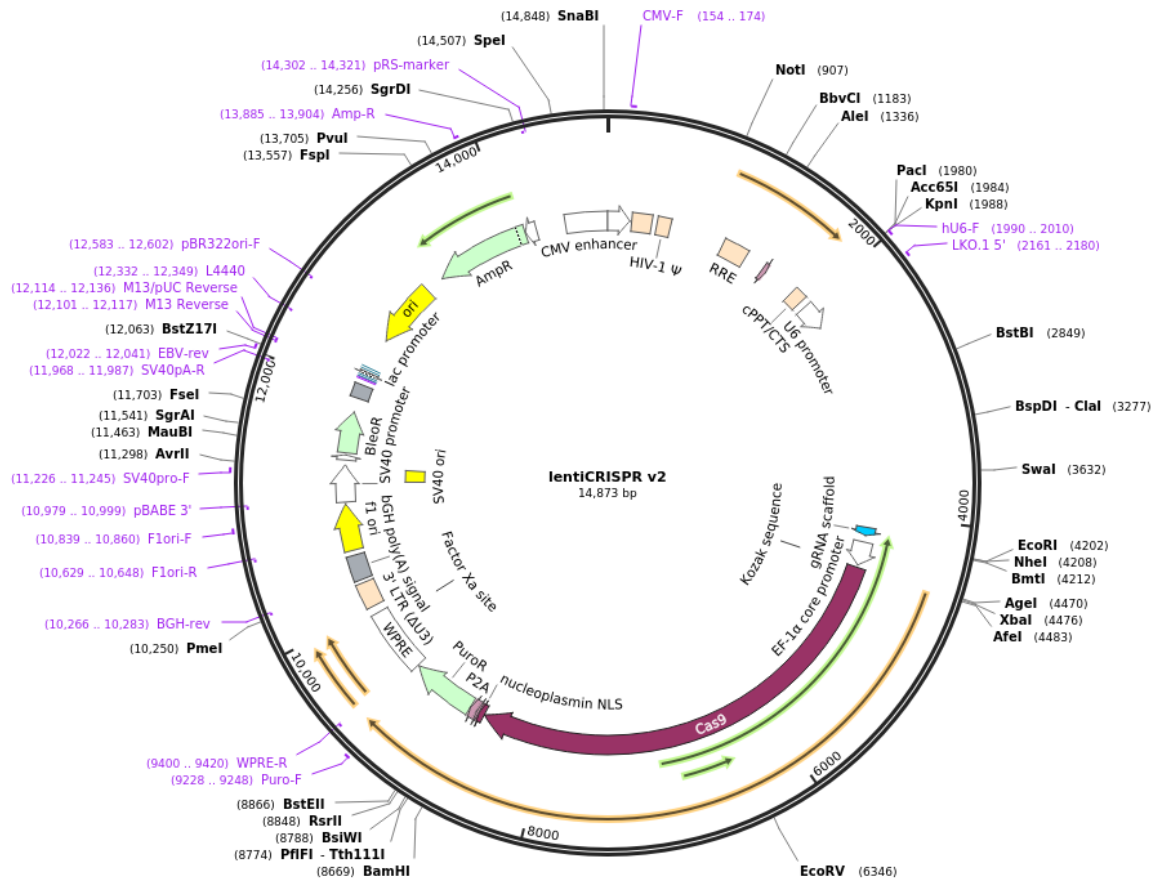


Figure 2-5 Vector map of LentiCRISPR V2 plasmid containing a puromycin-resistance marker for selection (Addgene plasmid #52961).

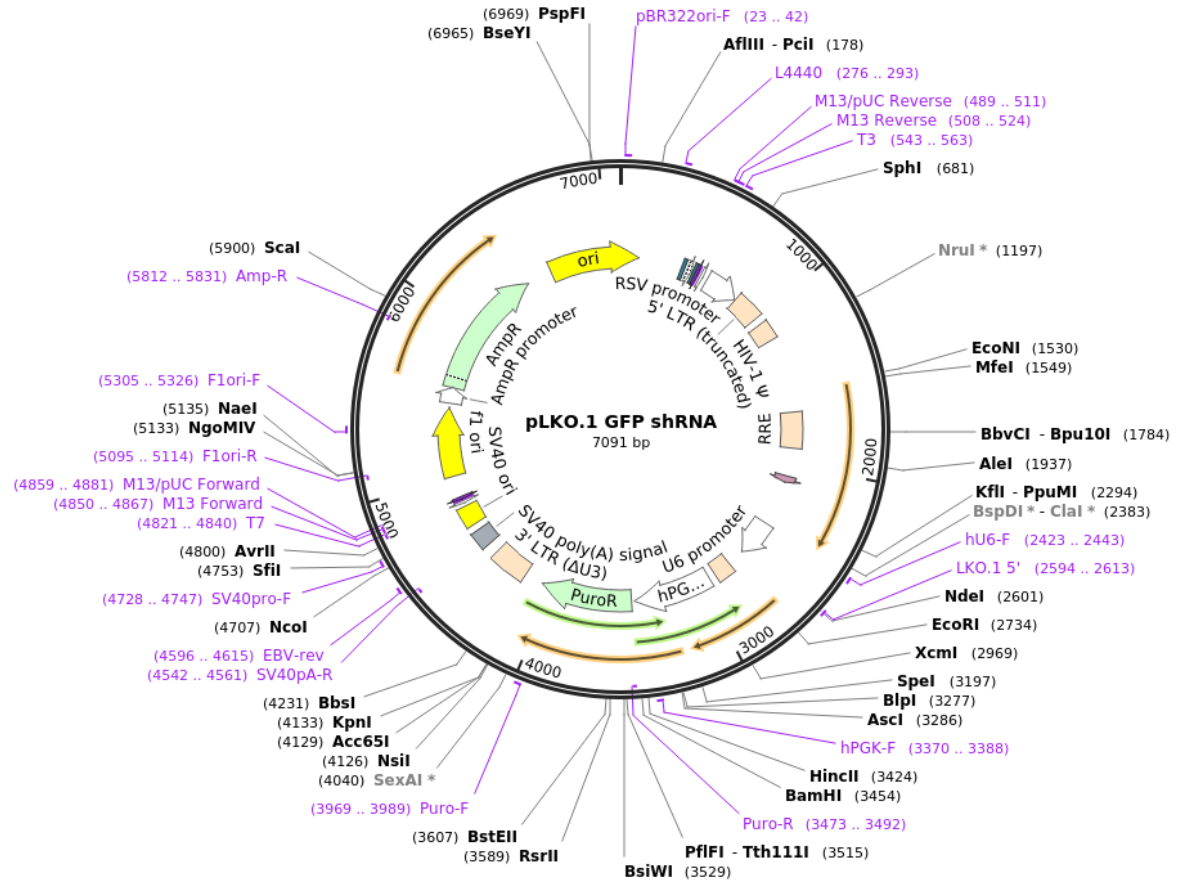


Figure 2-6 Vector map of pLKO.1 GFP shRNA (Addgene plasmid #30323).

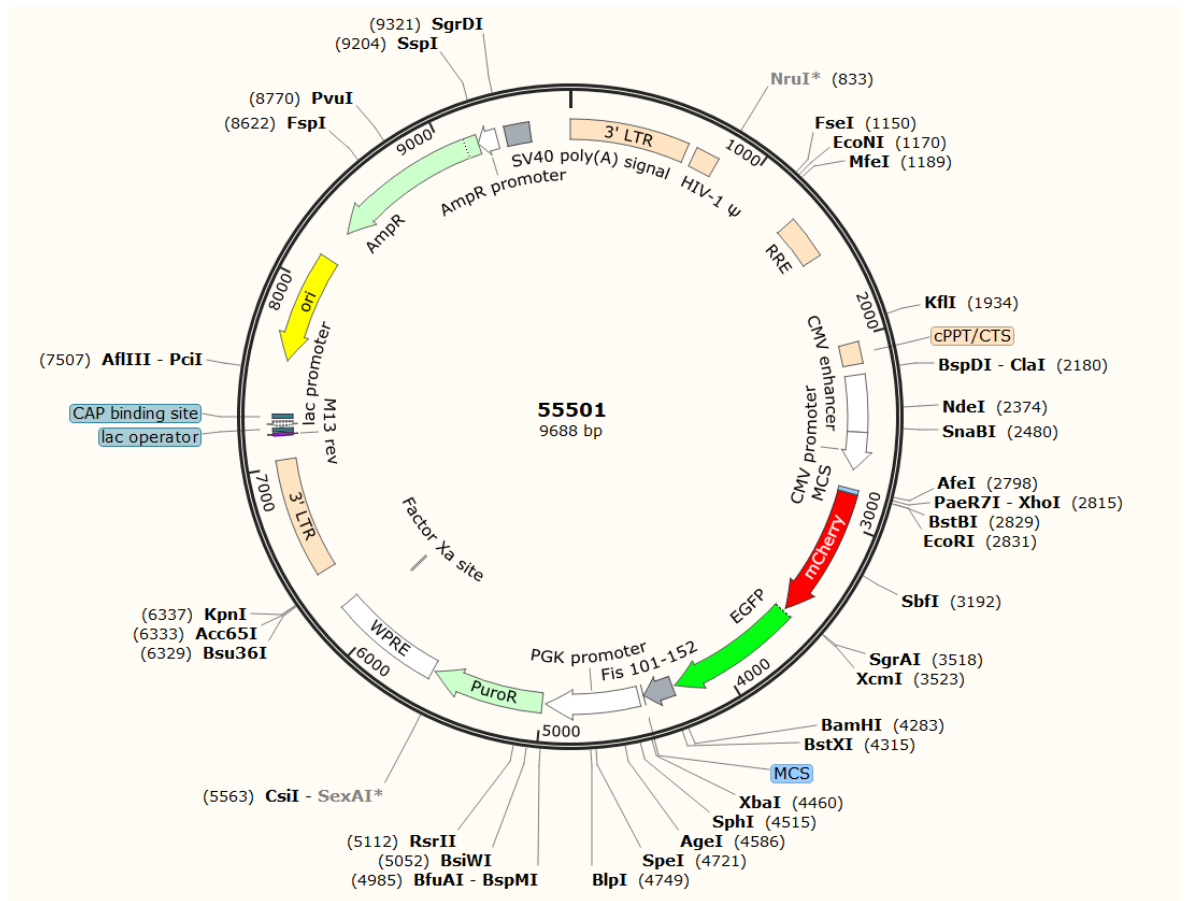


Figure 2-7 Vector map of pLVX mCherry-GFP-mtFIS1(101-152) was a gift from the Ganley lab from the University of Dundee.

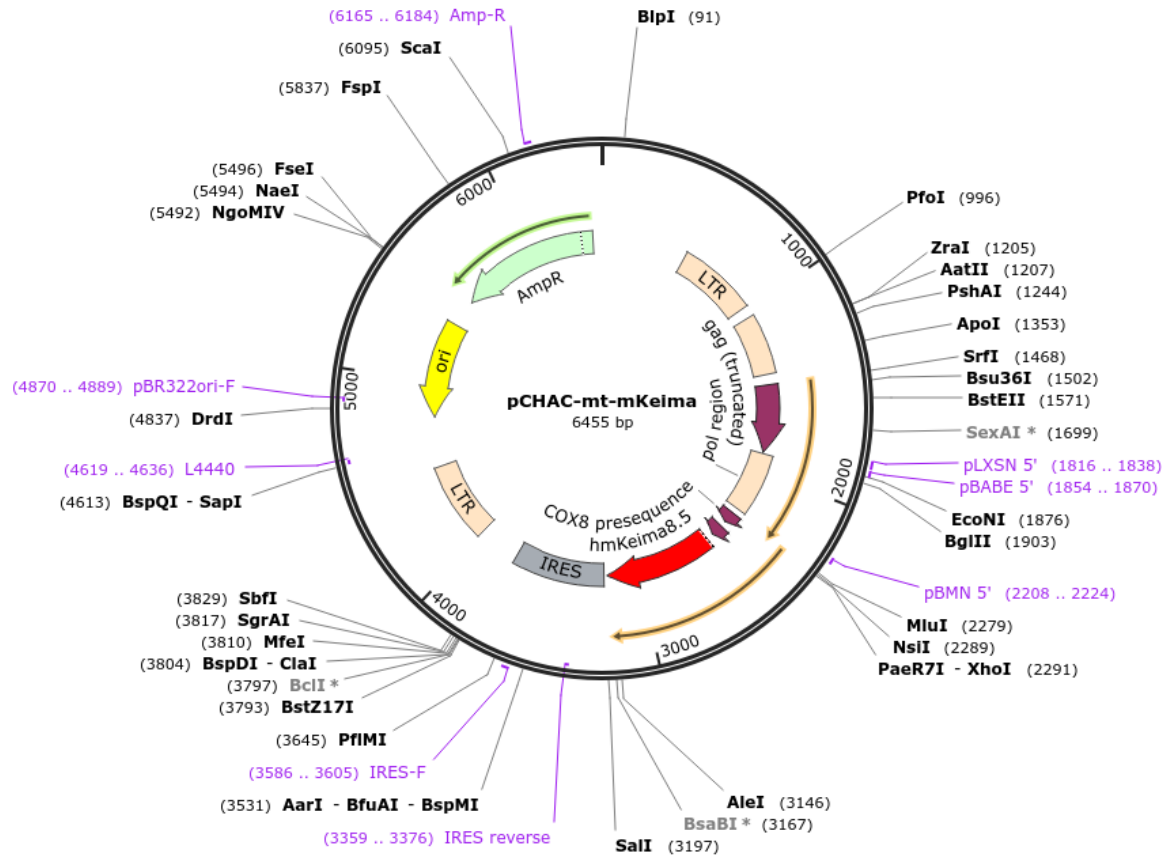


Figure 2-8 Vector map of mtKeima (Addgene plasmid # 72342).

### 2.9.4 Viral transduction of cell lines

HEK293 cells were seeded in a 10cm<sup>2</sup> culture dish with 0.8x10<sup>6</sup> cells/dish in 10mL DMEM and incubated to grow at 37°C in an incubator with 5% CO<sub>2</sub>. Once cells reached approximately 80% confluency (approximately 72 hours), culture medium was replaced with 9mL fresh medium.

Then the DNA mixture was prepared in distilled water as described in **Table 4** or **Table 5** and mixed. Then 500µL of 2XHBS was added and mixed again. Then 60µL CaCl<sub>2</sub> was added, and the solution was immediately mixed using a pipette by pipetting up and down 20 times. The mixture was incubated at 37°C for 30 minutes. Following incubation, the mixture was added dropwise onto the cells. The culture dish was gently swirled to distribute the DNA equally. The following day the medium was removed and discarded. 10mL fresh DMEM medium was added carefully to the cells. After 24 hours the medium was collected for the first transduction round. 10mL of fresh DMEM was added onto the HEK293 cells for a second round of transduction.

The medium containing the virus was subjected to centrifugation to remove contaminant cells or debris at 300xg for 5 minutes. The solution was filtered through a 0.45µm filter. After adding polybrene (8µg/mL), the solution was used to resuspend the target cells, 0.5x10<sup>6</sup> CML cells. This procedure was repeated the following day. 24 hours after the second transduction round, the CML cells were harvested by centrifugation and resuspended in fresh RPMI. Cells were left to recover for 48 hours, then antibiotic selection was started. Fluorescent cells were further subjected to FACS for purification. KO was validated via Western blotting.

**Table 4** Lentiviral transfection mix

DNA	Amount
Lentivector plasmid	10.0µg
Packaging plasmid psPAX2	7.5µg
Envelop plasmid VSVG	4.0µg
Milli-Q water	Make up to 440µL

Table 5 Retroviral transfection mix

DNA	Amount
Retro plasmid	10.0 $\mu$ g
Packaging plasmid gag/pol	7.5 $\mu$ g
Envelop plasmid VSVG	4.0 $\mu$ g
Milli-Q water	Make up to 440 $\mu$ L

## 2.10 Statistical analysis

The data were plotted and analysed using GraphPad Prism (GraphPad Software 10.1.2) as mean +/- standard error of mean (SEM) or as standard deviation (S.D.) as outlined in the figure legends. The statistical tests utilised are noted in the figure legends. Results were considered statistically different when P values were  $\leq 0.05$ .

## Chapter 3 Modelling GEMMs to track leukaemic cells in the BM niche and study the role of autophagy upon BM microenvironment interaction

### 3.1 Introduction

Although CML treatment has significantly advanced with the use of TKIs, TKI resistance in LSC remains a current focus for investigating novel curative therapies. The study of LSCs is challenged by their inaccessibility of their location within the bone. This chapter focuses on multiple approaches to track leukaemic cells and LSCs within the murine BM. The primary objectives revolve around localizing LSCs in the BM using *in vivo* imaging and exploring BM niche remodelling induced by LSCs. Additionally, the investigation aims to shed light on the role of autophagy in LSC persistence, observing autophagic flux, and employing autophagy inhibitors in an *ex vivo* setting.

To date, one of the most widely accepted mouse models for CML is the SCL-tTA/BCR::ABL1 model introduced by Koschmieder *et al.* in 2005<sup>371</sup>. These mice, referred to as double transgenic (DTG), are engineered to express BCR::ABL1<sup>p210</sup> under the HSC-specific SCL enhancer element. Using the Tet-off system, reporter genes can be silenced by the administration of tetracycline (tet) via drinking water, suppressing BCR::ABL1 expression. Upon removal of tetracycline from the drinking water, the mice exhibit the development of CML-like symptoms, including splenomegaly, leukocytosis, and infiltration of organs by extramedullary myeloid cells within a span of two to four weeks. Single transgenic mice (STG), possessing only one of the two necessary genes for BCR::ABL1 expression, serve as the control group.

Previously, our lab crossed SCL-tTA/BCR::ABL1 with the autophagy mouse model expressing GFP-LC3. In this chapter, we investigated the potential of leveraging GFP-LC3 as a marker for stem cells and assessed the model's suitability for monitoring autophagic flux *ex vivo* and *in vivo*. Furthermore, the chapter delves into examining the viability of *ex vivo* staining of stem cells before allografting into WT recipient mice for prolonged cell tracking. Additionally, we explored the use of different antibodies to label stem cells *in vivo*. Moreover, this chapter

encompasses the evaluation of a fluorescent mouse model expressing membrane-targeted tdTomato (mT) for tracking leukaemic cells and assesses various methods of transplanting donor BM cells into WT recipients while minimizing impact on BM architecture.

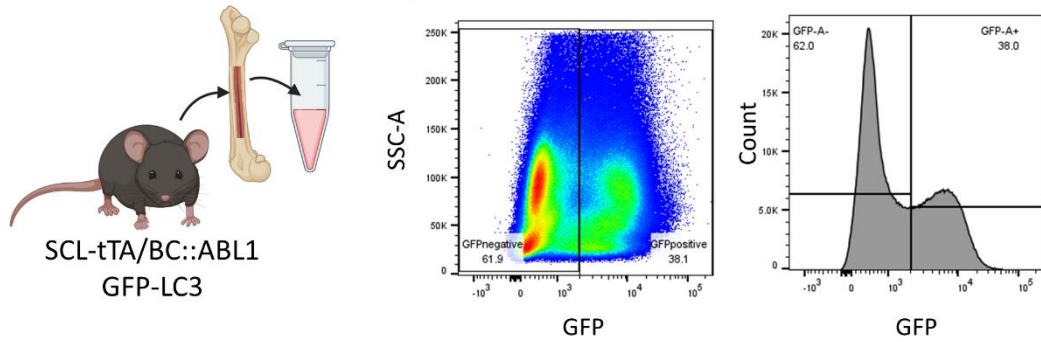
### **3.2 Validating the SCL-tTA/BCR::ABL1 GFP-LC3 model for *in vivo* LSCs localisation**

Our laboratory previously developed a CML mouse model that is suitable for studying autophagy. The SCL-tTA/BCR::ABL1 mouse was crossed with the GFP-LC3 mouse developed by the Ohsumi lab<sup>372</sup>. This specific mouse model expresses GFP-LC3 under the control of the CAG promoter, resulting in its constitutive overexpression<sup>372</sup>. LC3 is an abundantly expressed protein, involved in the formation and elongation of autophagosomal membranes and localises to the membrane of autophagosomes<sup>292</sup>. It serves as a marker to observe autophagic flux, evident by the formation of ‘puncta’ upon autophagy induction, referring to small fluorescent dots representing the number of autophagosomes per cell<sup>377</sup>. In this section we hypothesise that GFP-LC3 could not only be used as a readout for autophagic flux *in vivo* in HSCs, but can also serve as a marker for primitive cells in this GEMM.

#### **3.2.1 GFP as a marker for primitive cells in the SCL-tTA/BCR::ABL1 GFP-LC3 mouse model**

While Mizushima *et al.* confirmed that GFP-LC3 overexpression does not affect autophagic flux without an autophagy stimulus, such as fasting of the mice, they observed variations in GFP-LC3 expression levels across different organs<sup>372</sup>. However, their investigation did not encompass cells residing in the BM. The only haematopoietic cells they examined were peripheral blood cells, such as erythrocytes, which exhibited low to no GFP-LC3 expression<sup>372</sup>. Our lab has previously shown that haematopoietic cells isolated from the BM exhibit varying levels of GFP-LC3 expression<sup>365</sup>. In this section we address the question whether expression of GFP-LC3, henceforth referred to as GFP<sup>high/low</sup>, is correlated to cell stemness. Therefore, we first analysed GFP levels within stem cells compared to mature cells by flow cytometry.

## a. GFP levels in BM sample



## b. Gating strategy LSK-SLAM

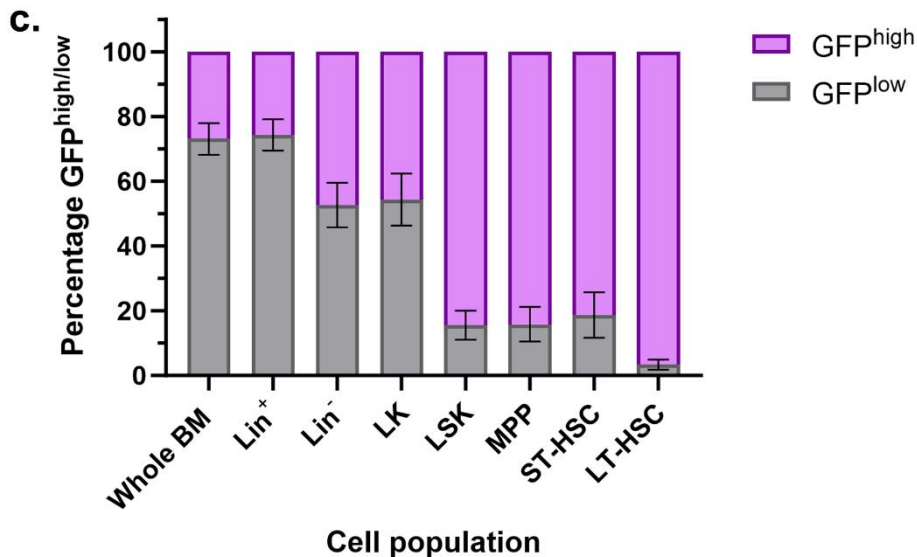
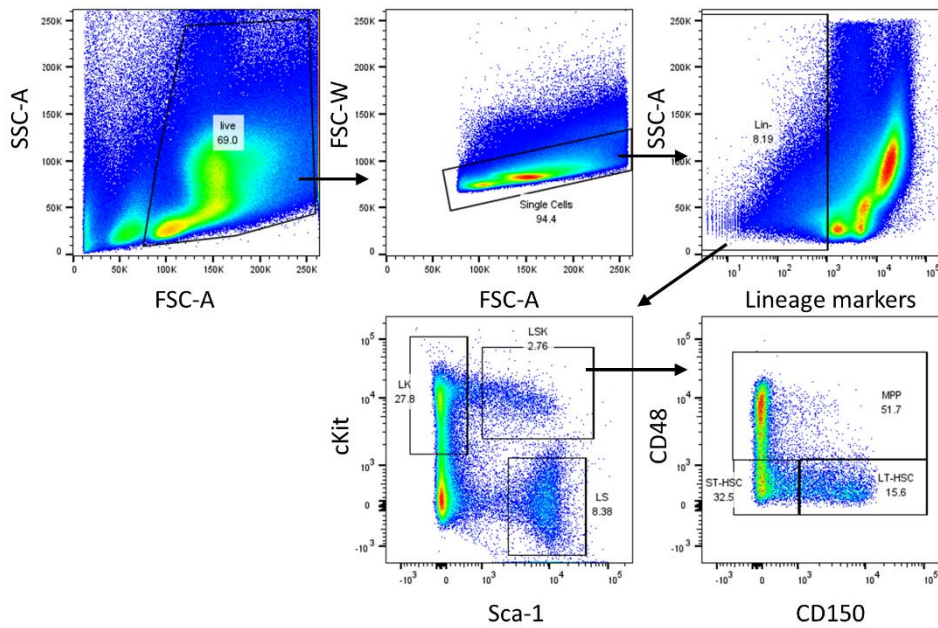


**Figure 3-1** GFP-LC3 expression is notably high in primitive BM cells within the SCL-tTA/BCR::ABL1 GFP-LC3 mouse model. The measurement of GFP expression in BM cells obtained from the leg bones of a SCL-tTA/BCR::ABL1 GFP-LC3 mouse is shown in (a). Utilising the LSK-SLAM gating strategy (b), increasingly primitive cells were isolated to measure the percentage of GFP<sup>high</sup> and GFP<sup>low</sup> cells in different cell populations (c). The graph illustrates the mean values +/- SEM of n=5 mice. Lin<sup>+/-</sup> = lineage-enriched/depleted population; LK = lineage-negative cKit<sup>+</sup> cells; LSK = lineage-negative cKit<sup>+</sup> Sca-1<sup>+</sup> cells; MPP = multipotent progenitor cells (CD150<sup>+/-</sup>CD48<sup>+</sup>); ST-HSCs = short-term haematopoietic stem cells (CD150<sup>-</sup>CD48<sup>-</sup>); LT-HSCs = long-term haematopoietic stem cells (CD150<sup>+</sup>CD48<sup>-</sup>).

Upon harvesting BM cells from SCL-tTA/BCR::ABL1 GFP-LC3 mice, we observed that the majority of BM-residing cells (~60%) did not exhibit GFP-LC3 expression, termed the GFP<sup>low</sup> population (**Figure 3-1a**). Employing the LSK-SLAM gating strategy, as illustrated in **Figure 3-1b**, we segregated more primitive cell populations from the more differentiated and mature BM cells. Initially, cells are gated for Lin<sup>-</sup> (excluding those expressing CD4, CD5, CD8a, CD11b, B220, Ter119, Gr-1 surface markers, thus constituting the Lin<sup>+</sup> population). From this Lin<sup>-</sup> subset, cells expressing both Sca-1<sup>+</sup> and cKit<sup>+</sup> were selected, forming the LSK population. Surface markers from the SLAM family can differentiate the LSK into subpopulations of ST-HSCs (CD150<sup>-</sup>CD48<sup>-</sup>), MPPs (CD150<sup>+/-</sup>CD48<sup>+</sup>) and LT-HSCs (CD150<sup>+</sup>CD48<sup>-</sup>).

To this date, there is no single surface marker for HSCs, and the combination of different markers is a useful strategy to highly enrich for stem cells. The LSK-SLAM gating strategy is a common method to further separate HSPCs into subpopulations. It should be noted that when referring to any subpopulation, for instance LT-HSCs, it comprises a heterogenous cell population that is highly enriched for the specific cell type.

Our analysis, conducted across multiple mice (n=5, **Figure 3-1c**) shows that LSK cells express higher levels of GFP compared to less primitive cell populations (Lin<sup>+</sup>, LK). Particularly, the LT-HSCs consistently demonstrated the highest levels of GFP-LC3 expression.

### **3.2.2 Autophagic flux induced by growth factor withdrawal *in vitro* in primary cells derived from GFP-LC3 mouse**

Prior to employing the GFP-LC3 model for *in vivo* studies, primary mouse cells were isolated to measure autophagic flux *in vitro*. The removal of cytokines from the growth medium induced metabolic stress due to reduced uptake of glucose in primary BM cells, resulting in the formation of 'puncta'<sup>358</sup>. To assess if autophagic flux can be measured in primary HSPCs, BM cells were incubated in primary cell medium supplemented with growth factors (+GF) and in medium without growth factors (-GF). Additionally, cells were incubated without GF but with the autophagy inhibitor HCQ to trap GFP-labelled autophagosomes before their fusion with lysosomes, which would lead to degradation of GFP-LC3. Flow

cytometry analysis of GFP in different cell populations, gated for GFP<sup>high</sup> and GFP<sup>low</sup> (**Figure 3-2**), indicated a reduction in the GFP<sup>high</sup> cell population within primitive cell subsets (LSK, ST-HSCs, MPPs and LT-HSCs) when cultured without GF (**Figure 3-2a&b, d&e**). Addition of HCQ to the medium restored GFP levels, indicating that autophagic flux is increased upon GF withdrawal and GFP-LC3 not degraded in HCQ treated cells (**Figure 3-2c&e**).

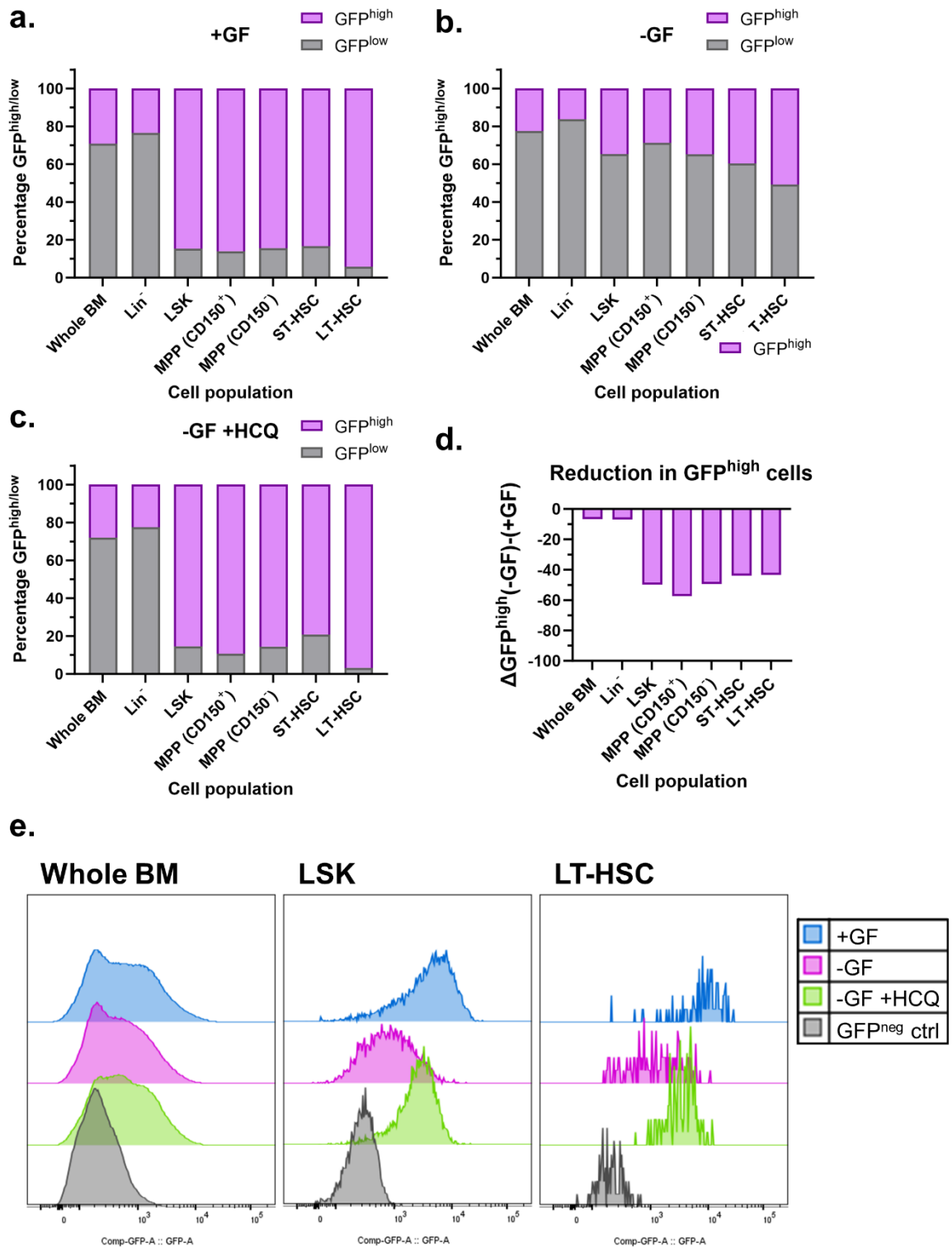


**Figure 3-2 GFP-LC3 enables the monitoring of autophagic flux in primary mouse BM cells.** BM cells from a WT GFP-LC3 mouse were harvested from leg bones and cultured in primary cell medium for 16 hours under three conditions: (a) containing the growth factors (GF) IL-3, IL-6 and SCF, (b) without GF, and (c) without GF but with the autophagy inhibitor HCQ. These cells were then stained for LSK-SLAM, and flow cytometry was utilised to measure GFP levels, assessing the percentage of GFP<sup>high</sup> and GFP<sup>low</sup> cells within each population. Bar chart (d) shows the difference of GFP<sup>high</sup> cells between the condition lacking GF compared to cells cultured with GF. Representative histograms of total BM cells, LSK and LT-HSCs are shown (e). These results represent one experiment with the BM of one mouse. Lin<sup>-</sup> = lineage-depleted population; LSK = lineage-negative cKit<sup>+</sup> Sca-1<sup>+</sup> cells; MPP = multipotent progenitor cells (CD150<sup>+</sup>/CD48<sup>+</sup>); ST-HSCs = short-term haematopoietic stem cells (CD150<sup>-</sup>CD48<sup>-</sup>); LT-HSCs = long-term haematopoietic stem cells (CD150<sup>+</sup>CD48<sup>-</sup>).

To confirm 'puncta' formation in primitive BM cells, high-throughput confocal microscopy was employed. Therefore, LSK-GFP<sup>high</sup> cells were sorted into a 96-well plate containing different medium conditions: +GF for steady state measurement, -GF to induce metabolic stress, +GF +HCQ to observe basal autophagic flux, and -GF +HCQ to measure autophagic flux upon metabolic stress. Cells were imaged after 16 hours of incubation, and representative microscopy images revealed cytosolic distribution of GFP-LC3 in steady state cells with occasional sparse GFP-'puncta' formation (**Figure 3-3a**). In line with flow cytometry data, cells under metabolic stress (**Figure 3-3b**) demonstrated an increased number of 'puncta' per cell or complete degradation of GFP-LC3. Both conditions containing the autophagy inhibitor HCQ exhibited formation of large GFP<sup>+</sup> 'puncta' (**Figure 3-3c&d**). Quantitative analysis was done by applying the Harmony software to count GFP<sup>+</sup>-spots per cell (**Figure 3-3e**), while excluding cells where GFP signal vanished (**Figure 3-3f**). Withdrawal of GF resulted in a 4-fold increase in 'puncta'-formation accompanied with an increase in GFP<sup>neg</sup> cells compared to the non-stressed cells. As expected HCQ treatment leads to accumulation of GFP<sup>+</sup>-puncta in both culture media demonstrating active autophagosome turnover without degradation by the lysosome. This *in vitro* study highlights the suitability of GFP-LC3 as a model for investigating autophagic flux in primitive BM cells.

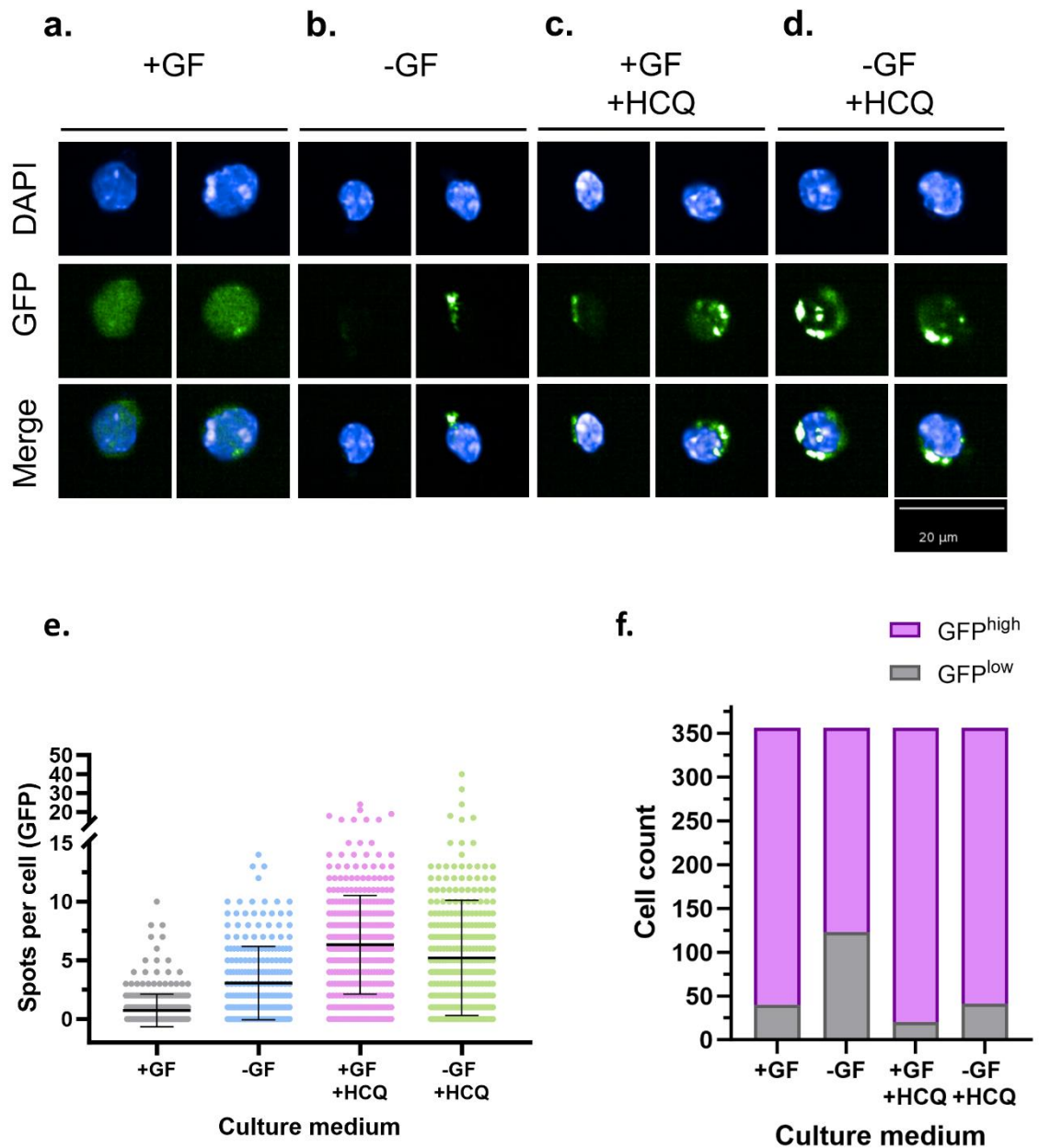


**Figure 3-3 Increased autophagosome formation in GFP<sup>+</sup> LSK cells upon metabolic stress.** LSK GFP<sup>high</sup> cells obtained from a WT GFP-LC3 mouse were sorted into a 96-well plate at a density of 500 cells per well. Cell cultures were subjected to four conditions: (a) with growth factors IL-3, IL-6 and SCF, (b) without growth factors, (c) with growth factors and hydroxychloroquine (HCQ), and (d) without growth factors but with HCQ. Imaging was conducted with the Opera Phenix, displaying two representative images with DAPI staining for the nucleus, GFP fluorescence, and merged images (a-d). Images show cytosolic diffused GFP-LC3 in (a), which localises to autophagosomal 'puncta' (b-d) and vanishes with high autophagic flux within the measured time period (b). Subsequent image analysis was performed using the Harmony software, quantifying GFP<sup>+</sup> spots per cell and the data is presented in a dot plot (e). A stacked bar chart illustrates the percentage of GFP<sup>high</sup> and GFP<sup>neg</sup> cells per condition after 16 hours of culture (f). Graphs indicate mean values  $\pm$  S.D. of one experiment analysing 356 cells per condition.

### 3.2.3 BM conditioning via irradiation was required for BM cell engraftment of BCR::ABL1 expressing leukaemia cells

Although cells transplanted into mice that underwent irradiation will ensure long-term repopulation of the recipient mice, irradiation does lead to damage of the BM microenvironment<sup>75,378,379</sup>. As the number of available niches is low in unconditioned mice<sup>380-382</sup>, we hypothesise that BM cells enriched for Ph<sup>+</sup> HSPCs could lead to successful engraftment as niche competition is reduced due to lack of carrier cells. In the following experiment, we aimed to ascertain the transplantability of the DTG model into non-conditioned mice to maintain the physiological microenvironment intact.

Generally, allografts are performed by conditioning recipient mice with a sublethal dose of 2x 4.25 Gray (minimum three hours apart) up to 24 hours before transplant or on the same day. To compare long-term reconstitution and engraftment of BM cells in non-irradiated and irradiated mice, we allografted three mice per arm with DTG GFP-LC3 cKit-enriched cells (**Figure 3-4**). Enrichment for primitive cells was done using magnetic cell separation selecting cKit<sup>+</sup> cells. Representative flow cytometry plots illustrate respective enrichment in primitive cells using this technique (**Figure 3-5**). Non-conditioned mice received 400,000 cells from cKit-enriched cell population, while irradiated mice received, in addition to 400,000 cKit<sup>+</sup> cells, one million carrier cells from WT CD45.1 littermates. We aimed to avoid competition for engraftment in non-conditioned mice, however irradiated recipients recover better when receiving a whole BM transplant. In addition, whole BM samples from GFP-LC3 mice might contain non-HSCs cells with high GFP levels, which could be depleted during cKit enrichment. The mice were induced after transplantation by tetracycline withdrawal, and one mouse per arm underwent BM analysis and assessment of leukaemic burden at three different time points.

The progression of leukaemia in DTG mice typically involves weight loss at later stages, concomitant with splenomegaly due to myeloid cell infiltration. To assess splenomegaly, the spleen-to-body ratio was calculated to adjust for varying body weight, particularly between female and male mice. A trend towards splenomegaly was observed in all three irradiated mice, but not in the non-irradiated mice (**Figure 3-6a-c, e**). Similarly, spleen cell counts (**Figure 3-6d**)

were slightly elevated in the irradiated arm, although this did not reach statistical difference.

BM analysis revealed successful engraftment and long-term reconstitution in the irradiated transplant arm, accompanied by the progressive expansion of CD45.2<sup>+</sup> cells due to expression of BCR::ABL1 (**Figure 3-7a&b, d**). Conversely, in the non-irradiated mice, no CD45.2<sup>+</sup> population was detected at either time point. Lower BM cell counts were detected in all three irradiated mice compared to non-irradiated mice (**Figure 3-7c**), which is a result of the irradiation. Mice in the irradiated transplant group have drastically reduced number of recipient cells compared to non-irradiated mice, while leukaemic CD45.2 donor cells were increasing over a timeframe of three weeks (**Figure 3-7d**). In conclusion, the experiment demonstrates that BM cells from the SCL-tTA/BCR::ABL1 successfully engrafted and induced leukaemia in conditioned mice, such as those subjected to sublethal irradiation, but failed to do so in non-conditioned mice.

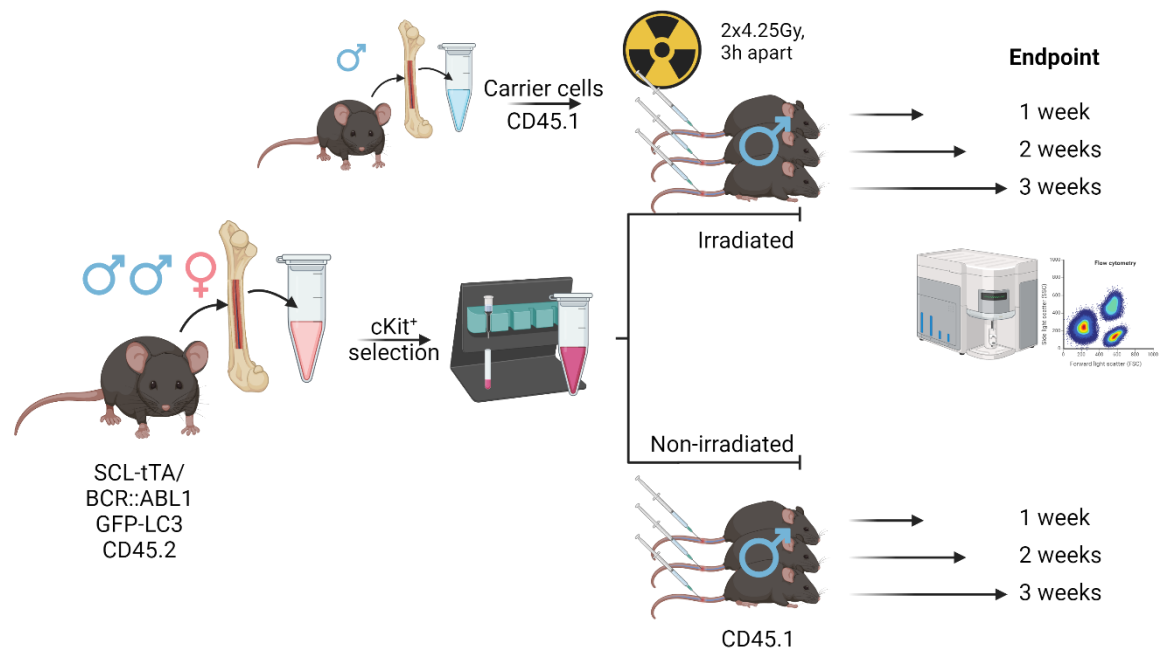


**Figure 3-4 Experimental setup for BM engraftment in conditioned and non-conditioned mice.** BM cells obtained from SCL-tTA/BCR::ABL1 mice (one female, two male), expressing the CD45.2 isotype were harvested and enriched for cKit<sup>+</sup> cells using magnetic separation columns. Subsequently, 400,000 cKit<sup>+</sup> cells were transplanted into three irradiated (male) and three non-irradiated (male) CD45.1 C57BL/6 mice. The irradiated mice received an additional one million CD45.1 carrier cells obtained from a littermate (male). Mice were not given tetracycline in the drinking water to induce BCR::ABL1 expression in CD45.2 cells. Over the following weeks, one mouse from each transplant group was humanely killed, and tissues analysed for engraftment and leukaemia development. Created with BioRender.com.

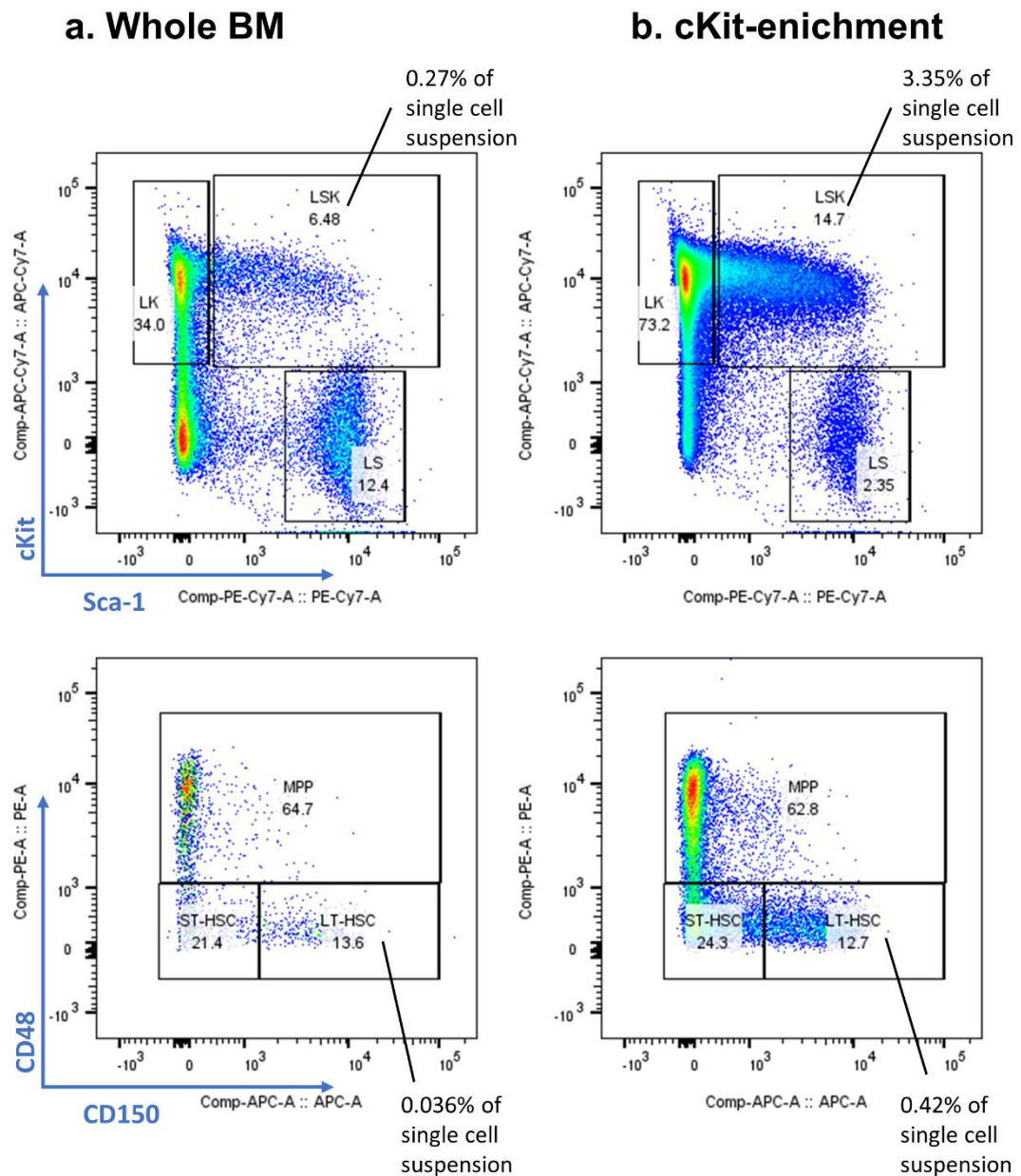


**Figure 3-5 LSK-SLAM populations in whole BM compared to cKit enriched sample.** Whole BM (a) single-cell suspension was stained with the LSK-SLAM markers and compared to the remaining cells that were enriched for cKit<sup>+</sup> cells (b) using magnetic cell sorting. Flow cytometry plots illustrate cKit and Sca-1 surface marker expression for the Lin<sup>-</sup> population. LSK cells were further gated for CD48 and CD150, as displayed in the bottom row. Percentages within the graphs refer to the parent population, while percentages for LSK and LT-HSCs from single cell suspension are noted.

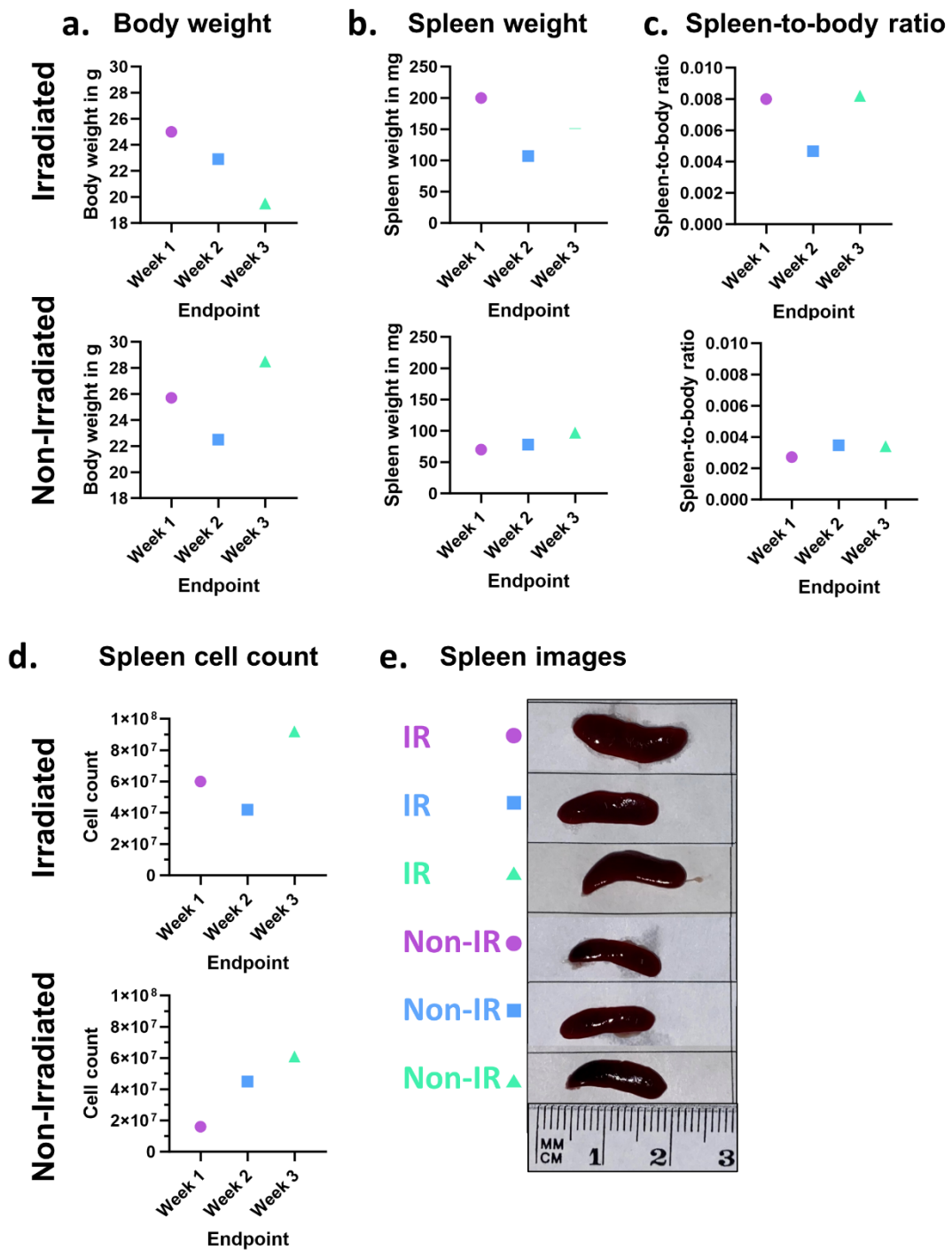


**Figure 3-6** Detection of leukaemia development indicated by trend towards splenomegaly in the irradiated transplant group. Body weight (a) and spleen weight (b) measurements were utilised to calculate the spleen-to-body ratio (c). Total spleen cell count (d) and corresponding spleen images (e) are depicted.

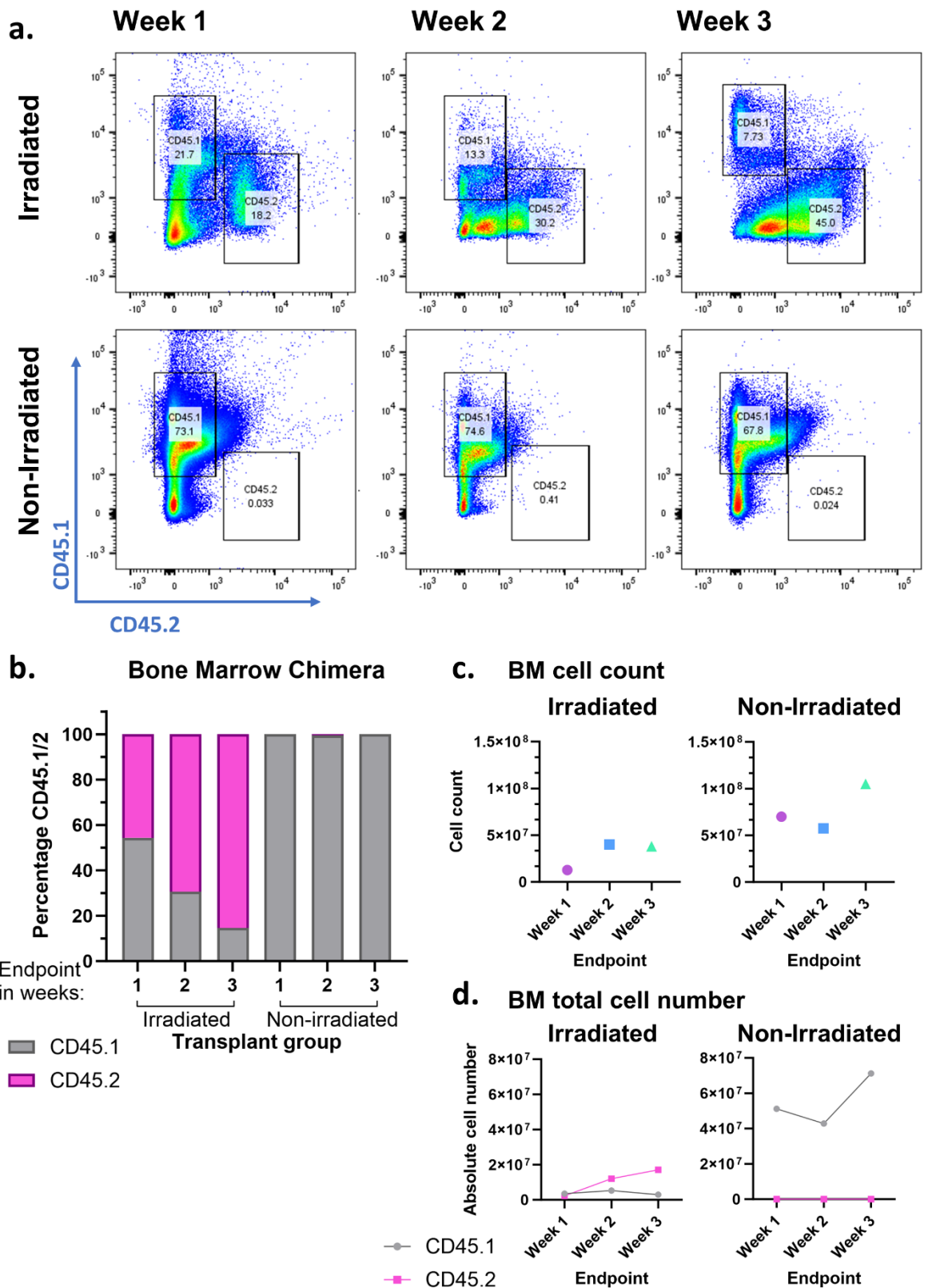


**Figure 3-7 BM transplant requires irradiation of recipient mice for long-term BM reconstitution.** Flow cytometry analysis of BM stained for CD45.1 and CD45.2 surface markers (a). The chimerism in the BM is illustrated as percentage in (b), alongside corresponding BM cell counts (c). Total cell number per CD45.1/CD45.2 illustrated in (d) was calculated from BM cell count (c) and percentage of CD45.1/CD45.2 cells (a).

### 3.2.4 Limited long-term engraftment potential in GFP-LC3<sup>low</sup> cells resulting from LT-HSCs depletion

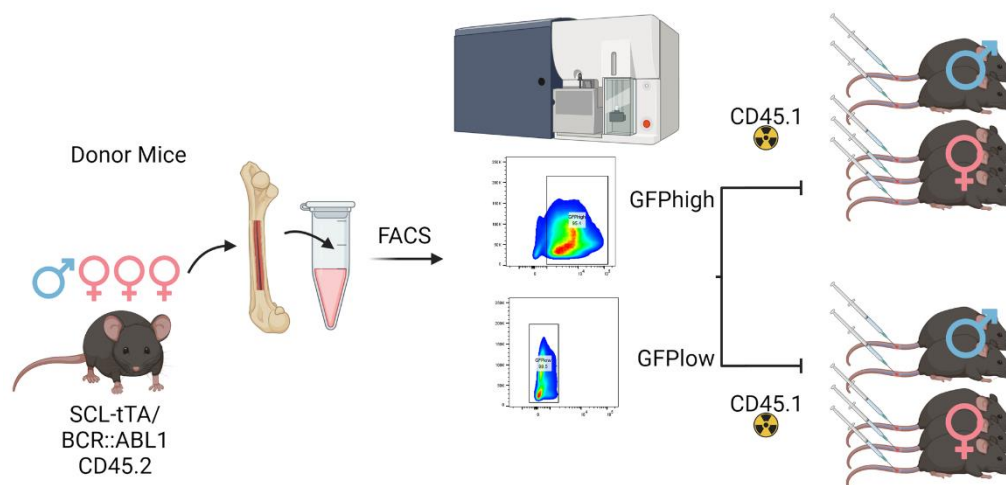


**Figure 3-8 Experimental setup for competitive transplant of GFP<sup>high</sup> and GFP<sup>low</sup> DTG cells.** BM cells from SCL-tTA/BCR::ABL1 GFP-LC3 mice (three female, one male) were harvested from the leg bones and sorted for GFP<sup>high</sup> and GFP<sup>low</sup> by FACS. Per mouse one million helper cells from C57BL/6 CD45.1 mice were mixed with 1.5 million of sorted cells and transplanted by tail vein injection. The mice were maintained on tetracycline for a three-week recovery period. Afterwards, tetracycline was removed from their drinking water for two weeks, then the animals were humanely killed, and tissue collected for further analysis. Created with BioRender.com.

As previously demonstrated in **Figure 3-1**, primitive haematopoietic cells exhibited high GFP-LC3 expression, which could potentially serve as a marker for stem cells in the SCL-tTA/BCR::ABL1 model. Surface markers, such as the LSK-SLAM panel (depicted in **Figure 3-1b**), are effective for identifying HSCs. Nevertheless, the most conclusive method to confirm stemness is to perform long-term multilineage engraftment to conditioned recipient mice. We next tested our hypothesis that enriching BM cells expressing high levels of GFP-LC3 would lead to long-term repopulation, whereas depletion of GFP<sup>high</sup> cells will lead to engraftment failure due to the lack of stem cells. Additionally, the competitive transplant assay will answer whether GFP-LC3 expression levels can serve as a suitable marker for primitive cells for *in vivo* localisation.

To validate the utility of GFP-LC3 expression as a stem cell marker in the SCL-tTA/BCR::ABL1 GFP-LC3 mouse model, a competitive transplant involving GFP<sup>high</sup> and GFP<sup>low</sup> cells with CD45.1 WT BM cells (**Figure 3-8**) was executed. Initially, BM cells from DTG GFP-LC3 mice were sorted into GFP<sup>high</sup> and GFP<sup>low</sup> cells by FACS (**Figure 3-9a**). Subsequently, the sorted cells underwent staining with the LSK-SLAM panel to assess the frequency of primitive cells compared to the whole

BM sample. The GFP<sup>high</sup> population exhibited a 35-fold increase in LSK cells compared to the whole BM sample (Figure 3-9b). Conversely, the GFP<sup>low</sup> population not only exhibited a reduction in LSK cells by 65% compared to the whole BM sample but were specifically depleted of LT-HSCs (Figure 3-9c).

The sorted cells, along with whole BM cells from WT CD45.1 mice, were then combined and transplanted into irradiated CD45.1 recipient mice. The mice were not induced to express BCR::ABL1 for three weeks to allow recovery from irradiation. Following this, tetracycline was removed from the drinking water to induce BCR::ABL1 expression. The entire experiment was concluded when continuous weight loss and poor body condition was observed in several mice in the GFP<sup>high</sup> group.

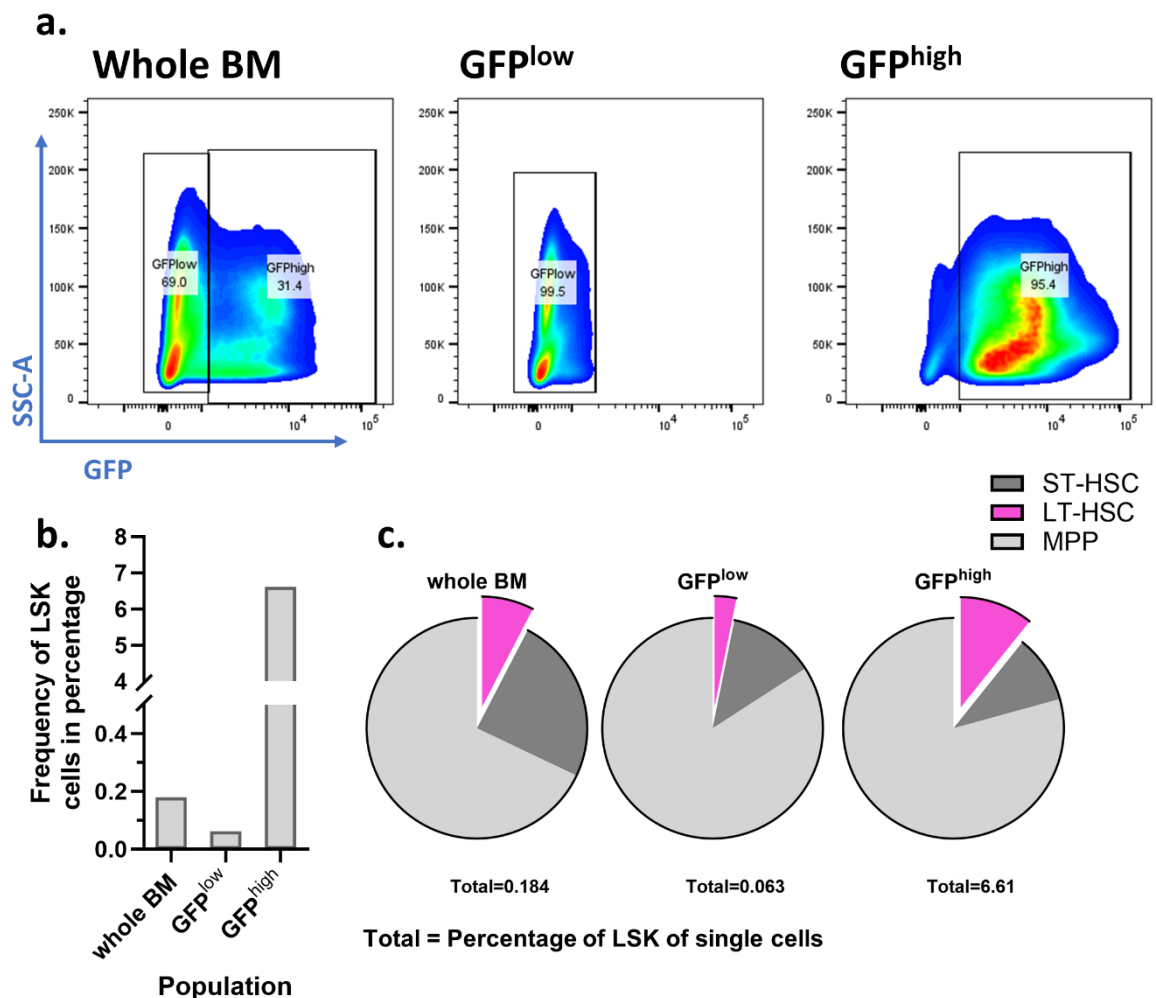


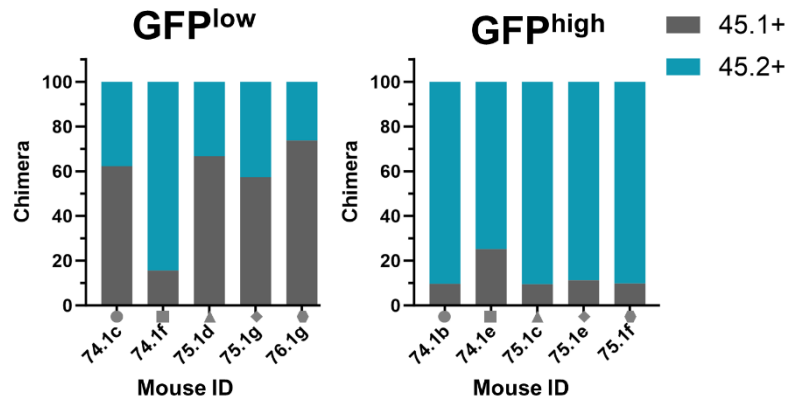
**Figure 3-9 GFP<sup>high</sup> cell population exhibits a substantial enrichment for primitive cells.** BM cells obtained from SCL-tTA/BCR::ABL1 GFP-LC3 mice (three female, one male) were sorted into GFP<sup>high</sup> and GFP<sup>low</sup> populations using FACS (a). Subsequently, the samples were stained using the LSK-SLAM panel to measure the percentage of LSK cells (b). Pie charts were utilised to illustrate the distribution of MPP, ST-HSC and LT-HSC within the LSK population (c).

Throughout the experiment, blood samples were utilised to estimate engraftment by assessing the CD45 isotype on blood leukocytes (**Figure 3-10**). Preceding the induction of BCR::ABL1 expression, blood samples were collected at two- and three-week post-transplantation. The GFP<sup>low</sup> cell population displayed a diminished capacity for engraftment at two weeks post-transplantation (**Figure 3-10a**), evident by the lower CD45.2 cell percentage in four mice (~40% in four mice, ~95% in one mouse) compared to mice transplanted with the GFP<sup>high</sup> population (~90% in four mice, ~75% in one mouse). This disparity became more pronounced three weeks after transplantation (**Figure 3-10b**), with the CD45.2 percentage declining in GFP<sup>low</sup> transplant arm to ~20% in four mice and reaching 0% in one mouse. In contrast, four out of five mice in the GFP<sup>high</sup> group maintained stable chimerism (~90% CD45.2<sup>+</sup> leukocytes), while one mouse exhibited a lower percentage, dropping to ~50% from previously 75% CD45.2<sup>+</sup> cells.

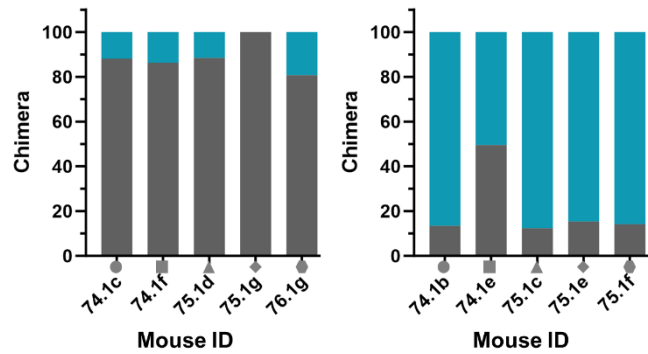
Withdrawal of tetracycline and consequently BCR::ABL1 expression, generally results in an expansion of the CD45.2<sup>+</sup> population. Further testing was conducted seven days (**Figure 3-10c**) and eleven days (**Figure 3-10d**) after induction, marked as the experiment's endpoint. Throughout this period, all GFP<sup>low</sup> mice displayed a decrease in CD45.2<sup>+</sup> cells, indicating a lack of long-term repopulating capacity and lack of myeloproliferation upon BCR::ABL1 expression. The GFP<sup>high</sup> group consistently maintained a chimerism of over 80% CD45.2<sup>+</sup> cells, except for one outlier mouse. This particular individual showed the most variation in blood chimerism, displaying 80% CD45.2<sup>+</sup> cells after seven days of BCR::ABL1 expression, then a reduction to 40% CD45.2<sup>+</sup> cells at the endpoint.

To evaluate the long-term repopulation capacity, chimerism levels in the BM are evaluated at the experiment's endpoint (**Figure 3-11b**). These findings further affirm that the GFP<sup>low</sup> population, except for one mouse displaying approximately 30% engraftment (**Figure 3-11b**), failed to achieve successful engraftment. Unlike in the blood and spleen (**Figure 3-11a&c**), where residual CD45.1<sup>+</sup> cells persisted in the GFP<sup>high</sup> transplant group, the leukaemic CD45.2<sup>+</sup> cells completely dominated over non-leukaemic cells CD45.1<sup>+</sup> cells in the BM across all five individuals.

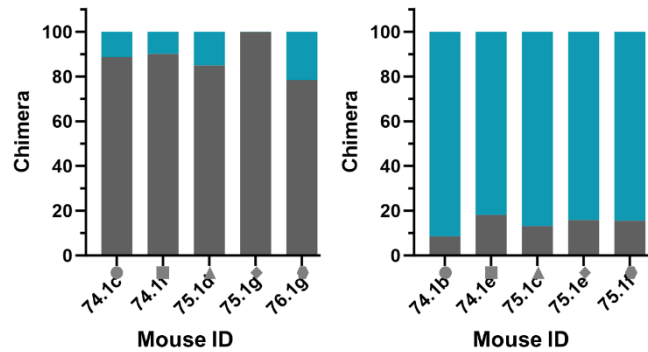
### a. Two weeks post-transplant



### b. Day 0 of induction



### c. Day 7 of induction



### d. Day 11 of induction - endpoint

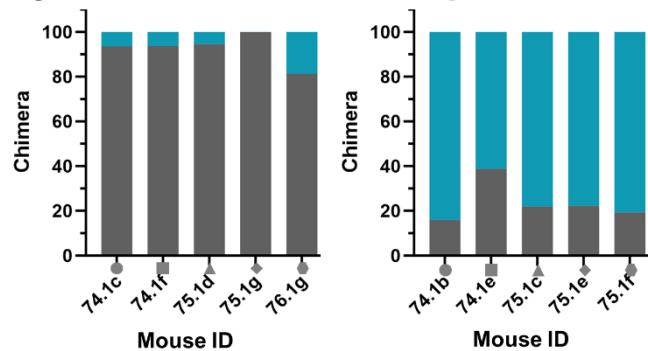


**Figure 3-10 Progression of long-term engraftment in GFP<sup>high</sup> transplant group measured by blood sampling.** Blood samples were collected beginning at two weeks post-transplantation (a), displaying the chimera of CD45.1/CD45.2 in the individual mice from both the GFP<sup>low</sup> and GFP<sup>high</sup> transplant groups. Induction was initiated three weeks after transplant (b), with blood sampling at seven days (c) and eleven days (d) post-induction.

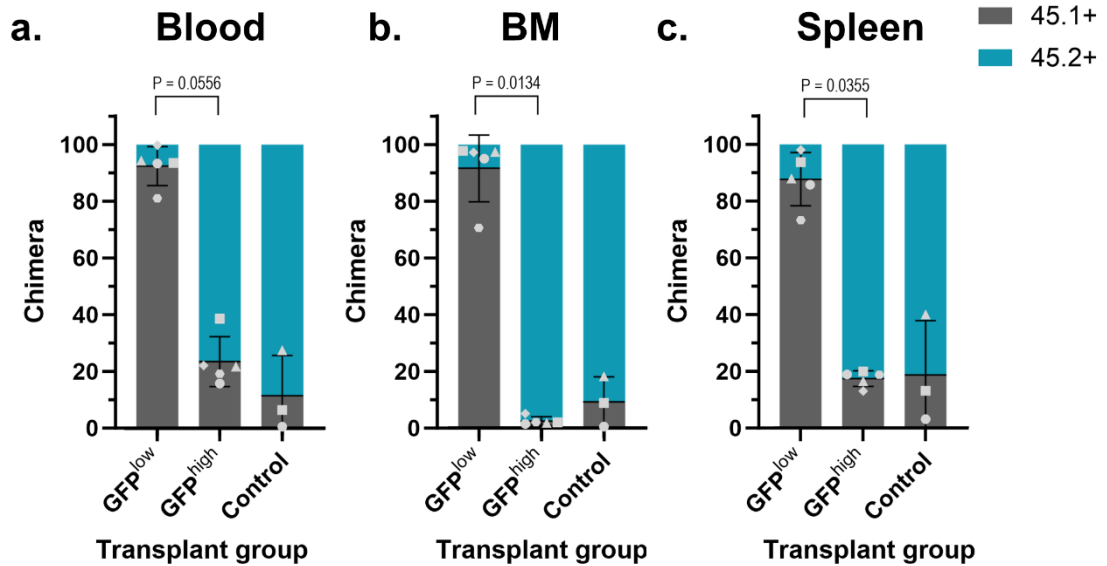


**Figure 3-11 Failure of GFP<sup>low</sup> population in long-term engraftment in irradiated recipient mice.** Chimerism in blood (a), BM (b) and spleen (c) was assessed at endpoint (32 days post-transplantation) using CD45.1 and CD45.2 surface markers by flow cytometry. Stacked bar charts illustrate CD45 isotype proportions. Mean values with error bars denoting +/- S.D. are shown with n=5 for both GFP<sup>low</sup> and GFP<sup>high</sup> groups, and n=3 for the control group. Individual data points, distinguished by specific shape (refer to Figure 3-10), are superimposed on the bar charts.

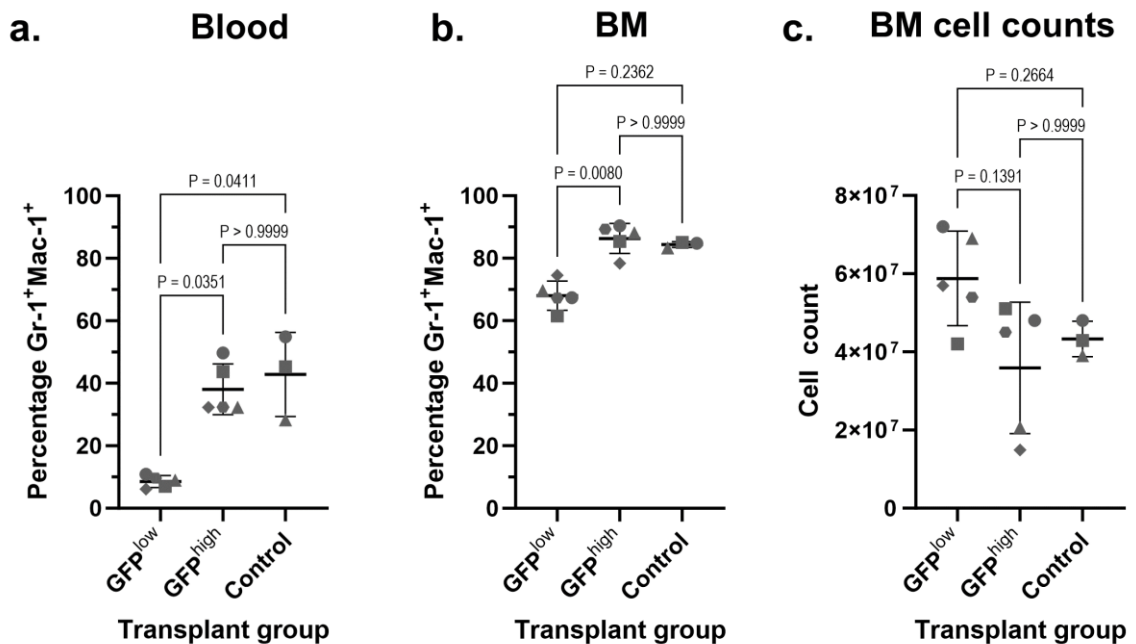


**Figure 3-12 Myeloproliferation in the GFP<sup>high</sup> transplant group was observed eleven days after induction.** The percentage of granulocytes (CD45<sup>+</sup>Gr1<sup>+</sup>Mac-1<sup>+</sup>) was assessed via flow cytometry in both the blood (a) and the BM (b). Cell counts of the BM are depicted in (c). The data were plotted as mean +/- S.D. of n=5 for GFP<sup>high</sup> and GFP<sup>low</sup>, n=3 for control arm. Data points are distinguished by specific shape corresponding to individual mice (refer to Figure 3-10). P-values were calculated with the non-parametric One-way ANOVA Kruskal-Wallis test with Dunn's multiple comparisons test.

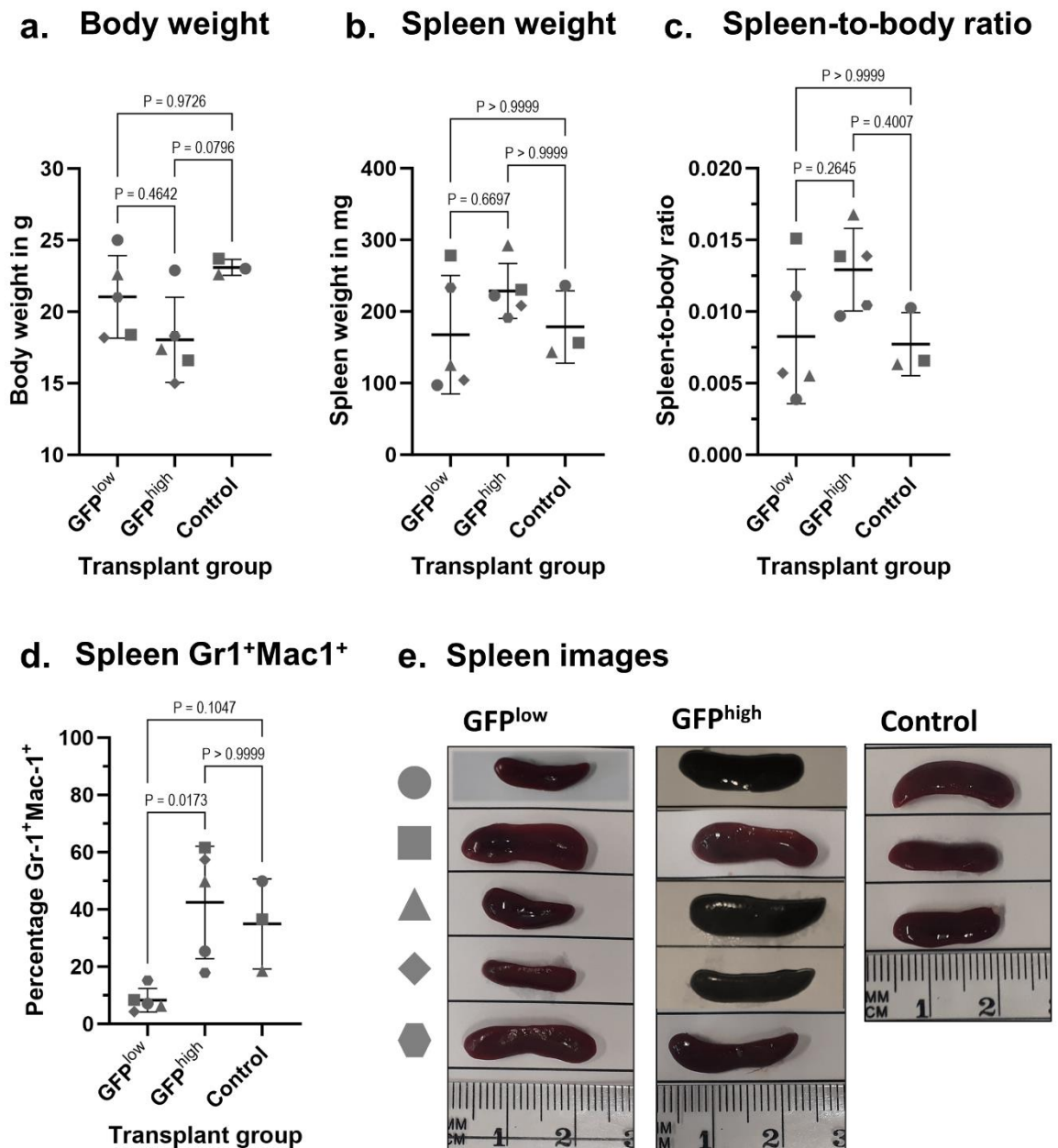


**Figure 3-13 Granulocyte infiltration of spleen observed in GFP<sup>high</sup> transplant group.** Body weight (a) and spleen weight (b) were utilised to calculate the spleen-to-body ratio (c). The percentage of granulocytes (CD45<sup>+</sup>Gr-1<sup>+</sup>Mac-1<sup>+</sup>) in the spleen was quantified (d) and images of the spleen are presented in (e). The data were presented as mean  $\pm$  S.D. of  $n=5$  for GFP<sup>high</sup> and GFP<sup>low</sup>,  $n=3$  for control arm. Individual data point, represented by distinct shapes corresponding to individual mice (refer to Figure 3-10), are displayed on the graphs. P-values were calculated with the paired non-parametric Wilcoxon test.

As leukaemia in the DTG model is associated with an expansion of CD45.2<sup>+</sup>, particularly in the myeloid lineage, the percentage of granulocytes were determined in the blood and BM (Figure 3-12a-b), as well as the spleen (Figure 3-13d). The GFP<sup>high</sup> transplant group consistently demonstrated higher percentages of granulocytes in all three organs, indicating both myeloproliferation and granulocyte infiltration in the spleen and peripheral blood. This observation correlated with a slight trend towards enlarged spleens

in this transplant arm (**Figure 3-13c&e**). In contrast, the GFP<sup>low</sup> arm showed no myeloid cell infiltration in the spleen (**Figure 3-13d**) and overall depicted smaller spleens (**Figure 3-13c&e**). However, two mice in this transplant group exhibited larger spleens that were not attributed to myeloid cell infiltration. BM cell counts in some mice from the GFP<sup>high</sup> group were decreased compared to the GFP<sup>low</sup> or control group, a common finding at the endpoint in this model. It is important to note that the control group more closely resembles the findings in the GFP<sup>high</sup> group, despite their BCR::ABL1 expression being suppressed by tetracycline in the drinking water. Although their spleen-to-body ratio (**Figure 3-13c**) was lower than that in the GFP<sup>high</sup> group, they exhibit a higher presence of myeloid cells in the spleen (**Figure 3-13d**), blood and BM (**Figure 3-12a-b**). Overall, this experiment confirms enrichment of primitive cells within the GFP<sup>high</sup> group and suggests that GFP-LC3 could potentially function as a marker for *in vivo* tracing of LSCs.

### 3.2.5 Visualisation of GFP<sup>+</sup> cells in the mouse calvarium

The objective of this section was to establish a suitable model for *in vivo* localisation of BM cells within their physiological environment to study LSCs persistence. At first, *ex vivo* localisation of BM cells was investigated using the DTG GFP-LC3 mouse model as previous experiments indicated higher GFP-LC3 expression in stem cells compared to differentiated precursor cells or mature blood cells.

*Ex vivo* microscopy of the calvarium involved sacrificing the animal and extracting the calvarium, which was affixed to a small cell culture dish filled with PBS. Imaging was conducted with an upright confocal microscope and a 20x magnification objective that is suitable for immersion in water or PBS. Numerous GFP<sup>+</sup> cells were detected in the calvarium from the DTG GFP-LC3 mouse (**Figure 3-14a**). To identify autofluorescence from GFP signal, a WT mouse was used as a control (**Figure 3-14b**), where no GFP signal was detected.

The next step was to localise GFP<sup>+</sup> cells transplanted to WT recipient mice, as the DTG model is used as a transplantable model. *Ex vivo* imaging was applied to the cohort from the previous experiment in section 3.2.3. The irradiated cohort exhibited high presence of GFP<sup>+</sup> cells in the BM, while the non-conditioned mice

did not and can be used as a control for GFP background signal. Surprisingly, a low frequency of GFP<sup>+</sup> cells in the calvarium was detected in the irradiated group with successful allograft (Figure 3-15a, Figure 3-16a, Figure 3-17a, Figure 3-18). Representative images show some GFP<sup>+</sup> cells, however the majority of the calvarium was non-fluorescent, similar to the non-conditioned mice (Figure 3-15b, Figure 3-16b, Figure 3-17b).

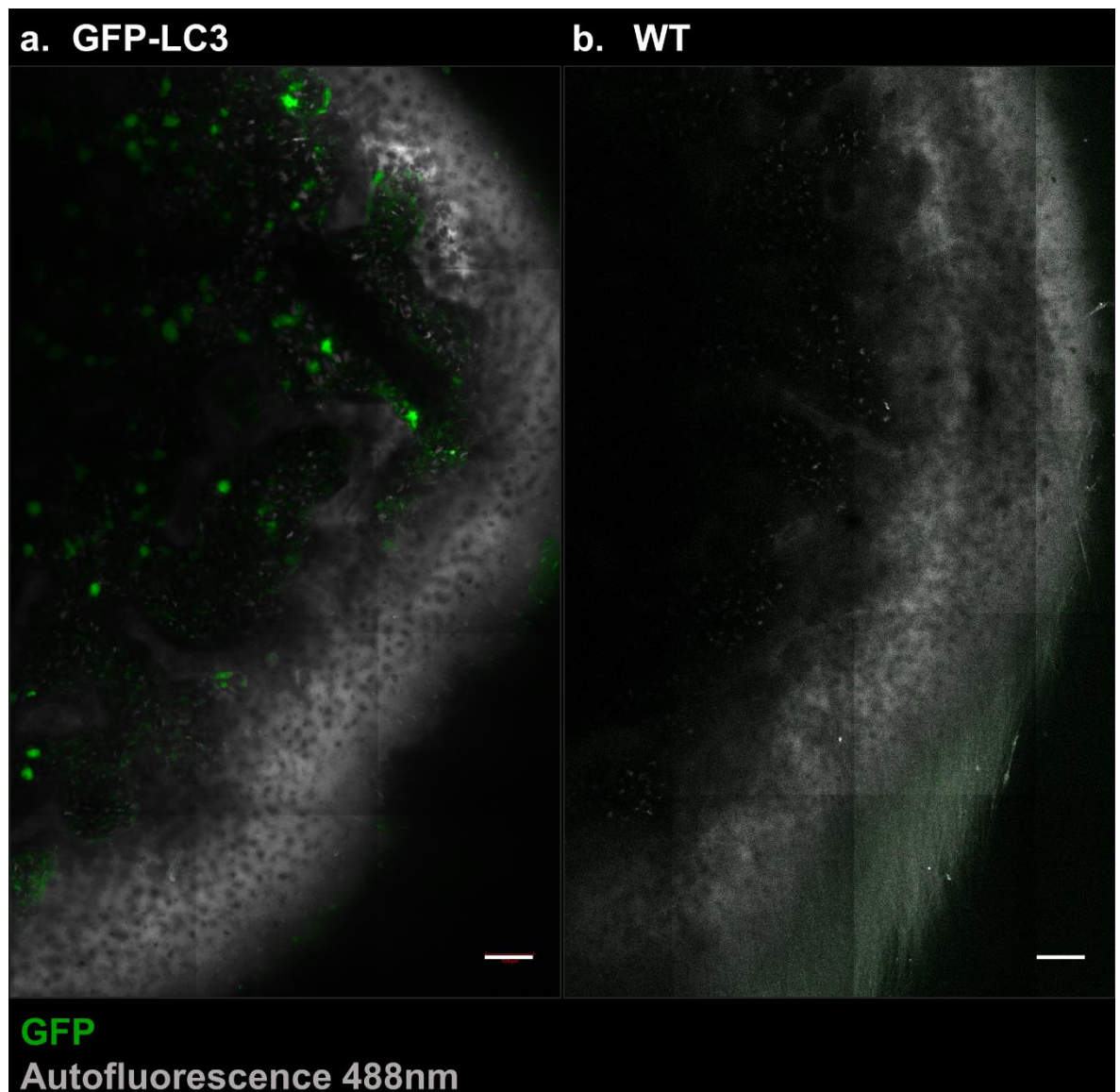


**Figure 3-14 Detection of GFP<sup>+</sup> cells in the calvarium isolated from a GFP-LC3 mouse using *ex vivo* microscopy.** Calvaria from a GFP-LC3 mouse (a) and a WT mouse (b) were extracted, affixed to a culture dish filled with PBS, and imaged in spectral mode. Tile scan images were captured using the 488nm laser and were processed by linear unmixing using Zen black. GFP signal is visualised in green, while autofluorescence signal is depicted in grey. Scale bar: 100 $\mu$ m.

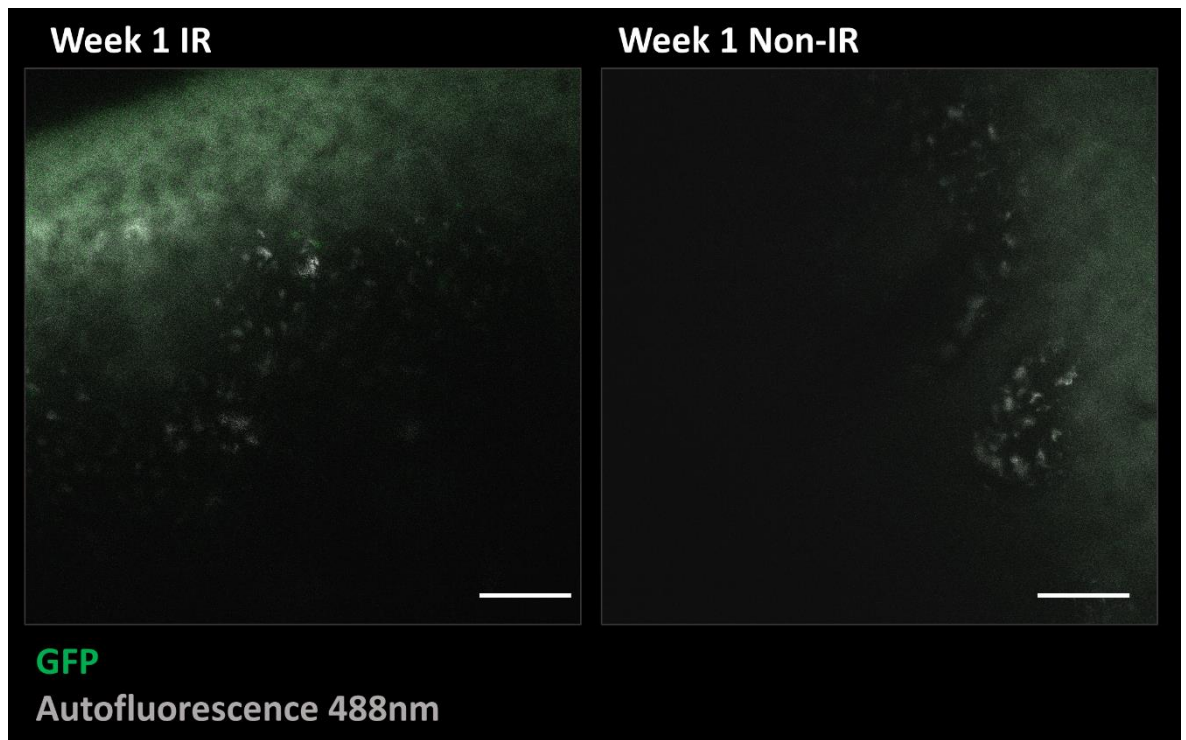


**Figure 3-15 Insufficient detection of GFP<sup>+</sup> cells in induced recipient mice transplanted with DTG GFP-LC3 BM cells.** The calvaria from both irradiated and non-irradiated recipients were imaged under spectral mode one week post-transplantation and BCR::ABL1 induction. These samples, affixed onto culture dishes filled with PBS, were subjected to imaging via the 488nm laser and subsequent analysis entailing linear unmixing utilising Zen black software. Visualisation highlights GFP signal in green against the backdrop of autofluorescence signal depicted in grey. Scale bar: 100 $\mu$ m.

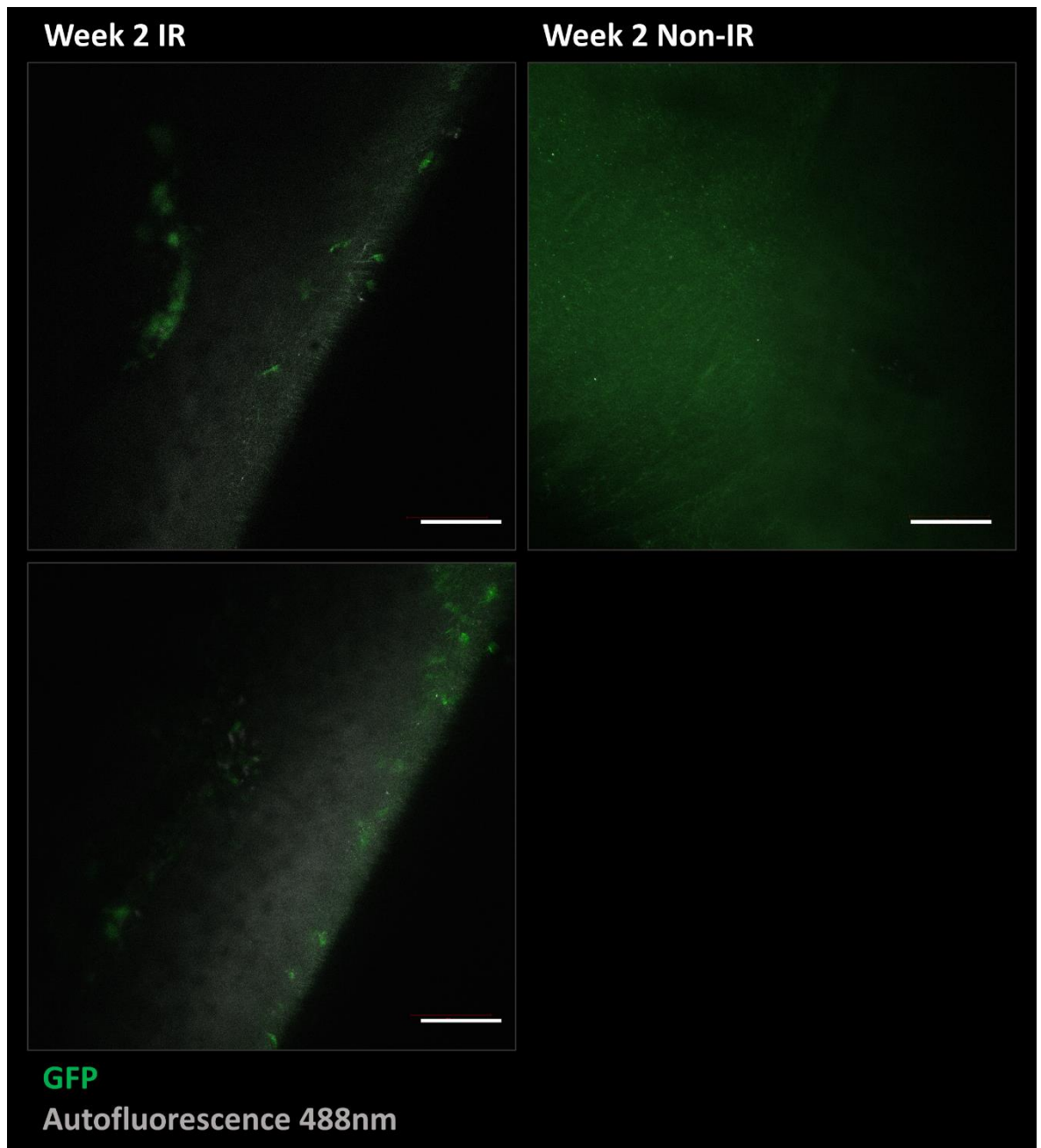


**Figure 3-16 Minimal detection of GFP<sup>+</sup> cells in the calvarium two weeks post-transplantation in DTG GFP-LC3 allografted mouse using *ex vivo* microscopy.** Calvaria from irradiated recipient and non-irradiated recipient two weeks after transplantation and induction of BCR::ABL1 expression were extracted, affixed to a culture dish filled with PBS, and imaged in spectral mode. Images were captured using the 488nm laser and were processed by linear unmixing using Zen black. GFP signal is visualised in green, while autofluorescence signal is depicted in grey. Scale bar: 100 $\mu$ m.

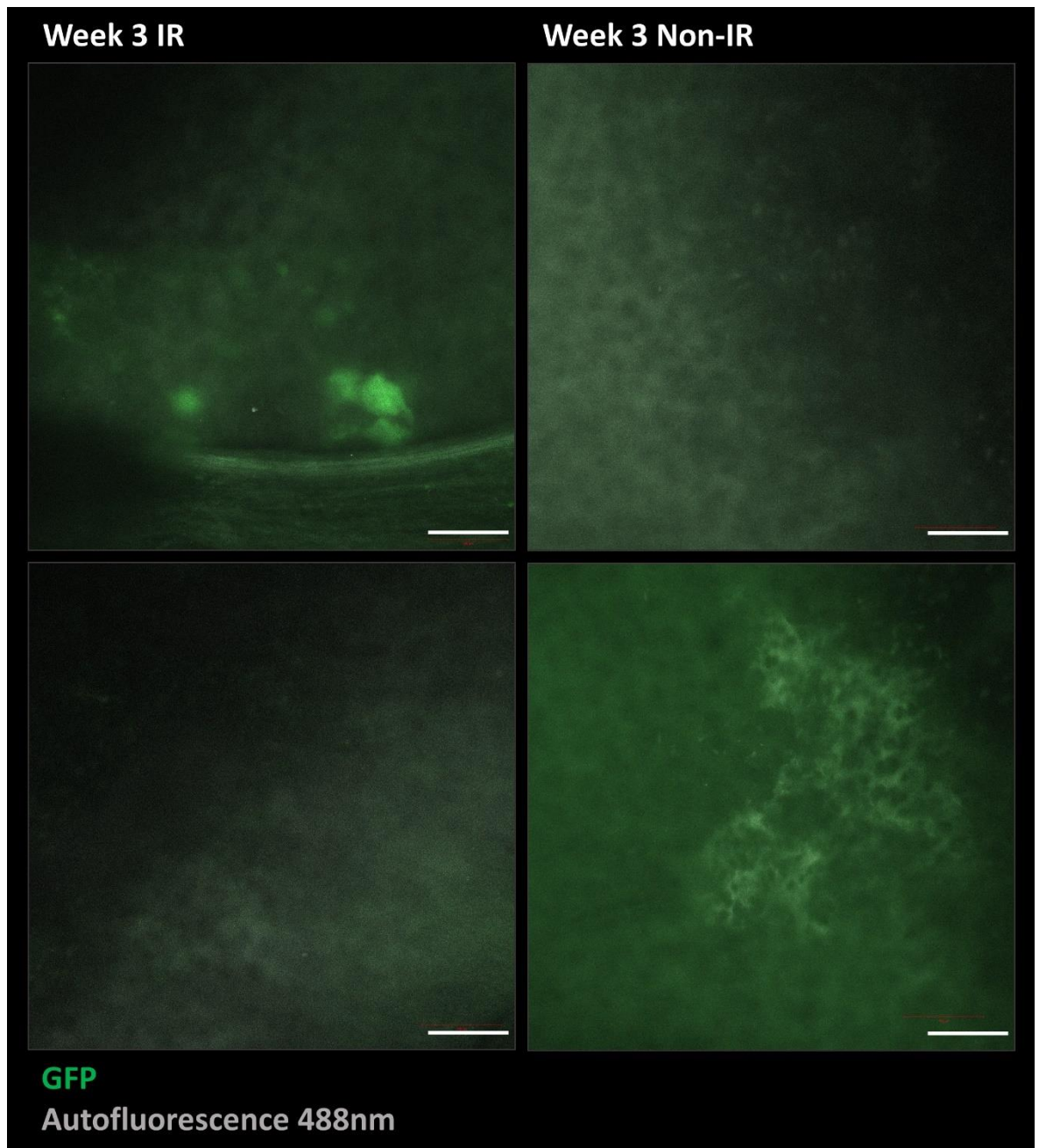


**Figure 3-17 Lack of detection of GFP<sup>+</sup> cells observed in the calvarium three weeks post-transplantation in DTG GFP-LC3 allografted mouse using *ex vivo* microscopy.** Calvaria collected from both an irradiated recipient and a non-irradiated recipient at the three-week mark post-transplantation and induction of BCR::ABL1 expression were attached to a culture dish filled with PBS and imaged under spectral mode. Imaging was performed using the 488nm laser, and subsequent analysis involved linear unmixing using Zen black software. GFP signal is represented in green, contrasting with autofluorescence signal displayed in grey. Scale bar: 100 $\mu$ m.

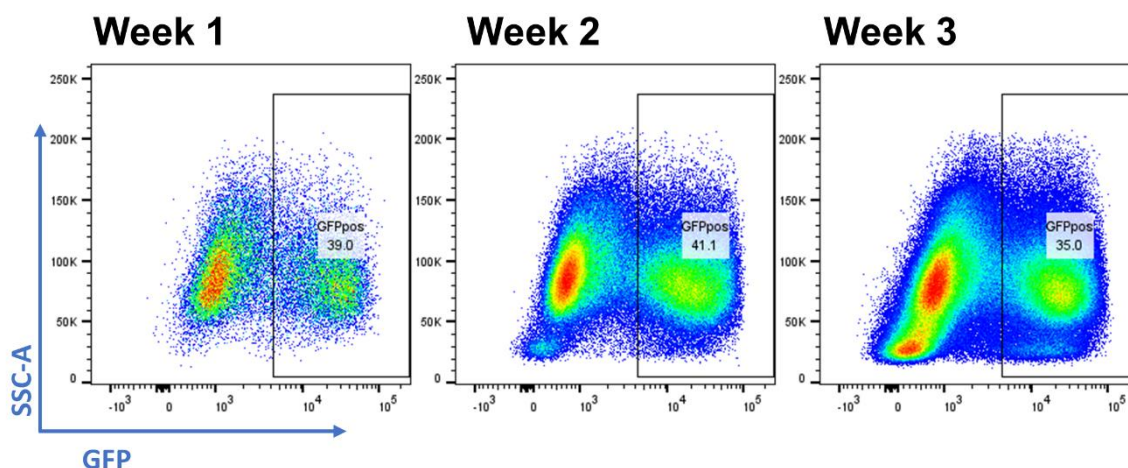


**Figure 3-18 Validation of GFP expression in CD45.2<sup>+</sup> cells in allografted mice was performed by analysing BM cells obtained from the leg bones of the irradiated cohort (refer to 3.2.3).** These mice were transplanted with cKit-enriched SCL-tTA/BCR::ABL1 GFP-LC3 cells and subjected to flow cytometry analysis at one week, two weeks and three weeks post-transplantation and induction of BCR::ABL1 expression.

### 3.2.6 Labelling LSCs *in vivo* using fluorescent antibodies

LSCs, as well as HSCs, cannot be identified by a single surface marker. However, similar to flow cytometry, a combination of surface markers can allow the study of a population highly enriched for stem cells. Therefore, one strategy to localise LSCs *in vivo* involved the combination of multiple surface markers and *in vivo* labelling with conjugated fluorescent antibodies, in combination with fluorescent reporter mice to mark leukaemic cells.

Notably, the combination of more surface markers results in higher purity of stem cells; however, in fluorescent microscopy there is a limit of fluorophores used simultaneously. Initially, we tested antibodies comprising the surface markers CD48, CD41 and CD150, with CD31 used for the vasculature. Kiel *et al.* demonstrated that the population CD41<sup>-</sup>CD48<sup>-</sup>CD150<sup>+</sup> is highly enriched for stem cells with a two-colour staining that is ideal for microscopy<sup>24</sup>.

Fluorescent antibodies were prepared in a total volume of 100µL PBS, and 5µg per antibody were injected 15 to 20 minutes before the mouse was humanely killed. While we initially obtained abundant staining using the CD48 antibody conjugated with the fluorophore PE (Figure 3-19), we could not replicate a similar staining with the same antibody clone but different fluorophores such as AlexaFluor488, BV421 or AlexaFluor700. Similarly, for CD41, we only attempted the antibody conjugated to BV421, which did not result in any detectable

staining in the calvarium. CD150 was conjugated to AlexaFluor647, and we observed some staining (**Figure 3-20**). However, as this was conducted in the GFP-LC3 mouse model, the staining of CD150 correlated with highly fluorescent GFP cells, which were larger in size and were previously shown to be most likely not haematopoietic cells.

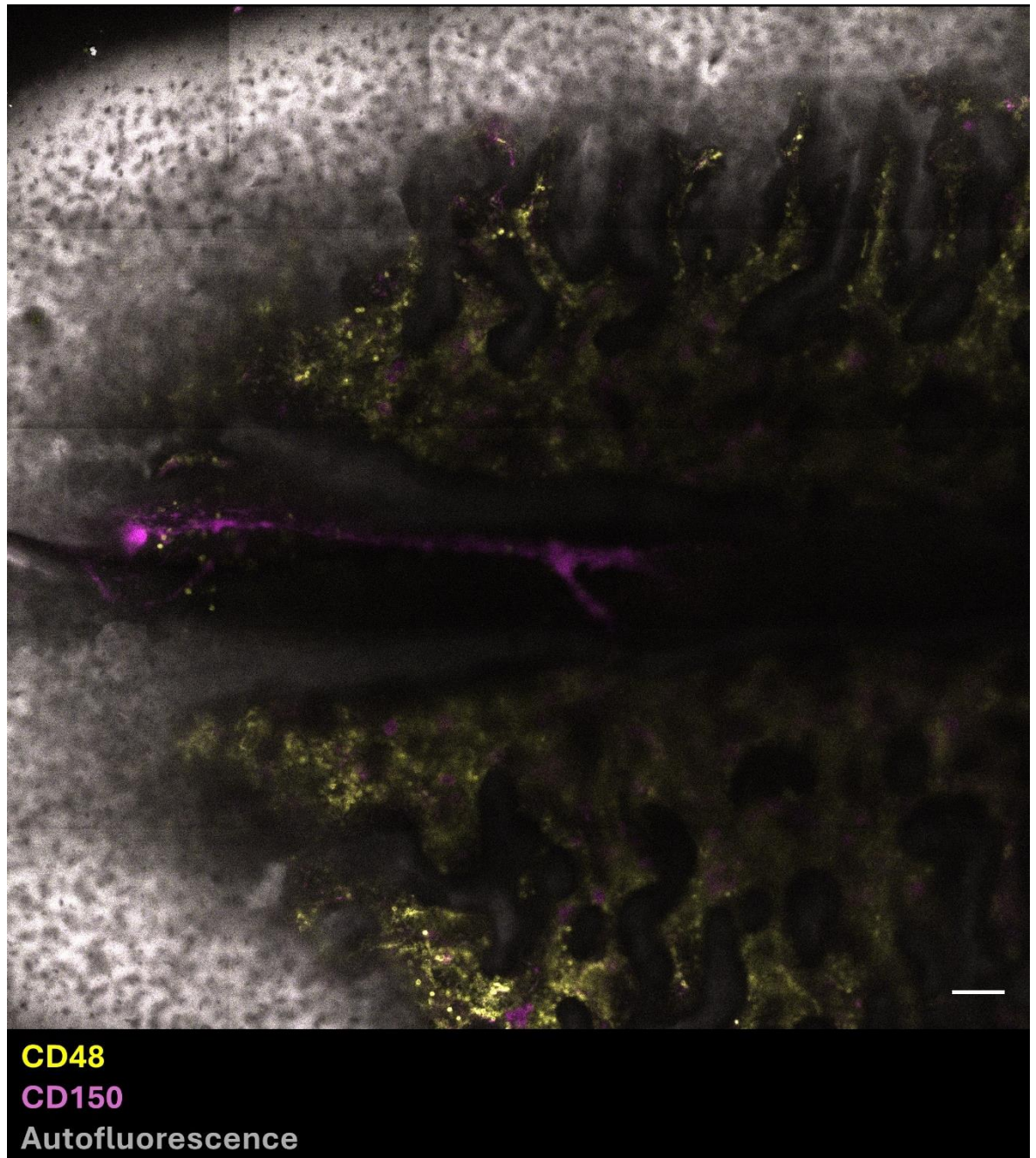


**Figure 3-19** *In vivo* labelling with fluorescent antibody targeting CD48 and CD150. One STG GFP-LC3 mouse was injected with 5 $\mu$ g of CD150-AlexaFluor647 (magenta) and CD48-PE antibody (yellow). After 15 minutes the mouse was humanely killed and the extracted calvarium was immediately used for confocal imaging. Spectral images were acquired as z-stacks and processed through linear unmixing in Zen black. Scale bar: 100 $\mu$ m.

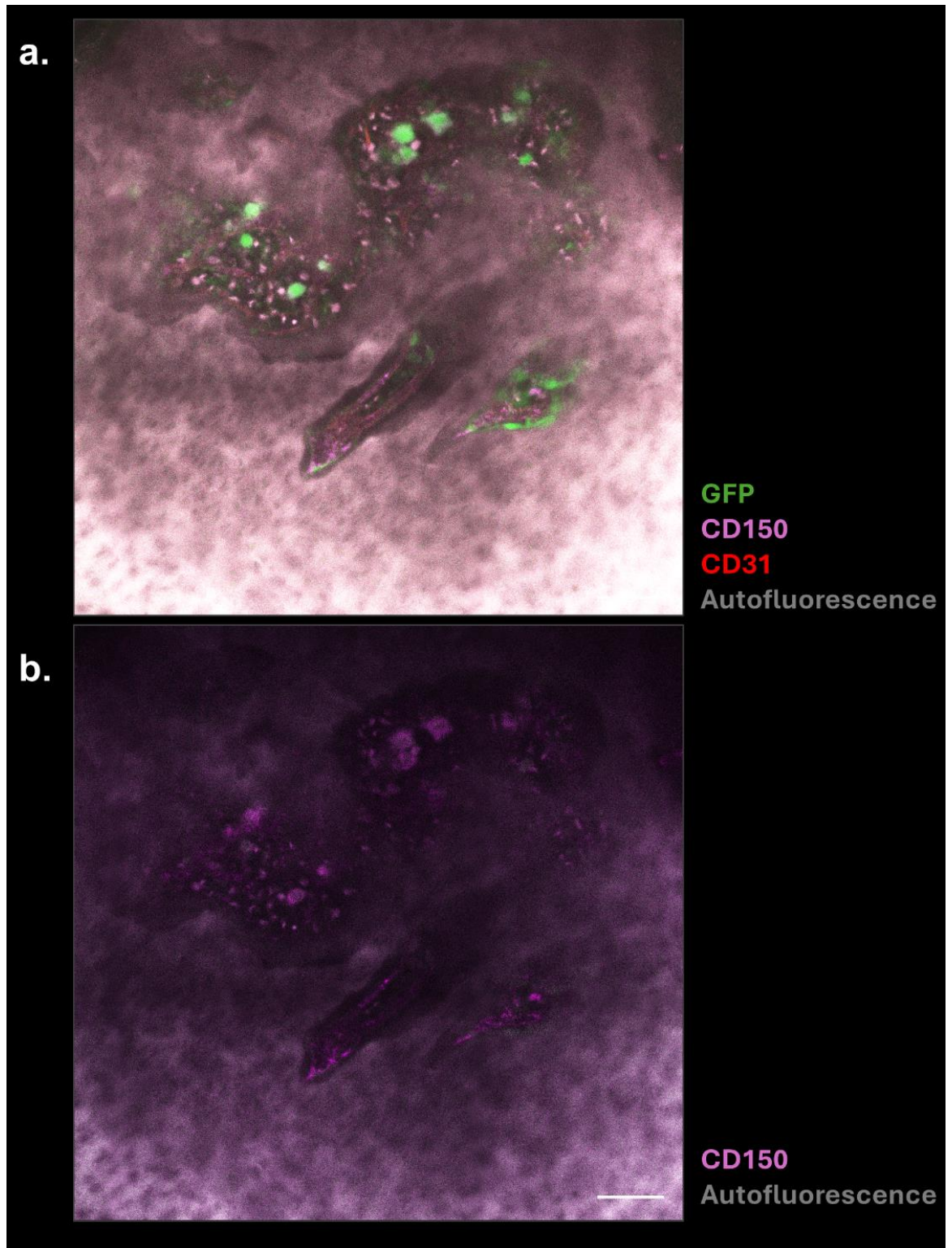


**Figure 3-20** *In vivo* labelling using a fluorescent antibody against CD150. One STG GFP-LC3 mouse was injected with 5 $\mu$ g of CD150-AlexaFluor647 (magenta) and CD48-PE antibody (yellow) as well as 10 $\mu$ g CD31-AlexaFluor594 (red). After 20 minutes the mouse was humanely killed and the extracted calvarium was immediately used for confocal imaging. Spectral images were acquired as z-stacks and processed through linear unmixing in Zen black. Scale bar: 100 $\mu$ m.

### 3.3 Investigating lipophilic dyes for *in vivo* tracking of LSCs in the BM microenvironment

Tracking LSCs *in vivo* presents a significant challenge due to their location within the BM. Other sections (3.2 and 3.4), discuss the use of fluorescent protein overexpression for this purpose. However, in this section, the focus shifts toward employing lipophilic dyes as an alternative method to label stem cells before transplantation.

Lipophilic carbocyanine dyes have emerged as promising tools for *in vivo* tracking of cells. Initially non-fluorescent in water, these dyes exhibit high fluorescence upon incorporation into the cell membrane. Their unique property of lateral diffusion within the membrane allows for comprehensive cell membrane labelling. A notable challenge in cell labelling methods is the potential dilution within actively cycling cells, resulting in their disappearance over time. This study aims to assess their detectability within a relevant timeframe in our mouse model. By exploring the effectiveness of these dyes *in vivo*, this research seeks to provide valuable insights into their potential as a reliable method for tracking LSCs within the BM microenvironment.

#### 3.3.1 Non-detection of DiD-labelled LT-HSC four to five weeks after transplantation to WT recipients due to insufficient staining

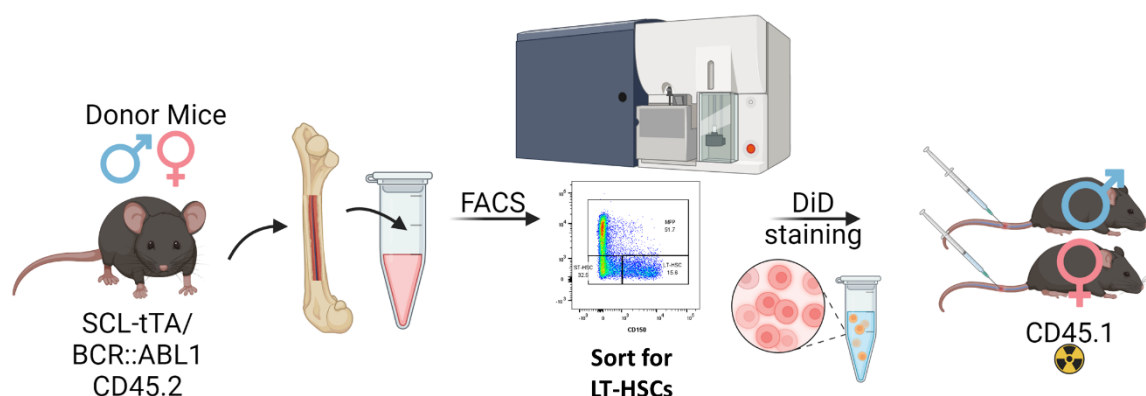


**Figure 3-21 Experimental design for *in vivo* tracing of DiD-stained LT-HSCs transplanted to WT recipient mice.** BM cells harvested from the leg bones of SCL-tTA/BCR::ABL1 GFP-LC3 mice (one female, one male) were sorted to obtain LT-HSCs (LSK CD48<sup>-</sup>CD150<sup>+</sup>) via FACS. These LT-HSCs were then stained with the lipophilic dye DiD. Subsequently, 2,000 LT-HSCs, in combination with two million CD45.1<sup>+</sup> carrier cells, were transplanted per recipient mouse. Notably, the recipient mice were not induced to express BCR::ABL1 for the entire experiment. The mice were humanely killed after four weeks (female) and five weeks (male) post-transplantation for analysis. Created with BioRender.com.

The primary objective of the initial experiment was to determine detectability of transplanted DiD-dyed LT-HSCs within the BM using flow cytometry and confocal microscopy after four to five weeks (**Figure 3-21**). The mice were not induced to express BCR::ABL1 to establish if quiescent LT-HSCs could be detected. BM cells isolated from SCL-tTA/BCR::ABL1 GFP-LC3 mice were sorted to obtain LT-HSCs, which were subsequently stained using the DiD dye following the manufacturer's instructions. Staining validation was conducted alongside human cell lines via flow cytometry to ensure successful staining (**Figure 3-22**).

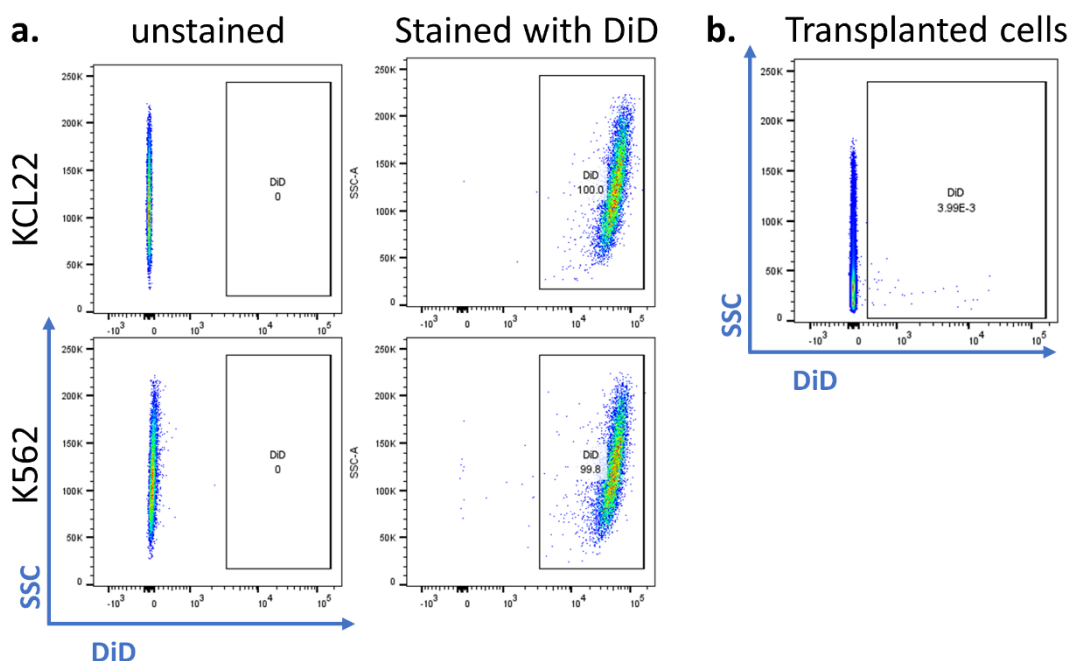


**Figure 3-22** DiD labelling of sorted LT-HSCs for transplantation involved testing the lipophilic dye DiD on human cell lines (a), including KCL22 and K562, both unstained and stained. The labelling process consisted of resuspending cells at a density of  $1 \times 10^6$  cell/mL, followed by the addition of 5  $\mu$ L of DiD cell labelling solution. After brief vortexing, the tubes were incubated at 37°C for 30 minutes. Subsequently, the cells underwent two washes with 2 mL of PBS to remove excess dye. For transplantation, 2,000 CD45.2<sup>+</sup> LT-HSCs were labelled with DiD and combined with two million carrier cells from CD45.1 littermates. This cell mixture was transplanted into CD45.1 WT mice and the remaining cells analysed by flow cytometry (b).

Upon sacrifice at four- and five-weeks post-transplantation, the calvarium was immediately imaged *ex vivo* to detect DiD<sup>+</sup> cells (**Figure 3-23b**). However, the obtained images were inconclusive, displaying minimal signal and overall low frequency of potential DiD<sup>+</sup> cells. To validate the frequency of DiD<sup>+</sup> by flow cytometry, BM cells were isolated from the leg bones. The female mouse, sacrificed after four weeks, exhibited a minimal number of positive hits, whereas the male mouse sacrificed after five weeks showed no detectable DiD<sup>+</sup> cells (**Figure 3-23a**). Contrary to the flow cytometry analysis, the microscopy imaging indicated a higher frequency of DiD<sup>+</sup> signal in the male mouse compared

to the female mouse. Nevertheless, both imaging methods exhibited inconsistencies regarding the presence of DiD<sup>+</sup> cells.

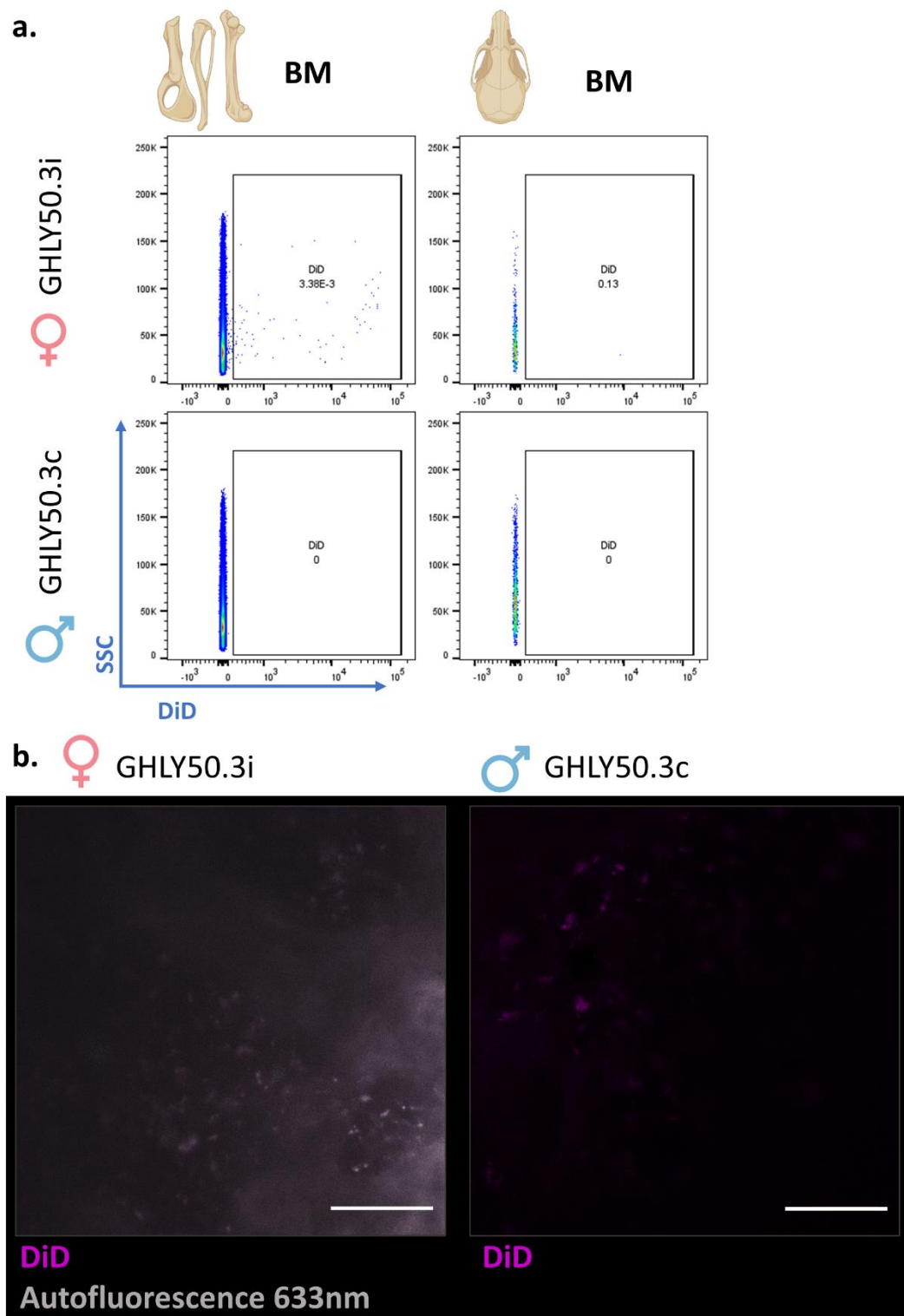


**Figure 3-23 Detection of DiD<sup>+</sup> LT-HSCs was inconclusive four to five weeks after transplantation.** BM cells obtained from leg bones and calvarium were analysed via flow cytometry to validate the presence of DiD<sup>+</sup> cells (a). Following animal sacrifice, *ex vivo* imaging was immediately performed on the calvarium to localise DiD<sup>+</sup> cells (b). Spectral images were acquired using the 633nm laser and processed by linear unmixing in Zen black. DiD signal is depicted in magenta, while autofluorescence signal is represented in grey. Scale bar 100µm.

### 3.3.2 Optimisation of DiD-labelling of primary BM-derived mouse cells

DiD labelling of primary BM-derived mouse cells had to be reevaluated, due to observations made during the initial transplant experiment. It was noted that while the staining protocol outlined by the manufacturer worked effectively for cell lines, its efficacy with BM cells was less satisfactory. Notably, less than half of the BM cells were successfully stained compared to the efficiency observed with human cell lines (**Figure 3-24a&b**). Considering the highly heterogenous nature of BM cells and the specific aim to label primitive cells, attempts were made to selectively stain the cKit-enriched cell population with a similar low output (~35% success, **Figure 3-24c**).

To improve the staining process, alterations were made by reducing the volume in which cells were resuspended, followed by vigorous vortexing and a shorter incubation period of only 10 minutes at 37°C. This modified approach demonstrated considerable enhancement in staining efficacy of cKit-enriched primary mouse cells, as depicted in **Figure 3-25**.

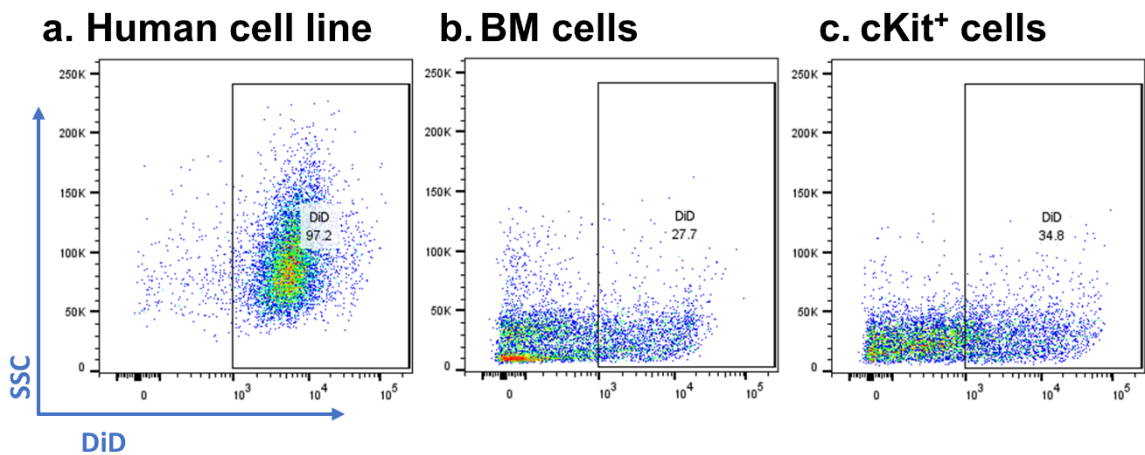


**Figure 3-24 Primary murine cells require an adjusted protocol compared to human cell lines for DiD cell labelling.** Cells were resuspended at a density of  $1 \times 10^6$  cell/mL, followed by the addition of 5  $\mu$ L of DiD cell labelling solution. After brief vortexing, the tubes were incubated at 37°C for 30 minutes. Subsequently, the cells were then washed twice with 2mL of PBS, and the fluorescent intensity was measured using flow cytometry.

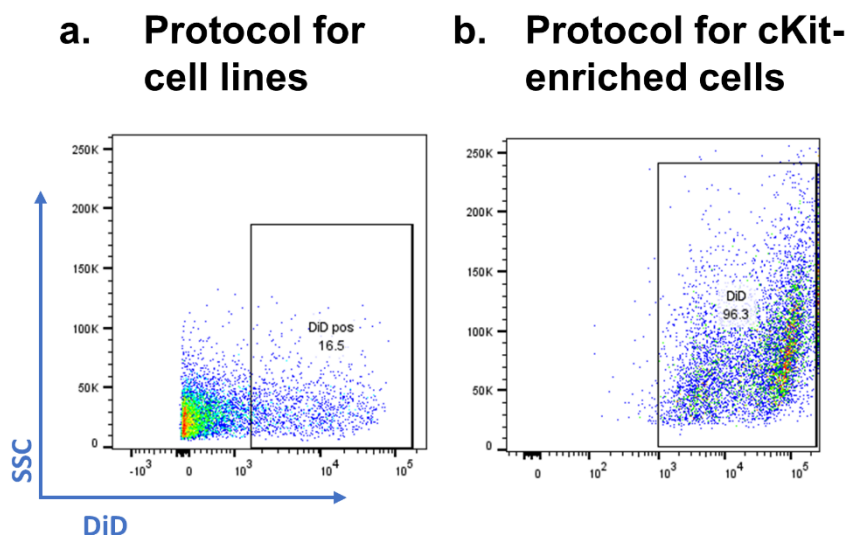


**Figure 3-25 Optimising DiD-labelling in cKit-enriched primary mouse BM cells.** Pelleted cells, up to  $1 \times 10^6$  cells, were resuspended in 400  $\mu$ L PBS, and 10  $\mu$ L of DiD cell labelling solution was added. Following vigorous vortexing, the tubes were incubated at 37°C for 10 minutes. Subsequently, cells underwent a wash with 2mL of PBS, and fluorescence was measured by flow cytometry. Panel (a) displays cKit-cells stained with the previous protocol, while panel (b) illustrates the fluorescent intensity obtained with the optimised protocol.

### 3.3.3 Transplantation of DiD-labelled cKit<sup>+</sup> cells to conditioned and non-conditioned WT mice

Transplantation of DiD-labelled cKit<sup>+</sup> cells into conditioned and non-conditioned WT mice were performed concurrently with the experiment previously described in section 3.2.3, involving engraftment of DTG cKit-enriched cells into irradiated and non-irradiated mice. We hypothesise that transplanted LSCs would be detected by the DiD signal within the calvarium of recipient mice with successful engraftment over a three-week period.

**Figure 3-26a** illustrates the staining of cKit cells using the optimised protocol. Typically, irradiated mice receive carrier cells (from CD45.1 WT mice) alongside the stem cell enriched transplanted cells to support recovery and prevent BM failure. Both cell populations were assessed for DiD fluorescence by flow cytometry using the remaining cells post-transplantation (**Figure 3-26b**).

Given the increased number of cells transplanted in this experiment and the improved labelling protocol, it was anticipated that the efficacy of DiD for long-term tracing would be clearer. However, it is important to note that, in this experiment, mice were not administered tetracycline, which induces BCR::ABL1

expression and subsequently increases cell cycling. This could significantly contribute to the dilution of the dye, even in primitive cells.

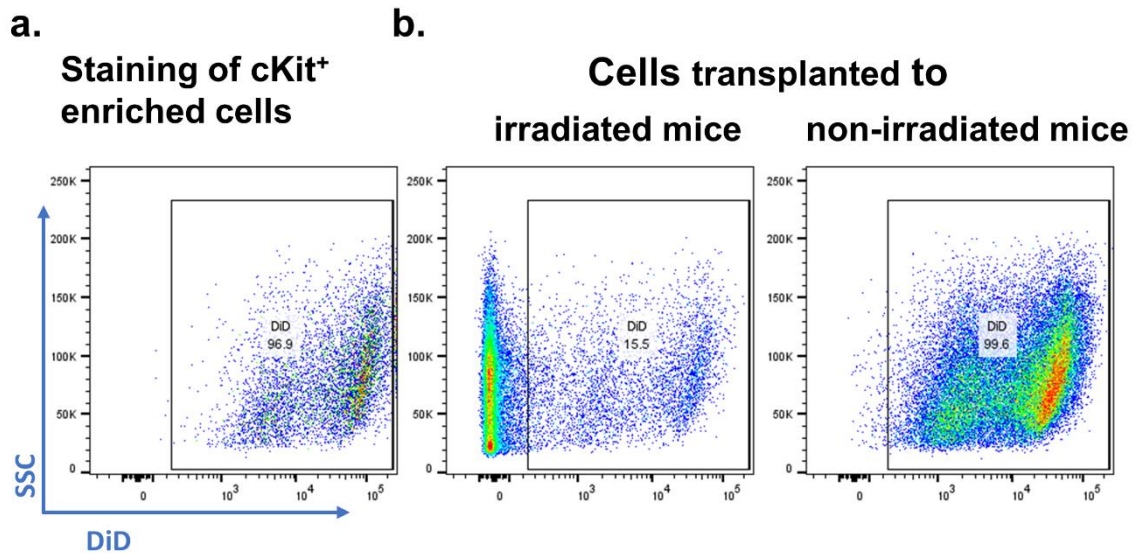


**Figure 3-26 Transplantation of cKit-enriched DiD<sup>+</sup> into conditioned and non-conditioned WT mice.** BM cells were isolated from SCL-tTA/BCR::ABL1 GFP-LC3 mice and enriched for cKit<sup>+</sup> cells using magnetic cell separation. The enriched cell population was then labelled with DiD by pelleting up to  $1 \times 10^6$  cells, resuspending them in 400  $\mu$ L PBS, and adding 10  $\mu$ L of DiD labelling solution. After incubation and washing, fluorescence was assessed by flow cytometry (a). Subsequently, 400,000 cKit<sup>+</sup> cells were transplanted into three irradiated and three non-irradiated male CD45.1 C57BL/6 mice, with irradiated mice receiving an additional one million CD45.1 carrier cells. DiD measurements were acquired for both transplant cell populations (b).

As established in section 3.2.3, cell transplants to non-conditioned mice failed to engraft, whereas CD45.2<sup>+</sup> cells transplanted to irradiated recipients exhibited successful engraftment and led to increased leukaemic burden with advancing time of the experiment. Flow cytometry analysis of BM from each mouse (**Figure 3-27**), revealed very low numbers of DiD<sup>+</sup> cells. Surprisingly, no difference was observed between BM from irradiated mice and non-irradiated mice, despite the lack of engraftment in the non-irradiated group. This observation was supported by comparing images from both transplant groups, where some DiD-signal was detected. Though, a comparable level or even higher level of signal was observed in the non-irradiated mice that lacked engraftment (**Figure 3-28**, **Figure 3-29**, **Figure 3-30**).

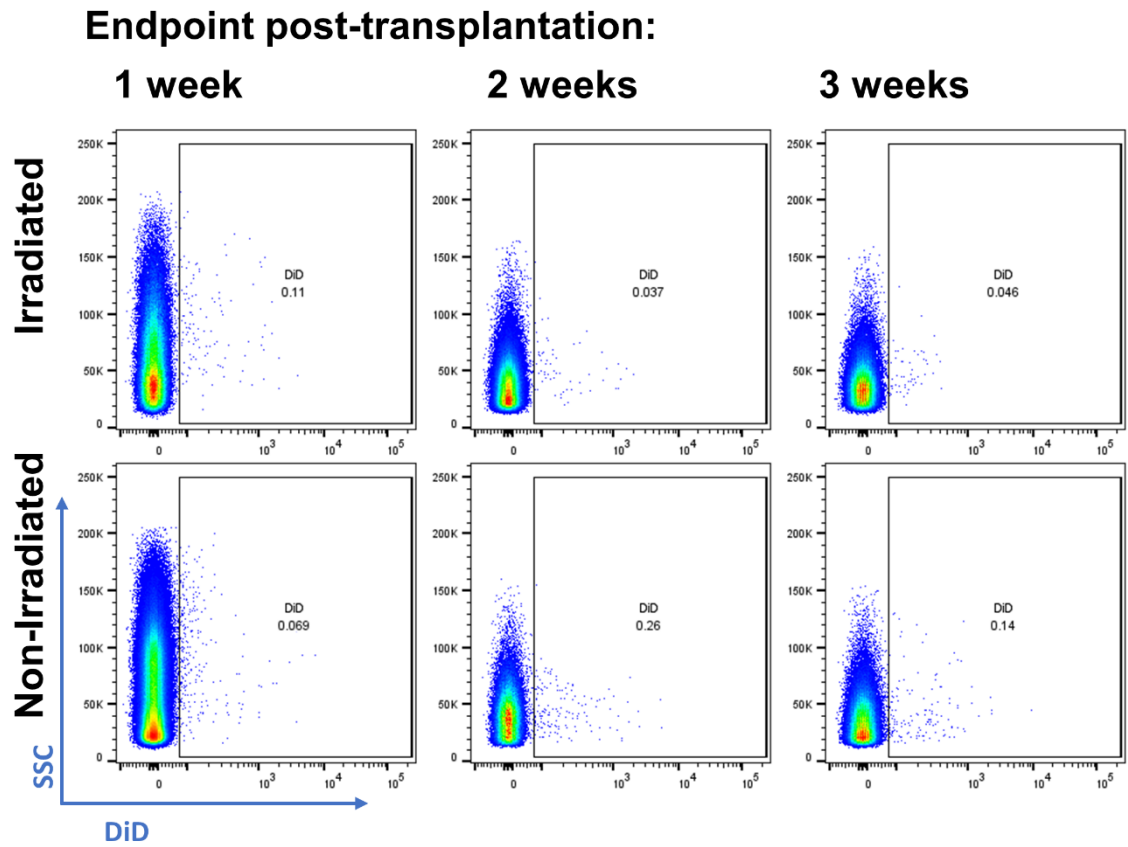


**Figure 3-27 Absence of DiD<sup>+</sup> cells in BM cells in induced mice one to three weeks post-transplantation.** BM cells from both transplant groups at each time point (one week, two weeks and three weeks) were analysed for presence of DiD-labelled cells.

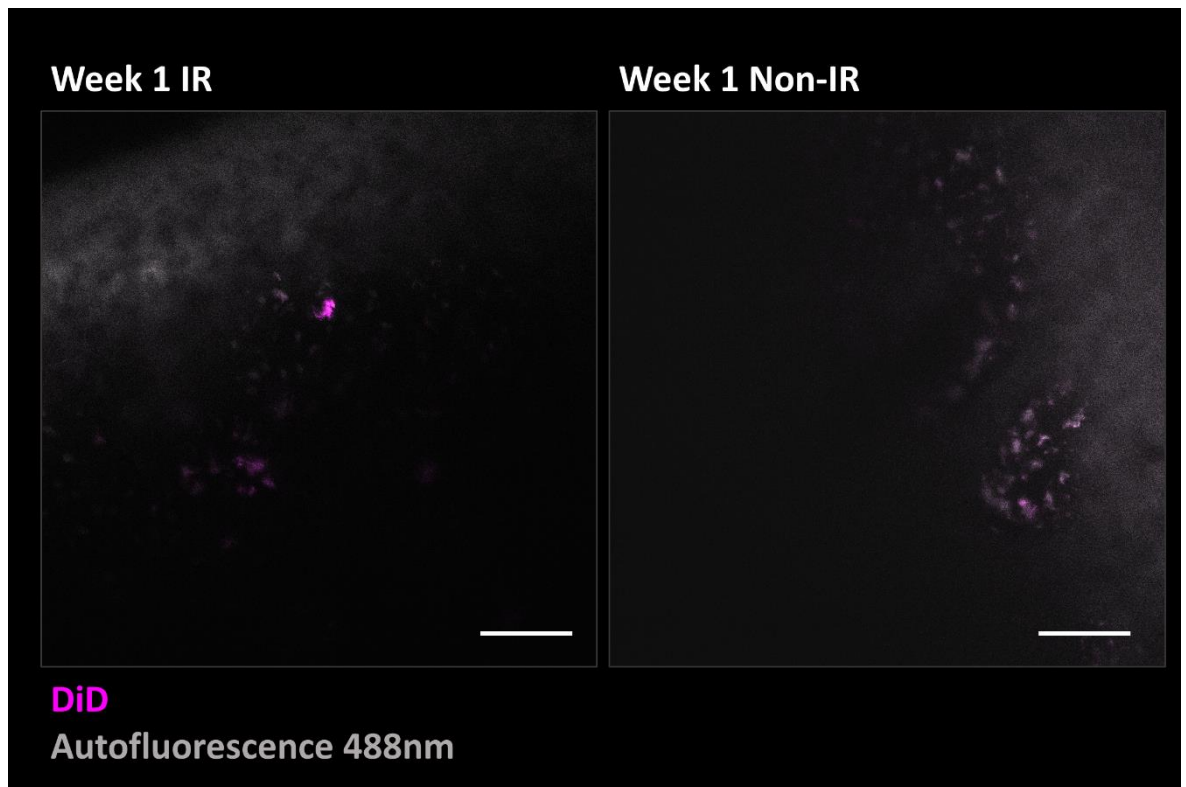


**Figure 3-28 Lack of clear localisation of DiD<sup>+</sup> cells observed one week post-transplantation using *ex vivo* microscopy.** Subsequently, each mouse was sacrificed, and the calvarium immediately prepared for microscopy to locate DiD<sup>+</sup> cells. Spectral images were acquired using the 488nm and 633nm lasers and processed through linear unmixing in Zen black. The DiD signal is depicted in magenta, while the autofluorescence signal appears in grey. Scale bar: 100 $\mu$ m.

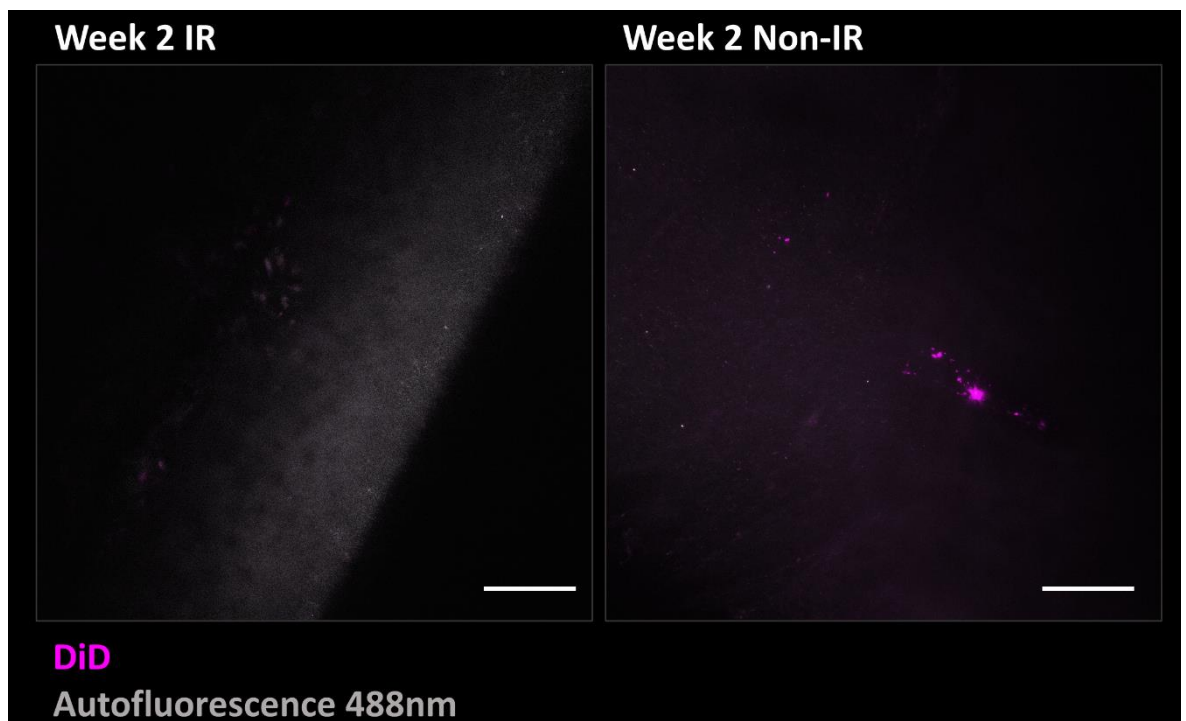


**Figure 3-29 Absence of DiD<sup>+</sup> cells in calvarium imaged two weeks post-transplantation using *ex vivo* microscopy.** Spectral images were acquired using the 488nm and 633nm lasers and processed through linear unmixing in Zen black. The DiD signal is depicted in magenta, while the autofluorescence signal appears in grey. Scale bar: 100 $\mu$ m.

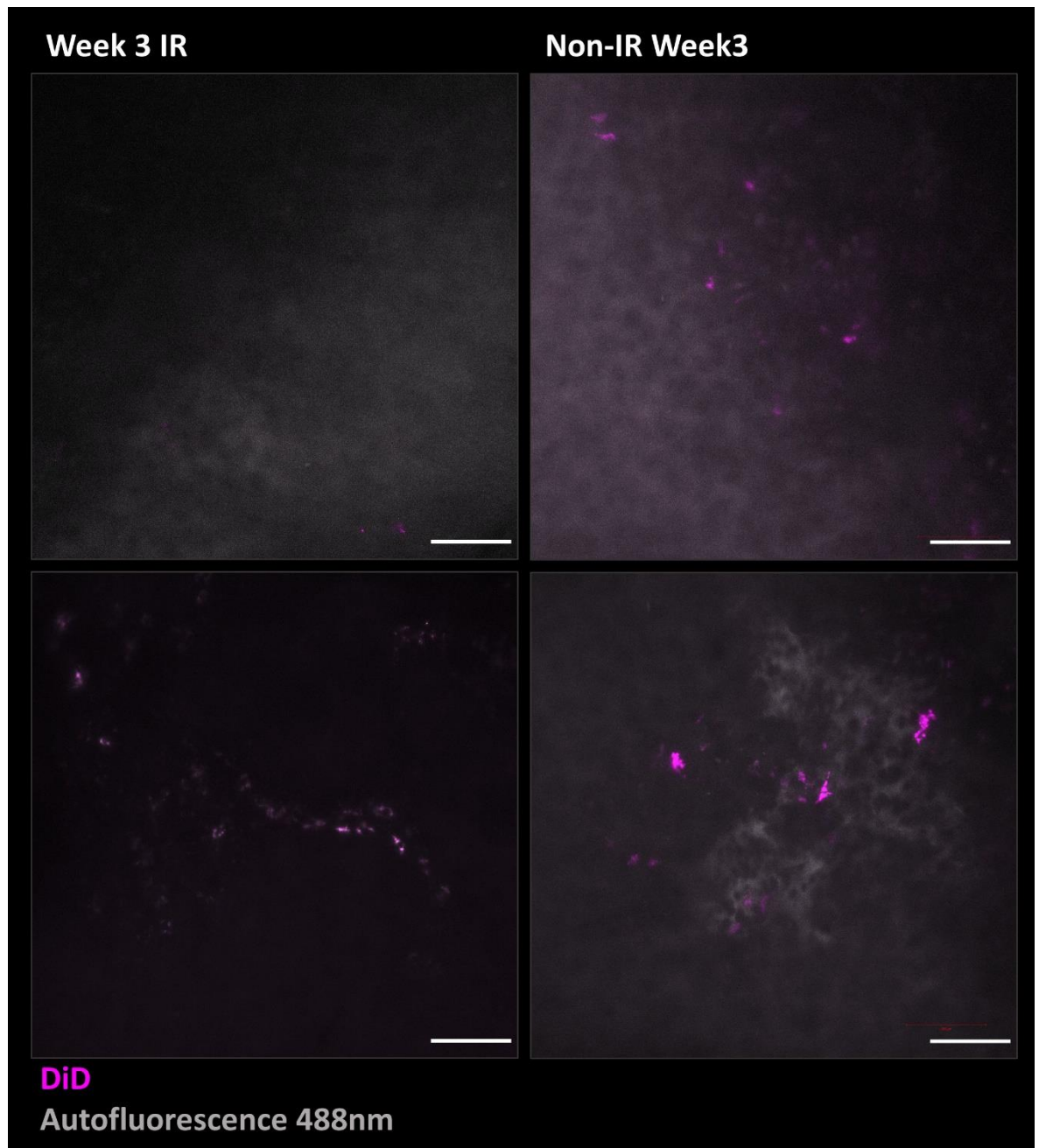


**Figure 3-30 Higher DiD-signal in calvarium obtained from the non-engrafted mouse compared to successfully engrafted mouse.** Subsequently, each mouse was sacrificed, and the calvarium immediately prepared for microscopy to locate DiD<sup>+</sup> cells. Spectral images were acquired using the 488nm and 633nm lasers and processed through linear unmixing in Zen black. All images were acquired as z-stack and are presented as maximum projections. The DiD signal is shown in magenta, while the autofluorescence signal appears in grey. Scale bar: 100 $\mu$ m.

### 3.3.4 DiD-labelling of LT-HSC impacted engraftment to WT recipient mice

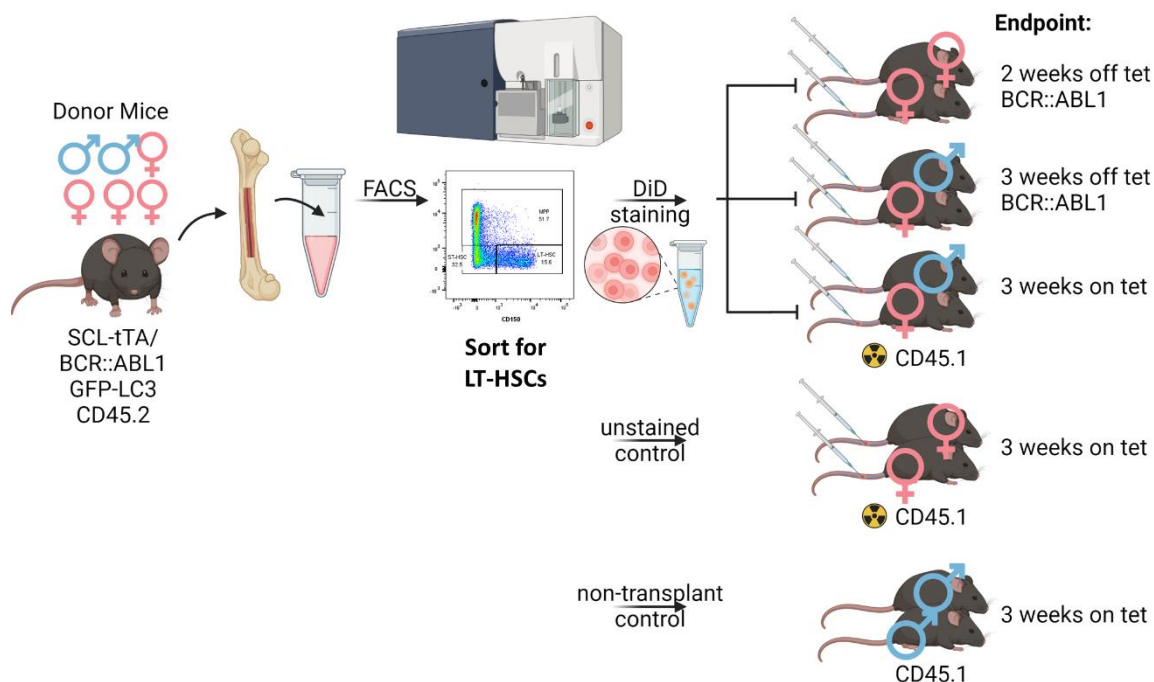


**Figure 3-31 Experimental design aimed to compare the suitability of DiD-labelled LT-HSC transplantation for *in vivo* tracing in leukaemic and non-leukaemic mice.** BM cells were obtained from SCL-tTA/BCR::ABL1 GFP-LC3 mice (four female, two male), extracted from the leg bones, and sorted to isolate LT-HSCs (LSK CD48<sup>-</sup>CD150<sup>+</sup>) using FACS. The LT-HSCs were then stained with the lipophilic dye DiD. Subsequently, 2,000 LT-HSCs were transplanted along with two million CD45.1<sup>+</sup> carrier cells into each recipient mouse (C57B/6 WT CD45.1), six mice in total. Two other mice received each 2,000 unstained (DiD<sup>-</sup>) LT-HSCs along with two million CD45.1<sup>+</sup> carrier cells. Two mice served as non-transplant controls. Following transplantation, all mice were allowed a recovery period of three weeks. Among the DiD-labelled transplant group, four mice were induced to express BCR::ABL1, with two mice induced for two weeks and two mice induced for three weeks. Created with Biorender.com

In the previous experiment, the irradiated mice were not given a recovery time and underwent immediate induction of BCR::ABL1 expression. Induction of BCR::ABL1 induces proliferation of stem cells, which could lead to rapid dilution of the signal, and could be the reason we were not able to detect DiD<sup>+</sup> cells previously. We hypothesise that DiD<sup>+</sup> stained HSCs transplanted to WT recipient mice should be detectable in mice that are not induced to express BCR::ABL1 compared to mice being induced.

An additional experiment was performed, to assess DiD-labelling for *in vivo* tracing in induced mice and non-induced mice (**Figure 3-31**). Therefore, LT-HSCs obtained from DTG GFP-LC3 mice via FACS, were subsequently labelled with DiD, and transplanted into irradiated recipients along with carrier cells. All mice were given three weeks of recovery time.

The experimental setup included three arms in the DiD-transplanted mice: one induced for two weeks, another induced for three weeks, and a third left non-induced. Additionally, two control arms were introduced: a non-transplant control as well as an unlabelled LT-HSCs transplant control to assess influence of labelling on engraftment. Unfortunately, all DiD-labelled samples failed to engraft as shown by the CD45 chimera (**Figure 3-32a**) when compared to non-transplant control (**Figure 3-32c**). Both mice in the unlabelled LT-HSCs transplant control had successful engraftment, although chimerism towards CD45.2 cells were low (**Figure 3-32b**). This indicates that more cells need to be transplanted and staining conditions need to be optimised to ensure labelling without compromising cell viability.

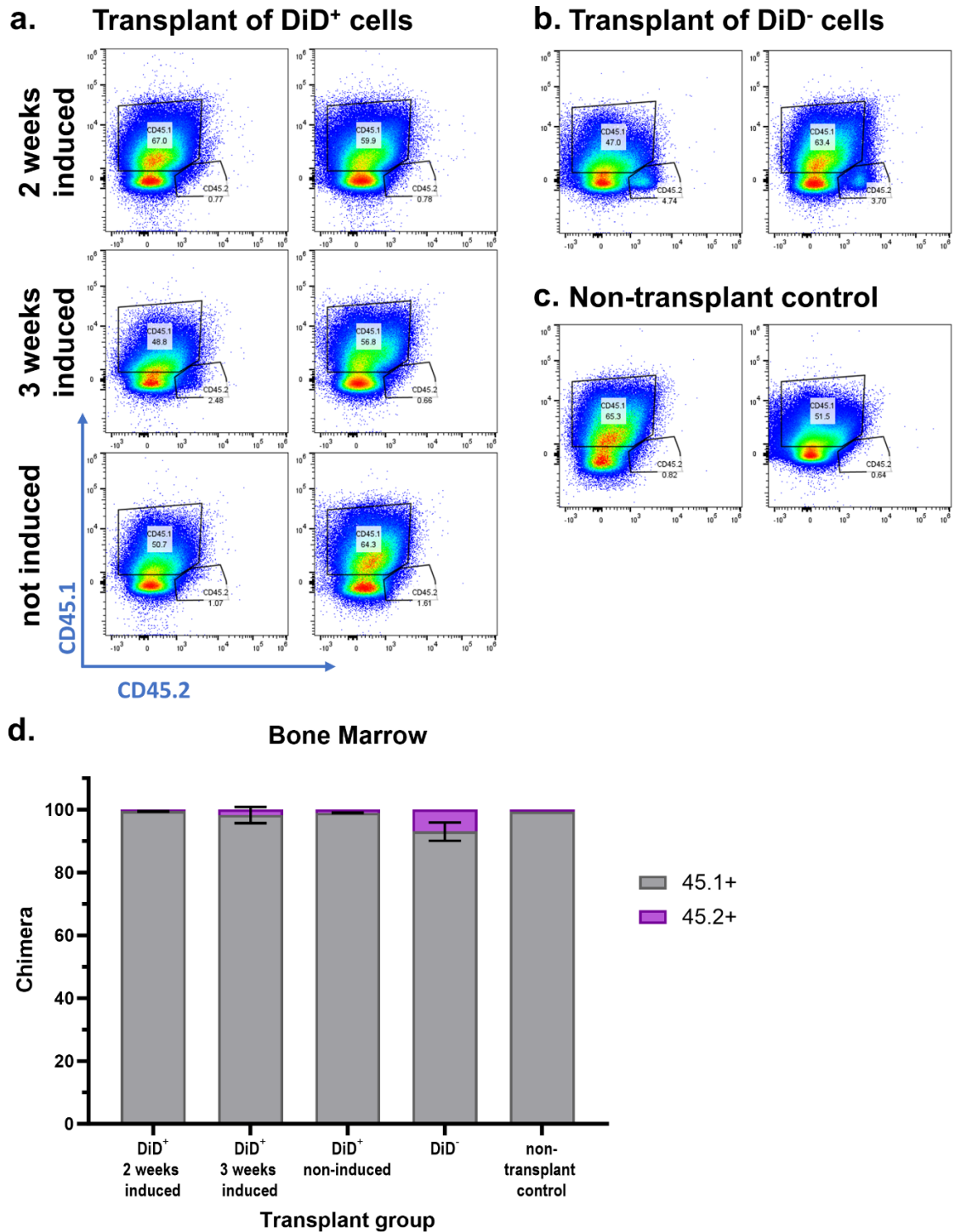


**Figure 3-32 BM chimerism reveals lack of engraftment of DiD-stained LT-HSCs.** BM cells isolated from leg bones were stained for CD45.1 and CD45.2 surface markers and acquired with flow cytometry (a-c). Chimerism in the BM (d) are shown. Data was plotted as mean  $\pm$  S.D. of  $n=2$  mice.

### 3.4 Establishing a fluorescent mouse model expressing tdTomato for *in vivo* tracing of LSCs in CML

In the following section, we aimed to utilise a different fluorescent reporter mouse model to study leukaemic cell location *in vivo*. By crossing the SCL-tTA/BCR::ABL1 mouse with the mTmG mouse<sup>373</sup>, we generated a valuable fluorescent mouse model tailored for studying leukaemic cells residing in the BM. In the mTmG model, the mTmG cassette was inserted into the ROSA26 locus on chromosome six, which enables the global expression<sup>373</sup>. Generally, the mTmG mouse expresses the membrane-targeted fluorescent protein tdTomato (mT)<sup>373</sup>. Activation of the Cre recombinase, triggers the conditional excision of mT, leading to expression of membrane-targeted GFP (mG)<sup>373</sup>. However, the SCL-tTA/BCR::ABL1 model has no Cre alleles, therefore cells express tdTomato (tdTom) allowing tracking of Ph<sup>+</sup> cells. Importantly, the CD45 allele expressed in the mTmG mice was confirmed to be the same as in the DTG mouse model (CD45.2), which additionally allows leukaemic cells to be distinguished from healthy cells in allograft experiments.

#### 3.4.1 Localising tdTom<sup>+</sup> cells in the calvarium allografted to a recipient mouse

First, we wanted to test our hypothesis that membrane-targeted tdTom-labelled cells are superior for *in vivo* tracking of BM cells compared to the GFP-LC3 model. Unlike GFP, which is excited by wavelengths in the blue/green spectrum of visible light, tdTom's excitation maximum is closer to the infrared spectrum. Therefore, it is excited by longer wavelength lasers, reducing scattering and allowing for deeper laser penetration<sup>258,261</sup>.

To assess the suitability of crossing the DTG model with the mTmG mouse for microscopy, LSK cells isolated from a WT mTmG mouse were transplanted into WT CD45.1 recipient mice (**Figure 3-33**). After three weeks, the mice were humanely sacrificed, and their calvarium immediately prepared for imaging. Therefore, the entire mouse was placed on the microscope stage, the calvarium was exposed, and a metal holder was attached to the skull bone using dental cement. The metal holder allows for stabilisation of the mouse during imaging as well as allowing creating a reservoir that is needed for imaging with an objective

(20x) designed for aqueous mounting medium immersion. A representative image (Figure 3-34c) displayed numerous tdTom<sup>+</sup> cells, confirming robust fluorescent detection of transplanted cells in the calvarium. A larger tile scan of the calvarium is shown in Figure 3-35. Further, BM chimera was assessed by flow cytometry, confirming high engraftment of the mTmG BM cells in both mice (Figure 3-34a). Additionally, the LSK-LSAM panel was used to assess the percentage of tdTom<sup>+</sup> and tdTom<sup>-</sup> cells in different populations (Figure 3-34b), indicating that most haematopoietic cells express evenly high levels of tdTom, except for ST-HSCs where 40% were found to express low levels of tdTom.

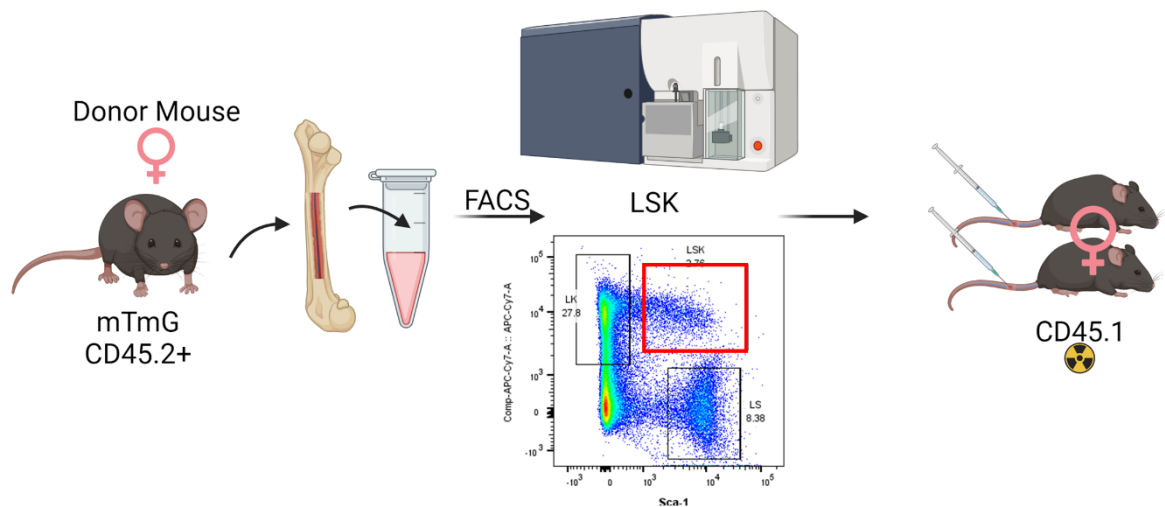


**Figure 3-33 Experimental design of allografting tdTom<sup>+</sup> BM cells to WT CD45.1 for *in vivo* tracing.** BM cells obtained from the leg bones of a mTmG mouse (one female) were sorted for LSK cells by FACS. Per mouse 25,000 LSK cells along with 1.75 million carrier cells from a CD45.1 mouse (one female) were transplanted by tail vein injection. Mice were allowed to recover for three weeks, then the animals were humanely killed, and tissue collected for analysis. Created with BioRender.com.

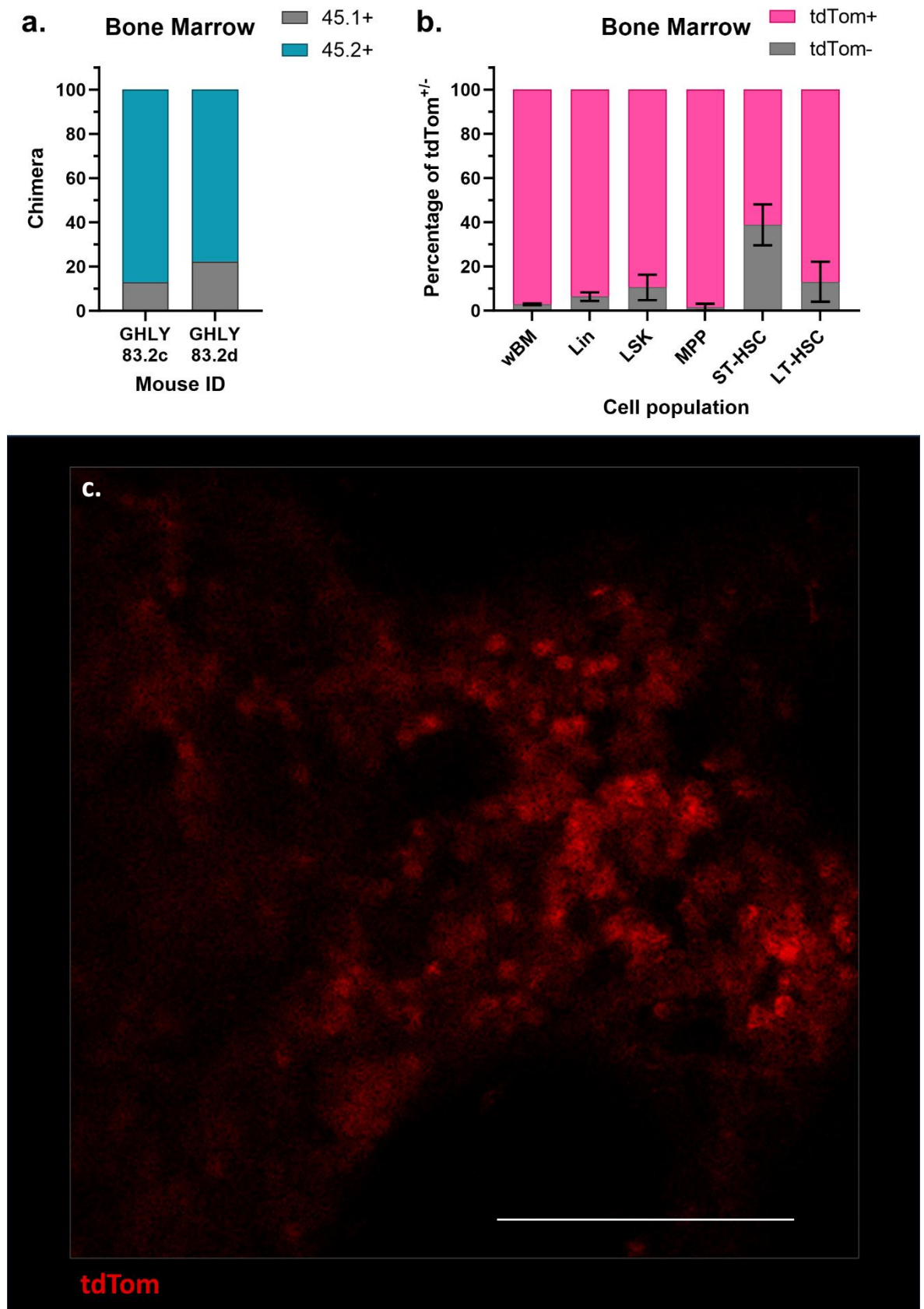


**Figure 3-34 Visualising mTmG BM cells transplanted to CD45.1 WT recipient mice via microscopy.** The BM chimerism in recipient mice is demonstrated in (a), and the expression of tdTom in different cell populations was assessed using flow cytometry (b). Microscopy on the calvarium was performed immediately after mice being sacrificed to visualise tdTom<sup>+</sup> cells. Image (c) was acquired in spectral mode, and the unmixed signal from tdTom<sup>+</sup> cells is depicted in red. Scale bar: 100 $\mu$ m.

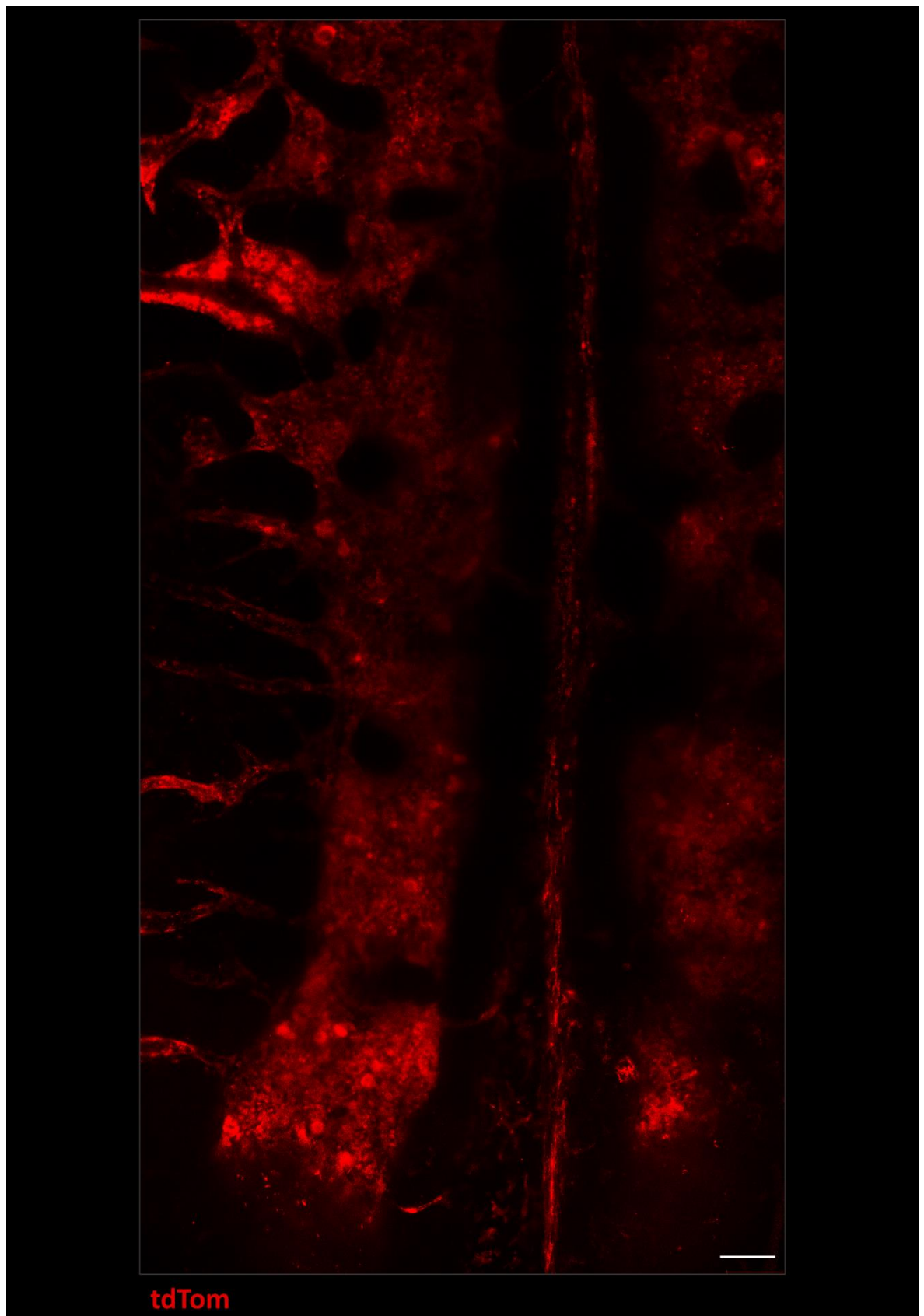


**Figure 3-35 Tile scan of the calvarium of mTmG chimeric mouse.** Microscopic imaging of the calvarium was conducted promptly after the mouse was humanely killed to observe tdTom<sup>+</sup> cell presence. Using spectral mode, a tile scan z-stack image was acquired, and the unmixed signal from tdTom<sup>+</sup> cells is depicted in red. Scale bar: 100 $\mu$ m.

### 3.4.2 Establishing DTG mTmG chimeras in busulfan-conditioned WT CD45.1 recipient mice

Busulfan, an alkylating drug, is used to condition mice for establishing allografts by targeting immune cells in the BM. This method is described as being less ablative on the BM compared to sublethal irradiation, eliminating the need for carrier marrow when transplanting more selective populations<sup>383</sup>.

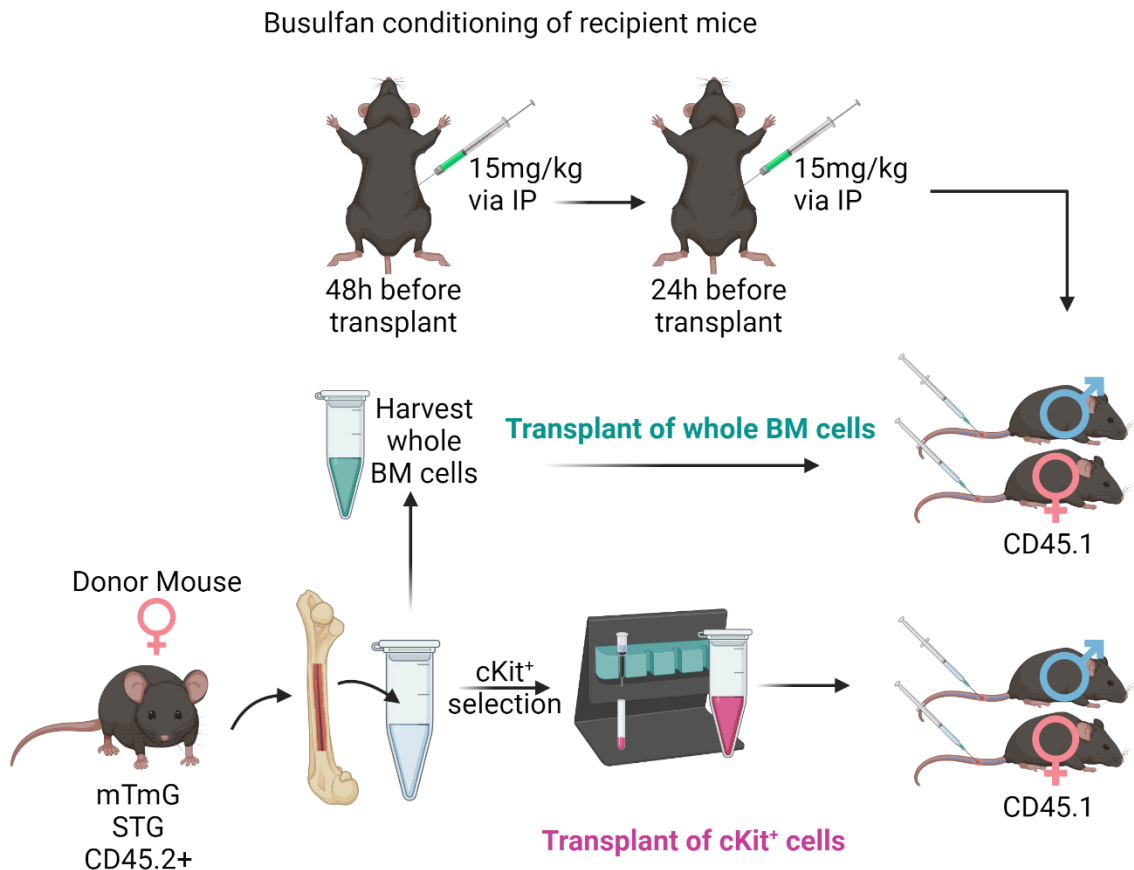


**Figure 3-36 Experimental design aimed to evaluate busulfan-conditioning of mice prior to transplant with whole BM and cKit-enriched tdTom<sup>+</sup> cells.** BM cells from a STG mTmG mouse (one female) were harvested from the leg bones and, and two million cells were transplanted to CD45.1 WT recipient mice (one female, one male). The remaining cells underwent enrichment for cKit<sup>+</sup> cells using magnetic cell separation. Subsequently, 500,000 cKit-enriched cells were transplanted per mouse (one female, one male). BM chimerism, characterised by CD45.1 and CD45.2 markers in the blood, was assessed over an eight-week period. Created with BioRender.com.

In this experiment, a small cohort of mice was set up to compare chimera development of busulfan-conditioned recipient mice after transplantation with whole BM or cKit-enriched cell population (**Figure 3-36**). The mice were treated with 15mg/kg busulfan 48 hours and 24 hours before transplantation, a protocol previously used successfully by other research groups within the institute. The development of chimerism was assessed by weekly bleeds up to eight weeks

post-transplantation, at which point the results indicated stable levels of chimerism with the previous weeks (**Figure 3-37a-b**). Notably, mice receiving the cKit-enriched transplant showed a similar degree of chimerism (~50% of CD45.2 cells), while only one out of two mice transplanted with whole BM exhibited engraftment (~30% of CD45.2 cells). After eight weeks, all mice were humanely killed to validate the chimerism in the BM, which was overall higher than the blood but clearly reflects the chimerism detected in the blood (**Figure 3-37c-d**). Transplant of cKit-enriched cells resulted in a stable engraftment of 60% in both mice, while only one mouse in the whole BM transplanted group exhibited engraftment at all, with approximately 50% CD45.2 cells.

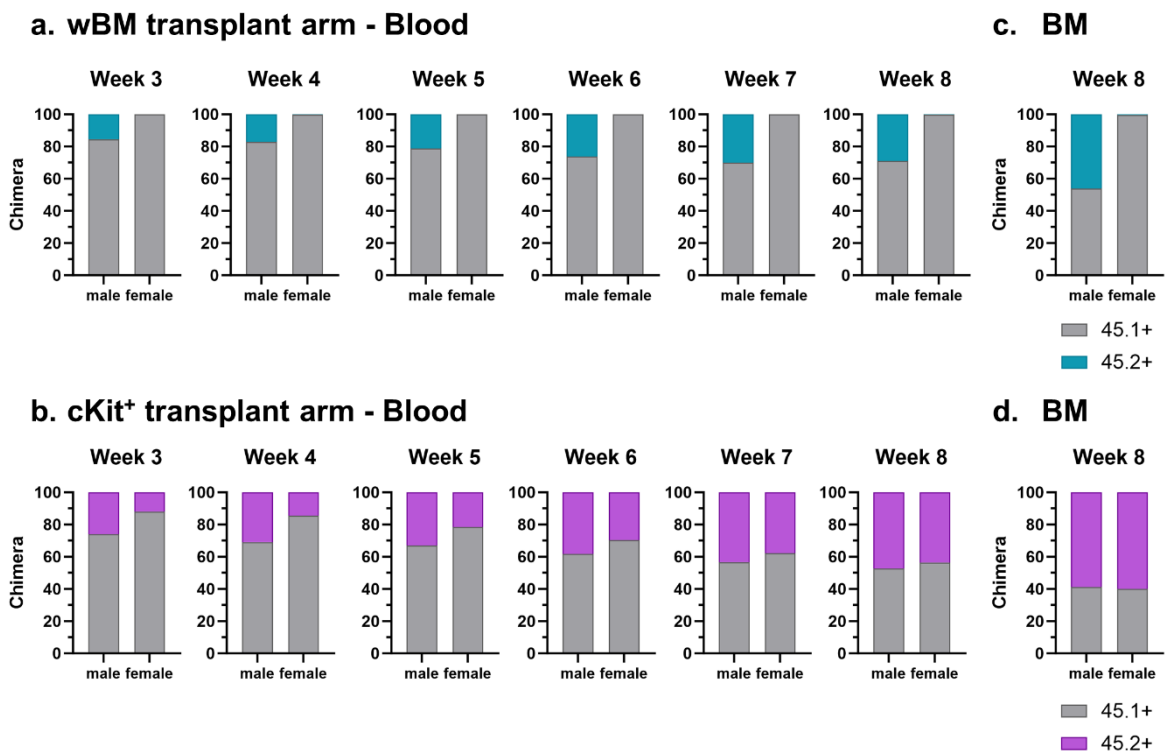


**Figure 3-37 Chimerism in cKit<sup>+</sup> recipient mice established eight weeks after transplantation.** Weekly blood samples were analysed for CD45 isotype in busulfan-conditioned recipient mice, as depicted in (a-b). Validation of engraftment in both transplant groups was performed by measuring CD45 isotype in the BM after eight weeks (c, d).

After establishing busulfan-conditioning as a successful method to transplant Ph<sup>+</sup> cells to WT recipient mice, we wanted to use this method to investigate leukaemic cells in the BM niche using tdTom as a label. We hypothesised that therapy-resistant leukaemic cells reside in a certain niche supporting their needs to endure TKI therapy. Since the cKit-enriched population resulted in a more consistent engraftment in the initial experiment with busulfan conditioning, a new cohort was set up. This cohort comprised ten mice transplanted with cKit<sup>+</sup>

BM cells from STG or DTG mTmG mice (**Figure 3-38**). STG mice lacked either the SCL-tTA or the BCR::ABL1 gene and therefore cannot express BCR::ABL1, even when tetracycline is removed from the drinking water, serving as the non-leukaemic transplant control. Once the cells engrafted and chimerism remained stable, measured through weekly bleeds, the mice were to be induced to develop leukaemia for *in vivo* localisation of leukaemic and non-leukaemic cells in the calvarium. Therefore, mice will be injected with fluorescent dextran to visualise the vasculature during IVM.

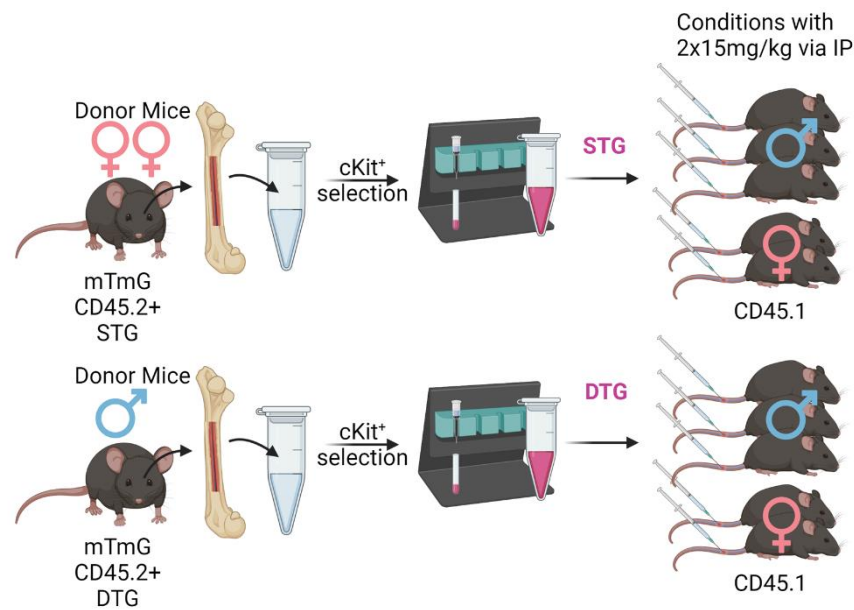
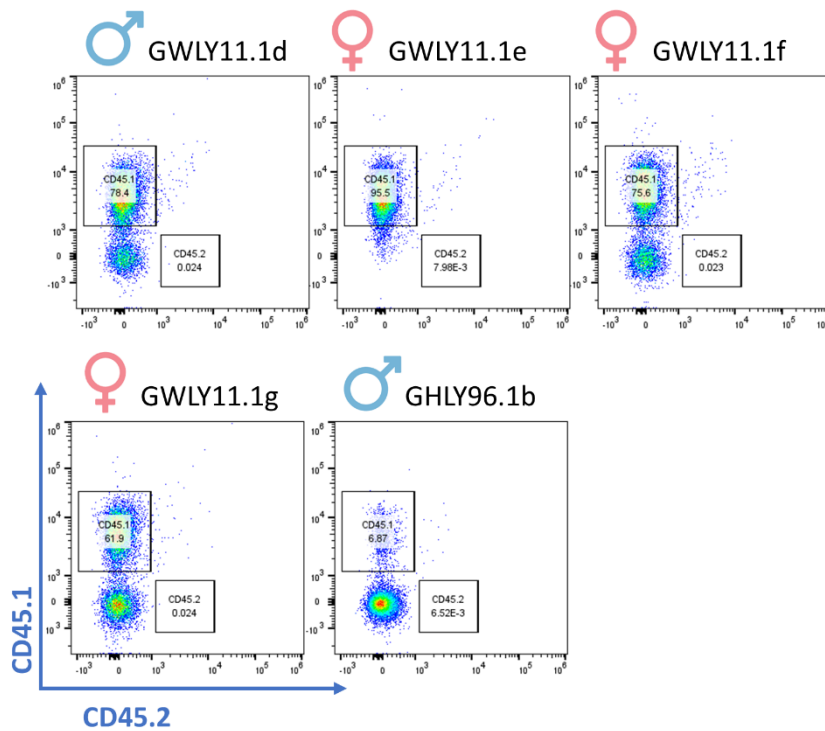


**Figure 3-38 Experimental setup of investigating leukaemic vs non-leukaemic BM cells in busulfan conditioned mice.** BM cells from two STG mTmG mice (two females) and a DTG mTmG mouse (male) were isolated from the leg bones and enriched for cKit<sup>+</sup> cells. Per mouse 500,000 cKit<sup>+</sup> enriched cells were transplanted to busulfan-conditioned mice (2x 15mg/kg via IP 48 hours and 24 hours prior to transplant). Chimera with CD45.1 and CD45.2 markers in the blood were assessed over five weeks. Created with BioRender.com.

Unfortunately, the first cohort entirely failed engraftment of donor cells (**Figure 3-39**). Subjecting the mice to weekly bleeds, no CD45.2<sup>+</sup> cells were detected after five weeks. As both transplant arms were affected, it is unlikely that the issue stemmed from the donor cells, which were harvested the same day from different donor mice. As in the previous experiment (**Figure 3-37**), the cells were isolated from donor marrow, purified by magnetic cell separation, and transplanted (500,000 cells per mouse) within a span of three hours. One possibility is precipitation of busulfan before dosing of the mice, thereby lowering the required dose.

### a. STG transplant arm - Blood Chimera



### b. DTG transplant arm - Blood Chimera

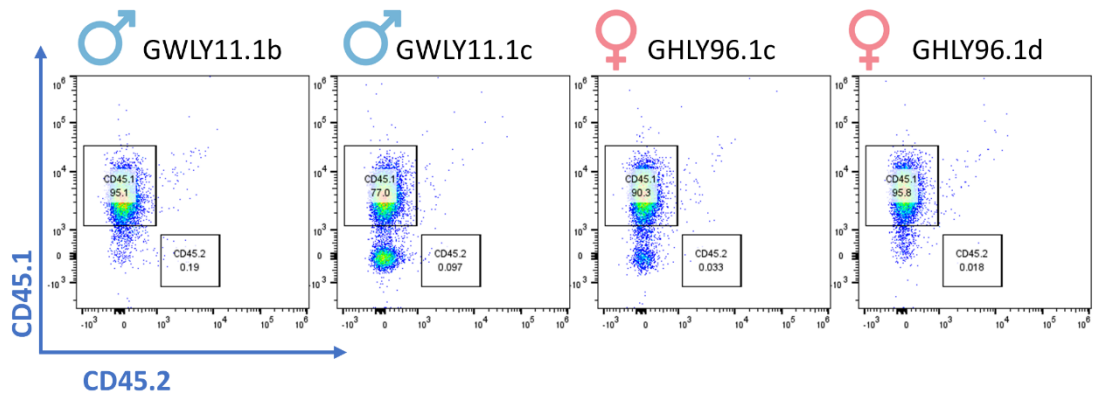


**Figure 3-39 Unsuccessful engraftment of STG and DTG mTmG BM cells in busulfan conditioned mice.** Blood samples were collected from STG (a) and DTG (b) recipient mice four weeks after allograft and analysed for CD45 isotype. One mouse in the DTG transplant arm was lost due to an unrelated condition.

Therefore, this experiment was repeated with a cohort of ten mice, with five mice per transplant arm. Steps were taken to ensure that busulfan remained in solution by dosing as quickly as possible after preparing the drug and maintaining it in a water bath at 37°C. However, engraftment was inconsistent, not only between the transplant arms but also within them (**Figure 3-41**). Out of five mice in the STG transplant group, only one mouse exhibited small percentage of engraftment (<20%), while in the DTG group, two out of five mice showed good engraftment (~50%). Consequently, no further analysis was performed with this

cohort due to lack of consistent engraftment of STG or DTG mTmG cells and it is apparent that optimisation of busulfan conditioning for successful allografts is required before proceeding.

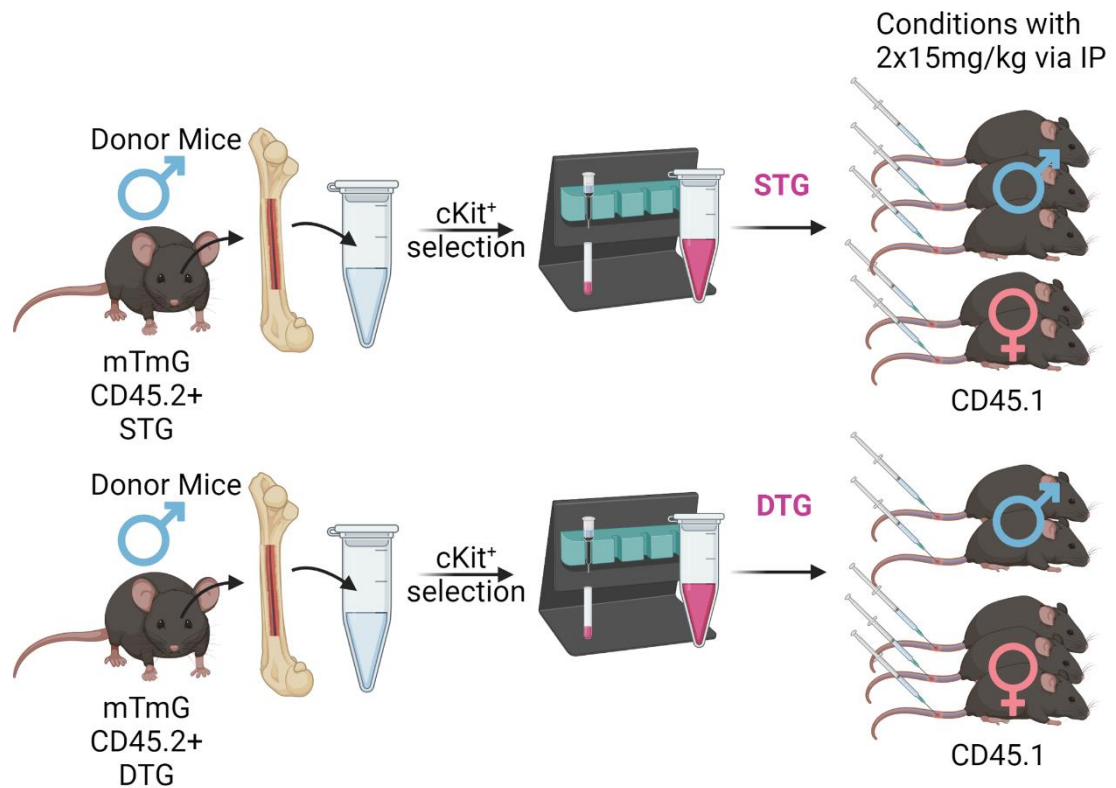


**Figure 3-40 Experimental setup of allografting DTG and STG cKit<sup>+</sup> cells to busulfan conditioned mice.** BM cells from a male STG mTmG mouse and a male DTG mTmG mouse were harvested from the leg bones, enriched for cKit<sup>+</sup> cells via magnetic cell separation and transplanted into busulfan conditioned mice (500,000 cKit-enriched per mouse; busulfan administrated at 2x 15mg/kg via IP 48 hours and 24 hours prior to transplant). Chimera with CD45.1 and CD45.2 markers in the blood were assessed over six weeks. Created with BioRender.com.

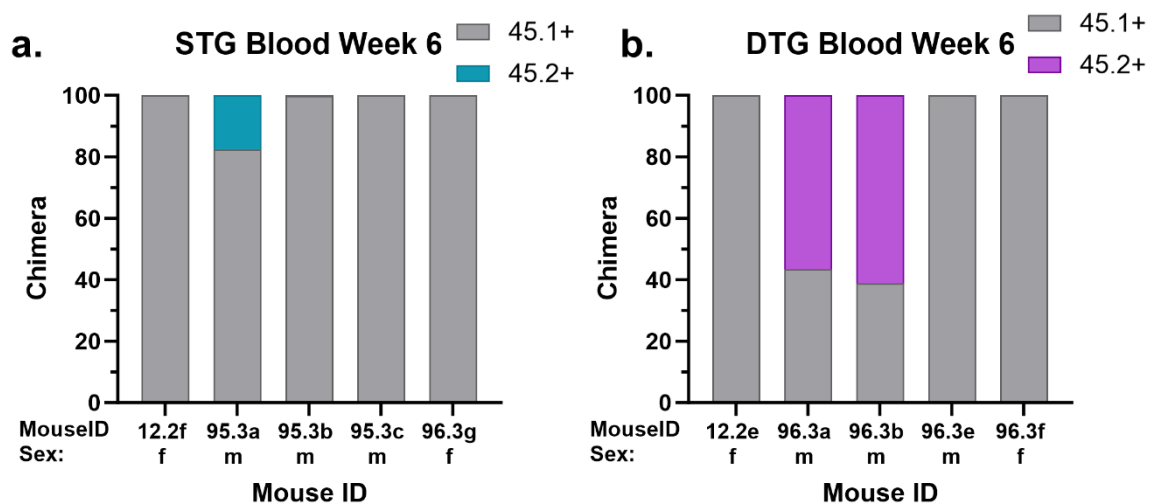


**Figure 3-41 Highly variable engraftment of STG and DTG mTmG BM cells in busulfan conditioned mice.** Blood samples from STG (a) and DTG (b) recipient mice were collected six weeks after allograft and analysed for CD45 isotype. Stacked bar charts depict the ratio of CD45.1<sup>+</sup>/CD45.2<sup>+</sup> BM cells.

### 3.4.3 Localising tdTom<sup>+</sup> cells in leukaemic and non-leukaemic mice transplanted into irradiated recipient mice

Although irradiation is more damaging to the BM and has a higher chance of developing severe complications within the initial three weeks of irradiation (BM failure, intestinal damage), it is consistent regarding the generation of chimeras with BM transplants. To study LSCs in the BM niche, we set up a cohort of ten mice, which are transplanted with cKit-enriched BM cells from STG or DTG mTmG donor mice. After a recovery time of three weeks, BCR::ABL1 expression was induced for two weeks to allow leukaemia development, with the intention of following up with two to four weeks of TKI treatment. Ideally, non-recovery IVM is done with one mouse at beginning of treatment and then weekly with one DTG mouse each. The STG mice are used as non-leukaemic healthy control (Figure 3-42).

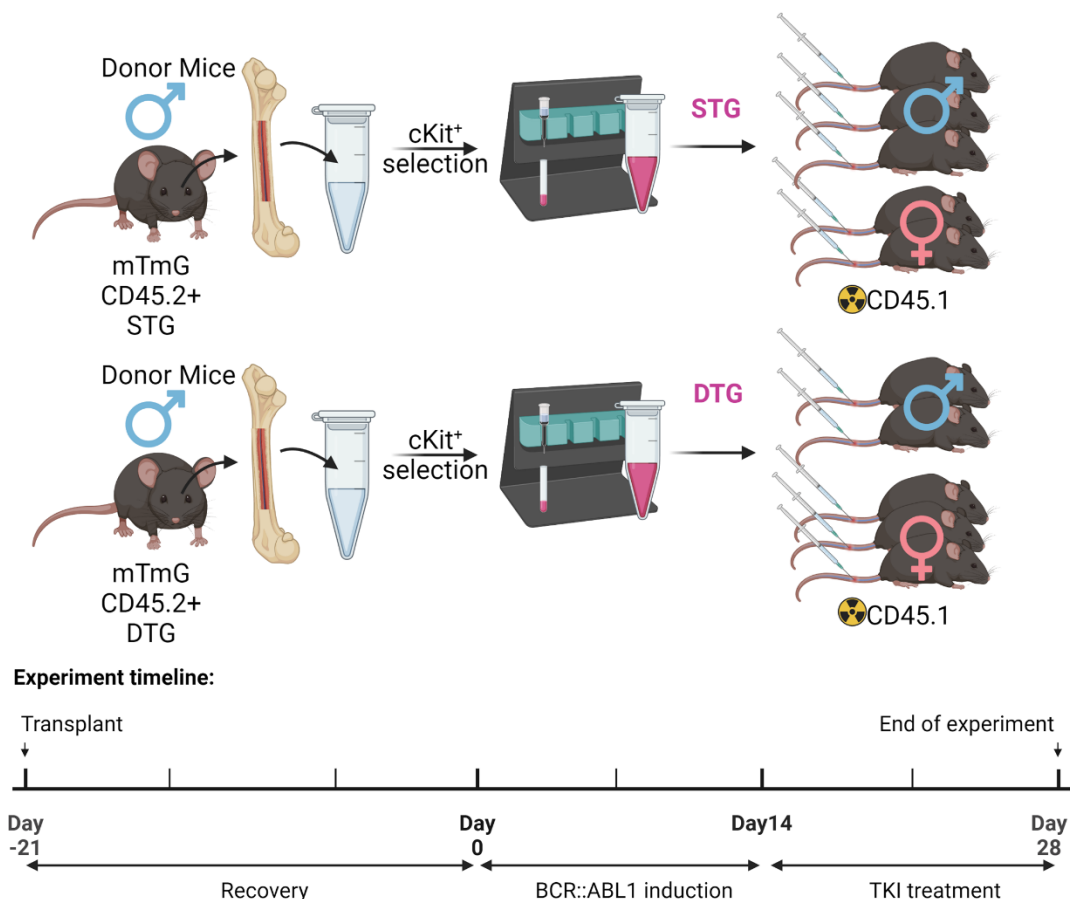
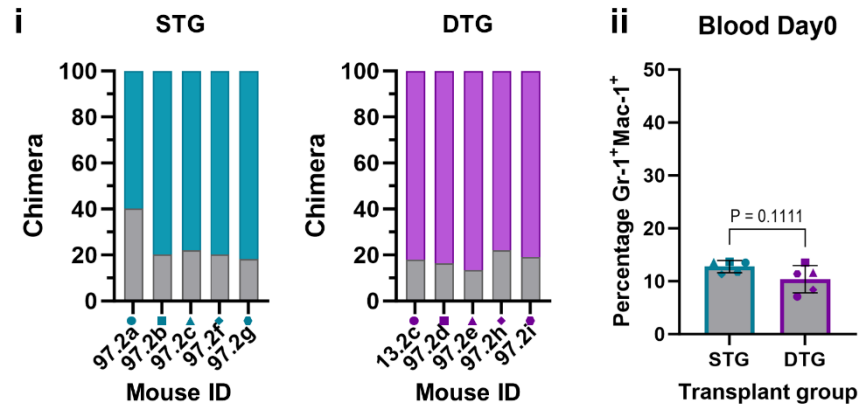


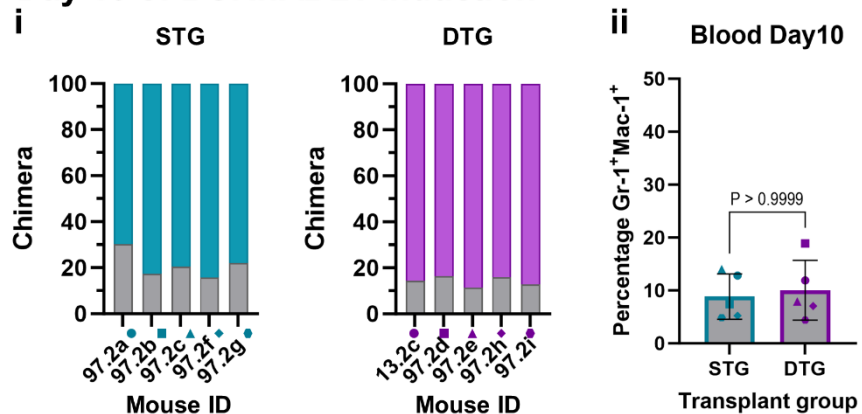
**Figure 3-42 Experimental design for localising therapy resistant LSCs within the BM niche.** BM cells were obtained from both STG and DTG mTmG mice, and cKit<sup>+</sup> cells were isolated. Subsequently, one million cKit<sup>+</sup> cells along with one million carrier cells (WT CD45.1) were transplanted into irradiated recipient mice. After allowing a recovery period of three weeks, tetracycline was removed from the drinking water to induce BCR::ABL1 expression. The intended protocol included inducing leukaemia for two weeks, followed by a two-week period of TKI treatment. However, unexpected deterioration of mice in the DTG arm led to premature termination of this experiment.

The initial assessment involved measuring CD45.2 cell engraftment through blood sampling (**Figure 3-43a i**). Most mice exhibited high engraftment of CD45.2 cells, with approximately 80% detected in the blood. Leukaemia development was monitored by evaluating granulocyte levels in the blood. On the day of tetracycline removal (day 0), all mice displayed an average 10% of Gr-1<sup>+</sup>Mac-1<sup>+</sup> granulocyte within the CD45<sup>+</sup> cell population after erythrocyte lysis (**Figure 3-43a ii**). Surprisingly, ten days post-induction, DTG mice did not show an increased percentage of granulocytes in the blood compared to day 0 or the control group (**Figure 3-43b ii**). Unexpectedly, the experiment had to be terminated after 14 days of induction due to sudden deterioration and death of mice in the DTG group. Blood samples showed elevated values of granulocytes in three DTG mice. Blood from one DTG mouse GWLY13.3c was unavailable for sampling. The remaining DTG mice did show a non-significant increase in granulocytes in the peripheral blood with high variability compared to the STG group (**Figure 3-43c ii**). Analysis of the spleen revealed granulocyte infiltration in the DTG group, with larger spleens observed compared to the control group (**Figure 3-44**).

## a. Day 0 of BCR::ABL1 induction



## b. Day 10 of BCR::ABL1 induction



## c. Day 14 of BCR::ABL1 induction

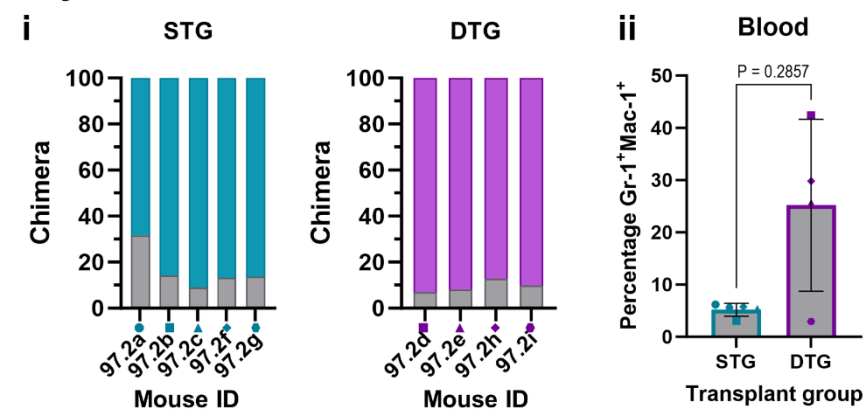


**Figure 3-43 Leukaemia development was detected in DTG mice after two weeks of BCR::ABL1 expression.** Blood samples were collected at day 0 (a), day 10 (b) and day 14 (c) following BCR::ABL1 induction in both transplant arms to analyse the CD45 isotype and the percentage of granulocytes (CD45<sup>+</sup>Gr-1<sup>+</sup>Mac-1<sup>+</sup>) in the blood. Graphs are displayed as mean  $\pm$  S.D., with a sample size of  $n=5$ . P-values were calculated using the unpaired, non-parametric Mann-Whitney test.

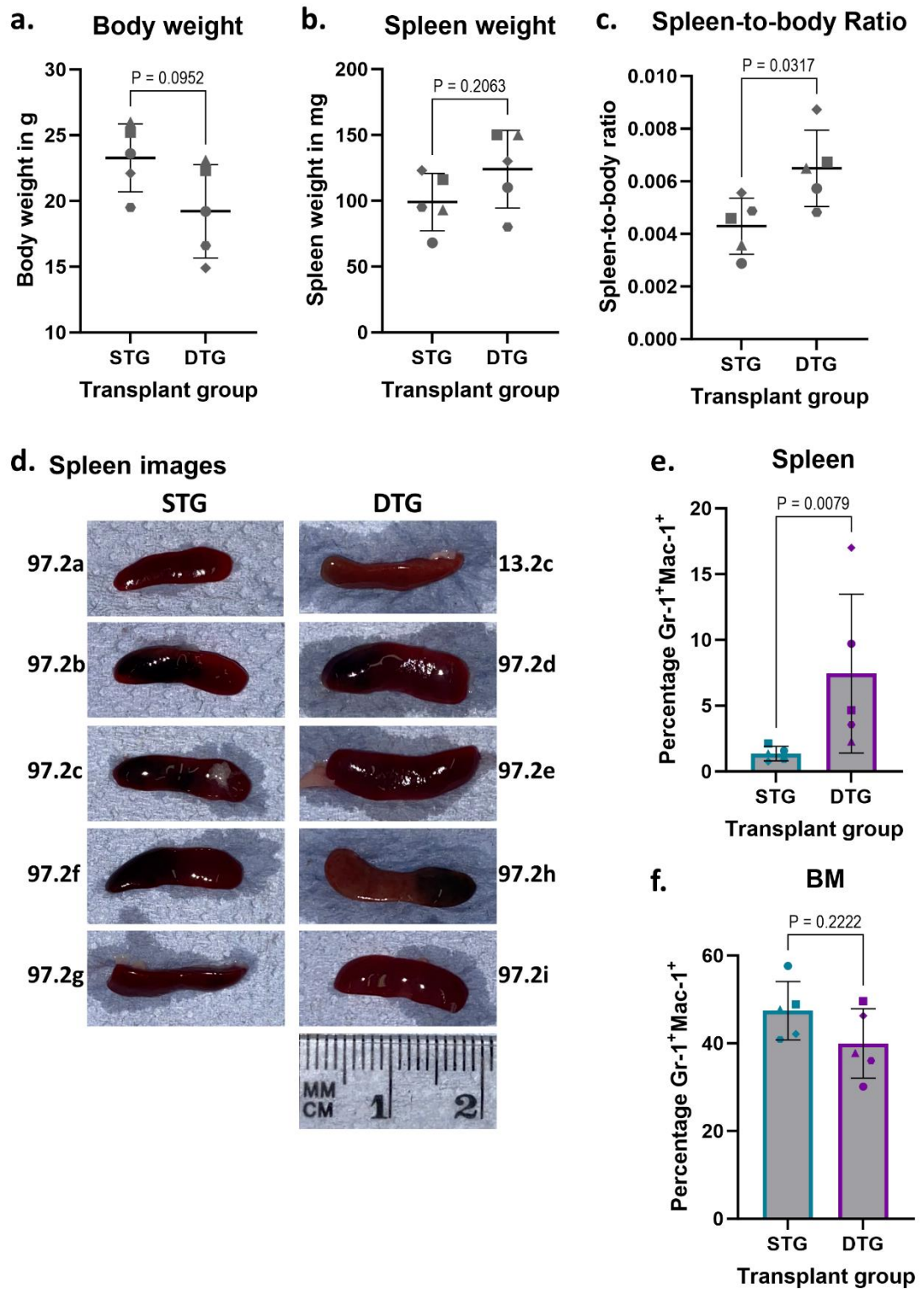


**Figure 3-44 Splenomegaly and myeloid cell infiltration were observed in the spleens of DTG recipient mice.** Body weight (a) and spleen weight (b) were measured to calculate the spleen-to-body ratio (c). Images of the spleen are presented in (d). Quantification of granulocytes (CD45<sup>+</sup>Gr-1<sup>+</sup>Mac-1<sup>+</sup>) in the spleen and the BM is shown (e-f). The data were presented as mean  $\pm$  S.D. of  $n=5$ . P-values were determined using the Mann-Whitney test.

## 3.5 Discussion

The aim of this project was to develop suitable genetic engineered mouse models to study LSCs in their physiological environment, the BM niche. Localising LSCs and identifying how the niche contributes to LSC persistence is a crucial step in developing new curative therapies.

### 3.5.1 Fluorescent model to localise LSCs and study autophagy

Firstly, the SCL-tTA/BCR::ABL1 GFP-LC3 mouse model was investigated for suitability for localising and studying LSCs *in vivo*. These studies elucidated that the GFP-LC3 expression in primitive cell populations is consistently higher than in more differentiated and matured haematopoietic cells (**Figure 3-1**). Next, *in vitro* studies aimed to elucidate autophagic flux in response to metabolic stress stimuli and treatment with autophagic inhibitors. Indeed, flow cytometry and microscopy analysis provided evidence of the model's reliability in recapitulating autophagy modulation in primary mouse BM cells (**Figure 3-2, Figure 3-3**). Confocal microscopy analysis confirmed increased autophagosome formation in LSK cells under metabolic stress, further emphasizing the model's potential for investigating autophagic processes in primitive BM cells *in vivo* (**Figure 3-3**).

Further, a competitive transplant of sorted DTG GFP-LC3 BM cells to irradiated WT recipient mice highlighted the lack of long-term engraftment potential in the GFP<sup>low</sup> cell population, specifically resulting from depletion of LT-HSCs (**Figure 3-9, Figure 3-10, Figure 3-11**). On the other hand, GFP<sup>high</sup> population resulted in a high engraftment and subsequently into development of CML-like symptoms after 11 days of BCR::ABL1 induction, indicated by splenomegaly, increased granulocytes in the blood and myeloid cell infiltration to the spleen (**Figure 3-12, Figure 3-13**). Surprising results were detected in the non-induced control group that were transplanted with whole BM, isolated before sorting the cells into GFP<sup>high</sup> and GFP<sup>low</sup>. Depending on availability of mice and aim of the experiment, different controls groups can be set up. A non-leukaemic control can comprise recipient mice transplanted with DTG cells that are continuously treated with tetracycline and therefore BCR::ABL1 expression is not induced. Alternatively, STG cells can be transplanted, which might result in a more accurate control group as both leukaemic and non-leukaemic mice will be taken

off tetracycline treatment, which is not the case if DTG cells are transplanted to the control arm. However, in this experiment the aim was to compare engraftment potential followed by level of leukaemia upon BCR::ABL1 induction. Therefore, the control arm was transplanted with the same cells as GFP<sup>low</sup> and GFP<sup>high</sup> before sorting, but the mice remained on tetracycline treatment. Surprisingly, levels of granulocytes in the blood between control arm and GFP<sup>high</sup> arm were similar at the endpoint (**Figure 3-12**). Nonetheless, unlike mice in the GFP<sup>high</sup> group, the control mice showed an overall smaller size of spleen accompanied with no external signs of the disease, such as weight loss, change in natural behaviour or pale bones. Tetracycline is administered via drinking water (0.5g/L) and mice have free access to drinking water. However, mice that have been irradiated are generally given soft foods (DietGel 76A), during their recovery period from irradiation. Additionally, this type of food supplement is also given during onset of leukaemia, indicated by weight loss. Generally, all mice are treated the same, therefore control mice were given soft foods as well despite no indication of weight loss. This could potentially lead to reduced water intake, consequently reducing tetracycline dosing and result in a 'leaky' BCR::ABL1 gene. However, this has not been seen in previous studies in our laboratory where mice have been housed similarly. This is a speculative explanation and was not confirmed in this experiment. Future experiments with this model should include more control groups, like a non-leukaemic STG control. In addition, activity of BCR::ABL1 should be examined via Western blotting or qPCR. Despite inconsistencies in the control group, the competitive transplant of sorted DTG GFP-LC3 BM cells into irradiated WT recipient mice revealed distinct outcomes between the GFP<sup>high</sup> and GFP<sup>low</sup> transplant group. The GFP<sup>low</sup> cells demonstrated a lack of long-term engraftment potential due to LT-HSCs depletion, while the GFP<sup>high</sup> population exhibited high engraftment followed by development of neutrophilia and splenomegaly, suggesting suitability of GFP-detection for primitive cells in this model.

Initial *ex vivo* microscopy of the calvarium of DTG GFP-LC3 mice revealed cells exhibiting a robust GFP signal that was absent in WT mice (**Figure 3-14**), indicating the signal to emerge from GFP-LC3 signal and not autofluorescence. Despite high engraftment levels of DTG GFP-LC3 cells in recipient mice post-transplantation, GFP<sup>+</sup> cells were not detectable in the calvarium by *ex vivo*

microscopy (**Figure 3-15**, **Figure 3-16**, **Figure 3-17**). Notably, isolated primitive BM cells subjected to microscopy after *in vitro* culture exhibited detectable GFP signals (**Figure 3-3**), leading to the conclusion that the cells observed in *ex vivo* microscopy of the calvarium likely represent non-haematopoietic cells, while the cells of interest express levels insufficient for *in vivo* detection. Imaging the BM within the whole bone causes scattering, potentially limiting the fluorescence detection compared to direct imaging of the cells. Furthermore, these cells in the calvarium appeared larger (~20µm diameter) compared to cells imaged *in vitro* (~10µm diameter), indicating another cell type present in the BM expressing an even higher level of GFP-LC3 compared to HSPCs.

In summary, the SCL-tTA/BCR::ABL1 GFP-LC3 mouse model stands as a valuable tool for studying autophagy in primitive leukaemic cells, demonstrating its potential in understanding the molecular process underlying LSC persistence. However, challenges persist in detecting GFP<sup>+</sup> LSCs within the BM niche, thus presenting unsuitable to localise LSCs in their physiological environment. Further development needs to be performed for this model to contribute to studying LSC interaction and modification in the BM microenvironment. Initial experiments with injectable fluorescent antibodies were performed (**Figure 3-19**, **Figure 3-20**) to label HSCs *in vivo*. This showed high variability between detection of different fluorophores but could be a suitable method when further optimised.

### 3.5.2 Evaluating *ex vivo* cell-labelling for *in vivo* tracking of LSC

This study aimed to evaluate the suitability of utilising lipophilic dyes, specifically DiD, for tracking LSCs within the BM microenvironment. Therefore, cells were isolated from donor BM and stained *ex vivo* before transplantation to conditioned recipient mice via IV injection into the tail vein. Membrane dyes have been used like this to study BM homing *in vivo* for up to two days post-transplantation<sup>75</sup>, however no data about long-term usage was available. Therefore, we performed a set of experiments to evaluate if *ex vivo* staining would be feasible for the required timeframe of the DTG model.

Initial challenges were presented by discrepancies between staining success in human cell-lines versus primary mouse BM cells (**Figure 3-24**). Adjustments to the staining protocol involved reducing the suspension volume, enhanced

vortexing and shorter incubation times, which significantly improved efficiency in staining cKit<sup>+</sup> primary cells (**Figure 3-25**). DiD-label retention for *in vivo* tracking was assessed over three weeks, with weekly analysis, while mice were induced to express BCR::ABL1. However, a significant presence of DiD<sup>+</sup> cells could not be detected in any of the mice (**Figure 3-27**). Overall, minimal detected signal in *ex vivo* microscopy of the calvarium was shown in both transplant arms and suggests background signal rather than specific cell tracking (**Figure 3-28**, **Figure 3-29**, **Figure 3-30**). Another experiment was conducted with the aim to compare DiD-tracking in non-leukaemic cells versus leukaemic mice transplanted with DiD<sup>+</sup> LT-HSCs. However, DiD<sup>+</sup> LT-HSCs failed to engraft, indicating that conditions during DiD-labelling might have been too harsh.

Overall, the study encountered challenges in achieving sustained and detectable tracking of DiD-labelled primitive cells in the BM microenvironment. The limitations in the protocol, particularly in optimisation in DiD-labelling of primary mouse cells, warrant further refinement and exploration. Further, suitability of long-term retainment of DiD-label could be investigated *in vitro* using primary mouse cells in long-term culture, which could provide a more direct and resource saving method. Long-term *ex vivo* expansion cultures, as published by Wilkinson *et al.*, could be useful for evaluating this<sup>384</sup>.

### 3.5.3 Conditioning mice for BM transplantation

In this study, we investigated different methods of BM transplantation aimed at reducing the impact on the BM microenvironment while successfully transplanting DTG cells into WT recipients. Total-body irradiation is a widely applied technique for allografting BM cells but carries several disadvantages. Although complications such as intestinal toxicity are rare, they can occur, and BM failure is a recognized side effect. Generally, whole BM transplants decrease the risk of BM failure by ensuring the survival of myeloablated recipients until the donor HSCs generate enough mature blood cells. Therefore, when purified HSPCs were transplanted to irradiated mice, carrier cells in the form of whole BM from a WT recipient littermate were co-transplanted. However, irradiation has been demonstrated to induce damage to the microvasculature, resulting in temporary vascular permeability accompanied by a reduction in endothelial cell

count<sup>75,385</sup>. Moreover, it has shown that irradiation affects BM stromal cells, crucial for regulating and maintaining HSCs<sup>386</sup>.

One approach to reduce impact on the BM microenvironment is conditioning mice using the alkylating agent busulfan, which reduces the number of native HSCs while avoiding extensive ablation of the BM. Generally, recipient mice were treated with busulfan (30mg/kg via IP) split in two doses administered 48 hours and 24 hours before transplantation of donor cells as established by Montecino-Rodriguez *et al.*<sup>383</sup>, which was further optimized in house by other research groups to be suitable for the CD45.1 recipient mice. Initially, the transplantation of cKit-enriched cells exhibited more consistent engraftment rates compared to whole BM cells in busulfan-conditioned mice (**Figure 3-37**). Despite this success, attempts to replicate consistent engraftment with STG or DTG mTmG cells using busulfan-conditioning presented significant challenges, resulting in unpredictable and varied engraftment levels (**Figure 3-39**, **Figure 3-41**). Generally, transplantation of BM cells, that are enriched for cKit<sup>+</sup> cells by magnetic cell separation, have consistently resulted in a successful engraftment to irradiation-conditioned mice (**Figure 3-7**, **Figure 3-43**). In the experiments described using busulfan-conditioned mice, the cells were isolated the same way and therefore should have engrafted. One potential reason for inconsistent engraftments could be the handling the freshly prepared drug resulting in inconsistent dosing of the mice. Although preparation of busulfan was done as described by Montecino-Rodriguez *et al.* and first dissolved in pure anhydrous DMSO, then resuspended in warm PBS, it was noted that the drug precipitates quickly if not kept at 37°C. Consistent dosing of the drug immediately after preparation is crucial for successful engraftment and needs further optimization in establishing stable chimeras.

Another approach to mitigate BM niche damage for studying LSCs in an unaltered environment and evaluating their impact on a healthy niche was the transplantation of DTG cKit-enriched BM cells into non-conditioned mice. However, over a three-week period and induction of BCR::ABL1 expression, no observable engraftment occurred (**Figure 3-7**). While it was previously believed that non-conditioned mice lacked the necessary space for donor HSCs, recent evidence suggests otherwise, indicating that transplantation of a higher number

of LT-HSCs can indeed establish chimerism in unconditioned mice<sup>387</sup>. While in our experiment, 400,000 cKit-enriched cells, containing approximately 400 LT-HSCs, were transplanted without successful engraftment, Shimoto *et al.* achieved 50% chimerism by transplanting 250,000 LT-HSCs (LSK CD150<sup>+</sup>CD48<sup>-</sup>CD34<sup>-</sup>)<sup>387</sup>. However, transplanting such a high number of LT-HSCs per mouse is not feasible with the DTG model at our institute due to the mating strategies of these mice. Generally, two STG mice or alternatively a WT mouse is mated with a DTG mouse, to prevent multiple copies of the BCR::ABL1 reporter gene and have residual expression even though tetracycline is given to the mice. An alternative approach could involve *ex vivo* expansion of LT-HSCs before transplantation, as demonstrated by Wilkinson *et al.*<sup>384</sup>. They achieved a 15% BM chimerism in non-conditioned mice using only 50 LSK CD150<sup>+</sup>CD34<sup>-</sup> donor BM cells, which were expanded to approximately 800,000 cells within 28 days of *ex vivo* culture<sup>384</sup>.

### 3.5.4 Evaluation of generating chimeras with Ph<sup>+</sup> mTmG cells

The provided section details the establishment of a fluorescent mouse model for *in vivo* tracing for LSCs in CML utilising the mTmG mouse model, which expresses membrane-targeted tdTom. The initial experiment involved transplanting LSK cells from mTmG mice into WT CD45.1 recipient mice, allowing for the observation and localization of tdTom<sup>+</sup> cells in the calvarium (**Figure 3-34**, **Figure 3-35**). Further, irradiation was used to establish STG and DTG mTmG chimeric mice to study leukaemic progression and location of therapy-resistant LSCs in their physiological environment using IVM (**Figure 3-42**, **Figure 3-43a**). However, unforeseen complications arose during leukaemia induction, leading to unexpected deterioration and mortality in the DTG mice. While the mice were induced for 10 days, blood samples did not show an abnormal presence of granulocytes in DTG mice compared to the STG group (**Figure 3-43b**). However, on day 14 of induction, the planned beginning of two-weeks TKI treatment, the experiment had to be terminated due to sudden health deterioration in the DTG group (**Figure 3-43c**, **Figure 3-44**). Induction of the mice for two to three weeks, followed by TKI treatment up to four weeks is a common practice in our lab<sup>365</sup>. However, in whole BM transplants with two million BM cells, approximately 200 LT-HSCs are transplanted, while transplantation of one million cKit-enriched cells resulted in approximately 1,000 LT-HSCs being transplanted. This high frequency of LSCs might have led to sudden and more

aggressive onset of leukaemia. As engraftment of cKit-enriched cells in irradiation-conditioned mice leads to high engraftment, a lower cell number of BCR::ABL1 inducible HSCs could be transplanted. Overall, the inconsistency in engraftment levels using busulfan and unexpected complications during leukaemia induction in irradiated recipient mice emphasize the need for meticulous consideration and further refinement of methodologies in this research area.

## Chapter 4 Investigating leukaemic cell location in the BM niche by developing a cell line xenograft mouse model

### 4.1 Introduction

Immortalised human haematopoietic cell lines are widely used to study CML. In general, these CML cell lines are derived from patients diagnosed with CML following identification of Ph<sup>+</sup> cells. Cell lines provide an unlimited source of reproducible cellular material, offering a wide range of *in vitro* applications, and have been invaluable in identifying the mechanism of BCR::ABL1 oncogene-mediated cell transformation.

Human cell lines are also used in preclinical mouse models, such as xenograft experiments, to test novel treatment strategies for CML in an *in vivo* setting. *In vivo* models are important as they not only validate whether a drug targeting a specific survival pathway is successful in a mammalian organism, but also allow us to better understand the physiological conditions and the influence of the microenvironment on cell survival compared to *in vitro* experiments. Severely combined immunocompromised (SCID) mice are routinely used as xenograft recipients because they allow engraftment of human cells. Initially, CB-17Prkd<sup>scid</sup> mice were found to have dysfunctional B and T cells and to be susceptible to engraftment of human haematopoietic cells<sup>388</sup>. Since then, many versions of SCID mice have been generated, such as the NRGW mouse, which is homozygous for the Rag1<sup>null</sup> allele and lacks functional T, B and NK cells<sup>374</sup>. Additionally, NRGW lack *Ckit* alleles disrupting HSC maintenance and downstream maturation of erythroid progenitors to the extent that human cell transplantation is supported<sup>374</sup>. Patient-derived xenografts (PDX), such as transplant of human primary LSCs (CD34<sup>+</sup>), can be used to evaluate the effect of different treatments on long-term leukaemia-initiating capacity. As human primary cells are limited in availability and are more challenging to modify *in vitro*, CML cell lines are an alternative and a more versatile option for xenotransplantation. Transplantation of human-derived immortalised cell lines has been used to measure tumour-initiating capacity by observing the formation of extramedullary tumours<sup>389</sup>.

The aim our study was to develop a suitable xenograft mouse model to visualise Ph<sup>+</sup> cells in the BM using advanced microscopy and to observe their response to targeted treatment. Identifying the location of leukaemic cells directly in the BM improves our understanding of their interactions with the BM niche and other cells residing there.

## 4.2 Generating GFP<sup>+</sup> human CML cell lines for the xenograft mouse model

To study the homing and engraftment of human leukaemic Ph<sup>+</sup> cells in the BM by microscopy, the K562 and KCL22 cell lines were engineered to stably express GFP via lentiviral transduction. Although the level of transduction was high, FACS was used to purify GFP<sup>high</sup> cells from remaining GFP<sup>neg/low</sup> cells (Figure 4-1).

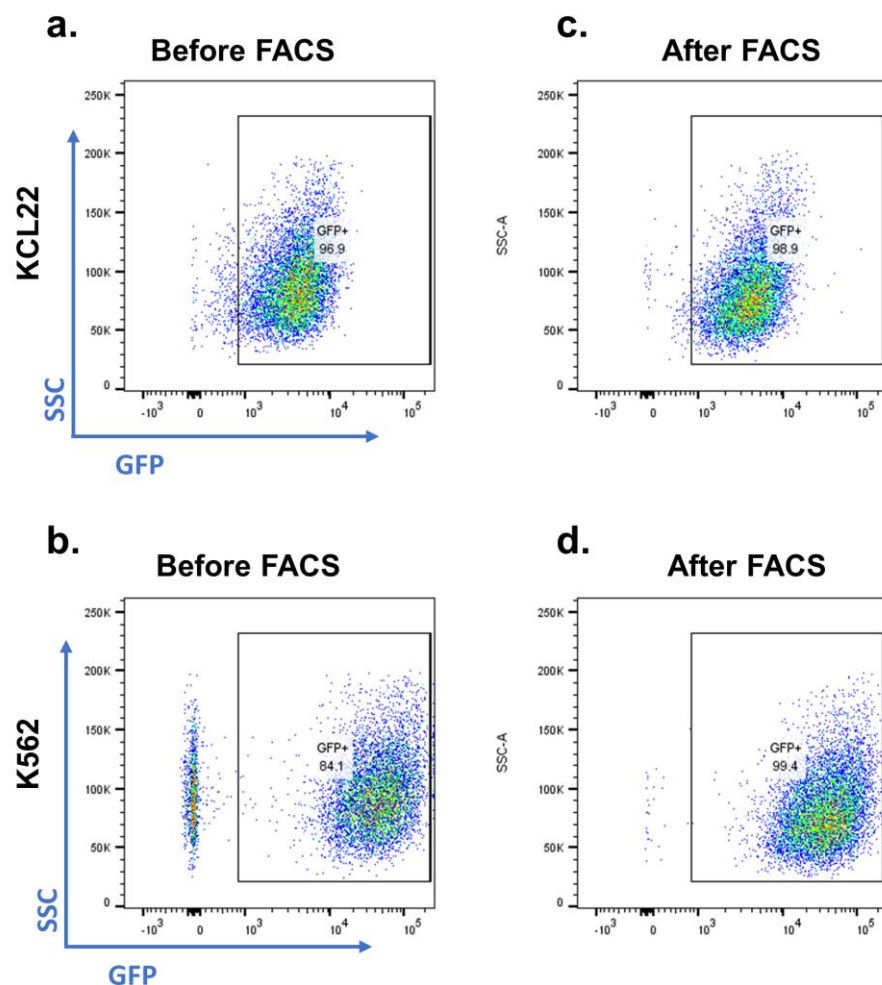


**Figure 4-1 Generation of GFP-expressing human CML cell lines.** Flow cytometry plots showing KCL22 (a) and K562 (b) expressing GFP following lentiviral transduction. FACS was performed to eliminate cells with low GFP expression (c, d).

Flow cytometry was used to measure the expression level of human CD45 (hCD45), a marker expressed on all haematopoietic cells (**Figure 4-2**). This marker was used in addition to GFP expression to identify the cells in mouse tissue. Both cell lines showed a small population (7%) that did not express hCD45. This may lead to a slight underestimation of the percentage of human cells being present in the mouse tissue but could be compensated by comparison with GFP<sup>+</sup> cells.

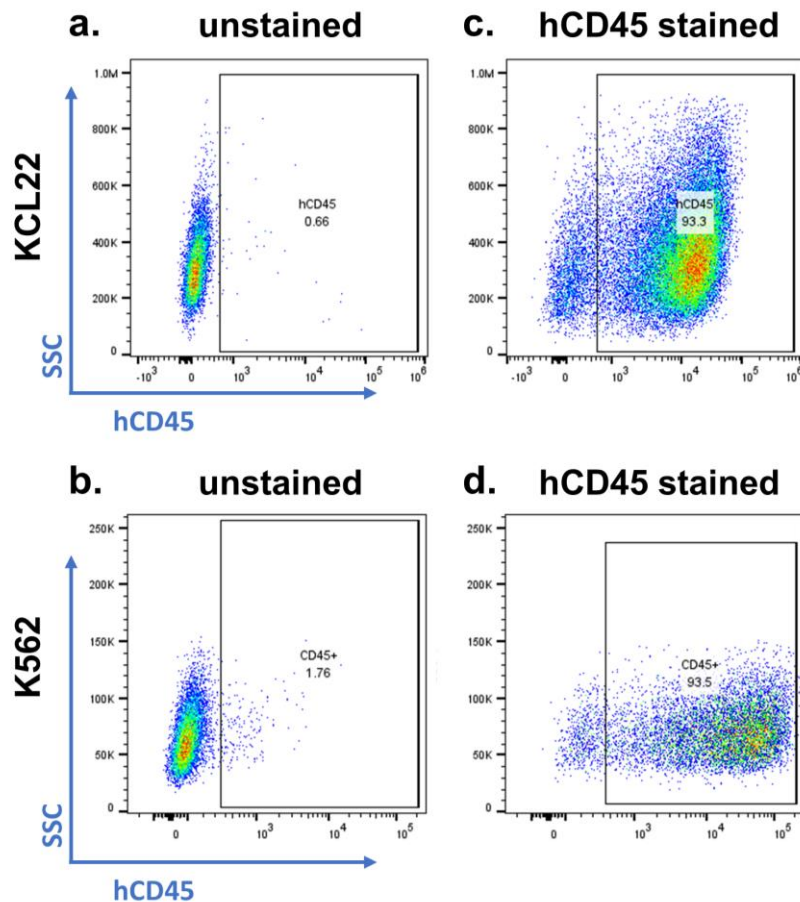


**Figure 4-2 Expression levels of hCD45 on human CML cell lines.** Left panel shows unstained control of KCL22 (a) and K562 (b). Right panel shows KCL22 (c) and K562 (d) stained with hCD45 conjugated to the fluorescent marker AlexaFluor647. Both cell lines have over 90% surface marker expression.

### 4.3 Investigating short- and long-term homing to the BM by K562-GFP cells

First, we decided to address the question whether human CML cells exhibit a preference for homing to the BM microenvironment of immunocompromised mice. This would allow us to study human CML cells in a more physiological environment compared to tissue culture. To determine whether human cell lines engraft quickly into the BM or require extended time, mice were sacrificed three

days and 21 days after transplantation. A total of four female mice of the same age (two mice per cell line) were transplanted with four million cells by tail vein injection and monitored for tumour development (**Figure 4-3**).

To assess engraftment dynamics, one mouse from each transplant arm was humanely killed three days after transplantation and blood, spleen, calvarium and leg bones were collected. Mice were examined for extramedullary tumour development at necropsy, but no tumour tissue was found. Tissue samples were processed by flow cytometry to assess the levels of cells expressing mouse CD45 (mCD45) and hCD45 (**Figure 4-4**). None of the tissues showed the presence of hCD45<sup>+</sup> cells. To discern any human cells not expressing hCD45 as mentioned above, GFP levels in the whole BM (and other tissues, not shown) was measured and found to be negative (**Figure 4-5**).

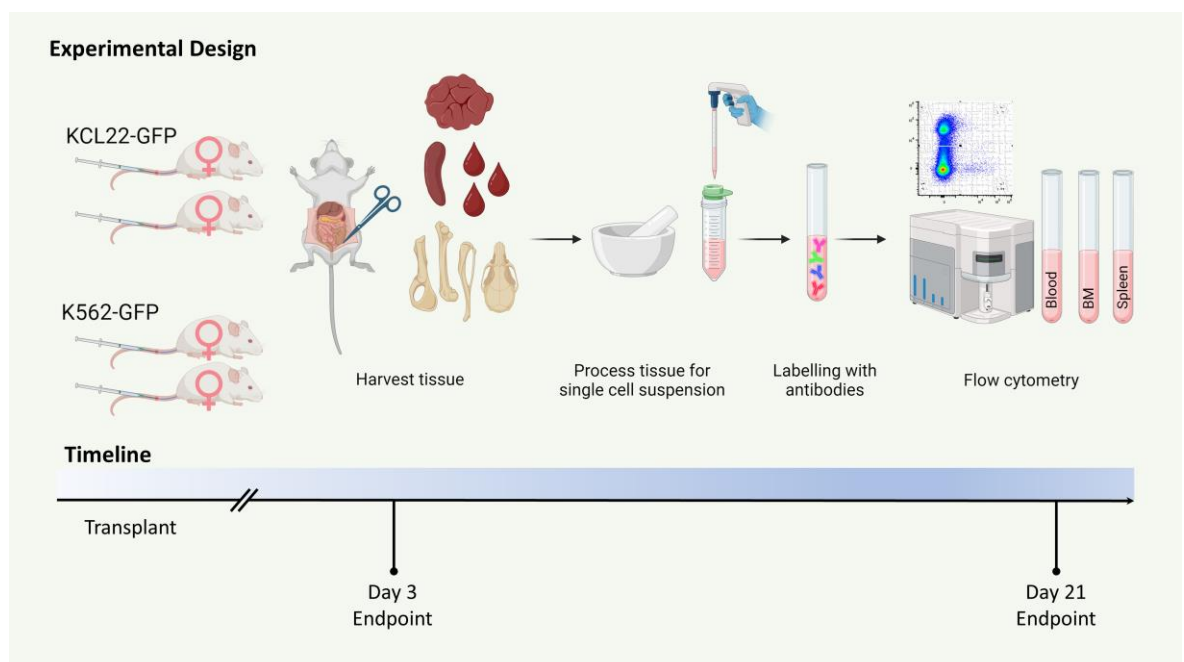


**Figure 4-3 Experimental design aimed to investigate BM engraftment of human cell lines.** Two immunocompromised mice received an injection of four million cells, either KCL22-GFP or K562-GFP. After three- and 21-days post-injection, one mouse from each group was humanely killed to assess the presence of human cells in the BM, blood, spleen, and extramedullary tumour. Bones samples were gently crushed in a mortar and strained through a cell strainer, while spleen samples were pressed through the cell strainer using a plunger. Blood samples underwent incubation in red blood cell lysis buffer. All tissues were stained with conjugated antibodies targeting mCD45 and hCD45 markers, followed by analysis using flow cytometry. Created with BioRender.com.

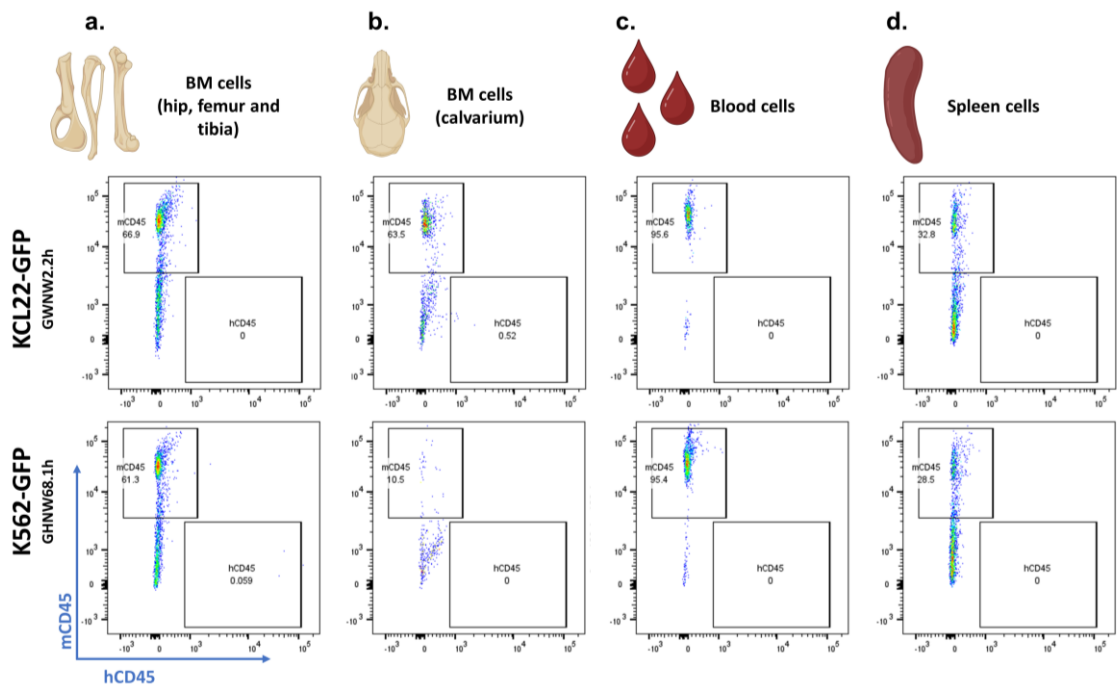


**Figure 4-4 Neither KCL22 nor K562 cells showed engraftment in the BM within three days post-injection.** Flow cytometry dot plots illustrate the absence of human cells expressing hCD45 (x-axis) against murine cells expressing mCD45 (y-axis) in the BM harvested from leg bones (a) or calvarium (b) of KCL22 recipient mouse (top row) and K562 recipient mouse (bottom row). Additionally, no hCD45<sup>+</sup> cells were detected in the blood sample (c) and spleen (d) in either group.

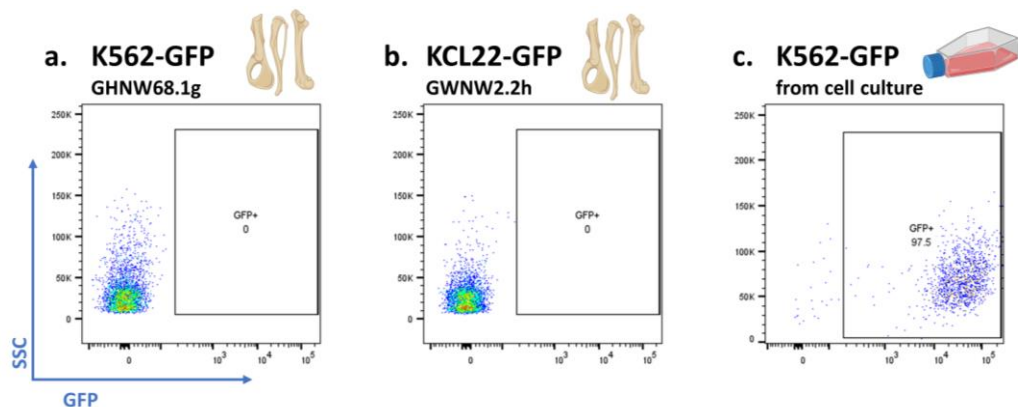


**Figure 4-5 Absence of GFP<sup>+</sup> cells in the BM of mice sacrificed three days after transplantation.** BM single cells isolated from the leg bones were analysed for GFP fluorescence of both K562 (a) and KCL22 (b) and compared with cells remaining in culture (c).

The remaining mice were sacrificed at the endpoint when tumour development was detected. Both mice had one large tumour of similar weight in the abdomen (**Figure 4-7c&d**). Besides non-haematological cells, both tumours consisted exclusively of hCD45<sup>+</sup> cells, with no mCD45<sup>+</sup> cells present (**Figure 4-6c**). No human cells were detected in the blood or spleen (**Figure 4-6d&e**). Notably, a small population of human cells engrafted into the BM of the K562 recipient mouse, accounting for 0.5% in the leg bones and 2.2% in the crushed calvarium among total cells, whereas KCL22 did not engraft into the BM (**Figure 4-6a&b**). BM and spleen total cell counts were slightly lower in mice reaching endpoint

compared to mice sacrificed early on day three (**Figure 4-7a&b**). All tissues were gated for GFP in the single cell population, as it was shown above that not all K562-GFP express hCD45. This revealed a higher percentage of human cells present in the BM (~1% in leg bones, ~5.5% in calvarium; **Figure 4-8a&b**) and the tumour tissue (43% in tumour; **Figure 4-8c**). To ensure that GFP was not transferred from the human cells to mouse cells, GFP fluorescence on mCD45<sup>+</sup> population was assessed, which was negative (**Figure 4-9**).

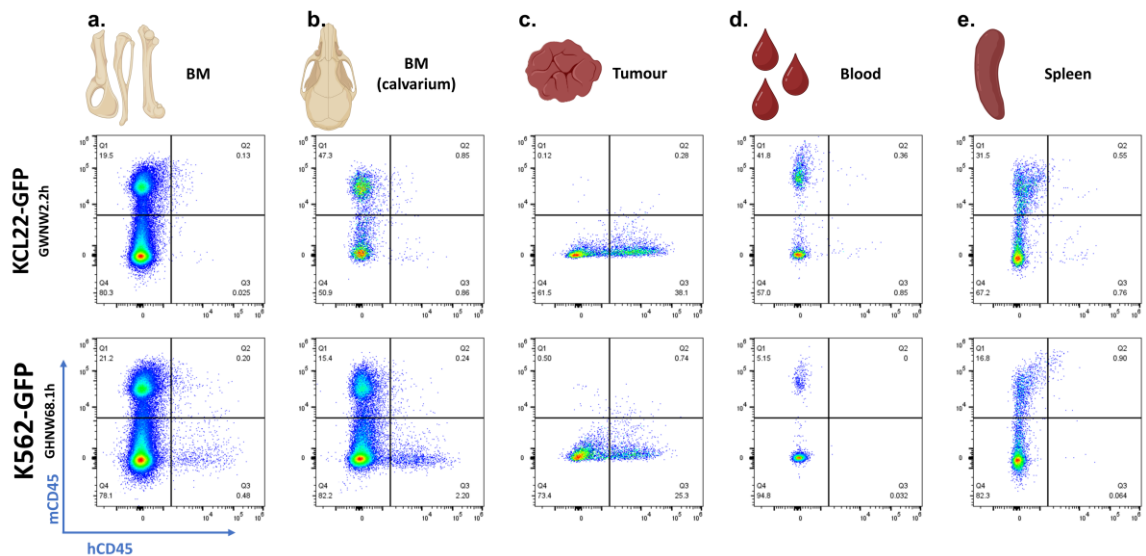


**Figure 4-6 BM engraftment of K562-GFP 21 days after transplantation.** Dot plots display levels of mCD45<sup>+</sup> and hCD45<sup>+</sup> cells in the KCL22 (top row) and the K562 (bottom row) recipient mouse 21 days post-injection. BM from leg bones (a) and the calvarium (b) were analysed along with tumour (c), blood (d) and spleen (e) with flow cytometry.

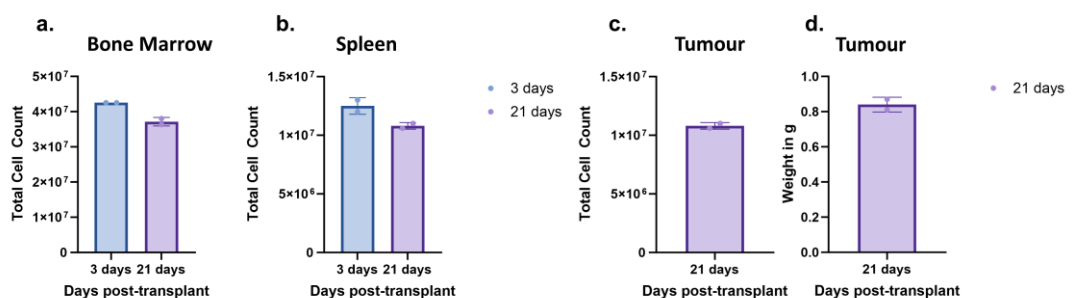


**Figure 4-7 Total cell count of the BM, spleen, and tumour at three and 21 days post-transplantation.** Absolute cell counts in BM (a), spleen (b) and tumour (c) are presented as mean  $\pm$  S.D. of  $n=2$ . Extramedullary tumour cell counts shown in (d). Notably, no extramedullary tumour was present in mice at the three day-endpoint.

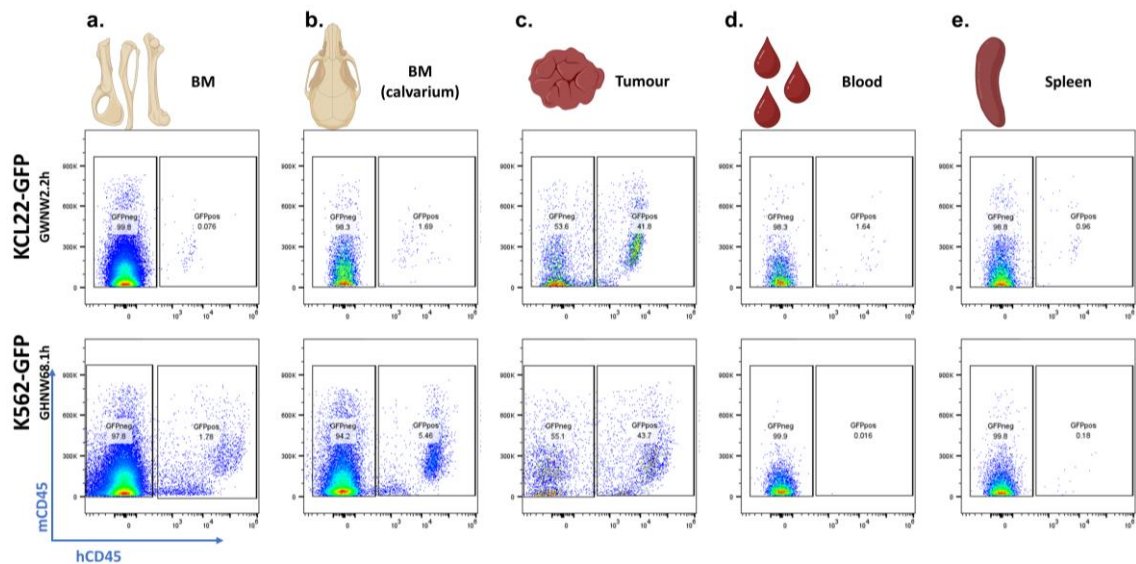


**Figure 4-8** GFP<sup>+</sup> cells detected in the BM and tumour of the K562 recipient mouse 21 days post-transplant. Dot plots show levels of GFP<sup>neg/low</sup> and GFP<sup>high</sup> cells in BM (a-b), tumour (c), blood (d) and spleen (e). The top row depicts tissues from the KCL22 recipient mouse, while the bottom row presents results from the K562 recipient.

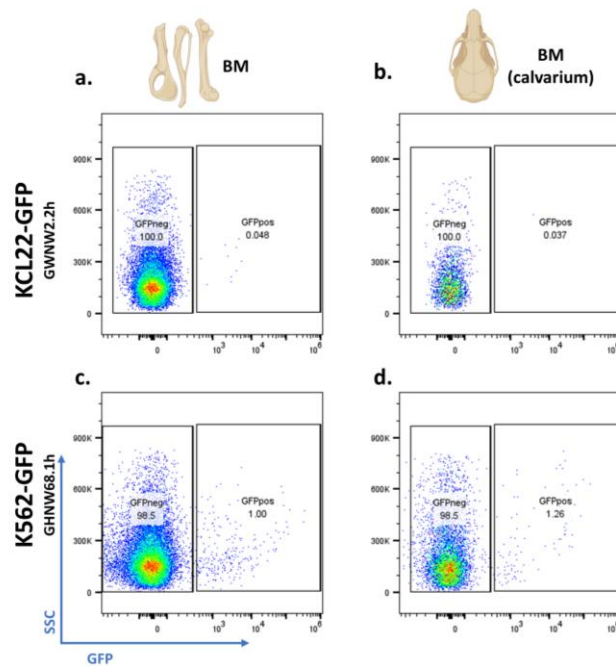


**Figure 4-9** Haematological mouse cells remained GFP<sup>neg</sup>. BM cells from KCL22 (top row) or K562 (bottom row) recipient mouse gated for mCD45<sup>+</sup>, were plotted for GFP fluorescence. The percentages in the graphs are based on the parent population of mCD45<sup>+</sup> cells in the total BM fraction (refer to Figure 4-6).

## 4.4 Visualising K562-GFP<sup>+</sup> cells in murine calvarium

Next, we wanted to determine whether Ph<sup>+</sup> cells localise in the BM microenvironment to a certain niche to identify potential cues relevant to TKI resistance and influence of BM environment. As K562-GFP cells have the potential, albeit small, to engraft in the BM of immunocompromised mice, four mice were transplanted with four million cells via tail vein with the intention to localise them in the BM niche using *ex vivo* confocal microscopy on the freshly excised calvarium (**Figure 4-10**). Mice were injected with fluorescent dextran to label the vasculature and sacrificed after one minute to allow dextran to evenly distribute in the vascular system. Mice were sacrificed at a time point based on the previous experiment (three weeks), although the mice did not develop an extramedullary tumour as in the previous specimens. As in preceding experiments, no hCD45<sup>+</sup> cells were detected in the blood and spleen (**Figure 4-11b&c**). Flow cytometry analysis of the BM showed no evidence of human cell engraftment in any of the four mice, as no population of hCD45<sup>+</sup> was detected that was distinctive from non-transplanted controls (**Figure 4-11a** and **Figure 4-12a**). Because of mouse availability, this experiment was performed in male mice, which have been shown to have slightly delayed engraftment of human CD34<sup>+</sup> HSCs<sup>374</sup>, while the previous experiment was with female mice. Although K562 cells cannot be compared to engraftment of primary human cells, a longer time point could potentially result in a higher engraftment.

Notably, confocal spectral microscopy of the calvarium revealed the presence of GFP<sup>+</sup> cells in all four mice transplanted with K562-GFP (**Figure 4-13**). While two mice displayed few cells (**Figure 4-13a&c**), the other two mice exhibited an accumulation of GFP<sup>+</sup> cells in close proximity to the vasculature or within blood vessels (**Figure 4-13b&d**). The fluorescent dextran used had a molecular weight (MW) of 70kDa, and it seems that the dextran was leaking into the BM space. Certain areas display a sinusoidal network (**Figure 4-13b**). Using a higher molecular weight dextran (500kDa) might enhance staining quality by reducing the likelihood of leakage.

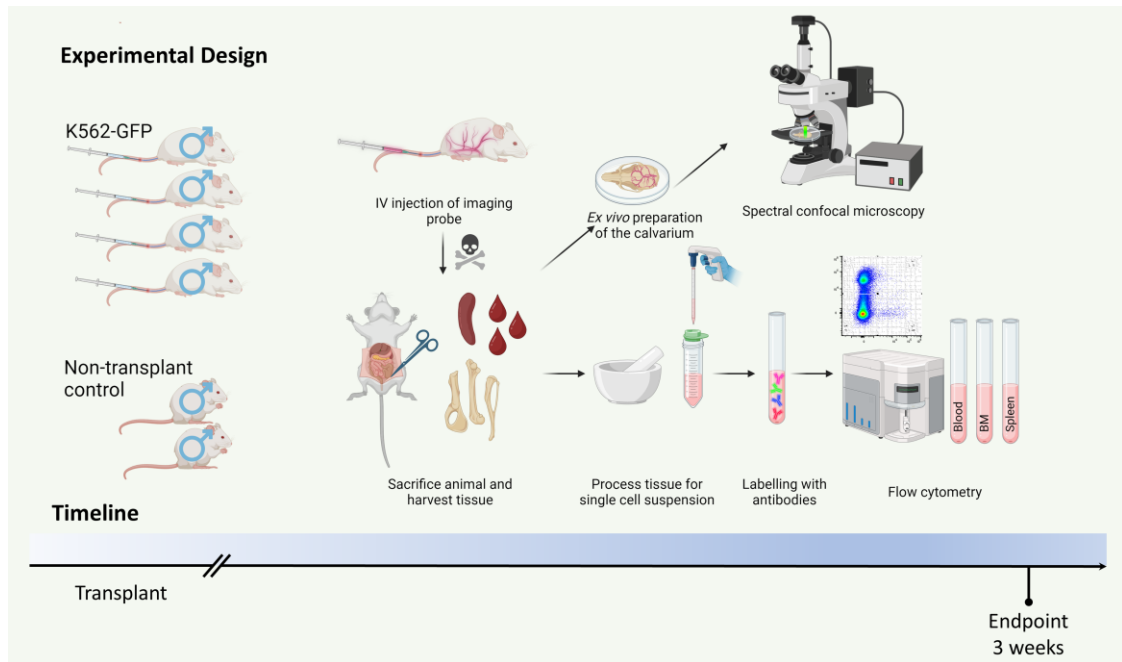


**Figure 4-10 Experimental design aimed to localise K562-GFP cells in mouse BM.** Four immunocompromised mice were transplanted with four million K562-GFP cells, while two littermate mice served as non-transplant controls. The experiment was concluded after three weeks, based on the timeline from the previous experiment. Mice were injected with fluorescent dextran and then humanely killed. Blood was collected in EDTA-coated tubes to prevent clotting. The calvarium was removed and placed in a small petri dish filled with PBS, fixed in place with a small amount of glue to prevent movement to perform *ex vivo* microscopy. The leg bones and spleen were collected and processed to a single cell solution. Blood samples underwent red blood cell lysis. All tissues were stained with conjugated antibodies targeting mCD45 and hCD45 and analysed by flow cytometry. Created with BioRender.com.



## K562-GFP transplanted mice

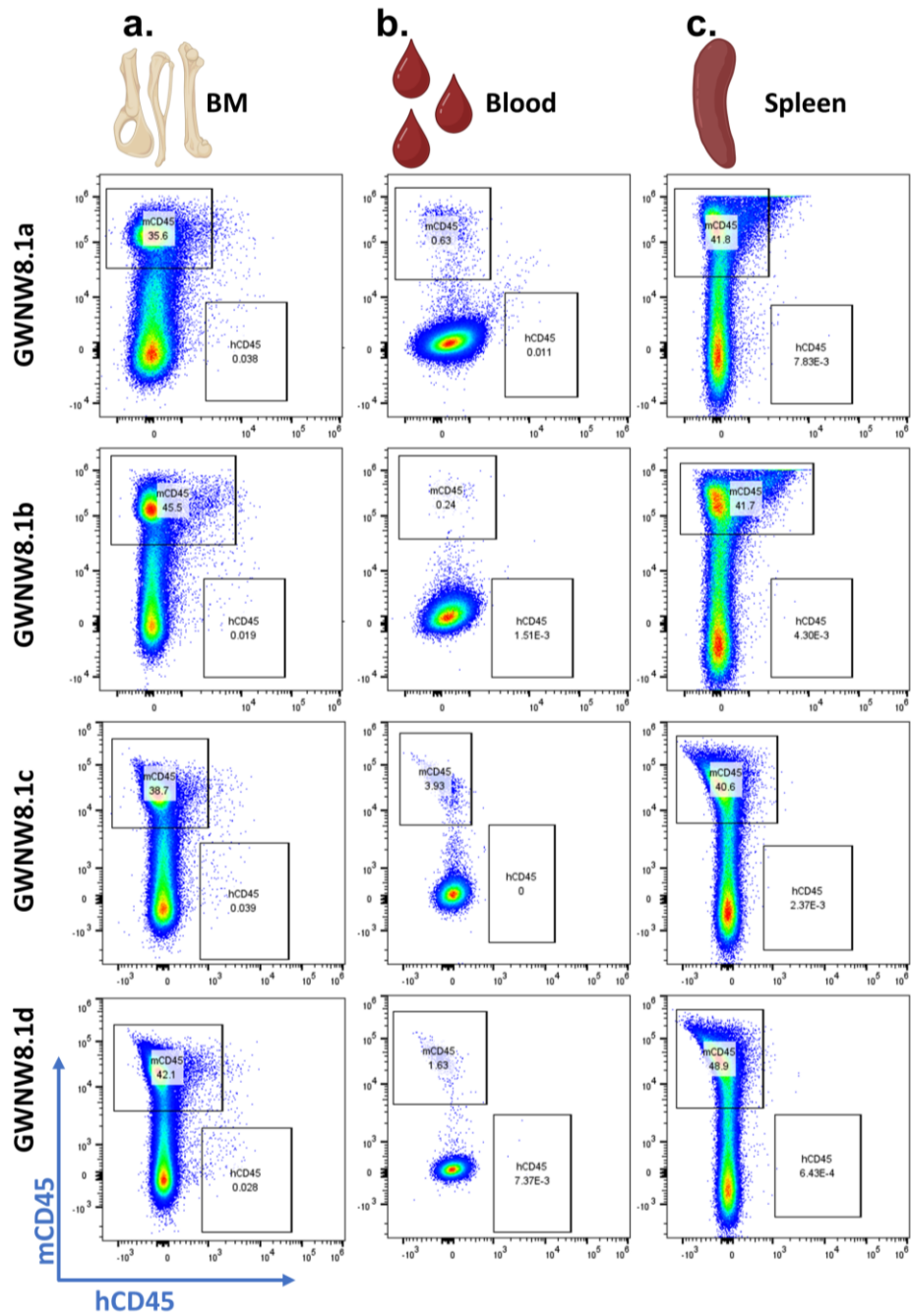


**Figure 4-11 K562-GFP showed no engraftment in male recipient mice within 23 days post-transplantation.** Four male SCID mice were transplanted with four million K562-GFP cells and humanely killed after 23 days. BM (a), blood (b) and spleen (c) samples were stained with hCD45 and mCD45, then analysed by flow cytometry.



### Non-transplant control mice

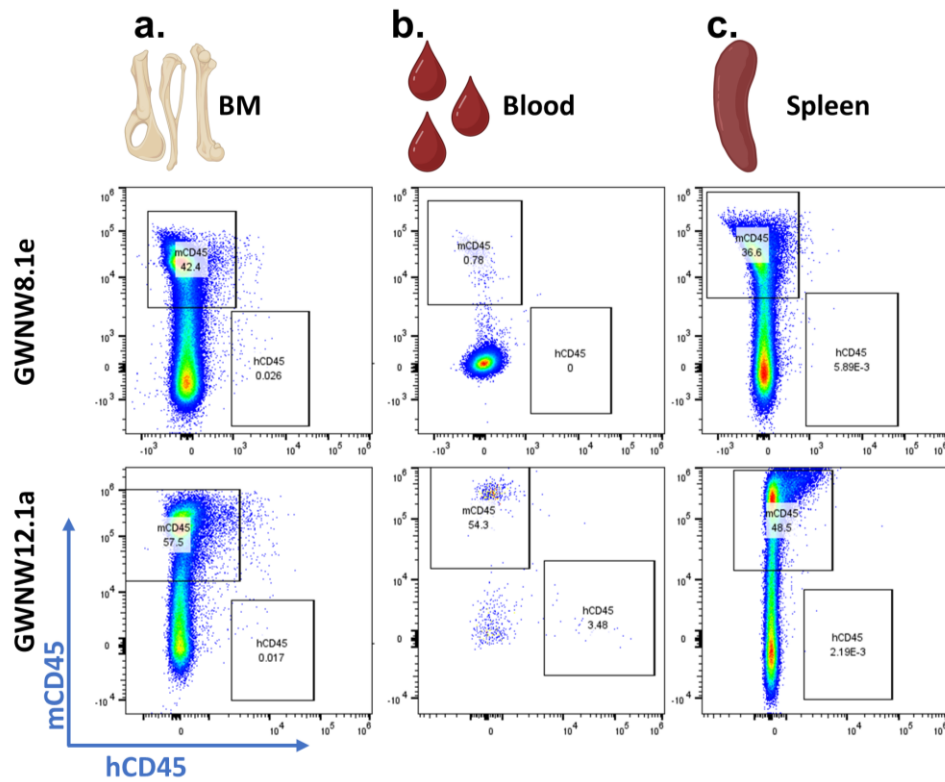


**Figure 4-12 Non-transplanted control mice assayed for hCD45<sup>+</sup> to identify background staining.** Dot plots depict levels of mCD45<sup>+</sup> and hCD45<sup>+</sup> cells within BM (a), blood (b) or spleen (c) samples of control mice, that did not receive any cell transplants.

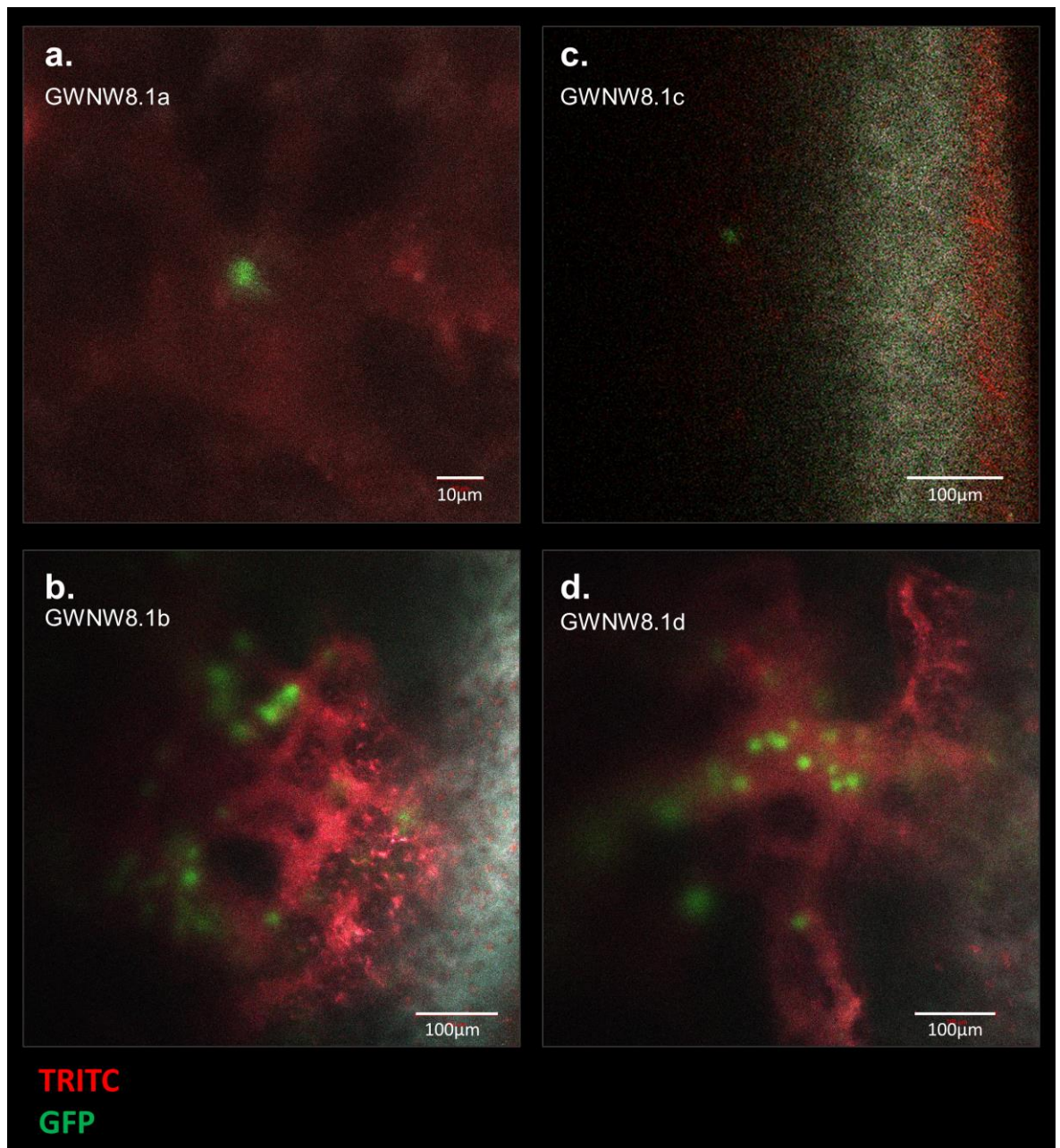


**Figure 4-13 Confocal microscopy detection of GFP<sup>+</sup> cells in the calvarium of xenograft mice.** Prior to sacrifice, mice were injected with fluorescent dextran and imaging was conducted immediately after extracting the calvarium. Spectral imaging was employed, and images were processed by linear unmixing in Zen (black). GFP<sup>+</sup> cells (green) were observed in proximity to the vasculature (red). Bone was identified by the autofluorescence signal (grey). Scale bars represent 10µm (a) or 100µm (b-d).

## 4.5 Hypoxia-priming of K562-GFP cells prior to xenograft did not impact BM engraftment

The BM has been shown to be a hypoxic environment for BM resident cells<sup>125</sup>. Exposing cells to hypoxia leads to stabilisation of HIF1 $\alpha$ , leading to metabolic adaption and inducing activation of multiple hypoxia-related genes<sup>121</sup>. Different studies have shown that hypoxia influences CXCR4 expression, which is known to mediate BM homing via CXCL12<sup>390-392</sup>. Therefore, priming K562-GFP cells in hypoxia (1% O<sub>2</sub>) was hypothesised to enhance BM engraftment to select for hypoxia-adapted cells, although K562 cells show reduced proliferation in hypoxia (**Figure 4-14**). To directly compare engraftment into female and male mice, three female and two male mice per arm (hypoxia-primed/normoxia-primed) were transplanted with four million cells each through tail vein injection (**Figure 4-15**). Hypoxia-primed cells were incubated in an incubator set to 1% O<sub>2</sub> for 72 hours before transplantation, while normoxia-primed cells were cultured in a standard incubator with atmospheric oxygen.

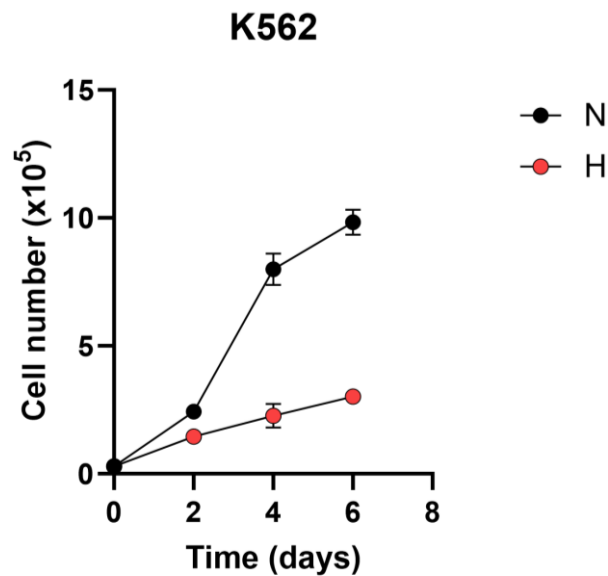


**Figure 4-14 Reduced cell proliferation of K562 in hypoxia.** K562 cells were cultured in a hypoxic (H) incubator (1% O<sub>2</sub>) and a general incubator with atmospheric O<sub>2</sub> (N) for six days to assess cell counts every two days. Data were presented as mean  $\pm$  S.D. with a sample size of  $n=3$ . Experiment performed by Mr. Daniele Sarnello.

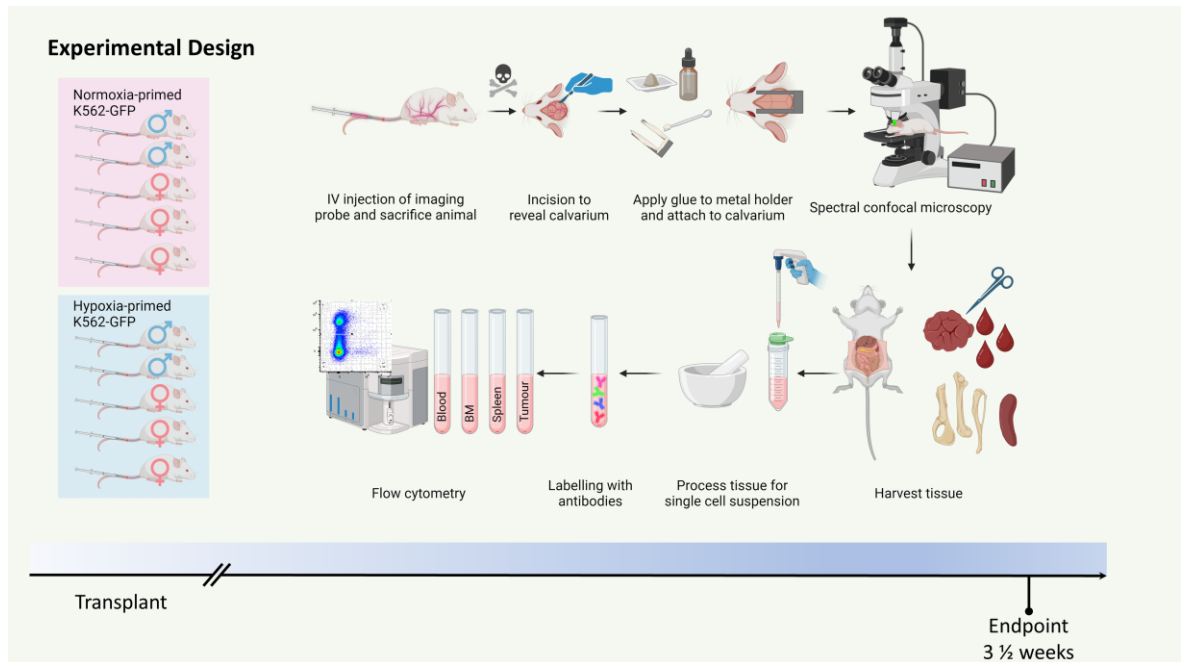


**Figure 4-15 Experimental design aimed to investigate BM engraftment of hypoxia-primed K562-GFP cells.** A total of ten SCID mice of mixed sex (three females, two males per group) were transplanted with four million K562-GFP cells. Half of the cohort received cells cultured in a regular incubator with atmospheric oxygen (normoxia), while the other half received cells that were cultured in an incubator with 1% oxygen (hypoxia) for 72 hours before transplantation. The experiment was concluded after 3 ½ weeks upon detecting tumour formation. Mice were injected with fluorescent dextran, then humanely killed, and blood samples were immediately collected. The mouse cadaver was prepared for microscopy by removing the skin from the skull to expose the bone. A metal holder was attached to the bone using freshly mixed dental cement. After the dental cement had set (~5-10 minutes), the mouse was secured onto the microscope stage, and PBS was placed on the skull for spectral imaging. Following imaging, the leg bones, spleen, and tumour tissues were collected. Blood samples underwent red blood cell lysis. Single-cell suspensions were stained with antibodies targeting mCD45 and hCD45, then analysed by flow cytometry. Created with BioRender.com.

All mice were humanely killed upon the first signs of extramedullary tumour growth in several mice, marking the endpoint, which occurred 3 ½ weeks post-transplantation. Consistent with previous experiments, the female mice exhibited faster tumour development, whereas males showed no formation of extramedullary tumours at this time point (**Figure 4-16**). Moreover, among the female mice, the hypoxia group displayed a lower tumour burden. While all females in the normoxia group had developed two abdominal tumours, only two out of three females in the hypoxia arm developed tumours.

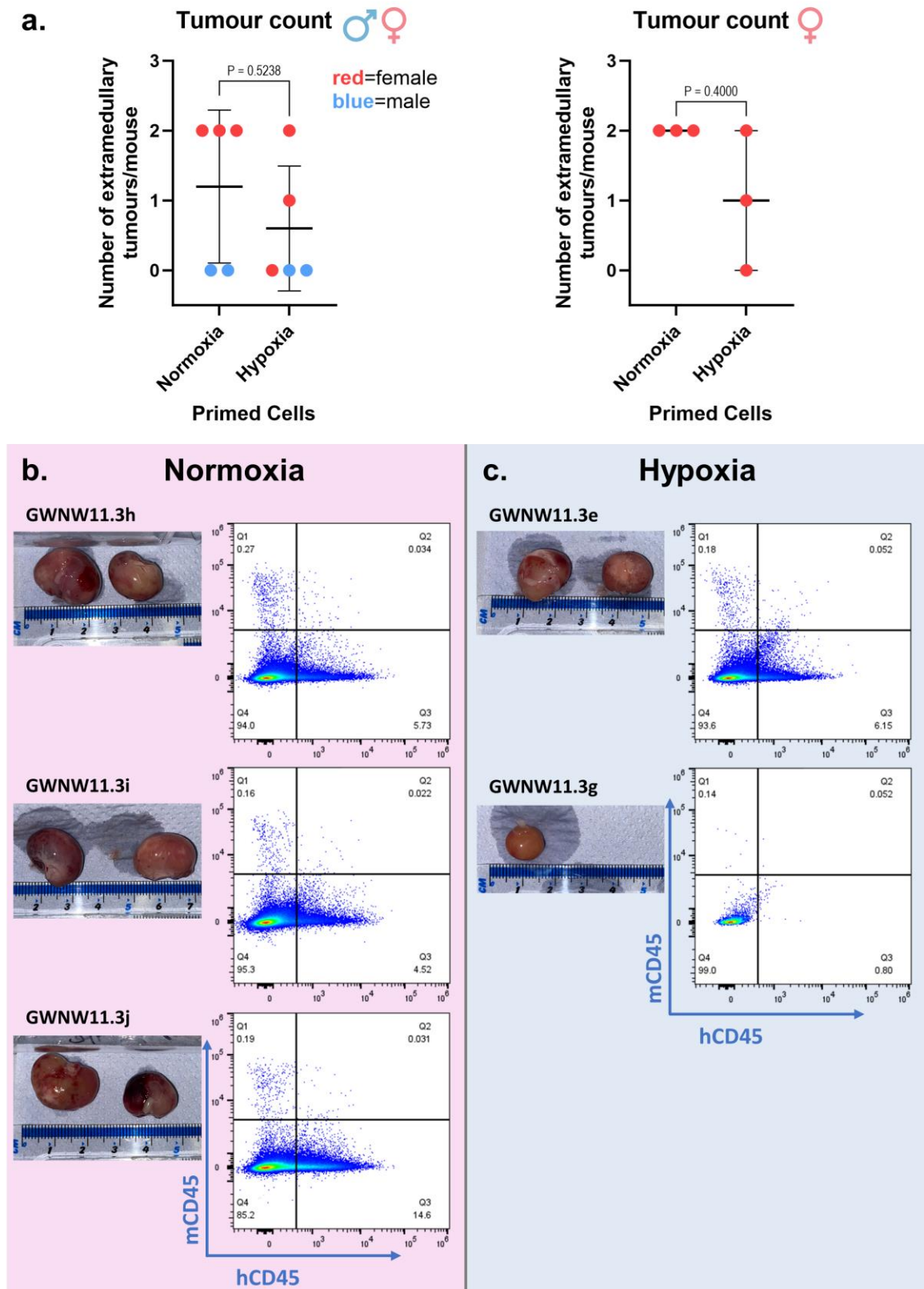


**Figure 4-16 Indication of reduced tumour formation of hypoxia-primed K562-GFP cells.** K562-GFP cells were primed in hypoxia (1%) for three days, followed by transplantation of four million cells per mouse into a cohort of five mice (three females, two males). The second experimental arm involved K562-GFP cells cultured in normoxia (21%). Mice were sacrificed when the first mouse reached the endpoint at 3 ½ weeks. The scatter plot (a) depicts the number of tumours per arm for all mice, distinguished by sex (red for females, blue for males), and specifically for female mice. Images of tumours per mouse along with their flow cytometry analysis for hCD45 and mCD45 are presented for the normoxia arm (b) and the hypoxia arm (c). Graphs are displayed as mean  $\pm$  S.D. with a sample size of  $n=5$  (all mice) or  $n=3$  (females). Statistical analysis was conducted with the non-parametric Mann-Whitney test.

Total BM cell counts were similar between both arms when all mice were included in the analysis. When tumour-free mice were excluded from the analysis, there was a trend towards lower BM cellularity in the normoxia arm than those mice injected with hypoxia primed cells (**Figure 4-17c**). There was no BM engraftment in the male mice regardless of pre-conditioning the cells (**Figure 4-17a-b, d-e**). The female mice exhibited a mean BM engraftment of approximately 0.8% in either transplant group, with higher variability in the hypoxia arm (**Figure 4-17d**). As in previous experiments, there were no to negligible numbers of hCD45<sup>+</sup> cells detected in the blood and spleen (**Figure 4-18, Figure 4-19**).

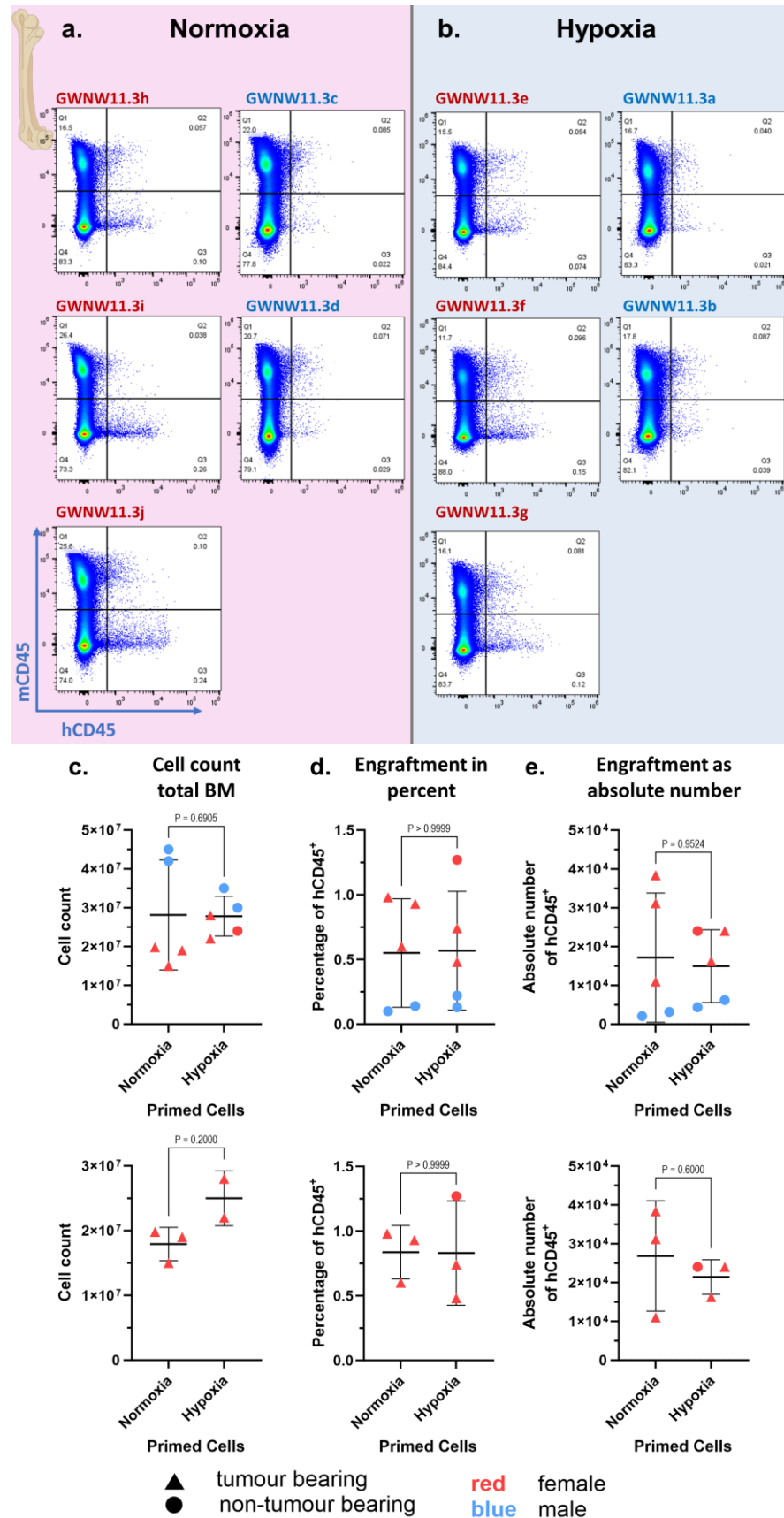


**Figure 4-17 BM engraftment of hCD45<sup>+</sup> of hypoxia- vs. normoxia-primed cells.** Flow cytometry analysis show BM levels of mCD45<sup>+</sup> and hCD45<sup>+</sup> cells from the hypoxia (a) and the normoxia (b) transplant group. Total BM cell counts (c), engraftment of hCD45<sup>+</sup> cells presented as percentages (d), and as absolute numbers (e) were plotted for all mice, distinguished by sex (top row), and specifically for females or tumour-bearing mice, respectively (bottom row). The graphs are presented as mean  $\pm$  S.D. with  $n=5$  (all mice) or  $n=3$  (females). Statistical analysis was conducted using the non-parametric Mann-Whitney test.

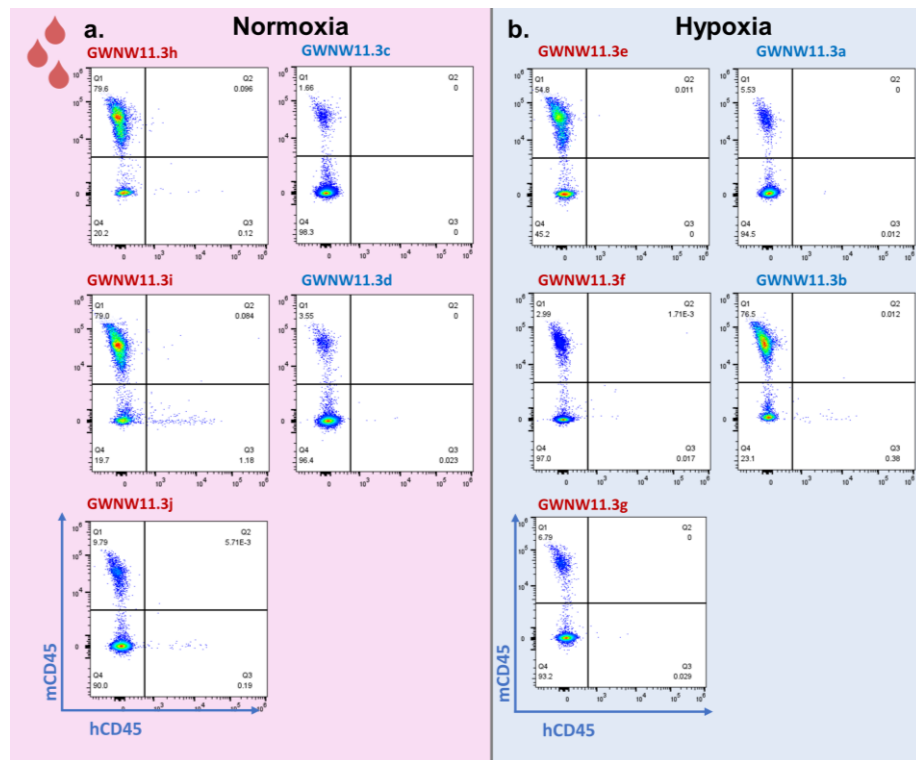


**Figure 4-18 Human cells were not detected in the blood of immunocompromised mice.** Blood samples from the normoxia (a) and hypoxia (b) transplant group were stained with anti-mCD45 and anti-hCD45 antibodies.

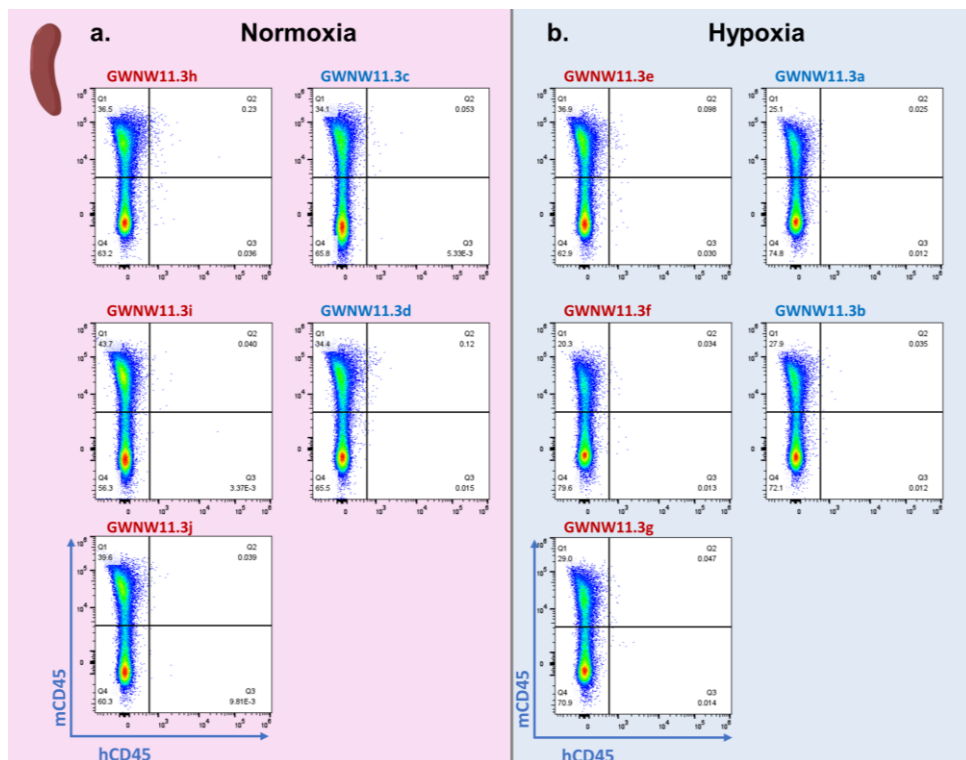


**Figure 4-19 K562-GFP cells did not localise to the spleen when primed in hypoxia.** Splens from normoxia (a) and hypoxia (b) transplant group were analysed by flow cytometry to assess levels of mCD45<sup>+</sup> and hCD45<sup>+</sup> cells.

Before conducting flow cytometry analysis, all mice underwent post-mortem microscopy to locate leukaemic cells expressing GFP<sup>+</sup> in the BM. However, none of the mice showed a high accumulation of human cells, and the majority exhibited few to no cells in the calvarium. Representative images displayed in **Figure 4-20** show rare individual GFP<sup>+</sup> cells located in the BM. There was no discernible distinction between the two transplantation groups regarding engraftment.

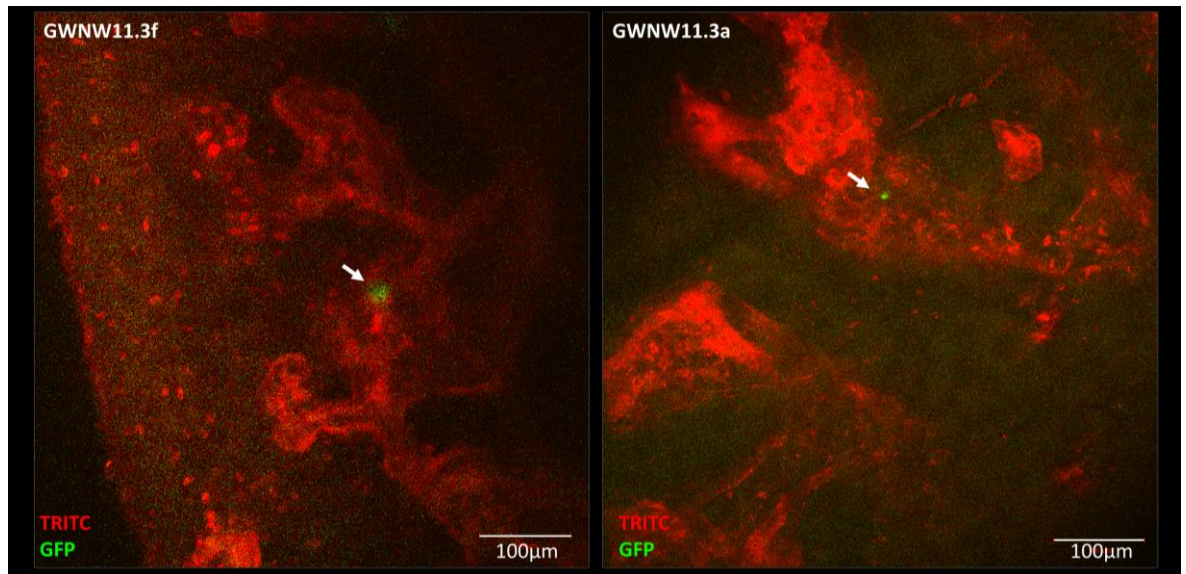


**Figure 4-20 Hypoxia-priming had no effect on BM engraftment in the calvarium of NRGW mice.** Prior to sacrifice, mice were injected with fluorescent dextran (TRITC, red), and imaging was immediately conducted. Images were acquired using spectral imaging and processed by linear unmixing in Zen (black). Representative images depict one GFP<sup>+</sup> cell (green, arrow) in two different specimens from the hypoxia group whereas the other mice showed a comparable number of GFP<sup>+</sup> cells or no cells at all. Scale bar indicates 100µm.

## 4.6 Migration of K562-GFP to the brain in male mice instead of BM engraftment or formation of extramedullary tumours

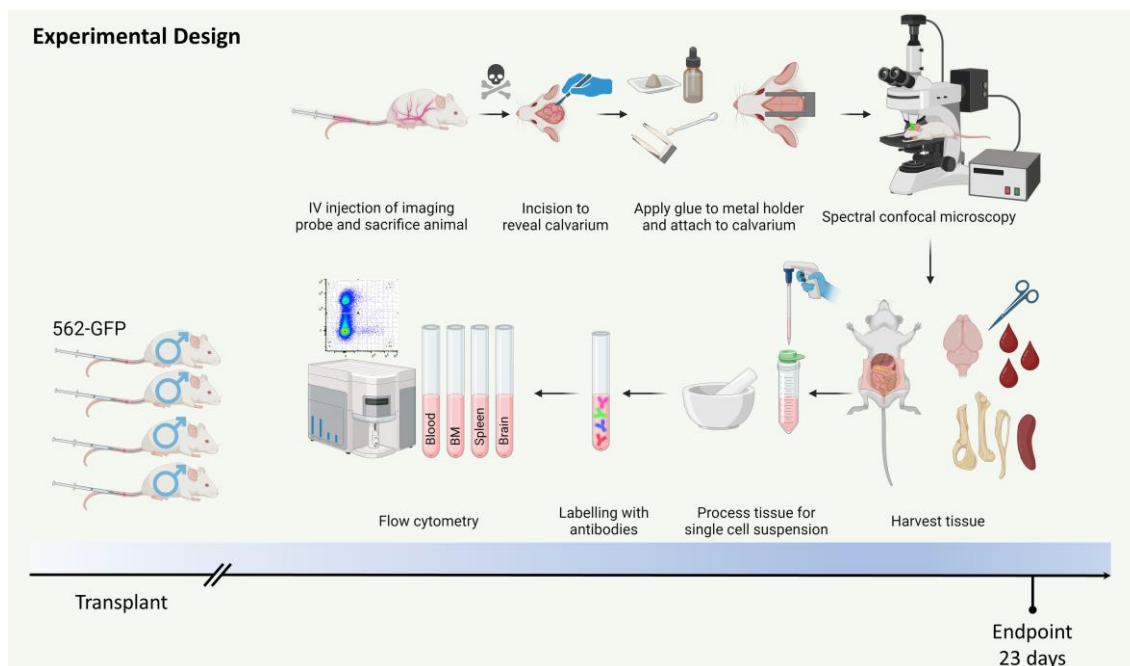


**Figure 4-21 Experimental design aimed to investigate BM engraftment of human cells in male mice.** Four male SCID mice were transplanted with four million K562-GFP cells. The experiment was terminated upon the onset of discomfort in the mice. Mice were injected with fluorescent dextran, then humanely killed, and subjected to microscopy. The mouse cadaver was prepared for microscopy by removing the skin from the skull to expose the bone. A metal holder was attached to the bone using freshly mixed dental cement. After the dental cement had set (~5-10 min), the mouse was secured on the microscope stage. Subsequently, PBS was placed on the skull and spectral imaging was performed. Afterwards, the leg bones, spleen and tumour samples were processed to obtain single-cell solutions. Blood samples underwent red blood cell lysis. All tissues were stained with antibodies targeting mCD45 and hCD45 and analysed by flow cytometry. Created with BioRender.com.

Previous experiments consistently demonstrated that female mice developed tumours within three weeks after transplantation, while male mice did not exhibit tumour development or BM engraftment within the same timeframe. We hypothesise that K562 engraftment and metastasis is delayed in male mice compared to female mice as seen in experiments with CD34<sup>+</sup> cord blood-derived cells<sup>374</sup>. Therefore, a separate experiment was conducted specifically in male mice to monitor both BM engraftment and tumour development upon transplantation of K562-GFP cells until the mice reached their endpoint.

Four male mice of the same age were transplanted with four million K562-GFP cells (**Figure 4-21**). By day 23, three out of the four mice showed signs of discomfort, although external examination and necropsy did not reveal any evidence of tumour formation. Notably, alongside mice displaying general signs

of discomfort and reduced alertness upon provocation, one mouse exhibited hind limb paralysis, indicating metastasis to the lumbar spinal cord.

Subsequently, all mice were humanely killed at the same time, and BM, blood, and spleen as well as the brain were harvested. Flow cytometry analysis indicated an absence of human cell engraftment in the BM (**Figure 4-22a**). Furthermore, the spleens appeared of normal size and did not harbour any hCD45<sup>+</sup> cells (**Figure 4-22c**). However, as suspected, the brains of the diseased mice contained a distinct population of hCD45<sup>+</sup> cells (**Figure 4-22d**). Two mice showed hCD45<sup>+</sup> circulating in the blood (**Figure 4-22b**), an occurrence rarely observed in previous experiments.

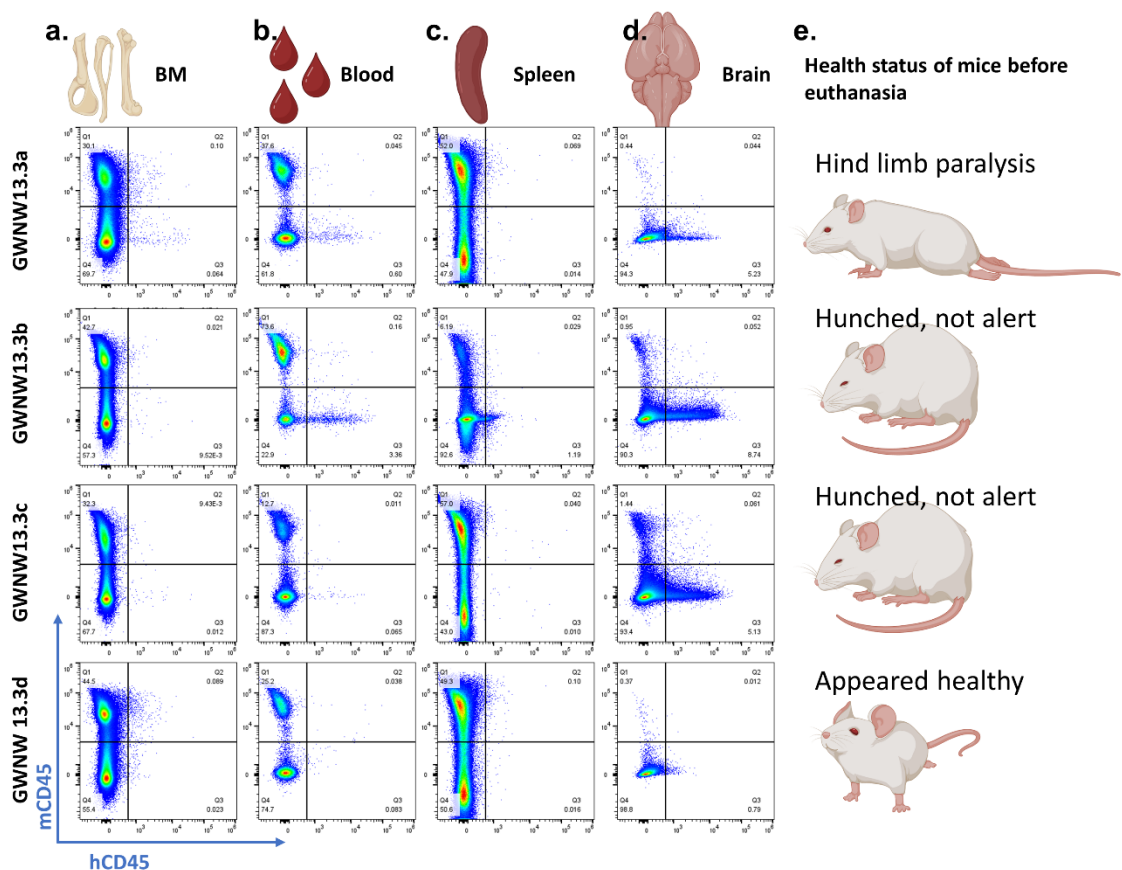


**Figure 4-22 Male xenograft recipients showed proliferation of K562 in the brain.** Male mice were transplanted with four million K562-GFP cells by tail vein injection and sacrificed after 23 days, when the first mouse displayed symptoms of discomfort (e). Mice were hunched and less mobile and alert (middle rows). One mouse additionally had hind limb paralysis. Only one mouse appeared healthy and showed no signs of discomfort. BM (a), blood (b), spleen (c) and brain (d) were analysed by flow cytometry for hCD45<sup>+</sup> cells.

Post-mortem confocal microscopy was performed on the calvarium. Therefore, IV injection of fluorescent dextran was administered 1-5 minutes before sacrificing the mice. The maximum projections of the tile scans displayed in

**Figure 4-23**, **Figure 4-25** and **Figure 4-26**, indicate the absence of GFP<sup>+</sup> cells, except in the case of one mouse depicted in **Figure 4-25**. In this instance, the GFP signal was detected deep within the tissue, making focusing unfeasible. Notably, this mouse exhibited a high number of human cells in the brain. Consequently, it is possible that the detected GFP signal originated from GFP<sup>+</sup> cells situated in the brain tissue beneath the calvarium.

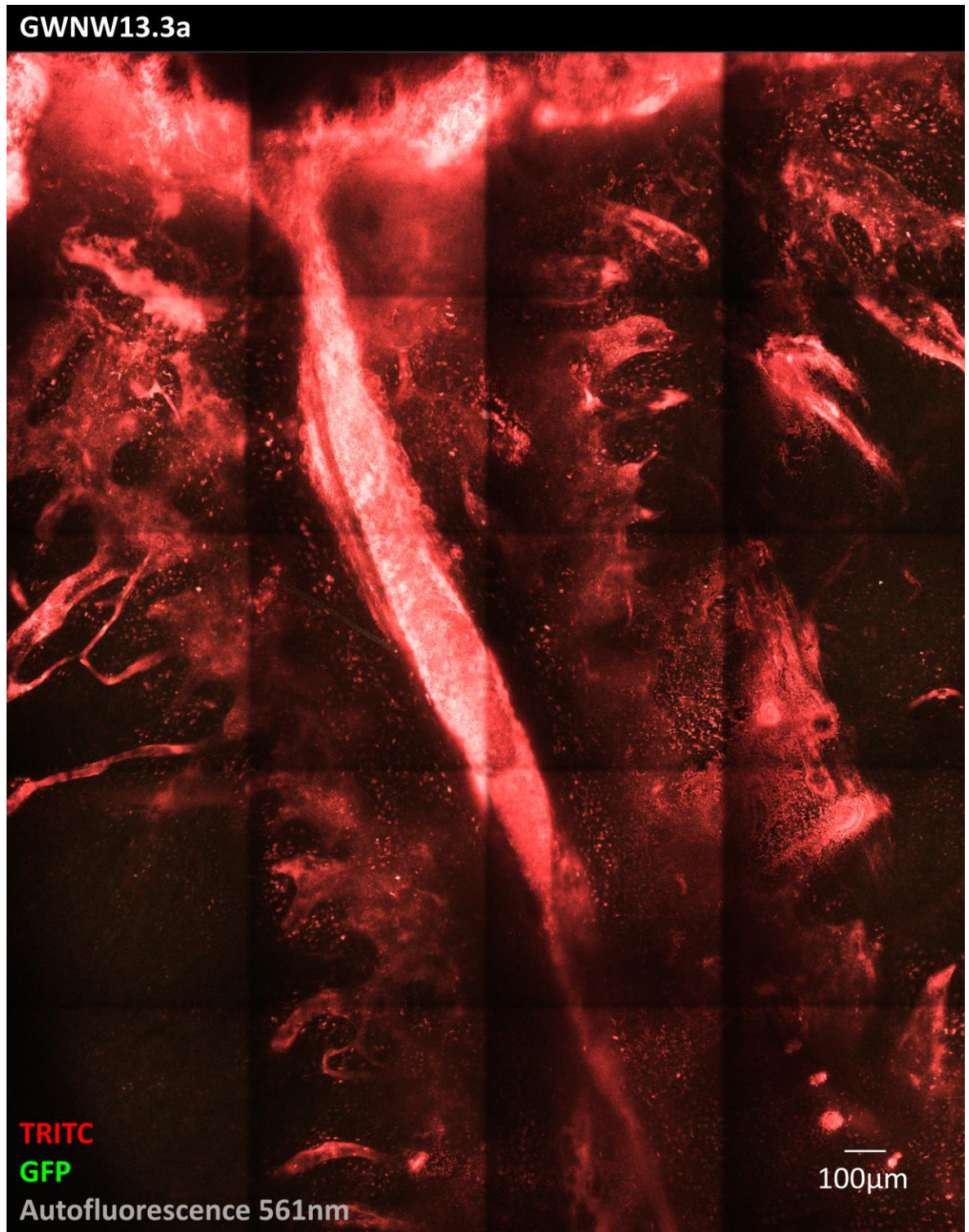


**Figure 4-23 Microscopy image of K562-GFP recipient male GWNW13.3a.** Image shows a representative tile scan acquired using spectral imaging with the lasers 488nm for GFP (green, no signal) and 561nm for TRITC (red). The image was processed with the Zen black software using linear unmixing, stitching and maximum projection (stack of 26 slices, 282.6µm). Strong signal from the central sinusoid and smaller vasculature was detected, while the calvarium was thoroughly scanned for GFP<sup>+</sup> cells. Scale bar: 100µm.

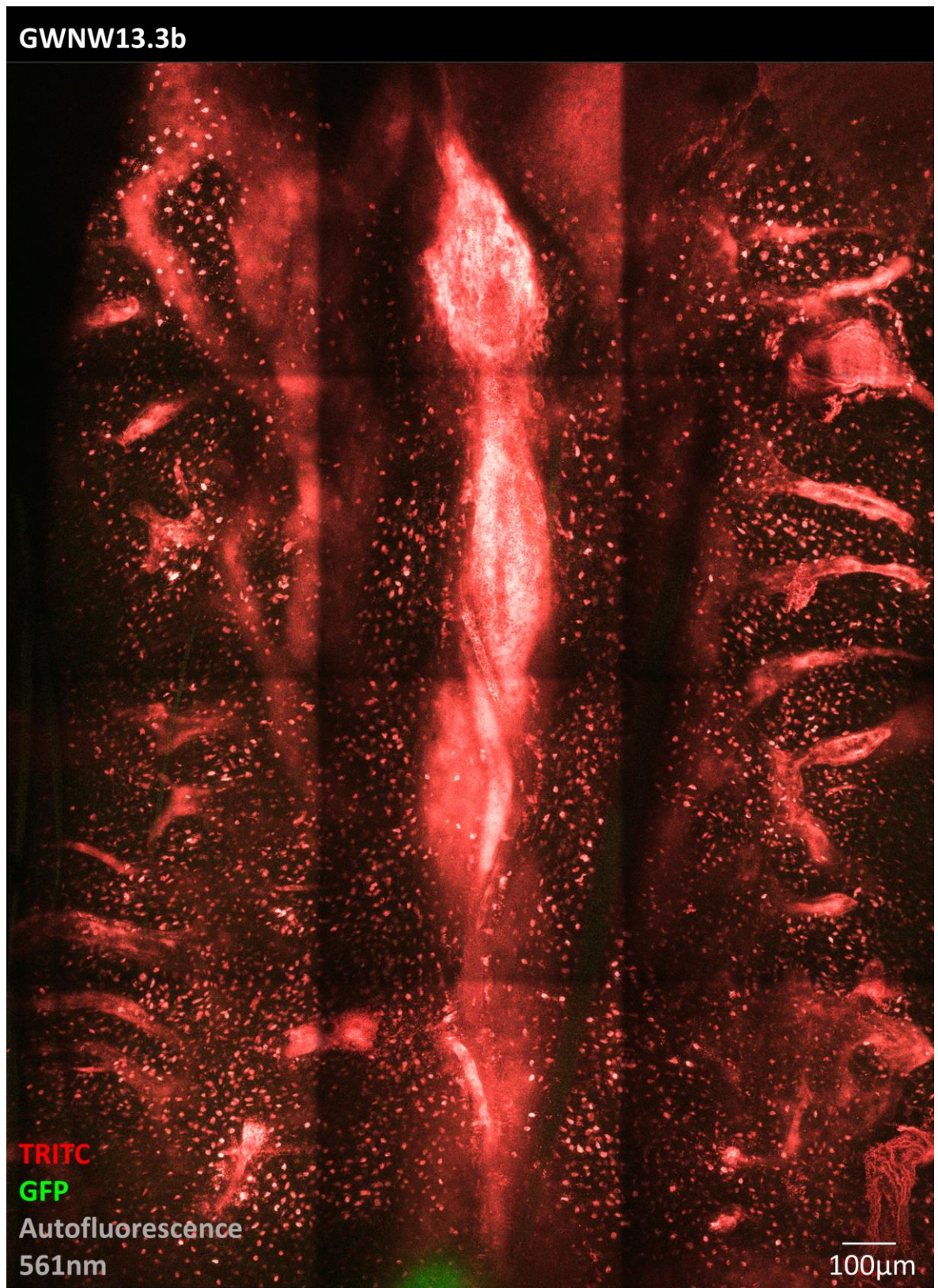


**Figure 4-24** Microscopy image of K562-GFP recipient male mouse GWNW13.3b. The image displays a representative tile scan obtained via spectral imaging employing lasers at 488nm for GFP (green, no signal) and 561nm for TRITC (red). The image underwent processing using Zen black software, involving linear unmixing, stitching and maximum projection (from a stack comprising 25 slices at 271.3µm with piezo). Robust signal from the central sinuous and smaller vasculature was detected, while no GFP<sup>+</sup> could be detected throughout the calvarium. Nuclei from osteoblasts contribute to strong background signal in the red channel, which could not be removed by linear unmixing. Scale bar: 100µm.

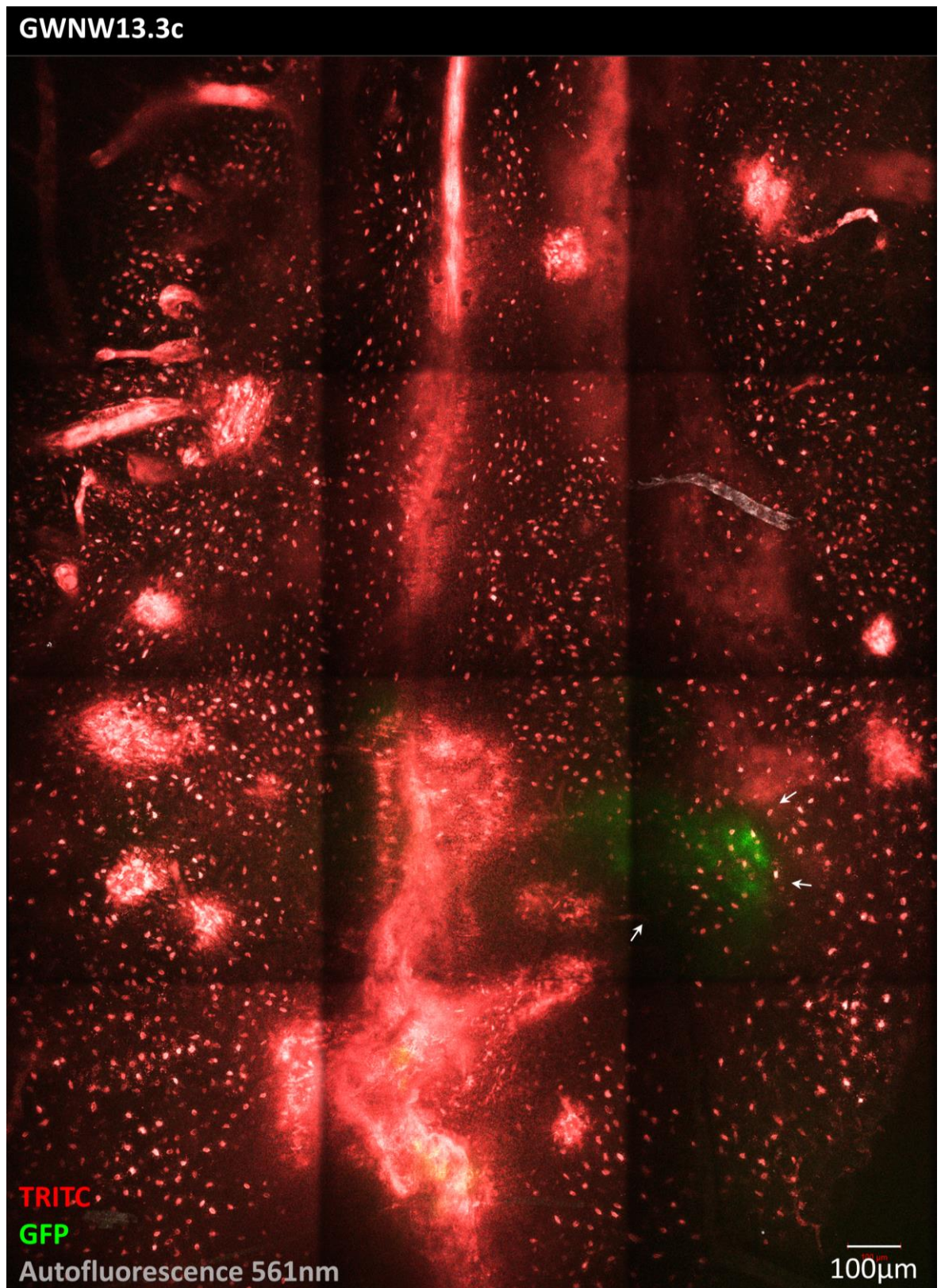


**Figure 4-25** Microscopy image of K562-GFP recipient male mouse GWNW13.3c. The image displays a representative tile scan captured using spectral imaging with the 488nm lasers (GFP, green) and the 561nm laser (TRITC, red). The image was processed with the Zen black software using linear unmixing, stitching and maximum projection (stack composed of 25 slices, yielding a total thickness of 271.3µm with a piezo stage). A diffuse GFP signal was detected deep within the tissue (white arrow). Scale bar: 100µm.

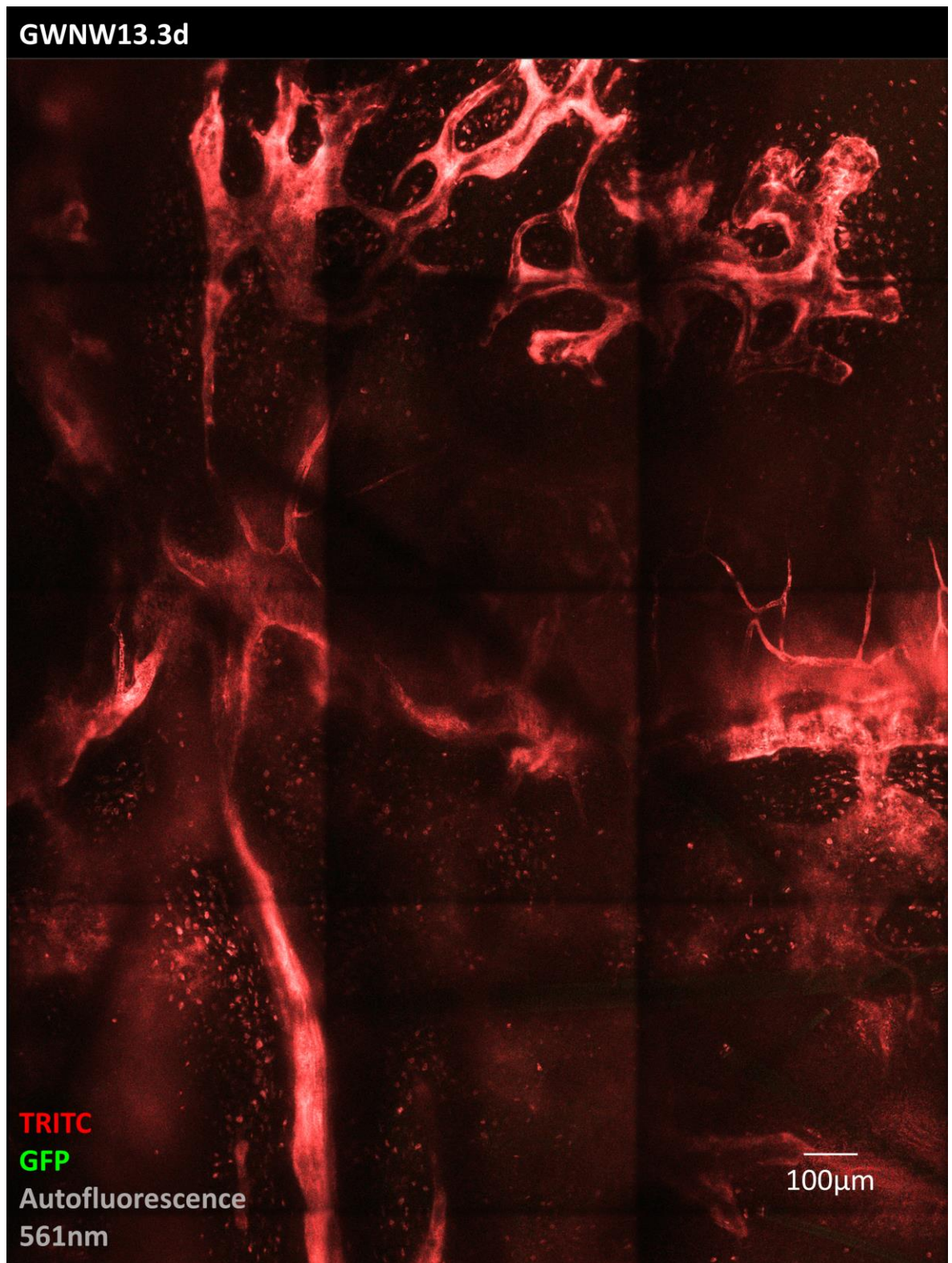
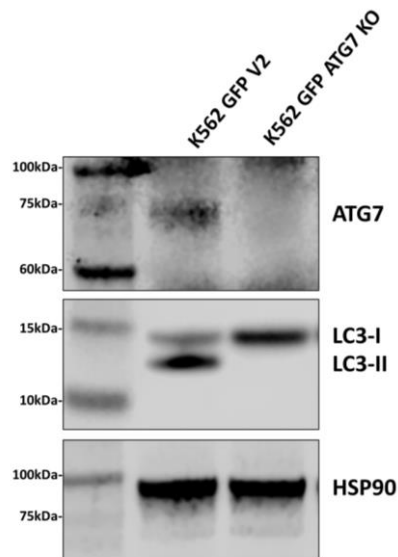


**Figure 4-26** Microscopy image of K562-GFP recipient male mouse GWNW13.3d. Image shows a representative tile scan acquired using spectral imaging utilising the lasers 488nm for GFP (green, no signal) and 561nm for TRITC (red). The image underwent processing with the Zen black software using linear unmixing, stitching and maximum projection (stack of 25 slices, covering a total thickness of 271.3µm with a piezo stage). Vasculature is detected, however no GFP<sup>+</sup> cells were detected across the entirety of calvarium. Scale bar: 100µm.

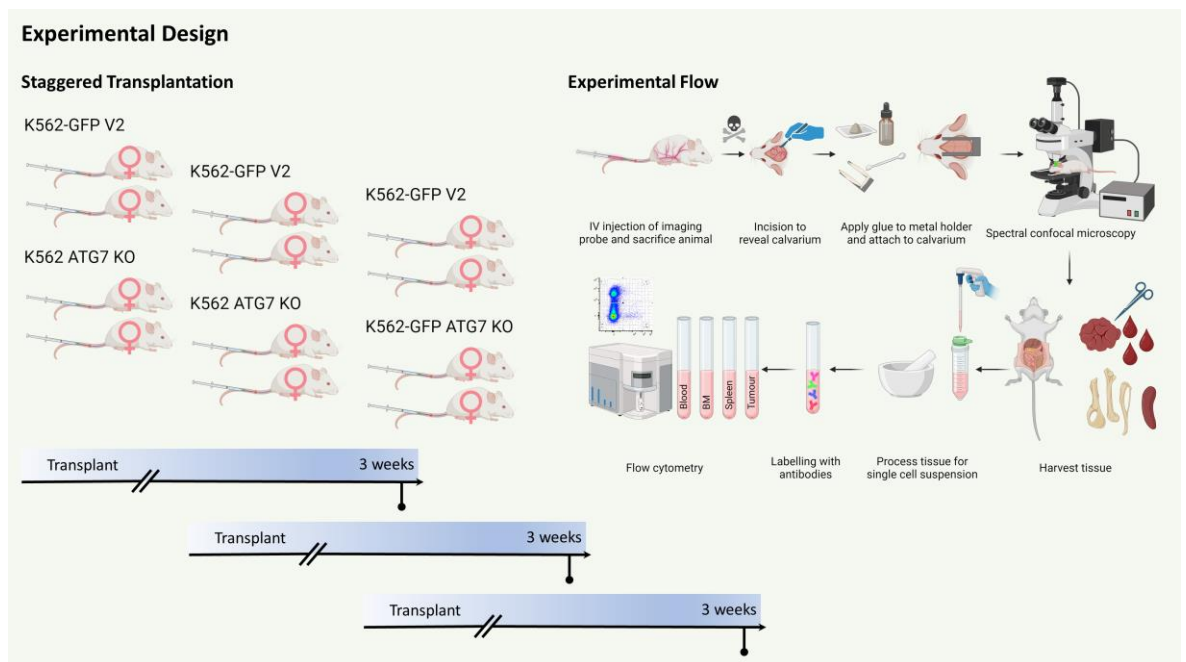
## 4.7 Autophagy-deficient K562 cells had reduced tumour formation capacity

The next step was to address the hypothesis that autophagy is required for tumour formation and influences engraftment and location in the BM *in vivo*. Autophagy is an important survival pathway that involves the recycling of intracellular material to ensure sufficient energy supply when cells are deprived of nutrients. BCR::ABL1 signalling reduces autophagic flux by activating mTOR<sup>143</sup>. Previous studies have shown that TKI treatment induces autophagic flux and ensures cell survival despite BCR::ABL1 inhibition<sup>365</sup>. Furthermore, a combination of targeted therapy and an autophagy inhibitor can induce differentiation in LSCs<sup>367</sup>. While primary cells pose challenges in genetic modification, cell lines offer a more straightforward approach. Alongside our efforts to develop a suitable xenograft mouse model for localising human leukaemic cells in the BM niche, we conducted experiments assessing the transplantation capacity of autophagy-deficient K562 cells. To achieve this, we utilised CRISPR-Cas9 to knock out the *ATG7* gene, which plays a pivotal role in the autophagy machinery. *ATG7* functions as a ubiquitin-activating enzyme E1 crucial for the ATG12-conjugation system<sup>393,394</sup>.

The KO was verified through Western blotting using an anti-ATG7 antibody (**Figure 4-27**). To further validate the complete inhibition of autophagy, LC3 conversion was visualised as a metric of autophagic flux. During autophagy induction, cytosolic LC3 (LC3-I) is conjugated to PE, now LC3-II, allowing it to integrate into the membrane of autophagosomes<sup>377</sup>. These two forms of LC3 can be distinguished by protein separation, as shown in **Figure 4-27**. This distinction is attributed to their difference in molecular weight and a higher hydrophobicity of LC3-II. In the vector control cells (V2), a strong band was detected for both LC3 forms indicating a level of basal autophagy. Conversely, in the *ATG7* KO cell line, the absence of LC3-II demonstrates the inability to undergo autophagy, resulting in accumulation of LC3-I.



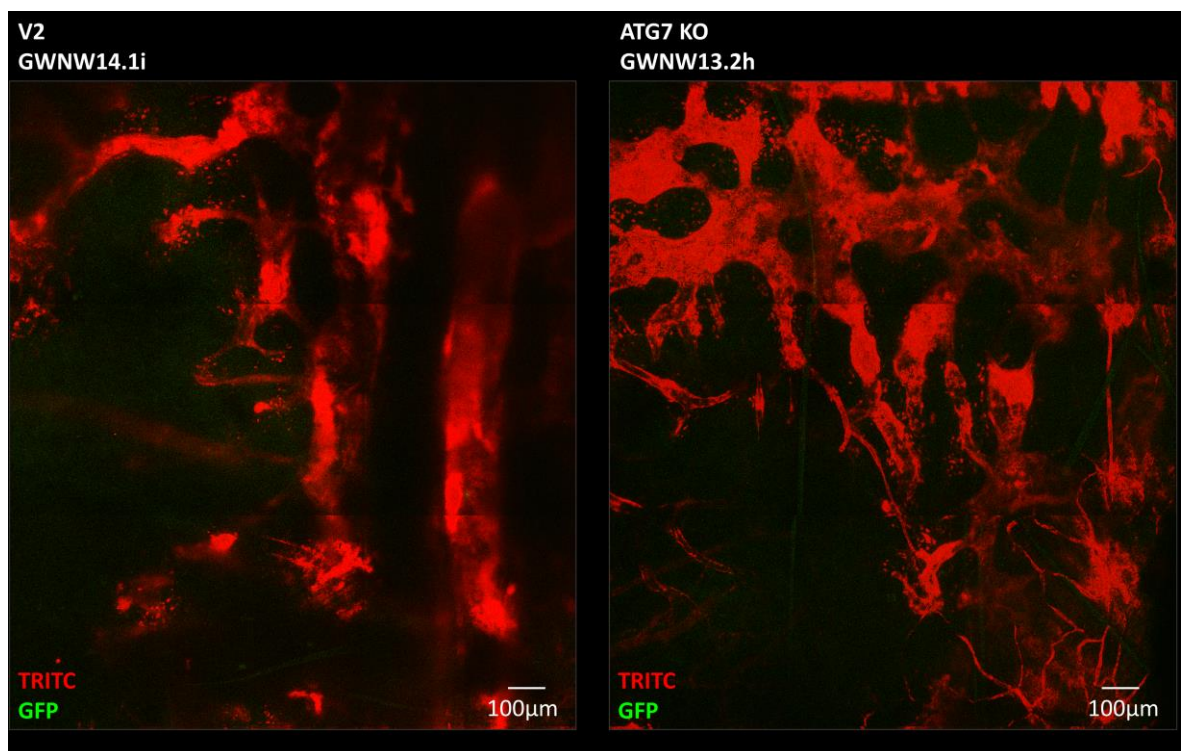
**Figure 4-27 Validation of ATG7 knockout in K562 GFP cells.** Western blot analysis shows successful KO of ATG7 in K562 cells compared to vector control (V2) cells. The inability to convert LC3-I to LC3-II demonstrates that KO cells were unable to undergo basal autophagy. HSP90 was used as a loading control.



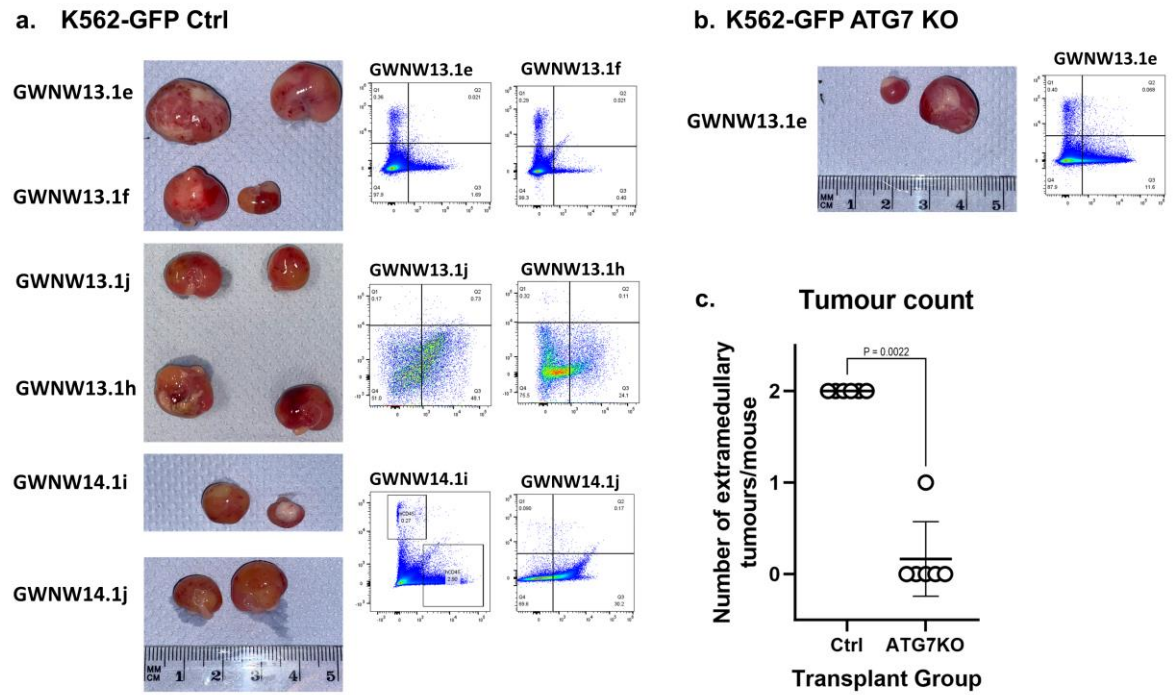
**Figure 4-28 Experimental design aimed to investigate BM engraftment of autophagy-deficient cells.** A total of six mice per group were transplanted with either K562-GFP vector control (V2) or ATG7 KO cells. The experiment was staggered, involving the transplantation of two mice per arm at the same time. All experiments were concluded three weeks post-transplantation. Following this period, mice were injected with fluorescent dextran and subsequently humanely killed. The mouse cadavers were prepared for microscopy by removing the skin from the skull to expose the bone. A metal holder was attached to the bone using dental cement to ensure the stable positioning of the mouse during microscopy. Subsequently, PBS was applied to the skull and spectral imaging was performed. Afterwards, single-cell suspensions were obtained from the leg bones, spleen, and tumour tissues. Blood samples underwent red blood cell lysis. All samples were stained with antibodies targeting mCD45 and hCD45 and analysed by flow cytometry. Created with BioRender.com.

In order to investigate cell localisation in BM, each transplant arm involved six mice injected with four million cells per mouse, either K562-GFP vector control (V2) or K562-GFP ATG7 KO cells. The experiment was staggered, involving the transplantation of two mice per group at the same time (Figure 4-28) due to the time-consuming nature of confocal microscopy. Representative images in Figure 4-29 demonstrate lack of GFP<sup>+</sup> cells in the BM niche in either transplant group.

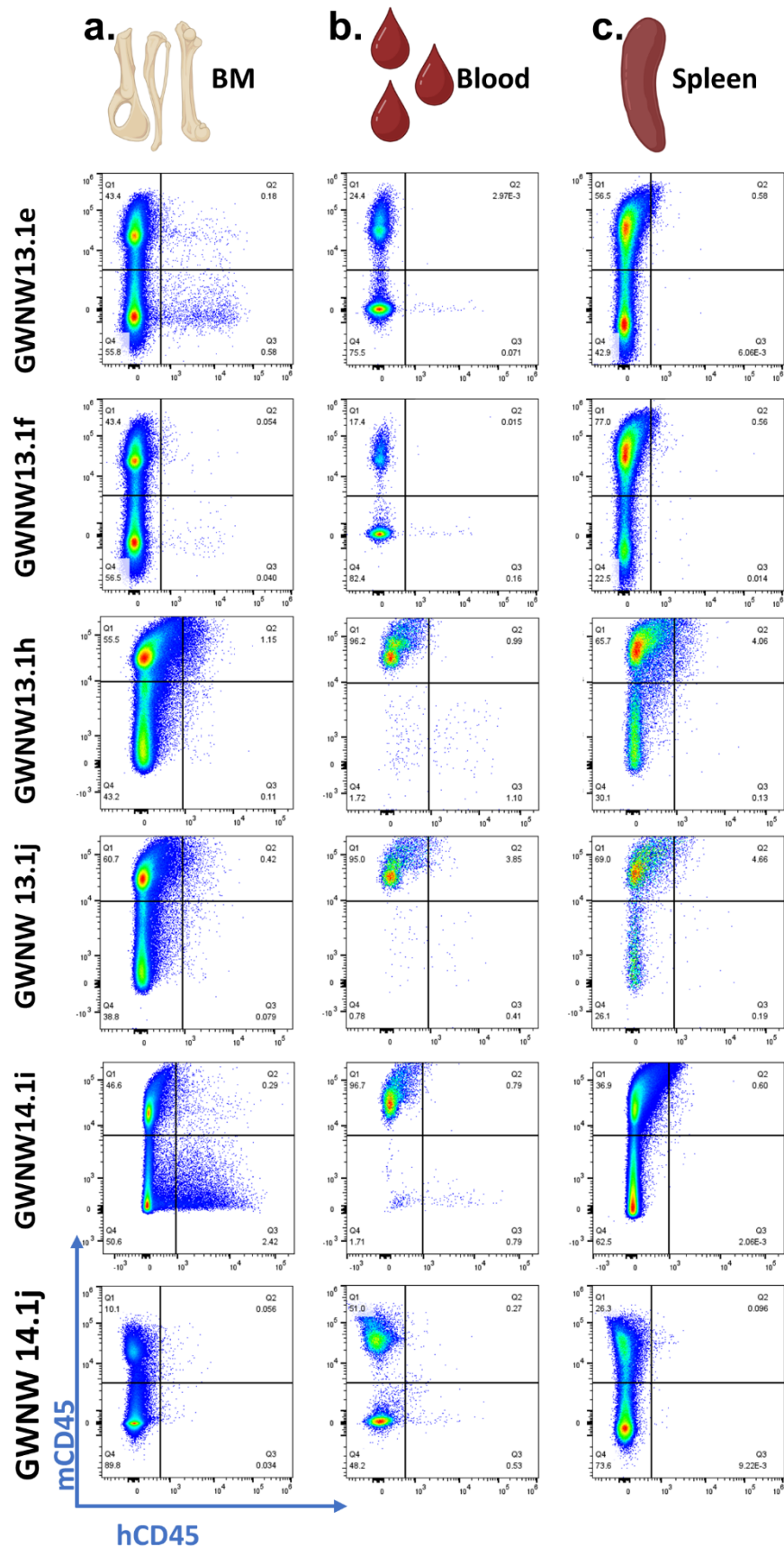
Following microscopy, tissues were collected, and flow cytometry was used to assess hCD45<sup>+</sup> cells in the BM, blood, spleen and tumour (Figure 4-31, Figure 4-32). Notably, tumour formation was significantly reduced in K562-GFP ATG7 KO cells compared to control cells (Figure 4-30). Despite this, overall engraftment into the BM remained limited for both transplant groups, with only one mouse per group exhibiting approximately 1.5% hCD45<sup>+</sup> cells from total BM cells (Figure 4-33). In contrast to male mice, K562 cells did not display migration of K562 cells to the brain in female mice (Figure 4-34).



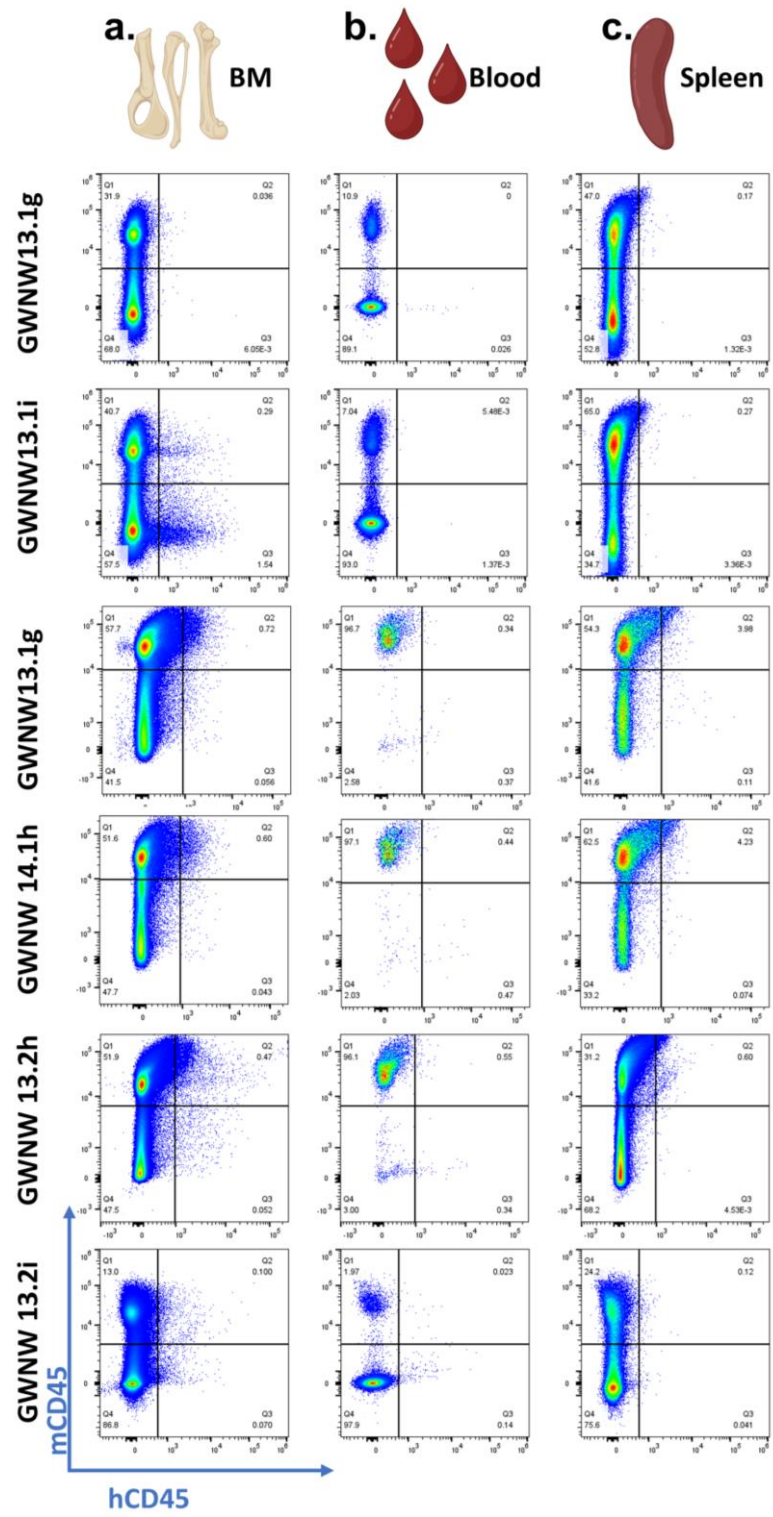
**Figure 4-29 K562-GFP WT or ATG7 KO cells are not able to be localised in the BM of the calvarium by microscopy.** Images shows a representative tile scan (left WT, right ATG7 KO transplant group) acquired using spectral imaging with the lasers 488nm for GFP (green, no signal) and 561nm for TRITC (red). The image was processed with the Zen black software using linear unmixing, stitching and maximum projection. Vasculature is detected, however no GFP<sup>+</sup> cells were detected throughout the calvarium. Scale bar 100µm.



**Figure 4-30 Tumour formation capacity reduced by ATG7 KO in K562-GFP cells.** Images show tumours harvested from the K562-GFP vector control (ctrl) group (a) and the K562-GFP ATG7 KO group (b) with corresponding flow cytometry analysis for mCD45<sup>+</sup> and hCD45<sup>+</sup> cells. Tumour count per transplant group was quantified in (c) with graph presented as mean  $\pm$  S.D. with  $n=6$ . Non-parametric Mann-Whitney test was used for statistical analysis.



**Figure 4-31 K562-GFP control cells showed limited potential of BM engraftment in female mice.** Recipients injected with four million K562-GFP WT cells were sacrificed three weeks after transplantation and BM (a), blood (b) and spleen (c) were stained with anti-human and anti-mouse CD45 antibodies.



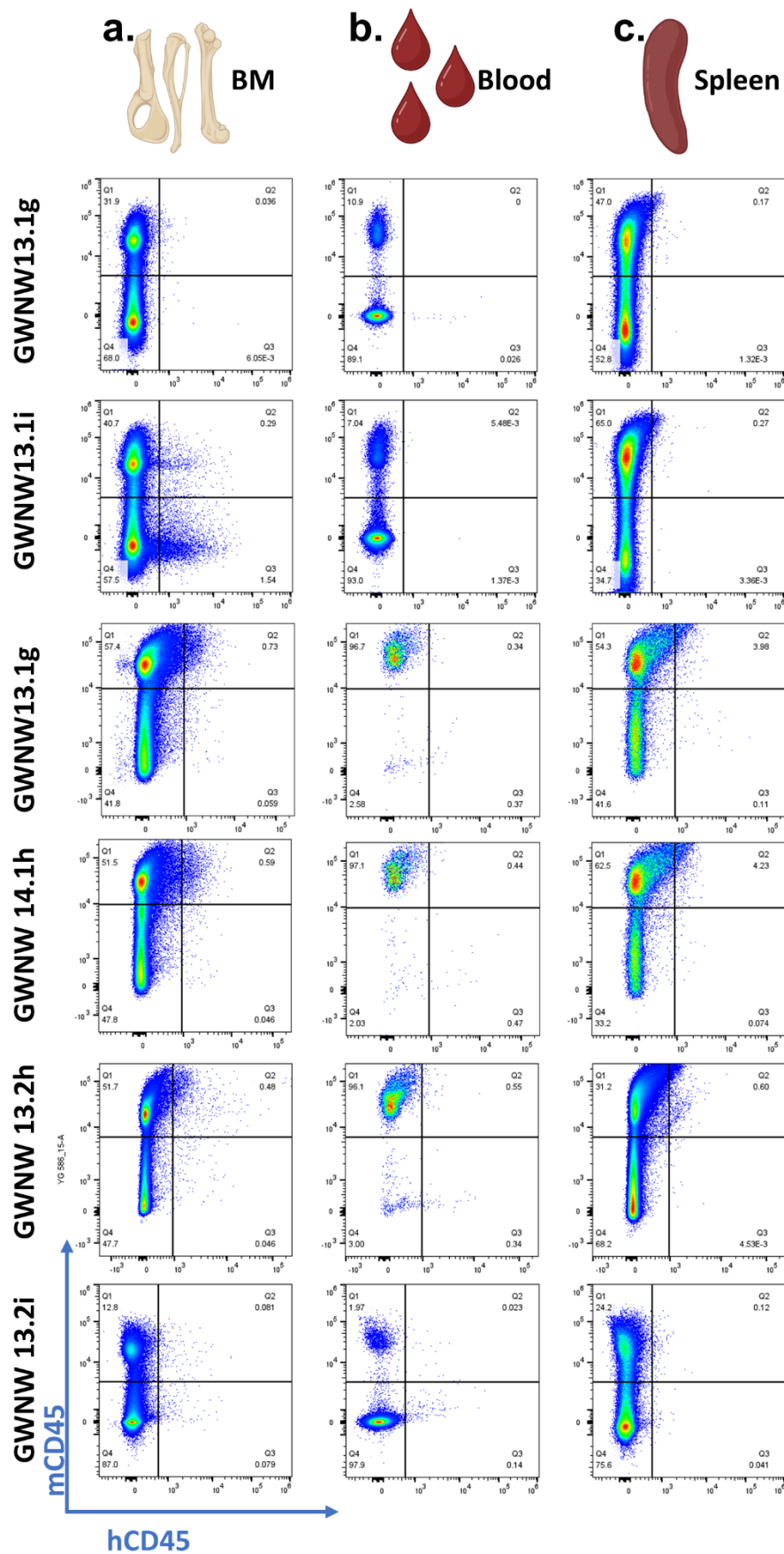


**Figure 4-32** BM engraftment of K562-GFP ATG7 KO cells in female NRGW mice. Recipients injected with four million K562-GFP ATG7 KO cells were sacrificed three weeks after transplantation and BM (a), blood (b) and spleen (c) were stained with antibodies targeting human and mouse CD45 surface markers.

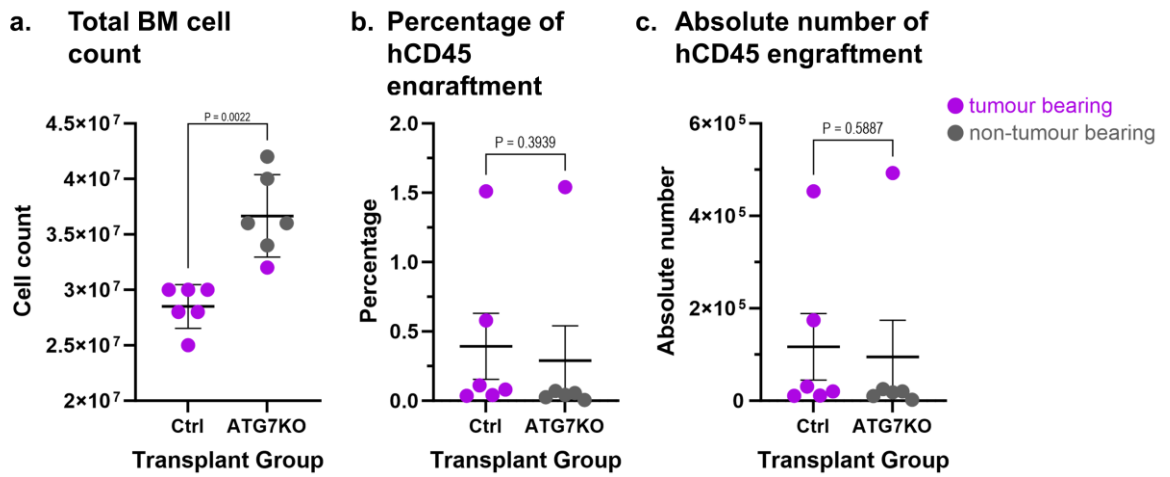


**Figure 4-33 Analysis of BM engraftment of K562-GFP ATG7 KO compared to control cells.** Graphs show total BM cell count (a) and BM engraftment of human cells in percentage of total BM cells (b) and as absolute number (c). Graphs were plotted as mean  $\pm$  S.D. with  $n=6$ . Non-parametric Mann-Whitney test was used for statistical analysis.

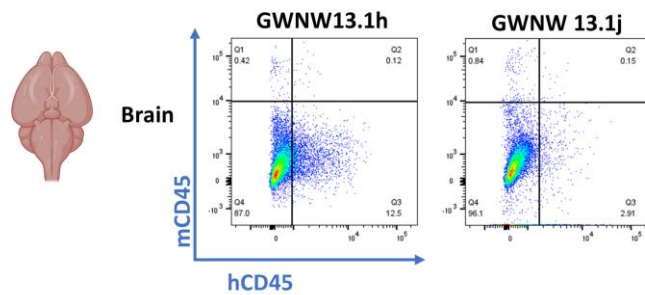


**Figure 4-34 K562-GFP cells tended to not migrate to the brain in female NRGW mice.** Representative flow cytometry analysis of brain cells harvested from mice transplanted with K562-GFP vector control cells three weeks after transplant. Single-cell suspension was stained with antibodies for hCD45 and mCD45 and analysed by flow cytometry.

## 4.8 Human Jurl cells engrafted close to vasculature in mouse calvarium BM

As BM engraftment of K562 displayed significant variability, rendering it unsuitable for xenograft experiments aimed at studying the localisation and interaction of leukaemic cells within the niche, we explored alternative Ph<sup>+</sup> cells for their potential to engraft. Jurl-MK1, derived from the peripheral blood of a male CML patient in BC, exhibits a high expression of the cytokine receptor cKit<sup>395</sup>. SCF, the ligand for cKit, has been shown to be crucial to maintain HSCs as well as being required for homing and long-term repopulation of transplanted HSCs<sup>82,93</sup>. Therefore, we hypothesise Jurl cells to have superior engraftment potential to the BM due to high expression of cKit compared to K562 or KCL22. Consequently, we genetically modified Jurl cells to express GFP similar to previous cell lines (Figure 4-35) and evaluated the levels of hCD45<sup>+</sup> through flow cytometry analysis (Figure 4-36).

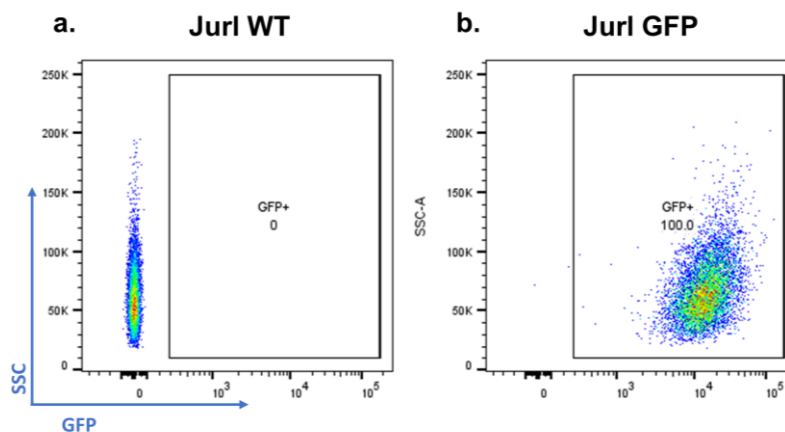


**Figure 4-35 Generation of Jurl cells to stably express GFP.** Jurl cells were lentivirally transduced to express GFP. Flow cytometry was used to measure GFP expression (b) compared to parental WT cells (a).

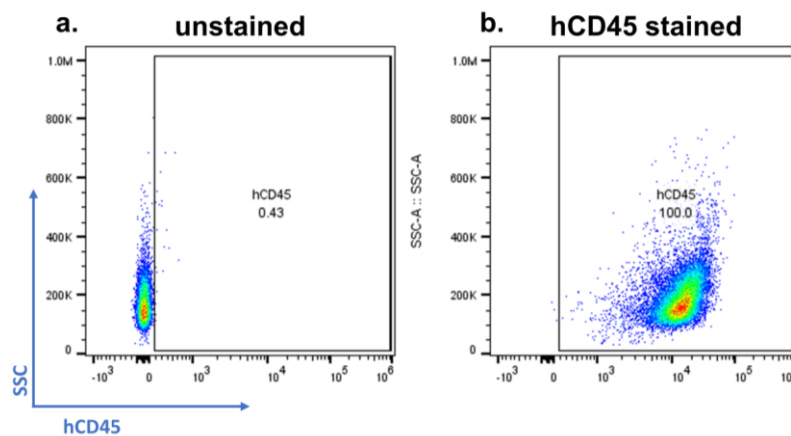


**Figure 4-36 Validation of human CD45<sup>+</sup> expression on Jurk-GFP cells.** Jurk-GFP cells were stained with an antibody targeting hCD45 (b) and compared to the unstained control cells (a).

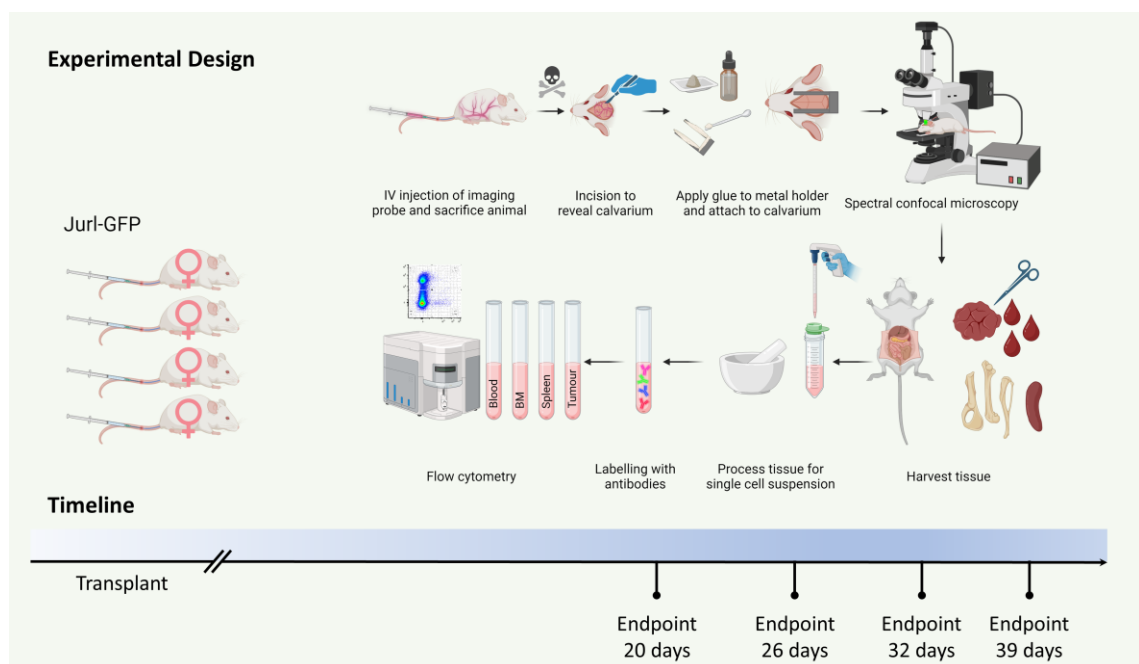


**Figure 4-37 Experimental design aimed to investigate BM engraftment dynamics of Jurk-GFP cells.** Four mice were transplanted with Jurk-GFP cells and were subsequently sacrificed between 20- and 39-days post-transplantation. To visualise the vasculature, mice were injected with fluorescent dextran, then humanely killed. The mouse cadaver was prepared for microscopy by removing the skin from the skull to expose the bone. A metal holder was then attached to the skull, securing the mouse on the microscope stage. PBS was applied to the skull for spectral imaging. Afterwards, single-cell suspensions were obtained from the of BM from leg bones as well as the spleen and tumour tissue. Blood samples underwent red blood cell lysis. All tissues were stained with antibodies targeting mCD45 and hCD45 and analysed by flow cytometry. Created with BioRender.com.

In the first transplantation experiment, four female mice received injections of four million Jurk-GFP cells each. These mice were then sacrificed between 20- and 39-days post-transplantation to monitor both tumour development and the dynamics of BM engraftment (**Figure 4-37**). Prior to sacrifice, mice were injected with fluorescent dextran to enable visualisation of the vasculature. Post-mortem microscopy of the calvarium was conducted before necropsy to

localise Jurl-GFP cells within the BM niche. Subsequently, samples of BM, blood, spleen and, if present, tumour were collected.

Flow cytometry analysis for mCD45<sup>+</sup> and hCD45<sup>+</sup> cells showed BM engraftment of human cells at 20 days with 0.73% of total BM cells (**Figure 4-39a**). While no human cells were detected in the blood, a small population was localised in the spleen (0.092% of total cells). Notably, no extramedullary tumour formation was observed. Despite flow cytometry detecting cells in the BM obtained from the leg bones, no GFP<sup>+</sup> cells were found in the calvarium during comprehensive microscopic examination (**Figure 4-40**).

Another mouse was sacrificed four weeks after transplantation and showed no signs of discomfort or tumour development on external examination. Flow cytometry analysis indicated an increase in hCD45<sup>+</sup> cells residing in the BM with 6.33% of total cells and 1.28% within the spleen (**Figure 4-39b**). However, no GFP<sup>+</sup> cells were detected through calvarium microscopy (**Figure 4-41**).

A similar profile was observed in the mouse sacrificed after 32 days. Despite fewer hCD45<sup>+</sup> cells residing in the BM (1.67% of total cells) and the spleen (2.44% of total cells) compared to the previous mouse (**Figure 4-39c**), few GFP<sup>+</sup> cells were detected in close proximity to the vasculature in the calvarium by microscopy (**Figure 4-42**).

The final mouse was sacrificed after 39 days upon external observation of tumour development in the abdomen. Flow cytometry analysis not only identified hCD45<sup>+</sup> cells in the spleen (comprising 3.47% of total cells) but also detected a small population in the blood (0.34% of total cells). Remarkably, the BM exhibited the highest percentage of engraftment with 11.2% hCD45<sup>+</sup> cells, marking the most substantial engraftment observed in the BM using human cell lines (**Figure 4-39d**). Confocal microscopy of the calvarium revealed scattered GFP<sup>+</sup> cells positioned close to the vasculature in various sites throughout the bone (**Figure 4-43**). Additionally, larger clusters of leukaemic cells were observed around larger vessels (**Figure 4-44**).

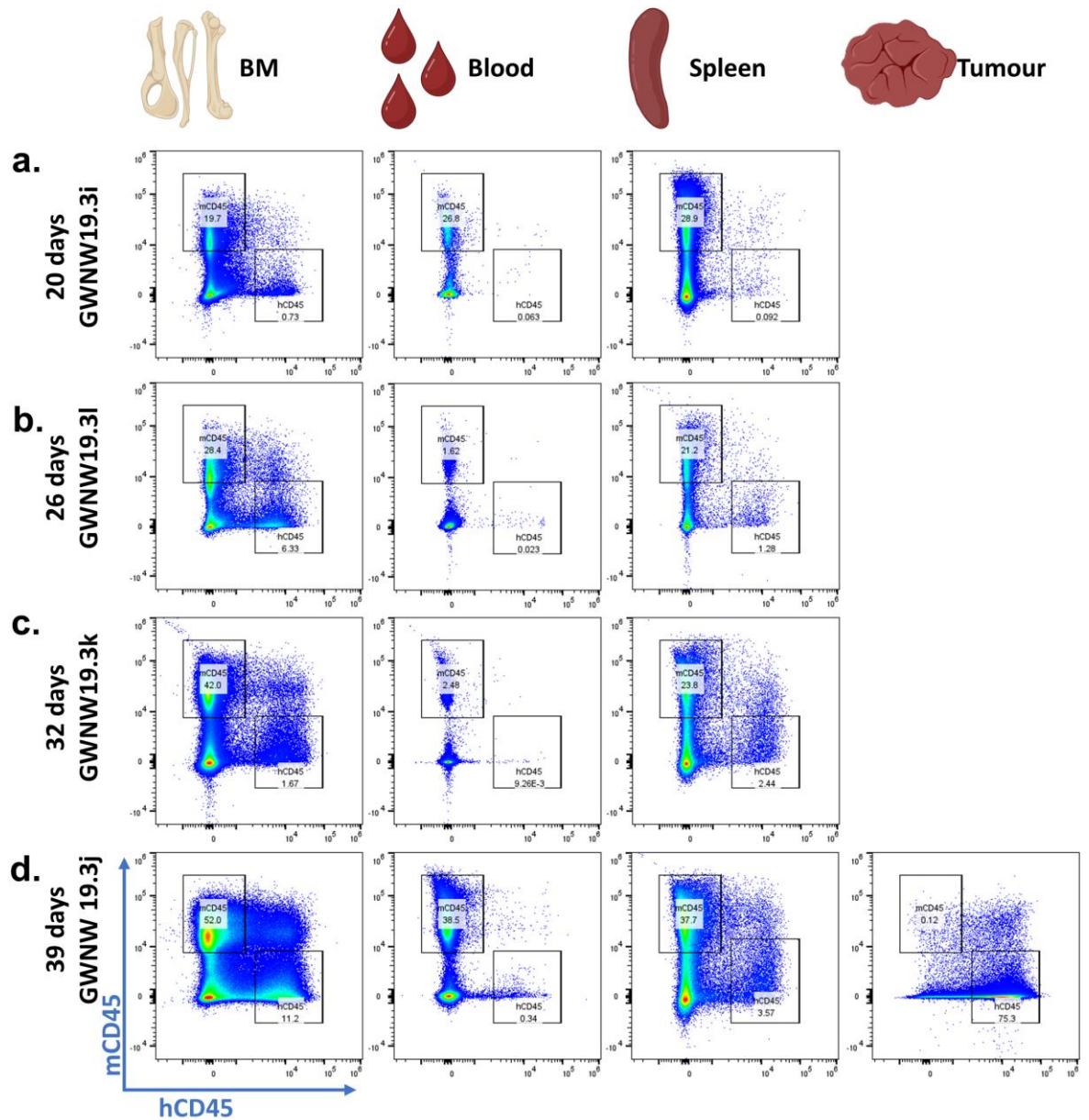


**Figure 4-38 Time course of Jurl-GFP engraftment in the BM.** Four mice were transplanted with four million Jurl-GFP cells via the tail vein injection. Mice were sacrificed sequentially between 20 to 39 days post-transplantation to determine engraftment dynamics and tumour development. BM from leg bones, blood, spleen, and tumour tissues were analysed for hCD45<sup>+</sup> cells in contrast to mCD45<sup>+</sup> cells by flow cytometry.

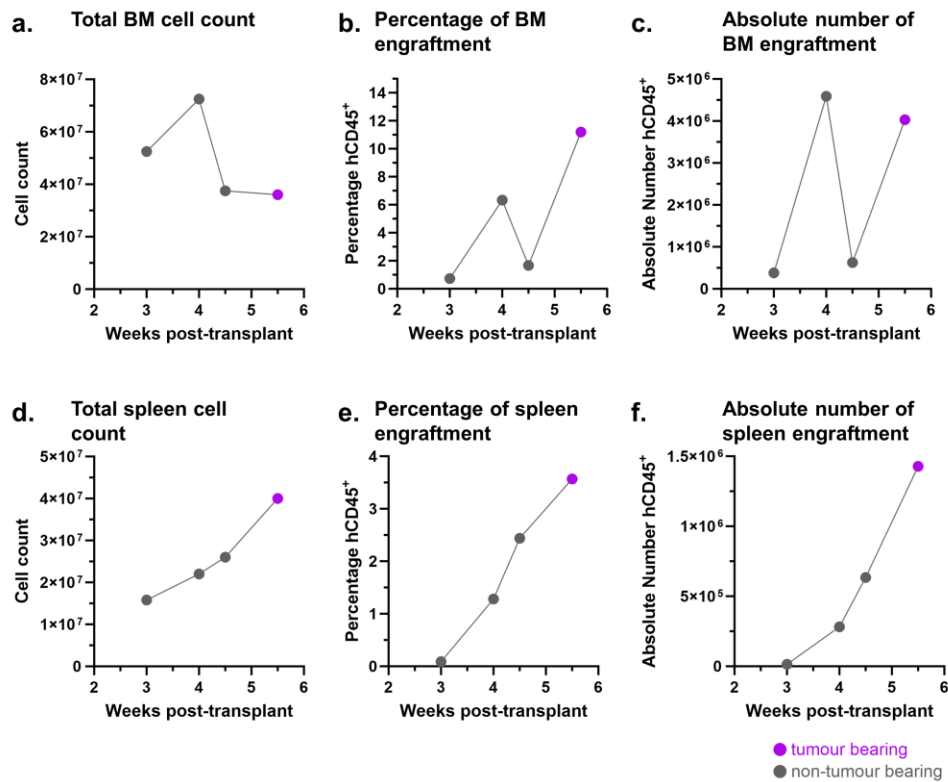


**Figure 4-39 Analysis of BM and spleen of Jurl-GFP recipient mice.** Total BM and spleen cell count (a, d) with engraftment of hCD45<sup>+</sup> cells in percentage (b, e) and as absolute number (c, f) were plotted over the time course of 20- to 39-days.

Despite the increasing cell number of hCD45<sup>+</sup> cells observed over the period of 20 to 39 days, the cellularity of the BM decreases concurrently with the rise in hCD45<sup>+</sup> cell count (**Figure 4-39a-c**). The bones of mice from the last two time points (day 32 and 39) appeared pale compared to the bones of mice at earlier time points, prone to breaking during harvesting (not shown). Pale bones often indicate potential signs of anaemia with a lower red blood cells counts. However, this was not confirmed by flow cytometry at that time and requires further investigation.

Spleens weights were not measured for this experiment; however, the total cell count indicated a consistent increase over time, correlating with increasing number of human cells localised in the spleen (**Figure 4-39d-f**).

These results suggest that Jurl-GFP cells possess a higher potential than K562-GFP cells for BM engraftment in SCID mice, which may allow the study of leukaemic cells in the BM niche. Nevertheless, it should be noted that this was a pilot study conducted with a limited number of mice to explore the potential dynamics of BM engraftment of Jurl cells in NRGW mice.

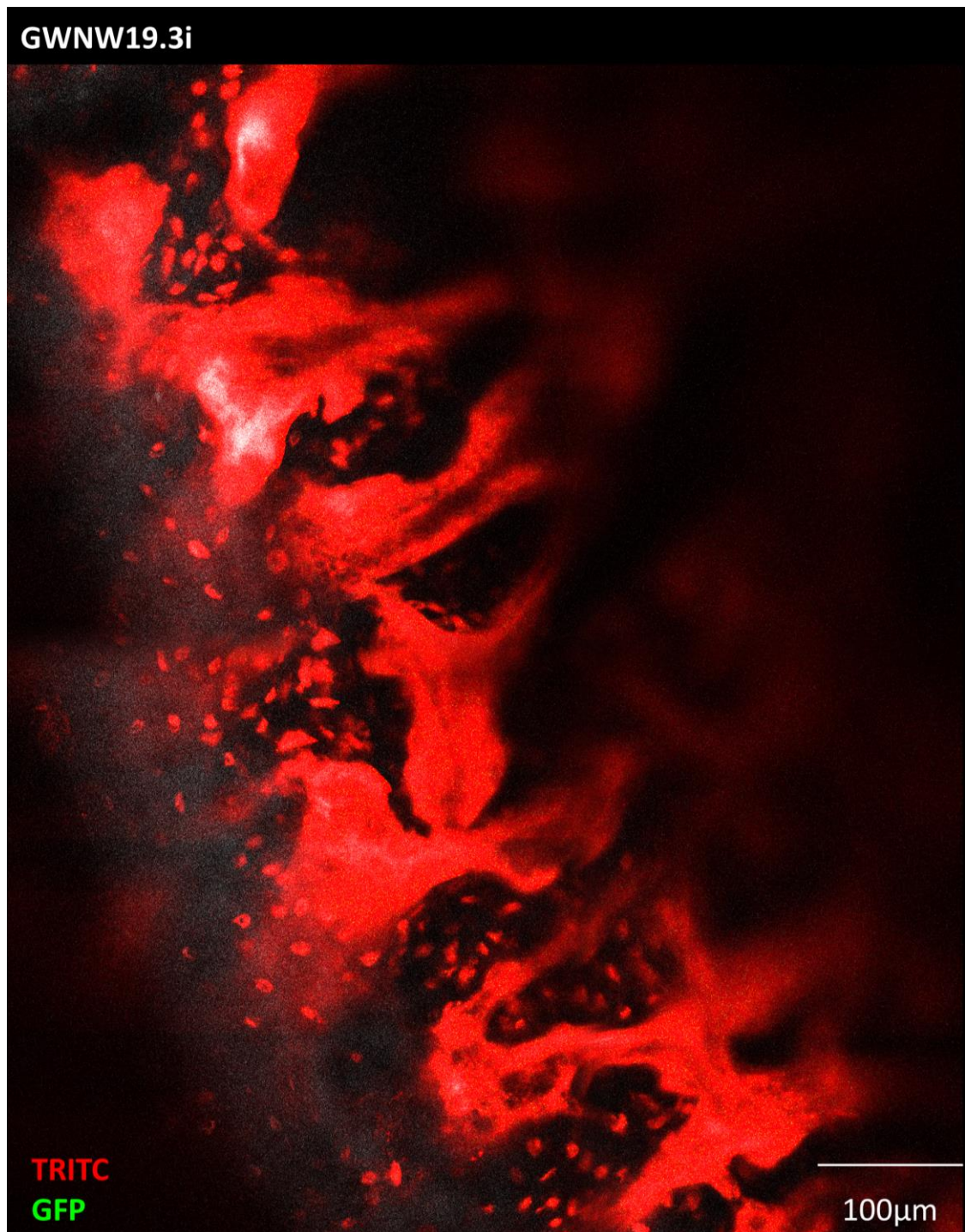


**Figure 4-40 Microscopy image of Jur1-GFP recipient 20 days post-transplantation.** The mouse received an injection of 640µg TRITC dextran 500,000 MW before sacrifice and was immediately prepared for microscopy. A representative tile scan of the calvarium is displayed here. Spectral imaging using lasers at 488nm for GFP (green, showing no signal) and 561nm for TRITC (red) was employed to acquire the image. Zen black was utilised for image processing, involving linear unmixing, stitching, and maximum projection (stack comprising 25 slices, thickness of whole image 96µm). The image shows the vasculature but there were no GFP<sup>+</sup> cells present in the calvarium which was thoroughly scanned during microscopy. Scale bar: 100µm.

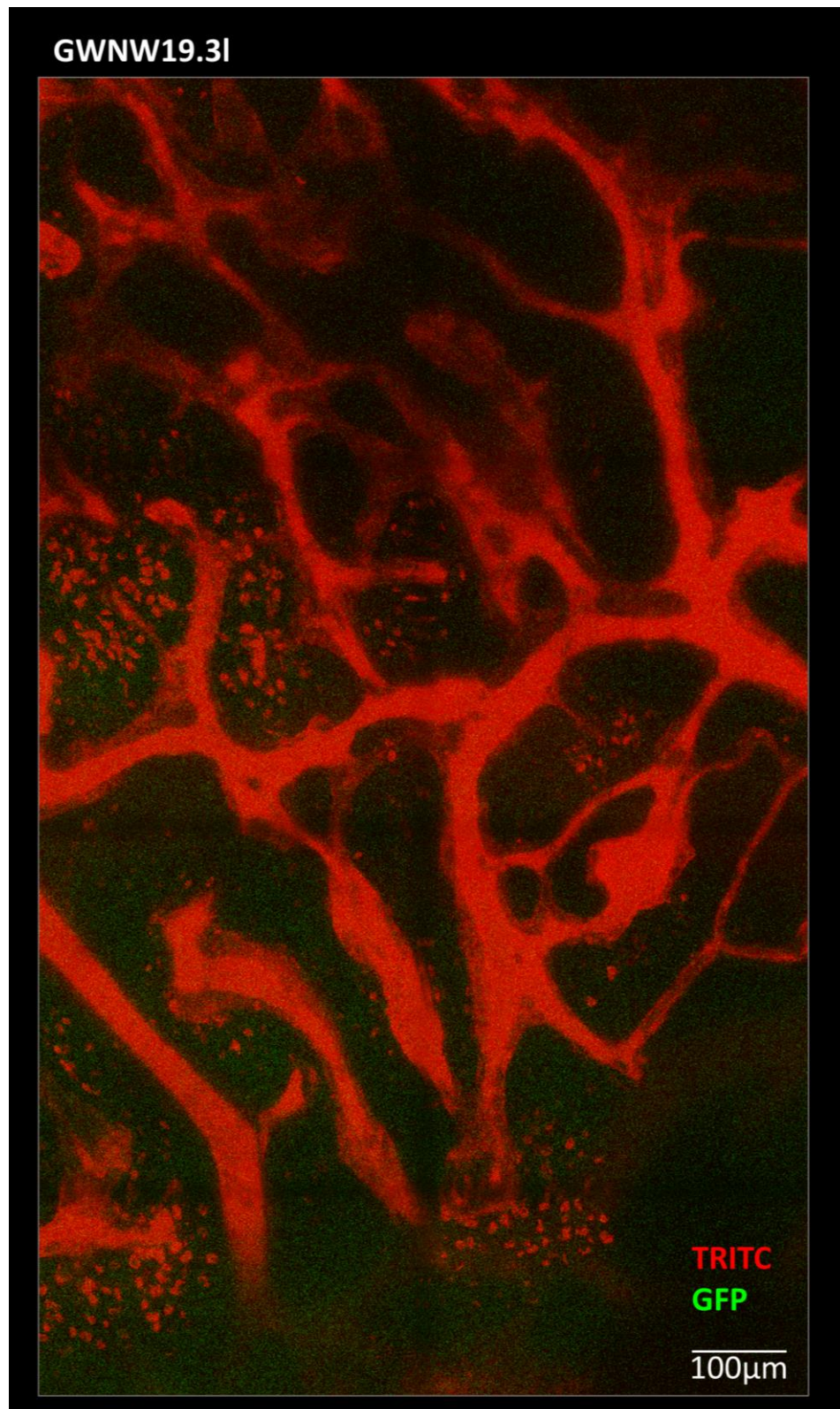


**Figure 4-41 Microscopy of calvarium from Jurl-GFP recipient mouse four weeks post-transplantation.** Mouse was injected with 640 $\mu$ g TRITC dextran prior euthanasia and immediately prepared for microscopy. A representative tile scan of the calvarium is shown here. The image was acquired using spectral imaging with the lasers 488nm for GFP (green, showing no signal) and 561nm for TRITC (red). The image was processed with the Zen black software using linear unmixing, stitching and maximum projection (stack comprising 22 slices, total thickness of image 113 $\mu$ m). Despite a comprehensive scan of the calvarium during microscopy, GFP<sup>+</sup> cells were observed. Scale bar: 100 $\mu$ m.

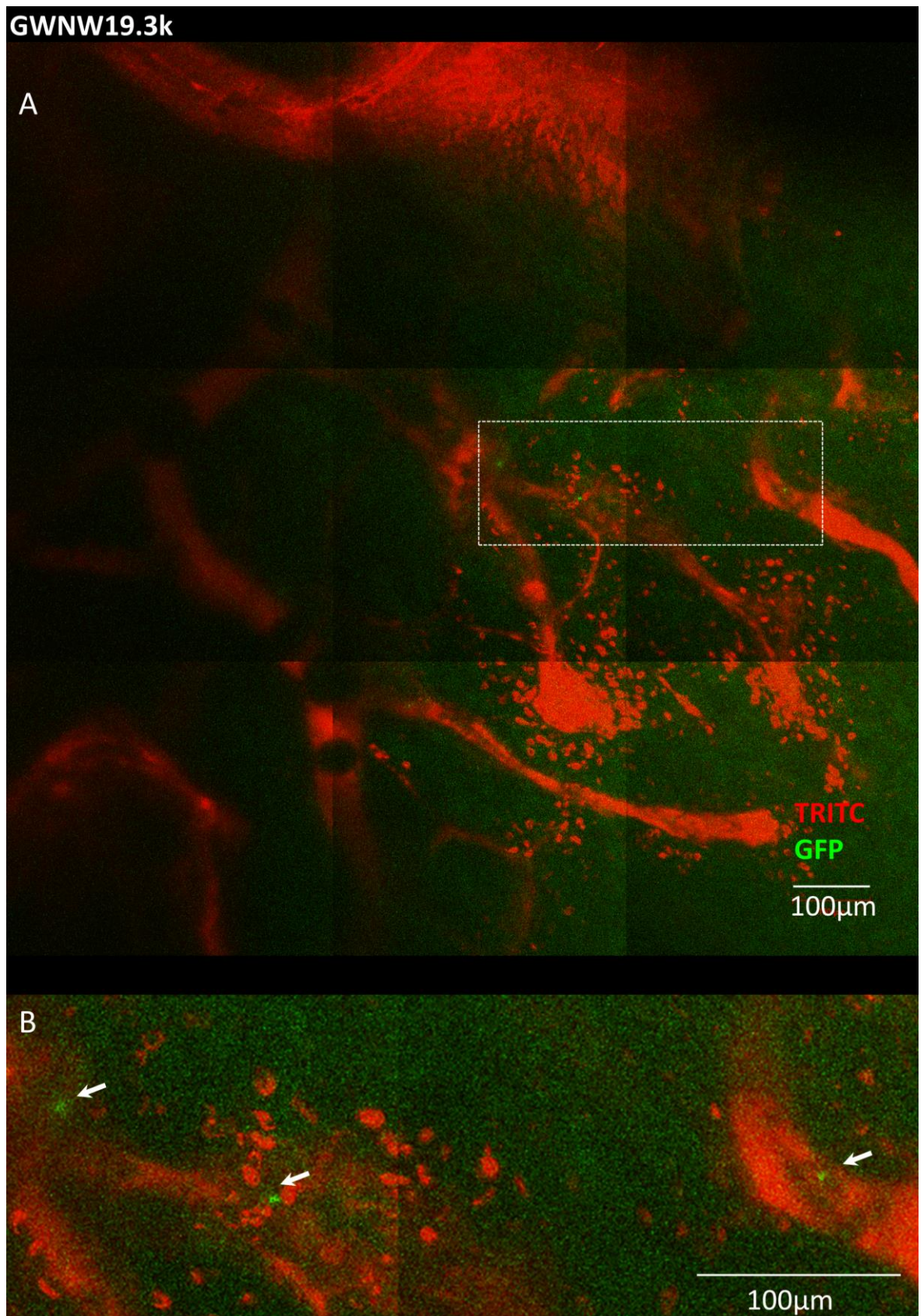


**Figure 4-42 Microscopy of calvarium from Jurl-GFP recipient mouse 32 days post-transplantation.** The mouse received an injection with 640µg TRITC dextran before being humanely killed and immediately prepared for microscopy. Spectral imaging using lasers at 488nm for GFP (green) and 561nm for TRITC (red) was employed to acquire the image. The Zen black software was utilised for image processing, involving linear unmixing, stitching and maximum projection (stack comprising of 22 slices, total thickness 133µm). The representative image (a) illustrates the vasculature, while a few rare GFP<sup>+</sup> cells were detected in the calvarium, as indicated in the zoomed-in view (b, white arrows). Scale bar: 100µm.

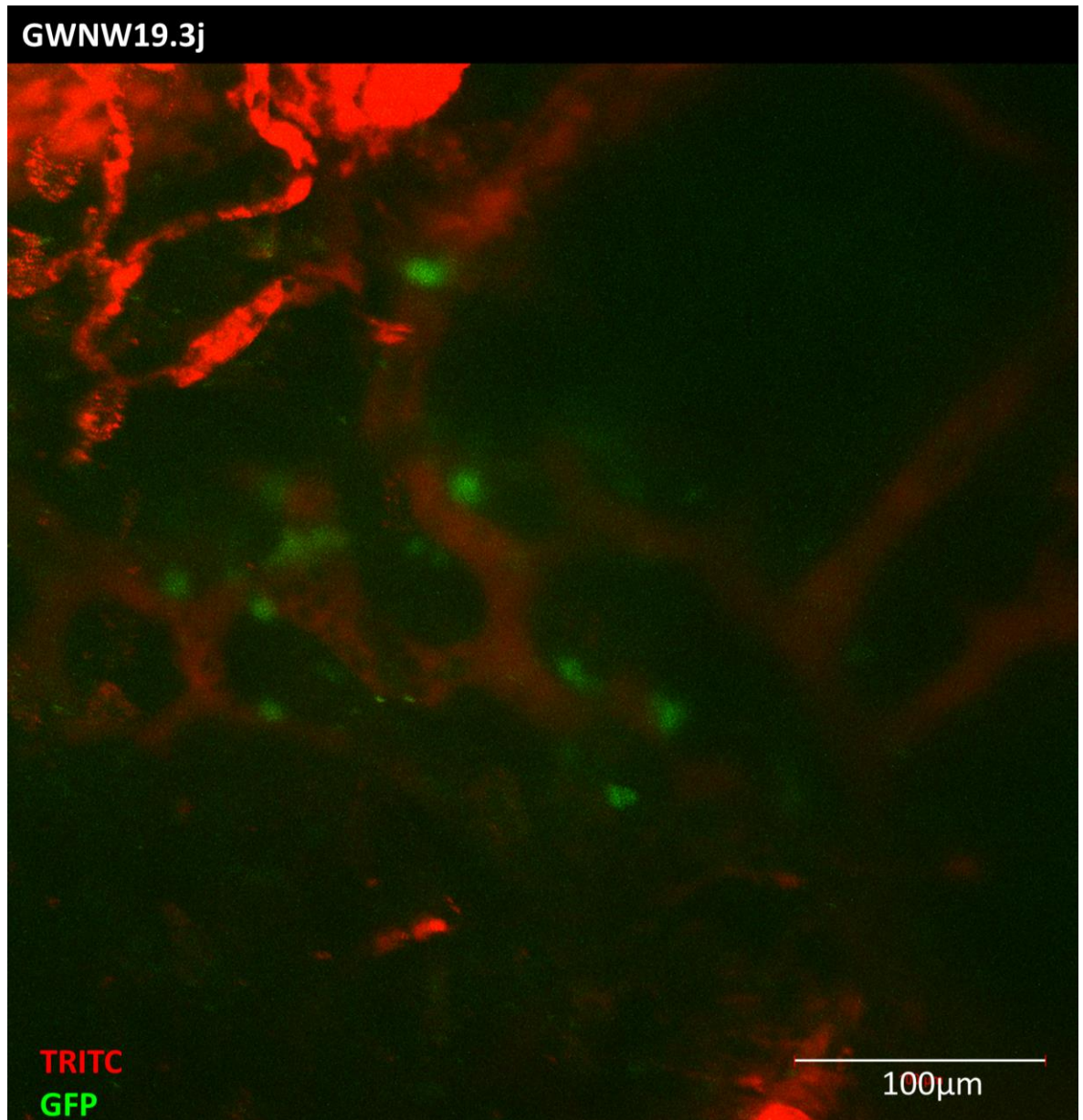


**Figure 4-43 Microscopy of calvarium from Jurl-GFP recipient mouse 39 days-post-transplantation detects GFP<sup>+</sup> close to vasculature.** The mouse received an IV injection of 640μg TRITC dextran. Post-mortem confocal microscopy was conducted with the lasers 488nm for GFP (green) and 561nm for TRITC (red). The z-stack images were maximum projected using the Zen black software (stack comprising 60 slices, total thickness 105.65μm). Sparsely scattered GFP<sup>+</sup> cells were detected close to the vasculature.

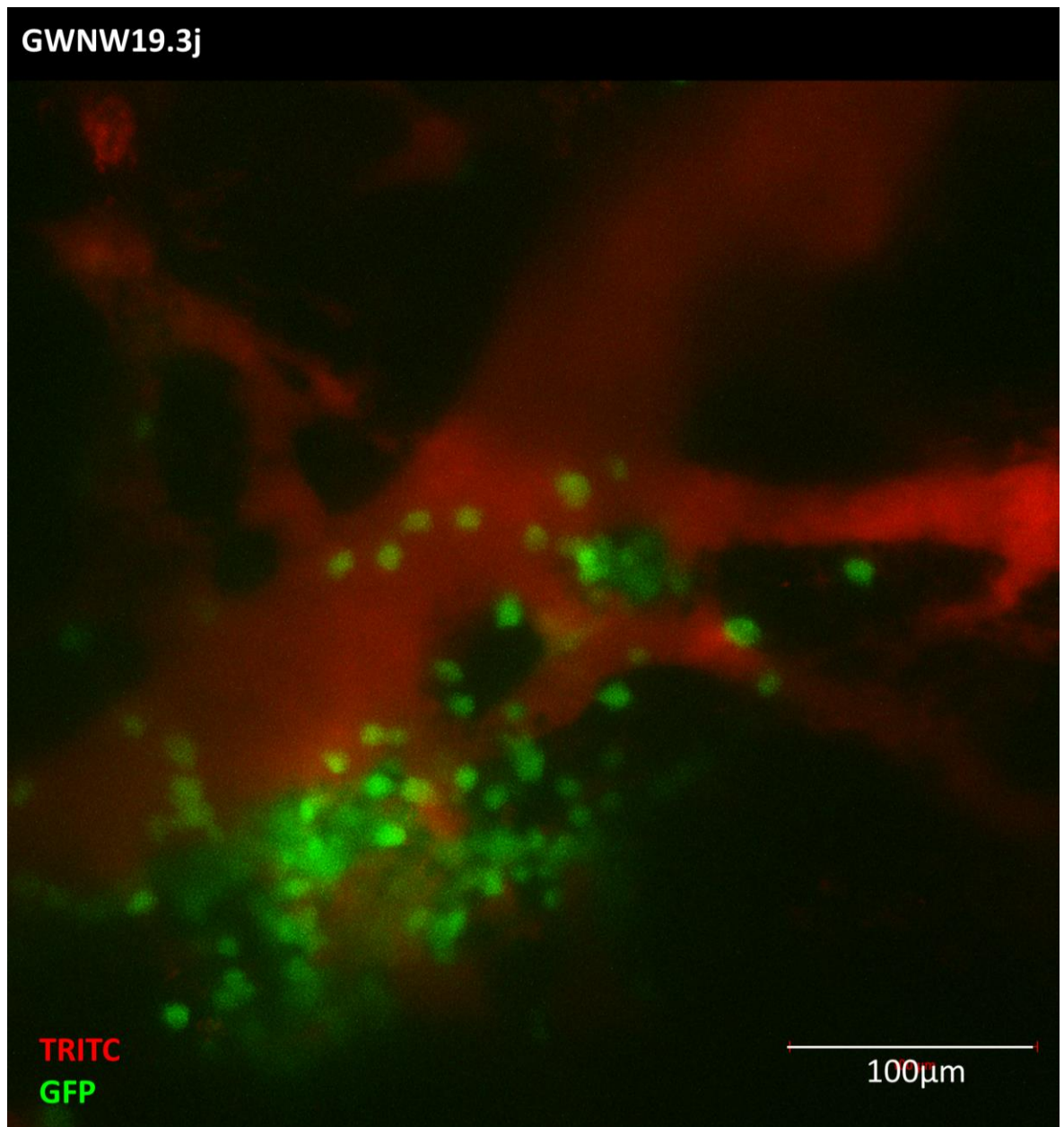


**Figure 4-44 Microscopy of calvarium from Jurl-GFP recipient mouse 39 days-post-transplantation detects accumulation of GFP<sup>+</sup> cells.** The mouse was injected with 640 $\mu$ g TRITC-dextran. Post-mortem microscopy was performed using the lasers 488nm for GFP (green) and 561nm for TRITC (red). The image was processed with the Zen black software for maximum projection of 93 z-stack slices (total thickness 164.74 $\mu$ m). Accumulation of GFP<sup>+</sup> detected close to the vasculature.

## 4.9 Intravital localisation of Jurk-GFP five weeks after transplantation in the BM

Next, we utilised IVM to investigate whether Jurk cells localise to a certain leukaemic niche in the BM that supports their engraftment. Following the previous experiment that concluded the engraftment dynamics of Jurk-GFP cells in NRGW mice, a new mouse cohort was set up. The cohort consisted of four female mice transplanted with four million Jurk-GFP cells and one non-transplant control mouse (**Figure 4-45**). The primary objective was to locate human leukaemic cells within the BM microenvironment using IVM.

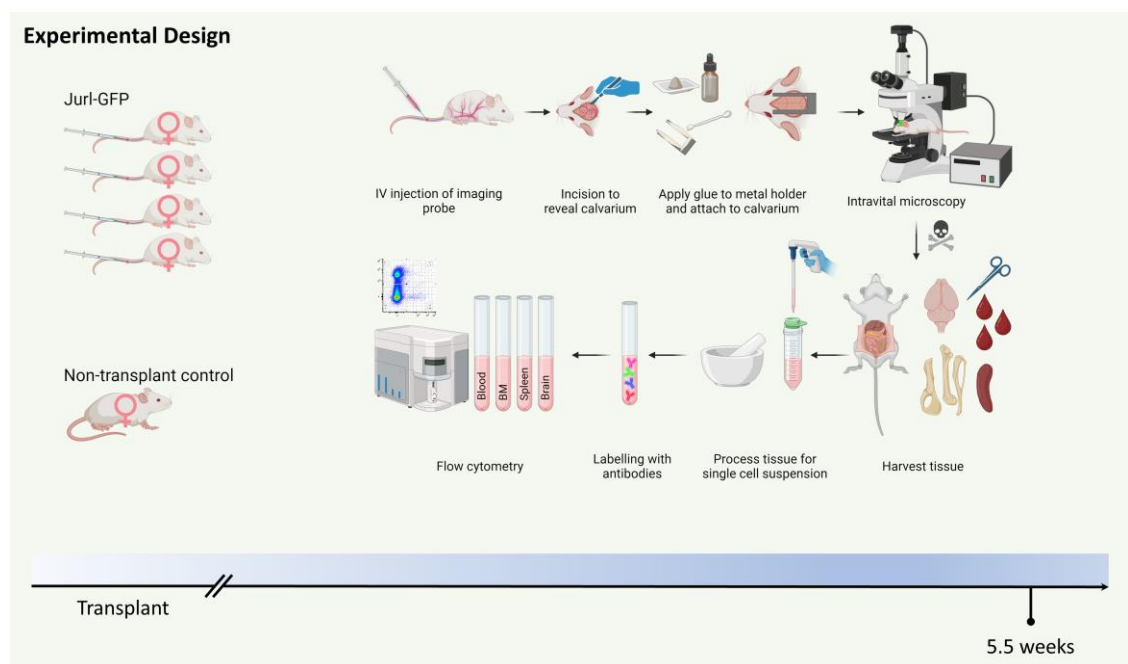


**Figure 4-45** Experimental design for localising Jurk-GFP in the BM microenvironment using IVM. Four mice were transplanted with four million Jurk-GFP cells, while one mouse was used as a non-transplant control. After five weeks, IVM was performed, followed by tissue analysis using flow cytometry. Prior to the mouse being anaesthetised with isoflurane, fluorescent dextran was injected via the tail vein. A metal holder was affixed to the skull bone using dental cement, which took approximately six minutes to set. The mouse was then secured onto the microscope stage to perform IVM. Afterwards, the mouse was humanely killed, and the leg bones, spleen, blood, and tumours were harvested to obtain single-cell suspensions for flow cytometry analysis to determine engraftment of hCD45<sup>+</sup> cells. Created with BioRender.com.

Based on the previous timeline experiment, it seemed appropriate to keep the mice for approximately five weeks post-transplantation to ensure a substantial presence of human cells within the BM. Flow cytometry analysis of the BM revealed a high engraftment, with hCD45<sup>+</sup> cells constituting approximately 25% of total cells, showing some variability (**Figure 4-46**). Notably, in three of the four mice, we observed extramedullary tumour development. Furthermore, we confirmed a significant localisation of Jurk-GFP cells in the spleen, supported by

splenomegaly observed in all transplanted mice (**Figure 4-47**). Moreover, human cells were also detected in the blood of two mice, accounting for 12.4% and 67.5% of the total cells in the blood after red blood cell lysis. In three mice, a substantial percentage of cells, ranging between 12-35% of the total, was found in the brain. This implies that overall, Jurl-GFP cells exhibit high potential of BM engraftment but also demonstrates localisation to multiple other organs.

Investigation through IVM aimed to locate human leukaemic cells residing within the BM niche in the calvarium. In a recipient mouse with the ID GWNW21.1e, which exhibited the lowest percentage in engraftment in the BM derived from the leg bones (9.7% of total cells, **Figure 4-46**), we could not detect any GFP<sup>+</sup> cells while scanning the calvarium (not shown). Two other recipient mice, with similar levels of engraftment within the BM, exhibited analogous localisation patterns of human cells within the BM (**Figure 4-48**, **Figure 4-49**). Here, we observed significant clusters of leukaemic cells occupying the entire BM cavity, alongside regions where sparse GFP<sup>+</sup> cells were scattered throughout the marrow, consistently in proximity to the vasculature. The final recipient mouse, despite exhibiting a similar level of human cells within the BM as determined by flow cytometry, displayed only few areas containing extremely sparse GFP<sup>+</sup> cells (**Figure 4-50**).

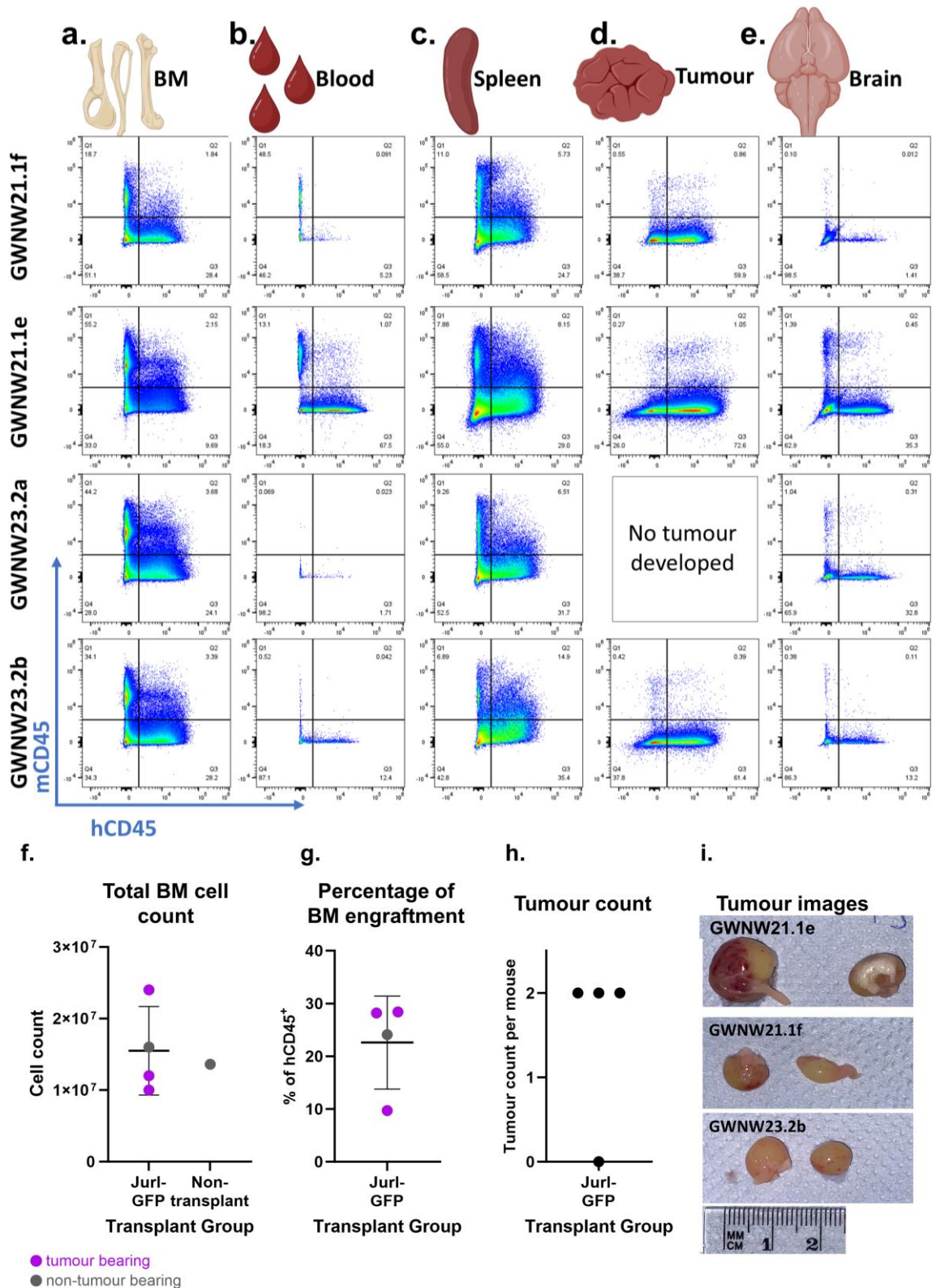


**Figure 4-46 Flow cytometry analysis of Jurl-GFP in NRGW mice five weeks after transplantation.** NRGW mice received a tail vein transplant of four million Jurl-GFP cells. Sequentially, the mice were sacrificed between day 36-38 post-transplantation. BM (a), blood (b), spleen (c), tumour (d) and brain (e) were stained with mCD45 and hCD45 antibodies. Non-transplant control is not presented. Total BM cell counts of leg bones (f) in the Jurl-GFP group are presented in comparison to the non-transplant control. BM engraftment in percentage (g) of human CD45<sup>+</sup> cells as well as tumour count per mouse (h) alongside corresponding tumours images (i) are provided.

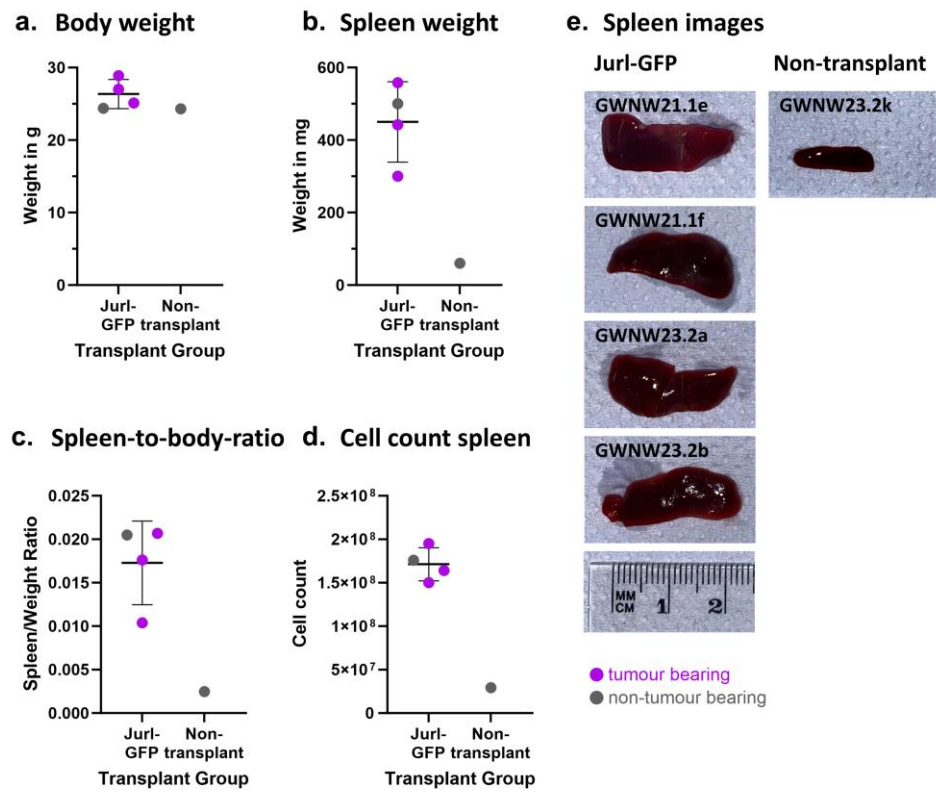


**Figure 4-47 Splenomegaly in NRGW mice five weeks after transplant with Jurl-GFP cells.** Body weight (a) and spleen weight (b) were used to calculate the spleen-to-body ratio (c) to assess splenomegaly in Jurl-GFP transplanted mice compared to non-transplant control. Spleen total cell counts (d) and images (e) are provided.

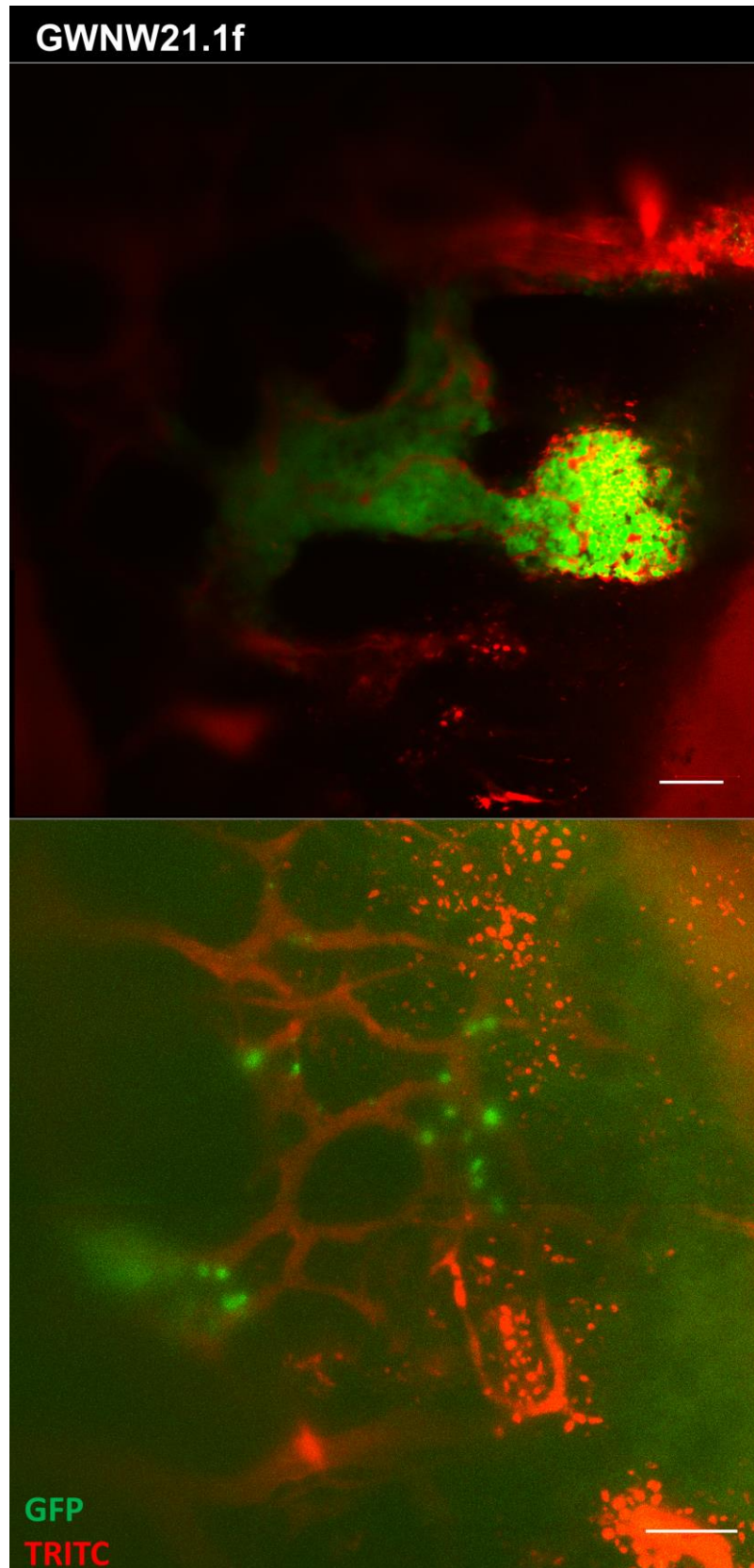


**Figure 4-48 IVM of xenograft mice transplanted with Jurk-GFP revealed large clusters of leukaemic cells.** Mouse was subjected to IVM 38 days post-transplantation to localise human cells within the BM niche. Prior to microscopy, fluorescent dextran was injected to visualise vasculature. The images display maximum projection tile scans comprising a thickness of 85.5 $\mu$ m (top) and 63 $\mu$ m (bottom). Scale bar: 100 $\mu$ m.

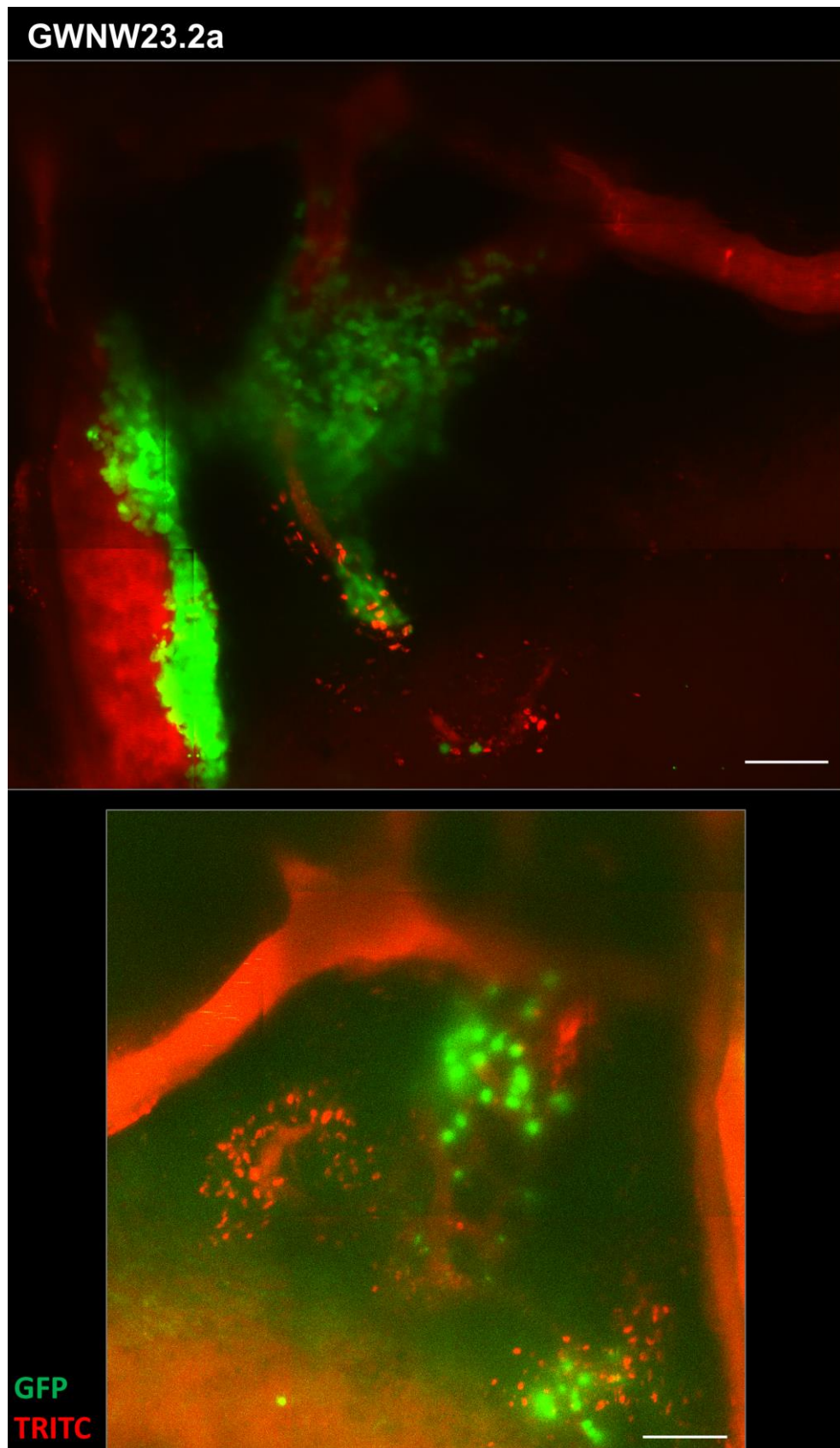


**Figure 4-49 IVM of xenograft mice transplanted with Jurk-GFP mice.** The IVM of a xenograft mouse, which had been transplanted 37 days earlier with Jurk-GFP cells, revealed to form large clusters of leukaemic cells (top) within the BM niche as well as localising around vasculature. Prior to microscopy, fluorescent dextran was injected to visualise vasculature. The images display maximum projection tile scans comprising a thickness of 81.70 $\mu$ m (top) and 62.38 $\mu$ m (bottom). Scale bar: 100 $\mu$ m.

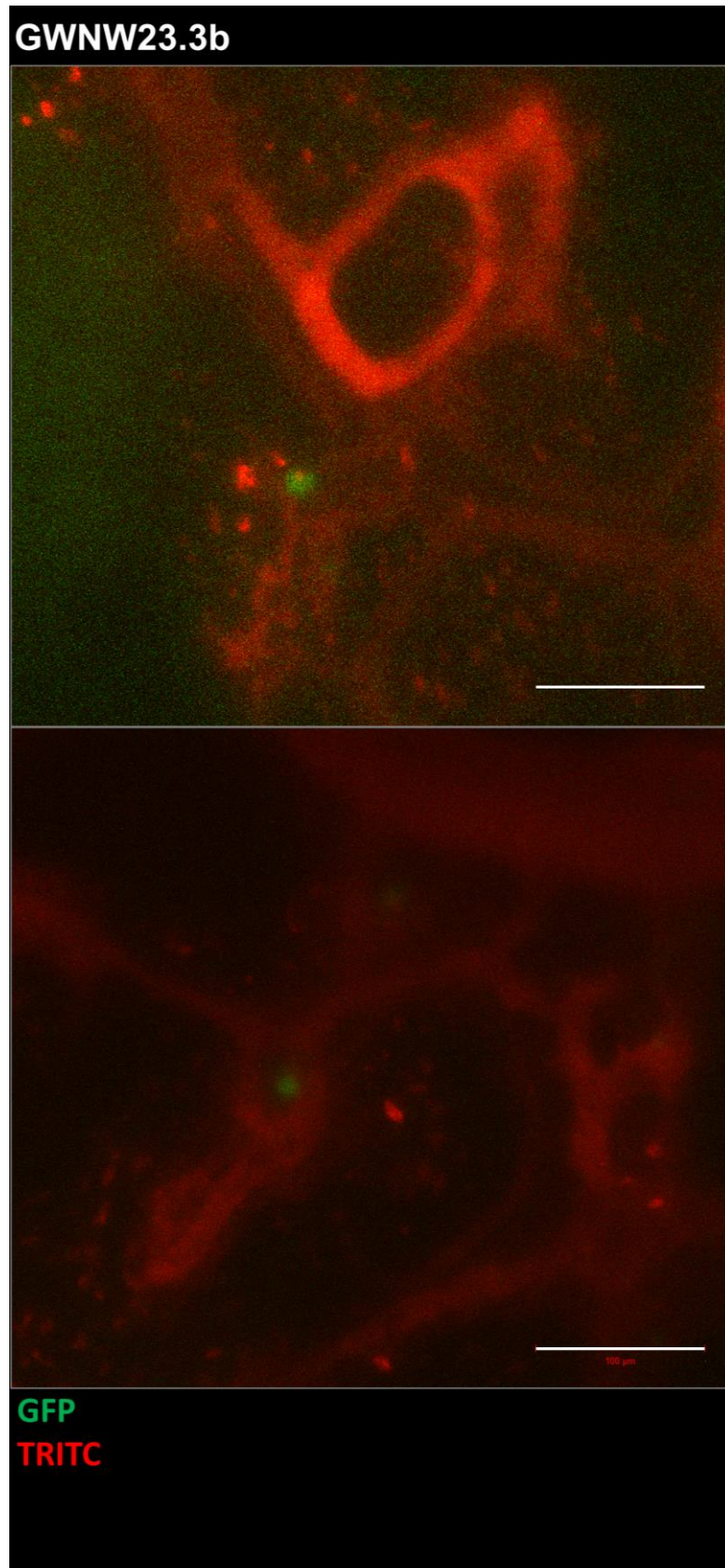


**Figure 4-50** IVM of xenograft mouse transplanted with JurI-GFP cells reveals minimal localisation within the calvarium. The mouse underwent IVM 37 days post-transplantation to localise human cells within the BM niche. Before microscopy, fluorescent dextran was injected to visualise vasculature. The images display maximum projection tile scans comprising a thickness of 60.89µm (top) and 39.40µm (bottom). Scale bar: 100µm.

## 4.10 Autophagy-deficient Jurl cells exhibited higher engraftment potential to control cells and increased localisation to the spleen

The objective of this experiment was to localise human leukaemic cells in the BM niche before mice developed extensive extramedullary tumours, capturing leukaemic cells in the BM before they occupy the entire medullary space. Additionally, we hypothesised that leukaemic cells require autophagy to induce extramedullary tumour formation as well as affecting BM location and engraftment.

Initially, we generated KO cell lines of Jurl-GFP cells and validated the KO via western blotting (Figure 4-51). Subsequently, a cohort of 10 mice, with five mice in each transplantation group, received an IV injection of four million Jurl-GFP control (ctrl) or ATG7 KO cells. After 4 ½ weeks, the mice underwent IVM followed by flow cytometry analysis of the tissues (Figure 4-52).

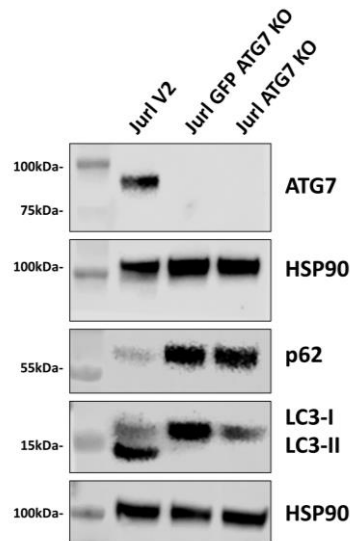


**Figure 4-51 Validation of ATG7 KO in Jurl-GFP cells.** Western blotting was used to validate successful KO of ATG7 in Jurl cells. p62 and LC3 protein levels validate inhibition of autophagic flux. HSP90 was used as loading control.

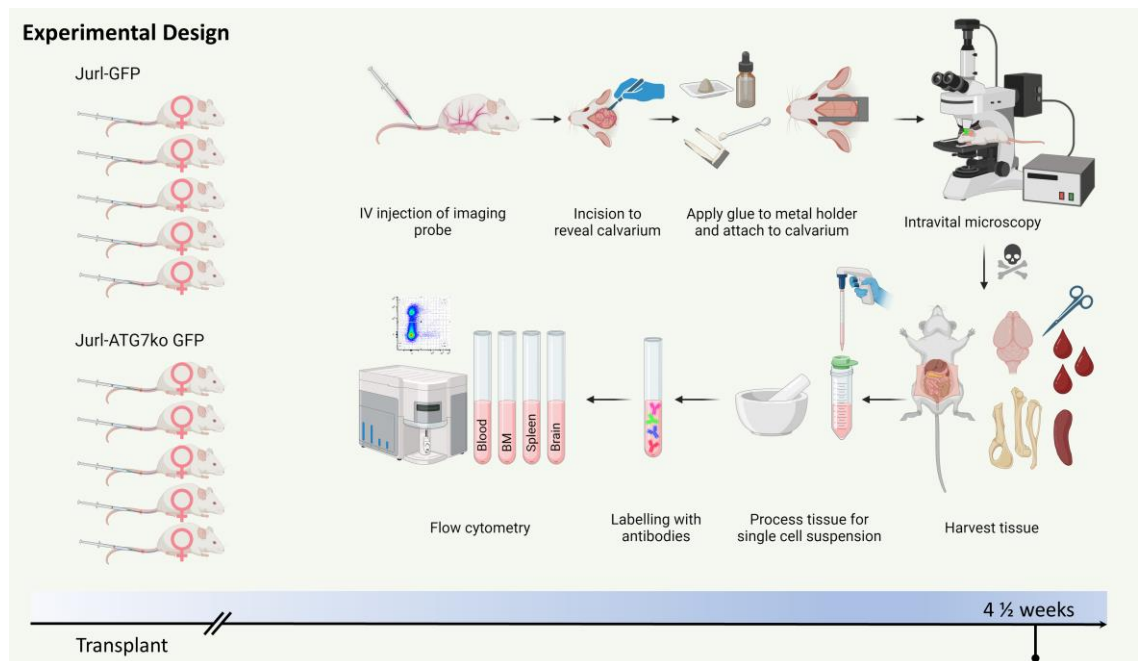


**Figure 4-52 Experimental design aimed to investigate the impact of autophagy deficiency on BM engraftment of Jurl-GFP.** Five mice per group were transplanted with either Jurl-GFP control (v2) or Jurl-GFP ATG7 KO cells. IVM was performed 4 ½ weeks post-transplantation. Prior to surgery to attach a metal holder to the skull bone, fluorescent dextran was injected via IV. The anesthetised mouse was then secured on the microscope stage and confocal microscopy was conducted. Tissue analysis of BM, spleen, blood, and tumours were collected and analysed by flow cytometry for hCD45<sup>+</sup> and mCD45<sup>+</sup> cells. Created with BioRender.com.

IVM microscopy revealed minimal localisation of GFP<sup>+</sup> cells within the BM niche in the calvarium in both transplant groups. Representative images from three mice per groups showed sparsely scattered GFP<sup>+</sup> cells (**Figure 4-58**). Analysis of the BM obtained from the leg bones revealed engraftment in every mouse, albeit with varying percentages (**Figure 4-53a**, **Figure 4-54a**). While total BM cell count was similar in both groups, BM engraftment in the ATG7 KO transplant group increased significantly by 12-fold compared to the control cells (**Figure 4-56**). Moreover, splenomegaly was detected in the ATG7 KO group, but not in the control mice (**Figure 4-55**). Correspondingly, the percentage of hCD45<sup>+</sup> cells detected in the spleen was 6.3-fold higher in the ATG7 KO compared to the control group (**Figure 4-55f**). With the exception of one mouse, no human cells were detected within the brain (**Figure 4-53e**, **Figure 4-54e**).

These mice were taken before reaching their endpoint, which was previously marked by detection of abdominal tumours during examination. During necropsy, some mice exhibited small onset of tumour formation, identifiable due to unusual tissue growth (**Figure 4-57a**, arrows). These smaller tumours allowed the identification of potential organs as the fallopian tubes and ovaries, which

were subsequently harvested from all mice (except one) to analyse for hCD45<sup>+</sup> cells despite lack of externally detectable tumours. This analysis revealed a high percentage of human cells residing within the female reproductive organs (**Figure 4-53d**, **Figure 4-54d**). For instance, recipient mouse with the ID GWNW26.1e, the onset of small tumours, as indicated in **Figure 4-57a** (arrows), contained 34% hCD45<sup>+</sup> cells. Conversely, in the image below, recipient mouse GWNW26.1f did not exhibit external tumour growth but showed 47% of hCD45<sup>+</sup> cells in flow cytometry analysis. Notably, in the control group such high values were only detected in tumour-bearing mice, while the overall tumour formation displayed a trend to be lower in ATG7 KO group (**Figure 4-57c**).

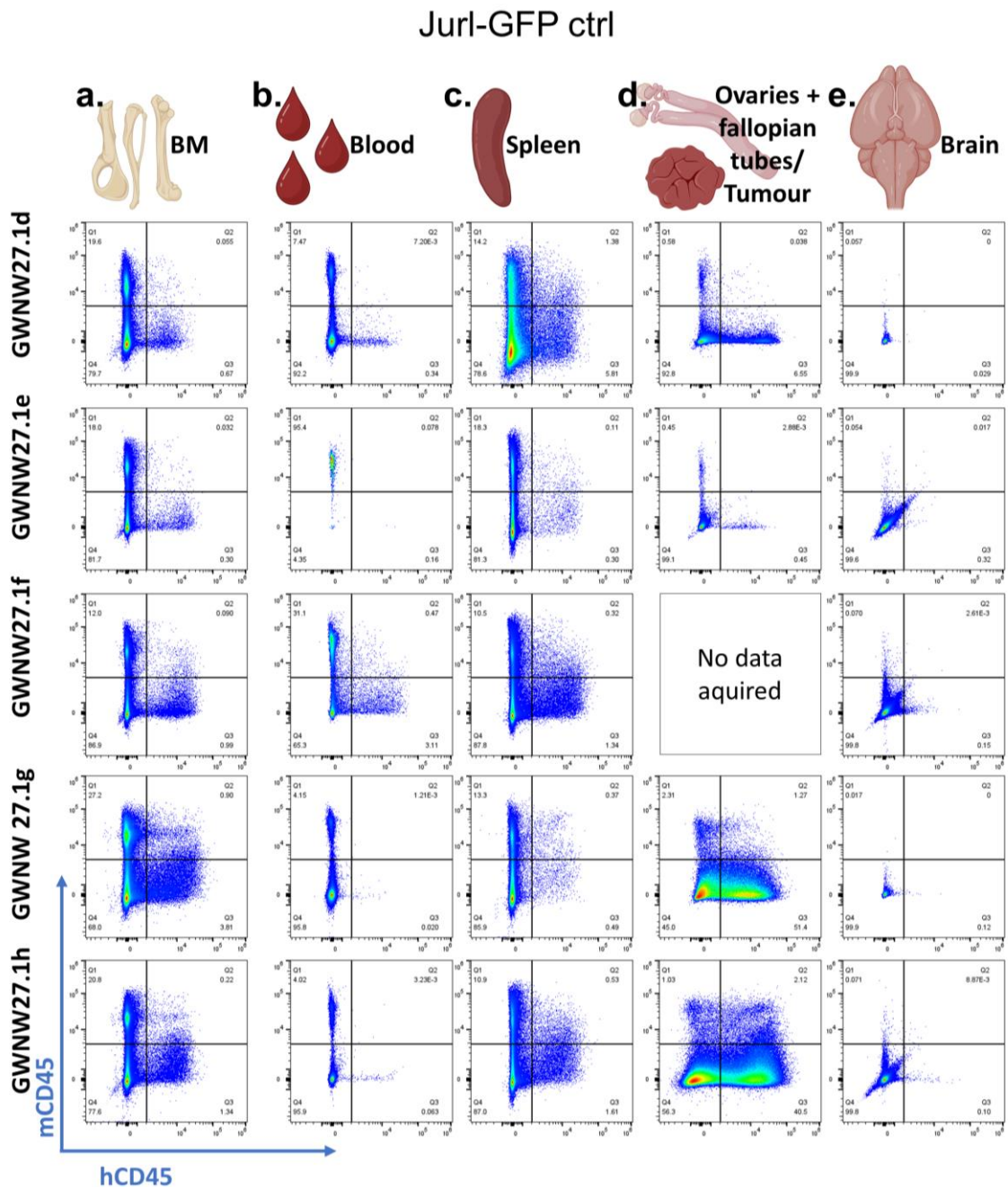


**Figure 4-53 Tissue analysis of Jurl-GFP control cells transplanted to NRGW mice.** NRGW mice were transplanted with four million Jurl-GFP control (ctrl) cells via tail vein and sacrificed sequentially between day 30 and 36 days after transplantation. BM (a), blood (b) and spleen (c) and brain (e) were stained with antibodies targeting mCD45 and hCD45 surface markers. Small tumours located in the female reproductive organ (d) were detected in two mice.

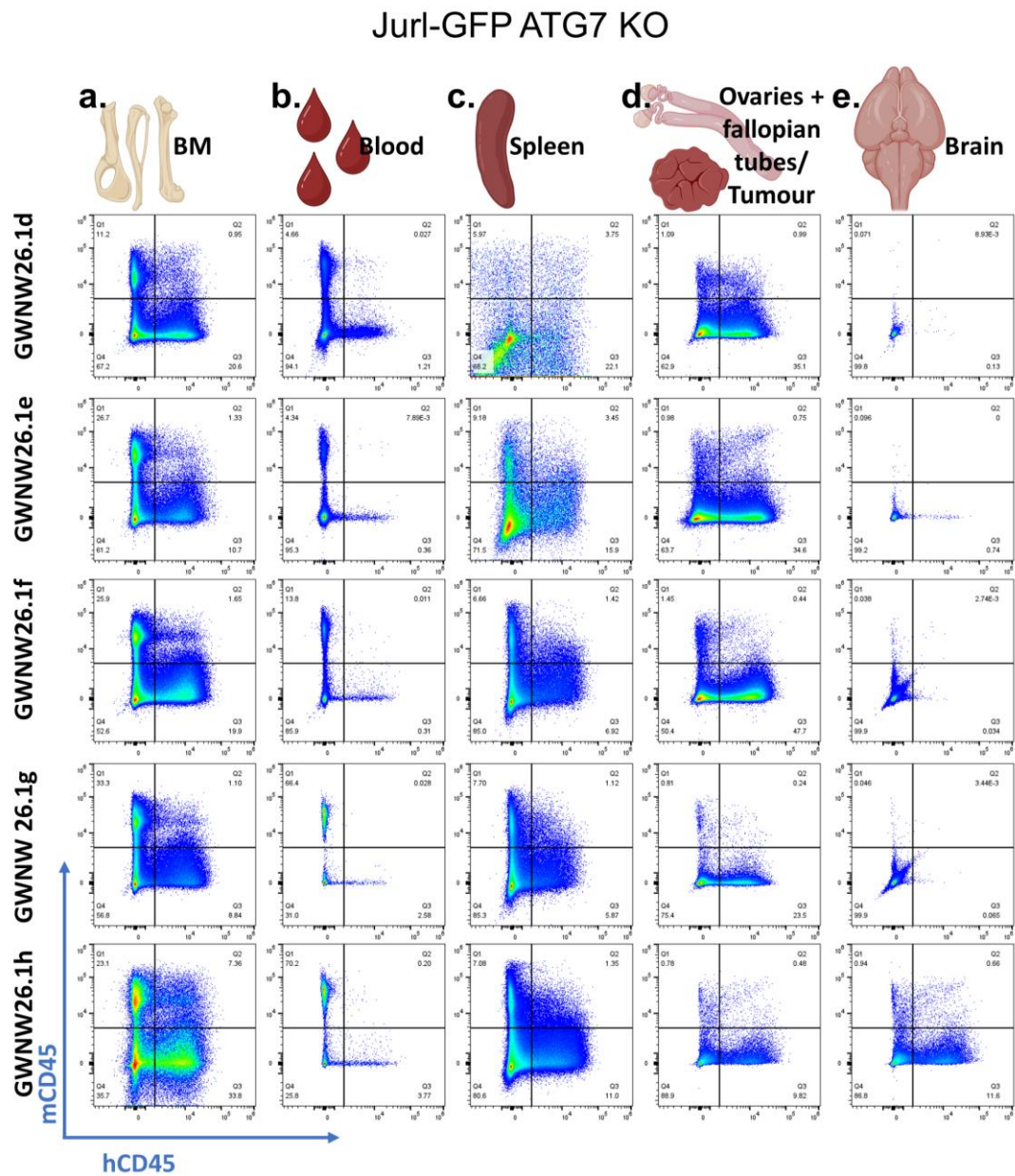


**Figure 4-54 Tissue analysis of Jurl-GFP ATG7 KO in NRGW mice.** NRGW mice were transplanted with four million Jurl-GFP ATG7 KO cells via the tail vein and were sequentially sacrificed between day 30 and 36 post-transplantation. Samples from the BM (a), blood (b) and spleen (c), and brain (e) were stained with antibodies targeting mCD45 and hCD45 surface markers. Small tumours located in the female reproductive organ (d) were detected in two mice.

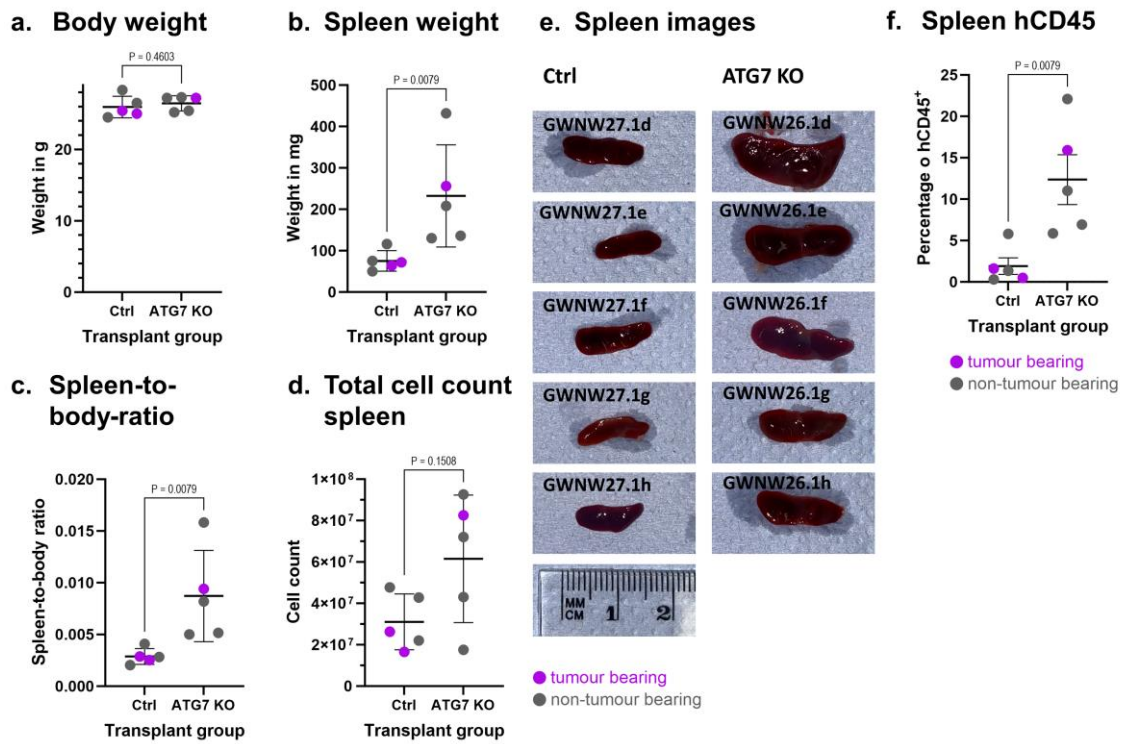


**Figure 4-55 Autophagy-deficient Jurl-GFP recipient mice exhibited splenomegaly.** The body (a) and spleen (b) weights at endpoint were used to calculate the spleen-to-body-ratio (c). Total cell counts of the spleen (d) and images of spleens from each mouse (e) confirmed increased spleen size in the autophagy-deficient group. Graphs are presented as mean  $\pm$  S.D. with  $n=5$ . Non-parametric Mann-Whitney test was used for statistical analysis.

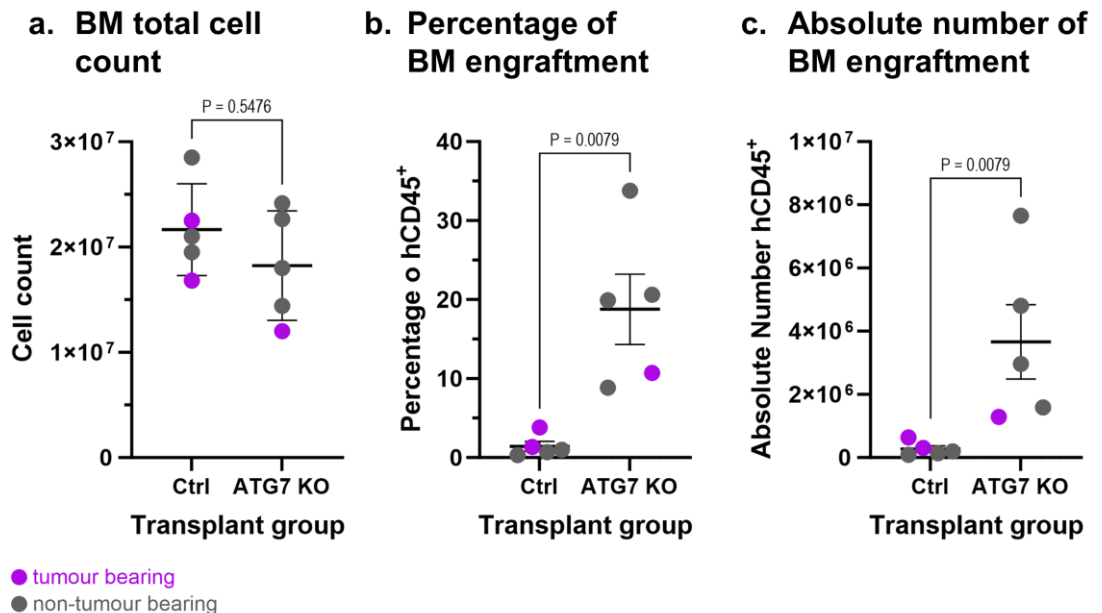


**Figure 4-56 Jurl-GFP ATG7 KO cells exhibited higher engraftment potential at 4 ½ weeks post-transplantation.** Graphs display total BM cell counts (a) and BM engraftment in percentage of total cells (b) as well the absolute number of hCD45 in the BM (c). Graphs are presented as mean  $\pm$  S.D. with  $n=5$ . Non-parametric Mann-Whitney test was used for statistical analysis.

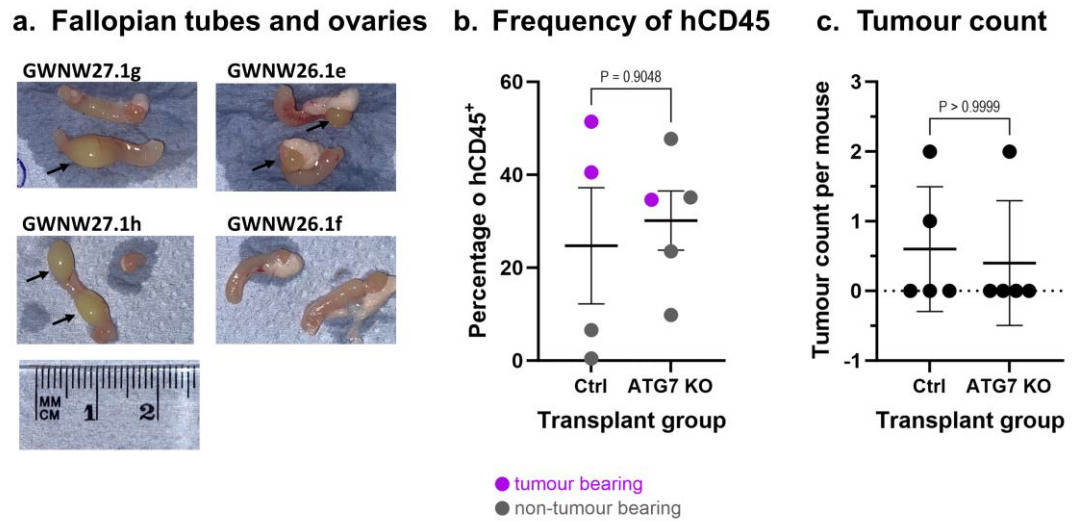


**Figure 4-57 Jurl cells detected in the female reproductive organs.** Fallopian tubes and ovaries (a) of some mice showed formation of small tumours (arrow). Fallopian tubes and ovaries, regardless of presence of tumours, were analysed for presence of hCD45<sup>+</sup> cells and are presented as percentage (b). Tumour count per mouse is displayed in (c). Graphs are presented as mean +/- S.D. with n=5. Non-parametric Mann-Whitney test was used for statistical analysis.

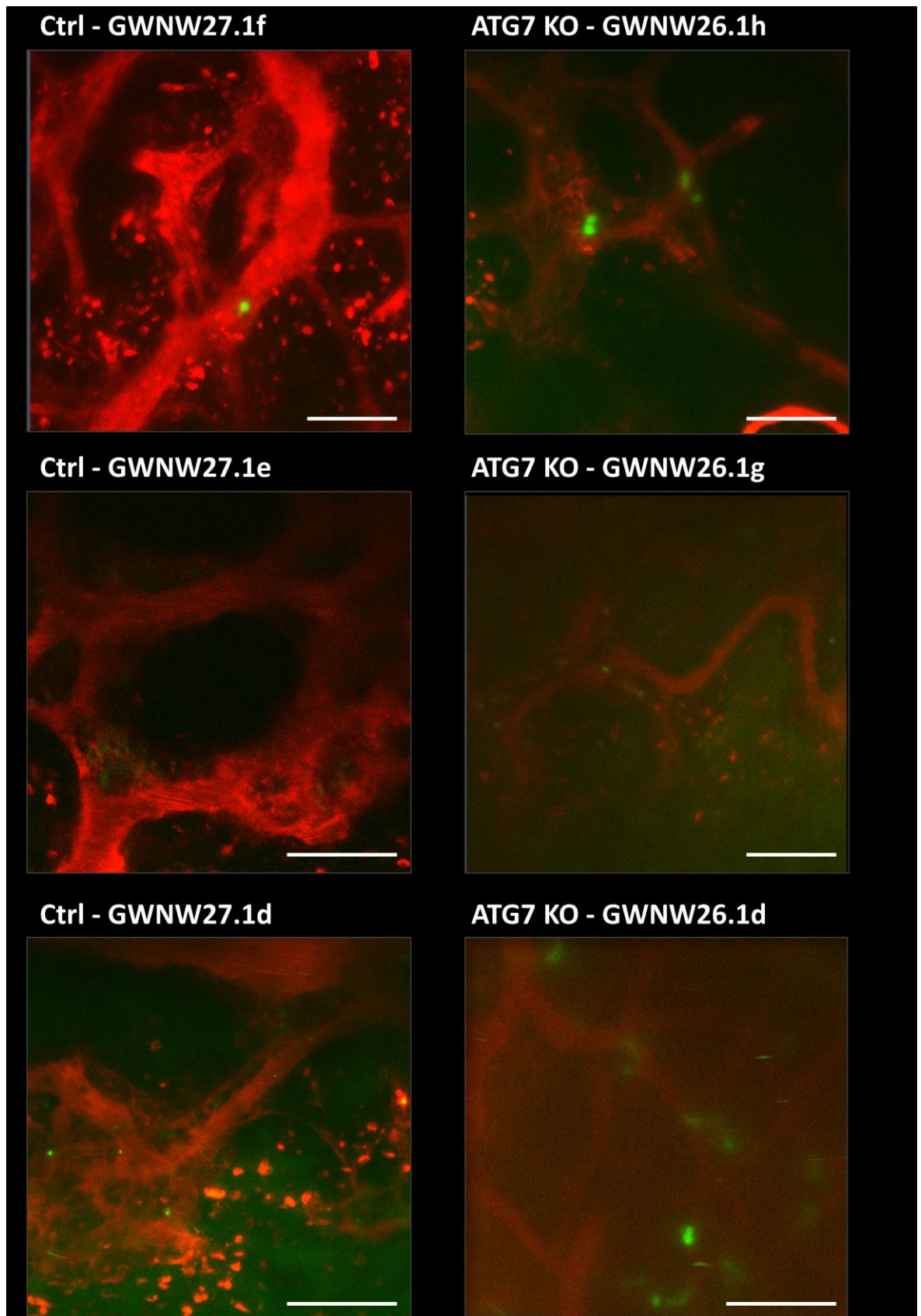


**Figure 4-58 Sparse localisation of Jurl-GFP cells in proximity to vasculature.** Representative IVM images were acquired of recipient mice transplanted with Jurl control (ctrl, left panel) or Jurl-ATG7 KO (right panel) 30 to 36 days post-transplantation. Vasculature is visualised by IV injection of fluorescent dextran (red). Scale bar: 100 $\mu$ m.

## 4.11 Discussion

Our project aimed to establish a xenograft mouse model to investigate the *in vivo* localisation and interactions of human leukaemic cells within the BM microenvironment to deepen our understanding of how the niche can influence cell localisation and contribute to TKI resistance. Due to greater genetic modifiability and availability of cell lines compared to primary cells, we initially assessed two Ph<sup>+</sup> human cell lines, K562 and KCL22, for their potential to be located in the BM. While KCL22 has been routinely utilised within our lab for assessing extramedullary tumour formation under various drug treatments, K562 had not been utilised in our previous *in vivo* studies. Our objective was to ascertain their engraftment potential within the BM to facilitate IVM examinations in response to TKI treatment and autophagy inhibition. To visualise human cell lines *in vivo*, we transformed the cells to stably overexpress GFP using lentiviral transduction.

Initially, we conducted a comparative analysis of both cell lines at two time points. After three days, we could not detect cells within the BM (**Figure 4-4**). However, by the 21-day mark, a small population (0.48%-2.2% of total cells) of K562 was found in the BM, contrasting with the absence of KCL22 cells (**Figure 4-6**). Notably, due to limited availability of recipient mice, only one mouse per time point and cell line was used. Thus, this initial experiment does not conclusively demonstrate that K562 exhibit higher engraftment potential over KCL22, necessitating further investigation with a larger cohort.

Subsequently, cohorts with K562-GFP revealed discrepancies between male and female mice. Female mice consistently developed extramedullary tumours in the abdomen, leading to their endpoint, whereas male mice did not exhibit tumour development within that timeframe (**Figure 4-11**, **Figure 4-16**). Instead, we observed migration of K562-GFP cells to the brain, causing neurological dysfunctions after 23 days or longer in male mice. While other studies have reported metastatic growth of K562 in the brain<sup>396,397</sup>, they did not specify variation upon different sex.

Moreover, male mice generally displayed a lack of human cell engraftment in the BM, blood or spleen (**Figure 4-11**, **Figure 4-17**, **Figure 4-18**, **Figure 4-19**).

Intriguingly, BM engraftment detected via flow cytometry from leg bones did not reflect cells residing in the calvarial BM space. **Figure 4-13** shows representative images of K562-GFP cells residing in the BM, while no cells were detected by flow cytometry (**Figure 4-11**). Contrary, in another experiment we could not detect human cells within the BM obtained from the leg bones (**Figure 4-22**) nor within the calvarium (**Figure 4-23**, **Figure 4-24**, **Figure 4-25**, **Figure 4-26**).

Female mice generally exhibited a small percentage of BM engraftment, albeit less than 1% of total BM cells when analysing BM obtained from the leg bones (**Figure 4-17**). Similar to male mice, no human cells were found in the spleen or the blood (**Figure 4-18**, **Figure 4-19**). However, confocal microscopy revealed poor detection of human cells within the calvarium (**Figure 4-20**). Experiments exploring hypoxia exposure to potentially select cells with higher BM homing potential indicated no significant difference in overall BM engraftment between cells exposed to 1% hypoxia for 72 hours before transplant compared to control cells cultured in normoxia (**Figure 4-17**). However, hypoxia exposure appeared to slightly affect extramedullary tumour formation, albeit non-significantly. Hypoxia influences many cellular responses and can suppress cell cycling<sup>398</sup>. Especially HSCs have been shown to exhibit high levels of HIF1 $\alpha$  that is important to maintain quiescence<sup>122</sup>. In CML, hypoxia has been shown to mediate TKI resistance<sup>399</sup>. However, the culture of K562 cells in hypoxia reduces cell proliferation (**Figure 4-14**) and might influence extramedullary tumour formation long-term.

In our final experiment with K562, we compared BM engraftment and tumour formation between control K562-GFP cells and those lacking ATG7, a vital player in CML cell survival<sup>367</sup>. Tumour formation was significantly reduced in the ATG7 KO transplant group (**Figure 4-30**), similar to our prior work with KCL22 cells and ULK1 inhibition<sup>367</sup>. However, BM engraftment between both groups did not differ (**Figure 4-33**). Despite one of each transplant group showing 1.5% of human cells residing in the BM, no GFP<sup>+</sup> cells were detected in the calvarium despite extensive imaging (**Figure 4-29**).

The BM spaces in the calvarium are relatively small compared to the BM in the leg bones. Therefore, the engraftment of such small percentages might be a reason for the lack of GFP<sup>+</sup> cells found by microscopy in the calvarium. It was

hypothesised that Jurl-GFP cells would exhibit higher BM engraftment potential than K562 cells due to higher expression of cKit<sup>395</sup>. cKit is involved in the BM homing of HSCs, making Jurl-GFP cells a potentially more relevant model to study engraftment dynamics and localisation patterns within the BM microenvironment. Initial experiments comparing BM engraftment between 20- to 39-days post-transplantation revealed comparable engraftment to K562 at the earlier time point with 0.79% of total cells (**Figure 4-38**). However, similar to K562, no GFP<sup>+</sup> cells were detected in the calvarium (**Figure 4-40**). The percentage increased over time, albeit inconsistently, with 6.33% human cells in the BM after 26 days, and 1.67% after 32 days. The last time point after 39 days revealed the highest percentage with 11.2% in the BM and was the only mouse where GFP<sup>+</sup> could be located in the calvarium using microscopy (**Figure 4-43**, **Figure 4-44**). The located cells were found to be diffused with close contact to the vasculature (**Figure 4-43**) or to reside as a large cluster around larger vessels (**Figure 4-44**). The mice were of the same age and sex, and a larger number of mice per time point would be needed to verify a linear increase in human cells with time.

To assess the reproducibility of BM engraftment of Jurl-GFP cells and determine niche localisation, we transplanted four female mice and observed more consistent BM engraftment in three, with over 20% of total cells, and approximately 10% in one (**Figure 4-46**). Nevertheless, IVM of the calvarium indicated substantial BM infiltration in only two mice (**Figure 4-48**, **Figure 4-49**) while the remaining two mice showed minimal to no GFP<sup>+</sup> cells (**Figure 4-50**). Longitudinal imaging at different time points could elucidate whether Jurl cells engraft to the BM forming a leukaemic niche, overtaking the entire BM over time or exhibit different proliferation dynamics upon BM localisation.

Finally, our investigation into the influence of leukaemic cells utilising autophagy compared to autophagy-deficient cells revealed differing engraftment potential between Jurl and K562 cells. For imaging purposes, the mice were analysed at a slightly earlier time point, after 4 ½ weeks instead of five. The mice were analysed before external detection of tumours, resulting in the discovery of smaller tumours located in the female reproductive organ (**Figure 4-57**), which has been shown by other studies<sup>397</sup>. Mice in the Jurl-GFP ATG7 KO

transplant group exhibited a higher BM engraftment (**Figure 4-56**) and larger spleens than the control group (**Figure 4-55**). Notably, detection of human cells in the spleen ranged between 5-22% in the ATG7 KO group (**Figure 4-54**), compared to 0.3-5% in the control group (**Figure 4-53**).

Notably, the engraftment of Jurl-GFP ATG7 KO cells was significantly increased when analysing BM obtained from the leg bones by 12-fold compared to the control cells (**Figure 4-56**). However, this stark difference was not observed in confocal microscopy of the calvarium, where only a few diffuse GFP<sup>+</sup> cells were found in the BM near the vasculature (**Figure 4-58**).

## Chapter 5 Investigating the role of mitophagy in TKI resistance in CML

### 5.1 Introduction

Autophagy is an intracellular mechanism that plays a pivotal role in ensuring cellular survival, adapting to metabolic stress, and mitigating oxidative damage from impaired mitochondria. Studies have highlighted its crucial role in sustaining functionality of HSCs<sup>46,355-357</sup>. Work from our lab has shown that autophagy is upregulated in LSCs after treatment with TKIs, such as imatinib<sup>363,365</sup>. This work has highlighted the need for clinically effective autophagy inhibitors with high selectivity. LifeArc has directed efforts towards designing drugs to target ULK1, which underwent further potency evaluations in our lab. LifeArc's candidate MRT403 (403) has shown promising results by sensitising LSCs to TKI treatment, consequently promoting LSC differentiation<sup>367</sup>. Current development of these molecules for clinical trials by industry partners may provide potential for a curative approach in CML and other cancers where autophagy provides resistance mechanism. Inhibition of autophagy has been shown to increase ROS levels in CML resulting in oxidative stress-induced differentiation<sup>367</sup>. A study in AML demonstrated that LSCs require mitophagy to maintain proliferation rates and stemness<sup>370</sup>.

The aim of our study was to investigate whether CML cells rely on a high turnover of mitochondria to evade targeted therapy and induce mitophagy upon TKI treatment. Understanding the metabolic reprogramming is crucial in deciphering TKI resistance in LSCs and developing novel treatments aimed at eradicating these cells.

First, we assessed mitochondrial content in CML cells following TKI treatment. Subsequently, we developed CML cell lines enabling the monitoring of mitophagy using the MitoQC reporter gene developed by the Ganley laboratory (refer to **Figure 5-4**)<sup>400</sup>. We applied high-resolution confocal microscopy to visualise mitophagy upon TKI treatment alone and in combination with autophagy inhibition and explored the role of different canonical mitophagy pathways.

Finally, we aimed to develop a high-throughput flow cytometry assay for broad drug screening.

## 5.2 Leukaemic cells displayed reduced mitochondrial mass upon TKI treatment

To assess whether TKI treatment induces mitochondrial degradation, two distinct flow cytometry methods were utilised: a fluorescent cell line overexpressing the outer mitochondrial membrane protein Tom20 fused to GFP and MitoTracker staining. Both methods can be used to assess mitochondrial mass within cells. First, KCL22 Tom20-GFP cells were treated with imatinib at concentrations of 2 $\mu$ M or 600nM for 6 or 24 hours, after which the median fluorescent intensity (MFI) was measured using flow cytometry. Notably, while minimal changes were observed at the 6h-time point, a substantial reduction of nearly 50% in mitochondrial mass was detected at the 24-hour mark (**Figure 5-1**).

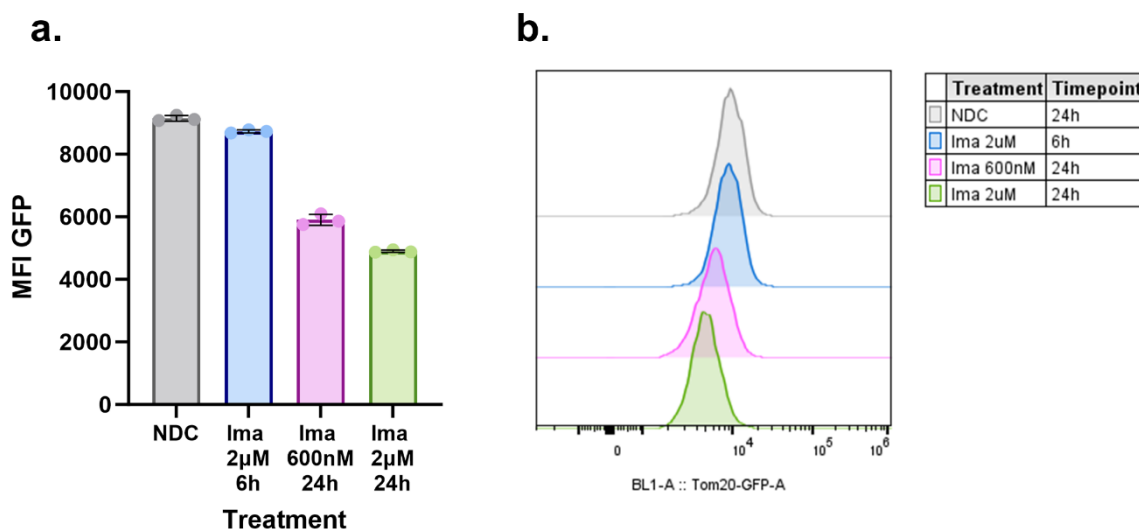


**Figure 5-1 Mitochondrial content reduced in KCL22 Tom20-GFP cells upon TKI treatment.** KCL22 cells overexpressing Tom20-GFP were treated with imatinib for 6 or 24 hours at a concentration of 2 $\mu$ M or 600nM. MFI was measured using flow cytometry (a) and representative histograms are shown in (b). The data shown in this figure corresponds to technical replicates (n=3), where each replicate represents an individual culture well derived from the same parental culture flask and conducted on the same day.

An alternative method was employed to measure mitochondrial content, which is independent of Tom20-GFP overexpression, as this could be affected by drug treatment. K562 cells were treated with 2 $\mu$ M imatinib for 24 hours and then stained with MitoTracker Green, a dye that localises to the mitochondria of live

cells. Similarly, MitoTracker staining revealed a consistent trend of reduced mitochondrial content comparable to that observed in KCL22 cells (**Figure 5-2a&b**).

In both assays, DAPI staining was used to exclude dead cells from the analysis revealing minimal cell death. Additionally, a cell viability assay was conducted to allow detection of early apoptosis following TKI treatment. Nuclear dyes like DAPI or 7-AAD can penetrate cells with a compromised cell membrane and are commonly used to measure late apoptosis. A marker for an early-stage apoptosis is AnnexinV, which exhibits high affinity to phosphatidylserine (PS), typically located on the cytoplasmic side of healthy cells but translocated to the extracellular side during apoptosis. Following 24 hours treatment with 2 $\mu$ M imatinib, K562 cells were stained with 7-AAD and AnnexinV, displaying a negligible increase in apoptosis (**Figure 5-2c&d**).

Furthermore, we assessed endogenous mitochondria protein levels using Western blotting utilising Tom20 as an indicator of mitochondrial mass. We used two control treatments known to induce mitophagy. CCCP, an uncoupling agent disrupting mitochondrial membrane potential and inducing Pink1/Parkin-mediated mitophagy<sup>326</sup>. Deferiprone (DFP) mimics a hypoxic state as an iron chelator leading to HIF1 $\alpha$  stabilisation<sup>400</sup>. K562 and KCL22 exhibited reduced levels upon TKI treatment in both cell lines, but more pronounced in KCL22 with a reduction by 70% compared to the no drug control (NDC) but only 20% in K562. An autophagy inhibitor blocking ULK1 activity, MRT403 (403), could partly restore Tom20 levels to normal levels although this seemed to be more variable across both cell lines (**Figure 5-3**).

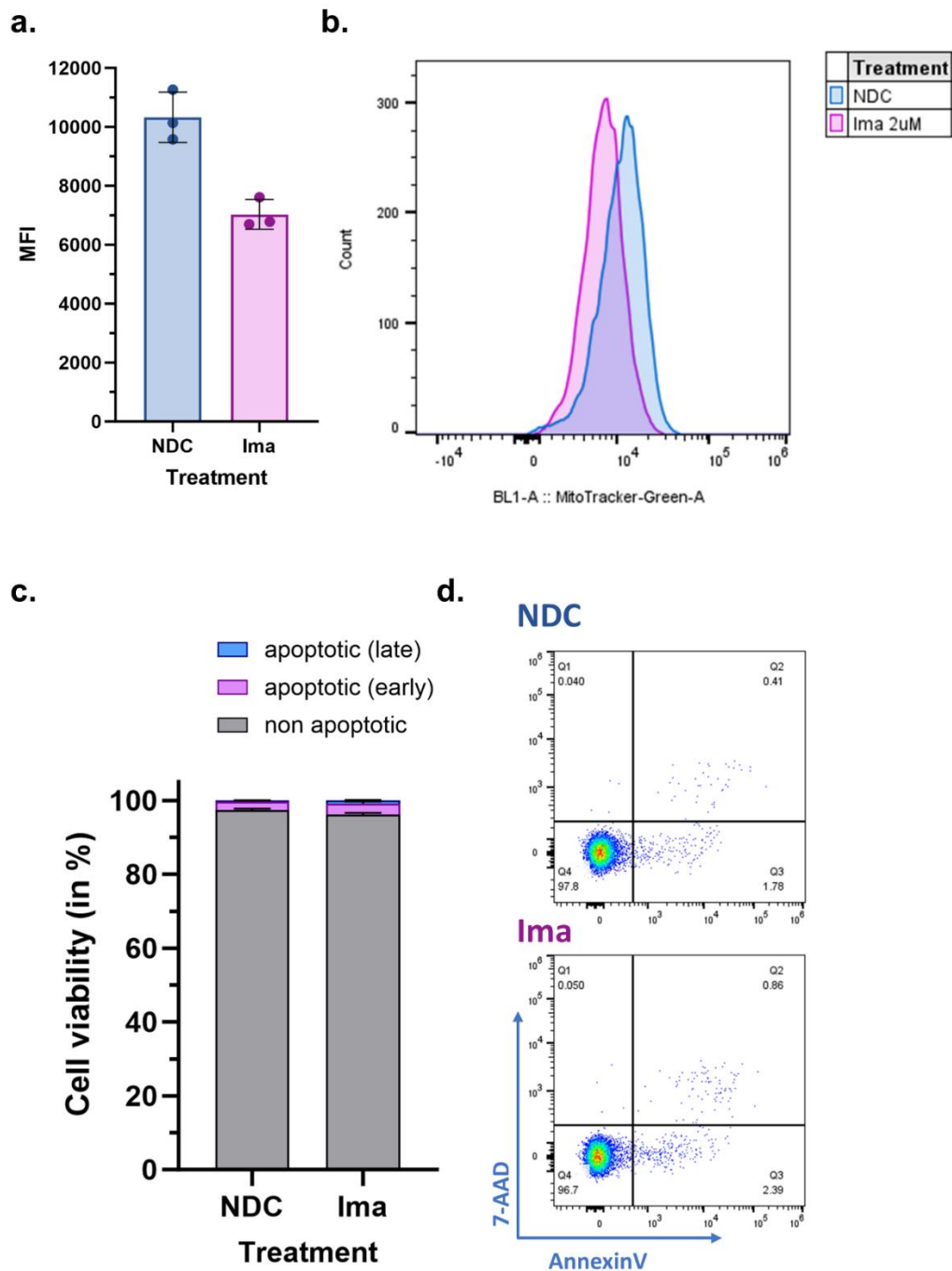


**Figure 5-2 Decrease of mitochondrial mass in TKI-resistant cells measured using MitoTracker.** K562 cells were treated with 2 $\mu$ M imatinib for 24 hours and MFI was measured using flow cytometry (a). Representative histograms displaying MitoTracker fluorescence is shown in (b). Apoptosis was evaluated using 7-AAD and AnnexinV antibody staining via flow cytometry. A bar plot (c) illustrates the percentage of non-apoptotic cells (AnnexinV<sup>-</sup>7AAD<sup>-</sup>), early apoptotic (AnnexinV<sup>+</sup>7AAD<sup>-</sup>) and late apoptotic (AnnexinV<sup>+</sup>7AAD<sup>+</sup>) cells. A representative dot blot is shown to depict the distribution of these cell populations (d). The data illustrated in this figure represent technical replicates (n=3), where each replicate signifies an individual culture well derived from the same parental culture flask and conducted on the same day.

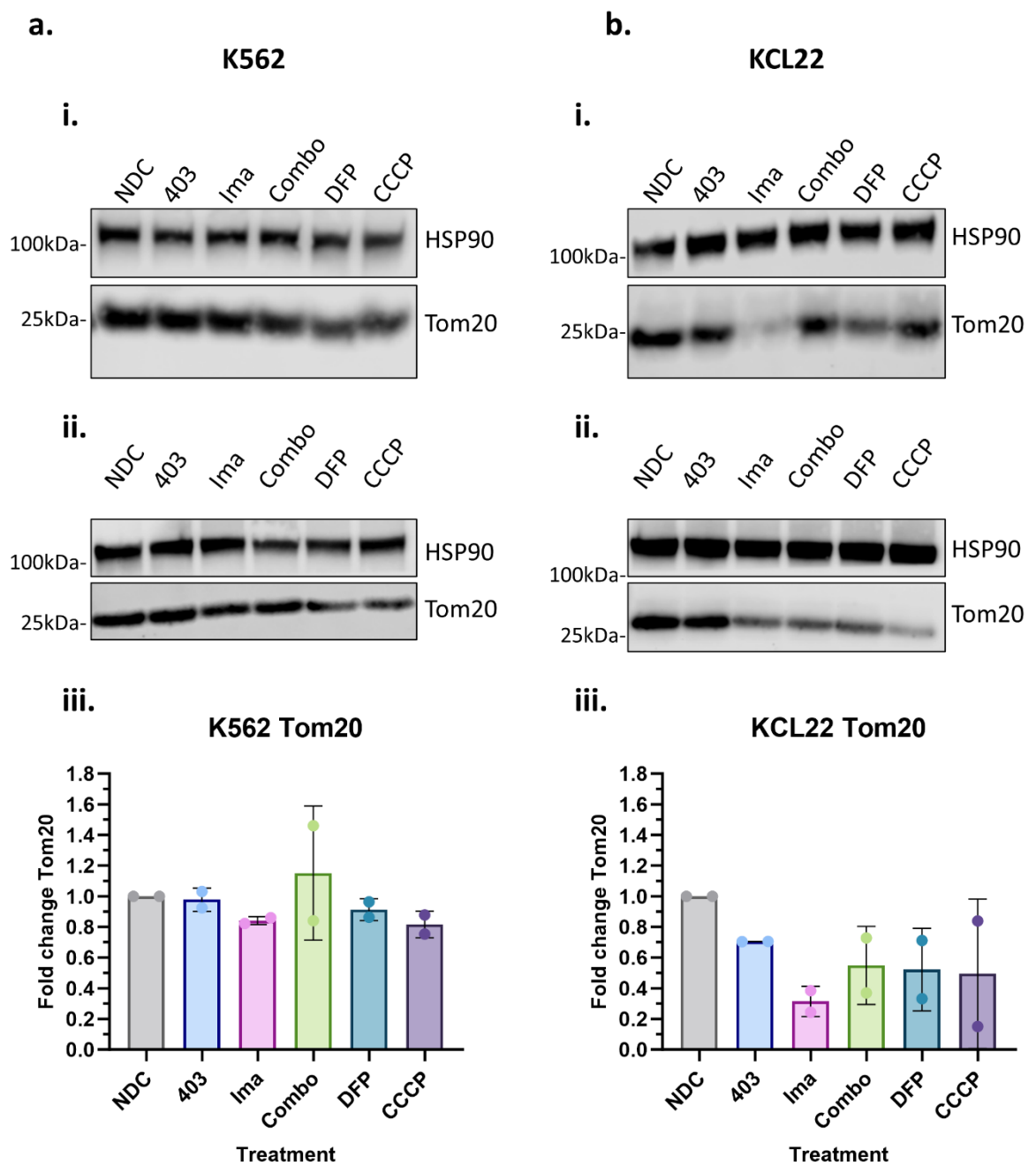


**Figure 5-3 Reduction in Tom20 protein levels following imatinib treatment.** Western blot images depicting Tom20 levels in K562 (a) and KCL22 (b) MitoQC cells treated with 3 $\mu$ M MRT403 (403), 2 $\mu$ M imatinib (Ima) and the combination of both for 24 hours. DFP (1mM for 24h) and CCCP (20 $\mu$ M for 4h) were used as controls to induce mitophagy. The results show Western blots of n=2 independent experiments in (i and ii). Protein levels first normalised to the loading control HSP90 and subsequently calculated as fold changes compared to the no drug control (NDC) (iii).

### 5.3 Generation of MitoQC stable CML cell lines

Next, our aim was to investigate the hypothesis that TKI treatment reduces mitochondrial content through increased mitophagy rather than a reduction in mitochondria biogenesis. For this purpose, we generated CML cell lines stably expressing the MitoQC reporter gene. MitoQC<sup>400</sup> stands for Mitochondria Quality Control and refers to a method designed to distinguish between healthy mitochondria and mitochondria that are in the process of being degraded (Figure 5-4). Therefore, cells were transduced to overexpress the tandem-dye mCherry-GFP linked to the outer mitochondrial membrane localisation signal derived from the protein Fis1 (residues 101-152). Notably, mCherry is a stable fluorophore, whereas GFP is sensitive to changing pH levels and non-fluorescent in an acidic environment like the lysosome. Consequently, healthy mitochondria exhibit red and green fluorescence, while during mitophagy and subsequent delivery to the lysosome, GFP fluorescence is quenched leading to formation of red 'puncta'. Following retroviral transduction, cells were selected with the antibiotic agent hygromycin B for seven days and purified by FACS to remove any non-transduced cells (Figure 5-5).

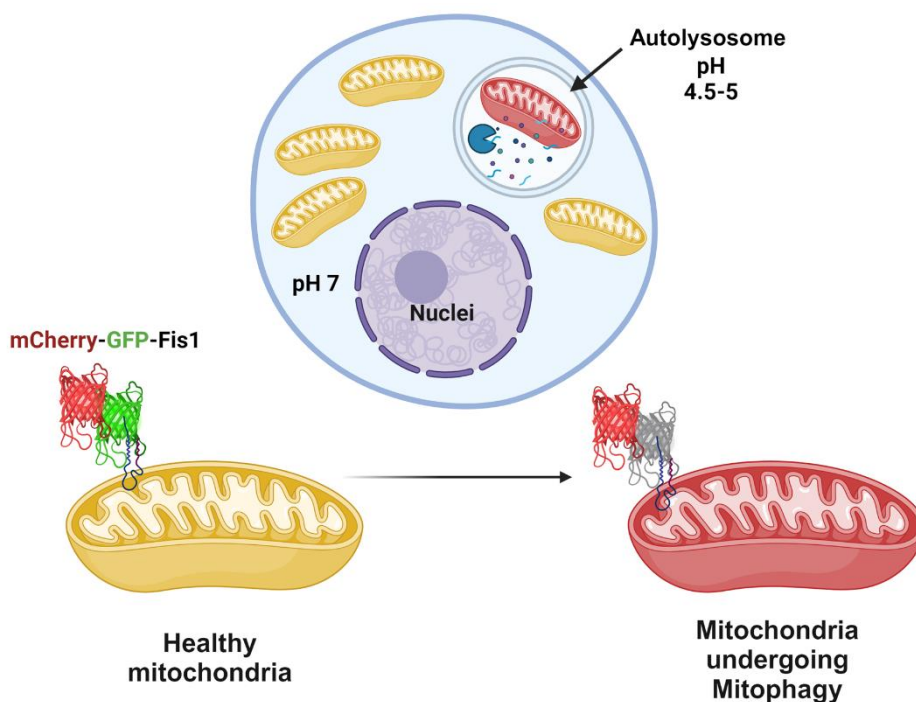


**Figure 5-4 The concept of MitoQC for measuring mitophagy.** Lysosomal turnover of mitochondria is measured by exploiting the pH sensitivity of GFP in the tandem-dye mCherry-GFP, that is localised to the outer mitochondrial membrane. Healthy mitochondria exhibit red and green fluorescence, while mitochondria enclosed by the lysosome lose GFP fluorescence in the low pH environment of the lysosome. Created with BioRender.com.

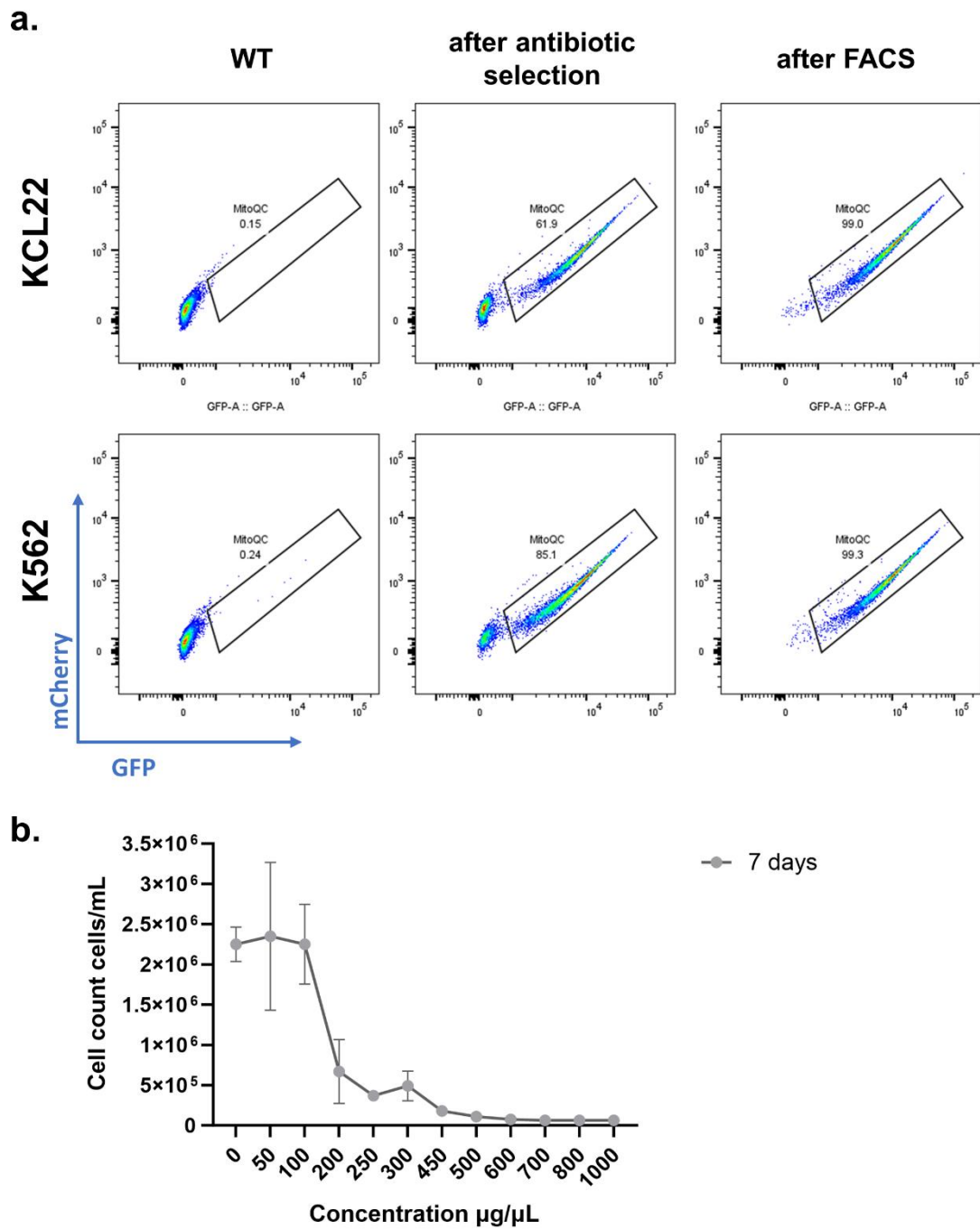


**Figure 5-5 Generation of MitoQC CML cell lines via retroviral transduction.** Flow cytometry plots (a) displaying the transduction of KCL22 and K562 with MitoQC (mCherry-GFP-Fis1<sup>101-152</sup>) after antibiotic selection. Following selection, cells were further purified using FACS. Ideal concentration for antibiotic selection with hygromycin B was determined assessing cell numbers after seven days to 250 $\mu\text{g}/\mu\text{L}$  (b).

## 5.4 TKI treatment led to mitophagy induction in CML cells

We applied super-resolution live-cell microscopy to visualise the mitochondria and allow quantification of ‘puncta’ formation in response to treatment. Multiple studies demonstrated the specificity of the MitoQC protein being targeted only to the mitochondria, through co-staining with different mitochondrial proteins, such as ATP synthase and Tom20<sup>400,401</sup>. Furthermore, co-localisation of mCherry-‘puncta’ with the lysosomal marker LAMP1 confirmed the functionality of the tandem-dye<sup>401</sup>.

Additionally, we demonstrated the co-localisation of red ‘puncta’ with lysosomal vesicles by utilising LysoTracker staining in CML cell lines upon TKI treatment (**Figure 5-6**). Therefore, K562 MitoQC cells were treated with imatinib for 24 hours, while one condition was left untreated. The cells were plated on glass-bottom chamber slides coated with poly-D-lysine to facilitate cell adherence to the surface. Approximately one hour prior to imaging, LysoTracker was added to the cell medium. Subsequently, high-resolution confocal images were acquired using a 63x objective at multiple fields with a microscope optimised for live-cell imaging. The untreated cells exhibited the presence of lysosomal vesicles, but rarely show any mCherry-‘puncta’. However, in the cells treated with imatinib, many cells displayed mCherry-‘puncta’ that are co-localised with the lysosomal marker.

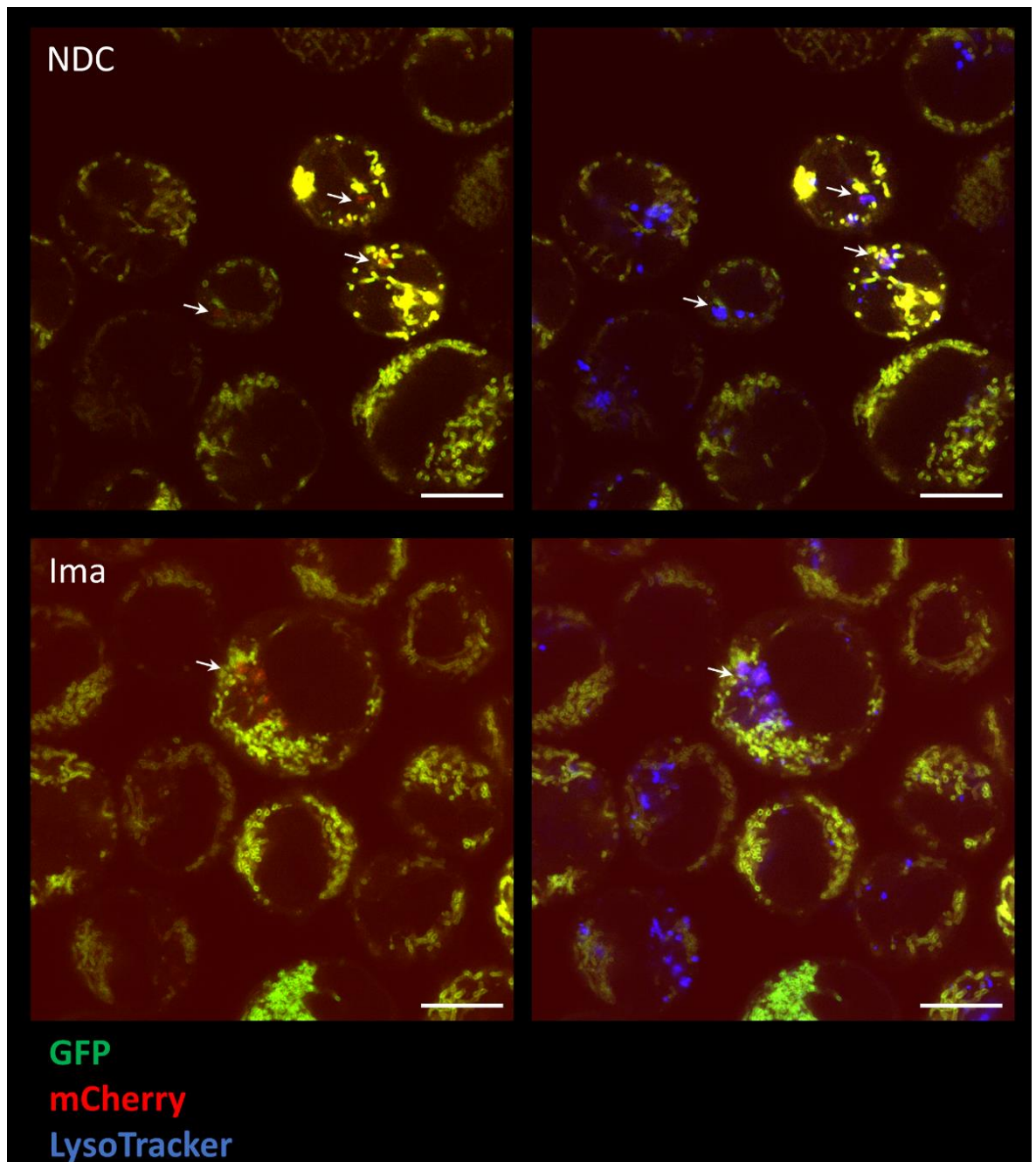


**Figure 5-6** Lysosomal staining co-localised with mCherry-'puncta' from MitoQC probe. K562 MitoQC cells were treated with 600nM imatinib (Ima) for 24 hours. No drug control (NDC) and Ima samples were imaged using confocal high-resolution microscopy employing the Zeiss LSM 880 with a 63x objective in Airyscan mode. Representative images depict the fluorescence of GFP (green) and mCherry (red), along with LysoTracker (blue). Arrows highlight red 'puncta' co-localised with the LysoTracker. Scale bar: 10 $\mu$ m.

### 5.4.1 TKI treatment triggered accumulation of mitolysosomes

Next, we quantified the number of mCherry-‘puncta’ per cell in KCL22 and K562 MitoQC cells treated with imatinib (2 $\mu$ M) for 24 hours compared to the untreated control cells (Figure 5-8, Figure 5-10). Across both cell lines, the baseline mean of mitolysosomes per cells ranged between 0.5 to 0.6 (Figure 5-7a, Figure 5-9a). However, following treatment with imatinib, a notable increase in mitolysosomes was observed. Specifically, the mean count rose to 2.5 or 2.7 in K562 and KCL22 cells, respectively, indicating an elevated induction of mitophagy, although this was only statistically significant in K562 cells.

Furthermore, the percentage of cells exhibiting one or more mitolysosomes was compared with cells showing no mitolysosomes. This analysis revealed an increase in cells actively undergoing mitophagy. Initially, only 15-20% in both cell lines displayed some degree of basal mitophagy. However, upon imatinib treatment, this percentage substantially increased to 60% or 70% (Figure 5-7b, Figure 5-9b).

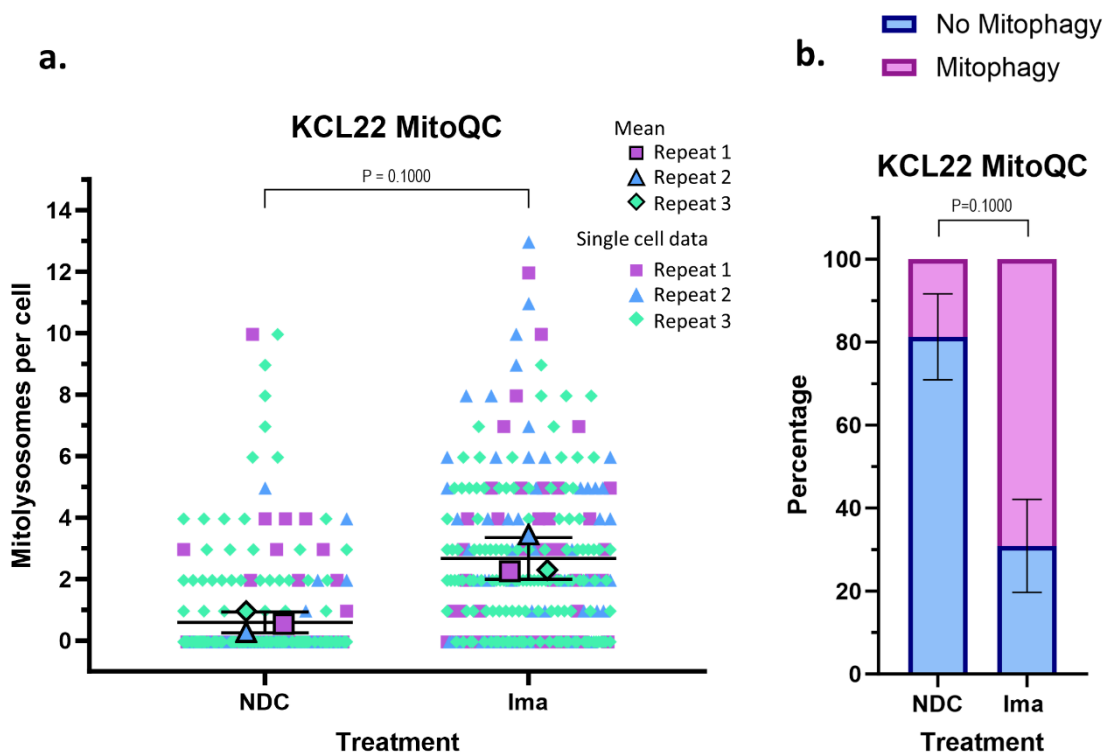


**Figure 5-7 Slightly increased mitophagy induction upon TKI treatment in CML cells.** KCL22 MitoQC cells were treated with 2 $\mu$ M imatinib (Ima) for 24 hours. Live-cell imaging was performed and mitolysosomes per cell were assessed (a). The data was plotted as mean  $\pm$  S.D. of n=3 independent experiments with single-cell data plotted in the background. P-values were calculated from the means applying the Mann-Whitney test. Bar charts illustrates ratio of cells undergoing mitophagy (detection of one or more mitolysosomes) versus cells not showing any mitolysosomes (b).

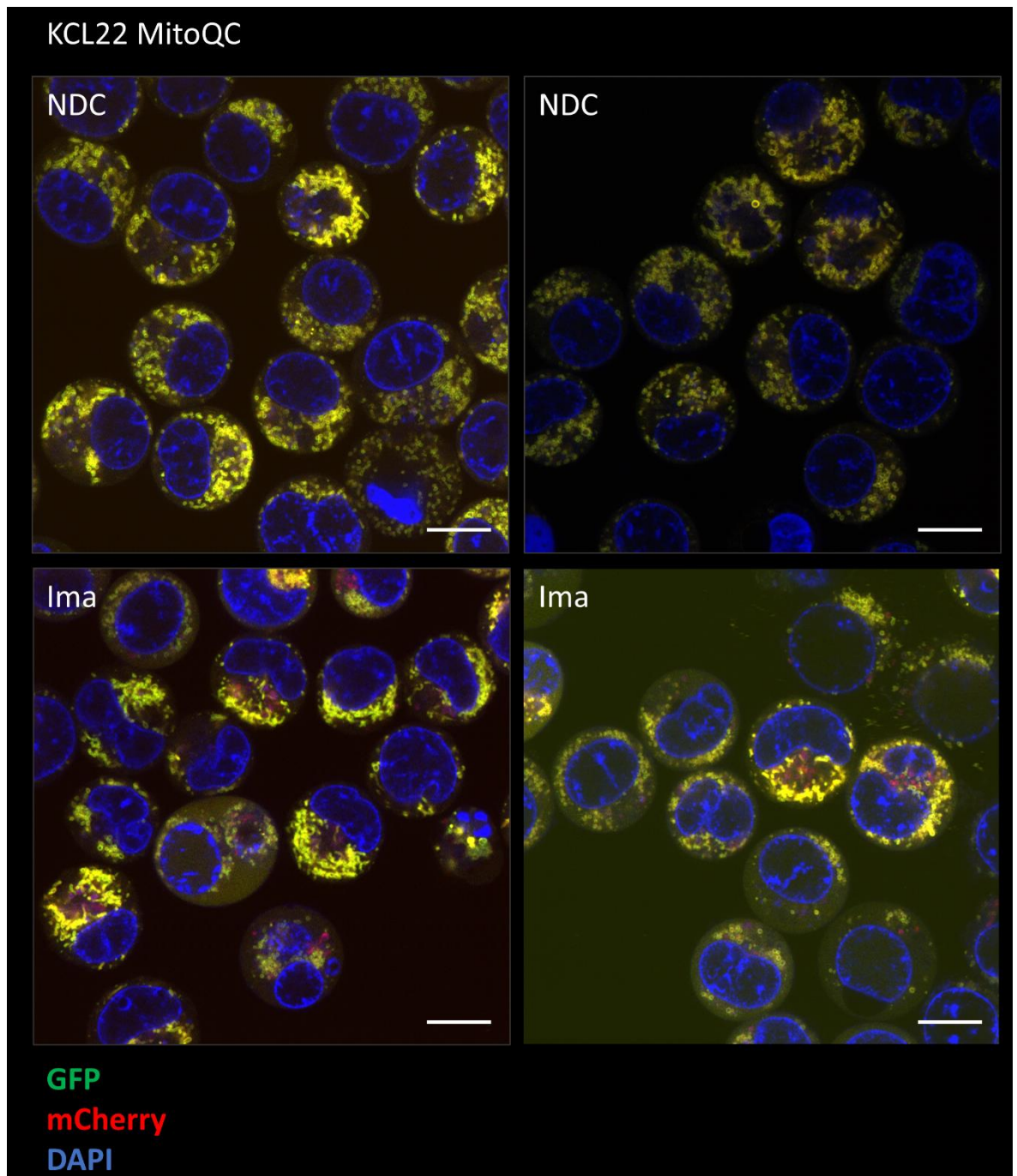


**Figure 5-8 mCherry-'puncta' formation in KCL22 upon TKI treatment.** Representative live-cell images of KCL22 MitoQC cells treated with 2 $\mu$ M imatinib (Ima) for 24 hours. Images were acquired with the LSM 880 using the Airyscan detector. GFP is shown in green and mCherry in red resulting in healthy mitochondria being visualised in yellow. The nucleus is shown in blue. Scale bar: 10 $\mu$ m.

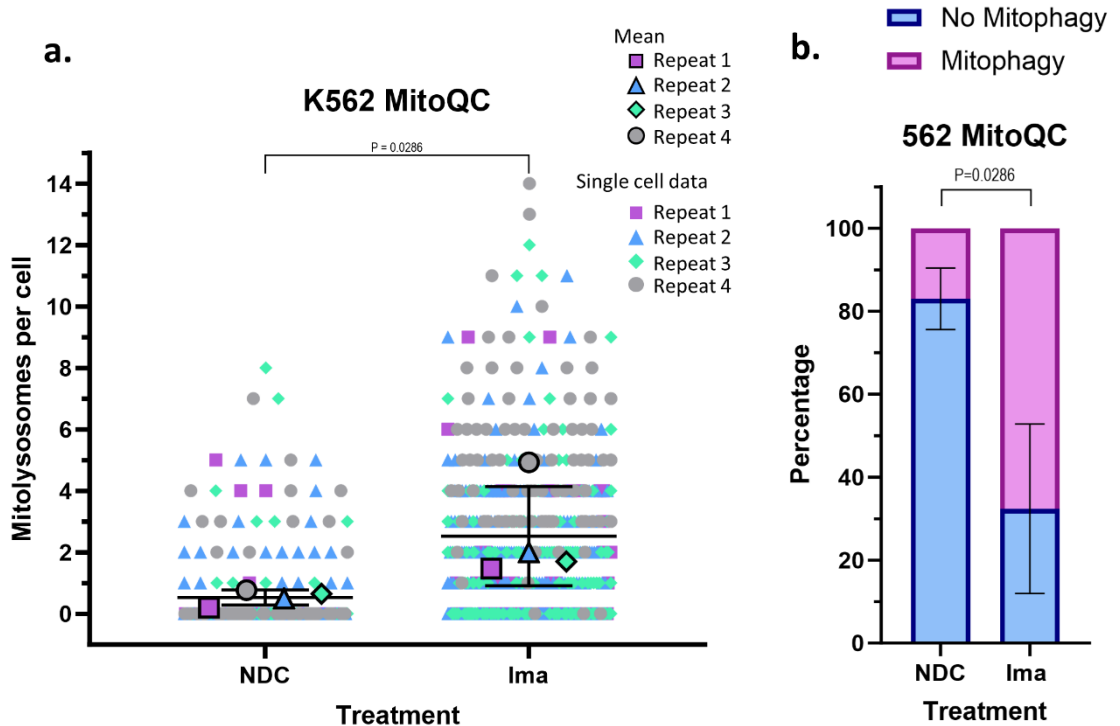


**Figure 5-9 Significant increase in mitophagy upon BCR::ABL1 inhibition in K562 MitoQC cells.** K562 MitoQC cells were treated with 2 $\mu$ M imatinib (Ima) for 24 hours. Live-cell imaging was performed to assess the number of mitolysosomes per cell (a). The data were plotted as mean  $\pm$  S.D. of  $n=4$  independent experiments, with single-cell data plotted in the background. P-values were calculated from the means using the Mann-Whitney test. The bar chart illustrates the ratio of cells actively undergoing mitophagy (detection of one or more mitolysosomes) compared to cells lacking mitolysosomes (b).

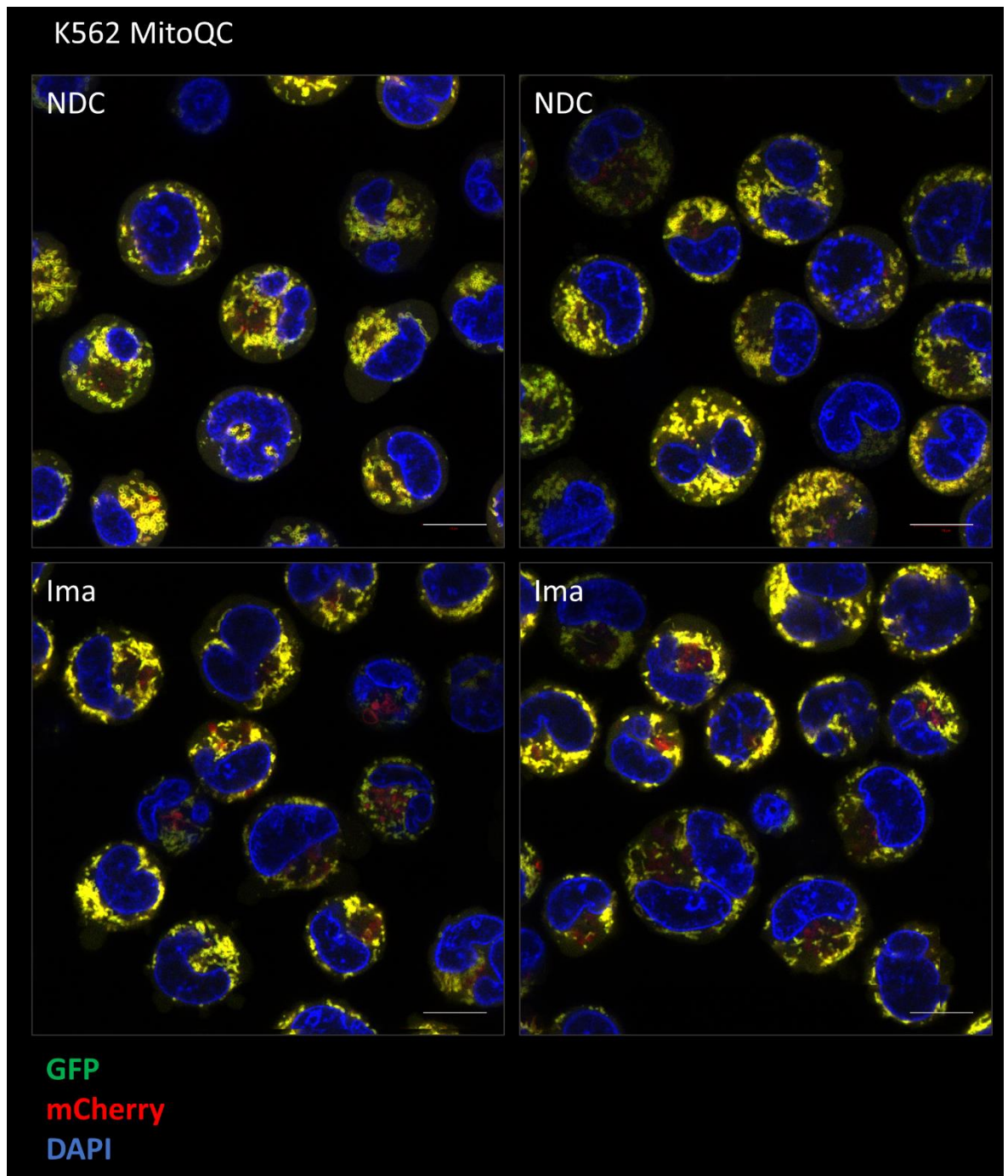


**Figure 5-10 Detection of mitophagy in K562 MitoQC cells upon TKI treatment.** Representative live-cell images of K562 MitoQC cells treated with 2 $\mu$ M imatinib (Ima) for 24 hours were acquired using the LSM 880 with the Airyscan detector. In these images, GFP is represented in green and mCherry in red, resulting the visualisation of healthy mitochondria displayed in yellow. Red 'puncta' represent mitochondria located inside the lysosome. The nucleus is depicted in blue. Scale bar: 10 $\mu$ m.

### 5.4.2 Autophagy inhibition prevented TKI-mediated mitophagy

As imatinib treatment of CML cells had previously demonstrated an increased appearance of mitochondria located within lysosomes, our aim was to inhibit autophagic flux to confirm whether this effect is mediated by autophagy. To validate this, we treated K562 MitoQC cells with the ULK1 inhibitor MRT403, imatinib alone, and a combination of both drugs. As previously published by our lab, MRT403 is an autophagy inhibitor highly specific for inhibiting the ULK1 kinase<sup>367</sup>.

First, Western blotting was utilised to confirm the inhibition of BCR::ABL1 signalling by imatinib treatment. CrkL, a downstream effector of BCR::ABL1, was not phosphorylated in presence of imatinib, validated by lack of phosphorylation (pCrkL), while levels of total CrkL remained unchanged (**Figure 5-11**). Treatment of cells with MRT403 showed inhibition of ULK1, evident by the absence of pAtg14, a protein phosphorylated at Ser29 by ULK1. Commonly used markers for assessing autophagic flux are p62 and LC3. The adaptor protein p62 is known to localise to autophagosomes and gets degraded during high autophagic flux<sup>377</sup>. Its accumulation signals that autophagy is inhibited, as observed in MRT403-treated cells (**Figure 5-12**). LC3 exists in two forms: cytosolic (LC3-I) and PE-conjugated LC3 (LC3-II) forming upon autophagy induction. These forms have different molecular weights. Despite LC3-II having a higher molecular weight, its binding to a phospholipid increases its hydrophobicity, resulting in faster migration during SDS-PAGE separation<sup>377</sup>. Hence, autophagic flux can be monitored by evaluation of levels of LC3-I and LC3-II. Compared to the untreated control cells, in imatinib-treated cells, both forms of LC3 exhibited lower levels, indicating degradation by high autophagic activity, coinciding with high levels of pATG14 and low levels of p62 (**Figure 5-12**). Conversely, exposure to MRT403 led to an accumulation of both LC3 forms, signifying inhibited autophagy. While LC3 levels suggested autophagy inhibition in the combination treatment of imatinib and MRT403, it did not entirely restore p62 to normal levels.

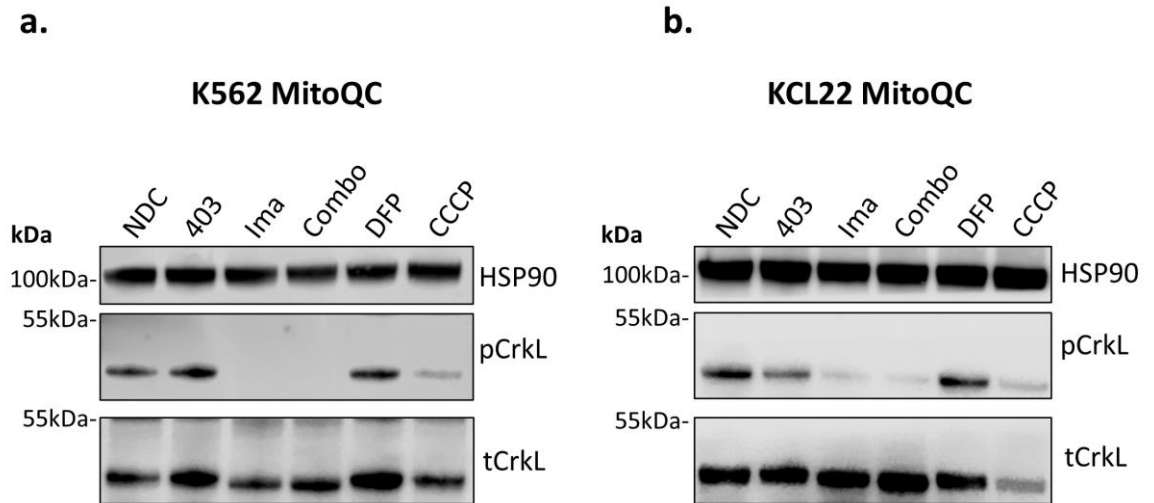


**Figure 5-11 Imatinib inhibited BCR::ABL1 signalling validated by reduced phosphorylation of CrkL.** K562 (a) and KCL22 (b) MitoQC cells were treated with 3 $\mu$ M MRT403 (403), 2 $\mu$ M imatinib (Ima) or a combination (Combo) of both for 24 hours. Control treatments involved 1mM DFP administered for 24 hours and 20 $\mu$ M CCCP for 4 hours. Western blots analysis depicts the levels of phosphorylated CrkL (pCrkL) and total CrkL (tCrkL), with HSP90 serving as the loading control. The results shown are representative of n=2 independent experiments.

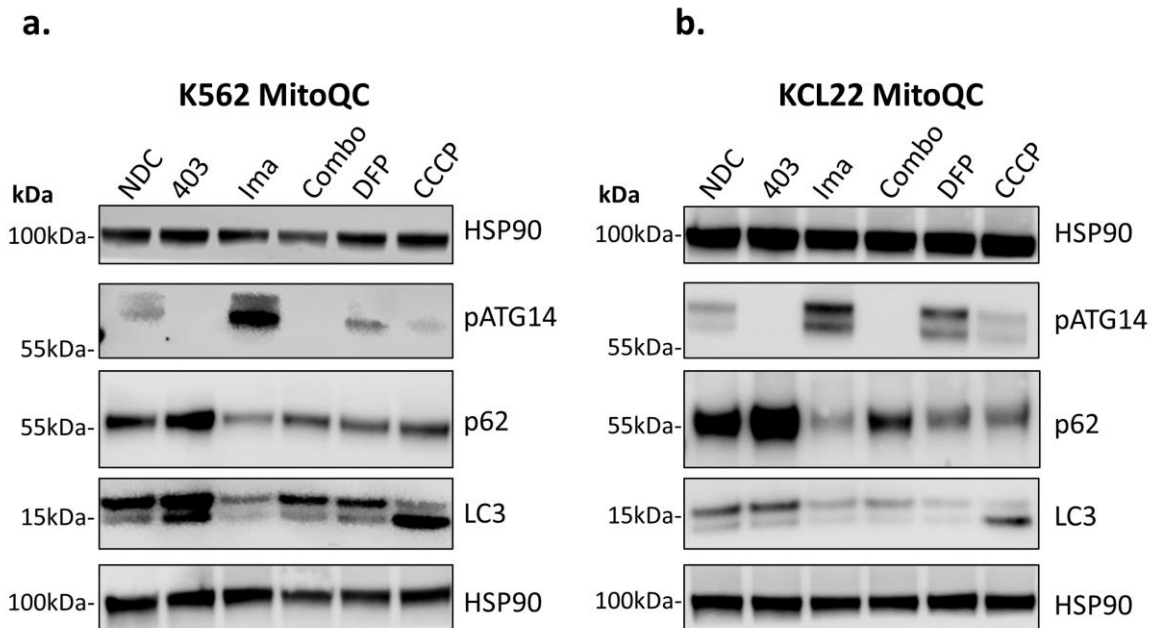


**Figure 5-12 Inhibition of ULK1 halts the autophagic flux triggered by TKI treatment.** Western blots display the levels phosphorylated Atg14 (pAtg14), p62 and LC3 in both K562 (a) and KCL22 (b) MitoQC cells treated with 3 $\mu$ M MRT403 (403), 2 $\mu$ M imatinib (Ima) and the combination of both for 24 hours. As controls, mitophagy inducers such as DFP (1mM for 24h) and CCCP (20 $\mu$ M for 4h) were used. HSP90 was used as a loading control. The results are representative of n=2 independent experiments.

Consistent with previous experiments, imatinib treatment resulted in a notable increase in both the number of mitolysosomes per cell in KCL22 cells, showing a fold increase of 6.5, and a substantial rise in the population of cells exhibiting an active level of mitophagy (**Figure 5-13a**), which increased from 15% in NDC to 85% upon TKI treatment (**Figure 5-13b**). Since the combination of autophagy inhibition with the previously used concentration of imatinib (2 $\mu$ M) significantly affected overall fluorescence of MitoQC cells, a lower concentration of imatinib (600nM) was applied. MRT403 treatment did not visibly alter the appearance of mitolysosomes, as basal mitophagy was already low in normal cell culture conditions. However, inhibiting ULK1 with MRT403 appeared to prevent TKI-mediated mitophagy induction and reduced the appearance of mitolysosomes to levels comparable no normal culture conditions (**Figure 5-13**). Similar results were observed with K562 MitoQC cells, where MRT403 treatment significantly reduced the formation of mitolysosomes upon TKI treatment (**Figure 5-14**), although this did not reach statistical significance.

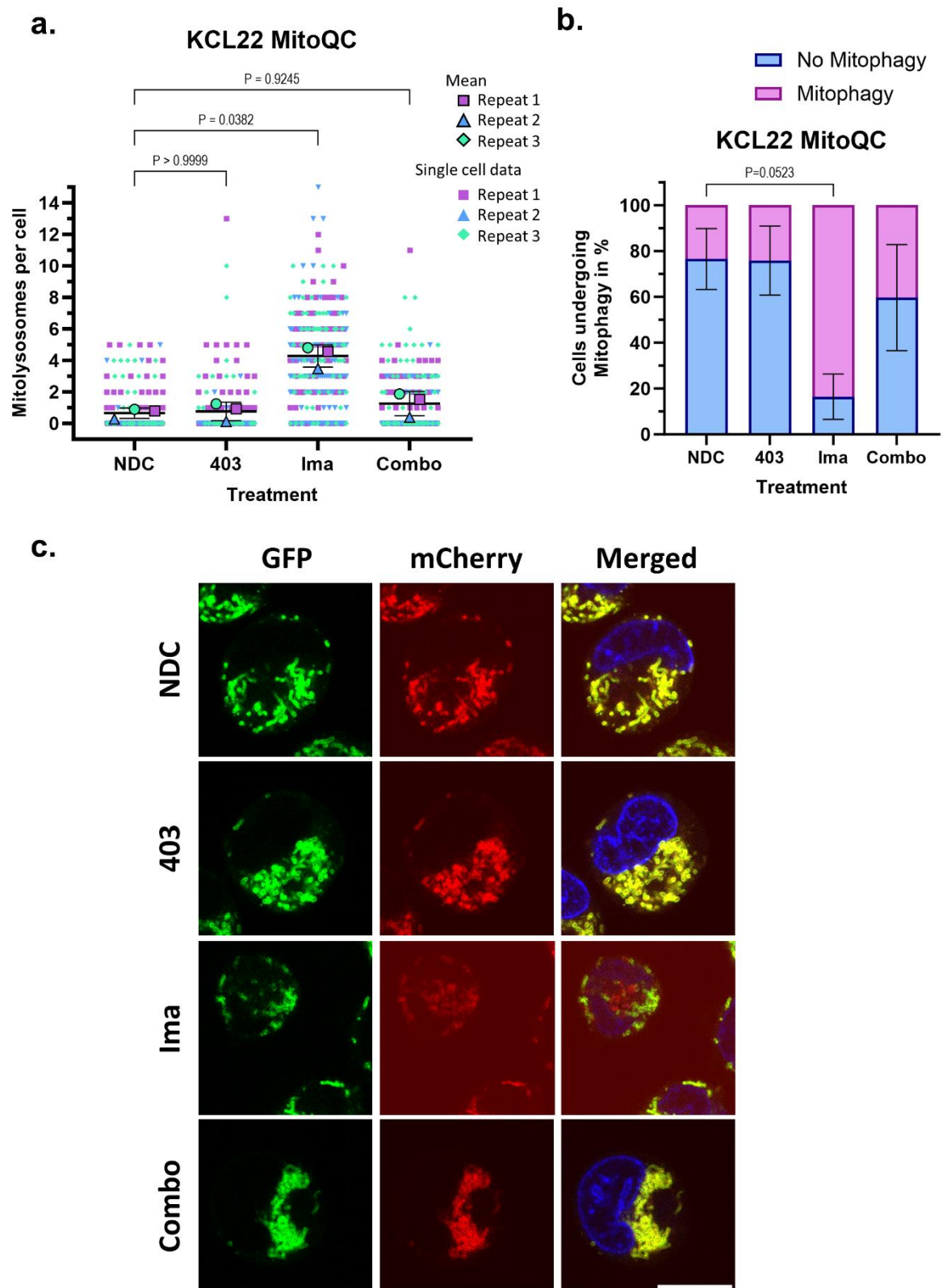


**Figure 5-13 MRT403 inhibits mitophagy induced by TKI treatment in KCL22 MitoQC cells.** KCL22 MitoQC cells were treated with 1 $\mu$ M MRT403 (403), 600nM imatinib (Ima) and a combination (Combo) of both for 24 hours. Live-cell microscopy was used to assess the number of mitolysosomes per cell (a). The mean  $\pm$  S.D. of  $n=3$  independent experiments were plotted, with single-cell data superimposed in the background. The bar chart illustrates the ratio of cells undergoing mitophagy (detection of one or more mitolysosomes) compared to cells lacking any mitolysosomes (b). Representative images are shown in (c). P-values were calculated using Kruskal-Wallis test and Dunnett's multiple comparison test.

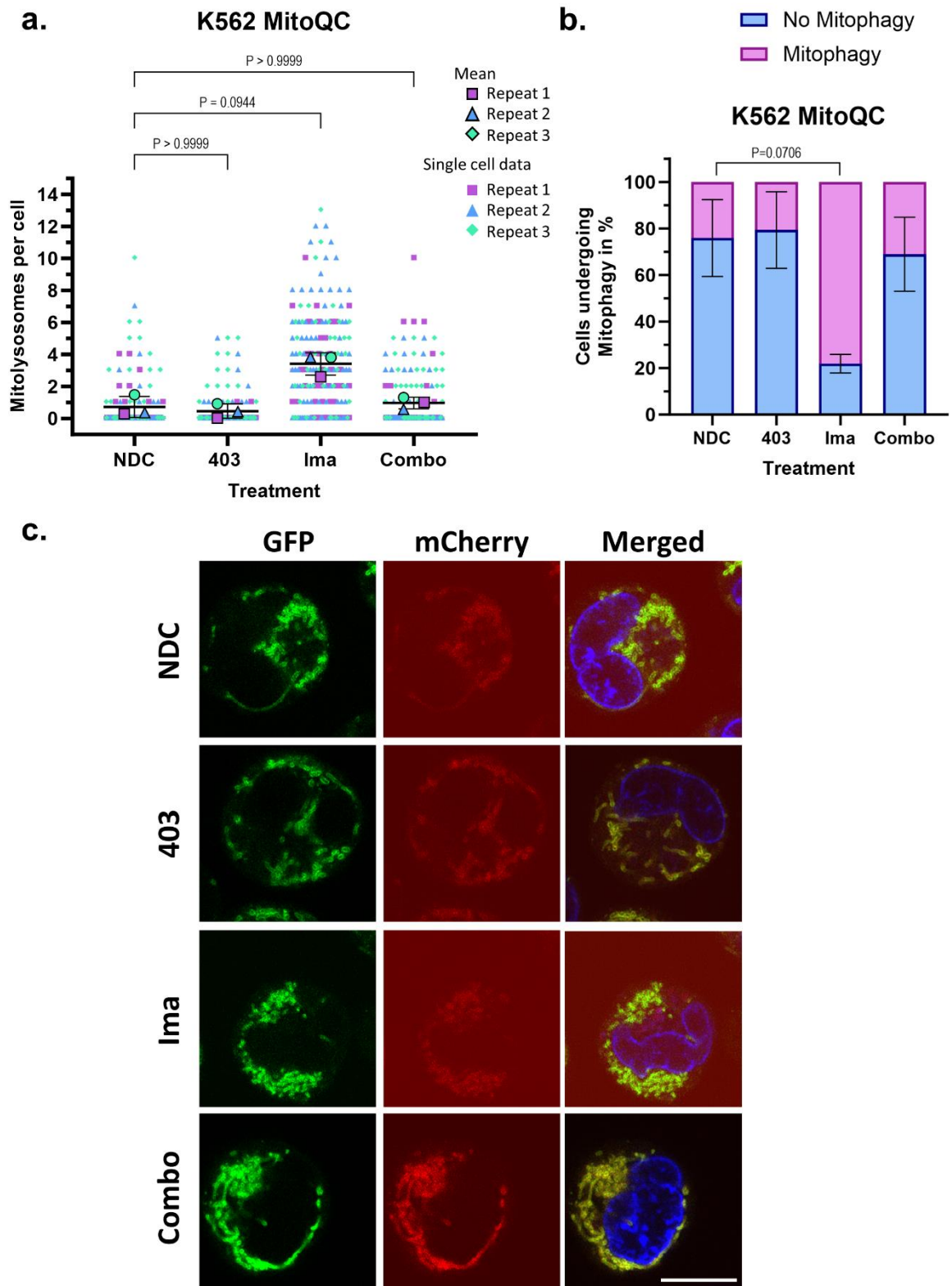


**Figure 5-14 ULK1 inhibition prevented TKI-mediated mitophagy induction in K562 MitoQC cells.** K562 MitoQC cells were treated with 1 $\mu$ M MRT403 (403), 600nM imatinib (Ima) and a combination (Combo) of both for 24 hours. Live-cell imaging was performed to assess the number of mitolysosomes per cell (a). The data were plotted as mean  $\pm$  S.D. of  $n=3$  independent experiments, with single-cell data superimposed in the background. The bar chart illustrates the ratio of cells undergoing mitophagy (detection of one or more mitolysosomes) versus cells showing no mitolysosomes (b). Representative images are shown in (c). P-values were calculated using Kruskal-Wallis test and Dunnett's multiple comparison test.

ATG7 is essential for autophagosome formation, serving as the E1-like enzyme that mediates both conjugation systems<sup>298</sup>. Consequently, it is a common target for genetic ablation in autophagy studies. Therefore, ATG7 was deleted using the CRISPR/Cas9 technique in KCL22 and K562 MitoQC cells and validated by Western blotting (**Figure 5-15c, Figure 5-16c**). Functional assessment of autophagy deficiency in the KO cells was shown by blotting for LC3, which cannot be converted to LC-II. Vector control cells convert LC3 on a basal level, as shown by the double band for LC3-I and LC3-II, while no LC3-II is detected in the ATG7 KO cell line.

Autophagy-deficient MitoQC (ATG7 KO) cells were exposed to imatinib to verify that mitophagy is autophagy-mediated in KCL22 and K562 cells (**Figure 5-15, Figure 5-16**). This was confirmed by the absence of mCherry-‘puncta’ in the ATG7 KO cells upon TKI treatment as mean of mitolysosomes per cells were restored to NDC levels, although the formation of mitolysosomes per cell in response to TKI treatment compared to NDC did not reach statistical significance.

The results obtained align with previous findings<sup>367</sup>, demonstrating that CML cells employ autophagy as a mechanism to evade TKI-induced cell death and differentiation. Notably, our experiments revealed an elevation in mitophagy, suggesting that CML cells respond to BCR::ABL1 inhibition not only by intensifying autophagic activity to ensure survival, but also by selectively targeting mitochondria.

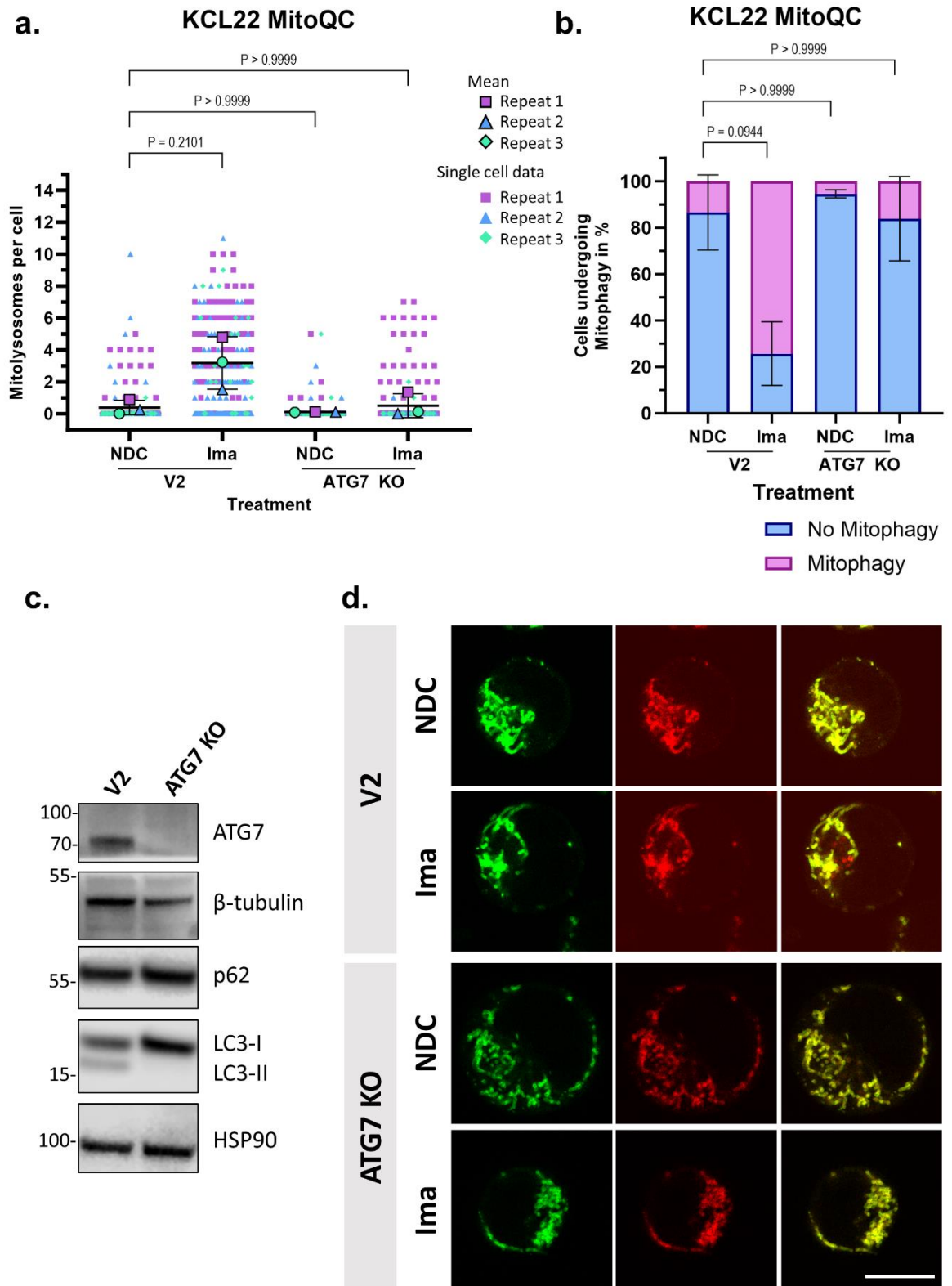


**Figure 5-15 ATG7 KO impeded TKI-mediated mitophagy induction in KCL22 cells.** KCL22 MitoQC ATG7 KO cells were subjected to 600nM imatinib for 24 hours alongside the vector control (V2). Live-cell imaging was conducted to measure the number of mitolysosomes per cell (a). The mean  $\pm$  S.D. of  $n=3$  independent experiments were plotted, with single-cell data superimposed in the background. The bar chart illustrates the ratio of cells exhibiting mitolysosomes compared to cells not undergoing mitophagy (b). P-values were calculated using Kruskal-Wallis test and Dunnett's multiple comparison test. Validation of ATG7 KO by Western blotting (c). Representative confocal microscope images are shown in (d). Scale bar: 10 $\mu$ m.

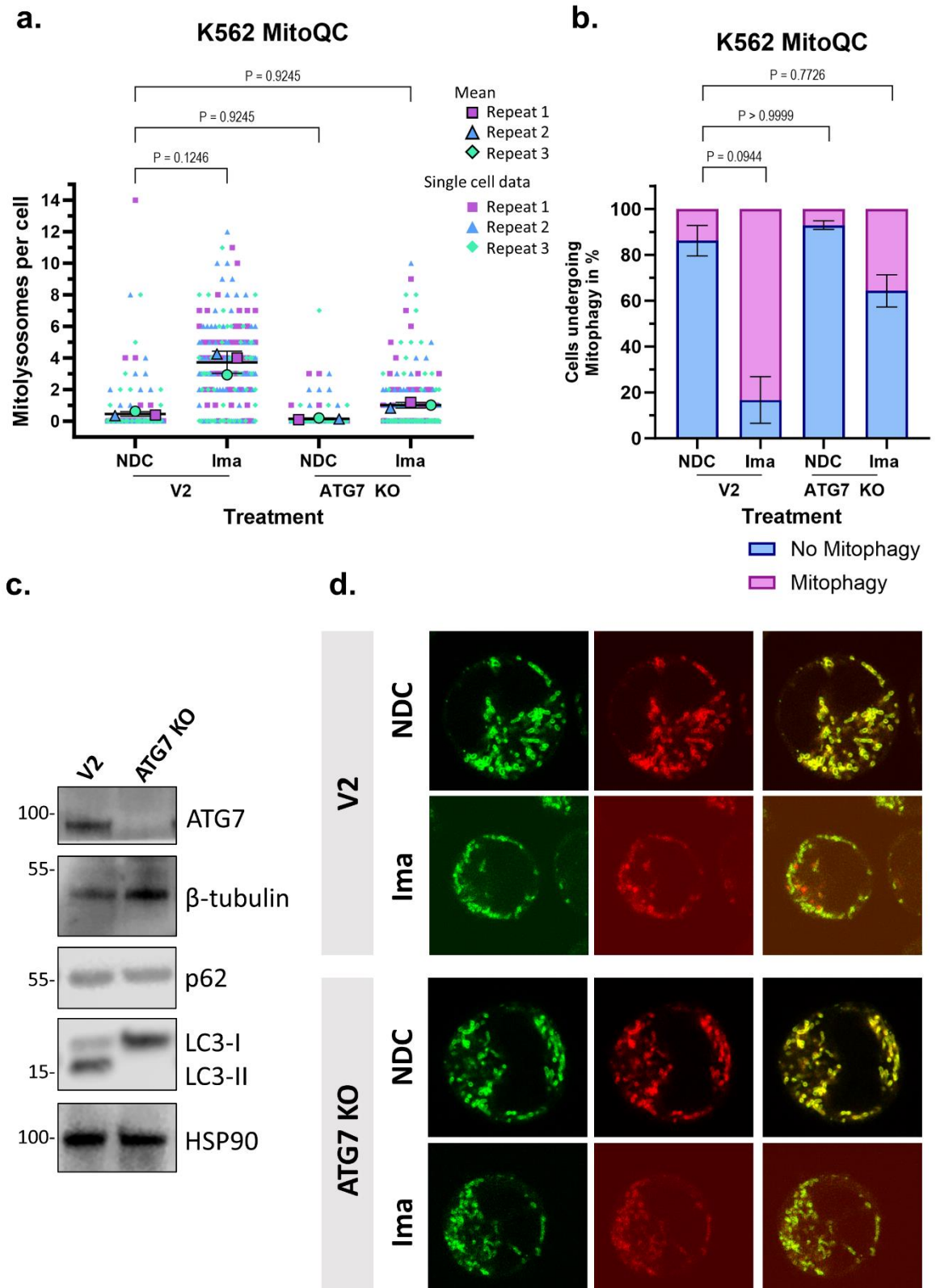


**Figure 5-16 TKI-mediated mitophagy induction required ATG7 for autophagic flux in K562 cells.** K562 MitoQC cells were genetically modified to be autophagy deficient by KO of ATG7 (ATG7 KO). Vector control (V2) and ATG7 KO cells were treated with 600nM imatinib, followed by live-cell imaging to measure the number of mitolysosomes per cell (a). The mean  $\pm$  S.D. of  $n=3$  independent experiments were plotted, with single-cell data superimposed in the background. The bar chart illustrates the ratio of cells undergoing mitophagy (detection of one or more mitolysosomes) versus cells showing no mitolysosomes (b). P-values were calculated using Kruskal-Wallis test and Dunnett's multiple comparison test. Validation of ATG7 KO via Western blotting (c). Representative confocal microscope images are shown in (d). Scale bar: 10 $\mu$ m.

### 5.4.3 Unravelling mitophagy pathways: the roles of Nix and BNIP3 in TKI-induced mitophagy

Next, our investigation aimed to explore the activation of different mitophagy pathways. The Pink1-Parkin pathway is typically activated by the accumulation of Pink1 on the outer mitochondrial membrane. While Pink1 is usually degraded within the mitochondria, its accumulation on the outer membrane triggers Parkin to ubiquitinate mitochondrial membrane proteins<sup>324,326</sup>. This polyubiquitination serves as a signal for the autophagosomal machinery to degrade this organelle<sup>321</sup>. Another canonical pathway involves the mitophagy adaptor proteins BNIP3 and Nix, proteins that facilitate mitophagy by direct binding to LC3<sup>337,338</sup>. Both proteins have been found to be upregulated by HIF1 $\alpha$  upon exposure to hypoxia and facilitate mitophagy, although this regulation appears to vary across different tissues<sup>402-404</sup>.

To assess the pathways involved in regulating mitophagy upon TKI treatment, we treated K562 and KCL22 cells with imatinib followed by Western blotting analysis of the key proteins Pink1, BNIP3 and Nix. As a control, we treated the cells with DFP leading to the stabilisation of Nix and BNIP3<sup>400</sup> and CCCP to trigger Pink1/Parkin-mediated mitophagy and induce accumulation of Pink1<sup>326</sup>.

Our findings suggest that the Pink1-Parkin pathway does not seem to be activated upon TKI treatment, as Pink1 levels are overall not detected unless the cells were cultured with CCCP (**Figure 5-17**). BNIP3 remained unchanged upon TKI treatment in either cell line but showed elevation in the control treatment with DFP. However, Nix seems to be upregulated upon imatinib treatment in both cell lines, although not as strongly as in the control treatment with DFP. This led to the hypothesis that Nix might constitute the primary pathway activated upon TKI treatment.

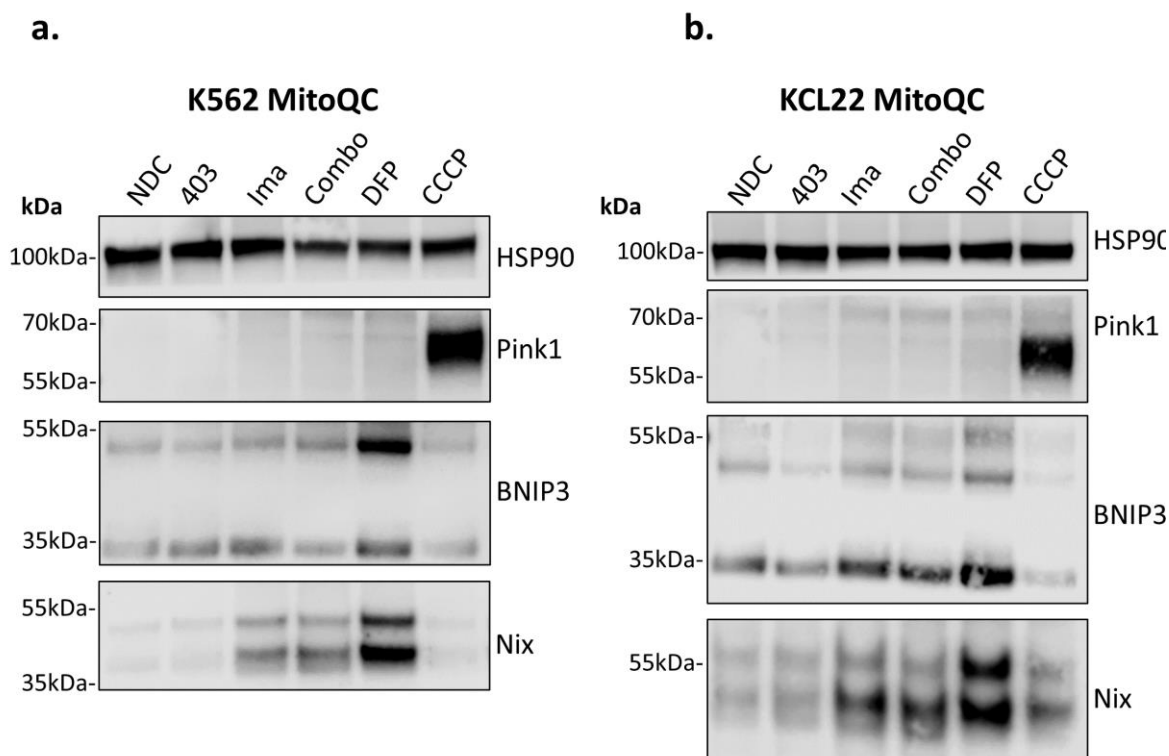


**Figure 5-17 Nix protein levels increased upon imatinib treatment.** Western blots showing levels Pink1, BNIP3 dimer and Nix in K562 (a) and KCL22 (b) cells treated with 3 $\mu$ M MRT403 (403), 2 $\mu$ M imatinib (Ima) or a combination of both for 24 hours. Mitophagy inducers like DFP (1mM for 24h) and CCCP (20 $\mu$ M for 4h) were used as control. HSP90 was used as a loading control. Representative of n=2 independent experiments.

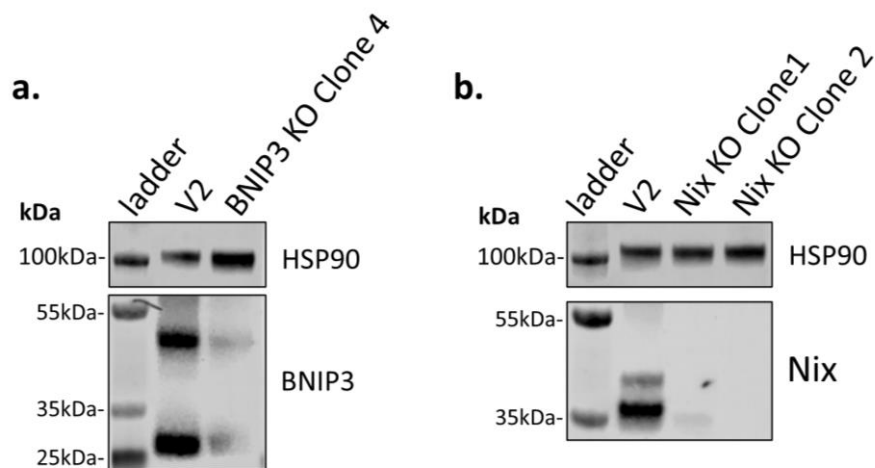
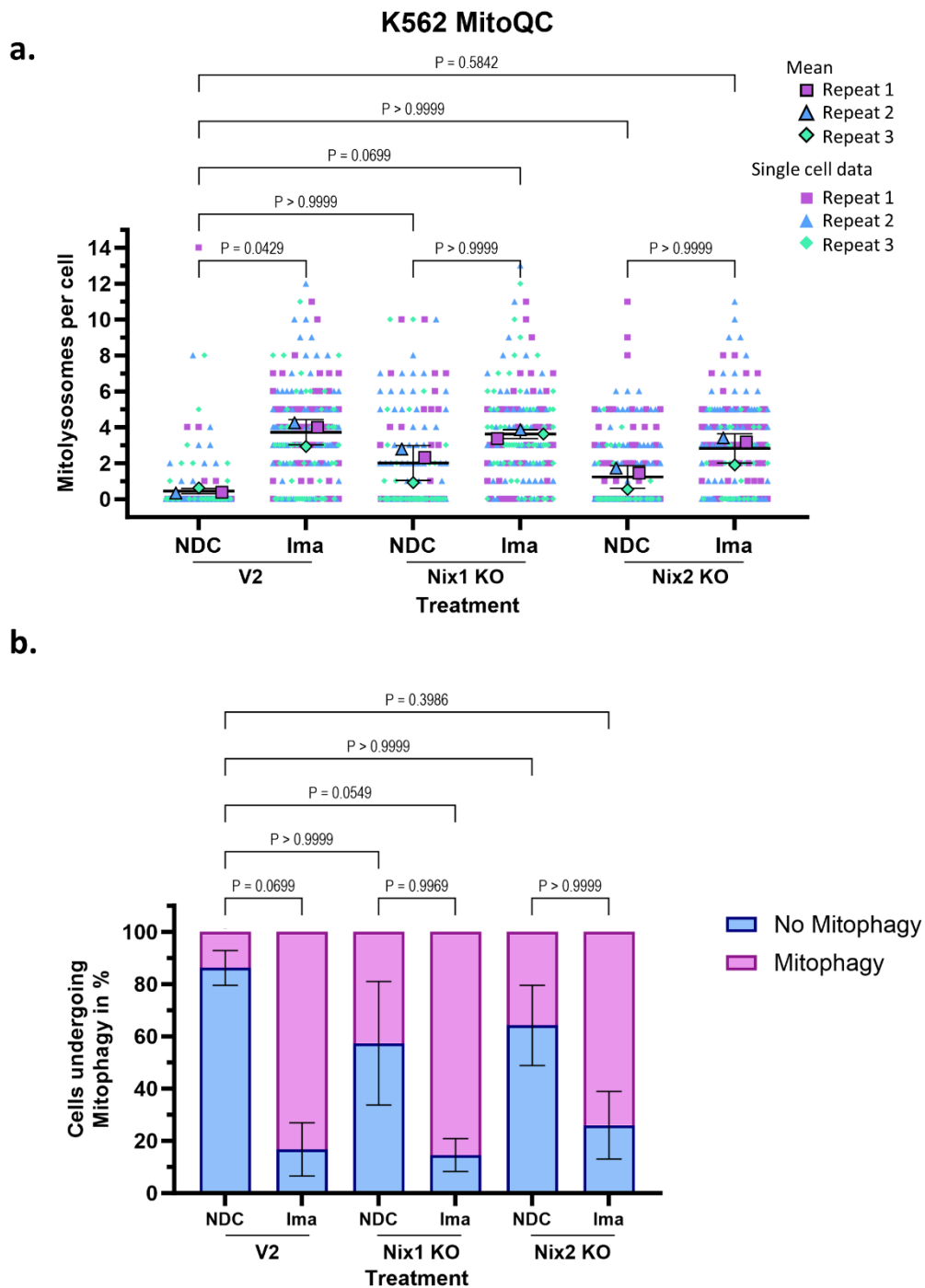


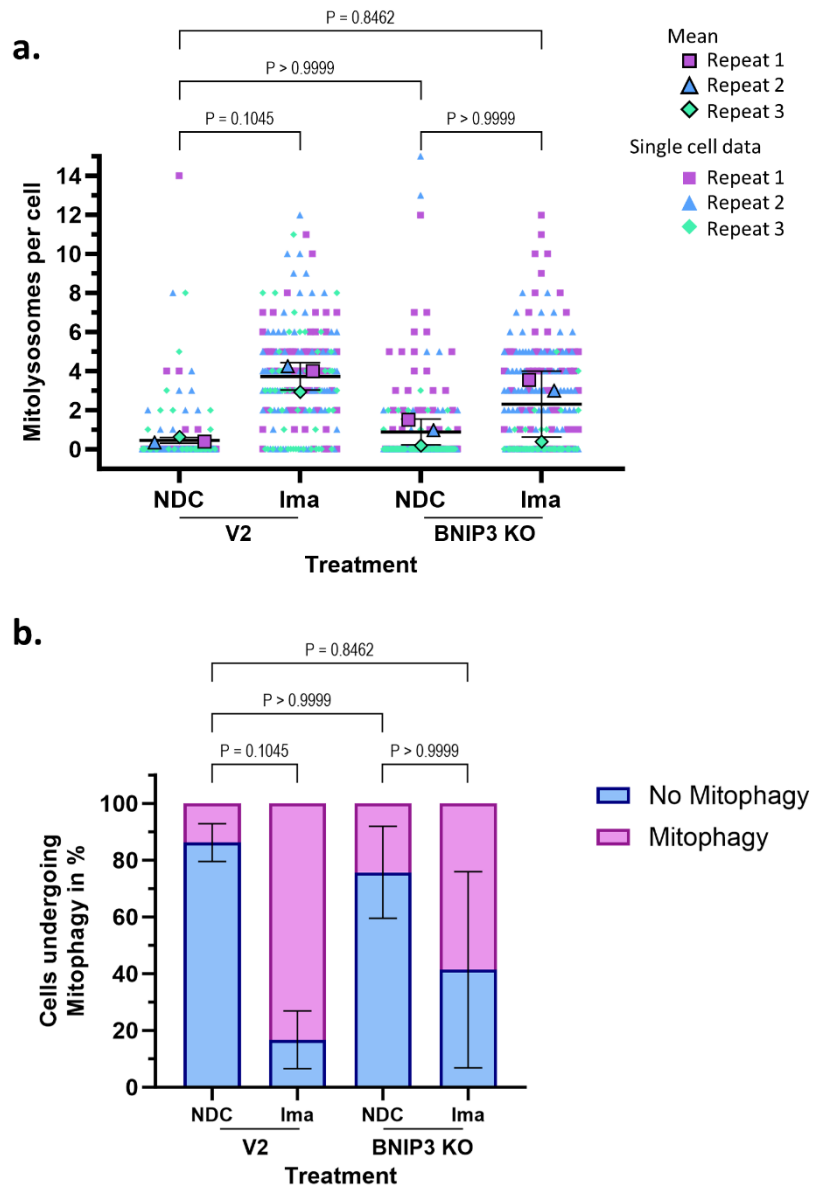
**Figure 5-18 Validation of BNIP3 and Nix knockout in K562 MitoQC cells.** KO cells for Nix and BNIP3 were generated by lentiviral transduction and CRISPR-Cas9 mediated genome editing. After single cell cloning, the purest clone was selected for subsequent transduction with the MitoQC reporter gene. Following this, K562 MitoQC vector control (V2), BNIP3 KO and Nix KO cells were exposed to hypoxia (1% O<sub>2</sub>) for 24 hours to induce upregulation of both proteins. The KO of Nix and BNIP3 was validated using Western blotting, with HSP90 serving as the loading control.

To validate this hypothesis, we utilised the CRISPR-Cas9 technique to generate K562 cells deficient in either Nix or BNIP3, followed by single-cell cloning to achieve a complete KO. Both procedures were conducted by Daniele Sarnello. Afterwards, the cells were retrovirally transduced to introduce the MitoQC reporter gene, a process that involved antibiotic selection and FACS purification. Following this step, K562 MitoQC V2 (vector control) and the respective KO cell lines were subjected to 24 hours of hypoxia (1%) to induce the upregulation of both Nix and BNIP3 (**Figure 5-18**) for the validation of successful KO via Western blotting.

To investigate whether Nix or BNIP3 mediate mitophagy induction in response to TKI treatment, K562 MitoQC control and the KO cells were treated with 600nM imatinib for 24 hours and subjected to live-cell microscopy. Consistent with previous experiments, (**Figure 5-9**) imatinib triggered an increase in mitolysosomes, with an average of four observed compared to almost none in the non-treated cells, showing considerable variability among individual cells. Intriguingly, all KO cells exhibited a trend of increased mCherry-‘puncta’ counts even without exposure to any drug, compared to the untreated control cells (**Figure 5-19a, Figure 5-20a**). Despite an observed increase in mitophagy upon TKI treatment, this rise was less pronounced and non-significant compared to the control cells (8-fold) due to elevated basal levels.

Furthermore, approximately half of the counted cells in the untreated Nix KO cells displayed induction of mitophagy, compared to only 20% in the control cells or 30% in BNIP3 KO cells (**Figure 5-19b, Figure 5-20b**). This suggests an increased basal mitophagy in cells lacking Nix. Although there was only a slight increase in mitolysosomes upon TKI treatment in the KO cells compared to their untreated counterparts, the percentage of cells displaying mitophagy across all KO cell lines increased to 80% in response to TKI treatment. Notably, this increase was less pronounced in the BNIP3 KO cells, which exhibited high variability between experiments. Representative images are illustrated in **Figure 5-21**.





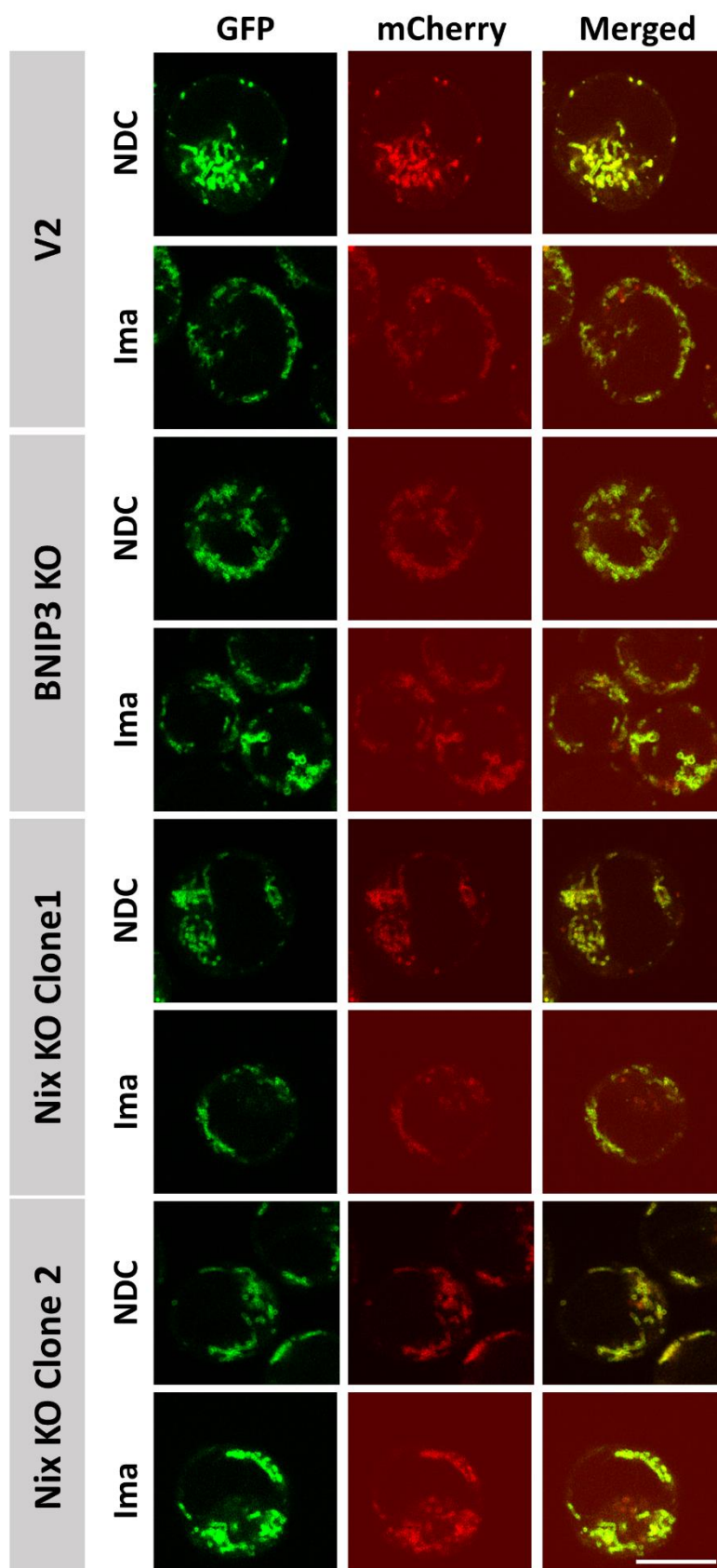


**Figure 5-21 Nix or BNIP3 are not essential for imatinib-mediated mitophagy.** Representative confocal images of K562 MitoQC vector control (V2), BNIP3 KO (clone 4) or Nix KO cells (clones 1 and 2) treated with 600nM imatinib (Ima) for 24 hours. Scale bar: 10 $\mu$ m.

## 5.5 Development of a high-throughput assay to measure mitophagy in CML cells

Another approach to measure mitophagy induction involved utilising flow cytometry, which is suitable for high-throughput applications, particularly considering that leukaemia cells are non-adherent. Consequently, MFI of GFP and mCherry was acquired, and their ratio normalised to NDC.

### 5.5.1 Assessing MitoQC flow cytometry-based assay using mitophagy inducers

Initially, the MitoQC assay was tested using known inducers of mitophagy. A time course experiment was conducted wherein CCCP was employed. Additionally, another method to stimulate mitophagy involved the inhibition of OXPHOS by treating cells with antimycin A (AA) and oligomycin (OL)<sup>377</sup>. KCL22 and K562 MitoQC cells were treated with either the combination of AA-OL or CCCP over a 24-hour time course and subsequently subjected to flow cytometry analysis (**Figure 5-22**, **Figure 5-23**).

Both cell lines exhibited increased mCherry fluorescence over GFP fluorescence shortly after two hours of treatment with either mitophagy inducer (AA-OL and CCCP), peaking between three and six hours in KCL22 (**Figure 5-22**) and three to four hours in K562 (**Figure 5-23**). Notably, after 24 hours of treatment, the ratio returned to normal levels comparable to NDC. Importantly, this effect was not due to the inclusion of dead cells, which were excluded from the analysis through DAPI staining. Throughout the treatment time course, overall cell death remained minimal (**Figure 5-24**). To interpret this outcome, we individually assessed the MFI of GFP and mCherry. Following four hours of treatment, a decrease in GFP intensity was detected, while mCherry remained unaffected (**Figure 5-25**). However, after 24 hours, reduced intensity was observed for both fluorophores, attributed to ongoing autophagic flux.

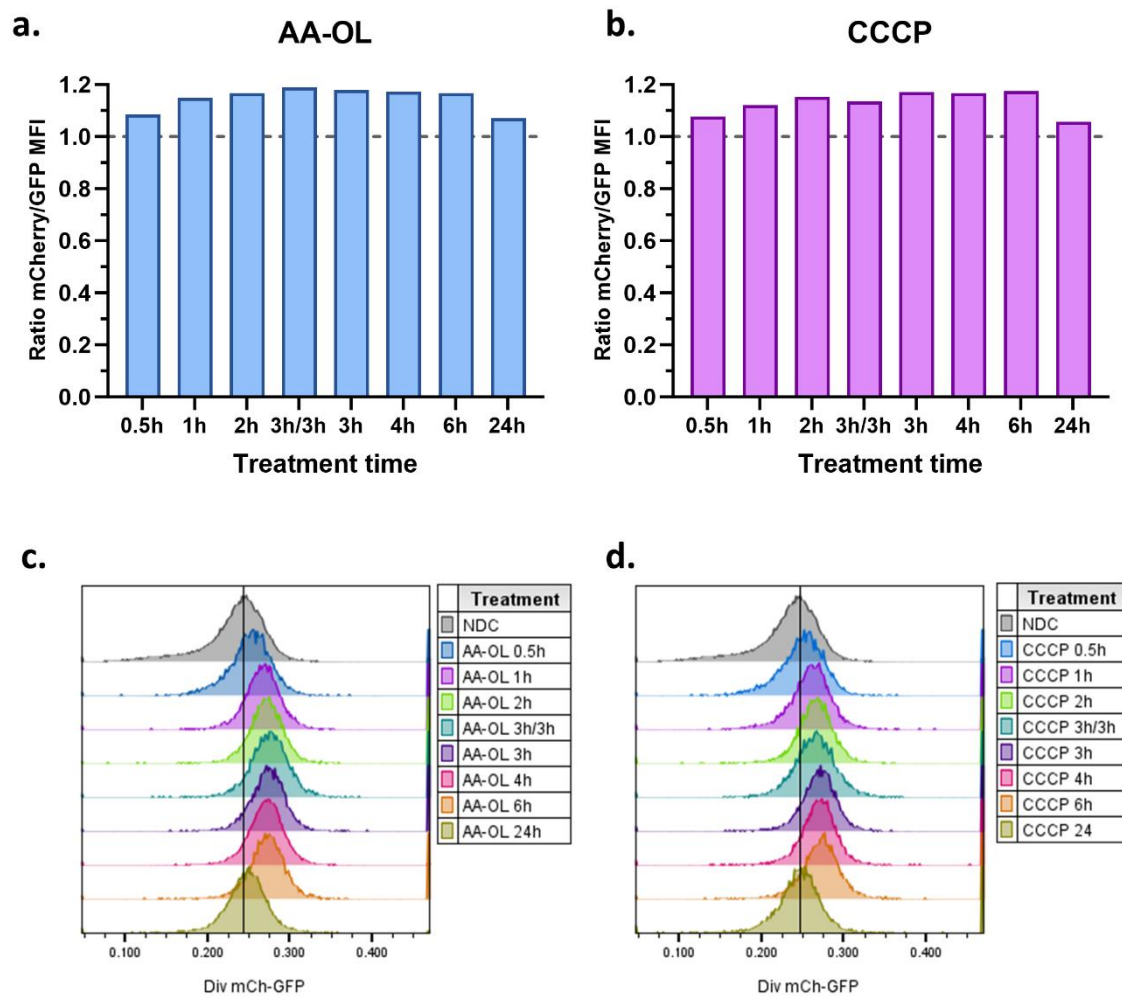


**Figure 5-22 Induction of mitophagy by CCCP and AA-OL peaked between three to six hours in KCL22 MitoQC cells.** KCL22 MitoQC cells were treated with 4 $\mu$ M antimycin A (AA) and 10 $\mu$ M oligomycin (OL) (a) or 20 $\mu$ M CCCP (b) for various durations: 0.5, 1, 2, 3, 4, 6, and 24 hours. Additionally, one condition (3h/3h) involved the respective treatment for 3 hours, followed by washing and resuspension in fresh medium without the drug and further incubation for 3 hours. Bar plots (a, b) show the ratio MFI (mCherry/GFP) normalised to the no drug control (NDC) with representative histograms displayed in (c, d). The data presented originate from a single experiment.

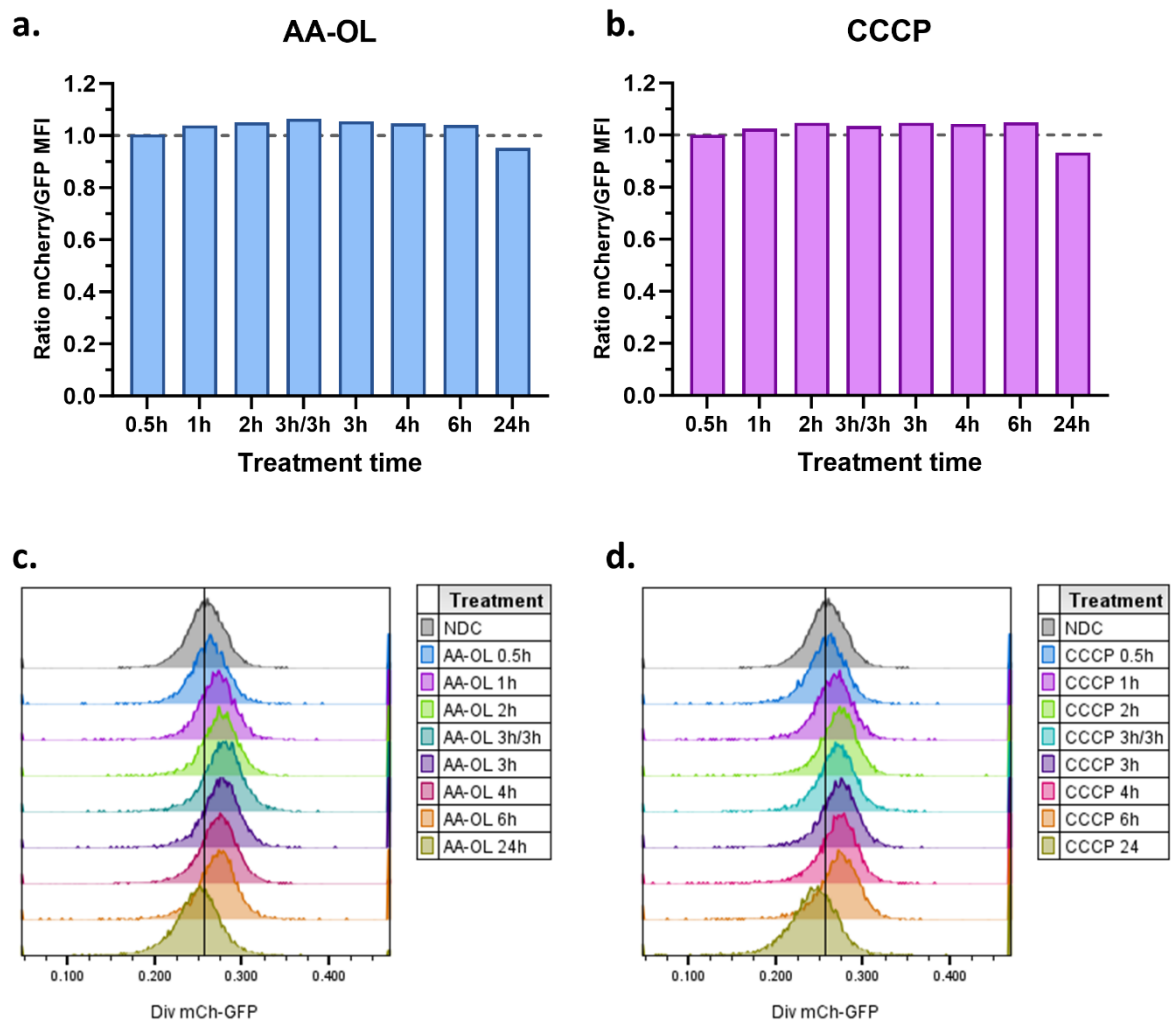


**Figure 5-23 Mitophagy induction by AA-OL or CCCP reaches maximum between three to six hours in K562 MitoQC.** K562 MitoQC cells were treated with 4 $\mu$ M antimycin A (AA) and 10 $\mu$ M oligomycin (OL) (a) or 20 $\mu$ M CCCP (b) for various durations (0.5h, 1h, 2h, 3h, 4h, 6h, and 24h). One condition (3h/3h) involved the respective treatment for 3 hours, after which cells were washed and resuspended in fresh medium without the drug. Bar plots (a, b) show the ratio MFI (mCherry/GFP) normalised to NDC and respective histograms are displayed in (c, d). The data presented originate from a single experiment.

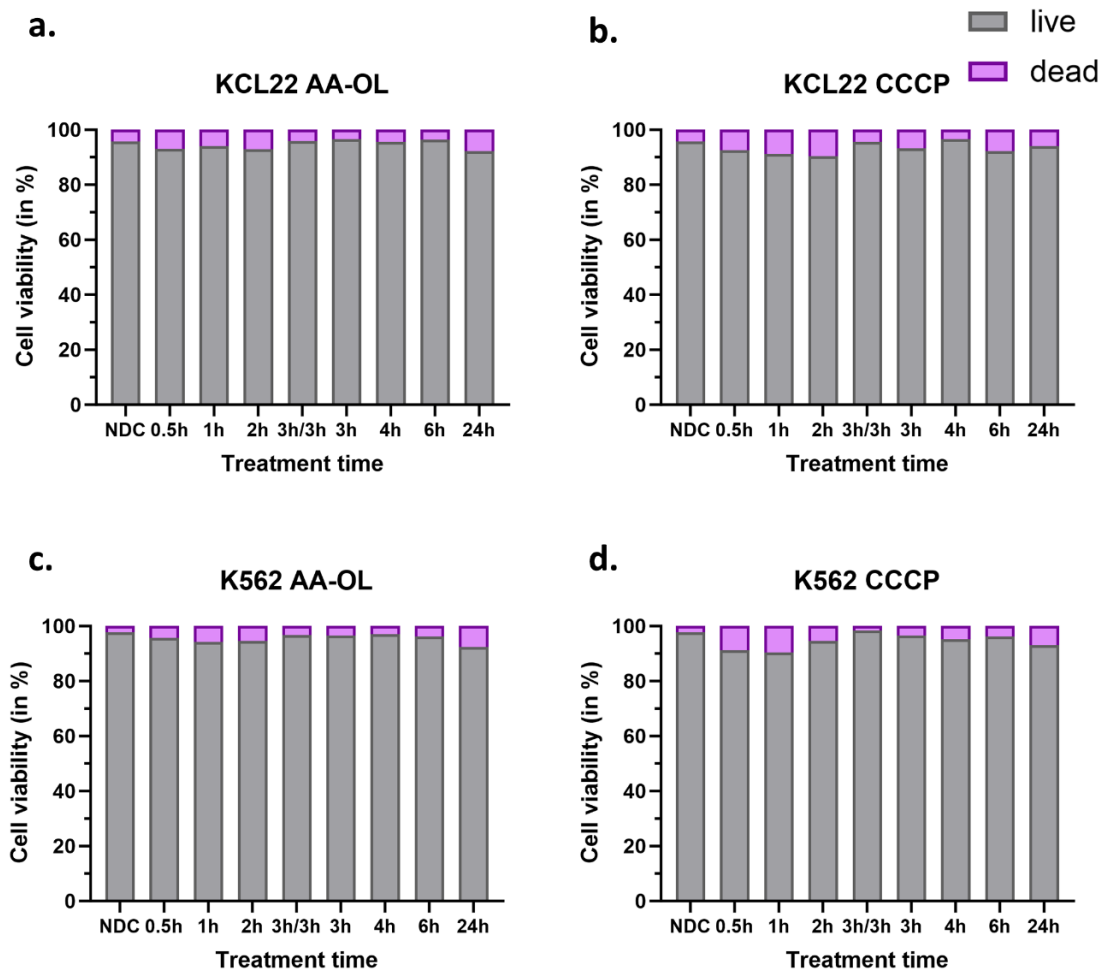
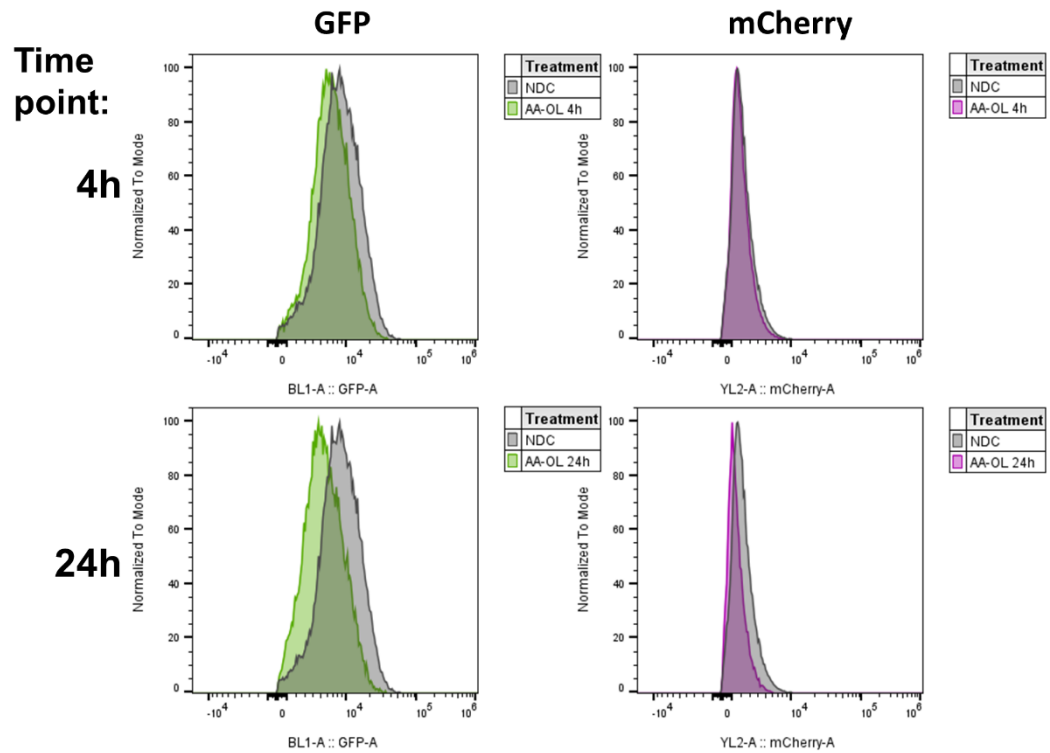


**Figure 5-24 Minimal cell death upon treatment with AA-OL or CCCP in KCL22 and K562 over 24 hours.** KCL22 MitoQC (a, b) and K562 MitoQC (c, d) cells were treated with  $4\mu\text{M}$  antimycin A (AA) and  $10\mu\text{M}$  oligomycin (OL) (a, c) or  $20\mu\text{M}$  CCCP (b, d) for various durations (0.5h, 1h, 2h, 3h, 4h, 6h, and 24h). One condition (3h/3h) involved the respective treatment for 3h, after which cells were washed and resuspended in fresh medium without the drug. Cells were stained with DAPI, followed by flow cytometry analysis. Bar plots show the percentage of live and dead cells. The data presented originate from a single experiment.

## a. KCL22 MitoQC



## b. K562 MitoQC

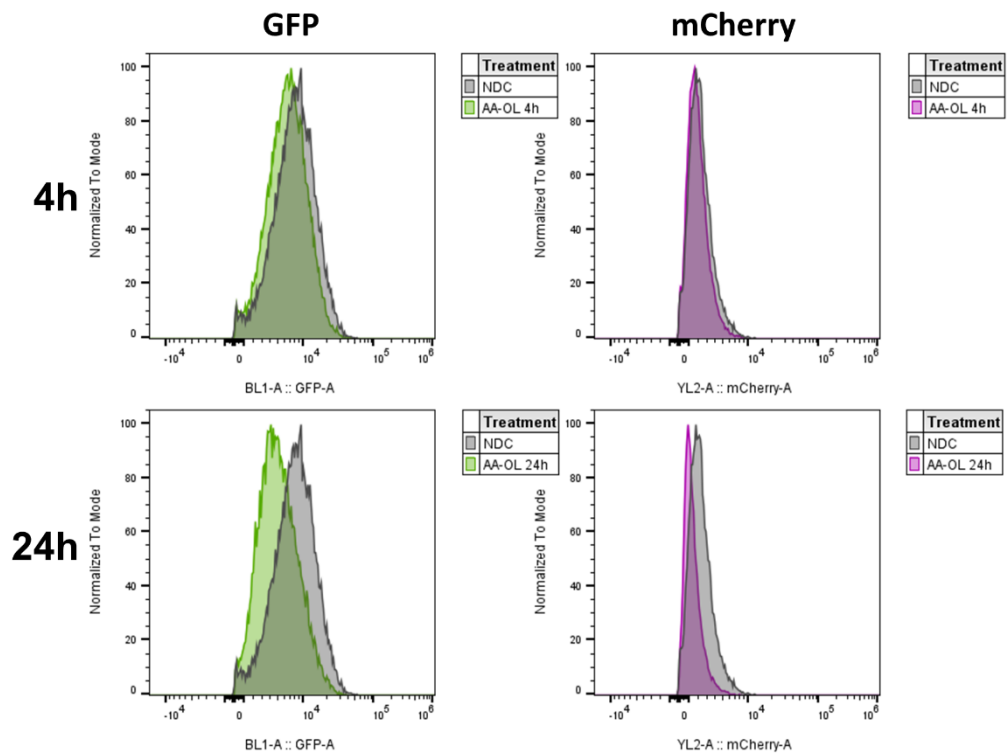


**Figure 5-25 Prolonged autophagic flux results in the degradation of GFP and mCherry.** KCL22 MitoQC (a) and K562 MitoQC (b) cells were treated with 4 $\mu$ M antimycin A (AA) and 10 $\mu$ M oligomycin (OL) for 4 and 24 hours. The histograms illustrate the MFI of GFP (left panel) or mCherry (right panel) from the no drug control (NDC, grey), overlaid with the MFI obtained from the treated cells.

### 5.5.2 TKI treatment induced mitophagy in a time-dependent manner

Imatinib has been demonstrated in **Figure 5-12** and in previous studies to increase autophagic flux<sup>367</sup>. In this experiment, the objective was to assess whether imatinib-mediated mitophagy can be measured using flow cytometry. Therefore, KCL22 and K562 MitoQC cells underwent imatinib treatment over a 24-hour time course. Flow cytometry analysis revealed a time-dependent increase in the ratio of MFI mCherry/GFP. This increase indicates higher levels of mCherry compared to GFP, using untreated cells as a baseline, suggesting induction of mitophagy after six hours (**Figure 5-26**). Notably, the K562 cells exhibited a more robust effect, contrary to the observations from the previous time course involving treatment with mitophagy inducers, where the response in KCL22 cells was stronger (**Figure 5-22, Figure 5-23**).

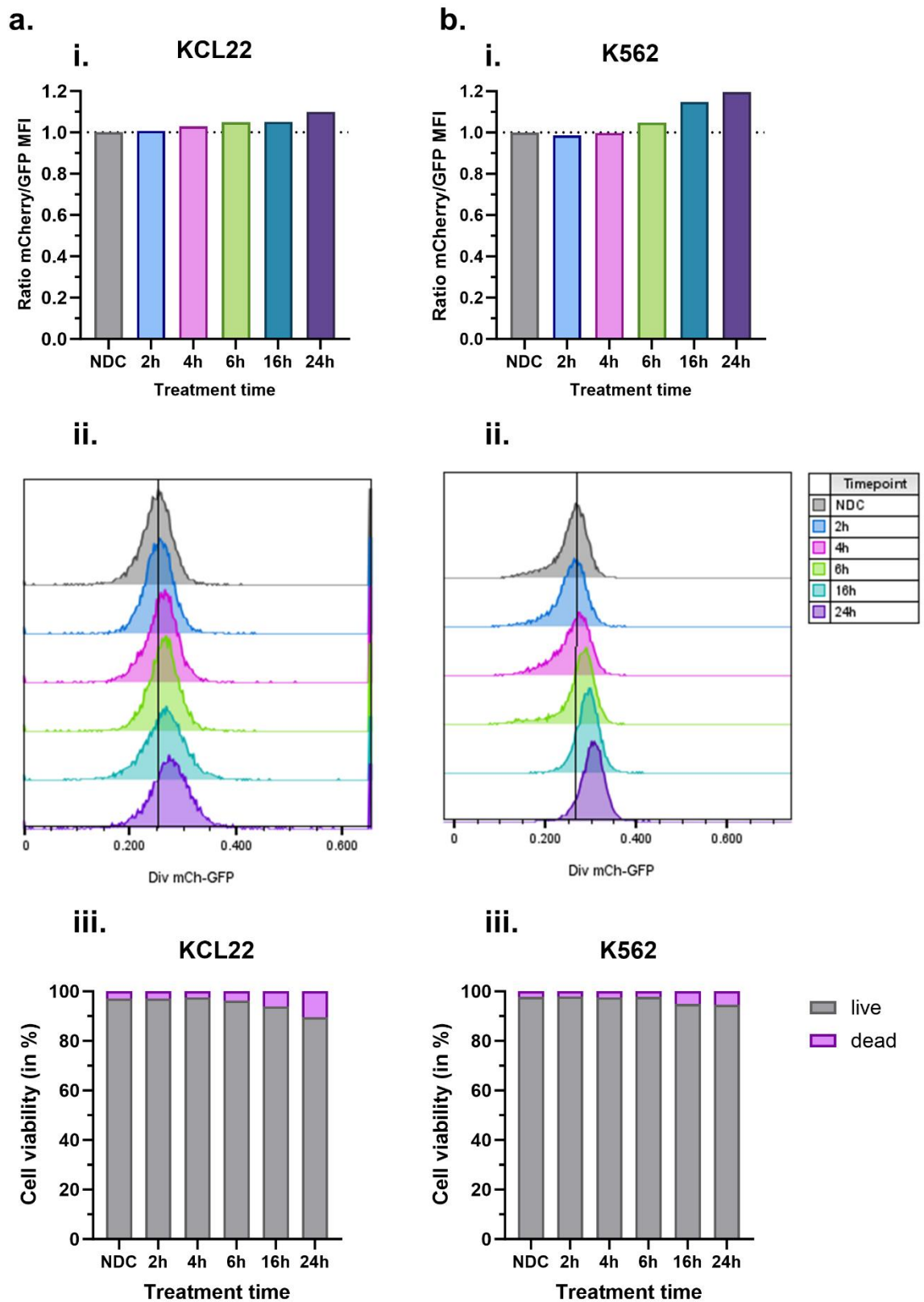


**Figure 5-26 Imatinib treatment induced mitophagy in a time-dependent manner in KCL22 and K562 cells.** KCL22 MitoQC (a) and K562 MitoQC (b) cells were exposed to 2 $\mu$ M imatinib for 2, 4, 6, 16 and 24 hours, alongside untreated cells (NDC). Bar plots (i) depict the ratio MFI (mCherry/GFP) normalised to NDC, with respective histograms displayed in (ii). Cell death, measured using DAPI staining, is presented as percentage (iii). The data presented originate from a single experiment.

### 5.5.3 Autophagy inhibitors failed to counteract TKI-induced mitophagy

The next step was to validate that autophagy inhibition restores fluorescent levels to baseline. Therefore, KCL22 MitoQC cells were subjected to single MRT403 treatment as well as in combination with imatinib (**Figure 5-27**).

Despite observing a slight decrease in ratio compared to imatinib treatment alone, it did not return to normal levels. DFP acts as a Pink1/Parkin-independent mitophagy inducer<sup>400</sup>, showed a similar level of mitophagy induction as seen with imatinib treatment or CCCP.

Subsequently, K562 MitoQC cells were treated with two different concentrations of MRT403, 1 $\mu$ M and 3 $\mu$ M. However, neither concentration, when combined with imatinib, effectively prevented the shift in MFI ratio compared to imatinib treatment alone (**Figure 5-28**). Another experiment was conducted to assess whether autophagic block must be established before TKI treatment. In this experiment, K562 MitoQC cells were pre-treated with MRT403 for six hours before the addition of imatinib to the culture medium (**Figure 5-29**).

Nevertheless, priming the cells to inhibit autophagy failed to reduce the induction of mitophagy upon imatinib treatment.

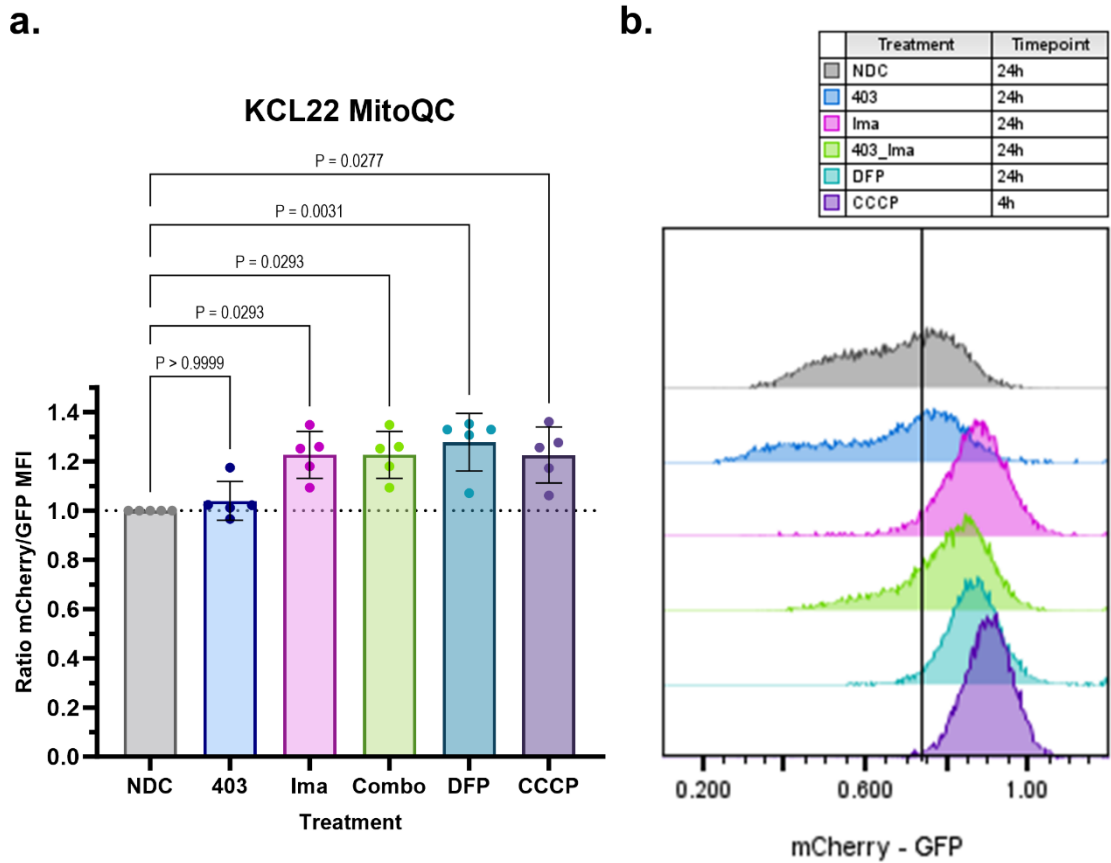


**Figure 5-27 Autophagy suppression with a ULK1 inhibitor did not prevent mitophagy induction.** KCL22 MitoQC cells were treated with 3 $\mu$ M MRT403 (403), 2 $\mu$ M imatinib (Ima) and the combination of both (Combo) for 24 hours. Control treatments involved exposing cells to 1mM DFP for 24 hours and 20 $\mu$ M CCCP for 4 hours. Bar blot (a) illustrates the ratio MFI (mCherry/GFP) normalised to the untreated cells (NDC). Representative histograms are illustrated in (b). Data are presented as mean  $\pm$  S.D. of n=5 independent experiments (each experiment calculated as mean from 2 individual wells on a plate). P-values were calculated using Kruskal-Wallis test and Dunnett's multiple comparison test.

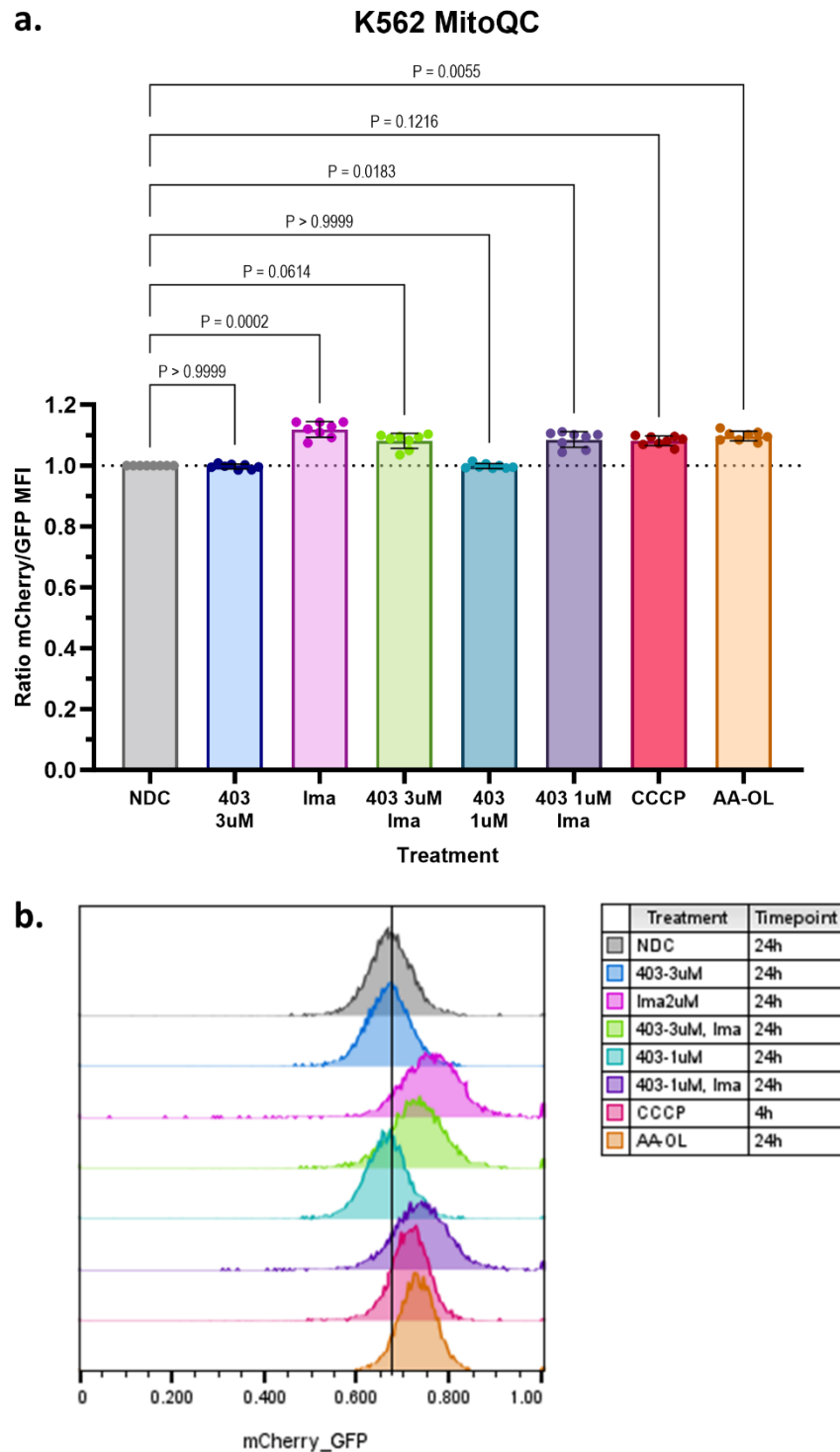


**Figure 5-28 ULK1 inhibition minimally reduced TKI-induced mitophagy in K562 MitoQC cells.** K562 MitoQC cells were treated with 1 $\mu$ M or 3 $\mu$ M MRT403 (403), 2 $\mu$ M imatinib (Ima) and the combination of both (403 Ima) for 24 hours. Control treatments were set up 20 $\mu$ M CCCP or 4 $\mu$ M antimycin A (AA) and 10 $\mu$ M oligomycin (OL) for 4h. Bar blot (a) represents the ratio MFI (mCherry/GFP), normalised to the no drug control (NDC). Representative histograms are illustrated in (b). The data were plotted as mean  $\pm$  S.D. of n=8 independent experiments (each experiment calculated as mean from 2 individual wells on a plate). P-values were calculated using Kruskal-Wallis test and Dunnett's multiple comparison test.

### K562 MitoQC pre-incubation with MRT403

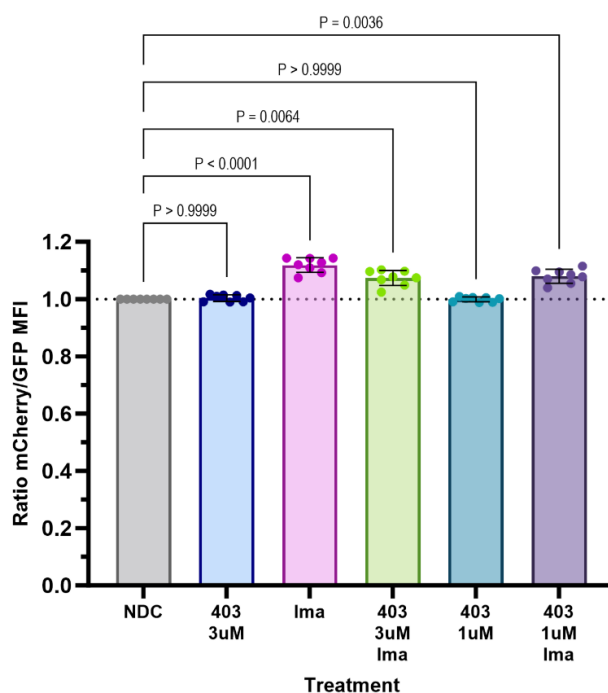


**Figure 5-29 Pre-treating K562 cells with an autophagy inhibitor did not counteract imatinib-induced mitophagy.** Initially, K562 MitoQC cells were exposed to 1 $\mu$ M or 3 $\mu$ M MRT403 (403) for 6 hours. In the combination (403 Ima) treatments, 2 $\mu$ M imatinib was introduced to the cell cultures for an additional 24 hours. Cells solely treated with 2 $\mu$ M imatinib (Ima) were incubated for 24 hours. The data were plotted as mean  $\pm$  S.D. of  $n=8$  independent experiments (each experiment calculated as mean from 2 individual wells on a plate). P-values were calculated using Kruskal-Wallis test and Dunnett's multiple comparison test.

To serve as controls, other autophagy inhibitors were employed in combination with imatinib. Bafilomycin A1 (BafA) is known for affecting the late stage of the autophagy machinery by inhibiting lysosomal acidification as well as blocking the fusion of the autophagosome with the lysosome<sup>405</sup>. While BafA is solely used for pre-clinical studies due to its high toxicity profile, hydroxychloroquine (HCQ), preventing the acidification of the lysosome, can be more safely used in clinical studies<sup>377</sup>. Similar to MRT403, both inhibitors failed to counteract the ratiometric change in fluorescence when combined with imatinib treatment (Figure 5-30).

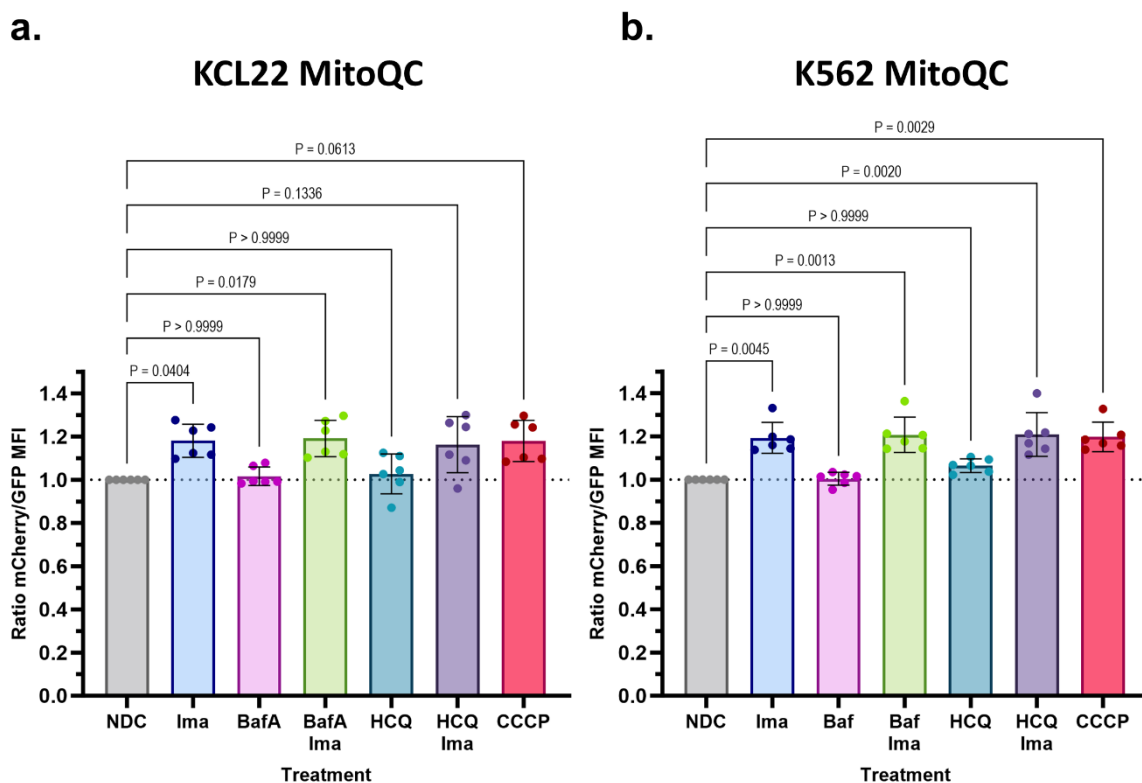


**Figure 5-30 Autophagy inhibitors BafA and HCQ failed to impede imatinib-induced mitophagy.** KCL22 MitoQC (a) and K562 MitoQC (b) cells were treated with 2 $\mu$ M imatinib (Ima), 100nM Bafilomycin (BafA), 20 $\mu$ M Hydroxychloroquine (HCQ) or a combination of Ima with either BafA or HCQ for 24 hours. A control treatment with 20 $\mu$ M CCCP was set up for 4 hours. The data were presented as mean  $\pm$  S.D. of n=6 independent experiments. P-values were calculated using Kruskal-Wallis test and Dunnett's multiple comparison test.

#### 5.5.4 Genetic ablation disrupting autophagic flux failed to mitigate TKI-induced mitophagy

Since autophagy inhibitors were not successful in counteracting TKI-induced mitophagy, a genetic approach was used to validate our results from this flow cytometry-based assay using ATG7 KO cells. Although autophagy is blocked, K562 and KCL22 MitoQC ATG7 KO cells treated with imatinib (Figure 5-31) exhibited a similar level of mitophagy induction as the respective WT cells (Figure 5-27, Figure 5-28). This is in contrast to data acquired using fluorescent microscopy, where we demonstrated that TKI-mediated mitophagy is abolished upon autophagy inhibition (Figure 5-15, Figure 5-16).

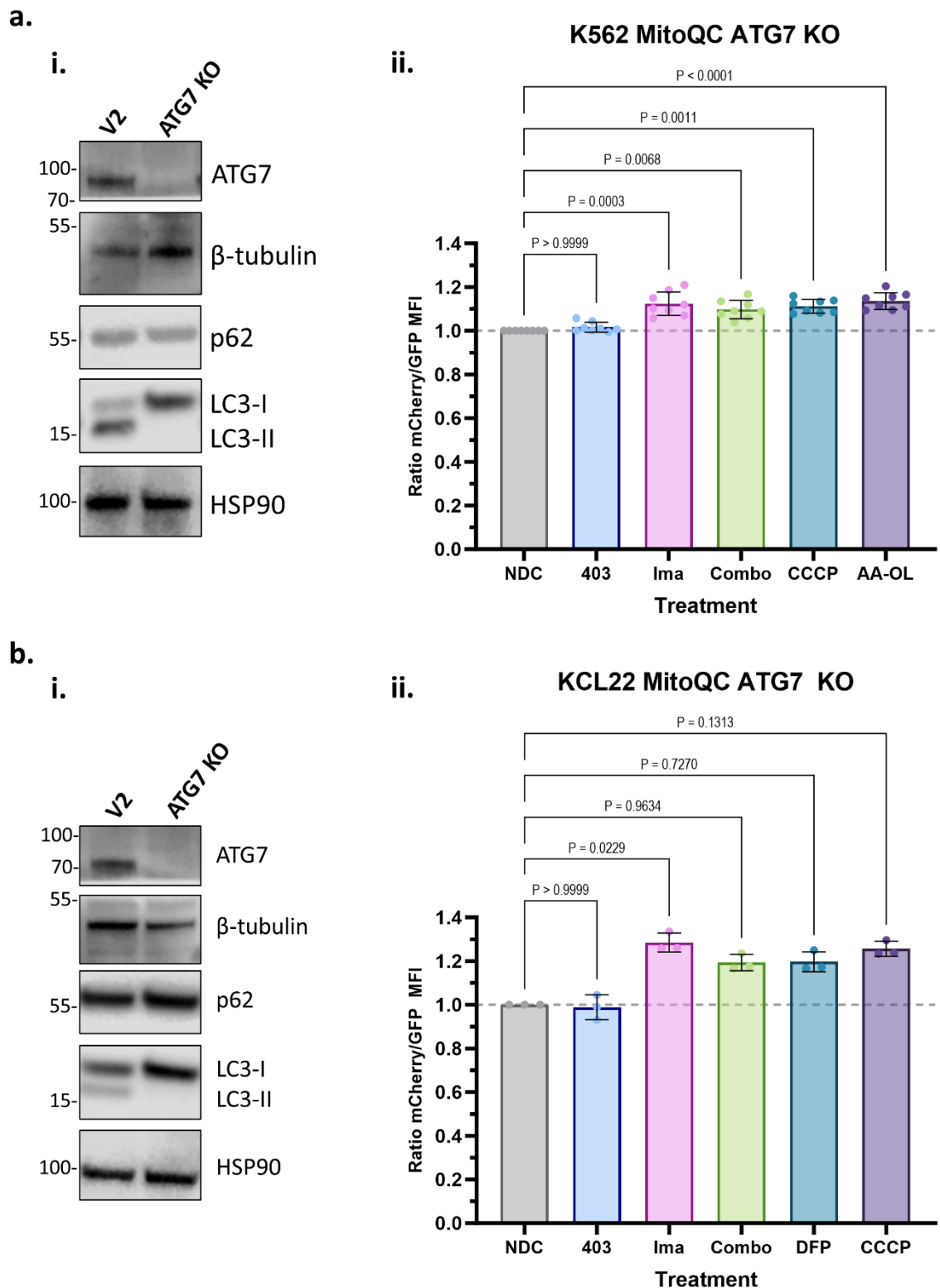


**Figure 5-31 Autophagy-deficient CML cells exhibited induction of mitophagy upon imatinib treatment.** Validation of ATG7 KO in K562 (a) and KCL22 (b) MitoQC cells was done via Western blotting using the antibodies for ATG7, p62 and LC3. As loading control HSP90 and  $\beta$ -tubulin were used (i). K562 (a) and KCL22 (b) MitoQC cells were treated with  $3\mu\text{M}$  MRT403 (403),  $2\mu\text{M}$  Imatinib (Ima), the combination of both (Combo) for 24h, followed by flow cytometry analysis. CCCP ( $20\mu\text{M}$ , 4h), DFP ( $1\text{mM}$ , 24h) or AA-OL ( $10\mu\text{M}$ ,  $5\mu\text{M}$ , 4h) and were used as control treatments. Bar charts illustrate Ratio MFI (mCherry/GFP) normalised to no drug control (NDC). The data presented in (a-ii) for K562 were plotted as mean  $\pm$  S.D. of  $n=5$  independent experiments (each experiment calculated as mean from 2 individual wells on a plate). The data plotted in (b-ii) represents  $n=3$  independent experiments. P-values were calculated using Kruskal-Wallis test and Dunnett's multiple comparison test.

### 5.5.5 Investigating an alternative mitophagy reporter gene mtKeima for flow cytometric analysis

Since the development of the MitoQC reporter gene, other constructs for measuring mitophagy have been developed, such as the mtKeima probe (**Figure 5-32a**). The Keima protein undergoes a change upon neutral or acidic pH and, similar to the MitoQC reporter gene, enables the measurement of mitochondria transferred to the lysosome<sup>406</sup>. The mtKeima probe has only one emission peak at 620nm, yet its excitation maximum shifts from 440nm at a neutral pH to 586nm under acidic conditions<sup>406</sup>. Studies have demonstrated that mtKeima probe exhibits a higher sensitivity in detecting mitophagy than the MitoQC probe due to its fluorescence shift and its higher resistance to lysosomal degradation<sup>406</sup>.

K562 mtKeima cells, generated by Daniele Sarnello, were treated with MRT403, imatinib and the combination of both for 24 hours (**Figure 5-32**). In contrast to findings in other cell lines where mtKeima demonstrated increased sensitivity in detecting mitophagy via flow cytometry<sup>407</sup>, our measurements showed similarity to those obtained with the MitoQC probe. The Combo treatment exhibited a slightly reduced level of mitophagy, comparable to that measured with the MitoQC assay. However, treatment with mitochondrial uncouplers, such as CCCP, and the combination of AA-OL led to a substantial increase in mitophagy with the mtKeima assay. Therefore, the mtKeima probe appears to be more sensitive in K562 cells during Pink1/Parkin-mediated mitophagy, however this was not observed when the cells were treated with TKI or DFP.

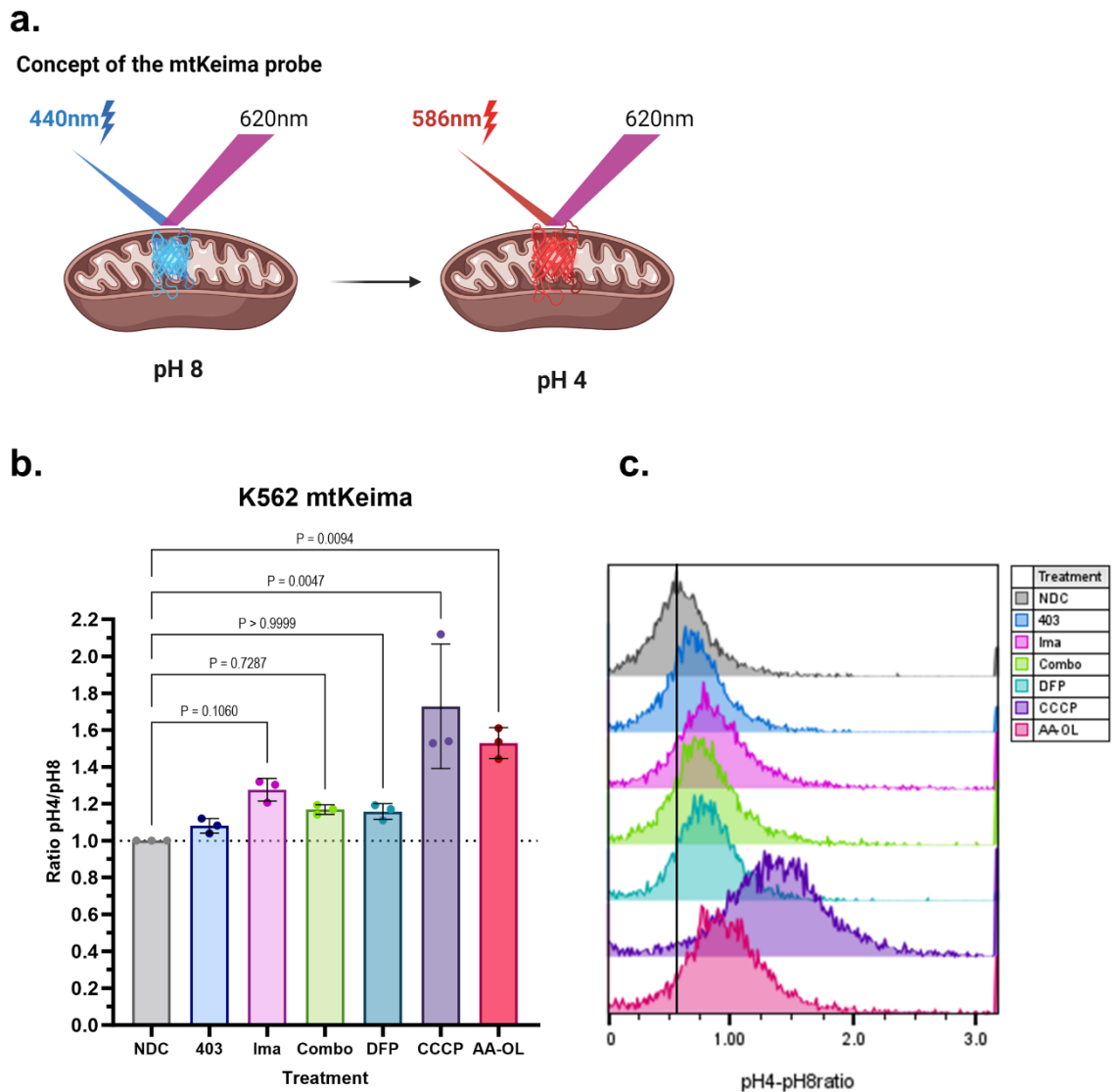


**Figure 5-32 Sensitivity of the mtKeima probe in flow cytometry analysis for detecting mitophagy induction in K562 cells.** The mtKeima probe allows to measure mitophagy due to its shift in excitation upon pH change (a). K562 mtKeima (b) cells were treated with 3 $\mu$ M MRT403 (403), 2 $\mu$ M imatinib (Ima) and a combination (Combo) of both for 24 hours. Control treatments were set up with 1mM DFP for 24 hours or 20 $\mu$ M CCCP and the combination of 4 $\mu$ M antimycin A and 10 $\mu$ M oligomycin (AA-OL) for 4 hours. The data were presented as mean  $\pm$  S.D. of n=3 independent experiments (each repeat was measured as a mean of 3 wells). P-values were calculated using Kruskal-Wallis test and Dunnett's multiple comparison test. Representative ratiometric histograms are plotted in (c). Created with BioRender.com.

## 5.6 Discussion

This section aimed to elucidate if human CML cells selectively degrade mitochondria in response to TKI treatment. Previous studies have established that autophagy plays a crucial role in LSC persistence following TKI therapy<sup>364,365</sup>. Detailed analyses using *in vitro* and *in vivo* data revealed that targeted therapy with TKIs, along with autophagy inhibitors, led to an oxidative-stress induced differentiation of LSCs<sup>367</sup>. As mitochondria are the primary source of ROS, and studies in other forms of leukaemia have demonstrated the necessity of a high turnover of mitochondria to maintain stemness in LSCs<sup>370</sup>, it led to the hypothesis that CML cells specifically target mitochondria for degradation to sustain survival.

At first, mitochondrial content was measured in cells treated with various concentrations of imatinib using two distinct assays. Mitochondrial content was assessed either through flow cytometry of KCL22 cells overexpressing Tom20-GFP (**Figure 5-1**) or by employing the MitoTracker dye with K562 cells (**Figure 5-2**). Both assays demonstrated a reduction in MFI upon treatment with imatinib suggesting mitochondria being degraded. Additionally, levels of Tom20, a mitochondrial protein, were assessed by Western blotting (**Figure 5-3**). Tom20 exhibited a reduction by 20% upon imatinib treatment in K562, with a partial lower induction in the combination treatment with the autophagy inhibitor MRT403. Conversely, KCL22 showed a more pronounced effect with 70% reduction in Tom20 levels following exposure to imatinib. While Western blotting confirmed previous results obtained from flow cytometry (**Figure 5-1**, **Figure 5-2**) and demonstrated reduced mitochondrial content, the levels of Tom20 exhibited considerable variability between experiments, requiring additional repetitions.

Besides increased mitophagy, a reduced mitochondrial mass could also result from reduced biogenesis upon treatment. The rate of mitophagy can be investigated using the tandem-reporter gene MitoQC, enabling the differentiation between healthy mitochondria and those undergoing mitophagy<sup>400</sup>. Overexpression of the GFP-mCherry-Fis1<sup>101-152</sup> protein, which localises to the mitochondrial membrane, takes advantages of the pH sensitivity of GFP. GFP is quenched in an acidic environment such as the lysosome, while

mCherry remains stable, leading to the formation of red 'puncta', signalling mitochondria being engulfed by the lysosome (**Figure 5-4**).

Therefore, K562 and KCL22 cell lines that stably express MitoQC, were developed using retroviral transduction followed by FACS purification (**Figure 5-5**). Super-resolution confocal live-cell microscopy was employed to visualise the mitochondria of the cells, revealing the presence of mCherry-'puncta' upon treatment with imatinib. The mean appearance of mitolysosomes per cell increased by approximately 5-fold in cells incubated with imatinib compared to untreated control (**Figure 5-7a**, **Figure 5-9a**). Moreover, the percentage of cells exhibiting any level of mitophagy was 4.6-times higher in the treated population compared to untreated cells. Approximately 15 to 20% of cells showed a level of basal mitophagy (**Figure 5-7b**, **Figure 5-9b**).

Subsequently, we treated both cell lines with the ULK1 inhibitor MRT403 to validate that the appearance of mitolysosomes is mediated by the autophagy machinery. Western blotting was performed to confirm the inhibition of BCR::ABL1 upon imatinib treatment (**Figure 5-11**) and to validate ULK1 inhibition following MRT403 treatment (**Figure 5-12**). While the single treatment with ULK1 did not affect appearance of mitolysosomes compared to the untreated cells, ULK1 inhibition successfully suppressed the formation of mitolysosomes to baseline in the combination treatment (**Figure 5-14**, **Figure 5-13**). These results were validated by using autophagy-deficient (ATG7 KO) cells, which were shown to prevent TKI-induced mitophagy in presence of imatinib (**Figure 5-15**, **Figure 5-16**). In both KO cell lines, an increase in mitophagy could be detected upon TKI treatment, unlike in the ATG7 KO cells where mitophagy was suppressed.

Next, we aimed to investigate whether mitophagy induction involved upregulation of a canonical mitophagy pathway. Initial assessment with Western blotting revealed an upregulation of Nix upon TKI treatment, while BNIP3 and Pink1 levels remained unaffected (**Figure 5-17**). Live-cell microscopy of KO cell lines for Nix and BNIP3 indicated that they are not essential for inducing mitophagy upon exposure to TKI (**Figure 5-19**, **Figure 5-20**, **Figure 5-21**). It should be noted that KO of either protein led to an overall increase in mitophagy at steady state, suggesting that the KO itself might introduce intracellular stress. Therefore, the observed mitophagy following TKI treatment in these cells

might not be solely mediated by the treatment itself but also be influenced by the KO-induced stress.

The potential of a high-throughput assay using flow cytometry was tested using known inducers of mitophagy; Both CCCP and AA-OL are recognised inducers of mitophagy, displaying an increase in mitophagy measured through ratiometric analysis of mCherry over GFP in a time-dependent manner (**Figure 5-22, Figure 5-23**). Apoptotic cells were excluded from flow cytometry analysis, though overall cell death within 24 hours was minimal (**Figure 5-24**). At four hours, the maximum reduction in GFP intensity was observed, while the mCherry signal remained consistent compared to the untreated cells (**Figure 5-25a**). Prolonged exposure (24 hours) resulted in the overall degradation of the mCherry-GFP labelled mitochondria, reverting the ratio analysis to baseline (**Figure 5-25b**). This indicates the necessity for careful evaluation of this assay to capture the precise moment when mitochondria are located within the lysosome.

We applied the flow cytometry assay to evaluate the induction of mitophagy by imatinib treatment over time, observing an increase in mitophagy after 16 to 24 hours (**Figure 5-26**), with a slightly more prominent effect in K562 cells. However, attempts to prevent mitophagy induction in KCL22 MitoQC cells by blocking autophagic flux using MRT403 (403), which inhibits ULK1, showed no success (**Figure 5-27**). Similarly, MRT403 treatment could only minimally decrease TKI-mediated mitophagy induction in K562 MitoQC cells (**Figure 5-28**). Under the circumstances that cells required priming for autophagy suppression, the inhibitor was added six hours before TKI treatment. However, this approach could not successfully prevent the TKI-mediated phenotype (**Figure 5-29**).

Other autophagy inhibitors, which act at a later stage by preventing autophagosome-lysosome fusion, such as BafA and HCQ, did not affect the induction of mitophagy when used in combination with imatinib either (**Figure 5-30**). Although the results of mitophagy induction appeared unaffected by autophagy inhibitors, the genetic approach using ATG7 KO was employed (**Figure 5-31**). However, flow cytometry analysis of autophagy-deficient cells yielded similar results to the control cells (**Figure 5-31**). Hence, it remains uncertain whether the observed effect is independent of the autophagy machinery or a

potential artifact from the assay itself. Notably, the dynamic range of this assay was small.

Recently, the MitoQC probe has been shown to exhibit variability in detecting mitophagy between cell lines as well as being less sensitive depending on the activated pathway compared to another mitophagy reporter gene, the mtKeima<sup>407</sup>. Similar to the MitoQC probe, this reporter gene utilised the pH difference between the cytosol and the lysosome and changes its excitation maximum from 440nm at a neutral pH to 586nm in an acidic environment<sup>406</sup>. The authors claim that the spectral switch in excitation results in a larger ratiometric change using the mtKeima probe compared to the MitoQC protein<sup>407</sup>. However, results obtained from K562 expressing mtKeima were found to be similar to those from the MitoQC assay when using flow cytometry to detect mitophagy following imatinib treatment. Although, the use of CCCP in mtKeima led to a 1.62-fold higher detection of mitophagy compared to measurements acquired in MitoQC cells (**Figure 5-28, Figure 5-32**). This was not the case for the mitophagy inducer DFP (**Figure 5-32**), indicating a higher sensitivity towards Pink1/Parkin-mediated mitophagy as previously demonstrated<sup>407</sup>.

## Chapter 6 Discussion

### 6.1 Introduction

The overarching aim of this study was to explore the CML BM niche, emphasising the significance of cell location in TKI resistance, particularly focusing on the role of non-selective and selective autophagy. Previous research has highlighted the vital role of autophagy as an important survival mechanism, especially in LSCs. However, whether autophagic degradation of specific proteins or organelles (such as mitochondria) occurs in this setting is not known. Autophagy is influenced by different metabolic environmental stressors such as hypoxia, nutrient deprivation, and inflammation. However, investigations into the interplay of leukaemic cells within the niche and the specific role of autophagy concerning their niche location remain unexplored in the context of CML.

To investigate this, we initially employed a genetic CML model and concurrently assessed a more tractable xenograft transplant model. Each models presented distinct challenges, underscoring the necessity for refinement. Finally, we aimed to unravel whether TKI treatment induces autophagy-mediated degradation of mitochondria and assessed the role of mitophagy in TKI resistance through *in vitro*-based assays. In this final chapter, we discuss potential avenues for future exploration and development.

### 6.2 Future outlook investigating LSCs in the BM niche

This project focused on applying different GEMM models to investigate LSCs within the BM niche. The SCL-tTA/BCR::ABL1 GFP-LC3 model proved effective in studying autophagy in primitive leukaemic cells *in vitro*. However, challenges arose in detecting GFP<sup>+</sup> LSCs within the BM niche, limiting the model's ability to localise LSCs in their physiological environment. Further experiments using injectable fluorescent antibodies showed some promise but requires optimisation and testing of different fluorophore conjugation and clones.

Furthermore, we assessed the potential of *ex vivo* dyes for long-term tracking, where many challenges arose during staining the cells, which either led to unequal staining or too harsh conditions of staining. Furthermore, there is

potential that these dyes give microenvironmental contamination when not optimised properly<sup>408</sup>. Too high usage of the dye can increase this potential and needs to be considered during optimisation. Moreover, staining optimisation and evaluation of long-term maintenance could be done using primary mouse HSCs *in vitro* in an expansion culture<sup>384</sup> compared to culture conditions maintaining cells in quiescence<sup>409</sup>.

This study also investigated various BM transplantation methods with the aim of minimising the impact on the BM microenvironment while successfully transplanting DTG cells into WT recipient mice. The widely used technique of total-body irradiation, although effective, poses complications such as gut toxicity and BM damage, including microvascular and stromal cell impairment<sup>75,386</sup>. To address this, an alternative approach using busulfan was explored to condition mouse BM<sup>383</sup>. While initially successful engraftment was achieved with cKit-enriched cells, challenges arose in replicating consistent engraftment in larger cohorts aimed to study the transplanted cells within the niche. One potential factor is consistent storage of the drug and dosing of the mice, and this should be addressed.

The transplant of cells into non-conditioned mice was tested with 400,000 cKit-enriched cells but the cells failed to engraft. Recently published data show that an increased number of transplanted LT-HSCs does indeed lead to successful engraftment<sup>384</sup>. To achieve such high numbers, the authors established an *ex vivo* expansion culture that increases the number of HSCs by 16,000-fold within four weeks<sup>384</sup>. Expanding cells this way could be an option to be explored for transplant into non-conditioned mice. Furthermore, cells could be modified via lentiviral transduction to introduce fluorescent markers or generate specific KO cells.

We generated another fluorescent model by crossing the SCL-tTA/BCR::ABL1 mouse with the mTmG model, which allows visualisation of cells within the BM niche as they express membrane-bound tdTom. This model was tested for establishing chimeras in CD45.1 recipient mice using the busulfan method for conditioning, as well as total-body irradiation. While busulfan-conditioning led to highly variable engraftments, as discussed above, complications arose during leukaemia induction in DTG mice conditioned with irradiation. Onset of

leukaemia was sudden and led to unexpected deterioration and mortality between 10 to 14 days post-induction, potentially due to high presence of Ph<sup>+</sup> LT-HSCs. Since purification of haematopoietic cells is required, lower numbers of LT-HSCs should be transplanted, and leukaemia development observed via blood tests for granulocyte percentage. A starting number would be 200,000 cKit enriched cells or 200 LT-HSCs along with up to two million carrier cells.

### **6.3 Future outlook on investigating the leukaemic niche by using xenograft mouse models**

This project aimed to establish a xenograft mouse model to investigate the *in vivo* localisation and potential interactions of human leukaemic cells within the BM microenvironment, with final objective of understanding how the niche contributes to TKI resistance. The study initially assessed two Ph<sup>+</sup> cell lines, K562 and KCL22, for their potential to engraft in the BM, with subsequent transformation for stable GFP expression for *in vivo* visualisation.

The findings revealed limited BM engraftment for both K562 and KCL22, with minimal and variable detection in the calvarium. Since the pilot experiment did not show any BM engraftment of KCL22, compared to a small percentage of K562 being located within the BM, the remaining work was mainly performed with K562 cells.

Discrepancies between male and female mice were observed, with female mice primarily developing extramedullary tumours, while we observed high infiltration of the brain in male mice. Notably, BM engraftment detected via flow cytometry did not always align with the presence of cells in the calvarial BM space, indicating complex migration dynamics to various bone regions. Overall, the majority of the conducted experiments showed few to no GFP<sup>+</sup> cells residing within the calvarium, with highly variable engraftment to the BM in the long bones. BM engraftment to male mice was rare, but even among females the engraftment was highly variable within experiments. Priming cells in hypoxia (1% O<sub>2</sub>) for 72 hours did not affect BM engraftment, but slightly reduced tumour formation. In an attempt to evaluate the role of autophagy upon BM engraftment and tumour formation, we transplanted K562 ATG7 KO cells, which had slightly reduced tumour formation but similarly low engraftment potential as control

cells. Attempts to condition the BM before transplantation with busulfan required optimisation of NRGW mice dosing, which is currently ongoing.

Further experiments involved Jurl cells, which were hypothesised to exhibit higher BM engraftment potential due to high expression levels of cKit<sup>395</sup>. Jurl cells did indeed show higher engraftment potential compared to K562, but we did not validate if this is due to elevated cKit expression. Mice exhibited an increasing population of Jurl cells within the BM over the time period of five weeks, although more mice per timepoint are required to validate this. While colonisation of the calvarial BM space is low at the four-week time point, we observed fully infiltrated BM pockets after five weeks. Longitudinal IVM could be used to analyse the colonisation dynamics of Jurl cells.

The role of autophagy was explored using Jurl ATG7 KO cells compared to control cells. This revealed a high tendency of ATG7 KO cells to localise to the spleen, while there were no control cells found to infiltrate the spleen, as in the previous experiment. BM engraftment was increased in the ATG7 KO group, while tumour formation was reduced compared to the control group. Overall, this shows different dynamics to K562 cells as well as previous experiments with Jurl WT cells. This requires not only repetition but should be supplemented with respective *in vitro* studies regarding the role of autophagy upon TKI treatment in Jurl cells.

Autophagic flux may be assessed by microscopy using the tandem-dye RFP-GFP-LC3 construct<sup>410</sup>, which forms red 'puncta' upon autophagy induction. GFP is quenched in the lysosome and more red 'puncta' are detected upon autophagy detection. A different construct is the GFP-LC3-RFP-LC3ΔG reporter gene, in which GFP-LC3 is fused RFP-LC3ΔG, lacking the c-terminal glycine<sup>411</sup>. After expression, the proteins are separated by action of endogenous ATG4 family proteases. As equal amounts of GFP-LC3 and RFP-LC3ΔG are expressed, but only GFP-LC3 can undergo lipidation and incorporated into autophagosome, RFP-LC3ΔG remains in the cytoplasm as an internal control<sup>411</sup>. This tool could also be used *in vivo* for analysing autophagic flux of cells engrafted to the BM compared to formation of extramedullary tumours or infiltration of the spleen.

Overall, it should be noted that while these findings provide insights into BM migration dynamics of leukaemic cells, this study was conducted with a restricted number of mice. Further investigations with larger cohorts are necessary to validate and generalise these observations. Moreover, in the absence of BM conditioning, both K562 and KCL22 demonstrated low potential for BM engraftment. While Jurk cells exhibit a higher potential to localise to the BM, their affinity to different BM niches, such as leg bones or the calvarium, showed considerable variability especially regarding autophagy-deficient cells. It should be noted that this project aimed to develop models for studying leukaemic cells in the BM niche, therefore numerous experiments were conducted over different timeframes, introducing another variable into the interpretation.

## **6.4 Investigation into the role of mitophagy in TKI resistance in CML**

### **6.4.1 Summary**

In parallel, the last chapter of this project focused on investigating whether CML cells selectively degrade mitochondria in response to TKI treatment. Previous research highlighted autophagy as an important survival mechanism in LSCs, maintaining cells in a state of low ROS<sup>367</sup>. However, whether selective autophagy is involved in this mechanism is not known. Various assays, including flow cytometry and Western blotting, were used to measure mitochondrial content in KCL22 and K562 cells, which was reduced upon exposure to the TKI imatinib, suggesting induction of mitophagy. More biological repeats should be performed to validate these measurements.

We then employed the tandem-reporter gene MitoQC, to visualise and quantify mitophagy occurring in KCL22 and K562 using live-cell microscopy, revealing an increase in mitolysosomes upon TKI treatment. We utilised MRT403, an autophagy inhibitor blocking ULK1 activity, as well as ATG7 KO cells to validate that the mitophagy induction was mediated by autophagy. Both assays showed reduction of mitophagy, which could be restored to basal levels in either the combination treatment of imatinib and MRT403, or treatment of imatinib in

autophagy-deficient cells. However, some of the data did not result in being statistically significant, and further repetitions are needed for validation.

Further exploration into the canonical mitophagy pathways involved assessing proteins levels by Western blotting, showing an accumulation of Nix but not BNIP3 or Pink1 upon TKI treatment in both KCL22 and K562 cells. Following this, KO cells of Nix or BNIP3 were exposed to imatinib to evaluate mitolysosomes formation using live-cell microscopy. The results obtained from these experiments were not clear, as the KO cells exhibited slightly increased mCherry-‘puncta’ indicating mitophagy without BCR::ABL1 inhibition. Therefore, only a small increase was observed comparing untreated KO cells with TKI-treated KO cells. Assessing percentages of cells undergoing mitophagy showed a higher basal mitophagy in the KO cells, with an increase upon TKI treatment. However, these results were variable across biological repeats and require more repetition to validate.

A high-throughput flow cytometry assay was assessed for compatibility with the MitoQC probe. Initially, a small increase in mitophagy measured by the ratio change of mCherry/GFP was noted upon TKI treatment as well as with known mitophagy inducers such as CCCP, AA-OL or DFP. However, attempts to block mitophagy using autophagy inhibitors, similarly to the live-cell microscopy, failed, raising questions about the specificity of the observed effect to be related to mitophagy or a mere artefact. We also employed another mitophagy reporter gene, mtKeima, with flow cytometry, as it was noted to be more sensitive than MitoQC<sup>407</sup>. Although, the mtKeima probe exhibited higher sensitivity to certain mitophagy inducers, such as CCCP, autophagy inhibition could not restore the TKI-mediated mitophagy and the dynamic range was equally as low as with MitoQC.

### 6.4.2 Future directions

It has been shown that Nix and BNIP3 can compensate for each other in some cell lines, where only a double KO could suppress hypoxia-induced mitophagy<sup>403</sup>. To assess if this is the case in TKI-mediated mitophagy, levels of Nix and BNIP3 could be measured via Western blotting upon TKI treatment in the respective KO cell line, to validate if the KO of one protein induces the upregulation of the

other. Furthermore, Nix requires dimerization to actively mediate mitophagy<sup>342</sup>. However, we were not able to detect the Nix dimers in whole protein lysates. Therefore, mitochondria could be isolated to validate that not only does Nix accumulate but is also forming dimers and actively recruiting the autophagy machinery. Further, the double KO of Nix and BNIP3 could be utilised to evaluate their role in TKI-mediated mitophagy. This could be done using live-cell microscopy or with a combined approach using “ImageStream”, an imaging flow cytometry technique where cells can be visualised directly in a high-throughput flow-based manner. Hereby, cells can be analysed by flow cytometry as well as acquiring microscopic images at the same time.

It should be noted that the single KO of either Nix or BNIP3 increased the rate of mitophagy in untreated cells, indicating that they might be required to maintain cell homeostasis. Therefore, oxidative stress should be measured in the KO cell lines using fluorogenic dyes, such as CellROX and MitoSOX. Additionally, cell viability assays should be performed as both proteins belong to the pro-apoptotic BH3-only family, a subfamily within the Bcl2 family and have been shown to bind other anti-apoptotic proteins such as Bcl2-XL or Bcl-2<sup>412</sup>. They have been shown to favour cell survival over their pro-apoptotic function in hypoxia<sup>403</sup>. As leukaemia cells reside in the BM, which is known to be an environment with low oxygen, it would be interesting to conduct these experiments in hypoxia. However, this would require a set up that allows researchers to maintain hypoxia throughout the imaging, or the fixation of cells. Overall, our investigations of mitophagy pathways exhibited a higher degree of variability and should be repeated and confirmed using additional cell lines, such as KCL22. Another canonical pathway that is less explored is mediated by the mitophagy receptor FUNDC1, which is, as BNIP3, phosphorylated by ULK1<sup>413,414</sup>, and could be activated upon TKI treatment.

While our experiments present intriguing findings and potential links between mitophagy and TKI therapy in CML, the variability in results emphasises the necessity for additional investigations and more comprehensive studies to delineate the precise role of mitophagy in CML pathogenesis. Our *in vitro* experiments suggest that TKI treatment indeed leads to some level of selective degradation of mitochondria, likely to promote survival by turning over excess

mitochondria. Our results suggest that Nix, and perhaps BNIP3, play a role in this process, although further investigation is required for full understanding of the underlying mechanisms of TKI-induced mitophagy.

To establish biological relevance, assessments should be conducted in primary CML LSCs using the MitoQC reporter gene. Moreover, exploring the disruption of mitochondrial fission by knocking down Fis1 could provide more insights into the significance of heightened mitophagy flux upon TKI treatment, similar to observations in AML LSCs<sup>370</sup>. Furthermore, *in vivo* studies could be conducted by using the available MitoQC mouse model, which could be crossed with the CML SCL-tTA/BCR::ABL1 model. This would allow assessment of the rate of mitophagy in LSCs compared to more differentiated progenitors as well as localisation of cells exhibiting high mitophagy in the BM if compatible with IVM.

## 6.5 Summary

Despite encountering numerous challenges in developing the tools to study leukaemic cells within their physiological environment, this endeavour has been invaluable in our learning process. This marks our lab's beginning at *in vivo* microscopy in the BM, integrating functional and analytical assays with real-time visual data. As we successfully adapted IVM at our institute, this achievement positions us to advance our research and opens new possibilities for discovery and innovation.

The application of advanced imaging techniques to unravel the roles of biological processes, such as autophagy and metabolism, which are highly influenced by the environment, remains an understudied frontier. Often hindered by a lack of imaging equipment and tools, our progress in this venture opens avenues for novel findings in the future, filling crucial gaps in our knowledge in leukaemia and perhaps other cancer types.

## List of References

- 1 Kaushansky, K. *et al.* in *Williams Hematology, 9e* (McGraw-Hill Education, 2015).
- 2 Hajdu, S. I. The first use of the microscope in medicine. *Ann Clin Lab Sci* **32**, 309-310 (2002).
- 3 Hajdu, S. I. A note from history: The discovery of blood cells. *Ann Clin Lab Sci* **33**, 237-238 (2003).
- 4 Forrester, J. M. Malpighi's *De polypo cordis*: an annotated translation. *Med Hist* **39**, 477-492 (1995). <https://doi.org/10.1017/s0025727300060385>
- 5 Boisset, J. C. & Robin, C. On the origin of hematopoietic stem cells: progress and controversy. *Stem Cell Res* **8**, 1-13 (2012). <https://doi.org/10.1016/j.scr.2011.07.002>
- 6 Ramalho-Santos, M. & Willenbring, H. On the origin of the term "stem cell". *Cell Stem Cell* **1**, 35-38 (2007). <https://doi.org/10.1016/j.stem.2007.05.013>
- 7 Till, J. E. & Mc, C. E. A direct measurement of the radiation sensitivity of normal mouse bone marrow cells. *Radiat Res* **14**, 213-222 (1961).
- 8 Becker, A. J., Mc, C. E. & Till, J. E. Cytological demonstration of the clonal nature of spleen colonies derived from transplanted mouse marrow cells. *Nature* **197**, 452-454 (1963). <https://doi.org/10.1038/197452a0>
- 9 Siminovitch, L., McCulloch, E. A. & Till, J. E. THE DISTRIBUTION OF COLONY-FORMING CELLS AMONG SPLEEN COLONIES. *J Cell Comp Physiol* **62**, 327-336 (1963). <https://doi.org/10.1002/jcp.1030620313>
- 10 Pietras, E. M. *et al.* Functionally Distinct Subsets of Lineage-Biased Multipotent Progenitors Control Blood Production in Normal and Regenerative Conditions. *Cell Stem Cell* **17**, 35-46 (2015). <https://doi.org/10.1016/j.stem.2015.05.003>
- 11 Cheng, H., Zheng, Z. & Cheng, T. New paradigms on hematopoietic stem cell differentiation. *Protein Cell* **11**, 34-44 (2020). <https://doi.org/10.1007/s13238-019-0633-0>
- 12 Sanjuan-Pla, A. *et al.* Platelet-biased stem cells reside at the apex of the haematopoietic stem-cell hierarchy. *Nature* **502**, 232-236 (2013). <https://doi.org/10.1038/nature12495>
- 13 Carrelha, J. *et al.* Hierarchically related lineage-restricted fates of multipotent haematopoietic stem cells. *Nature* **554**, 106-111 (2018). <https://doi.org/10.1038/nature25455>
- 14 Yamamoto, R. *et al.* Clonal analysis unveils self-renewing lineage-restricted progenitors generated directly from hematopoietic stem cells. *Cell* **154**, 1112-1126 (2013). <https://doi.org/10.1016/j.cell.2013.08.007>
- 15 Liggett, L. A. & Sankaran, V. G. Unraveling Hematopoiesis through the Lens of Genomics. *Cell* **182**, 1384-1400 (2020). <https://doi.org/10.1016/j.cell.2020.08.030>
- 16 Velten, L. *et al.* Human haematopoietic stem cell lineage commitment is a continuous process. *Nature Cell Biology* **19**, 271-281 (2017). <https://doi.org/10.1038/ncb3493>
- 17 Karamitros, D. *et al.* Single-cell analysis reveals the continuum of human lympho-myeloid progenitor cells. *Nature Immunology* **19**, 85-97 (2018). <https://doi.org/10.1038/s41590-017-0001-2>
- 18 Muller-Sieburg, C. E., Whitlock, C. A. & Weissman, I. L. Isolation of two early B lymphocyte progenitors from mouse marrow: a committed pre-pre-B cell and a clonogenic Thy-1-lo hematopoietic stem cell. *Cell* **44**, 653-662 (1986). [https://doi.org/10.1016/0092-8674\(86\)90274-6](https://doi.org/10.1016/0092-8674(86)90274-6)

- 19 Spangrude, G. J., Heimfeld, S. & Weissman, I. L. Purification and characterization of mouse hematopoietic stem cells. *Science* **241**, 58-62 (1988). <https://doi.org/10.1126/science.2898810>
- 20 Morrison, S. J. & Weissman, I. L. The long-term repopulating subset of hematopoietic stem cells is deterministic and isolatable by phenotype. *Immunity* **1**, 661-673 (1994). [https://doi.org/10.1016/1074-7613\(94\)90037-x](https://doi.org/10.1016/1074-7613(94)90037-x)
- 21 Baum, C. M., Weissman, I. L., Tsukamoto, A. S., Buckle, A. M. & Peault, B. Isolation of a candidate human hematopoietic stem-cell population. *Proc Natl Acad Sci U S A* **89**, 2804-2808 (1992). <https://doi.org/10.1073/pnas.89.7.2804>
- 22 Bhatia, M., Wang, J. C., Kapp, U., Bonnet, D. & Dick, J. E. Purification of primitive human hematopoietic cells capable of repopulating immune-deficient mice. *Proc Natl Acad Sci U S A* **94**, 5320-5325 (1997). <https://doi.org/10.1073/pnas.94.10.5320>
- 23 Osawa, M., Hanada, K., Hamada, H. & Nakauchi, H. Long-term lymphohematopoietic reconstitution by a single CD34-low/negative hematopoietic stem cell. *Science* **273**, 242-245 (1996). <https://doi.org/10.1126/science.273.5272.242>
- 24 Kiel, M. J., Yilmaz, O. H., Iwashita, T., Terhorst, C. & Morrison, S. J. SLAM family receptors distinguish hematopoietic stem and progenitor cells and reveal endothelial niches for stem cells. *Cell* **121**, 1109-1121 (2005). <https://doi.org/10.1016/j.cell.2005.05.026>
- 25 Purton, L. E. & Scadden, D. T. Limiting factors in murine hematopoietic stem cell assays. *Cell Stem Cell* **1**, 263-270 (2007). <https://doi.org/10.1016/j.stem.2007.08.016>
- 26 Goodell, M. A., Brose, K., Paradis, G., Conner, A. S. & Mulligan, R. C. Isolation and functional properties of murine hematopoietic stem cells that are replicating in vivo. *J Exp Med* **183**, 1797-1806 (1996). <https://doi.org/10.1084/jem.183.4.1797>
- 27 Phillips, R. L., Reinhart, A. J. & Van Zant, G. Genetic control of murine hematopoietic stem cell pool sizes and cycling kinetics. *Proceedings of the National Academy of Sciences* **89**, 11607-11611 (1992). <https://doi.org/doi:10.1073/pnas.89.23.11607>
- 28 Kim, M., Cooper, D. D., Hayes, S. F. & Spangrude, G. J. Rhodamine-123 staining in hematopoietic stem cells of young mice indicates mitochondrial activation rather than dye efflux. *Blood* **91**, 4106-4117 (1998).
- 29 Bowie, M. B. *et al.* Hematopoietic stem cells proliferate until after birth and show a reversible phase-specific engraftment defect. *J Clin Invest* **116**, 2808-2816 (2006). <https://doi.org/10.1172/jci28310>
- 30 Passegué, E., Wagers, A. J., Giuriato, S., Anderson, W. C. & Weissman, I. L. Global analysis of proliferation and cell cycle gene expression in the regulation of hematopoietic stem and progenitor cell fates. *J Exp Med* **202**, 1599-1611 (2005). <https://doi.org/10.1084/jem.20050967>
- 31 Wilson, A. *et al.* Hematopoietic stem cells reversibly switch from dormancy to self-renewal during homeostasis and repair. *Cell* **135**, 1118-1129 (2008). <https://doi.org/10.1016/j.cell.2008.10.048>
- 32 Foudi, A. *et al.* Analysis of histone 2B-GFP retention reveals slowly cycling hematopoietic stem cells. *Nature Biotechnology* **27**, 84-90 (2009). <https://doi.org/10.1038/nbt.1517>
- 33 Sun, J. *et al.* Clonal dynamics of native haematopoiesis. *Nature* **514**, 322-327 (2014). <https://doi.org/10.1038/nature13824>

- 34 Busch, K. *et al.* Fundamental properties of unperturbed haematopoiesis from stem cells in vivo. *Nature* **518**, 542-546 (2015).  
<https://doi.org/10.1038/nature14242>
- 35 Pietras, E. M., Warr, M. R. & Passegué, E. Cell cycle regulation in hematopoietic stem cells. *J Cell Biol* **195**, 709-720 (2011).  
<https://doi.org/10.1083/jcb.201102131>
- 36 Harrison, D. E. & Astle, C. M. Loss of stem cell repopulating ability upon transplantation. Effects of donor age, cell number, and transplantation procedure. *J Exp Med* **156**, 1767-1779 (1982).  
<https://doi.org/10.1084/jem.156.6.1767>
- 37 Allsopp, R. C., Morin, G. B., DePinho, R., Harley, C. B. & Weissman, I. L. Telomerase is required to slow telomere shortening and extend replicative lifespan of HSCs during serial transplantation. *Blood* **102**, 517-520 (2003).  
<https://doi.org/10.1182/blood-2002-07-2334>
- 38 Simsek, T. *et al.* The distinct metabolic profile of hematopoietic stem cells reflects their location in a hypoxic niche. *Cell Stem Cell* **7**, 380-390 (2010).  
<https://doi.org/10.1016/j.stem.2010.07.011>
- 39 Takubo, K. *et al.* Regulation of glycolysis by Pdk functions as a metabolic checkpoint for cell cycle quiescence in hematopoietic stem cells. *Cell Stem Cell* **12**, 49-61 (2013). <https://doi.org/10.1016/j.stem.2012.10.011>
- 40 Itkin, T. *et al.* Distinct bone marrow blood vessels differentially regulate haematopoiesis. *Nature* **532**, 323-328 (2016).  
<https://doi.org/10.1038/nature17624>
- 41 Miyamoto, K. *et al.* Foxo3a is essential for maintenance of the hematopoietic stem cell pool. *Cell Stem Cell* **1**, 101-112 (2007).  
<https://doi.org/10.1016/j.stem.2007.02.001>
- 42 Golan, K. *et al.* S1P promotes murine progenitor cell egress and mobilization via S1P1-mediated ROS signaling and SDF-1 release. *Blood* **119**, 2478-2488 (2012). <https://doi.org/10.1182/blood-2011-06-358614>
- 43 Katajisto, P. *et al.* Stem cells. Asymmetric apportioning of aged mitochondria between daughter cells is required for stemness. *Science* **348**, 340-343 (2015). <https://doi.org/10.1126/science.1260384>
- 44 Eliasson, P. & Jönsson, J. I. The hematopoietic stem cell niche: low in oxygen but a nice place to be. *J Cell Physiol* **222**, 17-22 (2010).  
<https://doi.org/10.1002/jcp.21908>
- 45 Tothova, Z. *et al.* FoxOs are critical mediators of hematopoietic stem cell resistance to physiologic oxidative stress. *Cell* **128**, 325-339 (2007).  
<https://doi.org/10.1016/j.cell.2007.01.003>
- 46 Ho, T. T. *et al.* Autophagy maintains the metabolism and function of young and old stem cells. *Nature* **543**, 205-210 (2017).  
<https://doi.org/10.1038/nature21388>
- 47 Yu, W. M. *et al.* Metabolic regulation by the mitochondrial phosphatase PTPMT1 is required for hematopoietic stem cell differentiation. *Cell Stem Cell* **12**, 62-74 (2013). <https://doi.org/10.1016/j.stem.2012.11.022>
- 48 Ito, K. & Suda, T. Metabolic requirements for the maintenance of self-renewing stem cells. *Nat Rev Mol Cell Biol* **15**, 243-256 (2014).  
<https://doi.org/10.1038/nrm3772>
- 49 Ansó, E. *et al.* The mitochondrial respiratory chain is essential for haematopoietic stem cell function. *Nat Cell Biol* **19**, 614-625 (2017).  
<https://doi.org/10.1038/ncb3529>
- 50 Kohli, L. & Passegué, E. Surviving change: the metabolic journey of hematopoietic stem cells. *Trends Cell Biol* **24**, 479-487 (2014).  
<https://doi.org/10.1016/j.tcb.2014.04.001>

- 51 Ito, K., Bonora, M. & Ito, K. Metabolism as master of hematopoietic stem cell fate. *Int J Hematol* **109**, 18-27 (2019). <https://doi.org/10.1007/s12185-018-2534-z>
- 52 Owusu-Ansah, E. & Banerjee, U. Reactive oxygen species prime *Drosophila* haematopoietic progenitors for differentiation. *Nature* **461**, 537-541 (2009). <https://doi.org/10.1038/nature08313>
- 53 Rattigan, K. M., Zarou, M. M. & Helgason, G. V. Metabolism in stem cell-driven leukemia: parallels between hematopoiesis and immunity. *Blood* **141**, 2553-2565 (2023). <https://doi.org/10.1182/blood.2022018258>
- 54 Mikkola, H. K. & Orkin, S. H. The journey of developing hematopoietic stem cells. *Development* **133**, 3733-3744 (2006). <https://doi.org/10.1242/dev.02568>
- 55 de Bruijn, M. F., Speck, N. A., Peeters, M. C. & Dzierzak, E. Definitive hematopoietic stem cells first develop within the major arterial regions of the mouse embryo. *Embo j* **19**, 2465-2474 (2000). <https://doi.org/10.1093/emboj/19.11.2465>
- 56 Ivanovs, A. *et al.* Highly potent human hematopoietic stem cells first emerge in the intraembryonic aorta-gonad-mesonephros region. *J Exp Med* **208**, 2417-2427 (2011). <https://doi.org/10.1084/jem.20111688>
- 57 Gekas, C., Dieterlen-Lièvre, F., Orkin, S. H. & Mikkola, H. K. The placenta is a niche for hematopoietic stem cells. *Dev Cell* **8**, 365-375 (2005). <https://doi.org/10.1016/j.devcel.2004.12.016>
- 58 Ottersbach, K. & Dzierzak, E. The murine placenta contains hematopoietic stem cells within the vascular labyrinth region. *Dev Cell* **8**, 377-387 (2005). <https://doi.org/10.1016/j.devcel.2005.02.001>
- 59 Gekas, C. *et al.* Hematopoietic stem cell development in the placenta. *Int J Dev Biol* **54**, 1089-1098 (2010). <https://doi.org/10.1387/ijdb.103070cg>
- 60 Ema, H. & Nakauchi, H. Expansion of hematopoietic stem cells in the developing liver of a mouse embryo. *Blood* **95**, 2284-2288 (2000).
- 61 Gao, X., Xu, C., Asada, N. & Frenette, P. S. The hematopoietic stem cell niche: from embryo to adult. *Development* **145** (2018). <https://doi.org/10.1242/dev.139691>
- 62 Schofield, R. The relationship between the spleen colony-forming cell and the haemopoietic stem cell. *Blood Cells* **4**, 7-25 (1978).
- 63 Dexter, T. M., Allen, T. D. & Lajtha, L. G. Conditions controlling the proliferation of haemopoietic stem cells in vitro. *J Cell Physiol* **91**, 335-344 (1977). <https://doi.org/10.1002/jcp.1040910303>
- 64 Kricun, M. E. Red-yellow marrow conversion: Its effect on the location of some solitary bone lesions. *Skeletal Radiology* **14**, 10-19 (1985). <https://doi.org/10.1007/BF00361188>
- 65 Pinho, S. & Frenette, P. S. Haematopoietic stem cell activity and interactions with the niche. *Nat Rev Mol Cell Biol* **20**, 303-320 (2019). <https://doi.org/10.1038/s41580-019-0103-9>
- 66 Standing, S. *Gray's anatomy: the anatomical basis of clinical practice*. Forty-second edn, (Elsevier, 2021).
- 67 Kunisaki, Y. *et al.* Arteriolar niches maintain haematopoietic stem cell quiescence. *Nature* **502**, 637-643 (2013). <https://doi.org/10.1038/nature12612>
- 68 Watson, E. C. & Adams, R. H. Biology of Bone: The Vasculature of the Skeletal System. *Cold Spring Harb Perspect Med* **8** (2018). <https://doi.org/10.1101/cshperspect.a031559>
- 69 Taichman, R. S. & Emerson, S. G. Human osteoblasts support hematopoiesis through the production of granulocyte colony-stimulating

- factor. *J Exp Med* **179**, 1677-1682 (1994).  
<https://doi.org/10.1084/jem.179.5.1677>
- 70 Visnjic, D. *et al.* Hematopoiesis is severely altered in mice with an induced osteoblast deficiency. *Blood* **103**, 3258-3264 (2004).  
<https://doi.org/10.1182/blood-2003-11-4011>
- 71 Calvi, L. M. *et al.* Osteoblastic cells regulate the haematopoietic stem cell niche. *Nature* **425**, 841-846 (2003). <https://doi.org/10.1038/nature02040>
- 72 Arai, F. *et al.* Tie2/angiopoietin-1 signaling regulates hematopoietic stem cell quiescence in the bone marrow niche. *Cell* **118**, 149-161 (2004).  
<https://doi.org/10.1016/j.cell.2004.07.004>
- 73 Zhang, J. *et al.* Identification of the haematopoietic stem cell niche and control of the niche size. *Nature* **425**, 836-841 (2003).  
<https://doi.org/10.1038/nature02041>
- 74 Kiel, M. J., Radice, G. L. & Morrison, S. J. Lack of evidence that hematopoietic stem cells depend on N-cadherin-mediated adhesion to osteoblasts for their maintenance. *Cell Stem Cell* **1**, 204-217 (2007).  
<https://doi.org/10.1016/j.stem.2007.06.001>
- 75 Lo Celso, C. *et al.* Live-animal tracking of individual haematopoietic stem/progenitor cells in their niche. *Nature* **457**, 92-96 (2009).  
<https://doi.org/10.1038/nature07434>
- 76 Xie, Y. *et al.* Detection of functional haematopoietic stem cell niche using real-time imaging. *Nature* **457**, 97-101 (2009).  
<https://doi.org/10.1038/nature07639>
- 77 Ellis, S. L. *et al.* The relationship between bone, hemopoietic stem cells, and vasculature. *Blood* **118**, 1516-1524 (2011).  
<https://doi.org/10.1182/blood-2010-08-303800>
- 78 Guezguez, B. *et al.* Regional localization within the bone marrow influences the functional capacity of human HSCs. *Cell Stem Cell* **13**, 175-189 (2013).  
<https://doi.org/10.1016/j.stem.2013.06.015>
- 79 Grassinger, J., Haylock, D. N., Williams, B., Olsen, G. H. & Nilsson, S. K. Phenotypically identical hemopoietic stem cells isolated from different regions of bone marrow have different biologic potential. *Blood* **116**, 3185-3196 (2010). <https://doi.org/10.1182/blood-2009-12-260703>
- 80 Nombela-Arrieta, C. *et al.* Quantitative imaging of haematopoietic stem and progenitor cell localization and hypoxic status in the bone marrow microenvironment. *Nat Cell Biol* **15**, 533-543 (2013).  
<https://doi.org/10.1038/ncb2730>
- 81 Ding, L. & Morrison, S. J. Haematopoietic stem cells and early lymphoid progenitors occupy distinct bone marrow niches. *Nature* **495**, 231-235 (2013). <https://doi.org/10.1038/nature11885>
- 82 Ding, L., Saunders, T. L., Enikolopov, G. & Morrison, S. J. Endothelial and perivascular cells maintain haematopoietic stem cells. *Nature* **481**, 457-462 (2012). <https://doi.org/10.1038/nature10783>
- 83 Greenbaum, A. *et al.* CXCL12 in early mesenchymal progenitors is required for haematopoietic stem-cell maintenance. *Nature* **495**, 227-230 (2013).  
<https://doi.org/10.1038/nature11926>
- 84 Frenette, P. S., Pinho, S., Lucas, D. & Scheiermann, C. Mesenchymal stem cell: keystone of the hematopoietic stem cell niche and a stepping-stone for regenerative medicine. *Annu Rev Immunol* **31**, 285-316 (2013).  
<https://doi.org/10.1146/annurev-immunol-032712-095919>
- 85 Sacchetti, B. *et al.* Self-renewing osteoprogenitors in bone marrow sinusoids can organize a hematopoietic microenvironment. *Cell* **131**, 324-336 (2007). <https://doi.org/10.1016/j.cell.2007.08.025>

- 86 Chan, C. K. *et al.* Endochondral ossification is required for haematopoietic stem-cell niche formation. *Nature* **457**, 490-494 (2009).  
<https://doi.org/10.1038/nature07547>
- 87 Sugiyama, T., Kohara, H., Noda, M. & Nagasawa, T. Maintenance of the hematopoietic stem cell pool by CXCL12-CXCR4 chemokine signaling in bone marrow stromal cell niches. *Immunity* **25**, 977-988 (2006).  
<https://doi.org/10.1016/j.immuni.2006.10.016>
- 88 Omatsu, Y. *et al.* The essential functions of adipo-osteogenic progenitors as the hematopoietic stem and progenitor cell niche. *Immunity* **33**, 387-399 (2010). <https://doi.org/10.1016/j.immuni.2010.08.017>
- 89 Méndez-Ferrer, S. *et al.* Mesenchymal and haematopoietic stem cells form a unique bone marrow niche. *Nature* **466**, 829-834 (2010).  
<https://doi.org/10.1038/nature09262>
- 90 Asada, N. *et al.* Differential cytokine contributions of perivascular haematopoietic stem cell niches. *Nat Cell Biol* **19**, 214-223 (2017).  
<https://doi.org/10.1038/ncb3475>
- 91 Acar, M. *et al.* Deep imaging of bone marrow shows non-dividing stem cells are mainly perisinusoidal. *Nature* **526**, 126-130 (2015).  
<https://doi.org/10.1038/nature15250>
- 92 Kokkaliaris, K. *et al.* Adult blood stem cell localization reflects the abundance of reported bone marrow niche cell types and their combinations. *Blood* (2020). <https://doi.org/10.1182/blood.2020006574>
- 93 Xu, C. *et al.* Stem cell factor is selectively secreted by arterial endothelial cells in bone marrow. *Nature Communications* **9**, 2449 (2018).  
<https://doi.org/10.1038/s41467-018-04726-3>
- 94 Naveiras, O. *et al.* Bone-marrow adipocytes as negative regulators of the haematopoietic microenvironment. *Nature* **460**, 259-263 (2009).  
<https://doi.org/10.1038/nature08099>
- 95 Yokota, T. *et al.* Adiponectin, a new member of the family of soluble defense collagens, negatively regulates the growth of myelomonocytic progenitors and the functions of macrophages. *Blood* **96**, 1723-1732 (2000).
- 96 Nakamura-Ishizu, A., Takubo, K., Fujioka, M. & Suda, T. Megakaryocytes are essential for HSC quiescence through the production of thrombopoietin. *Biochem Biophys Res Commun* **454**, 353-357 (2014).  
<https://doi.org/10.1016/j.bbrc.2014.10.095>
- 97 Heazlewood, S. Y. *et al.* Megakaryocytes co-localise with hemopoietic stem cells and release cytokines that up-regulate stem cell proliferation. *Stem Cell Res* **11**, 782-792 (2013). <https://doi.org/10.1016/j.scr.2013.05.007>
- 98 Bruns, I. *et al.* Megakaryocytes regulate hematopoietic stem cell quiescence through CXCL4 secretion. *Nat Med* **20**, 1315-1320 (2014).  
<https://doi.org/10.1038/nm.3707>
- 99 Sinclair, A. *et al.* CXCR2 and CXCL4 regulate survival and self-renewal of hematopoietic stem/progenitor cells. *Blood* **128**, 371-383 (2016).  
<https://doi.org/10.1182/blood-2015-08-661785>
- 100 Zhao, M. *et al.* Megakaryocytes maintain homeostatic quiescence and promote post-injury regeneration of hematopoietic stem cells. *Nat Med* **20**, 1321-1326 (2014). <https://doi.org/10.1038/nm.3706>
- 101 Pinho, S. *et al.* Lineage-Biased Hematopoietic Stem Cells Are Regulated by Distinct Niches. *Dev Cell* **44**, 634-641.e634 (2018).  
<https://doi.org/10.1016/j.devcel.2018.01.016>

- 102 Winkler, I. G. *et al.* Bone marrow macrophages maintain hematopoietic stem cell (HSC) niches and their depletion mobilizes HSCs. *Blood* **116**, 4815-4828 (2010). <https://doi.org/10.1182/blood-2009-11-253534>
- 103 Chow, A. *et al.* Bone marrow CD169+ macrophages promote the retention of hematopoietic stem and progenitor cells in the mesenchymal stem cell niche. *J Exp Med* **208**, 261-271 (2011). <https://doi.org/10.1084/jem.20101688>
- 104 Albiero, M. *et al.* Bone Marrow Macrophages Contribute to Diabetic Stem Cell Mobilopathy by Producing Oncostatin M. *Diabetes* **64**, 2957-2968 (2015). <https://doi.org/10.2337/db14-1473>
- 105 Ludin, A. *et al.* Monocytes-macrophages that express  $\alpha$ -smooth muscle actin preserve primitive hematopoietic cells in the bone marrow. *Nat Immunol* **13**, 1072-1082 (2012). <https://doi.org/10.1038/ni.2408>
- 106 Hur, J. *et al.* CD82/KAI1 Maintains the Dormancy of Long-Term Hematopoietic Stem Cells through Interaction with DARC-Expressing Macrophages. *Cell Stem Cell* **18**, 508-521 (2016). <https://doi.org/10.1016/j.stem.2016.01.013>
- 107 Luo, Y. *et al.* M1 and M2 macrophages differentially regulate hematopoietic stem cell self-renewal and ex vivo expansion. *Blood Adv* **2**, 859-870 (2018). <https://doi.org/10.1182/bloodadvances.2018015685>
- 108 Wright, D. E., Wagers, A. J., Gulati, A. P., Johnson, F. L. & Weissman, I. L. Physiological migration of hematopoietic stem and progenitor cells. *Science* **294**, 1933-1936 (2001). <https://doi.org/10.1126/science.1064081>
- 109 Hidalgo, A., Weiss, L. A. & Frenette, P. S. Functional selectin ligands mediating human CD34(+) cell interactions with bone marrow endothelium are enhanced postnatally. *J Clin Invest* **110**, 559-569 (2002). <https://doi.org/10.1172/jci14047>
- 110 Lapidot, T., Dar, A. & Kollet, O. How do stem cells find their way home? *Blood* **106**, 1901-1910 (2005). <https://doi.org/10.1182/blood-2005-04-1417>
- 111 Lo Celso, C. & Scadden, D. T. The haematopoietic stem cell niche at a glance. *J Cell Sci* **124**, 3529-3535 (2011). <https://doi.org/10.1242/jcs.074112>
- 112 Peled, A. *et al.* Dependence of human stem cell engraftment and repopulation of NOD/SCID mice on CXCR4. *Science* **283**, 845-848 (1999). <https://doi.org/10.1126/science.283.5403.845>
- 113 Zanjani, E. D., Flake, A. W., Almeida-Porada, G., Tran, N. & Papayannopoulou, T. Homing of human cells in the fetal sheep model: modulation by antibodies activating or inhibiting very late activation antigen-4-dependent function. *Blood* **94**, 2515-2522 (1999).
- 114 Papayannopoulou, T., Craddock, C., Nakamoto, B., Priestley, G. V. & Wolf, N. S. The VLA4/VCAM-1 adhesion pathway defines contrasting mechanisms of lodgement of transplanted murine hemopoietic progenitors between bone marrow and spleen. *Proc Natl Acad Sci U S A* **92**, 9647-9651 (1995). <https://doi.org/10.1073/pnas.92.21.9647>
- 115 Mazo, I. B. *et al.* Hematopoietic progenitor cell rolling in bone marrow microvessels: parallel contributions by endothelial selectins and vascular cell adhesion molecule 1. *J Exp Med* **188**, 465-474 (1998). <https://doi.org/10.1084/jem.188.3.465>
- 116 Frenette, P. S., Subbarao, S., Mazo, I. B., von Andrian, U. H. & Wagner, D. D. Endothelial selectins and vascular cell adhesion molecule-1 promote hematopoietic progenitor homing to bone marrow. *Proc Natl Acad Sci U S A* **95**, 14423-14428 (1998). <https://doi.org/10.1073/pnas.95.24.14423>

- 117 Scott, L. M., Priestley, G. V. & Papayannopoulou, T. Deletion of alpha4 integrins from adult hematopoietic cells reveals roles in homeostasis, regeneration, and homing. *Mol Cell Biol* **23**, 9349-9360 (2003). <https://doi.org/10.1128/mcb.23.24.9349-9360.2003>
- 118 Peled, A. *et al.* The chemokine SDF-1 activates the integrins LFA-1, VLA-4, and VLA-5 on immature human CD34(+) cells: role in transendothelial/stromal migration and engraftment of NOD/SCID mice. *Blood* **95**, 3289-3296 (2000).
- 119 van der Loo, J. C. *et al.* VLA-5 is expressed by mouse and human long-term repopulating hematopoietic cells and mediates adhesion to extracellular matrix protein fibronectin. *J Clin Invest* **102**, 1051-1061 (1998). <https://doi.org/10.1172/jci3687>
- 120 Parmar, K., Mauch, P., Vergilio, J. A., Sackstein, R. & Down, J. D. Distribution of hematopoietic stem cells in the bone marrow according to regional hypoxia. *Proc Natl Acad Sci U S A* **104**, 5431-5436 (2007). <https://doi.org/10.1073/pnas.0701152104>
- 121 Majmundar, A. J., Wong, W. J. & Simon, M. C. Hypoxia-inducible factors and the response to hypoxic stress. *Mol Cell* **40**, 294-309 (2010). <https://doi.org/10.1016/j.molcel.2010.09.022>
- 122 Takubo, K. *et al.* Regulation of the HIF-1alpha level is essential for hematopoietic stem cells. *Cell Stem Cell* **7**, 391-402 (2010). <https://doi.org/10.1016/j.stem.2010.06.020>
- 123 Kirito, K., Fox, N., Komatsu, N. & Kaushansky, K. Thrombopoietin enhances expression of vascular endothelial growth factor (VEGF) in primitive hematopoietic cells through induction of HIF-1alpha. *Blood* **105**, 4258-4263 (2005). <https://doi.org/10.1182/blood-2004-07-2712>
- 124 Pedersen, M. *et al.* Stem cell factor induces HIF-1alpha at normoxia in hematopoietic cells. *Biochem Biophys Res Commun* **377**, 98-103 (2008). <https://doi.org/10.1016/j.bbrc.2008.09.102>
- 125 Spencer, J. A. *et al.* Direct measurement of local oxygen concentration in the bone marrow of live animals. *Nature* **508**, 269-273 (2014). <https://doi.org/10.1038/nature13034>
- 126 CancerResearchUK. *Chronic myeloid leukaemia (CML) statistics*, <<https://www.cancerresearchuk.org/health-professional/cancer-statistics/statistics-by-cancer-type/leukaemia-cml#heading-Zero>> (2023).
- 127 Höglund, M., Sandin, F. & Simonsson, B. Epidemiology of chronic myeloid leukaemia: an update. *Ann Hematol* **94 Suppl 2**, S241-247 (2015). <https://doi.org/10.1007/s00277-015-2314-2>
- 128 Rowley, J. D. Letter: A new consistent chromosomal abnormality in chronic myelogenous leukaemia identified by quinacrine fluorescence and Giemsa staining. *Nature* **243**, 290-293 (1973). <https://doi.org/10.1038/243290a0>
- 129 Heisterkamp, N. *et al.* Localization of the c-ab1 oncogene adjacent to a translocation break point in chronic myelocytic leukaemia. *Nature* **306**, 239-242 (1983). <https://doi.org/10.1038/306239a0>
- 130 de Klein, A. *et al.* A cellular oncogene is translocated to the Philadelphia chromosome in chronic myelocytic leukaemia. *Nature* **300**, 765-767 (1982). <https://doi.org/10.1038/300765a0>
- 131 O'Hare, T., Zabriskie, M. S., Eiring, A. M. & Deininger, M. W. Pushing the limits of targeted therapy in chronic myeloid leukaemia. *Nat Rev Cancer* **12**, 513-526 (2012). <https://doi.org/10.1038/nrc3317>
- 132 Hehlmann, R. How I treat CML blast crisis. *Blood* **120**, 737-747 (2012). <https://doi.org/10.1182/blood-2012-03-380147>

- 133 Khoury, J. D. *et al.* The 5th edition of the World Health Organization Classification of Haematolymphoid Tumours: Myeloid and Histiocytic/Dendritic Neoplasms. *Leukemia* **36**, 1703-1719 (2022). <https://doi.org/10.1038/s41375-022-01613-1>
- 134 Nowell, P. C. Discovery of the Philadelphia chromosome: a personal perspective. *J Clin Invest* **117**, 2033-2035 (2007). <https://doi.org/10.1172/jci31771>
- 135 Zhang, X. & Ren, R. Bcr-Abl efficiently induces a myeloproliferative disease and production of excess interleukin-3 and granulocyte-macrophage colony-stimulating factor in mice: a novel model for chronic myelogenous leukemia. *Blood* **92**, 3829-3840 (1998).
- 136 Pendergast, A. M. *et al.* BCR-ABL-induced oncogenesis is mediated by direct interaction with the SH2 domain of the GRB-2 adaptor protein. *Cell* **75**, 175-185 (1993).
- 137 Sattler, M. *et al.* Critical role for Gab2 in transformation by BCR/ABL. *Cancer Cell* **1**, 479-492 (2002). [https://doi.org/10.1016/s1535-6108\(02\)00074-0](https://doi.org/10.1016/s1535-6108(02)00074-0)
- 138 Quintás-Cardama, A., Kantarjian, H. & Cortes, J. Flying under the radar: the new wave of BCR-ABL inhibitors. *Nat Rev Drug Discov* **6**, 834-848 (2007). <https://doi.org/10.1038/nrd2324>
- 139 Cortez, D., Reuther, G. & Pendergast, A. M. The Bcr-Abl tyrosine kinase activates mitogenic signaling pathways and stimulates G1-to-S phase transition in hematopoietic cells. *Oncogene* **15**, 2333-2342 (1997). <https://doi.org/10.1038/sj.onc.1201400>
- 140 Skorski, T. *et al.* Phosphatidylinositol-3 kinase activity is regulated by BCR/ABL and is required for the growth of Philadelphia chromosome-positive cells. *Blood* **86**, 726-736 (1995).
- 141 Naka, K. *et al.* TGF-beta-FOXO signalling maintains leukaemia-initiating cells in chronic myeloid leukaemia. *Nature* **463**, 676-680 (2010). <https://doi.org/10.1038/nature08734>
- 142 Markova, B. *et al.* Novel pathway in Bcr-Abl signal transduction involves Akt-independent, PLC- $\gamma$ 1-driven activation of mTOR/p70S6-kinase pathway. *Oncogene* **29**, 739-751 (2010). <https://doi.org/10.1038/onc.2009.374>
- 143 Cilloni, D. & Saglio, G. Molecular pathways: BCR-ABL. *Clin Cancer Res* **18**, 930-937 (2012). <https://doi.org/10.1158/1078-0432.ccr-10-1613>
- 144 He, Y. *et al.* Targeting PI3K/Akt signal transduction for cancer therapy. *Signal Transduction and Targeted Therapy* **6**, 425 (2021). <https://doi.org/10.1038/s41392-021-00828-5>
- 145 Naughton, R., Quiney, C., Turner, S. D. & Cotter, T. G. Bcr-Abl-mediated redox regulation of the PI3K/AKT pathway. *Leukemia* **23**, 1432-1440 (2009). <https://doi.org/10.1038/leu.2009.49>
- 146 de Jong, R., ten Hoeve, J., Heisterkamp, N. & Groffen, J. Tyrosine 207 in CRKL is the BCR/ABL phosphorylation site. *Oncogene* **14**, 507-513 (1997). <https://doi.org/10.1038/sj.onc.1200885>
- 147 Zhang, J. *et al.* CRKL Mediates p110 $\beta$ -Dependent PI3K Signaling in PTEN-Deficient Cancer Cells. *Cell Rep* **20**, 549-557 (2017). <https://doi.org/10.1016/j.celrep.2017.06.054>
- 148 Ilaria, R. L., Jr. & Van Etten, R. A. P210 and P190(BCR/ABL) induce the tyrosine phosphorylation and DNA binding activity of multiple specific STAT family members. *J Biol Chem* **271**, 31704-31710 (1996). <https://doi.org/10.1074/jbc.271.49.31704>

- 149 Hoelbl, A. *et al.* Stat5 is indispensable for the maintenance of bcr/abl-positive leukaemia. *EMBO Mol Med* **2**, 98-110 (2010).  
<https://doi.org/10.1002/emmm.201000062>
- 150 Gallipoli, P. *et al.* JAK2/STAT5 inhibition by nilotinib with ruxolitinib contributes to the elimination of CML CD34+ cells in vitro and in vivo. *Blood* **124**, 1492-1501 (2014). <https://doi.org/10.1182/blood-2013-12-545640>
- 151 Chen, H., Liu, H. & Qing, G. Targeting oncogenic Myc as a strategy for cancer treatment. *Signal Transduction and Targeted Therapy* **3**, 5 (2018).  
<https://doi.org/10.1038/s41392-018-0008-7>
- 152 Gómez-Casares, M. T. *et al.* C-myc expression in cell lines derived from chronic myeloid leukemia. *Haematologica* **89**, 241-243 (2004).
- 153 Albajar, M. *et al.* MYC in chronic myeloid leukemia: induction of aberrant DNA synthesis and association with poor response to imatinib. *Mol Cancer Res* **9**, 564-576 (2011). <https://doi.org/10.1158/1541-7786.Mcr-10-0356>
- 154 Sawyers, C. L., Callahan, W. & Witte, O. N. Dominant negative MYC blocks transformation by ABL oncogenes. *Cell* **70**, 901-910 (1992).  
[https://doi.org/10.1016/0092-8674\(92\)90241-4](https://doi.org/10.1016/0092-8674(92)90241-4)
- 155 Abraham, S. A. *et al.* Dual targeting of p53 and c-MYC selectively eliminates leukaemic stem cells. *Nature* **534**, 341-346 (2016).  
<https://doi.org/10.1038/nature18288>
- 156 Irvine, D. A. & Copland, M. Targeting hedgehog in hematologic malignancy. *Blood* **119**, 2196-2204 (2012). <https://doi.org/10.1182/blood-2011-10-383752>
- 157 Dierks, C. *et al.* Expansion of Bcr-Abl-positive leukemic stem cells is dependent on Hedgehog pathway activation. *Cancer Cell* **14**, 238-249 (2008). <https://doi.org/10.1016/j.ccr.2008.08.003>
- 158 Zhao, C. *et al.* Hedgehog signalling is essential for maintenance of cancer stem cells in myeloid leukaemia. *Nature* **458**, 776-779 (2009).  
<https://doi.org/10.1038/nature07737>
- 159 Irvine, D. A. *et al.* Deregulated hedgehog pathway signaling is inhibited by the smoothed antagonist LDE225 (Sonidegib) in chronic phase chronic myeloid leukaemia. *Sci Rep* **6**, 25476 (2016).  
<https://doi.org/10.1038/srep25476>
- 160 Shah, N. P. *et al.* Dasatinib Plus Smoothened (SMO) Inhibitor BMS-833923 in Chronic Myeloid Leukemia (CML) with Resistance or Suboptimal Response to a Prior Tyrosine Kinase Inhibitor (TKI): Phase I Study CA180323. *Blood* **124**, 4539 (2014).  
<https://doi.org/https://doi.org/10.1182/blood.V124.21.4539.4539>
- 161 Jamieson, C., Martinelli, G., Papayannidis, C. & Cortes, J. E. Hedgehog Pathway Inhibitors: A New Therapeutic Class for the Treatment of Acute Myeloid Leukemia. *Blood Cancer Discov* **1**, 134-145 (2020).  
<https://doi.org/10.1158/2643-3230.Bcd-20-0007>
- 162 Jamieson, C. H. *et al.* Granulocyte-macrophage progenitors as candidate leukemic stem cells in blast-crisis CML. *N Engl J Med* **351**, 657-667 (2004).  
<https://doi.org/10.1056/NEJMoa040258>
- 163 Karabay, A. Z. *et al.* Expression analysis of Akirin-2, NFκB-p65 and β-catenin proteins in imatinib resistance of chronic myeloid leukemia. *Hematology* **23**, 765-770 (2018).  
<https://doi.org/10.1080/10245332.2018.1488795>
- 164 Jin, B. *et al.* Anthelmintic Niclosamide Disrupts the Interplay of p65 and FOXM1/β-catenin and Eradicates Leukemia Stem Cells in Chronic Myelogenous Leukemia. *Clin Cancer Res* **23**, 789-803 (2017).  
<https://doi.org/10.1158/1078-0432.Ccr-16-0226>

- 165 Zhao, C. *et al.* Loss of beta-catenin impairs the renewal of normal and CML stem cells in vivo. *Cancer Cell* **12**, 528-541 (2007). <https://doi.org/10.1016/j.ccr.2007.11.003>
- 166 Hu, J. *et al.* Potential role of Wnt/ $\beta$ -catenin signaling in blastic transformation of chronic myeloid leukemia: cross talk between  $\beta$ -catenin and BCR-ABL. *Tumour Biol* (2016). <https://doi.org/10.1007/s13277-016-5413-3>
- 167 Heidel, F. H. *et al.* Genetic and pharmacologic inhibition of  $\beta$ -catenin targets imatinib-resistant leukemia stem cells in CML. *Cell Stem Cell* **10**, 412-424 (2012). <https://doi.org/10.1016/j.stem.2012.02.017>
- 168 Schürch, C., Riether, C., Matter, M. S., Tzankov, A. & Ochsenschein, A. F. CD27 signaling on chronic myelogenous leukemia stem cells activates Wnt target genes and promotes disease progression. *J Clin Invest* **122**, 624-638 (2012). <https://doi.org/10.1172/jci45977>
- 169 Flieswasser, T. *et al.* The CD70-CD27 axis in oncology: the new kids on the block. *J Exp Clin Cancer Res* **41**, 12 (2022). <https://doi.org/10.1186/s13046-021-02215-y>
- 170 Nolte, M. A., van Olfen, R. W., van Gisbergen, K. P. & van Lier, R. A. Timing and tuning of CD27-CD70 interactions: the impact of signal strength in setting the balance between adaptive responses and immunopathology. *Immunol Rev* **229**, 216-231 (2009). <https://doi.org/10.1111/j.1600-065X.2009.00774.x>
- 171 Riether, C. *et al.* Tyrosine kinase inhibitor-induced CD70 expression mediates drug resistance in leukemia stem cells by activating Wnt signaling. *Sci Transl Med* **7**, 298ra119 (2015). <https://doi.org/10.1126/scitranslmed.aab1740>
- 172 Ochsenschein, A. F. *et al.* Argx-110 Targeting CD70, in Combination with Azacitidine, Shows Favorable Safety Profile and Promising Anti-Leukemia Activity in Newly Diagnosed AML Patients in an Ongoing Phase 1/2 Clinical Trial. *Blood* **132**, 2680-2680 (2018). <https://doi.org/10.1182/blood-2018-99-118302>
- 173 Bigas, A. & Espinosa, L. Hematopoietic stem cells: to be or Notch to be. *Blood* **119**, 3226-3235 (2012). <https://doi.org/10.1182/blood-2011-10-355826>
- 174 Klinakis, A. *et al.* A novel tumour-suppressor function for the Notch pathway in myeloid leukaemia. *Nature* **473**, 230-233 (2011). <https://doi.org/10.1038/nature09999>
- 175 Reynaud, D. *et al.* IL-6 controls leukemic multipotent progenitor cell fate and contributes to chronic myelogenous leukemia development. *Cancer Cell* **20**, 661-673 (2011). <https://doi.org/10.1016/j.ccr.2011.10.012>
- 176 Santaguida, M. *et al.* JunB protects against myeloid malignancies by limiting hematopoietic stem cell proliferation and differentiation without affecting self-renewal. *Cancer Cell* **15**, 341-352 (2009). <https://doi.org/10.1016/j.ccr.2009.02.016>
- 177 Bowers, M. *et al.* Osteoblast ablation reduces normal long-term hematopoietic stem cell self-renewal but accelerates leukemia development. *Blood* **125**, 2678-2688 (2015). <https://doi.org/10.1182/blood-2014-06-582924>
- 178 Aljedai, A., Buckle, A. M., Hiwarkar, P. & Syed, F. Potential role of Notch signalling in CD34+ chronic myeloid leukaemia cells: cross-talk between Notch and BCR-ABL. *PLoS One* **10**, e0123016 (2015). <https://doi.org/10.1371/journal.pone.0123016>

- 179 Nakahara, F. *et al.* Hes1 promotes blast crisis in chronic myelogenous leukemia through MMP-9 upregulation in leukemic cells. *Blood* **123**, 3932-3942 (2014). <https://doi.org/10.1182/blood-2013-01-476747>
- 180 Nakahara, F. *et al.* Hes1 immortalizes committed progenitors and plays a role in blast crisis transition in chronic myelogenous leukemia. *Blood* **115**, 2872-2881 (2010). <https://doi.org/10.1182/blood-2009-05-222836>
- 181 Kode, A. *et al.* Leukaemogenesis induced by an activating  $\beta$ -catenin mutation in osteoblasts. *Nature* **506**, 240-244 (2014). <https://doi.org/10.1038/nature12883>
- 182 Duncan, A. W. *et al.* Integration of Notch and Wnt signaling in hematopoietic stem cell maintenance. *Nat Immunol* **6**, 314-322 (2005). <https://doi.org/10.1038/ni1164>
- 183 Naef, P. *et al.* IL-33-ST2 signaling promotes stemness in subtypes of myeloid leukemia cells through the Wnt and Notch pathways. *Sci Signal* **16**, eadd7705 (2023). <https://doi.org/10.1126/scisignal.add7705>
- 184 Kang, Y. A., Pietras, E. M. & Passegué, E. Deregulated Notch and Wnt signaling activates early-stage myeloid regeneration pathways in leukemia. *J Exp Med* **217** (2020). <https://doi.org/10.1084/jem.20190787>
- 185 Druker, B. J. *et al.* Efficacy and safety of a specific inhibitor of the BCR-ABL tyrosine kinase in chronic myeloid leukemia. *N Engl J Med* **344**, 1031-1037 (2001). <https://doi.org/10.1056/nejm200104053441401>
- 186 Druker, B. J. *et al.* Effects of a selective inhibitor of the Abl tyrosine kinase on the growth of Bcr-Abl positive cells. *Nat Med* **2**, 561-566 (1996). <https://doi.org/10.1038/nm0596-561>
- 187 Kantarjian, H. *et al.* Dasatinib versus imatinib in newly diagnosed chronic-phase chronic myeloid leukemia. *N Engl J Med* **362**, 2260-2270 (2010). <https://doi.org/10.1056/NEJMoa1002315>
- 188 Saglio, G. *et al.* Nilotinib versus imatinib for newly diagnosed chronic myeloid leukemia. *N Engl J Med* **362**, 2251-2259 (2010). <https://doi.org/10.1056/NEJMoa0912614>
- 189 Weisberg, E., Manley, P. W., Cowan-Jacob, S. W., Hochhaus, A. & Griffin, J. D. Second generation inhibitors of BCR-ABL for the treatment of imatinib-resistant chronic myeloid leukaemia. *Nat Rev Cancer* **7**, 345-356 (2007). <https://doi.org/10.1038/nrc2126>
- 190 Danhauser-Riedl, S., Warmuth, M., Druker, B. J., Emmerich, B. & Hallek, M. Activation of Src kinases p53/56lyn and p59hck by p210bcr/abl in myeloid cells. *Cancer Res* **56**, 3589-3596 (1996).
- 191 Warmuth, M. *et al.* The Src family kinase Hck interacts with Bcr-Abl by a kinase-independent mechanism and phosphorylates the Grb2-binding site of Bcr. *J Biol Chem* **272**, 33260-33270 (1997). <https://doi.org/10.1074/jbc.272.52.33260>
- 192 Tanis, K. Q., Veach, D., Duetzel, H. S., Bornmann, W. G. & Koleske, A. J. Two distinct phosphorylation pathways have additive effects on Abl family kinase activation. *Mol Cell Biol* **23**, 3884-3896 (2003). <https://doi.org/10.1128/mcb.23.11.3884-3896.2003>
- 193 Li, S. Src-family kinases in the development and therapy of Philadelphia chromosome-positive chronic myeloid leukemia and acute lymphoblastic leukemia. *Leuk Lymphoma* **49**, 19-26 (2008). <https://doi.org/10.1080/10428190701713689>
- 194 Olivieri, A. & Manzione, L. Dasatinib: a new step in molecular target therapy. *Ann Oncol* **18 Suppl 6**, vi42-46 (2007). <https://doi.org/10.1093/annonc/mdm223>

- 195 Talpaz, M. *et al.* Dasatinib in imatinib-resistant Philadelphia chromosome-positive leukemias. *N Engl J Med* **354**, 2531-2541 (2006). <https://doi.org/10.1056/NEJMoa055229>
- 196 O'Brien, S. G. *et al.* Imatinib compared with interferon and low-dose cytarabine for newly diagnosed chronic-phase chronic myeloid leukemia. *N Engl J Med* **348**, 994-1004 (2003). <https://doi.org/10.1056/NEJMoa022457>
- 197 Druker, B. J. *et al.* Five-year follow-up of patients receiving imatinib for chronic myeloid leukemia. *N Engl J Med* **355**, 2408-2417 (2006). <https://doi.org/10.1056/NEJMoa062867>
- 198 Holyoake, T. L. & Vetrie, D. The chronic myeloid leukemia stem cell: stemming the tide of persistence. *Blood* **129**, 1595-1606 (2017). <https://doi.org/10.1182/blood-2016-09-696013>
- 199 Ross, D. M. *et al.* Safety and efficacy of imatinib cessation for CML patients with stable undetectable minimal residual disease: results from the TWISTER study. *Blood* **122**, 515-522 (2013). <https://doi.org/10.1182/blood-2013-02-483750>
- 200 Mahon, F. X. *et al.* Discontinuation of imatinib in patients with chronic myeloid leukaemia who have maintained complete molecular remission for at least 2 years: the prospective, multicentre Stop Imatinib (STIM) trial. *Lancet Oncol* **11**, 1029-1035 (2010). [https://doi.org/10.1016/s1470-2045\(10\)70233-3](https://doi.org/10.1016/s1470-2045(10)70233-3)
- 201 Baccarani, M. *et al.* European LeukemiaNet recommendations for the management of chronic myeloid leukemia: 2013. *Blood* **122**, 872-884 (2013). <https://doi.org/10.1182/blood-2013-05-501569>
- 202 O'Hare, T. *et al.* AP24534, a pan-BCR-ABL inhibitor for chronic myeloid leukemia, potently inhibits the T315I mutant and overcomes mutation-based resistance. *Cancer Cell* **16**, 401-412 (2009). <https://doi.org/10.1016/j.ccr.2009.09.028>
- 203 Müller, M. C. *et al.* Ponatinib in chronic myeloid leukemia (CML): Consensus on patient treatment and management from a European expert panel. *Crit Rev Oncol Hematol* **120**, 52-59 (2017). <https://doi.org/10.1016/j.critrevonc.2017.10.002>
- 204 Cortes, J. E. *et al.* Final 5-Year Study Results of DASISION: The Dasatinib Versus Imatinib Study in Treatment-Naïve Chronic Myeloid Leukemia Patients Trial. *J Clin Oncol* **34**, 2333-2340 (2016). <https://doi.org/10.1200/jco.2015.64.8899>
- 205 Lang, K. *et al.* Mortality and Vascular Events Among Elderly Patients With Chronic Myeloid Leukemia: A Retrospective Analysis of Linked SEER-Medicare Data. *Clin Lymphoma Myeloma Leuk* **16**, 275-285.e271 (2016). <https://doi.org/10.1016/j.clml.2016.01.006>
- 206 Huang, X., Cortes, J. & Kantarjian, H. Estimations of the increasing prevalence and plateau prevalence of chronic myeloid leukemia in the era of tyrosine kinase inhibitor therapy. *Cancer* **118**, 3123-3127 (2012). <https://doi.org/10.1002/cncr.26679>
- 207 Fialkow, P. J., Jacobson, R. J. & Papayannopoulou, T. Chronic myelocytic leukemia: clonal origin in a stem cell common to the granulocyte, erythrocyte, platelet and monocyte/macrophage. *Am J Med* **63**, 125-130 (1977). [https://doi.org/10.1016/0002-9343\(77\)90124-3](https://doi.org/10.1016/0002-9343(77)90124-3)
- 208 Takahashi, N., Miura, I., Saitoh, K. & Miura, A. B. Lineage involvement of stem cells bearing the Philadelphia chromosome in chronic myeloid leukemia in the chronic phase as shown by a combination of fluorescence-activated cell sorting and fluorescence in situ hybridization. *Blood* **92**, 4758-4763 (1998).

- 209 Huntly, B. J. *et al.* MOZ-TIF2, but not BCR-ABL, confers properties of  
leukemic stem cells to committed murine hematopoietic progenitors. *Cancer*  
*Cell* **6**, 587-596 (2004). <https://doi.org/10.1016/j.ccr.2004.10.015>
- 210 Holyoake, T., Jiang, X., Eaves, C. & Eaves, A. Isolation of a highly  
quiescent subpopulation of primitive leukemic cells in chronic myeloid  
leukemia. *Blood* **94**, 2056-2064 (1999).
- 211 Bhatia, R. *et al.* Persistence of malignant hematopoietic progenitors in  
chronic myelogenous leukemia patients in complete cytogenetic remission  
following imatinib mesylate treatment. *Blood* **101**, 4701-4707 (2003).  
<https://doi.org/10.1182/blood-2002-09-2780>
- 212 Chomel, J. C. *et al.* Leukemic stem cell persistence in chronic myeloid  
leukemia patients with sustained undetectable molecular residual disease.  
*Blood* **118**, 3657-3660 (2011). <https://doi.org/10.1182/blood-2011-02-335497>
- 213 Corbin, A. S. *et al.* Human chronic myeloid leukemia stem cells are  
insensitive to imatinib despite inhibition of BCR-ABL activity. *J Clin Invest*  
**121**, 396-409 (2011). <https://doi.org/10.1172/jci35721>
- 214 Jiang, X., Lopez, A., Holyoake, T., Eaves, A. & Eaves, C. Autocrine  
production and action of IL-3 and granulocyte colony-stimulating factor in  
chronic myeloid leukemia. *Proc Natl Acad Sci U S A* **96**, 12804-12809  
(1999). <https://doi.org/10.1073/pnas.96.22.12804>
- 215 Wang, Y. *et al.* Adaptive secretion of granulocyte-macrophage colony-  
stimulating factor (GM-CSF) mediates imatinib and nilotinib resistance in  
BCR/ABL+ progenitors via JAK-2/STAT-5 pathway activation. *Blood* **109**,  
2147-2155 (2007). <https://doi.org/10.1182/blood-2006-08-040022>
- 216 Hamilton, A. *et al.* Chronic myeloid leukemia stem cells are not dependent  
on Bcr-Abl kinase activity for their survival. *Blood* **119**, 1501-1510 (2012).  
<https://doi.org/10.1182/blood-2010-12-326843>
- 217 Warburg, O. On the origin of cancer cells. *Science* **123**, 309-314 (1956).  
<https://doi.org/10.1126/science.123.3191.309>
- 218 Hanahan, D. & Weinberg, R. A. Hallmarks of cancer: the next generation.  
*Cell* **144**, 646-674 (2011). <https://doi.org/10.1016/j.cell.2011.02.013>
- 219 Vander Heiden, M. G., Cantley, L. C. & Thompson, C. B. Understanding the  
Warburg effect: the metabolic requirements of cell proliferation. *Science*  
**324**, 1029-1033 (2009). <https://doi.org/10.1126/science.1160809>
- 220 Kuntz, E. M. *et al.* Targeting mitochondrial oxidative phosphorylation  
eradicates therapy-resistant chronic myeloid leukemia stem cells. *Nat Med*  
**23**, 1234-1240 (2017). <https://doi.org/10.1038/nm.4399>
- 221 Abraham, A. *et al.* SIRT1 regulates metabolism and leukemogenic potential  
in CML stem cells. *J Clin Invest* **129**, 2685-2701 (2019).  
<https://doi.org/10.1172/jci127080>
- 222 de Beauchamp, L., Himonas, E. & Helgason, G. V. Mitochondrial  
metabolism as a potential therapeutic target in myeloid leukaemia.  
*Leukemia* **36**, 1-12 (2022). <https://doi.org/10.1038/s41375-021-01416-w>
- 223 Rattigan, K. M. *et al.* Pyruvate anaplerosis is a targetable vulnerability in  
persistent leukaemic stem cells. *Nat Commun* **14**, 4634 (2023).  
<https://doi.org/10.1038/s41467-023-40222-z>
- 224 Vetrie, D., Helgason, G. V. & Copland, M. The leukaemia stem cell:  
similarities, differences and clinical prospects in CML and AML. *Nature*  
*Reviews Cancer* **20**, 158-173 (2020). <https://doi.org/10.1038/s41568-019-0230-9>

- 225 Ye, H. *et al.* Leukemic Stem Cells Evade Chemotherapy by Metabolic Adaptation to an Adipose Tissue Niche. *Cell Stem Cell* **19**, 23-37 (2016). <https://doi.org/10.1016/j.stem.2016.06.001>
- 226 Welner, R. S. *et al.* Treatment of chronic myelogenous leukemia by blocking cytokine alterations found in normal stem and progenitor cells. *Cancer Cell* **27**, 671-681 (2015). <https://doi.org/10.1016/j.ccell.2015.04.004>
- 227 Giustacchini, A. *et al.* Single-cell transcriptomics uncovers distinct molecular signatures of stem cells in chronic myeloid leukemia. *Nature Medicine* **23**, 692-702 (2017). <https://doi.org/10.1038/nm.4336>
- 228 Zhang, B. *et al.* Altered microenvironmental regulation of leukemic and normal stem cells in chronic myelogenous leukemia. *Cancer Cell* **21**, 577-592 (2012). <https://doi.org/10.1016/j.ccr.2012.02.018>
- 229 Gallipoli, P. *et al.* Autocrine TNF- $\alpha$  production supports CML stem and progenitor cell survival and enhances their proliferation. *Blood* **122**, 3335-3339 (2013). <https://doi.org/10.1182/blood-2013-02-485607>
- 230 Zhang, B. *et al.* Inhibition of interleukin-1 signaling enhances elimination of tyrosine kinase inhibitor-treated CML stem cells. *Blood* **128**, 2671-2682 (2016). <https://doi.org/10.1182/blood-2015-11-679928>
- 231 Ågerstam, H. *et al.* IL1RAP antibodies block IL-1-induced expansion of candidate CML stem cells and mediate cell killing in xenograft models. *Blood* **128**, 2683-2693 (2016). <https://doi.org/10.1182/blood-2015-11-679985>
- 232 Schepers, K. *et al.* Myeloproliferative neoplasia remodels the endosteal bone marrow niche into a self-reinforcing leukemic niche. *Cell Stem Cell* **13**, 285-299 (2013). <https://doi.org/10.1016/j.stem.2013.06.009>
- 233 Agarwal, P. *et al.* Mesenchymal Niche-Specific Expression of Cxcl12 Controls Quiescence of Treatment-Resistant Leukemia Stem Cells. *Cell Stem Cell* **24**, 769-784.e766 (2019). <https://doi.org/10.1016/j.stem.2019.02.018>
- 234 Krause, D. S., Lazarides, K., von Andrian, U. H. & Van Etten, R. A. Requirement for CD44 in homing and engraftment of BCR-ABL-expressing leukemic stem cells. *Nat Med* **12**, 1175-1180 (2006). <https://doi.org/10.1038/nm1489>
- 235 Godavarthy, P. S. *et al.* The vascular bone marrow niche influences outcome in chronic myeloid leukemia via the E-selectin - SCL/TAL1 - CD44 axis. *Haematologica* **105**, 136-147 (2020). <https://doi.org/10.3324/haematol.2018.212365>
- 236 Zhang, B. *et al.* Bone marrow niche trafficking of miR-126 controls the self-renewal of leukemia stem cells in chronic myelogenous leukemia. *Nat Med* **24**, 450-462 (2018). <https://doi.org/10.1038/nm.4499>
- 237 Lechman, E. R. *et al.* Attenuation of miR-126 activity expands HSC in vivo without exhaustion. *Cell Stem Cell* **11**, 799-811 (2012). <https://doi.org/10.1016/j.stem.2012.09.001>
- 238 Lechman, E. R. *et al.* miR-126 Regulates Distinct Self-Renewal Outcomes in Normal and Malignant Hematopoietic Stem Cells. *Cancer Cell* **29**, 214-228 (2016). <https://doi.org/10.1016/j.ccell.2015.12.011>
- 239 Krause, D. S. *et al.* Differential regulation of myeloid leukemias by the bone marrow microenvironment. *Nat Med* **19**, 1513-1517 (2013). <https://doi.org/10.1038/nm.3364>
- 240 Brück, O. *et al.* Immune cell contexture in the bone marrow tumor microenvironment impacts therapy response in CML. *Leukemia* **32**, 1643-1656 (2018). <https://doi.org/10.1038/s41375-018-0175-0>

- 241 Rea, D. *et al.* Natural killer-cell counts are associated with molecular relapse-free survival after imatinib discontinuation in chronic myeloid leukemia: the IMMUNOSTIM study. *Haematologica* **102**, 1368-1377 (2017). <https://doi.org/10.3324/haematol.2017.165001>
- 242 Ilander, M. *et al.* Increased proportion of mature NK cells is associated with successful imatinib discontinuation in chronic myeloid leukemia. *Leukemia* **31**, 1108-1116 (2017). <https://doi.org/10.1038/leu.2016.360>
- 243 Hsieh, Y. C., Kirschner, K. & Copland, M. Improving outcomes in chronic myeloid leukemia through harnessing the immunological landscape. *Leukemia* **35**, 1229-1242 (2021). <https://doi.org/10.1038/s41375-021-01238-w>
- 244 Najima, Y. *et al.* Regulatory T cell inhibition by dasatinib is associated with natural killer cell differentiation and a favorable molecular response-The final results of the D-first study. *Leuk Res* **66**, 66-72 (2018). <https://doi.org/10.1016/j.leukres.2018.01.010>
- 245 Hughes, A. *et al.* CML patients with deep molecular responses to TKI have restored immune effectors and decreased PD-1 and immune suppressors. *Blood* **129**, 1166-1176 (2017). <https://doi.org/10.1182/blood-2016-10-745992>
- 246 Schürch, C., Riether, C., Amrein, M. A. & Ochsenbein, A. F. Cytotoxic T cells induce proliferation of chronic myeloid leukemia stem cells by secreting interferon- $\gamma$ . *J Exp Med* **210**, 605-621 (2013). <https://doi.org/10.1084/jem.20121229>
- 247 Gabilovich, D. I. & Nagaraj, S. Myeloid-derived suppressor cells as regulators of the immune system. *Nat Rev Immunol* **9**, 162-174 (2009). <https://doi.org/10.1038/nri2506>
- 248 Zhao, Y., Wu, T., Shao, S., Shi, B. & Zhao, Y. Phenotype, development, and biological function of myeloid-derived suppressor cells. *Oncoimmunology* **5**, e1004983 (2016). <https://doi.org/10.1080/2162402x.2015.1004983>
- 249 Giallongo, C. *et al.* Myeloid derived suppressor cells (MDSCs) are increased and exert immunosuppressive activity together with polymorphonuclear leukocytes (PMNs) in chronic myeloid leukemia patients. *PLoS One* **9**, e101848 (2014). <https://doi.org/10.1371/journal.pone.0101848>
- 250 Bronte, V., Serafini, P., Mazzoni, A., Segal, D. M. & Zanovello, P. L-arginine metabolism in myeloid cells controls T-lymphocyte functions. *Trends Immunol* **24**, 302-306 (2003). [https://doi.org/10.1016/s1471-4906\(03\)00132-7](https://doi.org/10.1016/s1471-4906(03)00132-7)
- 251 Giallongo, C. *et al.* Myeloid derived suppressor cells in chronic myeloid leukemia. *Front Oncol* **5**, 107 (2015). <https://doi.org/10.3389/fonc.2015.00107>
- 252 Stuckey, R., López Rodríguez, J. F. & Gómez-Casares, M. T. Discontinuation of Tyrosine Kinase Inhibitors in Patients with Chronic Myeloid Leukemia: a Review of the Biological Factors Associated with Treatment-Free Remission. *Curr Oncol Rep* **24**, 415-426 (2022). <https://doi.org/10.1007/s11912-022-01228-w>
- 253 Secklehner, J., Lo Celso, C. & Carlin, L. M. Intravital microscopy in historic and contemporary immunology. *Immunol Cell Biol* **95**, 506-513 (2017). <https://doi.org/10.1038/icb.2017.25>
- 254 West, J. B. Marcello Malpighi and the discovery of the pulmonary capillaries and alveoli. *Am J Physiol Lung Cell Mol Physiol* **304**, L383-390 (2013). <https://doi.org/10.1152/ajplung.00016.2013>

- 255 Wagner, D. D. & Frenette, P. S. The vessel wall and its interactions. *Blood* **111**, 5271-5281 (2008). <https://doi.org/10.1182/blood-2008-01-078204>
- 256 Landecker, H. Seeing things: from microcinematography to live cell imaging. *Nat Methods* **6**, 707-709 (2009). <https://doi.org/10.1038/nmeth1009-707>
- 257 Wollman, A. J., Nudd, R., Hedlund, E. G. & Leake, M. C. From Animaculum to single molecules: 300 years of the light microscope. *Open Biol* **5**, 150019 (2015). <https://doi.org/10.1098/rsob.150019>
- 258 Pawley, J. B. *Handbook of biological confocal microscopy*. (Springer, 2006).
- 259 Weigert, R., Sramkova, M., Parente, L., Amornphimoltham, P. & Masedunskas, A. Intravital microscopy: a novel tool to study cell biology in living animals. *Histochem Cell Biol* **133**, 481-491 (2010). <https://doi.org/10.1007/s00418-010-0692-z>
- 260 Schießl, I. M. & Castrop, H. Deep insights: intravital imaging with two-photon microscopy. *Pflugers Arch* **468**, 1505-1516 (2016). <https://doi.org/10.1007/s00424-016-1832-7>
- 261 Masedunskas, A. *et al.* Intravital microscopy: a practical guide on imaging intracellular structures in live animals. *Bioarchitecture* **2**, 143-157 (2012). <https://doi.org/10.4161/bioa.21758>
- 262 Oron, D. *et al.* Depth-resolved structural imaging by third-harmonic generation microscopy. *J Struct Biol* **147**, 3-11 (2004). [https://doi.org/10.1016/s1047-8477\(03\)00125-4](https://doi.org/10.1016/s1047-8477(03)00125-4)
- 263 Kim, J. & Bixel, M. G. Intravital Multiphoton Imaging of the Bone and Bone Marrow Environment. *Cytometry A* **97**, 496-503 (2020). <https://doi.org/10.1002/cyto.a.23937>
- 264 Campagnola, P. J. & Loew, L. M. Second-harmonic imaging microscopy for visualizing biomolecular arrays in cells, tissues and organisms. *Nat Biotechnol* **21**, 1356-1360 (2003). <https://doi.org/10.1038/nbt894>
- 265 Weigelin, B., Bakker, G. J. & Friedl, P. Third harmonic generation microscopy of cells and tissue organization. *J Cell Sci* **129**, 245-255 (2016). <https://doi.org/10.1242/jcs.152272>
- 266 Débarre, D. *et al.* Imaging lipid bodies in cells and tissues using third-harmonic generation microscopy. *Nat Methods* **3**, 47-53 (2006). <https://doi.org/10.1038/nmeth813>
- 267 Dickinson, M. E. D., Michael W. *Introduction to Spectral Imaging and Linear Unmixing*, <<https://zeiss-campus.magnet.fsu.edu/articles/spectralimaging/introduction.html>> (n.d.).
- 268 Larson, J. M. S., Stanley A.; Rainey, Adam M.; Davidson, Michael W. *Lambda Stacks and spectral signatures*, <<https://www.microscopyu.com/tutorials/lambda-stacks-and-spectral-signatures>> (2024).
- 269 Zimmermann, T. Spectral imaging and linear unmixing in light microscopy. *Adv Biochem Eng Biotechnol* **95**, 245-265 (2005). <https://doi.org/10.1007/b102216>
- 270 Lo Celso, C., Lin, C. P. & Scadden, D. T. In vivo imaging of transplanted hematopoietic stem and progenitor cells in mouse calvarium bone marrow. *Nat Protoc* **6**, 1-14 (2011). <https://doi.org/10.1038/nprot.2010.168>
- 271 Upadhaya, S. *et al.* Intravital Imaging Reveals Motility of Adult Hematopoietic Stem Cells in the Bone Marrow Niche. *Cell Stem Cell* **27**, 336-345.e334 (2020). <https://doi.org/10.1016/j.stem.2020.06.003>
- 272 Hawkins, E. D. *et al.* T-cell acute leukaemia exhibits dynamic interactions with bone marrow microenvironments. *Nature* **538**, 518-522 (2016). <https://doi.org/10.1038/nature19801>

- 273 Duarte, D. *et al.* Inhibition of Endosteal Vascular Niche Remodeling Rescues Hematopoietic Stem Cell Loss in AML. *Cell Stem Cell* **22**, 64-77.e66 (2018). <https://doi.org/10.1016/j.stem.2017.11.006>
- 274 Pirillo, C. *et al.* Metalloproteinase inhibition reduces AML growth, prevents stem cell loss, and improves chemotherapy effectiveness. *Blood Adv* **6**, 3126-3141 (2022). <https://doi.org/10.1182/bloodadvances.2021004321>
- 275 Haase, C. *et al.* Image-seq: spatially resolved single-cell sequencing guided by in situ and in vivo imaging. *Nat Methods* **19**, 1622-1633 (2022). <https://doi.org/10.1038/s41592-022-01673-2>
- 276 De Duve, C. The lysosome. *Sci Am* **208**, 64-72 (1963). <https://doi.org/10.1038/scientificamerican0563-64>
- 277 Huang, J. & Brumell, J. H. Bacteria-autophagy interplay: a battle for survival. *Nat Rev Microbiol* **12**, 101-114 (2014). <https://doi.org/10.1038/nrmicro3160>
- 278 Levine, B. & Klionsky, D. J. Development by self-digestion: molecular mechanisms and biological functions of autophagy. *Dev Cell* **6**, 463-477 (2004). [https://doi.org/10.1016/s1534-5807\(04\)00099-1](https://doi.org/10.1016/s1534-5807(04)00099-1)
- 279 Tsukada, M. & Ohsumi, Y. Isolation and characterization of autophagy-defective mutants of *Saccharomyces cerevisiae*. *FEBS Lett* **333**, 169-174 (1993). [https://doi.org/10.1016/0014-5793\(93\)80398-e](https://doi.org/10.1016/0014-5793(93)80398-e)
- 280 Cuervo, A. M. & Wong, E. Chaperone-mediated autophagy: roles in disease and aging. *Cell Res* **24**, 92-104 (2014). <https://doi.org/10.1038/cr.2013.153>
- 281 Wang, L., Klionsky, D. J. & Shen, H.-M. The emerging mechanisms and functions of microautophagy. *Nature Reviews Molecular Cell Biology* **24**, 186-203 (2023). <https://doi.org/10.1038/s41580-022-00529-z>
- 282 Tooze, S. A. & Yoshimori, T. The origin of the autophagosomal membrane. *Nat Cell Biol* **12**, 831-835 (2010). <https://doi.org/10.1038/ncb0910-831>
- 283 Sousa, C. M. *et al.* Pancreatic stellate cells support tumour metabolism through autophagic alanine secretion. *Nature* **536**, 479-483 (2016). <https://doi.org/10.1038/nature19084>
- 284 Poillet-Perez, L. *et al.* Autophagy maintains tumour growth through circulating arginine. *Nature* **563**, 569-573 (2018). <https://doi.org/10.1038/s41586-018-0697-7>
- 285 New, J. & Thomas, S. M. Autophagy-dependent secretion: mechanism, factors secreted, and disease implications. *Autophagy* **15**, 1682-1693 (2019). <https://doi.org/10.1080/15548627.2019.1596479>
- 286 Saxton, R. A. & Sabatini, D. M. mTOR Signaling in Growth, Metabolism, and Disease. *Cell* **168**, 960-976 (2017). <https://doi.org/10.1016/j.cell.2017.02.004>
- 287 Hosokawa, N. *et al.* Nutrient-dependent mTORC1 association with the ULK1-Atg13-FIP200 complex required for autophagy. *Mol Biol Cell* **20**, 1981-1991 (2009). <https://doi.org/10.1091/mbc.e08-12-1248>
- 288 Ganley, I. G. *et al.* ULK1.ATG13.FIP200 complex mediates mTOR signaling and is essential for autophagy. *J Biol Chem* **284**, 12297-12305 (2009). <https://doi.org/10.1074/jbc.M900573200>
- 289 Jung, C. H. *et al.* ULK-Atg13-FIP200 complexes mediate mTOR signaling to the autophagy machinery. *Mol Biol Cell* **20**, 1992-2003 (2009). <https://doi.org/10.1091/mbc.e08-12-1249>
- 290 Kim, J., Kundu, M., Viollet, B. & Guan, K. L. AMPK and mTOR regulate autophagy through direct phosphorylation of Ulk1. *Nat Cell Biol* **13**, 132-141 (2011). <https://doi.org/10.1038/ncb2152>

- 291 Garcia, D. & Shaw, R. J. AMPK: Mechanisms of Cellular Energy Sensing and Restoration of Metabolic Balance. *Mol Cell* **66**, 789-800 (2017). <https://doi.org/10.1016/j.molcel.2017.05.032>
- 292 Dikic, I. & Elazar, Z. Mechanism and medical implications of mammalian autophagy. *Nature Reviews Molecular Cell Biology* **19**, 349-364 (2018). <https://doi.org/10.1038/s41580-018-0003-4>
- 293 Fimia, G. M. *et al.* Ambra1 regulates autophagy and development of the nervous system. *Nature* **447**, 1121-1125 (2007). <https://doi.org/10.1038/nature05925>
- 294 Proikas-Cezanne, T. *et al.* WIPI-1alpha (WIPI49), a member of the novel 7-bladed WIPI protein family, is aberrantly expressed in human cancer and is linked to starvation-induced autophagy. *Oncogene* **23**, 9314-9325 (2004). <https://doi.org/10.1038/sj.onc.1208331>
- 295 Simonsen, A. & Tooze, S. A. Coordination of membrane events during autophagy by multiple class III PI3-kinase complexes. *J Cell Biol* **186**, 773-782 (2009). <https://doi.org/10.1083/jcb.200907014>
- 296 Mizushima, N. *et al.* A protein conjugation system essential for autophagy. *Nature* **395**, 395-398 (1998). <https://doi.org/10.1038/26506>
- 297 Mizushima, N., Noda, T. & Ohsumi, Y. Apg16p is required for the function of the Apg12p-Apg5p conjugate in the yeast autophagy pathway. *Embo j* **18**, 3888-3896 (1999). <https://doi.org/10.1093/emboj/18.14.3888>
- 298 Ohsumi, Y. Historical landmarks of autophagy research. *Cell Research* **24**, 9-23 (2014). <https://doi.org/10.1038/cr.2013.169>
- 299 Ichimura, Y. *et al.* A ubiquitin-like system mediates protein lipidation. *Nature* **408**, 488-492 (2000). <https://doi.org/10.1038/35044114>
- 300 Hansen, M., Rubinsztein, D. C. & Walker, D. W. Autophagy as a promoter of longevity: insights from model organisms. *Nat Rev Mol Cell Biol* **19**, 579-593 (2018). <https://doi.org/10.1038/s41580-018-0033-y>
- 301 Kirisako, T. *et al.* The reversible modification regulates the membrane-binding state of Apg8/Aut7 essential for autophagy and the cytoplasm to vacuole targeting pathway. *J Cell Biol* **151**, 263-276 (2000). <https://doi.org/10.1083/jcb.151.2.263>
- 302 Xie, Z., Nair, U. & Klionsky, D. J. Atg8 controls phagophore expansion during autophagosome formation. *Mol Biol Cell* **19**, 3290-3298 (2008). <https://doi.org/10.1091/mbc.e07-12-1292>
- 303 Pankiv, S. *et al.* p62/SQSTM1 binds directly to Atg8/LC3 to facilitate degradation of ubiquitinated protein aggregates by autophagy. *J Biol Chem* **282**, 24131-24145 (2007). <https://doi.org/10.1074/jbc.M702824200>
- 304 Itakura, E., Kishi-Itakura, C. & Mizushima, N. The hairpin-type tail-anchored SNARE syntaxin 17 targets to autophagosomes for fusion with endosomes/lysosomes. *Cell* **151**, 1256-1269 (2012). <https://doi.org/10.1016/j.cell.2012.11.001>
- 305 Wallace, D. C. A mitochondrial paradigm of metabolic and degenerative diseases, aging, and cancer: a dawn for evolutionary medicine. *Annu Rev Genet* **39**, 359-407 (2005). <https://doi.org/10.1146/annurev.genet.39.110304.095751>
- 306 Chen, H. *et al.* Mitofusins Mfn1 and Mfn2 coordinately regulate mitochondrial fusion and are essential for embryonic development. *J Cell Biol* **160**, 189-200 (2003). <https://doi.org/10.1083/jcb.200211046>
- 307 Cipolat, S., Martins de Brito, O., Dal Zilio, B. & Scorrano, L. OPA1 requires mitofusin 1 to promote mitochondrial fusion. *Proc Natl Acad Sci U S A* **101**, 15927-15932 (2004). <https://doi.org/10.1073/pnas.0407043101>

- 308 Okamoto, K. & Shaw, J. M. Mitochondrial morphology and dynamics in yeast and multicellular eukaryotes. *Annu Rev Genet* **39**, 503-536 (2005). <https://doi.org/10.1146/annurev.genet.38.072902.093019>
- 309 Friedman, J. R. & Nunnari, J. Mitochondrial form and function. *Nature* **505**, 335-343 (2014). <https://doi.org/10.1038/nature12985>
- 310 Song, Z., Ghochani, M., McCaffery, J. M., Frey, T. G. & Chan, D. C. Mitofusins and OPA1 mediate sequential steps in mitochondrial membrane fusion. *Mol Biol Cell* **20**, 3525-3532 (2009). <https://doi.org/10.1091/mbc.e09-03-0252>
- 311 Ban, T. *et al.* Molecular basis of selective mitochondrial fusion by heterotypic action between OPA1 and cardiolipin. *Nature Cell Biology* **19**, 856-863 (2017). <https://doi.org/10.1038/ncb3560>
- 312 Smirnova, E., Shurland, D. L., Ryazantsev, S. N. & van der Bliek, A. M. A human dynamin-related protein controls the distribution of mitochondria. *J Cell Biol* **143**, 351-358 (1998). <https://doi.org/10.1083/jcb.143.2.351>
- 313 Smirnova, E., Griparic, L., Shurland, D. L. & van der Bliek, A. M. Dynamin-related protein Drp1 is required for mitochondrial division in mammalian cells. *Mol Biol Cell* **12**, 2245-2256 (2001). <https://doi.org/10.1091/mbc.12.8.2245>
- 314 Lee, J. E., Westrate, L. M., Wu, H., Page, C. & Voeltz, G. K. Multiple dynamin family members collaborate to drive mitochondrial division. *Nature* **540**, 139-143 (2016). <https://doi.org/10.1038/nature20555>
- 315 Kraus, F. & Ryan, M. T. The constriction and scission machineries involved in mitochondrial fission. *J Cell Sci* **130**, 2953-2960 (2017). <https://doi.org/10.1242/jcs.199562>
- 316 Yoon, Y., Krueger, E. W., Oswald, B. J. & McNiven, M. A. The mitochondrial protein hFis1 regulates mitochondrial fission in mammalian cells through an interaction with the dynamin-like protein DLP1. *Mol Cell Biol* **23**, 5409-5420 (2003). <https://doi.org/10.1128/mcb.23.15.5409-5420.2003>
- 317 Stojanovski, D., Koutsopoulos, O. S., Okamoto, K. & Ryan, M. T. Levels of human Fis1 at the mitochondrial outer membrane regulate mitochondrial morphology. *J Cell Sci* **117**, 1201-1210 (2004). <https://doi.org/10.1242/jcs.01058>
- 318 Yu, R., Jin, S. B., Lendahl, U., Nistér, M. & Zhao, J. Human Fis1 regulates mitochondrial dynamics through inhibition of the fusion machinery. *Embo j* **38** (2019). <https://doi.org/10.15252/emj.201899748>
- 319 Sandoval, H. *et al.* Essential role for Nix in autophagic maturation of erythroid cells. *Nature* **454**, 232-235 (2008). <https://doi.org/10.1038/nature07006>
- 320 Ashrafi, G. & Schwarz, T. L. The pathways of mitophagy for quality control and clearance of mitochondria. *Cell Death Differ* **20**, 31-42 (2013). <https://doi.org/10.1038/cdd.2012.81>
- 321 Wang, S. *et al.* The mitophagy pathway and its implications in human diseases. *Signal Transduction and Targeted Therapy* **8**, 304 (2023). <https://doi.org/10.1038/s41392-023-01503-7>
- 322 Gan, Z. Y. *et al.* Activation mechanism of PINK1. *Nature* **602**, 328-335 (2022). <https://doi.org/10.1038/s41586-021-04340-2>
- 323 Jin, S. M. *et al.* Mitochondrial membrane potential regulates PINK1 import and proteolytic destabilization by PARL. *J Cell Biol* **191**, 933-942 (2010). <https://doi.org/10.1083/jcb.201008084>

- 324 Narendra, D. P. *et al.* PINK1 is selectively stabilized on impaired mitochondria to activate Parkin. *PLoS Biol* **8**, e1000298 (2010). <https://doi.org/10.1371/journal.pbio.1000298>
- 325 Hoshino, A. *et al.* The ADP/ATP translocase drives mitophagy independent of nucleotide exchange. *Nature* **575**, 375-379 (2019). <https://doi.org/10.1038/s41586-019-1667-4>
- 326 Narendra, D., Tanaka, A., Suen, D. F. & Youle, R. J. Parkin is recruited selectively to impaired mitochondria and promotes their autophagy. *J Cell Biol* **183**, 795-803 (2008). <https://doi.org/10.1083/jcb.200809125>
- 327 Okatsu, K. *et al.* A dimeric PINK1-containing complex on depolarized mitochondria stimulates Parkin recruitment. *J Biol Chem* **288**, 36372-36384 (2013). <https://doi.org/10.1074/jbc.M113.509653>
- 328 Durcan, T. M. & Fon, E. A. The three 'P's of mitophagy: PARKIN, PINK1, and post-translational modifications. *Genes Dev* **29**, 989-999 (2015). <https://doi.org/10.1101/gad.262758.115>
- 329 Ziviani, E., Tao, R. N. & Whitworth, A. J. Drosophila parkin requires PINK1 for mitochondrial translocation and ubiquitinates mitofusin. *Proc Natl Acad Sci U S A* **107**, 5018-5023 (2010). <https://doi.org/10.1073/pnas.0913485107>
- 330 Glauser, L., Sonnay, S., Stafa, K. & Moore, D. J. Parkin promotes the ubiquitination and degradation of the mitochondrial fusion factor mitofusin 1. *J Neurochem* **118**, 636-645 (2011). <https://doi.org/10.1111/j.1471-4159.2011.07318.x>
- 331 Vara-Perez, M., Felipe-Abrio, B. & Agostinis, P. Mitophagy in Cancer: A Tale of Adaptation. *Cells* **8** (2019). <https://doi.org/10.3390/cells8050493>
- 332 Geisler, S. *et al.* PINK1/Parkin-mediated mitophagy is dependent on VDAC1 and p62/SQSTM1. *Nat Cell Biol* **12**, 119-131 (2010). <https://doi.org/10.1038/ncb2012>
- 333 Narendra, D., Kane, L. A., Hauser, D. N., Fearnley, I. M. & Youle, R. J. p62/SQSTM1 is required for Parkin-induced mitochondrial clustering but not mitophagy; VDAC1 is dispensable for both. *Autophagy* **6**, 1090-1106 (2010). <https://doi.org/10.4161/auto.6.8.13426>
- 334 Okatsu, K. *et al.* p62/SQSTM1 cooperates with Parkin for perinuclear clustering of depolarized mitochondria. *Genes Cells* **15**, 887-900 (2010). <https://doi.org/10.1111/j.1365-2443.2010.01426.x>
- 335 Wong, Y. C. & Holzbaur, E. L. Optineurin is an autophagy receptor for damaged mitochondria in parkin-mediated mitophagy that is disrupted by an ALS-linked mutation. *Proc Natl Acad Sci U S A* **111**, E4439-4448 (2014). <https://doi.org/10.1073/pnas.1405752111>
- 336 Novak, I. & Dikic, I. Autophagy receptors in developmental clearance of mitochondria. *Autophagy* **7**, 301-303 (2011). <https://doi.org/10.4161/auto.7.3.14509>
- 337 Zhu, Y. *et al.* Modulation of serines 17 and 24 in the LC3-interacting region of Bnip3 determines pro-survival mitophagy versus apoptosis. *J Biol Chem* **288**, 1099-1113 (2013). <https://doi.org/10.1074/jbc.M112.399345>
- 338 Rogov, V. V. *et al.* Phosphorylation of the mitochondrial autophagy receptor Nix enhances its interaction with LC3 proteins. *Scientific Reports* **7**, 1131 (2017). <https://doi.org/10.1038/s41598-017-01258-6>
- 339 Schwarten, M. *et al.* Nix directly binds to GABARAP: a possible crosstalk between apoptosis and autophagy. *Autophagy* **5**, 690-698 (2009). <https://doi.org/10.4161/auto.5.5.8494>
- 340 Novak, I. *et al.* Nix is a selective autophagy receptor for mitochondrial clearance. *EMBO Rep* **11**, 45-51 (2010). <https://doi.org/10.1038/embor.2009.256>

- 341 Hanna, R. A. *et al.* Microtubule-associated protein 1 light chain 3 (LC3) interacts with Bnip3 protein to selectively remove endoplasmic reticulum and mitochondria via autophagy. *J Biol Chem* **287**, 19094-19104 (2012). <https://doi.org/10.1074/jbc.M111.322933>
- 342 Marinković, M., Šprung, M. & Novak, I. Dimerization of mitophagy receptor BNIP3L/NIX is essential for recruitment of autophagic machinery. *Autophagy* **17**, 1232-1243 (2021). <https://doi.org/10.1080/15548627.2020.1755120>
- 343 Kanki, T., Wang, K., Cao, Y., Baba, M. & Klionsky, D. J. Atg32 is a mitochondrial protein that confers selectivity during mitophagy. *Dev Cell* **17**, 98-109 (2009). <https://doi.org/10.1016/j.devcel.2009.06.014>
- 344 Okamoto, K., Kondo-Okamoto, N. & Ohsumi, Y. Mitochondria-anchored receptor Atg32 mediates degradation of mitochondria via selective autophagy. *Dev Cell* **17**, 87-97 (2009). <https://doi.org/10.1016/j.devcel.2009.06.013>
- 345 Marinković, M. & Novak, I. A brief overview of BNIP3L/NIX receptor-mediated mitophagy. *FEBS Open Bio* **11**, 3230-3236 (2021). <https://doi.org/10.1002/2211-5463.13307>
- 346 Landes, T. *et al.* The BH3-only Bnip3 binds to the dynamin Opa1 to promote mitochondrial fragmentation and apoptosis by distinct mechanisms. *EMBO Rep* **11**, 459-465 (2010). <https://doi.org/10.1038/embor.2010.50>
- 347 Lee, Y., Lee, H. Y., Hanna, R. A. & Gustafsson Å, B. Mitochondrial autophagy by Bnip3 involves Drp1-mediated mitochondrial fission and recruitment of Parkin in cardiac myocytes. *Am J Physiol Heart Circ Physiol* **301**, H1924-1931 (2011). <https://doi.org/10.1152/ajpheart.00368.2011>
- 348 Zhang, T. *et al.* BNIP3 Protein Suppresses PINK1 Kinase Proteolytic Cleavage to Promote Mitophagy. *J Biol Chem* **291**, 21616-21629 (2016). <https://doi.org/10.1074/jbc.M116.733410>
- 349 Gao, F. *et al.* The mitochondrial protein BNIP3L is the substrate of PARK2 and mediates mitophagy in PINK1/PARK2 pathway. *Hum Mol Genet* **24**, 2528-2538 (2015). <https://doi.org/10.1093/hmg/ddv017>
- 350 Liu, L. *et al.* Mitochondrial outer-membrane protein FUNDC1 mediates hypoxia-induced mitophagy in mammalian cells. *Nature Cell Biology* **14**, 177-185 (2012). <https://doi.org/10.1038/ncb2422>
- 351 Chen, M. *et al.* Mitophagy receptor FUNDC1 regulates mitochondrial dynamics and mitophagy. *Autophagy* **12**, 689-702 (2016). <https://doi.org/10.1080/15548627.2016.1151580>
- 352 Zhang, J. *et al.* Mitochondrial clearance is regulated by Atg7-dependent and -independent mechanisms during reticulocyte maturation. *Blood* **114**, 157-164 (2009). <https://doi.org/10.1182/blood-2008-04-151639>
- 353 Rossi, D. J., Jamieson, C. H. & Weissman, I. L. Stems cells and the pathways to aging and cancer. *Cell* **132**, 681-696 (2008). <https://doi.org/10.1016/j.cell.2008.01.036>
- 354 Chen, C., Liu, Y., Liu, Y. & Zheng, P. mTOR regulation and therapeutic rejuvenation of aging hematopoietic stem cells. *Sci Signal* **2**, ra75 (2009). <https://doi.org/10.1126/scisignal.2000559>
- 355 Liu, F. *et al.* FIP200 is required for the cell-autonomous maintenance of fetal hematopoietic stem cells. *Blood* **116**, 4806-4814 (2010). <https://doi.org/10.1182/blood-2010-06-288589>
- 356 Mortensen, M. *et al.* The autophagy protein Atg7 is essential for hematopoietic stem cell maintenance. *J Exp Med* **208**, 455-467 (2011). <https://doi.org/10.1084/jem.20101145>

- 357 Watson, A. *et al.* Autophagy limits proliferation and glycolytic metabolism in acute myeloid leukemia. *Cell Death Discovery* **1**, 15008 (2015).  
<https://doi.org/10.1038/cddiscovery.2015.8>
- 358 Warr, M. R. *et al.* FOXO3A directs a protective autophagy program in haematopoietic stem cells. *Nature* **494**, 323-327 (2013).  
<https://doi.org/10.1038/nature11895>
- 359 Jin, G. *et al.* Atad3a suppresses Pink1-dependent mitophagy to maintain homeostasis of hematopoietic progenitor cells. *Nat Immunol* **19**, 29-40 (2018). <https://doi.org/10.1038/s41590-017-0002-1>
- 360 Ito, K. *et al.* Self-renewal of a purified Tie2+ hematopoietic stem cell population relies on mitochondrial clearance. *Science* **354**, 1156-1160 (2016). <https://doi.org/10.1126/science.aaf5530>
- 361 Rimmelé, P. *et al.* Mitochondrial metabolism in hematopoietic stem cells requires functional FOXO3. *EMBO Rep* **16**, 1164-1176 (2015).  
<https://doi.org/10.15252/embr.201439704>
- 362 Galluzzi, L. *et al.* Autophagy in malignant transformation and cancer progression. *Embo j* **34**, 856-880 (2015).  
<https://doi.org/10.15252/embr.201490784>
- 363 Bellodi, C. *et al.* Targeting autophagy potentiates tyrosine kinase inhibitor-induced cell death in Philadelphia chromosome-positive cells, including primary CML stem cells. *J Clin Invest* **119**, 1109-1123 (2009).  
<https://doi.org/10.1172/jci35660>
- 364 Karvela, M. *et al.* ATG7 regulates energy metabolism, differentiation and survival of Philadelphia-chromosome-positive cells. *Autophagy* **12**, 936-948 (2016). <https://doi.org/10.1080/15548627.2016.1162359>
- 365 Baquero, P. *et al.* Targeting quiescent leukemic stem cells using second generation autophagy inhibitors. *Leukemia* **33**, 981-994 (2019).  
<https://doi.org/10.1038/s41375-018-0252-4>
- 366 Horne, G. A. *et al.* A randomised phase II trial of hydroxychloroquine and imatinib versus imatinib alone for patients with chronic myeloid leukaemia in major cytogenetic response with residual disease. *Leukemia* **34**, 1775-1786 (2020). <https://doi.org/10.1038/s41375-019-0700-9>
- 367 Ianniciello, A. *et al.* ULK1 inhibition promotes oxidative stress-induced differentiation and sensitizes leukemic stem cells to targeted therapy. *Sci Transl Med* **13**, eabd5016 (2021).  
<https://doi.org/10.1126/scitranslmed.abd5016>
- 368 Folkerts, H. *et al.* Inhibition of autophagy as a treatment strategy for p53 wild-type acute myeloid leukemia. *Cell Death Dis* **8**, e2927 (2017).  
<https://doi.org/10.1038/cddis.2017.317>
- 369 Qiu, S. *et al.* Autophagy inhibition impairs leukemia stem cell function in FLT3-ITD AML but has antagonistic interactions with tyrosine kinase inhibition. *Leukemia* **36**, 2621-2633 (2022). <https://doi.org/10.1038/s41375-022-01719-6>
- 370 Pei, S. *et al.* AMPK/FIS1-Mediated Mitophagy Is Required for Self-Renewal of Human AML Stem Cells. *Cell Stem Cell* **23**, 86-100.e106 (2018).  
<https://doi.org/10.1016/j.stem.2018.05.021>
- 371 Koschmieder, S. *et al.* Inducible chronic phase of myeloid leukemia with expansion of hematopoietic stem cells in a transgenic model of BCR-ABL leukemogenesis. *Blood* **105**, 324-334 (2005). <https://doi.org/10.1182/blood-2003-12-4369>
- 372 Mizushima, N., Yamamoto, A., Matsui, M., Yoshimori, T. & Ohsumi, Y. In vivo analysis of autophagy in response to nutrient starvation using

- transgenic mice expressing a fluorescent autophagosome marker. *Mol Biol Cell* **15**, 1101-1111 (2004). <https://doi.org/10.1091/mbc.e03-09-0704>
- 373 Muzumdar, M. D., Tasic, B., Miyamichi, K., Li, L. & Luo, L. A global double-fluorescent Cre reporter mouse. *Genesis* **45**, 593-605 (2007). <https://doi.org/10.1002/dvg.20335>
- 374 Miller, P. H. *et al.* Analysis of parameters that affect human hematopoietic cell outputs in mutant c-kit-immunodeficient mice. *Exp Hematol* **48**, 41-49 (2017). <https://doi.org/10.1016/j.exphem.2016.12.012>
- 375 Jinek, M. *et al.* A programmable dual-RNA-guided DNA endonuclease in adaptive bacterial immunity. *Science* **337**, 816-821 (2012). <https://doi.org/10.1126/science.1225829>
- 376 Jiang, F. & Doudna, J. A. CRISPR-Cas9 Structures and Mechanisms. *Annu Rev Biophys* **46**, 505-529 (2017). <https://doi.org/10.1146/annurev-biophys-062215-010822>
- 377 Klionsky, D. J. *et al.* Guidelines for the use and interpretation of assays for monitoring autophagy (4th edition)(1). *Autophagy* **17**, 1-382 (2021). <https://doi.org/10.1080/15548627.2020.1797280>
- 378 Mazo, I. B., Quackenbush, E. J., Lowe, J. B. & von Andrian, U. H. Total body irradiation causes profound changes in endothelial traffic molecules for hematopoietic progenitor cell recruitment to bone marrow. *Blood* **99**, 4182-4191 (2002). <https://doi.org/10.1182/blood.v99.11.4182>
- 379 Cao, X. *et al.* Irradiation induces bone injury by damaging bone marrow microenvironment for stem cells. *Proc Natl Acad Sci U S A* **108**, 1609-1614 (2011). <https://doi.org/10.1073/pnas.1015350108>
- 380 Mazo, I. B., Massberg, S. & von Andrian, U. H. Hematopoietic stem and progenitor cell trafficking. *Trends Immunol* **32**, 493-503 (2011). <https://doi.org/10.1016/j.it.2011.06.011>
- 381 Czechowicz, A., Kraft, D., Weissman, I. L. & Bhattacharya, D. Efficient transplantation via antibody-based clearance of hematopoietic stem cell niches. *Science* **318**, 1296-1299 (2007). <https://doi.org/10.1126/science.1149726>
- 382 Chen, J. *et al.* Mobilization as a preparative regimen for hematopoietic stem cell transplantation. *Blood* **107**, 3764-3771 (2006). <https://doi.org/10.1182/blood-2005-09-3593>
- 383 Montecino-Rodriguez, E. & Dorshkind, K. Use of Busulfan to Condition Mice for Bone Marrow Transplantation. *STAR Protoc* **1**, 100159 (2020). <https://doi.org/10.1016/j.xpro.2020.100159>
- 384 Wilkinson, A. C. *et al.* Long-term ex vivo haematopoietic-stem-cell expansion allows nonconditioned transplantation. *Nature* **571**, 117-121 (2019). <https://doi.org/10.1038/s41586-019-1244-x>
- 385 Kusumbe, A. P., Ramasamy, S. K. & Adams, R. H. Coupling of angiogenesis and osteogenesis by a specific vessel subtype in bone. *Nature* **507**, 323-328 (2014). <https://doi.org/10.1038/nature13145>
- 386 Abbuehl, J. P., Tatarova, Z., Held, W. & Huelsken, J. Long-Term Engraftment of Primary Bone Marrow Stromal Cells Repairs Niche Damage and Improves Hematopoietic Stem Cell Transplantation. *Cell Stem Cell* **21**, 241-255.e246 (2017). <https://doi.org/10.1016/j.stem.2017.07.004>
- 387 Shimoto, M., Sugiyama, T. & Nagasawa, T. Numerous niches for hematopoietic stem cells remain empty during homeostasis. *Blood* **129**, 2124-2131 (2017). <https://doi.org/10.1182/blood-2016-09-740563>
- 388 Ito, M. *et al.* NOD/SCID/gamma(c)(null) mouse: an excellent recipient mouse model for engraftment of human cells. *Blood* **100**, 3175-3182 (2002). <https://doi.org/10.1182/blood-2001-12-0207>

- 389 Lozzio, B. B., Lozzi, C. B. & Machado, E. Human myelogenous (Ph+) leukemia cell line: transplantation into athymic mice. *J Natl Cancer Inst* **56**, 627-629 (1976). <https://doi.org/10.1093/jnci/56.3.627>
- 390 Schioppa, T. *et al.* Regulation of the chemokine receptor CXCR4 by hypoxia. *J Exp Med* **198**, 1391-1402 (2003). <https://doi.org/10.1084/jem.20030267>
- 391 Mohammadali, F., Abroun, S. & Atashi, A. Mild hypoxia and human bone marrow mesenchymal stem cells synergistically enhance expansion and homing capacity of human cord blood CD34+ stem cells. *Iran J Basic Med Sci* **21**, 709-716 (2018). <https://doi.org/10.22038/ijbms.2018.26820.6561>
- 392 Ceradini, D. J. *et al.* Progenitor cell trafficking is regulated by hypoxic gradients through HIF-1 induction of SDF-1. *Nat Med* **10**, 858-864 (2004). <https://doi.org/10.1038/nm1075>
- 393 Tanida, I. *et al.* Apg7p/Cvt2p: A novel protein-activating enzyme essential for autophagy. *Mol Biol Cell* **10**, 1367-1379 (1999). <https://doi.org/10.1091/mbc.10.5.1367>
- 394 Tanida, I., Tanida-Miyake, E., Ueno, T. & Kominami, E. The human homolog of *Saccharomyces cerevisiae* Apg7p is a Protein-activating enzyme for multiple substrates including human Apg12p, GATE-16, GABARAP, and MAP-LC3. *J Biol Chem* **276**, 1701-1706 (2001). <https://doi.org/10.1074/jbc.C000752200>
- 395 Di Noto, R. *et al.* JURL-MK1 (c-kit(high)/CD30-/CD40-) and JURL-MK2 (c-kit(low)/CD30+/CD40+) cell lines: 'two-sided' model for investigating leukemic megakaryocytopoiesis. *Leukemia* **11**, 1554-1564 (1997). <https://doi.org/10.1038/sj.leu.2400760>
- 396 Lozzio, C. B. & Lozzio, B. B. Human chronic myelogenous leukemia cell-line with positive Philadelphia chromosome. *Blood* **45**, 321-334 (1975).
- 397 Ratajczak, M. Z. *et al.* In vivo treatment of human leukemia in a scid mouse model with c-myc antisense oligodeoxynucleotides. *Proc Natl Acad Sci U S A* **89**, 11823-11827 (1992). <https://doi.org/10.1073/pnas.89.24.11823>
- 398 Gardner, L. B. *et al.* Hypoxia inhibits G1/S transition through regulation of p27 expression. *J Biol Chem* **276**, 7919-7926 (2001). <https://doi.org/10.1074/jbc.M010189200>
- 399 Ng, K. P. *et al.* Physiologic hypoxia promotes maintenance of CML stem cells despite effective BCR-ABL1 inhibition. *Blood* **123**, 3316-3326 (2014). <https://doi.org/10.1182/blood-2013-07-511907>
- 400 Allen, G. F., Toth, R., James, J. & Ganley, I. G. Loss of iron triggers PINK1/Parkin-independent mitophagy. *EMBO Rep* **14**, 1127-1135 (2013). <https://doi.org/10.1038/embor.2013.168>
- 401 McWilliams, T. G. *et al.* mito-QC illuminates mitophagy and mitochondrial architecture in vivo. *J Cell Biol* **214**, 333-345 (2016). <https://doi.org/10.1083/jcb.201603039>
- 402 Sowter, H. M., Ratcliffe, P. J., Watson, P., Greenberg, A. H. & Harris, A. L. HIF-1-dependent regulation of hypoxic induction of the cell death factors BNIP3 and NIX in human tumors. *Cancer Res* **61**, 6669-6673 (2001).
- 403 Bellot, G. *et al.* Hypoxia-induced autophagy is mediated through hypoxia-inducible factor induction of BNIP3 and BNIP3L via their BH3 domains. *Mol Cell Biol* **29**, 2570-2581 (2009). <https://doi.org/10.1128/mcb.00166-09>
- 404 Field, J. T. & Gordon, J. W. BNIP3 and Nix: Atypical regulators of cell fate. *Biochim Biophys Acta Mol Cell Res* **1869**, 119325 (2022). <https://doi.org/10.1016/j.bbamcr.2022.119325>
- 405 Mauvezin, C. & Neufeld, T. P. Bafilomycin A1 disrupts autophagic flux by inhibiting both V-ATPase-dependent acidification and Ca-P60A/SERCA-

- dependent autophagosome-lysosome fusion. *Autophagy* **11**, 1437-1438 (2015). <https://doi.org/10.1080/15548627.2015.1066957>
- 406 Sun, N. *et al.* A fluorescence-based imaging method to measure in vitro and in vivo mitophagy using mt-Keima. *Nat Protoc* **12**, 1576-1587 (2017). <https://doi.org/10.1038/nprot.2017.060>
- 407 Liu, Y. T. *et al.* Mt-Keima detects PINK1-PRKN mitophagy in vivo with greater sensitivity than mito-QC. *Autophagy*, 1-10 (2021). <https://doi.org/10.1080/15548627.2021.1896924>
- 408 Lassailly, F., Griessinger, E. & Bonnet, D. "Microenvironmental contaminations" induced by fluorescent lipophilic dyes used for noninvasive in vitro and in vivo cell tracking. *Blood* **115**, 5347-5354 (2010). <https://doi.org/10.1182/blood-2009-05-224030>
- 409 Kobayashi, H. *et al.* Environmental Optimization Enables Maintenance of Quiescent Hematopoietic Stem Cells Ex Vivo. *Cell Rep* **28**, 145-158.e149 (2019). <https://doi.org/10.1016/j.celrep.2019.06.008>
- 410 Kimura, S., Noda, T. & Yoshimori, T. Dissection of the autophagosome maturation process by a novel reporter protein, tandem fluorescent-tagged LC3. *Autophagy* **3**, 452-460 (2007). <https://doi.org/10.4161/auto.4451>
- 411 Kaizuka, T. *et al.* An Autophagic Flux Probe that Releases an Internal Control. *Mol Cell* **64**, 835-849 (2016). <https://doi.org/10.1016/j.molcel.2016.09.037>
- 412 Zhang, J. & Ney, P. A. Role of BNIP3 and NIX in cell death, autophagy, and mitophagy. *Cell Death Differ* **16**, 939-946 (2009). <https://doi.org/10.1038/cdd.2009.16>
- 413 Poole, L. P., Bock-Hughes, A., Berardi, D. E. & Macleod, K. F. ULK1 promotes mitophagy via phosphorylation and stabilization of BNIP3. *Sci Rep* **11**, 20526 (2021). <https://doi.org/10.1038/s41598-021-00170-4>
- 414 Wu, W. *et al.* ULK1 translocates to mitochondria and phosphorylates FUNDC1 to regulate mitophagy. *EMBO Rep* **15**, 566-575 (2014). <https://doi.org/10.1002/embr.201438501>